AD-A240 420

91 9 4 099

INTERFACIAL PHENOMENA IN COMPOSITES

AND MECHANICAL PROPERTIES

S. Suresh and A. Needleman

INTERFACIAL PHENOMENA IN COMPOSITES:

PROCESSING, CHARACTERIZATION AND MECHANICAL PROPERTIES

INTERFACIAL PHENOMENA IN COMPOSITES:

PROCESSING, CHARACTERIZATION AND MECHANICAL PROPERTIES

Proceedings of the Symposium on Interfacial Phenomena in Composites: Processing, Characterization and Mechanical Properties, Newport, RI, June 1–3, 1988

EDITORS: S. SURESH AND
A. NEEDLEMAN

Reprinted from the journal
Materials Science and Engineering
Vol. A107, Nos. 1–2

ELSEVIER APPLIED SCIENCE
LONDON and NEW YORK

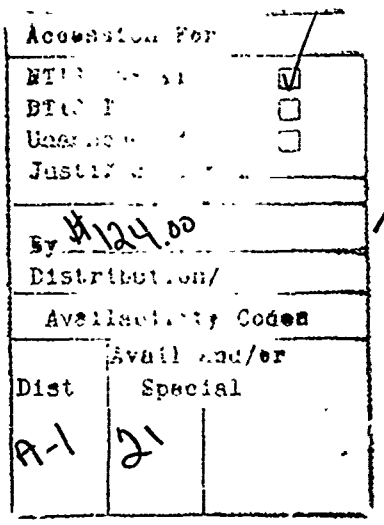

ELSEVIER APPLIED SCIENCE PUBLISHERS LTD
Crown House, Linton Road, Barking, Essex IG11 8JU, England

Sole Distributor in the USA and Canada
ELSEVIER SCIENCE PUBLISHING CO., INC.
52 Vanderbilt Avenue, New York, NY 10017, USA

British Library Cataloguing in Publication Data

Symposium on Interfacial Phenomena in Composites (1988: Newport, RI, U.S.A.)
Interfacial phenomena in composites: processing, characterization and mechanical properties
1. Composite materials. Interfaces
I. Title II. Suresh, S. III. Needleman, A.
IV. *Materials Science and Engineering*
620.1'18

ISBN 1-85166-987-6

Library of Congress Cataloging in Publication Data applied for

ISBN 1-85166-987-6

© ELSEVIER SEQUOIA S.A. 1989

The selection and presentation of material and the opinions expressed in this publication are the sole responsibility of the authors concerned

All rights reserved. No part of this publication may be reproduced, stored in a retrieval system, or transmitted in any form or by any means, electronic, mechanical, photocopying, recording, or otherwise, without the prior written permission of the copyright owner

Printed in The Netherlands by Krips Repro BV

Preface

With recent advances in processing technology, there is rapidly expanding research interest in composite materials with superior properties, hitherto unobtainable in monolithic systems, for a wide range of engineering applications. It is now generally recognized that the overall performance characteristics of composite materials are strongly influenced by the structure, chemistry and physical properties of the interfaces between the various components. Tailoring the interfaces to optimize the composite microstructure for superior performance will inevitably require a thorough fundamental understanding of the structure and properties of interfaces.

This volume contains the Proceedings of the Symposium on Interfacial Phenomena in Composites: Processing, Characterization and Mechanical Properties, held at Salve Regina College, Newport, Rhode Island, June 1–3, 1988. The symposium attracted over 100 participants representing academic institutions as well as government and industrial research laboratories.

The objective of the conference was to bring together scientists and engineers with different backgrounds and perspectives, but with a common interest in interfacial phenomena in composites. Sessions were held on the topics of physics of interfaces, characterization of interfaces, processing, and mechanics and micromechanics of interfacial deformation and failure. The conference format consisted of formal sessions restricted to the morning and early evening, with the afternoons and late evenings left free for informal discussion and relaxation.

Presentations were of two kinds: thirty formal presentations and fifteen shorter, more informal presentations. These proceedings contain the text of twenty-six of the formal presentations. It is a pleasure to thank all the speakers for making their presentations accessible to participants with a wide range of backgrounds. We are grateful to our colleagues in the Materials Research Group at Brown University for their advice in putting together the conference program and for their help and support in all phases of the organization of the conference. We are also thankful to them, and to all participants, for the cheerful encouragement that made organizing this conference such a pleasure. A special note of thanks is due to Ms. Pat Capece, secretary in the Division of Engineering at Brown University, for invaluable assistance before, during and after the conference. We are also grateful to Ms. Cheryl Hackett and other staff members at Salve Regina College for their enthusiastic help in organizing the symposium. As may be seen from the list of sponsors, support came from a variety of sources, and this support is much appreciated. The expeditious publication of this volume was made possible by the timely response of authors and referees in submitting and reviewing the papers.

While these proceedings document the formal part of the program, we hope that the interactions and collaborations that were initiated during the conference will serve as a less concrete, but not less substantial, confirmation of its success.

S. SURESH and A. NEEDLEMAN
Editors

Acknowledgments

The papers contained in this volume were peer-reviewed as per the normal editorial policies of the journal *Materials Science and Engineering*. Thanks are due to the following referees whose prompt reviews have enabled a timely publication of these proceedings.

P. F. Becher
J. Blume
T. Christman
K. Cho
J. Duffy
J. D. Embury
L. B. Freund
J. Gurland
J. W. Hutchinson
W. H. Kao
P. Lepetzky
M. Loretto
S. R. Nutt
M. Ortiz
C. F. Shih
V. Tvergaard
A. K. Vasudevan
J. H. Weiner
D. Wolf

Publication of this symposium was supported by National Aeronautics and Space Administration.

The editors are grateful to the following organizations for providing financial support for this symposium.

Brown University Materials Research Group on Plasticity and Fracture
Brown University Laboratory for Interface Science
Office of Naval Research
National Aeronautics and Space Administration
Aluminum Company of America

CONTENTS

Preface v

Acknowledgments vi

I PHYSICS AND MECHANICS OF INTERFACES

Role of the densest lattice planes in the stability of crystalline interfaces. a computer simulation study . . . 3
D. Wolf and S. Phillpot (Argonne, IL, U.S.A.)

Molecular dynamics study of a bicrystal at elevated temperatures 15
T. Nguyen and S. Yip (Cambridge, MA, U.S.A.)

Embrittlement of interfaces by solute segregation 23
J. R. Rice and J.-S. Wang (Cambridge, MA, U.S.A.)

Intrinsic toughness of interfaces 41
A. S. Argon, V. Gupta, H. S. Landis and J. A. Cornie (Cambridge, MA, U.S.A.)

On microstructural evolution and micromechanical modelling of deformation of a whisker-reinforced metal-matrix composite 49
T. Christman, A. Needleman, S. Nutt and S. Suresh (Providence, RI, U.S.A.)

The influence of hydrostatic pressure on the ductility of Al-SiC composites 63
A. K. Vasudevan, O. Richmond (Pittsburgh, PA, U.S.A.), F. Zok and J. D. Embury (Hamilton, Canada)

II PROCESSING

Microstructural aspects of aluminium silicon carbide particulate composites produced by a casting method 73
D. J. Lloyd, H. Lagace, A. McLeod and P. L. Morris (Kingston, Ont., Canada)

Development of nickel aluminide matrix composites 81
J.-M. Yang (Los Angeles, CA, U.S.A.), W. H. Kao (El Segundo, CA, U.S.A.) and C. T. Liu (Oak Ridge, TN, U.S.A.)

Processing and properties of metal matrix composites containing discontinuous reinforcement 93
M. G. McKimpson and T. E. Scott (Houghton, MI, U.S.A.)

Fabrication of intermetallic matrix composites 107
R. M. German and A. Bose (Troy, NY, U.S.A.)

Ceramic-ceramic composites with reaction bonded matrices 117
J. S. Haggerty (Cambridge, MA, U.S.A.)

Dispersion processing of creep resistant whisker-reinforced ceramic-matrix composites 127
J. R. Porter (Thousand Oaks, CA, U.S.A.)

III BIMATERIAL AND BICRYSTAL

Sandwich test specimens for measuring interface crack toughness 135
Z. Suo and J. W. Hutchinson (Cambridge, MA, U.S.A.)

Elastic-plastic analysis of a collinear array of cracks on a bimaterial interface 145
C. F. Shih and R. J. Asaro (Providence, RI, U.S.A.)

On the mechanics of adhesion testing of flexible films 159
N. Aravas (Philadelphia, PA, U.S.A.), K.-S. Kim (Urbana, IL, U.S.A.) and M. J. Loukis (Philadelphia, PA, U.S.A.)

Stress concentration along interfaces of elastic-plastic thin films 169
J. C. Lambropoulos and S.-M. Wan (Rochester, NY, U.S.A.)

On elasticity solutions for cracks on bimaterial and bicrystal interfaces 177
J. L. Bassani and J. Qu (Philadelphia, PA, U.S.A.)

CONTENTS *(continued)*

IV CHARACTERIZATION OF INTERFACES

Structure and chemistry of metal/ceramic interfaces 187
M. Rühle and A. G. Evans (Santa Barbara, CA, U.S.A.)

Characterization of internal interfaces in metals and alloys by high resolution electron microscopy 199
J. M. Penisson and G. Regheere (Grenoble, France)

High resolution interface analysis 207
R. W. Carpenter (Tempe, AR, U.S.A.)

Interfacial interactions in titanium-based metal matrix composites 217
D. G. Konitzer (Pittsburgh, PA, U.S.A.) and M. H. Loretto (Birmingham, U.K.)

V MICROMECHANICS

The mechanical performance of fiber-reinforced ceramic matrix composites 227
A. G. Evans (Santa Barbara, CA, U.S.A.)

Effects of matrix microstructure and particle distribution on fracture of an aluminum metal matrix composite 241
J. J. Lewandowski, C. Liu (Cleveland, OH, U.S.A.) and W. H. Hunt, Jr. (Pittsburgh, PA, U.S.A.)

Theoretical and experimental analysis of the toughening behavior of whisker reinforcement in ceramic matrix composites 257
P. F. Becher, C. H. Hsueh, P. Angelini and T. N. Tiegs (Oak Ridge, TN, U.S.A.)

Dynamic compressive fracture in fiber-reinforced ceramic matrix composites 261
J. Lankford (San Antonio, TX, U.S.A.)

Behavior of interface in alumina/glass composite 269
A. Maheshwari, K. K. Chawla (Socorro, NM, U.S.A.) and T. A. Michalske (Albuquerque, NM, U.S.A.)

AUTHOR INDEX 277

SUBJECT INDEX 279

I PHYSICS AND MECHANICS OF INTERFACES

Role of the Densest Lattice Planes in the Stability of Crystalline Interfaces: A Computer Simulation Study*

D. WOLF and S. PHILLPOT

Materials Science Division, Argonne National Laboratory, Argonne, IL 60439 (U.S.A.)

(Received June 1, 1988)

Abstract

The zero-temperature energies and equilibrium volume expansions of point-defect-free grain boundaries (GBs) on the two densest planes of f.c.c. copper, b.c.c. molybdenum and cubic diamond silicon have been determined, using an Embedded-Atom-Method potential for copper, a Finnis–Sinclair potential for molybdenum, and the Stillinger–Weber potential for silicon. It is found that in all three structures the energies of the GBs on the second-densest planes are about two to three times higher than of those on the densest planes. For the metals a strong correlation between GB energy and volume expansion at the GB is observed. Owing to its covalent nature of bonding such a correlation is not found for silicon. It is illustrated that atoms in very close contact (up to about 10% closer than the perfect-crystal nearest-neighbor distance) are mainly responsible for the very large anisotropy in the GB energy. Since the strong repulsive forces between such atoms should be active even in complex interface systems (such as metal–ceramic interfaces or strained-layer superlattices), we suggest that the energetics of even more general interfaces is strongly influenced by the Pauli principle.

1. Introduction

The relationship between the structure (geometrical and chemical) of crystalline interfaces and their physical properties has been a subject of considerable interest during the last decade. Although the anisotropy of mechanical properties (such as fracture and plasticity) is well understood for single crystals, the unraveling of structure–property correlations for composites and grain boundary materials is a much more complex endeavor. This complexity arises in part from the experimental difficulties in characterizing the chemical composition at interfaces surrounded by bulk material and in part from the difficulties in preparing well-oriented bicrystalline interfaces. Also, the fact that even a "simple" bicrystalline grain boundary (GB) requires the specification of *eight* degrees of freedom (d.o.f.) illustrates the bewildering variety of combinations which has to be considered in an attempt to unravel the complicated relationship between physical properties and geometrical structure even for bicrystalline materials.

Faced with the enormous complexity of the experimental task of unraveling structure–property correlations for interface materials, it appears that computer simulations can make an important contribution towards the understanding of such correlations and their underlying physical causes. In contrast to experiments, in a computer simulation study both the chemistry at the interface and the interface geometry can be controlled and systematically varied. The drawbacks of this approach are well known: a) the limitation to relatively small model systems containing, at most, thousands of atoms; b) problems of a systematic nature arising from insufficiently known interatomic interactions, and c) the limitation to coherent interfaces, *i.e.* those with a periodic arrangement of atoms parallel to the interface plane.

Within this framework grain boundaries are particularly suited for a systematic investigation of structure–property correlations for the following two reasons. First, interatomic potentials represent less of a problem for GBs than for dissimilar-material interfaces, particularly when—as in this study—segregation phenomena are ignored. Second, owing to the absence of a lattice-parameter mismatch at the interface, coher-

*Paper presented at the symposium on Interfacial Phenomena in Composites: Processing, Characterization, and Mechanical Properties, Newport, RI, June 1–3, 1988.

0921-5093/89/$3.50

© Elsevier Sequoia/Printed in The Netherlands

ent atom arrangements are obtained for many combinations of the degrees of freedom required to specify the GB. These combinations are readily identified by means of the coincident-site lattice CSL model [1, 2]. The main parameter in this model is the inverse density of CSL sites, Σ. Low values of Σ correspond to small unit cells of the three-dimensional coincident-site superlattice in common to the two halves of the bicrystal. In many cases this results in rather small *planar* unit-cell areas in the GB plane, and a subsequently small computational cell.

Given the suitability of GBs for structure-property studies, in this paper the correlation between the GB plane and the GB energy will be investigated. Considering that GBs are *planar* defects, this focus on the crystallographic plane on which the defect lies appears only natural, particularly since it is well established that properties such as fracture and plasticity are highly anisotropic. For example, in the absence of plasticity the criterion for crack growth along a GB "brittle fracture" involving the difference, $2\gamma - E^{GB}$, between the GB energy and the energies of the two free fracture surfaces plays a dominant role (see *e.g.* ref. 3). Recent TEM observations on faceting of GB planes and on the frequently observed preference of GBs for asymmetrical plane configurations [4, 5] also suggest an important role played by the GB plane. Thermal grooving experiments on 110 tilt GBs in aluminum suggest a strong anisotropy of the GB energy [6], and it has been pointed out that the deep cusps observed for the tilt angles for which the symmetrical plane is a 111 or 113 plane correspond to the densest and second densest planes for this misorientation [7]. Also, recent TEM work on the correlation between GB segregation and the GB geometry illustrates the "preponderant influence of the grain boundary plane on segregation" [8].

In the present article the zero-temperature energies of grain boundaries on the two densest planes in the f.c.c., b.c.c., and cubic diamond structures will be investigated together with the corresponding free surfaces. Although reconstruction and/or impurity segregation may be of major importance in "real" boundaries on which experiments are performed, we think of these point-defect-free interfaces as important model systems on which the structure-energy correlation can perhaps be understood prior to introducing additional parameters and therefore complications such as temperature, impurities, reconstruction, etc.

Volume-dependent interatomic potentials derived by means of the Embedded Atom Method (EAM) of Daw and Baskes for f.c.c. metals [9, 10] and of Finnis and Sinclair (F-S) for b.c.c. metals [11] are now available. Thus, in contrast to earlier calculations in which pair potentials were employed [12-14], the unidirectional volume expansion at GBs parallel to the GB plane normal can now be fully accounted for. Also, the covalent nature of bonding in the cubic diamond structure has been incorporated in the empirical bond-bending and bond-stretching three-body atomistic potential of Stillinger and Weber (S-W) for silicon [15]. This potential has recently been used with considerable success in studies of a variety of properties of the crystalline, liquid, and amorphous phases of silicon [15]. In particular the structure of both small clusters [16] and the reconstruction of the 100 surface [17] are well described. In each of these there are atoms in environments significantly different from the ideal crystal. By comparing our results for silicon with those for metals, we hope to gain some insight into how the nature of bonding (i.e. covalent *versus* metallic) influences the properties of GBs.

The article is organized as follows. In Section 2 the geometrical degrees of freedom of bicrystalline interfaces are briefly defined. A discussion of the interatomic potentials employed (Section 3) and the computational methods used (Section 4) follows. In Section 5 the energies and volume expansion of GBs on the two densest planes of f.c.c. copper are presented and discussed. A similar analysis for b.c.c. molybdenum and cubic diamond silicon follows in Sections 6 and 7, respectively. A discussion of ideal fracture energies is presented in Section 8, followed by our main conclusions in Section 9. Whereas all of the calculations presented in this paper are limited to zero temperature, we point out that the atomistic simulation of the high-temperature properties of grain boundaries is the subject of the following article in these proceedings [18].

2. Geometrical characterization of solid interfaces

As is well known, in addition to the crystal structure(s) and lattice parameter(s), eight geometrical parameters are needed to characterize a

bicrystalline interface. These eight degrees of freedom d.o.f. are usually subdivided into macroscopic and microscopic ones [19]. The latter are represented by the three d.o.f. associated with translations parallel and perpendicular to the interface plane, characterized by the translation vector T. By the very nature of T, only experiments which can measure translations on an atomic scale are capable of determining its three components.

The five macroscopic d.o.f. characterize the overall misorientation of the two halves of the bicrystal relative to each other as well as the interface plane. A simple—yet rather general—definition of these five parameters focuses on the crystallographic orientation of the interface plane with respect to the two crystals. If we define $\hat{n}_1$ and $\hat{n}_2$ as the interface-plane normals with respect to the principal coordinate systems of semi-crystals 1 and 2 (see Fig. 1), then the only remaining macroscopic d.o.f. is associated with a rotation, by the angle θ, about the interface-plane normal. All eight d.o.f. may be summarized as follows:

$$\hat{n}_1, \hat{n}_2, \theta, T \qquad (1)$$

The characterization method in (1) has several advantages over the usual definition of the five macroscopic d.o.f. for grain boundaries via the CSL misorientation. First, since the existence of a coincident-site superlattice is not required, (1) is applicable equally to coherent and incoherent interfaces as well as to grain boundaries and dissimilar-material interfaces. Second, symmetrical interfaces for which $\hat{n}_1 = \hat{n}_2$ are readily apparent. Finally, the tilt and twist components of a general GB are readily identified, the tilt axis and angle follow from the vector product of $\hat{n}_1$ and $\hat{n}_2$, whereas the twist component is given by the twist angle θ [20].

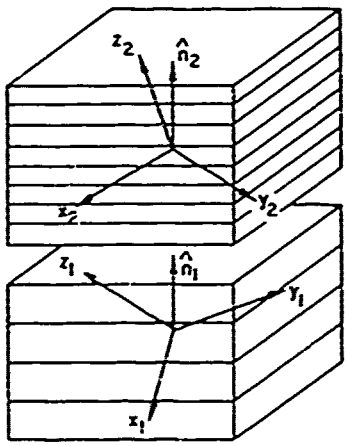

Fig. 1. GB plane orientations $\hat{n}_1$ and $\hat{n}_2$ in the principal coordinate systems associated with the two halves of the bicrystal.

Later in this paper twist boundaries on the densest planes of three cubic crystal structures will be investigated. Being symmetrical, these GBs are therefore characterized by three macroscopic d.o.f., two associated with the GB plane orientation, $\hat{n}_1 = \hat{n}_2$, and the twist angle. The twist angles together with the corresponding values of Σ for GBs on the {111}, {100}, and {110} planes of cubic crystals are listed in Tables 1–3. We point out that the particular rotation angles for which a certain value of Σ is obtained are entirely independent of the particular cubic crystal structure considered. Within the CSL model, therefore, no differences exist between GBs in different cubic structures. This fact is often misinterpreted such

TABLE 1 θ Σ combinations for {111} twist boundaries in cubic crystals

θ	Σ
7.34	183
9.43	111
13.17	57
15.18	43
16.43	147
17.90	31
21.79	21
27.80	13
32.20	39
38.21	7
42.10	93
43.57	49
44.82	129
46.83	19
50.57	37
52.66	61
60.00	3

TABLE 2 θ Σ combinations for {100} twist boundaries in cubic crystals

θ	Σ
10.34	61
12.68	41
14.28	65
15.26	25
16.02	97
22.62	13
28.07	17
30.51	85
36.87	53
43.60	5
45.23	113
53.13	29

TABLE 3 θ-Σ combinations for (110) twist boundaries in cubic crystals

θ	Σ
13.44	51a
20.05	33a
22.84	51b
26.53	19
31.59	27
38.94	9
44.00	57a
45.99	59
50.48	11
55.88	41
58.99	33b
70.53	3
80.63	43
82.94	57b
86.63	17

as to predict similar *physical* properties of GBs in different cubic crystal structures. Being entirely crystallographic in nature, however, this simple geometrical model makes no attempts, of course, to predict any physical properties of grain boundaries. Indeed, as demonstrated later in this paper, the energies of GBs in different cubic structures depend very strongly on the GB structure, in spite of their identical CSL characterization.

3. Interatomic potentials

In contrast to central-force potentials in which the potential energy arises from pair interactions only, in the Embedded Atom Method the total energy of the system also includes many-body contributions from a volume-dependent term. Starting from density functional theory, Daw and Baskes showed that under certain simplifying assumptions (see below) the total energy can be written as a sum of bonding and repulsive terms as follows [9, 10]:

$$V=\sum_i F_i(\rho_i^{\mathrm{T}})+\sum_i\sum_{j>i}\phi_{ij}(r_{ij}) \qquad (2)$$

The first term represents the embedding energy, $F_i(\rho_i^{\mathrm{T}})$, contributed by every atom i as it is embedded in the electron gas. Attractive in nature, $F_i(\rho_i^{\mathrm{T}})$ depends on the type of atom and on the total electron density, ρ_i^{T}, at its site. Assuming (a) centrally symmetric electron densities and approximating (b) the actual (self-consistent) electron densities in the expression for the total energy by superposing *atomic* electron densities ρ_i^{T} may be written as follows:

$$\rho_i^{\mathrm{T}}=\sum_{j\neq i}\rho_j^{\mathrm{a}}(r_{ij}) \qquad (3)$$

where $\rho_j^{\mathrm{a}}(r_{ij})$ is the atomic electron density of atom j at the distance r_{ij} (i.e. at the site of atom i). The second contribution in eqn. (2) represents the short-range repulsion between the atoms which is assumed (c) to be of a central-force type.

Within the framework of the three assumptions (a)–(c) stated above, the evaluation of the total energy of a system of particles is a straightforward matter for a given set of numerical tables for $\phi_{ij}(r)$, $\rho_j^{\mathrm{a}}(r)$, and $F_i(\rho_i^{\mathrm{T}})$. The computation is more CPU time intensive, however, than for a central-force potential of the same cut-off radius (typically by a factor of 2 in our codes).

Based on simple band-structure considerations, Finnis and Sinclair [11] have presented an empirical interatomic force description for metals which also uses eqn. (2). Although the interpretations of eqn. (2) differ slightly, the EAM and Finnis–Sinclair (F–S) potentials are essentially based on the same level of description of metallic bonding. In contrast to the EAM method, however, in the F–S approach the embedding functions are determined analytically from the relationship

$$F_i(\rho_i^{\mathrm{T}})=-A\rho_i^{\mathrm{T}} \qquad (4)$$

where A is a constant obtained from a fit to perfect-crystal properties. Similarly, ρ_j^{a} and ϕ_{ij} are written as analytical functions of the distance between atoms whereas in EAM potentials $F_i(\rho_i^{\mathrm{T}})$, ρ_j^{a}, and ϕ_{ij} are available numerically only as obtained from a complicated empirical fitting procedure which is not as transparent as in the F–S method. In the calculations described below, an EAM potential for copper appropriate for Cu/Ni alloys and the F–S potential for molybdenum will be employed. The latter will be used in the form proposed recently by Ackland and Thetford [21] in which the short-range repulsion has been enhanced by addition of a Born–Mayer term.

Finally, the empirical bond-bending and bond-stretching potential of Stillinger and Weber [15] (S–W) is employed in our simulations of silicon GBs. This potential consists of a two-body (central-force) and a three-body part. The first increases strongly at short distances, has a minimum at the nearest-neighbor distance, and goes smoothly to zero at less than the second-nearest-neighbor distance. The three-body (bond-bending) part of the potential is zero for tetrahedral bond angles. In the ideal crystal, therefore, the two-body potential couples only

nearest neighbors whereas the three-body part couples second-nearest neighbors through its angular dependence.

The validity of the S-W potential for GB simulations has been tested recently [22] in a comparison of the relaxed structure of the (221) symmetrical tilt GB with that obtained from electronic-structure calculations of Thomson and Chadi [23] and DiVincenzo *et al.* [24]. In agreement with intuitive arguments of Hornstra [25] and the electronic-structure calculations [23, 24] it was found that the glide-plane configuration has significantly lower energy than the mirror-plane translational configuration. Although the absolute values of the GB energies obtained do not agree too well with the electronic-structure results, the agreement in the choice of the optimum translational configuration is encouraging. In addition, as already pointed out in the Introduction, the S-W potential has been employed with considerable success on the simulation of a variety of physical properties of the crystalline, liquid, and amorphous phases of silicon [15, 16].

4. Computational procedure

In contrast to our earlier work on metals using pair potentials [7, 12-14], in all the studies presented here the volume expansion at the GB was fully accounted for. By its very nature this expansion is one-dimensional (parallel to the GB plane normal) since, in the GB plane, the unit-cell dimensions are fixed, *i.e.* they are determined by the surrounding bulk regions far away from the interface. We distinguish a three-dimensional expansion, ΔV, and a one-dimensional quantity which we shall call the free volume of the GB, δV. The two are related by the unit-cell area of the GB:

$$\Delta V = \delta V A \tag{5}$$

δV is hence a volume expansion per unit area. Throughout the rest of this paper δV will be expressed in units of the lattice parameter a_0.

One way to determine δV is illustrated in Fig. 2 for the $\Sigma 5$ (100) and $\Sigma 7$ (111) boundaries in copper. In these calculations the positions of the rigid blocks surrounding the GB [26] were fixed at a constant value of δV, and a constant-volume relaxation was performed. The iterative energy minimization procedure ("lattice statics") employed to determine the relaxed GB structure was described in detail in ref. 12. Similar to

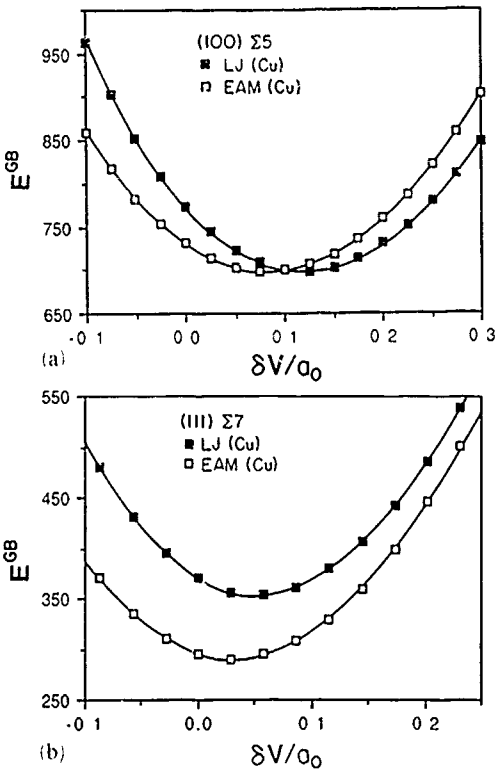

Fig. 2. GB energy (in erg cm^{-2}) vs. δV (in lattice parameter units) for the (a) $\Sigma 5$ (100) and (b) $\Sigma 7$ (111) boundary for both the Cu EAM, and a Lennard-Jones potential. Parameters for the latter are given in ref. 28.

earlier calculations for ionic bicrystals [26, 27], the GB energy shows a minimum at the equilibrium value of δV. For both GBs this value is smaller for the EAM potential than for a Lennard-Jones potential used for the purpose of comparison [28, 29]. If δV is increased well beyond the range shown in these figures, E^{GB} converges towards twice the energy, γ, of the corresponding free surface. This was previously illustrated in detail for ionic crystals (in refs. 26 and 27).

Figures 2(a) and (b) also demonstrate the effect of the restriction to $\delta V = 0$ [12-14] on the GB energy obtained. Lifting this restriction leads to a substantial decrease in the GB energy (for example, from about 965 erg cm^{-2} to about 700 erg cm^{-2} for the $\Sigma 5$ boundary with the EAM potential for copper).

This procedure of determining the optimum δV via constant-volume relaxations is rather time-consuming. By using the pressure exerted in the z direction on the rigid blocks by the atoms in the GB region, a constant-pressure simulation can be performed which yields the free volume in

a single simulation. Also, by computing the forces which the two parts of the bicrystal exert on each other, the two halves are able to translate relative to each other parallel to the GB plane. This so-called block-relaxation procedure, fully applied below, was described in detail in refs. 26 and 29.

5. (111) and (100) twist boundaries in Cu

5.1. Results

The energies and free volumes of grain boundaries on the two densest planes of copper, obtained in the manner described above and in ref. 29, are shown in Fig. 3. The Σ–θ combinations for these boundaries are listed in Tables 1 and 2. Owing to the fourfold rotation axis in the planar unit cell of the ideal crystal on the (100) plane, the results for the (100) boundaries are symmetrical with respect to 45°. Similarly, due to the threefold rotation axis on the (111) plane, the results for the (111) boundaries are symmetrical with respect to 60°. Several features in Figs. 3(a) and (b) are particularly interesting:

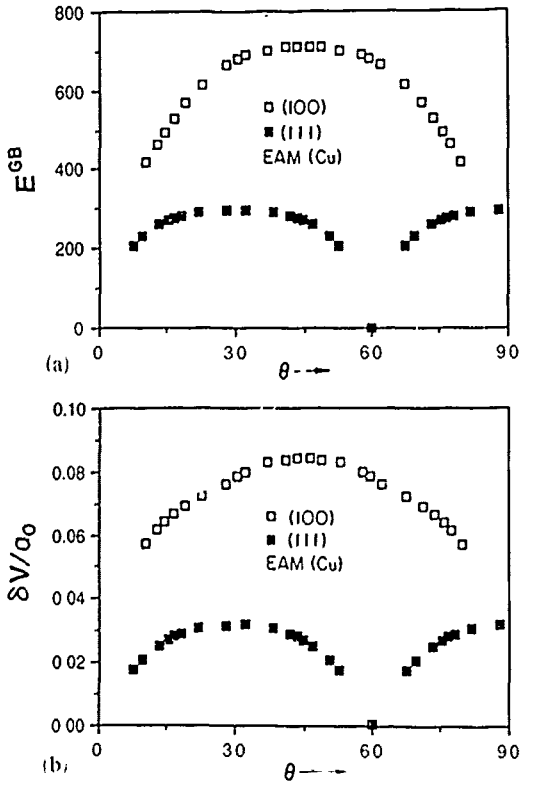

Fig. 3. (a) GB energy (in erg cm^{-2}) vs misfit angle for the (100) and (111) twist boundaries in Cu(EAM) listed in Tables 1 and 2. (b) Volume expansion per unit area for the boundaries in the top half.

(a) The $E^{GB}(\theta)$ and $\delta V(\theta)$ curves are remarkably smooth and of similar shape.

(b) Following the steep increase of E^{GB} and δV for low-angle boundaries [30], both quantities level off for larger angles. Since the dislocation cores overlap completely in this region, the GB is thought to be "saturated" with elastic stress energy. An increase in the angle, therefore, produces no further increase in E^{GB} and δV. Owing to the failure of the Read–Shockley model [30] in this plateau region, we consider these GBs to display behavior "typical" of high-angle grain boundaries.

(c) The energies and free volumes of GBs on the (111) plane are significantly lower (typically by a factor of two) than on the (100) plane.

(d) The (111) boundaries show a deep cusp for the (111) twin orientation ($\theta = 60°$). The energy of that interface is computed to be about 2 erg cm^{-2} while its volume expansion is negligible.

Finally in this section a Read–Shockley analysis of the above results for E^{GB} and δV is performed. The GB energy is an analytical function of θ according to the Read–Shockley dislocation model for *low-angle* boundaries [30]. For twist boundaries,

$$\frac{E^{GB}}{\theta} = \frac{E_c}{b} - \frac{Gb}{2\pi} \ln \theta \tag{6}$$

where b is the Burgers vector and E_c the core energy of the screw dislocations which form a network, thus accommodating the mismatch between the two crystals; G is the shear modulus. We assume that a similar relationship applies to δV:

$$\frac{\delta V}{\theta} = \delta V_c - \delta V_s \ln \theta \tag{7}$$

where δV_c is some effective core volume whereas δV_s may be thought of as arising from a volume change due to the strain field. The parameters of a least-squares fit of eqns. (6) and (7) for the boundaries in Figs. 3(a) and (b) in the low-angle regime ($\theta < 20°$) are listed in Table 4.

5.2. Discussion

The smoothness of the $E^{GB}(\theta)$ curves in Fig. 3(a) is similar to our results from earlier constant-volume calculations for f.c.c. metals [7, 12–14]. Since these calculations were first presented, the general shape of such a curve was investigated

TABLE 4 Values of E_c'/b and $Gb/2\pi$ (in erg cm^{-2}), and δV_c and δV_s (in units of the lattice parameter) obtained from the fit of eqns. (6) and (7) to the low-angle portions ($\ln \leqslant -1.0$) of the curves in Figs. 3, 6 and 8 for copper, molybdenum and silicon, respectively

		E_c'/b	$Gb/2\pi$	δV_c	δV_s
(111)	Cu(EAM)	−21.1	788.9	0.0378	0.0487
(100)	Cu(EAM)	637.4	970.6	−0.0096	0.1791
(110)	Mo(F-S)	251.1	2397.6	0.0140	0.0906
(100)	Mo(F-S)	1105.4	4435.6	0.0071	0.2464
(111)	Si(S-W)	−1016.2	2615.5	0.0048	−0.1174
(110)	Si(S-W)	811.3	2985.1	0.0851	0.2148

experimentally for (100) twist boundaries in gold by Chan and Balluffi [31]. Their "rotating crystallite" experiments demonstrated that—with the exception of a shallow cusp near the Σ5 orientation—the $E^{GB}(\theta)$ curve is, indeed, rather smooth and that it levels off for angles above the Σ5 orientation. Although effects arising from restructuring and/or impurity segregation have not been considered in the calculations, we consider the qualitative agreement with these experiments rather gratifying, particularly in view of the fact that the general shape of such $E^{GB}(\theta)$ curves has been predicted well prior to the experiment [7, 12–14, 26, 27].

In our earlier comparison of the energies of (111) and (100) twist boundaries in f.c.c. metals [13] seven different central-force potentials were employed with essentially the same result. Under the constant-volume constraint previously mentioned, all potentials yield roughly 2–3 times higher energies for the (100) boundaries than for ones on the (111) plane. Although by relaxing this constraint all GB energies were found to decrease substantially (see Figs. 2(a) and (b)), the ratio of the energies on the different planes is still of the same magnitude. This strongly suggests an important role played by the GB plane in determining the energy of the pure, point-defect-free GBs considered here. The interpretation given for the observed large energy differences is essentially based on the Pauli principle: Although, owing to the volume expansion at the GB, the density in the GB region has decreased and, hence, the average distance between atoms has increased, some atoms in a highly defected environment remain pushed more closely together than the crystalline nearest-neighbor distance. It appears that in any GB unit cell there are regions of very poor match across the interface which cannot be sufficiently relaxed even when the volume expands. This is demonstrated by the

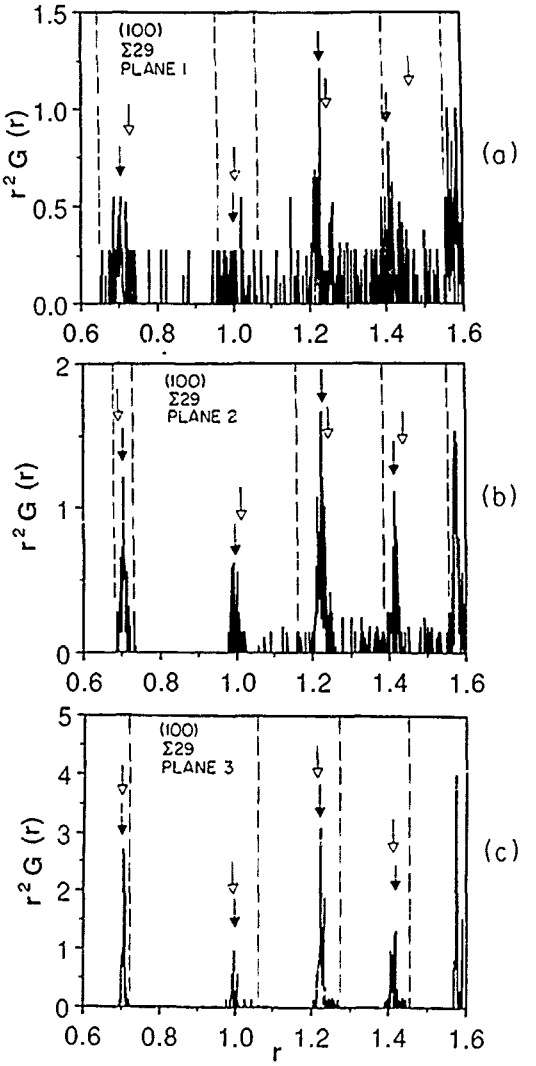

Fig 4. Radial distribution functions for the three planes nearest to the Σ29 (100) twist boundary. Full arrows indicate the corresponding perfect-crystal peak positions; open arrows show the average value of r in a given shell. The widths of these shells are indicated by the dashed lines. Whereas the atoms in the plane nearest to the interface [Fig. 5(a)] are very strongly affected by the presence of the interface, the atoms in the third-nearest plane [Fig. 5(c)] are found in an almost perfect-crystal environment.

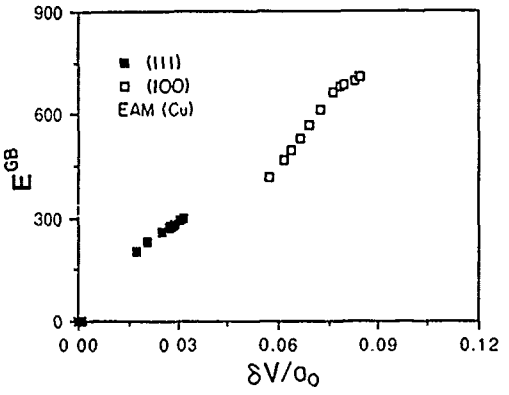

Fig. 5. GB energy *vs.* equilibrium free volume for the Cu boundaries in Fig. 3

radial distribution function, $r^2G(r)$, in Fig. 4 for the Σ29 (100) boundary. Figures 4(a)–(c) illustrate the rapid decrease of the structural disorder as the atoms become more perfectly coordinated with increasing distance from the interface. They also illustrate that, although the mean diameter of each shell has increased (due to the volume expansion), a significant number of atoms are at distances smaller than the corresponding ideal-crystal nearest-neighbor, second-nearest-neighbor distances, etc. (tallest peaks in these figures). A closer analysis shows that a larger number of atoms have been pushed together to distances below that for nearest neighbors in the (100) boundaries than in the (111) boundaries. Upon twisting (111) planes (with interplanar spacing $d(111)=0.577a_0$) less structural disorder is thus created than by twisting (100) planes (with $d(100)=0.5a_0$). Based upon the sharp increase of all interatomic interactions potentials for distances shorter than that for nearest neighbors (the Pauli principle!), the densest lattice planes (*i.e.* those with the largest interplanar lattice spacing) show less structural disorder than the less dense planes (*i.e.* those with smaller interplanar spacings). As a consequence, the GB energy increases dramatically with decreasing interplanar spacing (*i.e.* decreasing planar mass density).

Figure 5 shows a remarkable correlation between the volume expansion at a GB and its energy. (Notice, however, that the deviations from a straight line are well outside the scatter of our results.) This correlation is even more remarkable if we consider that the atomic structures and unit-cell dimensions are different for all the GBs considered. Although the atomic structure obviously controls the volume expansion, once the value of δV is known, according to Fig. 5, so is the energy. Almost 30 years ago Seeger and Schottky [32] presented a very simple model for the energy and electrical resistivity of high-angle GBs in metals in which δV is the key parameter. Two interesting aspects of their results are (a) the fact that the atomic structure of the GB does not enter at all except via the parameter δV and (b) the electrical resistivity is also controlled by δV.

We conclude this section by pointing out that in a recent rather detailed investigation of the role of the interatomic potential on the predicted GB energies, a Lennard-Jones potential for copper gave qualitatively the same results as those in Figs. 3 and 5 obtained for an EAM potential [29]. From this it was concluded that the local-volume dependence of interatomic potentials (incorporated only in the EAM potential) must not be a very important phenomenon in the energetics of metal grain boundaries. As pointed out above, the energetics of GBs appear to be dominated by the short-range repulsion between atoms in poor match across the interface. However, since in EAM potentials the short-range repulsion is assumed to be of a central-force nature (see eqn. (2)), this agreement of the qualitative generic properties of GBs obtained for the two types of potential is not very surprising.

6. (110) and (100) twist boundaries in molybdenum

If, as argued in the preceding section, the energy of high-angle twist GBs is indeed governed by the interplanar spacing of the lattice planes parallel to the GB plane, then one would expect an entirely different selection of low-energy GB planes in the b.c.c. lattice than in the f.c.c. lattice. The two densest planes in the b.c.c. structure are the (110) and (100) planes, with $d(110)=0.70^{7}a_0$ and $d(100)=0.50a_0$. The results obtained for twist boundaries on these planes in molybdenum are summarized in Figs. 6 and 7. Owing to the twofold rotation axis in the planar unit cell of the ideal crystal on the (110) plane, the results for the (110) boundaries are symmetrical with respect to 90°. The symmetry of the (100) planes with respect to $\theta=45°$ was already discussed above.

The qualitative features in Figs. 6(a) and (b) are rather similar to those in Figs. 3(a) and (b). The

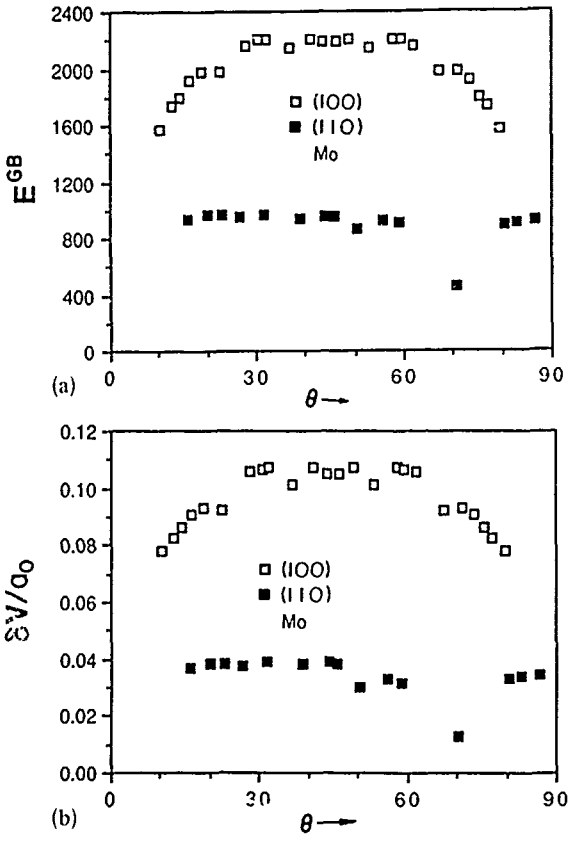

Fig. 6. (a) GB energy (in erg cm $^{-2}$) vs. misfit angle for (100) and (110) twist boundaries in molybdenum determined by means of a Finnis–Sinclair potential (see also Tables 1 and 3). (b) Volume expansion per unit area for the boundaries in the top half.

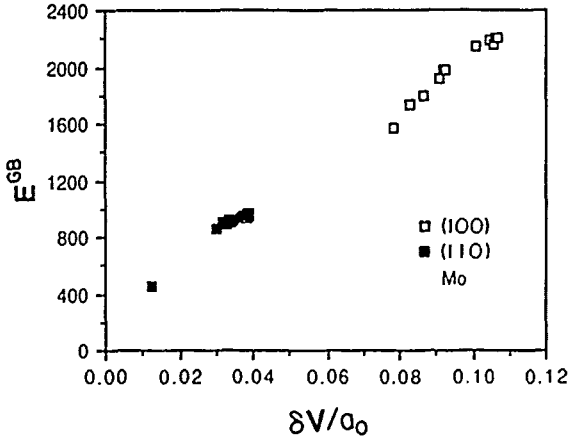

Fig. 7. GB energy vs. equilibrium free volume for the molybdenum boundaries in Fig. 6.

energies and free volumes of the boundaries on the densest plane are significantly lower than those on the second-densest plane. A deep cusp is observed for the Σ3 boundary on the (110) plane ($\theta = 70.53°$; see Table 3). The reason for the appearance of this cusp is similar to the reason for the existence of a deep cusp for the Σ3 (111) ($\theta = 60°$) twin boundary in Figs. 3(a) and (b). Both of these GBs have the smallest planar unit-cell area of any GB on the corresponding plane. Whereas for the Σ3 (111) boundary this unit-cell area is identical to the area of the perfect crystal on the (111) plane, the area of the Σ3 (110) boundary is three times as large as the corresponding perfect-crystal unit-cell area. As pointed out earlier [7], the sensitivity of the GB energy to translations parallel to the GB plane is greater for smaller planar unit cells. In the extreme case only one atom per lattice plane is found in the unit cell. An optimum translational configuration can then be found in which *all* atoms in the two opposing planes at the interface are simultaneously in their minimum energy state. Such is the case for all symmetrical tilt GBs and, in particular, for the Σ3 (111) GB. With three atoms per plane in the planar unit cell, the Σ3 (110) GB is not as sensitive to translation as if it accommodated only one atom per plane. However, its sensitivity to translation is still much greater than that of the Σ9 and Σ11 GBs on the (110) plane for which small cusps are seen in the $E^{GB}(\theta)$ and $\delta V(\theta)$ curves in Figs. 6(a) and (b) (for $\theta = 38.94°$ and $\theta = 50.48°$, respectively).

As for f.c.c. Cu, the $E^{GB}(\theta)$ and $\delta V(\theta)$ curves for b.c.c. molybdenum show remarkably similar shapes. Again, from Fig. 7 it appears that for a given free volume the GB energy is determined. Whether or not this is a general feature of all GBs in metals requires calculation for GBs on less dense planes, including symmetrical and asymmetrical tilt GBs.

Finally, a Read–Shockley analysis was performed for the low-angle portions of the curves in Figs. 6(a) and (b). The parameters obtained from the fit of eqns. (6) and (7) to these $E^{GB}(\theta)$ and $\delta V(\theta)$ portions of the curves have been included in Table 4.

We conclude by pointing out that in a recent, more complete investigation of GBs in b.c.c. metals [29] the results obtained for the molybdenum potential of Finnis and Sinclair were compared with those obtained for Johnson's well-known central-force potential for α-Fe [33]. As in a similar comparison between central force and EAM potentials for f.c.c. metals [29] the qualitative features of the $E^{GB}(\theta)$, $\delta V(\theta)$, and $E^{GB}(\delta V)$ curves were found to be the same for the two types of potential. This again indicates that the

basic generic properties of GBs in metals are governed by the short-range part of the interatomic potential employed in simulations.

7. (111) and (110) twist boundaries in silicon

The investigation of grain boundaries in silicon, with its covalent bonding, provides an opportunity to study whether and how the criteria for low GB energy established above for metals depend on the nature of atomic bonding. As already mentioned, the bond-bending (three-body) part of the Stillinger–Weber (S–W) potential is responsible for the tetrahedral coordination obtained for silicon; without this part the lattice would collapse into a close-packed structure. The bond-stretching (two-body) part, by contrast, is very similar in nature to the short-range repulsive contributions in EAM and F–S potentials. If the energetics of GBs are indeed governed by the atoms in very close contact, one would expect qualitative similarities between metals and covalent systems, particularly with respect to the effect of interplanar lattice spacing on the GB energy.

As is well apparent from the silicon structure (which, for our purposes, is best looked upon as an f.c.c. lattice with a basis of two atoms, with the basis vectors pointing in the ⟨111⟩ directions), the (111) planes form bilayers of separation $d(111)=0.433a_0$ and $0.144a_0$, respectively. The larger of these is a nearest-neighbor distance, since each of the four tetrahedral bonds points in a ⟨111⟩ direction. In our investigation the GBs were chosen to lie between the more widely spaced planes. The second largest interplanar spacing in the cubic diamond structure, then, is that of (110) planes, with $d(110)=0.354a_0$. Our results obtained for GBs on these two most widely spaced lattice planes are summarized in Fig. 8.

Figure 8(a) shows qualitatively the same features as our results for metals: GBs on the more widely spaced (111) planes show significantly lower energies than GBs on the (110) planes. The difference of approximately 22% in interplanar spacings translates into an energy difference of roughly a factor of two. Also, as for metals, energy cusps are observed whenever a particularly small planar unit-cell area is approached. This is the case for the Σ3 (111) ($\theta=60°$) boundary (see also Fig. 3(a)) and for the Σ3 (110) ($\theta=70.53°$) boundary (see also Fig. 6(a)). As in the metals, the difference between these energies

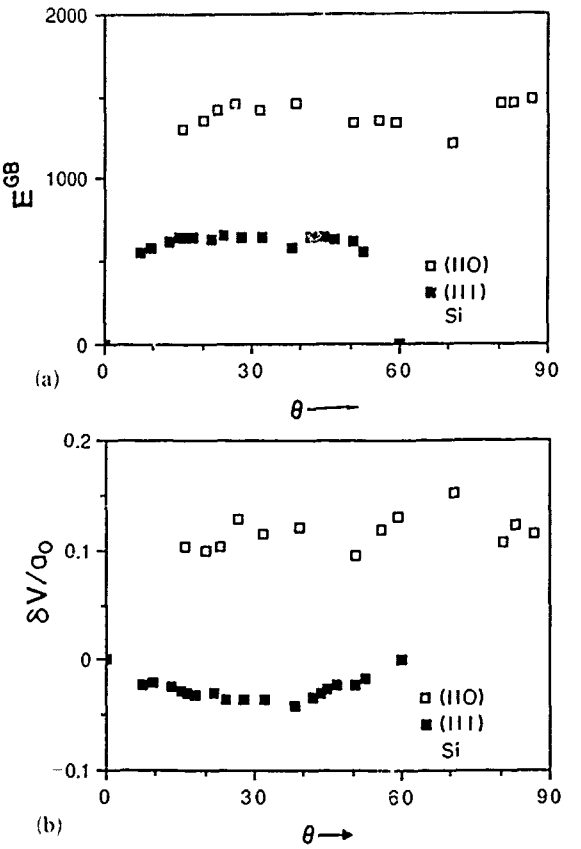

Fig. 8. (a) GB energy (in erg cm^{-2}) vs. misorientation angle for (111) and (110) twist boundaries in silicon determined by means of the Stillinger–Weber potential. (b) Volume expansion per unit area for the boundaries in the top half.

is a result of the differing degrees of disorder in the GBs on the two planes. In addition to radial distribution functions similar to Fig. 4, however, angular distribution functions have to be considered also. A detailed analysis of both types of distribution function was presented in ref. 22 for GBs on both sets of planes.

As for the (110) twist boundaries in molybdenum, the values of δV for the (110) twist boundaries in silicon are approximately constant (*i.e.* independent of θ), although the scatter is larger than for metals (see Fig. 8(b)). A particularly interesting feature in Fig. 8(b) is the fact that for the (111) twist boundaries all free volumes are *negative*, *i.e.* the GBs actually *contract*. At first sight this result appears paradoxical because the perfect stacking has been destroyed at the GB, in both a hard- and a soft-sphere material one would expect a subsequent expansion. The explanation for this phenomenon is closely connected with the covalent (*i.e.* directional) bonding of sili-

con: the bonds in the diamond structure point in the ⟨111⟩ directions. Hence, in a (111) free surface all bonds cut by creating this surface point in the direction of the surface normal. Therefore, when twisting two (111) planes relative to one another all bond lengths are stretched. Upon relaxation, the atoms attempt to recover their perfect-crystal bond lengths by contracting—with the net result of a contraction at the GBs. The strong correlation between GB energy and volume expansion does therefore not exist when the directionality of the bonding becomes an important consideration.

Finally, the parameters obtained from a fit of the Read–Shockley expressions (6) and (7) to the low-angle portions of the curves in Figs. 8(a) and (b) are listed in Table 4. Although the scatter of points is larger than for metals, overall the Read–Shockley expressions were satisfied rather well for low-angle boundaries.

8. Fracture energies

For the sake of completeness, in Table 5 we have listed the energies, γ, of the free surfaces obtained by separating the GBs considered in this paper at the GP plane. Surface reconstruction was not considered in these calculations. According to the Griffith criteria, the thermodynamic threshold for brittle fracture along a grain boundary is given by $2\gamma - E^{GB}$. Using the values of γ in Table 5 and the energies presented in Figs. 3(a), 5(a) and 8(a), the related ideal fracture energies can be determined for all GBs considered in this paper. In Table 5 we have included the approximate energies from the flat parts of the $E^{GB}(\theta)$ curves in these figures. As already pointed out, for GBs in these misorientation ranges the Read–Shockley description breaks down since the dislocation cores overlap completely. We consider these boundaries, therefore, to display behavior "typical" or "generic" for high-angle grain boundaries.

TABLE 5 Free-surface energies, γ, and energies of "typical" high-angle GBs (*i.e.* from the flat parts of the $E^{GB}(\theta)$ curves in Figs. 3(a), 6(a) and 8(a)). Also shown is the thermodynamic threshold energy, $2\gamma - E^{GB}$, for brittle bicrystal fracture. All energies are in units of erg cm^{-2}. $d(hkl)$ is the interplanar spacing of (hkl) planes (in units of the lattice parameter a_0)

		$d(hkl)/a_0$	γ	E^{GB}	$2\gamma - E^{GB}$
(111)	Cu(EAM)	0.577	1012	290	1734
(100)	Cu(EAM)	0.5	1125	700	1550
(110)	Mo(F-S)	0.707	1829	945	2713
(100)	Mo(F-S)	0.500	2100	2170	2030
(111)	Si(S-W)	0.433	1361	650	2072
(110)	Si(S-W)	0.354	1667	1400	1934

According to Table 5, the larger interplanar spacing of the densest planes gives rise not only to significantly lower GB energies but also to lower free-surface energies. Surprisingly, however, these planes are not the ones with the lower values of the ideal fracture energy, $2\gamma - E^{GB}$. In fact, in all three cubic structures considered this energy is lower for the second densest planes. What this means in reality is not obvious because impurity segregation is believed to play an important factor in the fracture of grain-boundary materials.

9. Conclusions

Before comparing the results of this study with experimental results one should keep in mind that we have considered the properties of very simple model systems at zero temperature which may or may not exist in this form in nature. These model systems exclude any effects arising, for example, from point defects in the GB region, such as impurity segregation and reconstruction. For these simple model systems we have demonstrated the following properties.

(a) Both the GB energy and volume expansion depend very strongly on the GB plane. In corresponding free surfaces the same effect is less pronounced. This illustrates the role of the structural disorder at the interface in enhancing the energy anisotropies already present at the related free surfaces.

(b) In metals the GB energy appears to be correlated with the volume expansion induced by the destruction of perfect stacking at the interface. This expansion is larger for GB planes with smaller interplanar spacing.

(c) In silicon, due to its covalent bonding, no such correlation between GB energy and free volume seems to exist. In fact, for the reasons discussed in Section 7, GBs on the (111) plane actually contract.

(d) The planar unit-cell area appears to be of importance also. Whenever, on a given plane, a twist angle is approached for which the GB unit-cell area is particularly small (such as for $\theta = 70.53°$ on (110) and $\theta = 60°$ on (111)), a cusp in the $E^{GB}(\theta)$ curve is observed.

(e) In all GBs investigated, a significant fraction of atoms in the planes nearest to the GB plane show interatomic separations which are less (up to about 10%) than the perfect-crystal nearest-neighbor distance. These atoms appear to be the ones contributing most to the GB energy. In silicon, the distribution of bond angles contributes in addition.

(f) The dominating nature of atoms in very close contact with one another is thought to be the main reason for the similarities in the structure–energy correlation for all three cubic lattices considered.

In summary, it appears that the energetics and, perhaps, other physical properties of grain boundaries are governed by the short-range repulsion between atoms in very close contact, *i.e.* by the Pauli principle. It appears reasonable to assume that in more complex interface materials, such as metal–ceramic interfaces, the structural disorder at the interface also gives rise to atoms in very close contact. Since, independent of the nature of chemical bonding, atoms repel each other when pushed closely together, we believe that the densest planes should play an equally important role in the energetics of more complex interfaces. That this is indeed the case is illustrated in these proceedings by the high-resolution TEM work of M. Rühle on metal–ceramic interfaces [34]. The preference of many GBs studied by means of high-resolution TEM for asymmetrical GB plane orientations [4, 5] (in which one of the two planes is a densest lattice plane) also supports this suggestion.

Acknowledgments

This work was supported by the U.S. Department of Energy, BES Materials Sciences, under Contract W-31-109-Eng-38.

References

1 D. G. Brandon, B. Ralph, S. Ranganathan and M. S. Wald, *Acta Metall., 12* (1964) 813.
2 W. Bollmann, *Crystal Defects and Crystalline Interfaces*, Springer, New York, 1970.
3 J. R. Rice, in R. M. Latanision and R. H. Jones (eds.), *Chemistry and Physics of Fracture*, Martinus Nijhoff, Dordrecht, 1987, pp. 22–43.
4 K. L. Merkle and D. J. Smith, *Ultramicroscopy, 22* (1987) 57; and *Phys. Rev. Lett., 39* (1987) 2887.
5 W. Krakow, J. T. Wetzel and D. A. Smith, *Philos. Mag. A, 53* (1986) 739.
6 G. Hasson, J. Y. Boos, I. Herbeuval, M. Biscondi and C. Goux, *Surf. Sci., 31* (1972) 115.
7 D. Wolf, *J. Phys. Coll. C4, 46* (1985) C4-197.
8 D. Bouchet and L. Priester, *Scripta Metall., 21* (1987) 475.
9 M. S. Daw and M. I. Baskes, *Phys. Rev. Lett., 50* (1983) 1285.
10 M. S. Daw and M. I. Baskes, *Phys. Rev. B, 29* (1984) 6443.
11 M. W. Finnis and J. E. Sinclair, *Philos. Mag. A, 50* (1984) 45.
12 D. Wolf, *Acta Metall., 32* (1984) 245 and 735.
13 D. Wolf, *Physica, 131B* (1985) 53.
14 D. Wolf, in R. J. Arsenault, J. R. Beeler and D. M. Esterling (eds.), *Computer Simulation in Materials Science*, American Society for Metals, Metals Park, OH, 1987, p. 111.
15 F. H. Stillinger and T. A. Weber, *Phys. Rev. B, 31* (1985) 5262.
16 B. P. Feuston, R. K. Kalia and P. Vashishta, *Phys. Rev. B, 35* (1987) 6222.
17 F. F. Abraham and I. P. Batra, *Surf. Sci., 163* (1985) 1752.
18 T. Nguyen and S. Yip, *Mater. Sci. Eng., A107* (1989) 15.
19 C. Goux, *Can. Metall. Q., 13* (1974) 9.
20 D. Wolf and J. F. Lutsko, to be published.
21 G. J. Ackland and R. Thetford, *Phil. Mag. A, 56* (1987) 15.
22 S. Phillpot and D. Wolf, *Proc. MRS Symp. on Interfacial Structure, Properties, and Design in Solids*, Reno, NV, April 1988.
23 R. E. Thomson and D. J. Chadi, *Phys. Rev. B, 29* (1984) 889.
24 D. P. DiVincenzo, O. L. Alerhand, M. Schluter and J. W. Wilkins, *Phys. Rev. Lett., 56* (1986) 1925.
25 J. Hornstra, *Physica, 25* (1959) 409.
26 D. Wolf, *J. Am. Ceram. Soc., 67* (1984) 1.
27 D. Wolf and R. Benedek, *Adv. Ceram., 1* (1981) 107.
28 T. Nguyen, S. Yip, D. Wolf and J. F. Lutsko, *Proc. Int. Conf. on Structure and Properties of Internal Interfaces*, Lake Placid, 1987, to be published.
29 D. Wolf, *Acta Metall.*, in press.
30 W. T. Read and W. Shockley, *Phys. Rev., 78* (1950) 275.
31 Siu-Wai Chan and R. W. Balluffi, *Acta Metall., 26* (1985) 1113.
32 A. Seeger and G. Schottky, *Acta Metall., 7* (1959) 495.
33 R. A. Johnson, *Phys. Rev., 134* (1964) A1329.
34 M. Ruhle and A. G. Evans, *Mater. Sci. Eng., A107* (1989) 187.

Materials Science and Engineering, A107 (1989) 15–22

Molecular Dynamics Study of a Bicrystal at Elevated Temperatures*

TUE NGUYEN and SIDNEY YIP

Department of Nuclear Engineering, Massachusetts Institute of Technology, Cambridge, MA 02139 (U.S.A.)

(Received June 1, 1988)

Abstract

The use of the molecular dynamics simulation technique to study interfacial properties at high temperatures is discussed in the context of an investigation of thermal disordering at a grain boundary. Using a bicrystal model of a high-angle symmetrical tilt boundary and an empirical interatomic potential function for aluminum, results are obtained which reveal that total loss of crystalline order can occur in the interfacial region at about 0.8 to 0.9 of the bulk melting point.

1. Introduction

In the mechanical behavior of crystalline materials, grain boundaries often play an important role because interfacial regions are general sources and sinks of point defects and they are also regions where stresses tend to nucleate and accumulate [1, 2]. In order to achieve a fundamental understanding of how grain boundaries behave under conditions of high temperature and finite stress, it has been necessary to consider simpler systems on which detailed calculations can be performed. From the standpoint of atomistic studies the bicrystal has become the standard model for theoretical discussions [3].

Since it is hardly feasible to observe directly the detailed atomic structure of the interface in a bicrystal specimen, attempts have been made to obtain such information through a discrete particle simulation approach, either molecular statics for the determination of low temperature structures and energies [4], or molecular dynamics for the calculation of properties at finite temperature [5, 6]. While the dynamic simulations have provided considerable insight into the importance of local structure and cooperative dynamics, the extent to which these results can have an impact on experiments is still an issue to be resolved.

The purpose of this contribution, which is largely pedagogical, is to discuss the capability of the molecular dynamics simulation technique for studying interfacial properties at high temperatures, through an investigation of structural stability of a bicrystal model. Results are presented which illustrate the advantage of atomistic simulation, namely availability of detailed information about particle positions and interactions which makes it possible to examine and correlate different physical properties under the same condition. It is also intended here to emphasize the limitations of the simulation approach, the approximate nature of the interatomic potential function and system-size effects associated with the use of a finite simulation cell.

2. Bicrystal models

Bicrystal models are commonly used to analyze and interpret physical properties of grain boundary solids [7]. In defining a bicrystal model one has to consider both the geometric structure of the interface (grain boundary) and the interatomic potential functions through which the particles are assumed to interact. Moreover, any actual calculation involves the use of a simulation cell which means specifying the geometry and dimensions of the cell and the conditions imposed on the cell borders. These factors in turn determine the spatial extent of the crystalline material on either side of the interface and the relation between the system under direct simulation and a specimen on the macroscopic scale. Since cells of varying sizes and border conditions of different types have been used, an appreciation of the cell-specific effects is helpful when discussing the physical significance of simulation results

*Paper presented at the symposium on Interfacial Phenomena in Composites: Processing, Characterization, and Mechanical Properties, Newport, RI, June 1–3, 1988.

0921-5093/89/$3.50

© Elsevier Sequoia/Printed in The Netherlands

Bicrystal models are generally based on the coincident-site-lattice concept which assumes perfect matching of atomic positions at the interface [8, 9]. In this construction the two halves of the bicrystal are single crystals which have been rotated relative to each other about an axis which lies either in the plane of the interface (tilt boundary) or normal to the plane (twist boundary). For reasons of computational economy, it is common to consider high-angle boundaries to take advantage of the smaller periodic structural units. This means choosing boundaries with a low value of Σ, where Σ is the inverse density of the coincident-site-lattice points. A number of tilt boundaries have been investigated on the grounds that these are low-energy boundaries and are therefore special [10]. Thus far molecular dynamics studies have been concerned only with tilt boundaries. However, there are actually cogent reasons for studying twist boundaries [10]. From a geometrical analysis it has been shown that a symmetrical tilt boundary is a special case of the twist boundary (180° angle of rotation). Moreover, the most physical parameters governing the grain boundary energy are shown to be the interplanar spacing normal to the interface and the area of the planar unit cell in the plane of the interface, the boundary plane. It follows from these considerations that studies of twist boundaries can best lead to a general understanding of interfacial properties.

While the role of the interatomic forces may not be so obvious as the structure of the interface, it is well to keep in mind that the relaxed configurations given by molecular statics and the atomic trajectories produced by molecular dynamics are direct consequences of the forces assumed to be acting among the particles. In ascribing the calculated properties to physical systems one is assuming the potential function used is sufficiently realistic. Unfortunately, there is no simple method of validating such an assumption short of comparing predicted properties with measured values. The problem is made even more difficult by the fact that different properties are sensitive to different aspects of the potential function. In the absence of direct validation by experiment, one can investigate the sensitivity of the calculation by using different potentials. Because of the effort and expense involved in repeating the calculation, such procedure is seldom followed.

The bicrystal models which have been studied by molecular dynamics have mostly employed empirical potential functions such as the Lennard-Jones (6-12) potential [5, 6, 11-14], which is known to be appropriate for noble gas solids, and the Morse potential or spline potentials fitted to certain properties of f.c.c. or b.c.c. metals [15-17]. The latter potentials were not considered particularly satisfactory, they were clearly compromises motivated by availability and computational simplicity. Improved potential functions for metals have become available recently following the development of the so-called embedded atom method (EAM) [18]. Although the resulting potential is still effectively fitted to known properties of the metal, the variation with local electron density is now taken into account explicitly, and this eliminates the major objection to the empirical potential, namely the electronic contributions are neglected. The EAM potentials for f.c.c. metals have given very encouraging results in a number of calculations of materials properties [19].

The development of appropriate border conditions for atomistic calculations is another issue which deserves attention. The basic function of the border conditions imposed on the simulation cell is to keep the computational burden within reasonable limits without introducing artificial constraints on the bicrystal system. This means the borders must ensure that the interface is properly surrounded by bulk matter while keeping the simulation cell size to a minimum. In the two directions parallel to the interface, the periodic nature of the coincident-site-lattice model makes the use of periodic border conditions a natural choice. In the perpendicular (z) direction it is not clear what is the best choice. Early studies have employed periodic borders [11-13] or fixed borders [15-17], each with some unsatisfactory consequences. Recently, a method which permits the simulation cell to expand or contract in the z direction as well as independent x-y translations for the two halves of the bicrystal has been proposed [20].

To make the foregoing remarks more specific we show in Fig. 1 a bicrystal model [16, 17] for which some illustrative results will be discussed in the following. The interface in this case is a $\Sigma = 5$ tilt boundary in an f.c.c. lattice with the tilt axis directed along [001] and the boundary plane is chosen to be $(\bar{1}30)$. The misorientation or rotation angle is 53.13°. The intention of this study is to model aluminum using a Morse potential function with parameters determined by fitting the

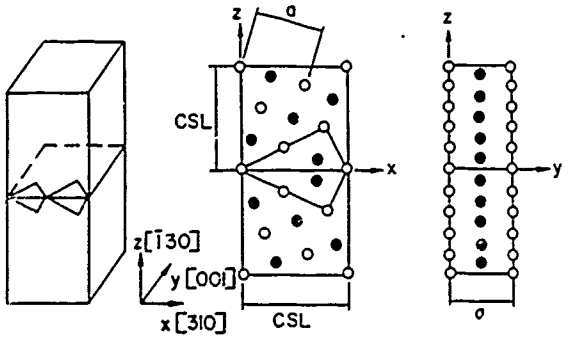

Fig. 1. Simulation cell showing the crystallographic orientation of the bicrystal model of a $\Sigma = 5$ (001)/(1̄30) symmetrical tilt boundary. Cell is periodic along the x and y directions and has fixed borders along the z direction. Also shown are the x–z and y–z plane projections of two adjacent layers of atoms (open and solid circles) in the two CSL structural units [1 CSL = $a(2.5)^{1/2}$] across the boundary plane (1̄30).

known vacancy formation energy [21]. One can question whether potential functions of this type are adequate in representing a metal. Certainly, more realistic results can be expected from the use of the EAM potentials. Such calculations are currently in progress [22].

In specifying the simulation cell we choose coordinate axes such that the x direction is along [310], the y direction [001], and the z direction [1̄30]. The cell is periodic along the x and y directions, but along the z direction a fixed border condition is imposed. This means that atoms are placed beyond the z borders of the cell at the positions of the initial configuration and they are held fixed throughout the simulation. The constraint on the cell imposed by the fixed border is in principle highly undesirable, it is hoped that in practice the actual effects are small so far as the behavior of the interfacial region is concerned. However unsatisfactory it may be, the fixed border is regarded as an alternative to the periodic border condition which gives rise to a second interface in the simulation cell. The latter is undesirable since the two interfaces will interact and at sufficiently high temperatures boundary migration will be thermally activated, leading eventually to the annihilation of the two interfaces. It is possible to formulate a border condition which does not introduce a second interface into the simulation and which allows the cell to expand or contract in the z direction according to the stresses produced in the cell, as well as independent translations of the two halves of the bicrystal [20].

Since the constraining effects of the fixed border are a concern, two simulation cells of different sizes will be used. The smaller cell (model B) contains 840 particles with x and z dimensions of 2 and 14 CSL units and y dimension of 3 lattice constants. The larger cell (model D), containing 2520 particles, has the same x and y dimensions, but the z dimension is 3 times longer. We anticipate that any property which is significantly affected by the fixed border will show variation with cell size; conversely, if the same property values are obtained from both models this would constitute numerical evidence that the border effects on that property are not serious.

3. Calculation of properties

Standard molecular dynamics are employed for the simulation of the bicrystal model [5, 6]. Newton's equations of motion for the atoms in the simulation cell are integrated using a Gear fifth-order predictor–corrector algorithm. To keep the computational burden within limits, the interatomic potential function is cut off at 1.49 lattice constants and a shift is introduced in the energy and the force at the cut-off distance to eliminate the unphysical discontinuities associated with a truncated potential. The choice of the range cut-off is again a compromise between computational efficiency and reality of simulation.

The $\Sigma = 5$ symmetrical tilt bicrystal constructed by the coincident site lattice method is not stable because there is a pair of atoms which are too close to each other in each of the two CSL units across the interface in every other (001) plane (see Fig. 1). To relieve the strong repulsion between this pair we first remove one of the two atoms and then allow the two halves of the bicrystal to have independent rigid translations in all three directions. The relaxed structure which serves as the initial configuration for the molecular dynamics simulation is taken to be that configuration having the lowest potential energy. The resulting structure obtained in this manner is essentially the same as that found in an earlier study [23].

The purpose of the initial relaxation is to start the dynamic simulation with a stress-free configuration. Actually the precise details of the initial configuration should not matter too much, since during the simulation at high temperatures the atoms can have large amplitudes of displacement, thus facilitating the relief of local stresses.

The basic output of the simulation runs are the particle positions and velocities at each time step Δt. The choice of the time step size is governed by the stability of the numerical solution to the equations of motion. Over the range of temperatures studied Δt varies from 0.45 to 2.58×10^{-15} s. Roughly there are about 50 time steps in a lattice vibration period. A particular run is specified by the number of time steps N_t and the temperature of the system which is maintained at the desired value by rescaling the velocities once every 10 steps. Since the shape and volume of the simulation cell does not change during the run, a substantial pressure increase can result if the system temperature is raised from one run to the next. We therefore adjust the lattice constant a at the beginning of each run to keep the pressure more or less constant throughout the entire series.

Given the particle positions and velocities at every time step one can calculate essentially all the physical properties of interest. In this study we are primarily concerned with those properties which are well defined at any temperature and which reveal some aspects of structural order. We therefore consider the following collection, the internal energy U, the internal stress tensor π, the static structure factor $S(\boldsymbol{K})$, and the mean-square displacement function Δr^2. These quantities are defined as

$$U = \sum_{i<j} u_{ij}$$

$$\pi = \frac{1}{\Omega}\left[N k_B T I - \sum_{i} \sum_{j>i} (u'_{ij}/r_{ij})\, r_{ij} r_{ij} \right]$$

$$S(\boldsymbol{K}) = \frac{1}{N} \sum_{i,j} \exp[i\boldsymbol{K}(r_i - r_j)]$$

$$\Delta r^2(t) = \frac{1}{N} \sum_{i} [r_i(t) - r_i(0)]^2$$

where $u_{ij} = u(|r_i - r_j|)$ is the interatomic pair potential, r_i is the position of atom i, Ω is the atomic volume, N is the number of atoms in the simulation cell (in the case where local properties are calculated N will refer to the number of atoms in the region of interest), k_B is the Boltzmann constant, T is the system temperature, defined as $3k_B T = \Sigma_i m v_i^2$, v_i being the velocity of particle i, and $\boldsymbol{K}$ is a prescribed wavevector. The pressure P is given by $[\mathrm{Tr}(\pi)/3]$.

All the quantities defined can be calculated once the particle positions are known; they pertain to the entire system and they will vary with time since the particles are always in motion. Because of the intrinsic fluctuations in a thermodynamic system it is often more useful to consider time-averaged properties. We will denote such averages by the angular brackets $\langle\ \rangle$. There are, however, different time averages. One can take the instantaneous value (at time step t_n) of a property such as the internal energy $U = U(t_n)$, and calculate a cumulative average over the first s time steps

$$\bar{U}(t = s\Delta t) = \frac{1}{s} \sum_{1}^{s} U(t_n)$$

For small values of s or when the system is initially not in equilibrium, the time variation of $\bar{U}$ will show fluctuations, but when the average is over a large number of time steps during which the system has reached equilibrium, then $\bar{U}$ will converge to an essentially constant value which we will denote as $\langle U \rangle$. The significance of $\langle U \rangle$ is that it is the thermodynamic or ensemble average in the sense of the ergodic hypothesis, the time average being equivalent to ensemble average. On the other hand, the instantaneous value U will always fluctuate in time regardless of whether or not the system is in a state of equilibrium. The same remarks apply also to the other properties.

In terms of the properties U, π, $S(\boldsymbol{K})$, and Δr^2, one can achieve a quite detailed and unified characterization of the simulation model. In order to isolate the behavior specific to the interface, it is of great value to consider a reference system with which one can compare the various properties being calculated. Given the choice of the bicrystal model and the simulation cell, it is clear that an appropriate reference system is a single crystal with the same orientation as either the upper or lower half of the bicrystal. By using the same potential function and applying the same border conditions one can make the simulation cell for the reference system identical to the bicrystal system except for the interface. In this way, the difference in any property can be attributed to the presence of the interface.

Since the bicrystal system is not homogeneous, it is essential to be able to identify the interfacial region as being distinct from the bulk crystal. As an operating procedure we divide the simulation cell into equal layers along the z direction, and calculate the above properties as local quantities for each layer. The combination of layer calculations and the availability of the reference system

data for comparison makes it possible to follow the deformation and disordering of the interface at elevated temperatures.

4. Microstructural behavior at high temperatures

We now describe some simulation results obtained using the bicrystal model discussed above [17]. Two series of simulations have been performed, one in which the bicrystal temperature was raised in a stepwise manner and the other in which the temperature was lowered similarly. In the heating series the range covered was from about half the melting point of the bulk T_m to a temperature close to T_m, T_m being the value determined from a study of the reference system. In the cooling series the starting configuration was that of a melt and the system was cooled down to various temperatures below T_m. Since the results of the cooling series are consistent with those of the heating series, they will not be discussed any further.

The behavior of the bicrystal that is of primary interest is the stability of the interfacial structure against thermal disordering. Specifically, we would like to establish whether the interface undergoes a structural transition prior to the melting transition occurring in the bulk system. We begin with the internal energy results shown in Fig. 1. First we note the reference system results which indicate an essentially linear increase of U starting at 500 K up to about 950 K where a sudden jump occurs. Examination of the static structure factor $S(K)$ shows that the particle configuration has become structurally disordered as manifested by an essentially zero value of $S(K)$. Also the mean-square displacement increases sharply to a value that appears to be unbounded. We interpret this behavior as signifying a melting transition, and accordingly we will take T_m to be 950 K. That this value turns out to be close to the known melting point of aluminum (930 K) should be regarded as largely fortuitous since the potential function used is crude and also one expects a certain amount of superheating given the present border conditions. It is, however, self-consistent to adopt the reference system result as the bulk melting point.

In Fig. 2 the bicrystal results are shown separately for the interfacial region and the bulk regions. This division is based on the properties which have been calculated layer by layer and the

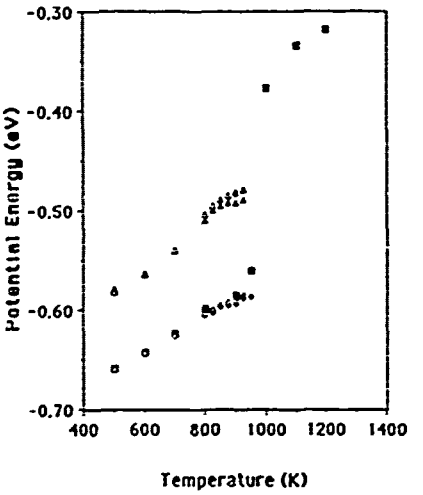

Fig. 2. Variation of potential energy per particle with temperature of the bicrystal model and the reference single-crystal system. Triangles denote the results for the grain boundary layers and diamonds for the bulk region in the bicrystal (solid and open symbols are for the smaller and larger cells respectively). Single-crystal results are denoted by the solid squares.

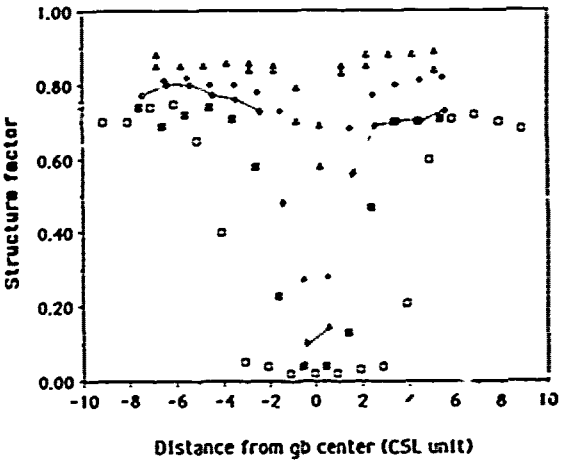

Fig. 3. Profiles of the static structure factor $S(K)$ of the bicrystal cell at various temperatures below bulk melting. 500 K solid triangles, 600 K open triangles, 700 K solid diamonds, 800 K open diamonds, 850 K solid squares, 900 K open squares.

fact that the interfacial region is less well ordered compared to the bulk. The results most useful for the delineation of the interface is the static structure factor $S(K)$. Figure 3 shows the profile of $S(K)$ along the z direction at various temperatures. Because we are interested in the effect of thermal disordering and not the difference between the bicrystal and the reference single crystal, the wavevector K should be chosen such that projections of the atomic positions along this

direction are the same for the two systems. In this case we take $\boldsymbol{K}$ along the y direction. With the interfacial region being characterized by a lower value of $S(\boldsymbol{K})$, one has a convenient measure of the extent of the interface. At 800 K and below, the interfacial width L appears to be temperature independent, although there is increasing disorder with temperature in the interfacial region as well as in the bulk. At 850 K complete disorder has set in in the interfacial region along with some width expansion. At 900 K it is clear that the extent of the region of disorder has increased considerably. From these profiles we can systematically decide which layer should be treated as belonging to the interface.

It can be seen in Fig. 2 that the bulk region energies are in agreement with the values obtained from the reference system. This is as it should be if the bicrystal simulation cell is chosen large enough so that part of it indeed behaves like a bulk crystal. The internal energy of the interface, denoted by closed and open triangles in Fig. 2, shows linear behavior parallel to that of the bulk for temperatures up to about 800 K. Then its variation seems to change character, the precise details being system size dependent. Over the temperature region from 825 to 950 K the grain boundary core region is found to undergo a volume expansion, and in the case of the smaller cell the expansion is accompanied by an appreciable pressure increase (see Table 1). The pressure increase also occurs in the larger cell at a higher temperature. Our interpretation is that the pressure increase is responsible for the energy leveling off seen in Fig. 2, and this is an unphysical behavior caused by the fixed border condition used in our simulation.

TABLE 1 Calculated pressure (kbar) in the bicrystal models and the reference single crystal cell. Values shown are averages taken over 1000 time steps at the end of every run; they are also averages over the entire cell excluding several layers next to the fixed boundaries

Temperature (K)	*Model B*	*Model D*	*Ref*
500	−5.52	−4.94	−4.64
600	−6.25	−5.83	−5.99
700	−6.04	−6.38	−7.27
800	−4.14	−6.44	−7.61
825	−1.98	−4.96	
850	−0.41	−4.03	
875	4.13	−0.22	
900	9.31	4.13	−7.87
925	12.02	8.10	
950	20.61		−4.71

The profiles of $S(\boldsymbol{K})$ given in Fig. 3 allow us to extract an interfacial width L. We regard a layer as belonging to the interface if its $S(\boldsymbol{K})$ value is less than or equal to $(S_B - S_{min})/2$, where S_B is the maximum value of $S(\boldsymbol{K})$ averaged over both sides of the interface excluding the interfacial region, and S_{min} is the minimum value of $S(\boldsymbol{K})$ at the given temperature. The layers regarded as bulk are those with $S(\boldsymbol{K}) \simeq S_B$. A plot of the variation of L with temperature is given in Fig. 4. One can see that L is essentially unchanged from 500 to 700 K, and within the error bars it is also size independent. Up to 800 K the change is still quite small, but beyond this temperature a rapid increase in width occurs. This behavior is quite consistent with the foregoing discussion of the internal energy results, and together they suggest a grain boundary melting transition in the sense of loss of local crystalline order.

In Fig. 4 the error bars are determined from the time-dependent fluctuations in $S(\boldsymbol{K})$. It is reasonable that at 800 K and above the larger cell gives higher values of L because the greater pressure rise in the smaller cell is likely to inhibit the transition. This then implies that the true increase of L with temperature above 875 K is probably greater than the present estimate. A logarithmic variation of the boundary width has been previ-

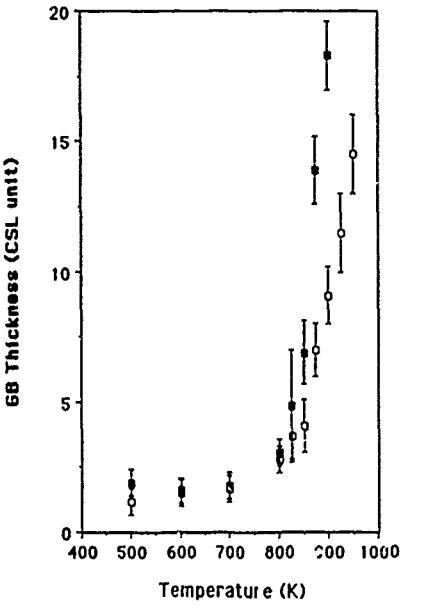

Fig. 4. Variation of grain boundary width (in CSL units) with temperature, smaller cell (open squares) and larger cell (solid squares). Error bars are a measure of the dynamical fluctuations encountered in defining the interfacial layer.

ously suggested [14, 24], but no actual results for a liquid-like film thickness have been reported.

5. Discussion

Molecular dynamics results can provide unique insight into local structure and dynamics of material interfaces because the atomistic simulation approach allows one to study in detail the highly non-linear interactions among particles distributed in any configuration dictated by the interatomic forces between neighboring particles and the stresses mediated by their local environment. Combining this feature with the capability of treating entropic effects associated with thermal fluctuations, one has a powerful tool for probing interfacial properties. There are practical limitations concerning the availability of realistic interatomic potential functions and the need for flexible border conditions which do not involve an excessive number of particles. The embedded atom method of deriving potential functions is an encouraging development from the standpoint of applications to material systems of practical interest [19]. It apears that there is considerable potential for atomistic simulations to make significant contributions to our understanding of the physical properties of interfacial systems.

We have described a study of the structural stability of a particular bicrystal model at elevated temperatures. This serves to illustrate some of the unique features of the atomistic simulation approach as well as some of the difficulties. The existence of grain boundary premelting is still an open question despite several attempts to obtain definitive results [11, 13, 14, 16, 17]. In a larger sense the problem is of interest from the standpoint of phase transitions at internal interfaces [25]; there is also an analogy with surface-induced disorder transitions and wetting [26]. It seems reasonable to conclude that the basic phenomenon of structural behavior at interfaces at finite temperatures is rich and worthy of continued investigations. Eventually one would like to make contact with experimental observations [27], in which case further issues of the effects of impurities and secondary boundary dislocations will have to be addressed.

Acknowledgments

We would like to acknowledge the collaboration of P. S. Ho, T. Kwok and C. Nitta in the aluminum bicrystal study discussed here. The computations were carried out at the IBM Watson Research Center. We also want to thank D. Wolf and J. Lutsko for useful discussions. The work of one of us (T.N.) has been supported by a Department of Energy Fellowship in Radioactive Waste Management.

Note added in proof

Since the writing of this paper we realized that the temperature T_m referred to in Section 4 is actually a mechanical instability temperature which is known to be higher than the melting point. Although the simulation results presented here are not affected, the conclusion to be drawn from our work is that melting at the grain boundary occurs at 0.8 to 0.9 of the instability temperature. It has been shown elsewhere (S. R. Phillpot, J. F. Lutsko, and D. Wolf, to be published; T. Nguyen, *Ph.D. Thesis*, MIT, September 1988; to be published) that grain boundary melting in fact occurs at the melting point of the bulk solid. We are grateful to D. Wolf, J. F. Lutsko, and S. R. Phillpot for sharing their results on melting at surfaces and interfaces with us prior to publication.

References

1 For a general discussion of the effects of interfaces on mechanical properties, see J. P. Hirth, *Metall. Trans., 3* (1972) 3047.
2 Panel Report on Interfacial Bonding and Adhesion, *Mater. Sci. Eng., 83* (1986) 169.
3 For a review see R. J. Harrison, G. A. Bruggeman and G. H. Bishop, in G. A. Chadwick and D. A. Smith (eds.), *Grain Boundary Structure and Properties*, Academic Press, London, 1976, Chap. 2.
4 See the conference proceedings on Grain Boundary Structure and Properties, *J. Phys. Coll. C6, 43* (1982), contributions by P. D. Bristowe, p. C6-33, and by V. Vitek and G. J. Wang, p. C6-147. See also *Surf. Sci., 144* (1) (1984), and D. Wolf, *Acta Metall., 32* (1984) 245.
5 G. H. Bishop, R. J. Harrison, T. Kwok and S. Yip, in J. W. Christian, P. Haasen and T. B. Massalski (eds.), *Progress in Materials Science, Chalmers Anniversary Volume*, Pergamon, Oxford, 1981, p. 49.
6 S. Yip, *Comments Solid State Phys., 11* (1984) 125.
7 G. Hasson, M. Biscondi, P. Lagarde, J. Levy and C. Goux, in H. Hu (ed.), *The Nature and Behavior of Grain Boundaries*, Plenum Press, New York, 1972, p. 3.
8 W. Bollman, *Crystal Defects and Crystalline Interfaces*, Springer, Berlin, 1970.
9 G. H. Bishop and B. Chalmers, *Scr. Metall., 2* (1968) 133.
10 D. Wolf, *J. Phys. Coll. C4, 46* (1985) C4-197.

11 G. Ciccotti, M. Guillope and V. Pontikis, *Phys. Rev. B, 27* (1983) 5576; M. Guillope, G. Ciccotti and V. Pontikis, *Surf. Sci., 144* (1984) 67.

12 F. Carrion, G. Kalonji and S. Yip, *Scr. Metall., 17* (1983) 915; P. Demeyier, G. Kalonji, R. Najafabadi and S. Yip, *Surf. Sci., 144* (1984) 77.

13 P. Demeyier and G. Kalonji, *J. Chem. Phys., 85* (1986) 2937, *Acta Metall., 35* (1987) 2719.

14 J. Q. Broughton and G. H. Gilmer, *Phys. Rev. Lett., 56* (1986) 2692.

15 T. Kwok, P. S. Ho and S. Yip, *Phys. Rev. B, 29* (1984) 5354, 5363.

16 T. Nguyen, P. S. Ho, T. Kwok, C. Nitta and S. Yip, *Phys. Rev. Lett., 57* (1986) 1919. In this simulation the force expression is missing a factor of 2 so the model studied was a system in which the forces are smaller by a factor of 2 than those corresponding to the potential. For corrected results see ref. 17.

17 T. Nguyen, P. S. Ho, T. Kwok, C. Nitta and S. Yip, unpublished work.

18 M. S. Daw and M. I. Baskes, *Phys. Rev. B, 29* (1984) 6443; S. M. Foiles, M. I. Baskes and M. S. Daw, *Phys. Rev. B, 33* (1985) 7983.

19 M. Baskes, M. Daw, B. Dodson and S. Foiles, *MRS Bull., 13* (2) (1988) 28.

20 J. F. Lutsko, D. Wolf, S. Yip, S. R. Phillpot and T. Nguyen, *Phys. Rev. B.*, in press.

21 R. M. J. Cotterill and M. Doyama, in R. Hasiguti (ed.), *Lattice Defects and Their Interactions*, Gordon and Breach, New York, 1967, p. 1.

22 J. F. Lutsko and D. Wolf, *Scr. Metall.*, in press; T. Nguyen, *Ph.D. Thesis*, Massachusetts Institute of Technology, 1988.

23 M. Hasimoto, Y. Ishida, R. Yamamoto and M. Doyama, *J. Phys. F, 10* (1980) 1109.

24 R. Kikuchi and J. Cahn, *Phys. Rev. B, 21* (1980) 1893.

25 C. Rottman, *J. Phys. Coll.*, to be published.

26 R. Lipowsky, *Phys. Rev. Lett., 57* (1986) 2876.

27 S. W. Chan, J. S. Liu and R. Balluffi, *Scr. Metall., 19* (1985) 1251.

Materials Science and Engineering, A107 (1989) 23–40

Embrittlement of Interfaces by Solute Segregation*

JAMES R. RICE and JIAN-SHENG WANG

. 'vision of Applied Sciences, Harvard University, Cambridge, MA 02138 (U.S.A.)

(Received June 1, 1988)

Abstract

We discuss theoretical models of interfacial embrittlement by solute segregation. Of properties susceptible to alteration by segregation, the ideal work of interfacial separation, $2\gamma_{int}$, is predicted to have an important but probably not exclusive role in controlling embrittlement. A thermodynamic framework for estimating $2\gamma_{int}$ from data available through free surface and grain boundary adsorption studies is outlined, and relevant segregation energies are given for carbon, phosphorus, tin, antimony and sulphur segregation in iron. Data from intergranular fracture experiments involving these same segregants is also summarized in an attempt to test the idea that segregation-induced embrittlement (or ductilization) can be understood in terms of the segregant's effect on $2\gamma_{int}$. Uncertainties in present data do not allow a convincing test, but it is not implausible that the deleterious effects of phosphorus, tin, and sulphur in iron can be understood in this way. The effect of carbon does not seem to be similarly understandable, although that may be due to the inappropriateness of the only available surface segregation data in that case, which are for a (001) surface rather than a general polycrystalline surface created by intergranular fracture.

1. Introduction

Several examples are known whereby the alteration of chemical composition of grain boundaries, by the atomic-scale segregation of solutes present only as minute impurities in the bulk, causes intergranular brittleness of normally ductile solids. Examples are provided by bismuth in copper, sulphur in nickel and a range of segregants, including arsenic, oxygen, phosphorus, tin, antimony, sulphur, tellurium and presumably hydrogen in iron [1–3]. Sometimes the presence of a segregant at grain boundaries may improve the ductility of a polycrystal that is susceptible to brittle intergranular failure. This seems to be the case for carbon in iron that has been embrittled by some of the segregants just mentioned, and also for boron in the ordered Ni_3Al alloy [4, 5].

Here we focus on the much studied cases of segregants in iron. The idea is to use the results now available from extensive experiments dealing with that case to evaluate and test theoretical concepts on interfacial cohesion, and thus to develop ideas which may find wider application to interfacial failure in other systems, including composites.

The next section examines available theory for understanding the brittle decohesion cracking of interfaces in terms of parameters susceptible to alteration by segregation. That section emphasizes the expected important, if not exclusive, role of $2\gamma_{int}$ as a controlling interfacial property in determining resistance to brittle decohesion cracking. Here $2\gamma_{int}$ is the ideal work of reversibly separating an interface against atomic cohesion. It is equal to the area under the stress σ *vs.* separation distance δ curve for the interface; Fig. 1.

The section which follows then reviews a thermodynamic framework which relates changes in interfacial chemical composition, due to solute segregation, to changes in $2\gamma_{int}$. The reductions (or increases) in $2\gamma_{int}$ in separations at fixed composition are shown to be related to differences between initial and final free energies of segregation. These differences are between an initial state in which the segregants are situated on unstressed interfaces, *i.e.* grain boundaries, and a final state in which they reside on the pair of free surfaces created by fracture.

Although the fractures of interest generally occur at low temperature, when the interface is out of composition equilibrium with the bulk, the

*Paper presented at the symposium on Interfacial Phenomena in Composites: Processing, Characterization, and Mechanical Properties, Newport, RI, June 1–3, 1988.

0921-5093/89/$3.50

© Elsevier Sequoia/Printed in The Netherlands

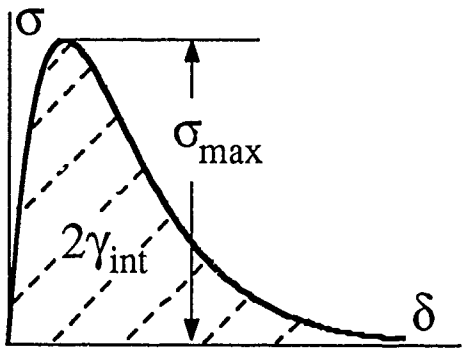

Fig. 1. Tensile stress *vs.* separation distance normal to an interface.

relevant free energies of segregation can be estimated from high temperature equilibrium segregation experiments. While there is substantial uncertainty and some inconsistency in reported experimental values, data exist allowing estimates of approximate ranges for the free energies both for grain boundary and free surface impurity segregation in the cases of carbon, phosphorus, tin, antimony and sulphur in α-Fe.

Thus one has the means of determining how segregation of so. ·es at interfaces affects $2\gamma_{int}$. The question arises. is understanding of the alteration of $2\gamma_{int}$ by solute segregation really relevant to explaining segregation-induced embrittlement in ductile or normally du .tile systems, for which total works of fracture are usually much larger than $2\gamma_{int}$?

To address this we close by indicating a method of testing, with data from fracture experiments, the hypothesis that embrittlement (or ductilization) by impurity solute segregation at interfaces is explainable in terms of the effect of the segregation on $2\gamma_{int}$. The uncertainties in currently available data, both for fracture properties of solute embrittled iron alloys and for thermodynamic properties of the grain boundary and surface segregants, are so great that a convincing test of the hypothesis cannot be made at this time. The data on phosphorus, tin, antimony and sulphur in polycrystalline iron is nevertheless such that it is not implausible that their deleterious effects can be understood in terms of their alteration of $2\gamma_{int}$, which they decrease. The available data for carbon in iron do not fit the same trend, although the interpretation is unclear since a critical surface segregation energy is available only for carbon segregation on (100) planes in iron crystals rather than for general polycrystal surfaces formed by intergranular fracture.

2. Brittle decohesion cracking of interfaces

Here we briefly review theoretical models of the cracking process in order to identify material or interfacial properties relevant to crack growth resistance.

2.1. Griffith crack

In the elastic-brittle Griffith model, all plastic flow processes are neglected. The amount G per unit crack area by which the work done by external loads exceeds the change in elastic strain energy, both calculated according to continuum elasticity, is equated to the energy $2\gamma_{int}$ per unit crack area residing in the newly separated bonds. (G is proportional to the square of the stress intensity factor for the common linear elastic model of the adjoining solids; see *e.g.* [6].) Thus $G=2\gamma_{int}$ for crack growth, so that the effect of alteration of interfacial chemical composition shows only through its effect on $2\gamma_{int}$ in this model. Sometimes the energy of the bonds is written

$$2\gamma_{int}=f_s^A+f_s^B-f_b^{A/B} \quad (1)$$

where A and B denote the solids that join along the interface (Fig. 2(a)) or as $2f_s-f_b$ when the solids have identical properties, where the fs denote excess free energy per unit area for a surface (f_s) or for a grain boundary interface (f_b). A different expression, as discussed later, applies for separation of an interface in presence of a mobile segregant which can diffuse to or from the interfacial region during separation.

2.2. Cohesive zone model

This model incorporates more detail of the separation process, but does not represent the effects of atomic discreteness. In it, the interfacial region is represented as two joined elastic continua which interact with one another such that a stress-separation relation, $\sigma=\sigma(\delta)$ like in Fig. 1, applies along the gradually decohering interface according to the local separation δ (Fig. 2(b)). The two solids are, for the present, assumed to separate without dislocation or other inelastic processes within them and without significant shear parallel to the interface. The latter assumption may not generally be reasonable for interfaces between solids of strong dissimilarity in elastic constants, even when loaded only by tensile forces acting perpendicular to the interface (see ref. 7 and references therein). We neglect

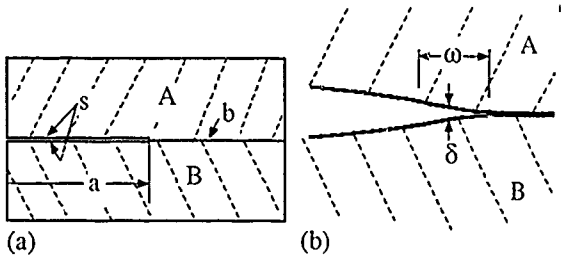

Fig. 2. (a) Interfacial elastic-brittle crack. (b) Region of gradual decohesion near tip, over size scale ω.

such effects here, although they may be important for many types of composite interfaces.

Clearly, if the interface is initially unseparated and if stressing is uniform all along it, then the failure criterion is that $\sigma = \sigma_{max}$ of Fig. 1. However, there is a different result when the failure occurs within a transition region between a much longer crack-like zone, where the sides of the interface have been pulled out of interaction range of one another, and an also long region where the interface remains essentially unseparated, $\delta = 0$. This defines a non-singular, cohesive crack model and a well known application of the J-integral shows that the condition for crack growth reduces, in this limit, to [6, 8]

$$G = \int_0^\infty \sigma(\delta)\,d\delta \equiv 2\gamma_{int} \tag{2}$$

where G is the energy release rate for the equivalent elastic-brittle crack model, Fig. 2(a). Thus the cohesive zone model then gives complete agreement with the Griffith model.

The transition zone itself, over which the decohesion occurs, has a length ω along the interface which may be estimated from the Dugdale/BCS model. For the isotropic material of tensile modulus E and Poisson ratio ν, this gives (see, for example, [9])

$$\omega = \frac{\pi}{8(1-\nu^2)}\frac{EG}{\sigma_{max}^2} = \frac{\pi}{4(1-\nu^2)}\frac{E\gamma_{int}}{\sigma_{max}^2} \approx 0.9\,\frac{E\gamma_{int}}{\sigma_{max}^2} \tag{3}$$

which is a lower bound to the size since it is based on σ being uniform at σ_{max} all along the cohesive zone. Guided by analogous discussion in [10], we shall thus estimate ω as (1 to 1.5) $E\gamma_{int}/\sigma_{max}^2$.

If one now assumes a σ vs. δ relation compatible with the $(1+x)e^{-x}$ type fit to the energy of the universal bonding correlation of Rose *et al.* [11, 12] and Ferrante and Smith [13], then

$$\sigma = E_0\left(\frac{\delta}{h}\right)\exp\left(-\alpha\frac{\delta}{h}\right) \tag{4}$$

Here h represents an unstressed separation distance between planes joining at the interface, and is of order of the atomic spacing or a little larger, and E_0 is the initial modulus for one-dimensional tensile straining of the interface layer. It then follows from $d\sigma/d\delta = 0$ that

$$\sigma_{max} = \frac{E_0}{e\alpha} \tag{5}$$

with $\delta = h/\alpha$ at the maximum and

$$2\gamma_{int} = \int_0^\infty \sigma\,d\delta = \frac{E_0 h}{\alpha^2} \tag{6}$$

either of which determine α and, together, imply $\sigma_{max}^2 = 2E_0\gamma_{int}/e^2 h$.

Thus the estimate of the cohesive zone ω at the crack tip as 1 to 1.5 times $E\gamma_{int}/\sigma_{max}^2$ gives $\omega \approx (4\text{–}6)(E/E_0)h$. For the cleavage of a lattice plane, considered as an interface, $E_0 > E$ because of the Poisson effect (*e.g.* $E_0 = 1.35E$ when $\nu = 0.3$) and $\omega \approx 3\text{–}4$ lattice spacings. In this case the separation process may be highly localized to the crack tip and may bear little resemblance to the spread-out zone of gradual decohesion envisioned in the present model. By contrast, for a high-angle grain interface, weakened by segregation, it is plausible that h is a little larger than an atomic spacing and that the interfacial layer is elastically compliant so that $E_0 < E$. For example $(E/E_0)h = 2$ lattice spacings results in $\omega \approx 8\text{–}12$ lattice spacings. Thus weak interfaces not only require less of a stress intensity factor for elastic-brittle crack growth but also spread the decohesion zone out over a greater size scale. Both factors reduce the near-tip shear stresses generated during the separation process, and hence reduce the stresses tending to cause those dislocation processes that have been neglected in the modelling discussed thus far.

2.3. *Effects of lattice discreteness*

While $G = 2\gamma_{int}$ is the condition for growth of a (long) crack according to the continuum elastic models, lattice calculations are not in perfect agreement. Even when the assumed interaction potentials among the atoms is consistent with

allowing brittle decohesion of bonds along the fracture path, without nucleation of dislocations, one finds [6, 14–17] that loads corresponding to the value G^+ of the continuum G must be achieved for the onset of crack growth, and lower loads corresponding to a value G^- for the onset of healing, where

$$G^- < 2\gamma_{int} < G^+ \tag{7}$$

(The fact that $2\gamma_{int}$ must fall in the range between G^- and G^+, as required by thermodynamics, was not recognized in some of the earlier works on the subject [16], due primarily to ambiguities in defining G so as to properly agree with that for the anisotropic elastic continuum limit of the adopted lattice model [18].)

The excess of G^+ over $2\gamma_{int}$ is referred to as lattice trapping, and it is G^+ rather than $2\gamma_{int}$ which provides the correct criterion for (non-thermally activated) crack growth. Unfortunately, it is not known in much detail how G^+ depends on the shape of the σ vs. δ relation, or on the "shape" of potentials describing interatomic interactions, and thus there is little basis for addressing how alterations of chemical composition of the interface might affect G^+. However, with an important caveat to be discussed, recent calculations for elastic-brittle cracks in crystal lattices suggest that $G^+ - 2\gamma_{int}$ is only a small fraction of $2\gamma_{int}$, of the order of 10% or less [14, 15]. Thus, to a reasonable approximation, the effect of segregants on G^+ may be expected to be similar to their effect on $2\gamma_{int}$. Also, the difference $G^+ - 2\gamma_{int}$ is relatively small when the decohesion process is gradual, extending over many atomic spacings at the crack tip, and this is the situation to be expected with a strongly embrittled interface.

The caveat refers to the possibility [19, 20] that some incipient dislocation-like shear rearrangement of atomic bonds may occur near the crack tip in loading towards G^+. Even if this does not involve full nucleation of a dislocation, *e.g.* with the incipient dislocation structure disappearing due to image-like attractions at the free surface after the crack grows ahead, it still might serve to make $G^+ - 2\gamma_{int}$ significantly greater than lattice calculations thus far reported have shown. As a possible example, de Cellis *et al.* [17] found an incipient twin-like shear zone in a lattice simulation of cracking of iron.

Lattice trapping effects allow the possibility of thermally activated growth, and the kinetics of crack growth or healing must always satisfy [21]

$$(G - 2\gamma_{int})\dot{a} \geq 0 \tag{8}$$

where a = crack length. Thus $2\gamma_{int}$ is the thermodynamic threshold for growth. A similar thermodynamic restriction applies for growth in presence of a mobile solute, which can diffuse to the interfacial region during separation, or for crack growth in an environment which adsorbs onto the fresh fracture surface, provided that $2\gamma_{int}$ is appropriately re-defined using adsorption data.

2.4. Competition between cleavage and dislocation blunting

Another perspective on the effects of solute segregation on embrittlement is provided by their effect on the competition between cleaving and dislocation blunting at the tip of an atomistically sharp interfacial crack [15, 8, 22–27], Fig. 3. According to this viewpoint, an interface is regarded as intrinsically cleavable if the local stress concentration at the tip (here phrased in terms of G) necessary for cleavage decohesion, namely $G_{cleave} = G^+ \approx 2\gamma_{int}$, is less than the value G_{disl} corresponding to nucleation of a dislocation from the crack tip. Conversely, if $G_{disl} < 2\gamma_{int}$, the crack tip will first begin to blunt by dislocation emission and, presumably, a more ductile failure mode will result.

Some relevant comments on this approach are as follows [25].

(a) G_{disl} is not a fixed number for a given interface, but depends on the direction of crack growth along it [23, 25, 26], because of the different orientations of the potentially relaxing slip planes, and on the mixity of shear with tensile loading relative to the crack [15, 25]. Thus it may be the case the $G_{disl} < 2\gamma_{int}$ for some directions of cracking along a given interface, whereas

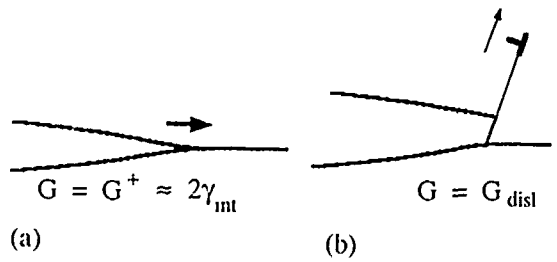

Fig. 3. Competition between (a) interfacial decohesion and (b) dislocation blunting of crack tip. System is regarded as intrinsically cleavable if G for (a) is less than for (b).

$G_{disl} > 2\gamma_{int}$ for other directions. Hence it over simplifies to say that an interface is intrinsically cleavable. Available calculations, for that special set of cracking directions which are such that the crack tip lies in a slip plane [23, 25, 26], suggest that

$$G_{disl} = AEb^2/r_0 \quad (9)$$

where b is the Burgers vector of the relaxing dislocation, r_0 its core size, and A a factor which depends on ν, the load mixity, and the particular orientation of the relaxing slip system, and which also includes a factor representing the resistance to formation of the dislocated ledge at the crack tip.

(b) Even when the intrinsic cleavability condition $G_{disl} > 2\gamma_{int}$ is met, interfaces may actually show brittleness only if there is a mechanism to nucleate the hypothesized atomistically sharp cracks, *e.g.* by stress concentrations owing to local heterogeneity of plastic flow, and if stress levels ahead of those cracks are not so much reduced by plastic flow, due to pre-existing or non-tip-nucleated dislocations, so as to cause the local crack-tip G to fall below $2\gamma_{int}$.

(c) Conversely, if the intrinsic cleavability condition is not met, in that $G_{disl} < 2\gamma_{int}$, cleavage may still occur if the mobility of tip-nucleated dislocations is sufficiently low that they cannot be driven out from the near-crack-tip region, so that stresses reaching levels of order σ_{max}, Fig. 1, develop along the interface ahead of the crack.

Thus, while the comparison of G_{disl} with $2\gamma_{int}$ in terms of the crack-tip competition provides important insight on intrinsic cleavability, the approach is not sufficient on its own to incorporate the factors mentioned in (b) and (c) which result in the strong observed dependence of brittleness on temperature and strain rate due to the dependence of plastic flow processes on those same factors. To examine the effects of alterations of composition of an interface on its intrinsic cleavability, one should therefore examine the effects on $2\gamma_{int}$ (or, more precisely, G^+) and G_{disl}. Thus if the effect of interfacial solute segregation is the typical one, of reducing $2\gamma_{int}$, this, in isolation, would make the interface more cleavable. Similarly, an effect of increasing $2\gamma_{int}$ would, in isolation, make it less cleavable. However, the segregation might also affect G_{disl} and the ease of dislocation passage through the interface, as a part of larger scale plastic stress relaxation near the tip. For example, G_{disl} depends somewhat on the energy of the ledge left at the dislocated tip, and that is likely to have a dependence on chemical composition along the interface [24]. In addition, it has recently been observed that solutes of large atomic size relative to the host lattice, which retain some residual volume misfit even after segregating to the interface, may inhibit dislocation nucleation (*i.e.* increase G_{disl}) through an elastic interaction analogous to that in solute hardening [27]. None of these possible effects of segregation on G_{disl} and on dislocation passage through the interface can be quantified with much accuracy. Thus it is not clear if cases could exist for which, as an example, a solute segregation that decreased $2\gamma_{int}$ could have a net result of less cleavability of the interface.

2.5. *Crack nucleation*

In some cases interface cracks may pre-exist, but in ductile systems it is likely that most such cracks have been safely blunted in high temperature heat treatments prior to use. Thus the occurrence of interfacial fracture will require a process of crack nucleation. Sometimes this process simply occurs by the early cracking of a brittle phase, *e.g.* a carbide. Here we consider direct nucleation due to local stresses generated by the heterogeneity of flow. This is illustrated in terms of a simple dislocation pile-up in Fig. 4. It is clear that once the crack has become several atomic spacings long it is like any other interface crack and hence the controlling property in $2\gamma_{int}$, subject to the various reservations already noted. When the crack is nearer to birth, other characteristics of atomic bonding, *e.g.* as reflected in the peak strength σ_{max} and the overall shape of the σ vs. δ relation, are important too. Segregant effects that reduce σ_{max} will ease the birth of cracks at

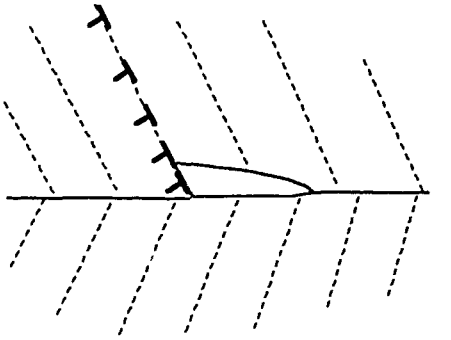

Fig. 4. Interfacial crack nucleation at a dislocation pile-up.

local stress concentrations and those that lower $2\gamma_{int}$ make it easier for them to spread to a mature size along the interface.

In the spirit of the sort of competition discussed in the last section, stress concentration at the pile-up tip may be relaxed [20] by crack nucleation or by nucleating new dislocations in the adjoining crystal and perhaps in the interface too. Segregant effects on σ_{max} and $2\gamma_{int}$ are evidently relevant to the former, it is presently unknown to what extent segregants may act to aid or inhibit the latter.

2.6. *Cleavage cracking with extensive surrounding plasticity*

It is normally the case in ductile systems that fractures which appear to occur by cleavage, whether of lattice planes or grain interfaces, are accompanied by significant plastic flow. Figure 5 is intended to illustrate a tensile decohesion zone that is embedded within a much larger plastic zone. The value of G, in circumstances for which the plastic zone is of small enough scale that G can be defined, is often written as

$$G = w_p + 2\gamma_{int} \qquad (10)$$

where the plastic work term w_p is frequently inferred to be much greater than $2\gamma_{int}$.

For cleavage of ferrite grains adjacent to crack-nucleating carbides in steels [20] w_p is inferred to be only 1.3 to 2.5 times $2\gamma_{int}$, but it is approximately 500 to 1000 times based on G at the onset of low temperature transgranular cleavage of polycrystalline mild steel [20, 28], taking

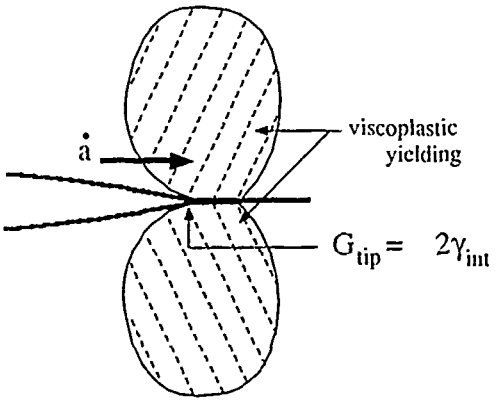

Fig. 5 Plastic/viscoplastic zone near tip of a crack growing by interfacial decohesion. In some circumstances an elastic-type stress singularity remains at a propagating crack tip, so that an energy flow to the decohesion process may be defined.

$2\gamma_{int} = 4\ J\ m^{-2}$ in both cases [29]. The great difference between single- and polycrystalline values has been attributed to energy absorbed in ductile tearing between the inevitably misaligned cleavage facets formed when a cleavage crack crosses a grain boundary. For cleavage of the more brittle of a suite of copper bicrystals [30] containing 0.003 at.% Bi, which segregates to and embrittles the bicrystal interface, w_p is approximately 5 times the estimated [26] $2\gamma_{int} = 2\ J\ m^{-2}$ for a $\Sigma 5$ symmetric tilt about [100], with (031) boundary plane, in the as-grown condition, and 25 times $2\gamma_{int}$ for a high-angle random boundary after vacuum annealing for 96 h at 723 K and some fatigue hardening. These values are based on loads on pre-cracked specimens at the onset of crack growth and might overestimate the w_p prevailing during the rapid crack propagation which followed. The same is true for polycrystalline mild steel, above. In contrast, copper bicrystals with symmetric tilt about [110], with $\Sigma 11\ (1\bar{1}3)$ or $\Sigma 9\ (2\bar{2}1)$ boundary planes, were not brittle after similar heat treatments and mechanical testing, although the latter could be embrittled by holding for 24 h in bismuth vapor at 1123 K prior to annealing for 96 h at 723 K. Presumably, w_p is a much greater multiple of $2\gamma_{int}$ for such boundaries.

Since w_p is often much larger than $2\gamma_{int}$, it is sometimes assumed that $2\gamma_{int}$ is an irrelevant parameter for such fractures. However, various authors have pointed out (*e.g.* [31]) that if the mechanism of fracture is, in fact, the tensile decohesion of atomic bonds, then w_p must depend in some way on the stress *vs.* separation curve as in Fig. 1, as well as on the plastic flow properties of the material. For example, if somehow both $2\gamma_{int}$ and σ_{max} could be reduced towards zero, it is evident that a vanishingly small stress concentration would be required at the tip for cleavage, and thus w_p would reduce towards zero too. It is not known on what features of the σ *vs.* δ relation w_p depends. Presumably, w_p would decrease (increase) under segregation-induced alterations of the σ *vs.* δ relation which decreased (increased) both $2\gamma_{int}$ or σ_{max}, but whether $2\gamma_{int}$ or σ_{max}, or something else, is the most important variable is not known in general and, probably, has no universally valid answer.

A convincing case can be made that w_p is a function only of $2\gamma_{int}$ for cleaving materials which exhibit a sufficiently strong rate sensitivity to plastic flow at high strain rates. This is rooted in

previous work of Hart [32], Hui and Riedel [33], and Lo [34], and has been developed by Freund and Hutchinson [28] and Mataga *et al.* [35]. Essentially, it is found that within a continuum plasticity formulation for a propagating, mathematically sharp-tipped crack (*i.e.* without account for a finite-sized cohesive zone), a classical inverse-square-root stress singularity of elastic type is retained at the tip, provided that the plastic constitutive response is sufficiently rate sensitive. The plastic shear strain rate $\dot{\varepsilon}^p = \dot{\varepsilon}^p(\tau)$ must increase with shear stress τ no more rapidly than τ^3, *i.e.* $\dot{\varepsilon}^p(\tau)/\tau^3 \to 0$ as $\tau \to \infty$, for this to occur. Since an elastic singular field is then retained at the crack tip, an energy flow to the tip, say G_{tip}, can be defined. Presuming that in Fig. 5 the actual decohesion process takes place over a size scale that is well embedded within the zone dominated by this near-tip elastic singular field, the sorts of results discussed in Sections 2.1 to 2.3 suggest that the condition for crack propagation is that

$$G_{tip} = G^+ \approx 2\gamma_{int} \tag{11}$$

Here G_{tip} is determined from the continuum plasticity analysis in terms of the history of crack growth and load variation, as well as in terms of the viscoplastic constitutive properties. For example, Freund and Hutchinson [28] and Mataga *et al.* [35] give results for the ratio G_{tip}/G as a function of crack speed $\dot{a}$ for steady-state growth of the crack under small-scale yielding conditions such that there is net energy flux G per unit crack area. That is $G = w_p + G_{tip}$, and G corresponds to what would be called the fracture energy in such a situation. What is important for the present discussion is that the only parameter entering the fracture description that is susceptible to alteration by solute segregation is $2\gamma_{int}$, which determines the value which G_{tip} must attain for the postulated crack growth history to occur. In this model, alterations of $2\gamma_{int}$ have a "valve-like" effect on the (sometimes) much larger plastic dissipation w_p.

In other cases of crack growth with substantial plasticity, under conditions for which the very large stresses of materials with strong viscoplastic effects cannot be generated, it may be the case that σ_{max} of Fig. 1 plays a more decisive role. For example, rate-independent models of the plastic flow process lead to maximum achievable stress levels ahead of initially sharp cracks in ductile solids [36]. Under plane-strain-like constraint, a maximum tension of about $3 \times \sigma_y$ (the tensile yield strength) results for a non-hardening material, and higher multiples of σ_y result in strain hardening materials; these factors ignore heterogeneities of the stress field at the dislocation scale, as in Fig. 4. If conditions appropriate to such rate-dependent plasticity models apply, then it would seem that cleavage of an interface would become much more difficult when σ_{max} exceeds the maximum achievable tensile stress (unless a more readily cracked brittle phase is present). Thus, in such cases, the understanding of segregant-induced alterations of σ_{max} could be critical to understanding embrittlement. Needleman [37] has developed a numerical modelling approach to interface decohesion in ductile surroundings which may be useful in assessing the effect of σ_{max} and the shape of $\sigma(\delta)$ relation.

2.7. Summary

The discussion leads us to suspect that of the parameters susceptible to change by alteration of the chemical composition of an interface, $2\gamma_{int}$ is an important parameter in determining embrittlement. The rest of the paper focuses on that parameter, but other parameters, notably σ_{max}, may also be important, and there remain possibilities that segregation might affect embrittlement by little-understood effects on dislocation generation and mobility in the immediate vicinity of the interface.

3. Interfacial decohesion in presence of a segregated solute

A thermodynamic framework [22, 38] now reviewed enables use of results from solute segregation studies to estimate effects of segregation on $2\gamma_{int}$.

With reference to Fig. 6, we focus on the interface as a thermodynamic system which is assumed to be in local equilibrium but which may be (and typically is, at low temperatures) out of composition equilibrium with adjoining bulk phases, both before and after separation. Interfacial thermodynamic quantities are defined as Gibbs-like excesses relative to those of the two adjoining phases. In defining excesses, each adjoining phase is regarded as a homogeneous system having the same mass as that phase and sustaining homogeneous deformations equivalent to those prevailing a few atomic layers away from the interface in that phase. Thus δ is defined as

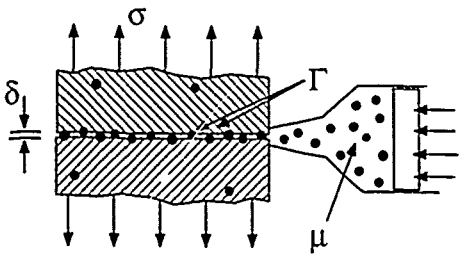

Fig. 6. Interfacial region with solute segregation, treated as a thermodynamic system that may be constrained against composition equilibrium with the adjoining bulk phase; μ is the chemical potential equilibrating solute of coverage Γ in the interfacial region.

the excess interfacial opening, *i.e.* the separation between two points, one in each of the adjoining phases, in excess of that separation which is accountable by homogeneous strain of the phases in which the two points reside. For the present discussion, the two adjoining phases are taken to be identical to one another (*e.g.* a symmetrical grain boundary) as a simplification.

We deal exclusively with solutes which are far more abundant along the interface than in a few atomic layers, well removed from the interface, in either adjoining phase. In that case Γ^i, the concentration of segregant i per unit area of interface, is well defined and we assume that an equilibrating chemical potential μ^i can be associated with each segregating species i as it exists at the interface.

Thus, where u and s are the excesses of energy and entropy per unit area of interface, in a formulation which treats the interface region as being constrained against the necessity of solute composition equilibrium with the adjoining phases, one has

$$\mathrm{d}u = T\mathrm{d}s + \sigma\,\mathrm{d}\delta + \sum_i \mu^i\,\mathrm{d}\Gamma^i \tag{12}$$

for reversible changes of state. Here σ is the stress acting perpendicular to the interface and the summation extends just over the segregants. We do not consider work modes that stretch the interface in its own plane.

The key assumption, embedded in the above equation, is that all thermodynamic functions referring to the interface, *e.g.* u, s, σ and the μ^i, are determined by the values of T, δ and Γ^i, regardless of the solute concentrations (say, x_1, x_2, ...) in the adjoining phases. If eqn. (12) holds throughout a separation process (one in which δ is increased towards indefinitely large values) as assumed in the present modelling, then any distinction is neglected between the pair of free surfaces resulting from such a decohesion fracture and free surfaces having the same T and Γ^i, but produced by a different thermal/mechanical route. The latter route might for instance have involved equilibrium solute segregation to the free surfaces at a higher temperature and, possibly, a surface reconstruction.

If $\delta_0\{=\delta_0(T, \Gamma^1, \Gamma^2, \ldots)\}$ is the separation for an unstressed interface (*i.e.* with $\sigma=0$) having composition Γ^1, Γ^2, ... then the work of separation is

$$2\gamma_{\mathrm{int}} = \int_{\delta_0}^{\infty} \sigma\,\mathrm{d}\delta \tag{13}$$

which is consistent with Fig. 1. This expression does not define a unique value until one characterizes the path of variation (if any) of T and the Γ^i with δ during separation. We regard T as constant during separation and thus work in terms of the excess Helmholtz function $f=u-Ts=f(\delta, \Gamma^1, \Gamma^2, \ldots)$, omitting explicit reference to T as a variable. At fixed T

$$\mathrm{d}f = \sigma\,\mathrm{d}\delta + \sum_i \mu^i\,\mathrm{d}\Gamma^i \tag{14}$$

Thus, when there is a single segregant of amount Γ and equilibrating potential μ, one has for separation at constant Γ (the normal case at low T and with non-mobile segregants)

$$\begin{aligned}(2\gamma_{\mathrm{int}})_{\Gamma=\mathrm{const}} &= f(\infty, \Gamma) - f(\delta_0(\Gamma), \Gamma) \\ &= 2f_s(\Gamma/2) - f_b(\Gamma)\end{aligned} \tag{15}$$

Here $f(\infty, \Gamma)=2f_s(\Gamma/2)$ is the free energy excess for the pair of distantly separated surfaces, so that $f_s(\Gamma/2)$ is the excess for a single one of them, where the total segregant Γ is assumed to divide equally between the two. In the usual notation, $\Gamma_s=\Gamma/2$. Also, $f(\delta_0(\Gamma), \Gamma)=f_b(\Gamma)$ refers to the unstressed grain boundary. One may then obtain the alternative expression that [22, 38]

$$(2\gamma_{\mathrm{int}})_{\Gamma=\mathrm{const}} = (2\gamma_{\mathrm{int}})_0 - \int_0^{\Gamma} \{\mu_b(\Gamma) - \mu_s(\Gamma/2)\}\,\mathrm{d}\Gamma \tag{16}$$

where $(2\gamma_{\mathrm{int}})_0$ is the work to separate a clean interface (with $\Gamma=0$), $\mu_b(\Gamma)$ is the equilibrating

potential for segregant coverage Γ on an unstressed grain boundary and $\mu_s(\Gamma/2)$ for coverage $\Gamma/2$ on a single free surface.

This last equation links $2\gamma_{int}$, for separation at fixed composition, to quantities which can, in principle, be estimated from solute segregation studies. One expects that normally the potential necessary to equilibrate Γ on a grain boundary will be larger than the potential to equilibrate the same amount on a pair of free surfaces (as $\Gamma/2$ on each), $\mu_b(\Gamma) > \mu_s(\Gamma/2)$. There are, apparently, exceptions, but with this normal type of segregation behavior, the segregation reduces $2\gamma_{int}$ and thus is expected to promote embrittlement.

If $\mu = \mu(\delta, \Gamma)$ denotes the equilibrating potential for the interfacial region (with for instance $\mu(\infty, \Gamma)$ corresponding to $\mu_s(\Gamma/2)$ above), then the normal type of segregation just discussed is such that $\mu(\delta_0, \Gamma) > \mu(\infty, \Gamma)$. If, in fact, μ diminishes continuously with δ during the decohesion, such that $\partial\mu(\delta, \Gamma)/\partial\delta < 0$, then it may be proven that the peak strength σ_{max} (Fig. 1) of the interface is also reduced by segregation. This is because of the relation [22] that

$$\frac{d}{d\Gamma}\left\{(\sigma_{max})_{\Gamma=const}\right\} = \left\{\frac{\partial\mu(\delta,\Gamma)}{\partial\delta}\right\}_{\delta=\delta_m(\Gamma)} \qquad (17)$$

where $\delta = \delta_m(\Gamma)$ is the value of δ at which the peak strength σ_{max} occurs.

For separation at constant composition in presence of multi-component segregation, the generalization of (16) is [38, 39]

$$2\gamma_{int} = (2\gamma_{int})_0 - \int_{(0,0,\ldots)}^{(\Gamma^1,\Gamma^2,\ldots)} \sum_i (\mu_b{}^i - \mu_s{}^i)\, d\Gamma^i \qquad (18)$$

While separation at fixed composition seems to be the normal failure mode in low temperature embrittlement, it is useful to consider an opposite limiting case. This we consider for a single segregant of amount Γ at potential μ. This limit is separation at constant potential μ, implying that there is (for "normal" segregators) solute inflow to the interface region during separation so as to maintain μ fixed, *e.g.* at the value for an adjoining bulk phase with which there is composition equilibrium. Such conditions require mobility. They are probably met approximately in low temperature hydrogen assisted cracking of some interfaces (*e.g.* prior austenite grain boundaries in high strength quenched and tempered steels). It has been argued that they may be met also in high temperature stress relief cracking of grain boundaries in steels due to sulphur segregation [20].

The Γ = constant and μ = constant paths are compared in Fig. 7 which has been drawn using Langmuir-McLean adsorption isotherms (see below). For separations at fixed μ the relevant thermodynamic function is $\gamma \equiv f - \mu\Gamma = \gamma(\delta, \mu)$, and

$$\begin{aligned}(2\gamma_{int})_{\mu=const} &= \gamma(\infty, \mu) - \gamma(\delta_0(\mu), \mu) \\ &= 2\gamma_s(\mu) - \gamma_b(\mu)\end{aligned} \qquad (19)$$

Here we have rewritten the opening of the unstressed boundary as $\delta = \delta_0(\mu)$; $\gamma_s(\mu)$ and $\gamma_b(\mu)$ denote the γ function for a single free surface and for the unstressed grain boundary, respectively. Also, it follows that [22]

$$(2\gamma_{int})_{\mu=const} = (2\gamma_{int})_0 - \int_{-\infty}^{\mu} \{2\Gamma_s(\mu) - \Gamma_b(\mu)\}\, d\mu \qquad (20)$$

Here $\Gamma_s(\mu)$ gives the segregant coverage on a single free surface, and $\Gamma_b(\mu)$ on a grain boundary, at equilibrating potential μ.

Some relevant observations are as follows:

(1) Normal segregators have been characterized above as having $\mu_b(\Gamma) > \mu_s(\Gamma/2)$, and might analogously be expected to show $2\Gamma_s(\mu) > \Gamma_b(\mu)$. That is, at a given potential, such

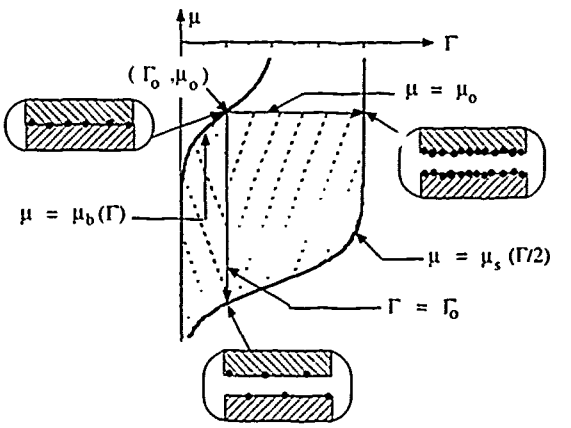

Drawn for L-McL with $\Gamma_s^{max} = \Gamma_b^{max}$, $RT = 0.1\,(\Delta g_b^o - \Delta g_s^o)$

Fig. 7. Plots of μ vs. Γ for unstressed boundary ($\mu = \mu_b(\Gamma)$) and pair of free surfaces created by fracture ($\mu = \mu_s(\Gamma/2)$). Paths shown for separation at constant Γ and for separation at constant μ. The μ vs. Γ plots, or adsorption isotherms, shown have been based on the Langmuir McLean model.

segregators are situated more abundantly on a pair of free surfaces than on an unstressed grain boundary. For both separation routes considered, $2\gamma_{int}$ is reduced by such a segregator, so that they are expected to embrittle. Nevertheless, thermodynamics does not preclude the existence of anomalous segregators for which the above unequalities are reversed, *e.g.* $2\Gamma_s(\mu) < \Gamma_b(\mu)$. This means that an anomalous segregator tends to situate more abundantly on an unstressed grain boundary than on a pair of free surfaces. Such anomalous segregators increase $2\gamma_{int}$ and hence are expected to decrease interfacial brittleness. It is of interest in this regard that boron appears to be an anomalous segregator in the ordered alloy Ni_3Al, and that it reduces the severe grain boundary brittleness of that alloy [4, 5].. We discuss later the possibility that carbon may be an anomalous segregator in iron.

(2) A segregant in mobile conditions, allowing separation at constant μ, always reduces $2\gamma_{int}$ relative to the value for separation at constant Γ. That is, $2\gamma_{int}$ for "slow" separation, at fixed μ, is always less than $2\gamma_{int}$ for "fast" separation, at fixed Γ. This is because [22, 38]

$$(2\gamma_{int})_{\Gamma=\Gamma_0} - (2\gamma_{int})_{\mu=\mu_0} = \int_{\Gamma_s}^{2\Gamma_s(\mu_0)} \{\mu_0 - \mu_s(\Gamma/2)\}\, d\Gamma > 0 \qquad (21)$$

(if $d\mu_s(\Gamma_s)/d\Gamma_s > 0$, as reasonably assumed) for paths beginning at (Γ_0, μ_0) in Fig. 7. The inequality applies for normal as well as anomalous segregators. The difference in $2\gamma_{int}$ at constant Γ compared with that at constant μ can be numerically significant, showing that mobility (or slowness of the attempted separation) is an important factor for worsening the already deleterious effect of a normal segregator on $2\gamma_{int}$, and for reducing the beneficial effect of an anomalous one. The above difference in $2\gamma_{int}$ corresponds to the cross-hatched area between the two paths in Fig. 7, whereas $(2\gamma_{int})_0 - (2\gamma_{int})_{t=t_0}$ corresponds to the cross-hatched area to the left of the $\Gamma = \Gamma_0$ path in the figure.

(3) In rapid separation at fixed composition, a thermodynamic argument drawing on the inequality nature of the second law shows that $2\gamma_{int}$ of (16) and (18) gives the least possible work to separate an interface [8]. More work could be expended if, for instance, on an atomic scale, the cracking process acted to decohere some other set of atomic bonds than those producing the thermodynamic minimum [40].

(4) Embrittlement, at least as it mirrors $2\gamma_{int}$, is always seen to depend on differences between segregant effects on the initial grain boundary and on the two free surfaces created by the fracture. Thus a focus on the electronic alterations induced by segregants in grain boundaries, without corresponding study of what they induce on free surfaces, is unlikely to prove definitive in explaining solute embrittlement. Rather, the focus should be on the calculation of energies and entropies of segregation for both the initially coherent interface and for the surfaces created by fracture. Specifically, the differences in energy and entropy between the two states are of primary interest.

(5) When the grain boundary and surface coverages Γ entering the above formulae are less than values corresponding to full coverage of a set of adsorption sites, idealized as all having the same low energy relative to solute sites in the bulk, the simple Langmuir–McLean model [41, 42] may be adopted. Thus

$$\mu_b(\Gamma_b) = \Delta g_b^0 + RT \ln\{\Gamma_b/(\Gamma_b^{max} - \Gamma_b)\}$$
$$\mu_s(\Gamma_s) = \Delta g_s^0 + RT \ln\{\Gamma_s/(\Gamma_s^{max} - \Gamma_s)\} \qquad (22)$$

where the (inherently negative) Δg^0 terms are referenced to a bulk phase at the same temperature, that is they are based on the expression $\mu = RT \ln\{x/(1-x)\} \approx RT \ln x$ for the equilibrating potential when a fraction x of available solute sites are occupied in the bulk. The Δg^0 terms have the form

$$\Delta g_b^0 = \Delta h_b - T\Delta s_b^0 \qquad \Delta g_s^0 = \Delta h_s - T\Delta s_s^0 \qquad (23)$$

Here the Δh terms are the enthalpies of segregation (essentially identical to energies of segregation in the present context since pressure times volume terms are negligible for the unstressed boundary and free surface), and the Δs^0 terms are entropies of segregation relating to changes in the atomic vibrational spectrum. Estimated values of the Δh and Δs^0, or of the Δg^0 at particular temperatures, are given in the next section for several segregants in iron.

Consider now a grain boundary separation at fixed composition. If the initial coverage Γ on the boundary falls within the Langmuir–McLean range, then the coverage $\Gamma/2$ on the separated surfaces is sure to do so and the equations above

for the μ can be used directly in the calculation of $2\gamma_{int}$ by eqn. (16). The integrand of (16) is then

$$\mu_b(\Gamma)-\mu_s(\Gamma/2)=(\Delta g_b^0-\Delta g_s^0)+RT\ln\left(\frac{2\Gamma_s^{max}-\Gamma}{\Gamma_b^{max}-\Gamma}\right) \quad (24)$$

For representative boundary coverages $\Gamma=0.25$ to $0.75\Gamma_b^{max}$, and with $\Gamma_b^{max}\approx\Gamma_s^{max}$, the last term, containing the ln, varies from 0.8 to $1.6RT$. It is $0.7RT$ when $\Gamma=0$. Since at $T=300$ K, typical of low temperature fractures, $RT=2.5$ kJ mol^{-1}, and since $(\Delta g_b^0-\Delta g_s^0)$ is of order 50 to 100 kJ mol^{-1} (see next section) for representative embrittling solutes in iron, one is usually justified in neglecting the ln term. In that case (16) reduces to

$$2\gamma_{int}\approx(2\gamma_{int})_0-(\Delta g_b^0-\Delta g_s^0)\Gamma \quad (25)$$

(Since the Δg^0 have only mild temperature dependence, because representative Δs^0 vary from 0 to 0.04 kJ mol^{-1} K^{-1} (see next section), one might set $T=0$ and hence write

$$2\gamma_{int}\approx(2\gamma_{int})_0-(\Delta h_b-\Delta h_s)\Gamma \quad (26)$$

which is the form given by Rice [8]. We have a preference for (25) since it is more accurate and its terms are found by a slightly smaller range of the error-prone extrapolation in T, from a high T at which there is segregation equilibrium with solutes in the bulk.)

For multicomponent segregation within the Langmuir–McLean range, μ vs. Γ relations incorporating site competition may be assumed [42], *e.g.*

$$\mu^i(\Gamma^1,\Gamma^2,\ldots)=\Delta g^{0i}+RT\ln\left\{\Gamma^i/(\Gamma^{max}-\sum_i\Gamma^i)\right\} \quad (27)$$

Again, the last term, while decisive for high temperature equilibrium, is negligible for low temperature fracture, in which case (18) reduces to

$$2\gamma_{int}=(2\gamma_{int})_0-\sum_i(\Delta g_b^{0i}-\Delta g_s^{0i})\Gamma^i \quad (28)$$

4. Auger-electron-spectroscopy-based segregation energies of impurity solutes in iron

Auger electron spectroscopy (AES) has been the primary technique for recent studies of solute segregation on grain interfaces, that can be broken open by fracture, and on the surfaces thus created. However, considerable uncertainties are introduced by the experimental conditions and assumptions which must be made in converting Auger peak height ratios, diagnostic of different solutes, into coverages Γ^i of those solutes along the boundaries under study. Quantification of the technique has not been fully developed yet. Also, there are several factors which affect the coverage of segregated atoms on an interface or exposed surface. Among them are the orientations of the interface and the surface, the composition of the examined material and the existence of other residual impurities.

The standard method of analyzing data, for a boundary or free surface thought to be in high temperature composition equilibrium with the adjoining bulk phases, is to equate μ_b or μ_s to $RT\ln x$, so that the data is represented in the Langmuir–McLean form

$$\Gamma/(\Gamma^{max}-\Gamma)=x\exp(-\Delta g^0/RT) \quad (29)$$

It is necessary to first choose a value of Γ^{max}. Then, presuming that x is known, the adopted conversion factor is used to convert the AES peak height ratio to an estimate of Γ/Γ^{max}. When this is done at a single temperature, the results enable calculation of a value of Δg^0 at that temperature for the data to be represented by (29). When results are obtained over a range of temperature, the procedure is to extract a Δh and Δs^0 which enable the best representation of the results over that range with $\Delta g^0=\Delta h-T\Delta s^0$.

This is the route to the values of Δh, Δs^0 or Δg^0 that we list shortly. However, it is well to recognize that the concept of the segregation energy, particularly on a polycrystal surface, is only a macroscopic average based on the Langmuir–McLean segregation law. Atomistic calculations show that even for a single macroscopically planar interface, the bonding energy of a segregant atom may change from site to site. There is no unique segregation energy, and even on the average, the Langmuir–McLean equation is not always valid. Keeping all this in mind, one is not too surprised at the large scatter of the available data.

AES-based (mostly) segregation data in iron are listed in Table 1 for that set of impurity solutes for which results are available constraining, somewhat, both grain boundary and free surface segregation energies, so that eqns. 25

TABLE 1 AES-based surface and grain boundary segregation data in iron (in kJ mol^{-1})

Impurity	*Segregation point*	$-\Delta g_{s/b}^0$ (at T)	$-\Delta h_{s/b}$	$\Delta s_{s/b}^0 \times 1$K	*Reference*
C	(100) surface		84	±0.004	Grabke [55, 56]
	Grain boundary		57	0.022	Grabke [55, 56]
			38	0.043	Hänsel and Grabke [43]
			79[a]	−0.013[a]	Papazian *et al.* [65]
Sn	Polycrystal surface	77 (823 K)	46	0.045[b]	Seah and Lea [61]
	Low-index surface		> 200		Grabke [55]
	Grain boundary	45 (823 K)	13	0.045[b]	Seah and Lea [61]
			23	0.026	Grabke [55]
?	Polycrystal surface	> 80 (973 K)			Guttmann [63]
			75		Grabke [56]
	Low-index surface[c]		180[c]		Grabke [55]
	Grain boundary		34	0.022	Grabke [55, 56]
			32	0.022	Guttmann *et al.* [52]
			21	0.037	Hänsel and Grabke [43]
Sb	Polycrystal surface	> 105 (1023 K)			Dumoulin *et al.* [64]
	Grain boundary	20–40 (1023 K)			Guttmann [66]
			13[d]		Guttmann [67]
S	Polycrystal surface		165		Tauber and Grabke [57]
			190		Grabke [56]
	Grain boundary	75 (1143 K)			Suzuki *et al.* [47]

[a] Autoradiography data.
[b] Based on assumed entropy expression by Seah and Lea [61], evaluated at 823 K.
[c] Apparently for low-index crystal surface; data and details of study unpublished.
[d] Rutherford back scattering spectroscopy data.

and (28) can be applied. The elements for which such are currently available are carbon, phosphorus, tin, antimony and sulphur. The uncertainties are seen to be sufficiently large that sometimes data obtained by the same research group scatter widely. Based on these data we estimate values of $\Delta g_b^0 - \Delta g_s^0$ at $T = 300$ K. These will be used in the next section in a comparison with fracture data.

We start with carbon. Carbon is known as a grain boundary cohesion enhancer in steels [43–48]. It has been confirmed that the role of carbon in improving ductility of iron alloys and steels is two-fold. One effect is to displace harmful impurities, such as phosphorus [43, 46, 49–54], tin [55], and sulphur [47, 56–58] from grain boundaries and thus reduce the detrimental effects of these impurities. Carbon is thought to be effective in this way due to its unusually large value of $-\Delta g_b^0$, compared to other segregants, which favors it in site competition. The other effect is an inherent one in that carbon itself increases the grain boundary cohesion. To obtain reliable AES data for carbon is a very difficult task since the exposed surface of the specimen is easily contaminated by carbon even in an extra-high-vacuum AES chamber.

The only available value for surface segregation of carbon was measured on the (100) crystallographic plane, and gives $-\Delta h_s = 84$ kJ mol^{-1}. There are reasons to suspect that this value may be too high to be representative of polycrystalline surfaces created by intergranular fracture. First, since carbon can be displaced from an iron surface by tin [59], one expects $-\Delta h_s^C$ to be less than $-\Delta h_s^{Sn}$ (strictly, $-\Delta g_s^{oC}$ should be less than $-\Delta g_s^{0Sn}$ at the displacement temperature). The values reported in Table 1 do not support this. Thus we have reinterpreted the 84 kJ mol^{-1} for $-\Delta h_s^C$ as the upper limit of a possible range, 74–84 kJ mol^{-1}, with a corresponding range allowed later for tin. Second, since the 84 kJ mol^{-1} is for a (100) crystal surface, it is well to observe that with phosphorus and tin, for which segregation energies have been estimated both for low-index crystal surfaces and for polycrystal surfaces, the low-index surface values are considerably higher than those for polycrystal surfaces

(Table 1). A low energy electron diffraction study [60] showed that the segregated carbon atoms sit in octahedral sites on the (100) plane as interstitials. For an average polycrystal surface the number of this type of interstitial site is less than on a {100} plane, and it is expected that the surface segregation enthalpy for non-(100) planes might be lower than the range of $-\Delta h_s = 74$–84 kJ mol^{-1}. However, based on that range and other data listed in Table 1, *e.g.* for grain boundaries, a range of $\Delta g_b^0 - \Delta g_s^0$ for carbon at 300 K is estimated to be -2 to 35 kJ mol^{-1}. The lower end of this range is based on the Δh_h^C from autoradiography measurements; AES results support the upper end. If $-\Delta h_s^C$ has been overestimated as discussed above, then the difference $\Delta g_b^0 - \Delta g_s^0$ could take more strongly negative values, consistent with carbon acting to increase $2\gamma_{int}$.

The segregation of tin on iron surfaces was studied by Rüsenberg and Viefhaus [59] on (100), (110) and (111) crystallographic planes of Fe–4wt.%Sn alloy single crystals and by Seah and Lea [61] on pol, crystal surfaces of Fe–Sn alloys with much lower tin concentrations (0.001–1.0 wt.% Sn). It was found that an order–disorder transition occurred at high coverage leading to a multilayer segregation, and the Langmuir–McLean type segregation law is then invalid. No unique segregation enthalpy and entropy could be derived. Based on the fact that even at low bulk concentration saturated structures were always observed, Grabke [55] estimated that the enthalpy for surface segregation of tin on the low-index crystal surfaces mentioned must be relatively high, $-\Delta h_s \geqslant 200$ kJ mol^{-1}. Considering that tin can be displaced by sulphur from the iron surface when the bulk concentration of sulphur is much lower than that of tin [61, 62], this value of $-\Delta h_s$ is far too high to be representative of polycrystalline surfaces. Seah and Lea [61] obtained a much lower polycrystal value of $-\Delta h_s = 46$ kJ mol^{-1} (based on a polycrystalline value of $-\Delta g_s^0 = 77$ kJ mol^{-1} at 823 K; from this they inferred, based on an assumed form for Δs^0 (giving 0.045 kJ mol^{-1} K^{-} at 823 K), that $-\Delta h_s = 46$ kJ mol^{-1}). Lea and Seah [62] found that multilayer segregation would not occur if the bulk concentration is lower than 0.005 wt.%. As an impurity in steels this condition is usually satisfied and Seah and Lea's value for Δg_s^0 might be appropriate. Considering that tin can displace carbon from iron surfaces, this value is taken as the lower limit and a range $-\Delta g_s^0 = 77$–87 kJ mol^{-1} at 823 K is assumed. Also, assuming what seems to be a more typical $\Delta s_s^0 = 0$–0.03 kJ mol^{-1} K^{-1} and $\Delta s_b^0 = 0.02$–0.03 kJ mol^{-1} K^{-1} to extrapolate in T, rather than the larger values of Seah and Lea, a range of $\Delta g_b^0 - \Delta g_s^0$ at 300 K for tin of 26–57 kJ mol^{-1} is estimated.

Grabke [55, 56] reported two contrasting values of segregation enthalpy of phosphorus on iron surfaces, $-\Delta h_s = 75$ kJ mol^{-1} as a polycrystal v lue and what, from context, appears to be a low-index crystal surface value of 180 kJ mol^{-1}. Details and supporting data for the latter are unpublished. Guttmann [63] gave $-\Delta g_s^0 > 80$ kJ mol^{-1} at 973 K. We interpret this as 80–90 kJ mol^{-1} and selecting Δs_s^0 as 0.01–0.03 kJ mol^{-1} K^{-1} gives a $-\Delta h_s$ approximately consistent with the 75 kJ mol^{-1} noted above. Thus we estimate a range of $\Delta g_b^0 - \Delta g_s^0$ at 300 K for phosphorus of 35–48 kJ mol^{-1}.

Segregation of antimony has been less investigated. Dumoulin and Guttmann [64] showed that in Fe–Sb alloys with 0.06 at.% Sb an equilibrium surface segregation could be reached with the saturation level less than 1 monolayer and the segregation process could be described in the framework of the Langmuir–McLean theory below 973 K when the evaporation rate is very low. The surface segregation energy was estimated only as $-\Delta g_s^0 > 105$ kJ mol^{-1} at 1023 K. We interpret this as 105–130 kJ mol^{-1}. Using the estimated values of $\Delta s_s^0 = 0$–0.03 and $\Delta s_b^0 = 0.02$–0.03 kJ mol^{-1} K^{-1}, we estimate $\Delta g_b^0 - \Delta g_s^0 = 58$–$122$ kJ mol^{-1} at 300 K for antimony.

It has been known that sulphur is of strong embrittlement potential if manganese does not exist [56]. Sulphur is most susceptible to surface segregation. The polycrystalline surface segregation enthalpy, $-\Delta h_s^0$, was reported to be 165 kJ mol^{-1} [57] and 190 kJ mol^{-1} [55]. Ignoring the modest entropy corrections for the surface segregation, in view of this range, and assuming $\Delta s_b^0 = 0.02$ kJ mol^{-1} K^{-1}, we estimate $\Delta g_b^0 - \Delta g_s^0 = 107$–$140$ kJ mol^{-1} at 300 K for sulphur.

The estimated data for the Δg^0 quantities at 300 K for carbon, tin, phosphorus, antimony and sulphur are summarized in Table 2. Also shown is a measured of embrittlement sensitivity, to be discussed in the next section.

To understand the order of the reduction of $2\gamma_{int}$ that is implied by the results just summar-

TABLE 2 Summary of ranges of Δg^0 at 300 K (in kJ mol^{-1}) and embrittlement sensitivities, ξ (in K/at.% in g.b.)

Impurity	$-\Delta g_s^0$	$-\Delta g_b^0$	$\Delta g_b^0 - \Delta g_s^0$	ξ
C	73–85	50–75	−2–35	−20–−10
Sn	61–87	30–35	26–57	15–38
P	76–80	32–41	35–48	5–20
Sb	83–130	8–25	58–122	28–67
S	165–190	50–58	107–140	35–45

To get $-\Delta h_s$, decrease $-\Delta g_s^0$ by approximately 0 to 9, to get $-\Delta h_b$, decrease $-\Delta g_b^0$ by approximately 6 to 9.

ized, we may note that $\Delta g_b^0 - \Delta g_s^0 = 50$ to 100 kJ mol^{-1} is representative for deleterious segregants in Table 2. If we consider a grain boundary with a square network of possible adsorption sites, spaced 0.25 nm from one another, and suppose that only one quarter of these are taken by the segregant, then $\Gamma = 4 \times 10^{18}$ m$^{-2} = 7 \times 10^{-6}$ mol m^{-2}. Thus for separation at this composition

$$2\gamma_{int} \approx (2\gamma_{int})_0 - (0.35 \text{ to } 0.70)\ \text{J m}^{-2} \qquad (30)$$

Since $(2\gamma_{int})_0 \approx 3.1$ J m^{-2} for a typical boundary in pure iron [29], this is a significant alteration.

The reductions from $(2\gamma_{int})_0$ will be yet greater when conditions of mobility allow separation at constant μ. Typically, in that case the surface ends up fully covered (Fig. 7) according to the Langmuir–McLean model for surface segregation, which means that the Langmuir–McLean model will not necessarily apply and, instead, multilayer coverage may occur. However, from the geometry of Fig. 7, we may expect that a calculation based on (20) with Langmuir–McLean for the surface could only underestimate the reductions of $2\gamma_{int}$ that would be calculated from the actual surface adsorption isotherm, since $\mu \to \infty$ as $\Gamma \to 2\Gamma_s^{max}$ in the Langmuir–McLean model, so we proceed on that basis. Assume then, that $\Gamma_s^{max} = \Gamma_b^{max}$ both correspond to coverage of half the network of adsorption sites mentioned above, and that the segregation energy difference is large compared with RT. As a specific illustration, assume that the fixed μ at which the separation is imagined to occur is such as to equilibrate $\Gamma = 0.5\ \Gamma_b^{max}$ (*i.e.* a quarter of the network of sites covered) on the unstressed boundary. This is the case illustrated in Fig. 7. Then the reduction from $(2\gamma_{int})_0$ is approximately four times that in the previous example for separation at constant Γ. That is the reduction would range from 1.4 to 2.8 J M^{-2} in the imagined separation at constant μ, which is substantial but possibly underestimates the actual effect.

5. Fracture tests and embrittlement sensitivities

There do not seem to exist results of fracture experiments which would enable a careful test of the degree to which alterations of $2\gamma_{int}$ control solute embrittlement. What is widely available is the characterization of segregant effects on the ductile–brittle transition temperature (DBTT) in the Charpy impact test of iron and steels. Here the concern is with a low temperature brittle mode that involves intergranular fracture, or some mixture of it with transgranular cleavage, that transitions into a ductile tearing mode of rupture with increase of temperature. Most commonly, these effects have been reported as a variation δ(DBTT) in DBTT associated with variations $\delta\Gamma'$ in solute coverages, under conditions for which microstructural dimensions and plastic flow resistance (in practical terms, as measured by hardness at a given temperature) are held constant. This correlation has been reported extensively as the linear form

$$\delta(\text{DBTT}) = \sum_i \xi_i \delta\Gamma' \qquad (31)$$

where the constants ξ_i are called embrittlement sensitivities.

We give values, or approximate ranges, of the ξ_i later. The most reliable values of the Γ' are determined by AES measurements on the intergranular fracture surface, as discussed earlier. Unfortunately, there are several possible definitions of the DBTT, *e.g.* as the temperature at which (a) the Charpy energy exceeds some fixed value (say, 2.7 J), or (b) the energy is half way between its upper and lower shelf values, or (c) the fracture surface area is of half intergranular (possibly with transgranular) cleavage and half ductile rupture appearance.

In principle, if the uncertainties in all quantities concerned were not so large, the values of the ξ_i could be used to test the hypothesis that $2\gamma_{int}$ controls interfacial embrittlement. We recognize that if the hypothesis is correct, then

$$\text{DBTT} = F(2\gamma_{int}, \text{microstructure}) \qquad (32)$$

That is, solute segregation influences DBTT only through its effect on $2\gamma_{int}$, under conditions as assumed above for which "microstructure" (*i.e.*

microstructural dimensions and parameters like dislocation density and entanglements determining plastic flow resistance) are unaffected by the segregation treatment.

Current theory is, of course, unable to predict the above function F but, if it exists, then

$$\delta(\mathrm{DBTT}) = \frac{\partial F}{\partial(2\gamma_{\mathrm{int}})}\,\delta(2\gamma_{\mathrm{int}}) \tag{33}$$

in alterations of the material which leave microstructural dimensions and plastic flow resistance unchanged. In the sub-monolayer coverage range for which the linear form of (31) is contemplated, one can use (28) and thus write

$$\begin{aligned}\delta(2\gamma_{\mathrm{int}}) &= \sum_i [\partial(2\gamma_{\mathrm{int}})/\partial\Gamma^i]\delta\Gamma^i + [\partial(2\gamma_{\mathrm{int}})/\partial T]\delta T \\ &= -\sum_i (\Delta g_b^{0i} - \Delta g_s^{0i})\delta\Gamma^i - 2s_{\mathrm{int}}\delta(\mathrm{DBTT})\end{aligned} \tag{34}$$

where $2s_{\mathrm{int}} = -\partial(2\gamma_{\mathrm{int}})/\partial T$ at fixed composition. The second term on the right above arises because of the temperature dependence of $2\gamma_{\mathrm{int}}$, eqn. (32) is actually an implicit equation for DBTT since $2\gamma_{\mathrm{int}}$ depends not only on the Γ^i but also on T(=DBTT, for the purposes of that equation).

Thus, if the hypothesis is correct that solute effects are to be understood solely through effects of segregation on $2\gamma_{\mathrm{int}}$, then from the last two equations

$$\delta(\mathrm{DBTT}) = A\sum_i (\Delta g_b^{0i} - \Delta g_s^{0i})\delta\Gamma^i \tag{35}$$

where the interpretation of A is

$$A = \frac{-\partial F/\partial(2\gamma_{\mathrm{int}})}{1 + 2s_{\mathrm{int}}\partial F/\partial(2\gamma_{\mathrm{int}})} \tag{36}$$

Comparison with (31) then shows that the hypothesis is supported if the embrittlement sensitivities from fracture tests and the segregation energies from adsorption studies satisfy

$$\xi_i = A(\Delta g_b^{0i} - \Delta g_s^{0i}) \tag{37}$$

with the same coefficient A for every segregating chemical species i.

Since temper embrittlement of alloy steels by impurity segregation is an important, widely studied, embrittlement phenomena, data for embrittlement sensitivities for steels (and otherwise "pure" iron) are available in the literature. Early data on embrittlement sensitivities of impurities in steels were summarized by Seah [68, 69] in terms of Kelvins per ppm by mass of the solute concentration in the bulk. These data are irrelevant to our comparison since they are not based on grain boundary coverage. As quantitative AES advanced in recent years measurements of the interfacial concentration of impurities became possible. Embrittlement sensitivities are typically reported in units of Kelvins per atomic % of solute coverage on grain boundaries. They are available for several detrimental impurities in steels, including phosphorus, tin, antimony and sulphur for which there are segregation energy data (Tables 1 and 2) and also for the important element carbon. Published values are listed in Table 3. The available data spread widely. As we pointed out previously, the shift of the ductile-brittle transition temperature, measured by standard Charpy impact tests, is not only dependent on the grain boundary segregation, but also a function of the resistance of the steel to plastic flow, which is determined by microstructure. Comparisons between different steels or for the same steel under different conditions are inappropriate. The most strictly comparable data are those for 3.5Ni-1.7Cr steels after heat treatments to obtain the same grain size and hardness. However, as we see from the table, data for this steel obtained by different research groups are

TABLE 3 Embrittlement sensitivities for steels (in K/at.% in g.b.)

Impurity	*System*	ξ	*Reference*
P	low-alloy steel	5.4	Guttmann [63]
	12%Cr-Ni-Mo	6.0	Guillou *et al.* [70]
	34CrMo4	6.7	Erhart *et al.* [51]
	16MCND6	5.9	Guttmann [71]
	16NC6	7.3	Guttmann [71]
	Z12CND12	7.6	Guttmann [71]
	3.5Ni-1.7Cr steel	16	McMahon *et al.* [72]
		10	Guttmann [66]
	Fe-P-C	20	Suzuki *et al.* [46, 54]
Sn	3.5Ni-1.7Cr steel	38	McMahon *et al.* [72]
		15	Guttmann [66]
Sb	3.5Ni-1.7Cr steel	67	McMahon *et al.* [72]
		28	Guttmann [66]
S	Fe-S-C	40	Suzuki *et al.* [47]
C	Fe-S-C	−10	Suzuki *et al.* [47]
	Fe-P-C	−20	Suzuki *et al.* [46, 54]

still scattered widely, probably owing to the difference in experimental conditions and calibration procedures for converting the Auger peak height ratio to the fracture surface coverage.

Ranges for the embrittlement sensitivities ξ_i, based on Table 3, have been summarized in the last column of Table 2. The plot of the ranges for the ξ_i against those for $(\Delta g_b^{0\prime} - \Delta g_s^{0\prime})$ at 300 K, also from Table 2, are shown in Fig. 8. These ranges are based on the values reported in different studies (often as few as two, defining the upper and lower limit to a range), and on other consideration as we have discussed, but include no account of uncertainties, or error bars, in any individual study. Thus, for example, we cannot at this point be certain that correct values for the ξ and $\Delta g_b^0 - \Delta g_s^0$ actually fall within the box shown for each segregant.

If there were none of the uncertainties or ambiguities mentioned in the values for the ξ_i and $\Delta g_b^{0\prime} - \Delta g_s^{0\prime}$, then the hypothesis could be judged as being supported if the data points fell approximately on a straight line, and not supported if otherwise. In the present situation there is little to conclude from Fig. 8. The trend for the detrimental segregants phosphorus, tin, antimony and sulphur cannot be judged as contradicting the hypothesis, given present uncertainties.

The straight line in Fig. 8 corresponds to $A = 0.37$ (K/at.% on g.b.)/(kJ mol^{-1}) = 1400 K/(J m^{-2}) in (37). Thus, from (36) if we assume $2s_{int} = (0.5 \text{ to } 1.0) \times 10^{-3}$ J m^{-2} K^{-1} [74, 75], that straight line implies

$$\partial F/\partial(2\gamma_{int}) \approx -(580 \text{ to } 820) \text{ K/(J m}^{-2}) \qquad (38)$$

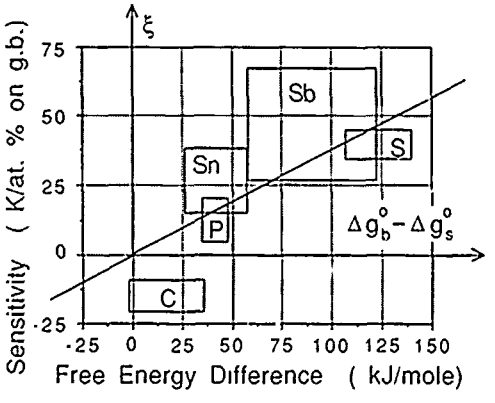

Fig 8 Plot of approximate ranges for embrittlement sensitivities, ξ, against approximate ranges for difference in free energy of segregation, $\Delta g_b^{0\prime} - \Delta g_s^{0\prime}$. See Tables 1–3 and text for discussion of data.

That is, each 0.1 J m^{-2} reduction in $2\gamma_{int}$ due to segregation of solutes such as phosphorus, tin, antimony or sulphur increases the DBTT by the order of 60 to 80 K.

Results for carbon in Fig. 8 are inconsistent with the trend of the other segregants. The $\Delta g_b^0 - \Delta g_s^0$ range that we give for carbon suggests that it is a mildly embrittling element. Such is not inconsistent with the net effect of carbon being beneficial, because it also displaces worse embrittlers from grain boundaries by site competition. However, there is evidence that after accounting for displacement effects, there is an additional effect of carbon as a cohesion enhancer (see for example refs. 46 and 54), signified by the negative ξ in Tables 2 and 3. This may mean that effects of carbon segregation on embrittlement cannot be understood in terms of an alteration of $2\gamma_{int}$. It is, nevertheless, well to remember that we have had to use the (100) crystal surface segregation energy for carbon, in absence of results for carbon adsorption on polycrystal surfaces created by intergranular fracture. As remarked, this may result in our reported range for $\Delta g_b^0 - \Delta g_s^0$ being a significant overestimate. The possibility cannot presently be ruled out that a more appropriate, polycrystalline range of $\Delta g_b^0 - \Delta g_s^0$ for carbon would be negative, in better agreement with the trend of proportionality of the ξ to the $\Delta g_b^0 - \Delta g_s^0$ that is required when $2\gamma_{int}$ controls embrittlement.

6. Summarizing remarks

We have reviewed theoretical models of intergranular fracture with an emphasis on understanding effects of solute segregation on the process. Of parameters susceptible to alteration by solute segregation, the models point to an important role for alterations of $2\gamma_{int}$, the ideal work of separation of an interface, in governing embrittlement. Nevertheless, alterations of the peak strength σ_{max}, the shape of the σ vs. δ relation and of other potentials for the interfacial region, and of poorly understood parameters characterizing dislocation generation at, and mobility through, the interface may also be important for embrittlement.

A thermodynamic framework is outlined which allows results of solute adsorption studies for grain boundaries and free surfaces to be used to estimate alterations in $2\gamma_{int}$ due to solute segregation. For light, sub-monolayer coverage, the

critical parameter giving the decrease of $2\gamma_{int}$ per unit increase of solute coverage is $\Delta g_b^0 - \Delta g_s^0$. This is the difference in the (inherently negative) free energies of segregation from the bulk to a grain boundary and from the bulk to a free surface. That is, it is the reversible work of moving a solute atom from a specific adsorption site along a free surface to a specific site along a grain boundary.

For the special case of dilute temper embrittling solutes in steels, or iron, we summarize data giving approximate ranges of the free energy difference. This can be done, with various uncertainties, for carbon, phosphorus, tin, antimony and sulphur.

The effects of such solute segregation on shifting the DBTT in the Charpy impact test has been summarized in terms of embrittlement sensitivities ξ. Values have been summarized here from the literature. We show that the hypothesis that embrittlement can be understood solely in terms of the effects of solute segregation on $2\gamma_{int}$ requires that the ratio of ξ to $\Delta g_b^0 - \Delta g_s^0$ be the same for every segregant. We attempt to use the available data to test the hypothesis, but the uncertainties in the data are too great to allow any sharp conclusions. Results for the detrimental segregants, phosphorus, tin, antimony and sulphur may plausibly support the hypothesis, but not those that we show for carbon. This may be either because carbon's effects (beyond those due to its displacement of deleterious segregants through site competition) are not explicable in terms of the effect of carbon segregation on $2\gamma_{int}$, or because the surface segregation energy that we have used in the correlation, available only for carbon on (100) surfaces, overestimates the magnitude of segregation energy for a polycrystal surface formed by intergranular fracture. If the latter is true, the hypothesis regarding $2\gamma_{int}$ may hold for carbon also.

It is unlikely that experimental techniques for study of surface and grain boundary adsorption will improve enough in the near future to significantly reduce the uncertainties that we have encountered. Possibly, first-principles quantum electronic calculations of the difference in bonding energies for a solute in a grain boundary and in a free surface environment will provide a quicker and more accurate route to understanding alterations of $2\gamma_{int}$ by solute segregation. Such calculations are encouraged and should also provide useful guidelines on what factors make for large or small, positive or negative (i.e. cohesion enhancing), values of $\Delta g_b^0 - \Delta g_s^0$.

More definitive fracture experiments than those provided by the Charpy test would also be of great help in testing theoretical concepts. Ideally, one might measure the macroscopic fracture energy G for bicrystal specimens, for a fixed set of adjoining crystal orientations and with variable amounts and types of segregated solutes for each such orientation, and characterize the extent to which G correlates with $2\gamma_{int}$ or with other quantities susceptible to alteration by solute segregation.

Acknowledgments

This study was supported by the NSF Materials Research Laboratory at Harvard University, and by the University of California through subcontract to Harvard based on support by the Office of Naval Research contract N00014-86-K-0753. We are grateful to Greg Olson for helpful discussion.

References

1 M. Guttmann and D. McLean, in W. C. Johnson and J. M. Blakely (eds.), *Interfacial Segregation*, ASM, Metals Park, OH, 1979, p. 261.
2 C. L. Briant and S. K. Banerji, in C. L. Briant and S. K Banerji (eds.), *Embrittlement of Engineering Alloys*, Academic Press, New York, 1983, p. 21.
3 A. Fraczkiewicz and M. Biscondi, *J. Phys. Paris Colloq. C4, 46* (1985) 497.
4 C. T. Liu, C. L. White and J. A. Horton, *Acta Metall., 33* (1985) 213.
5 C. L. White, *J. Vac. Sci. Technol. A, 4* (1986) 1633.
6 B. R. Lawn and T. R. Wilshaw, *Fracture of Brittle Solids*, Cambridge University Press, Cambridge, 1975.
7 J. R. Rice, *J. Appl. Mech., 55* (1988) 98.
8 J. R. Rice, in R. M. Latanision and R. H. Jones (eds.), *Chemistry and Physics of Fracture*, Martinus Nijhoff, Dordrecht, 1987, p. 22.
9 J. R. Rice, in H. Liebowitz (ed.), *Fracture: An Advanced Treatise*, Vol. 2, Academic Press, New York, 1968, p. 191.
10 A. C. Palmer and J. R. Rice, *Proc. R. Soc. London Ser. A, 332* (1973) 527.
11 J. H. Rose, J. R. Smith and J. Ferrante, *Phys. Rev. B, 28* (1983) 1835.
12 J. H. Rose, J. R. Smith, F. Guinea and J. Ferrante, *Phys. Rev. B, 29* (1984) 2963.
13 J. Ferrante and J. R. Smith, *Phys. Rev. B, 31* (1985) 3427.
14 R. Thomson, in R. M. Latanision and J. Pickens (eds.), *Atomistics of Fracture*, Plenum, New York, 1983, p. 167.
15 R. Thomson, in H. Ehrenreich and D. Turnbull (eds.), *Solid State Physics*, Vol. 39, Academic Press, New York, 1986, p. 1.
16 D. M. Esterling, *J. Appl. Phys., 47* (1976) 486.

17 B. de Cellis, A. S. Argon and S. Yip, *J. Appl. Phys., 54* (1983) 4864.
18 J. R. Rice, in R. E. Kelly (ed.), *Proc. 8th U.S. Natl. Congr. on Applied Mechanics*, Western Periodicals, N. Hollywood, 1979, p. 191.
19 J. F. Knott, in R. M. Latanision and J. Pickens (eds.), *Atomistics of Fracture*, Plenum, New York, 1983, p. 209.
20 J. F. Knott, in R. M. Latanision and R. H. Jones (eds.), *Chemistry and Physics of Fracture*, Martinus Nijhoff, Dordrecht, 1987, p. 44.
21 J. R. Rice, *J. Mech. Phys. Solids, 26* (1978) 61.
22 J. R. Rice, in A. W. Thompson and I. M. Bernstein (eds.), *Effect of Hydrogen on Behavior of Materials*, The Metallurgical Society of AIME, Warrendale, PA, 1976, p. 455.
23 D. D. Mason, *Philos. Mag., 39* (1979) 455.
24 M. P. Seah and D. Hondros, in R. M. Latanison and J. Pickens (eds.), *Atomistics of Fracture*, Plenum, New York, 1983, p. 855.
25 P. M. Anderson and J. R. Rice, *Scr. Metall., 20* (1986) 1467.
26 J.-S. Wang, P. M. Anderson and J. R. Rice, in M. G. Yan, S. H. Zhang and Z. M. Zheng (eds.), *Mechanical Behavior of Materials—V*, Pergamon, Oxford, 1987, p. 191.
27 J. Yu and J. R. Rice, in M. H. Yoo, C. L. Briant and W. A. T. Clark (eds.), *Interfacial Structure, Properties and Design*, Materials Research Society, Vol. 122, 1988, in press.
28 L. B. Freund and J. W. Hutchinson, *J. Mech Phys. Solids, 33* (1985) 169.
29 J. P. Hirth and J. Lothe, *Theory of Dislocations* (Appendix 2), McGraw-Hill, New York, 1968.
30 J. S. Wang, in M. H. Yoo, C. L Briant and W. A. T. Clark (eds.), *Interfacial Structure, Properties and Design*, Materials Research Society, Vol. 122, 1988, in press.
31 M. L. Jokl, V. Vitek and C. J. McMahon, Jr., *Acta Metall., 28* (1980) 1479.
32 E. W. Hart, *Int. J. Solids Struct., 16* (1980) 807.
33 C. Y. Hui and H. Riedel, *Int. J. Fracture, 17* (1981) 409.
34 K. K. Lo, *J. Mech. Phys. Solids, 31* (1983) 287.
35 P. A. Mataga, L. B. Freund and J. W. Hutchinson, *J. Phys. Chem. Solids, 48* (1987) 985.
36 J. R. Rice and M. A. Johnson, in M. F. Kanninen, W. F. Adler, A. R. Rosenfield and R. I. Jaffee (eds.), *Inelastic Behavior of Solids*, McGraw-Hill, New York, 1970, p. 641.
37 A. Needleman, submitted to *Int. J. Fracture.*
38 J. P. Hirth and J. R. Rice, *Metall. Trans. A, 11* (1980) 1502.
39 R. J. Asaro, *Phil. Trans. R. Soc. London Ser. A, 295* (1980) 150.
40 M. E. Eberhart, K. H. Johnson, R. P. Messner and C. L. Briant, in R. M. Latanision and J. Pickens (eds.), *Atomistics of Fracture*, Plenum, New York, 1983, p. 255.
41 D. McLean, *Grain Boundaries in Metals*, Oxford University Press, Oxford, 1957.
42 E. D. Hondros and M. P. Seah, *Metall. Trans A, 8* (1977) 1363.
43 H. Hänsel and H. J. Grabke, *Scr. Metall., 20* (1986) 1641.
44 H. Kimura, K. Abiko, S. Suzuki, M. Obata, J.-I. Kumagai and H. Kimura, in *Grain Boundary Structure and Related Phenomena*, Proc. JIMIS-4, 1986, p. 53.
45 H. Kimura, K. Abiko and S. Suzuki, in M. H. Yoo, C. L. Briant and W. A. T. Clark (eds.), *Interfacial Structure, Properties and Design*, Materials Research Society, Vol. 122, 1988, in press.
46 S. Suzuki, M. Obata, K. Abiko and H. Kamura, *Trans. Iron Steel Inst. Jpn., 25* (1985) 62.
47 S. Suzuki, S. Tani, K. Abiko and H. Kimura, *Metall. Trans. A, 18* (1987) 1109.
48 K. Abiko, S. Suzuki and H. Kimura, *Trans. Jpn. Inst. Metals, 23* (1982) 43.
49 R. Moller and H. J. Grabke, *Scr. Metall., 18* (1984) 527.
50 H. Erhart and H. J. Grabke, *Metall. Sci., 15* (1981) 401.
51 H. Erhart, H. J. Grabke and R. Möller, *Arch. Eisenhüttenwes, 52* (1981) 451.
52 M. Guttmann, Ph. Dumoulin and M. Wayman, *Metall. Trans. A, 13* (1982) 1693.
53 Y. E. Glickman, V. F. Kotyshev, Y. L. Cherpakov and R. E. Bruver, *Phys. Met. Metallogr. (U.S.S.R.), 36* (1973) 126.
54 S. Suzuki, M. Obata, K. Abiko and H. Kimura, *Scr. Metall., 17* (1983) 1325.
55 H. J. Grabke, in R. M. Latanision and R. H. Jones (eds.), *Chemistry and Physics of Fracture*, Martinus Nijhoff, Dordrecht, 1987, p. 388.
56 H. J. Grabke, *Steel Research, 57* (1986) 178.
57 G. Tauber and H. J. Grabke, *Ber. Bunsenges Phys. Chem., 82* (1978) 298.
58 K. S. Shin and B. H. Tsao, *Scr. Metall., 22* (1988) 585.
59 M. Rušenberg and H. Viefhaus, *Surf. Sci., 159* (1985) 1.
60 H. J. Grabke, W. Pualitschke, G. Tauber and H. Viefhaus, *Surf. Sci., 63* (1977) 377.
61 M. P. Seah and C. Lea, *Philos. Mag., 31* (1975) 627.
62 C. Lea and M. P. Seah, *Surf. Sci., 53* (1975) 273.
63 M. Guttmann, in R. M. Latanision and J. R. Pickens (eds.), *Atomistics of Fracture*, Plenum, New York, 1983, p. 465.
64 Ph. Dumoulin and M. Guttmann, *Mater. Sci. Eng., 42* (1980) 249.
65 J. M. Papazian and D. N. Beshers, *Metall. Trans., 2* (1971) 491.
66 M. Guttmann, *Phil. Trans. R. Soc. London Ser. A, 295* (1980) 169.
67 M. Guttmann, *Surf. Sci., 53* (1975) 168.
68 M. P. Seah, *Surf. Sci., 53* (1975) 213.
69 M. P. Seah, *Proc. R. Soc. London Ser. A, 349* (1976) 535.
70 R. Guillou, M. Guttmann and Ph. Dumoulin, *Metal Sci., 15* (1981) 63.
71 M. Guttmann, in R. M. Latanision and R. J. Courtel (eds.), *Advances in the Mechanics and Physics of Surfaces*, Vol. 1, Harwood Academic Publishers, Chur., 1981, p. 1.
72 C. J. McMahon, Jr. and L. Marchut, *J. Vac. Sci. Technol., 15* (1978) 450.
73 M. Guttmann, *Mater. Sci. Eng., 42* (1980) 227.
74 W. R. Tyson, *Can. Metall. Q, 14* (1975) 307.
75 L. E. Murr, *Interface Phenomena in Metals and Alloys*, Addison-Wesley, Boston, MA, 1975.

Materials Science and Engineering, A107 (1989) 41–47

Intrinsic Toughness of Interfaces*

A. S. ARGON, V. GUPTA, H. S. LANDIS† and J. A. CORNIE

Massachusetts Institute of Technology, Cambridge, MA 02139 (U.S.A.)

(Received June 1, 1988)

Abstract

The intrinsic delamination toughness of interfaces between thin coatings of SiC and substrates of either silicon single crystals or Pitch-55 carbon fibers can be determined accurately in many instances from the analysis of the spontaneous delamination phenomenon of such coatings when they are under residual tension or compression. When the thickness of such stressed coatings reach a critical threshold value, the elastic strain energy of material misfit stored in the coating becomes a driving force for delamination of the coatings in quasi-static equilibrium, starting from defects on the interfaces or edges. The analysis of this phenomenon has given delamination toughnesses for interfaces between SiC coatings and silicon single crystals and Pitch-55 carbon fibers, which range from 5.1 J m^{-2} to 5.95 J m^{-2}. Although somewhat high, these toughness levels are well within a factor of 2 of the expected true intrinsic interface toughnesses for these systems in the absence of any accompanying inelastic deformation.

1. Introduction

Interfaces play a key role in the mechanical behavior of heterogeneous solids. They govern the mode and extent of traction transmission between phases of different elastic and inelastic properties. When local tractions across interfaces reach a critical magnitude, the parting of interfaces initiates microcracks or voids, which transform a previously continuous solid into a discontinuous one, and set the stage for final fracture.

In many aligned fiber reinforced composites, the structural service requirements are almost entirely met by the volume fraction of stiff and strong, but brittle fibers. The matrix then acts merely to position the fibers in space and to impart to the composite a minimum level of transverse and longitudinal shear properties. It is now well recognized, however, that in such composites, the evolution of sub-critical damage under stress by correlated fiber fractures is governed by the mechanical coupling between fibers through the matrix. When the interfaces transmit all tractions fully and the coupling between fibers is too good, isolated fractures in fibers with small variability in strength tend to spread more readily to surrounding fibers, and hasten the development of a super-critical damage cluster (see *e.g.* Argon [1, 2]). In such instances, the strength of the composite is often less than the average strength of an unbonded bundle of similar fibers of equal length [2]. Thus, aligned fiber composites can often be made more damage tolerant, by decoupling fractured fibers from their neighbors through controlled delamination of their interfaces. Since many modern reinforcing carbon fibers are provided with protective coatings, it becomes possible to tailor the strength and toughness of the interfaces between coating and fiber to act as mechanical fuses to decouple broken fibers from their surroundings [3]. While considerable inelastic deformation in the surrounding matrix can accompany the propagation of a crack along the interface between the coating and the fiber, the intrinsic toughness of the interface sets the overall scale of the delamination toughness [4]. Thus, in controlling the performance of the composite through the control of the intrinsic interface toughness, it becomes of paramount importance to measure this toughness reliably.

Here, we will report briefly how, under special circumstances, the intrinsic toughness between certain coatings and substrates can be determined unambiguously through the analysis of the phen-

*Paper presented at the symposium on Interfacial Phenomena in Composites: Processing, Characterization, and Mechanical Properties, Newport, RI, June 1–3, 1988.

†Now with GTE Laboratories, Waltham, MA, U.S.A.

0921-5093/89/$3.50

© Elsevier Sequoia/Printed in The Netherlands

omenon of "spontaneous" delamination of coatings when they are residually stressed. A more detailed discussion of this phenomenon and its potential for interface toughness determination can be found elsewhere [5].

2. Residual stresses in vapor-deposited SiC coatings

Because of its hardness, low density, and chemical stability, SiC is the coating of choice for carbon fibers. It adheres well to carbon fibers and to most metal matrixes in which carbon fibers are used. In the cases to be discussed here, the SiC coatings have been applied by plasma-assisted chemical vapor deposition to both Pitch-55 carbon fiber and single crystal silicon substrates with (100) plane surfaces. In all instances, the as-deposited coatings of SiC were found to entrap large quantities of hydrogen gas—apparently in solid solution, resulting in significant incorporation of positive misfit in the plane of the coating, and establishment of biaxial residual compressive stress. When the coatings were applied to thin disk-shaped silicon single-crystal wafers on only one side, the level of these residual compressive stresses could be readily measured from the changed curvature of the disk from the simple relation:

$$\sigma = \frac{E_s h^2}{6(1-\nu_s)tR} \tag{1}$$

where R is the spherical radius of curvature of the substrate silicon disk, E_s and ν_s its Young's modulus and Poisson's ratio respectively, h its thickness, and t the thickness of the coating. This established that the residual compressive stresses in the as-deposited coatings were independent of the thickness of the coating, but were dependent only on the ion beam energy of the coating process, as shown in Fig. 1. Upon annealing of the coatings at 600 °C for 30 min, the entrapped hydrogen gas producing the positive misfit could be readily driven out, resulting in substantial reduction in coating thickness, but also in the development of substantial net negative biaxial misfit in the plane of the coating and associated biaxial residual tensile stresses. These tensile stresses could be as readily measured by changing curvature of the substrate disks. They too were found to be independent of coating thickness, but dependent on ion beam energy in a symmetrically reverse way for the levels of compressive stress in the as-deposited coatings, as shown also in Fig. 1.

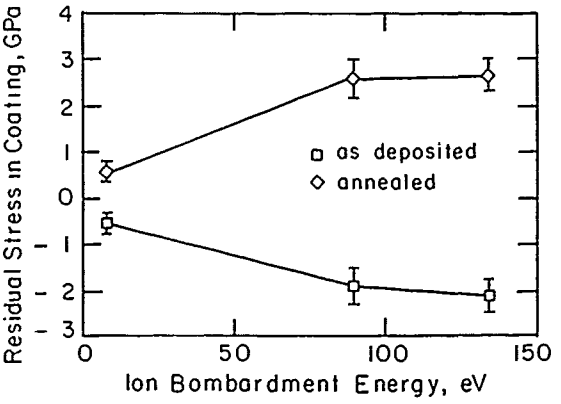

Fig. 1. Measured residual stresses in SiC coatings as a function of ion beam energy of the coating process for as-deposited coatings in compression and annealed coatings in tension.

Coatings applied to Pitch-55 carbon fiber in the same manner were of uniform thickness around the circumference of the fiber. Therefore, they did not produce curvature changes in the fibers, but showed identical changes in thickness and other delamination behavior upon annealing, which are presented below. From this, it is concluded that they too were under very similar sets of residual stresses, which also depended only on ion beam energy and not on the thickness of the coatings.

3. "Spontaneous" delamination of coatings

3.1. Threshold thickness of delamination

While thin coatings of submicron thicknesses were found to remain intact on both silicon and carbon fiber substrates for indefinitely long times, regardless of the level or type of the residual stresses, thicker coatings were found to delaminate from the substrates when their thicknesses exceeded a critical level. The forms of this delamination were radically different for coatings in compression from coatings in tension. In both cases, it was observed that when the coatings exceeded a threshold thickness, different in tension from that in compression, the rate of delamination increased with increasing thickness of coatings when the samples were observed in laboratory air. Beyond a certain thickness in excess of the threshold thickness, the delamination was nearly spontaneous upon removal of the samples from the coating apparatus, and happened even in the apparatus in vacuum. This suggests an element of stress corrosion cracking

in the delamination process occurring in laboratory air that needs to be investigated further. This conjecture is reinforced by the observation that coatings with thicknesses in excess of the threshold thickness for long-term delamination in air could be maintained intact when samples were stored in vacuum.

3.2. Delamination of coatings with tensile misfit strain

In annealed coatings with tensile misfit strain on silicon single-crystal substrates, the first form of delamination was the formation of columnar cracks in the coatings, parallel to the ⟨110⟩ directions of the silicon single-crystal substrates. These directions are 16% stiffer in the (100) surface of the crystal than the corresponding orthogonal set of ⟨100⟩ directions. Upon cracking, coatings were found to delaminate in ribbon-shaped slabs, starting from the free ends where parallel coating cracks were arrested by a previously established crack of the orthogonal family, as shown in Figs. 2(a) and 2(b). In Fig. 2(a), the extent of coating delamination from the substrate is clearly visible from the darker contrast of the ribbon relative to its surroundings. The delaminated ribbon continues to lie flat on the substrate, clearly because the residual tensile stress in it that has been relieved by the delamination was uniform across the thickness. Figure 2(b) shows a gap at the end of the ribbon between it and the upper portion of the surrounding coating which still remains attached to the substrate. These gaps, which could be readily measured at many places, when divided by the length of the delaminated ribbon furnished an independent measure of the initial material misfit strain ε_m. These misfit strains, when divided into the residual tensile stress in the coatings prior to the onset of the delamination, permitted the determination of the Young's modulus of the coatings from eqn. (2) below:

$$E = \frac{(1-\nu)\sigma}{\varepsilon_m} \tag{2}$$

where the Poisson's ratio of the coating was taken to be 0.3, since it could not be measured independently. These measurements established that the Young's modulus of the annealed SiC coatings depended uniquely on the initial ion beam energy of the coating process, as shown in Fig. 3, and indicated that the ion beam energy governs the structure of the coating.

The observations of a well-defined delamination threshold in the thickness of the coatings with tensile misfit indicate that this delamination is driven by the elastic strain energy stored in the coating. In such problems of biaxially stressed

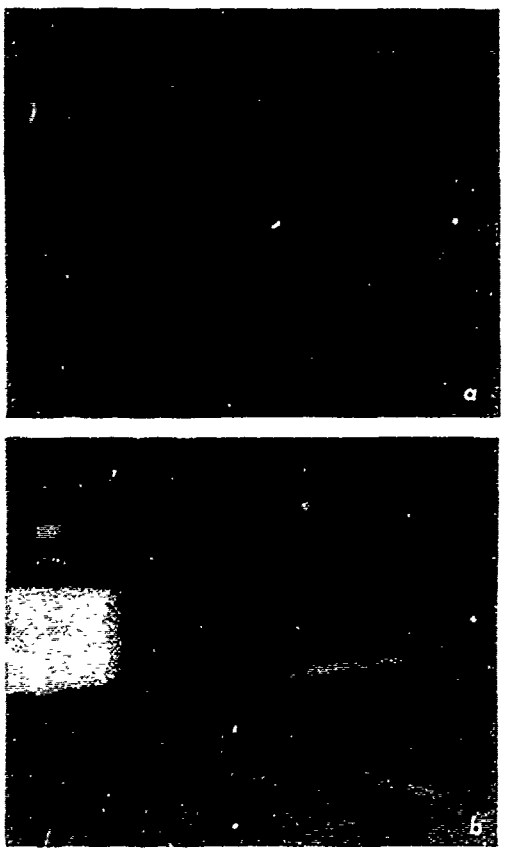

Fig. 2. Example of a ribbon-like delamination of an annealed SiC coating in tension: (a) low magnification view showing extent of delaminated ribbon, (b) high magnification view showing the initial tensile material misfit displacement.

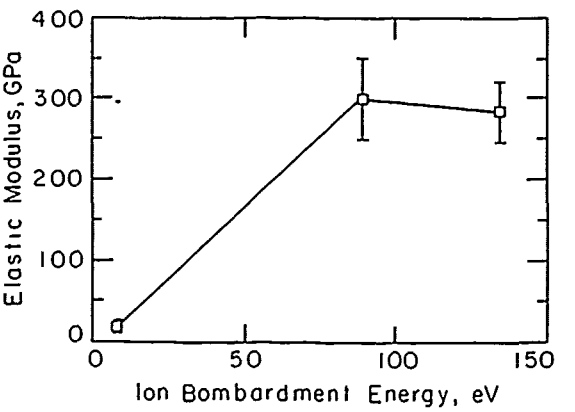

Fig. 3. Dependence of the Young's modulus of SiC coatings in tension, on the ion beam energy of the coating process.

thin coatings resulting from a constant material misfit independent of thickness, the elastic strain energy almost entirely resides in the coating, with only a negligible contribution coming from the much thicker substrate [5]. Thus, for very thin coatings where the elastic strain energy per unit area of the interface is less than the interface toughness, the coating remains intact indefinitely. As the thickness of the coating increases, the available elastic strain energy per unit area increases monotonically until it becomes equal to the intrinsic interface toughness* (or energy release rate) G_{co}. Then, the coating can delaminate away from the substrate under quasi-static conditions, starting from any interface defect or pre-crack. For thicknesses greater than the critical thickness, the delamination will occur with increasing velocity. From elementary considerations, the G_{co} is given by [5]:

$$G_{co}=\frac{\sigma^2(1-\nu)t_c}{E}=\frac{\varepsilon_m{}^2 E t_c}{(1-\nu)} \qquad (3)$$

where σ, ε_m, E, ν, t_c are respectively the biaxial residual tensile stress, the biaxial material misfit strain, the Young's modulus, the Poisson's ratio, and the critical (threshold) thickness—all of the coating. This interface toughness, determined from evaluation of eqn. (3) is shown in Fig. 4. It is found from here that the interface toughness is constant, within experimental error, and does not depend on ion beam energy. Its average value is 5.1 J m^{-2} for coatings in residual tension.

3.3. Delamination of coatings with compressive misfit strain

In the as-deposited coatings, the residual stress is compressive, as stated above. There too, the elastic strain energy stored in the coating per unit area of the interface increases monotonically with thickness of the coating. The delamination of these coatings from the substrate, however, exhibits a very different form. Here, it is found that coatings of considerably greater thickness remain attached intact to the substrate. When they reach a new critical thickness in the range of 1.0 μm, they are found to separate by forming a blister which lifts off the substrate in a regularly buckled form, as shown in Fig. 5, where a number of blisters in various stages of separation can be seen. At (A), the blisters are just large enough to produce two half waves of vertical buckling; at (B), large blisters have settled into a form where they propagate radially outward in quasi-static equilibrium, with a self-similar circumferential buckling

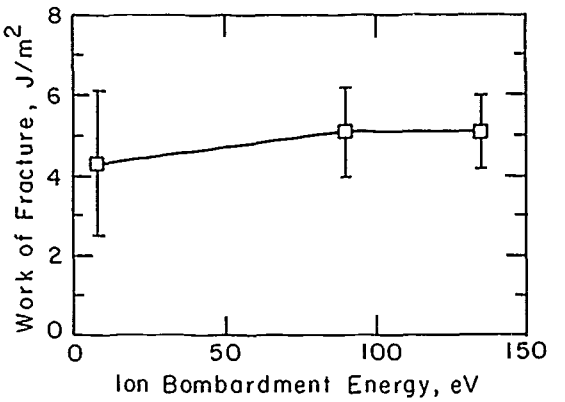

Fig. 4. Interface toughness as a function of ion beam energy.

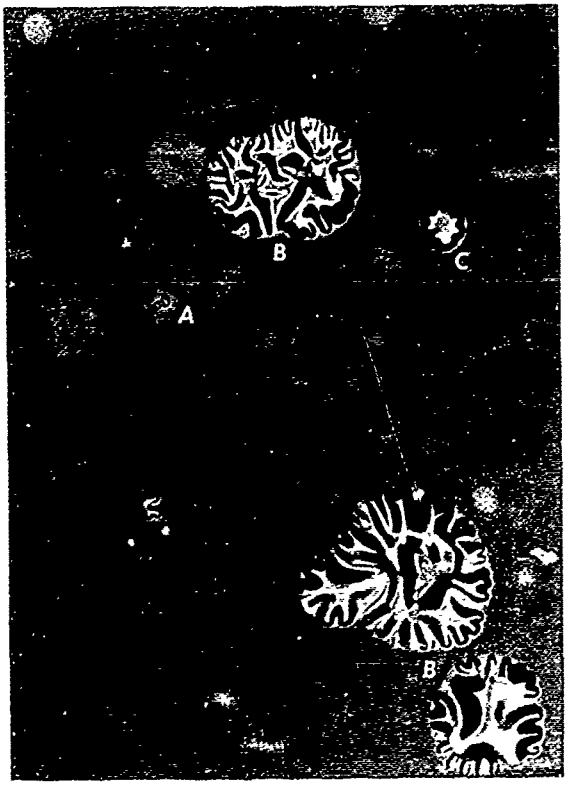

Fig. 5. Delamination blisters in an as-deposited coating in biaxial compression. (A) smallest size blister just lifting off, B. large blisters growing radially outward, with a self-similar and regular circumferential buckled form, (C) a blister just large enough to assume a regular circumferential buckled shape.

*Although unconventional, we use the word toughness here for G_{co} in preference to "specific work of fracture" or "critical energy release rate"

wavelength l. This wavelength appears just established in the small blister shown at (C).

Detailed observations of the growth of the blister with Nomarski interference contrast microscopy showed that, as the blister front advances radially outward, first the radial residual stress is relieved, apparently by slippage of the coating radially inward over a process zone of several μm in width. This is followed by the partial relief of the circumferential stress by the formation of the circumferential buckles, with a wavelength l, that depends on the initial biaxial residual compressive stress σ given by eqn. (4) below [5]:

$$l = \pi t \left\{ \frac{E}{3(1-\nu^2)\sigma(1-\nu)} \right\}^{1/2} \tag{4}$$

In eqn. (4), E is the Young's modulus of the coating, t its thickness, and ν its Poisson's ratio, which we take to be 0.3. Since the residual compressive stress can be measured independently from the curvature of the substrate attached to the coating, and l can be measured from the micrographs, such as Fig. 5, the modulus of the coating can be calculated from eqn. (4). When this was done for a coating of 1.1 μm threshold thickness with a measured l of 20 μm, and residual compressive stress of 2 GPa, E was found to be 116 GPa.

Further elementary analysis of the remaining elastic strain energy U_t per unit area of interface in the post buckled shape of the coating establishes it to be [5]

$$U_t = \frac{\pi^4 E t^5}{9(1-\nu^2)^2 l^4} \tag{5}$$

In the same fundamental parameters, the initial strain energy per unit area of interface prior to the formation of the blister is [5]

$$U_i = \frac{\pi^4 E t^5}{9(1-\nu^2)^2(1-\nu) l^4} \tag{6}$$

At the critical threshold thickness t_c, the difference between (6) and (5) should provide for the intrinsic toughness G_{co} of the interface, *i.e.*

$$G_{co} = \frac{\nu \pi^4 E t_c^5}{9(1-\nu^2)^2(1-\nu) l^4} \tag{7}$$

Evaluation of typical cases already referred to above gave an interface toughness of $G_{co} = 5.95$ J m^{-2}, which is 14% higher than the value determined for coatings in residual tension. This difference is attributed to the additional and possibly different dissipative work of slippage between coating and substrate during the release of the radial stress.

3.4. Delamination of coatings from Pitch-55 carbon fibers

The same phenomenon of spontaneous delamination of SiC coatings with tensile misfit was found also with Pitch-55 carbon fibers. When such fibers were coated followed by the annealing treatment of 600 °C for 30 min, the coatings were found to remain stable and intact, if their thicknesses were less than 0.33 μm for coatings deposited at low ion beam energy. When coatings with thickness slightly exceeding this thickness, having the above process history, were left in laboratory air with the usual relative humidity of 60% for several months, they were found to undergo copious and complete delamination by cracking and flaking, as shown in Fig. 6.

The initial biaxial misfit strain ε_m between coating and fiber could again be determined from the ratio of the average gap size between flakes to the average dimension of the flakes. With this information, and the assumption that the modulus of the coating in tension is given uniquely by Fig. 3 as being a function of only the ion beam energy, and the further assumption that the Poisson's ratio remained at 0.3, the threshold elastic strain energy of the coating per unit area could be calculated and equated to the fracture toughness of the interface to simply result in [5]

$$G_{co} = \frac{\varepsilon_m^2 E t_c}{(1-\nu)} \tag{8}$$

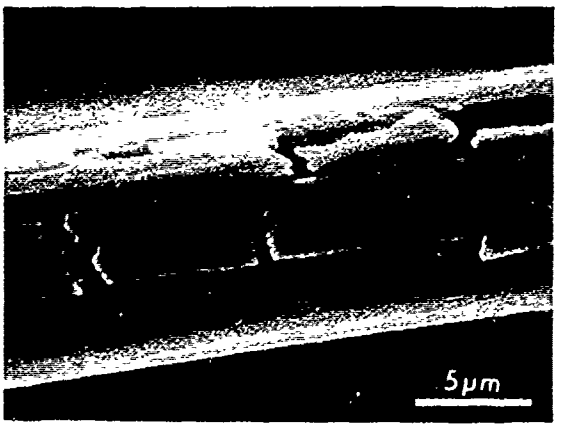

Fig. 6. Flakes of delaminated SiC coatings on a Pitch-55 carbon fiber.

for coating thickness to fiber radius ratio $t/R \ll 1$. Evaluation of these results for a typical case of coating with a modulus of 16 GPa threshold thickness of 0.33 μm, and misfit strain of 2.7×10^{-2} on a fiber with a radius of 5 μm, the interface toughness was calculated to be $G_{co} = 5.47$ J m^{-2}. This is quite close to the value of 5.1 J m^{-2} determined for the SiC/Si pair.

4. Discussion

The phenomenon of spontaneous delamination of coatings under residual stress from more massive substrates occurs quasi-statically when the elastic strain energy of misfit per unit area equals the intrinsic work of separation of the coating from the interface. The analysis of the conditions of such delamination provides the much-needed informaton on the intrinsic toughness of the interface. Apart from small differences between the various modes of separation presented above, the interface toughness is independent of the state of stress in the coating. Furthermore, the toughness of the interface between SiC coatings and carbon fibers is also quite close to that measured for the SiC/Si pair.

Observation of such delamination events is not new. Evans and Hutchinson [6] have reported somewhat similar delamination phenomena for interfaces between surface layers and substrates in microelectronics components, but observed a rather different process in the delamination of the layers in compression, which was less informative.

It must be noted that the simplicity of the phenomenon reported above results from the sharply defined nature of the interface, and the condition that the interface toughness is evidently less than the toughness of either the coating or the substrate, so that delamination cracks remain in the interface and do not wander into either of the two adjoining materials.

Under these conditions, furthermore, where the elastic strain energy of misfit is overwhelmingly stored in the coating, the nature of the stress intensity at the tip of the interface crack must be even more complicated than the complex stress intensities and their associated oscillatory tractions that have been extensively discussed in the literature [7–9]. Clearly, in this case, the singular component of the stress field ahead of the crack must be of very short range and, while it must be of opposite sign for the two cases of tensile and compressive misfit, the delamination remains in the plane of the interface. A clue to this unique behavior is likely to be the Nomarski interference contrast microscopy observation noted above and discussed in more detail elsewhere [5] that, at least in the case of the enlargement of the compression blister, the delamination may be preceded by some slippage in the interface prior to lift off of the coating. This may also account for the magnitudes of the interface toughness that have been obtained. Thus, in the absence of any dissipative work, the toughness of an interface must be:

$$G_{co} = \chi_A + \chi_B - \chi_{AB} \tag{9}$$

where χ_A and χ_B are the surface energies of components A and B, and χ_{AB} the specific interface energy between A and B. Although good measurements of either the surface energies of silicon, or SiC, or their interface energy do not exist, a simple estimate can show that the measured interface toughnesses are considerably in excess of what could be expected. The surface energy of silicon measured by Gilman [10] in cleavage experiments is 1.24 J m^{-2}. If the surface energy of SiC is estimated to be higher in the ratio of the Young's moduli of SiC to silicon, *i.e.* by a factor of 2.04, it should be 2.53 J m^{-2}. Thus, considering the interface energy between silicon and SiC to be somewhere of the order of 1 J m^{-2}, it is clear that the measured interface toughnesses are about twice what might be expected from eqn. (9). Clearly, therefore, even in this very short-range crack tip stress field, as it propagates along the interface, additional dissipative work is done which we propose is expended by some relative slippage between coating and substrate prior to lift off of the coating.

On the whole, however, we conclude that the interface toughnesses that we have reported are quite meaningful and that the spontaneous delamination experiment can be used within these limitations to monitor changes of interface adhesion in tailoring the properties of interfaces in the quest of making tougher and more damage-tolerant composites.

Acknowledgments

This research has been supported by DARPA, ONR, and Naval Air Development Center under Contract No. N00014-84-K and IST/SDIO under Contract No. N00014-85-K-0645. Addi-

tional support also came from the MIT Consortium for Processing and Evaluation of Metal and Ceramic Matrix Composites.

References

1 A. S. Argon, in H. Herman (ed.), *Treatise on Materials Science and Technology*, Academic Press, New York, 1972, p. 79.
2 A. S. Argon, in L. J. Broutman and R. H. Krock (eds.), *Composite Materials: Fracture and Fatigue*, Academic Press, New York, 1974, p. 253.
3 V. Gupta, A. S. Argon and J. A. Cornie, *J. Mater. Sci.*, in the press.
4 J. R. Rice, in T. Yokobori *et al.* (eds.), *Proc. 1st Int. Conf. on Fracture*, Japanese Society for Strength and Fracture of Materials, Sendai, Japan, 1965, p. 309.
5 A. S. Argon, V. Gupta, H. S. Landis and J. A. Cornie, *J. Mater. Sci.*, in the press.
6 A. G. Evans and J. W. Hutchinson, *Int. J. Solids Struct.*, *20* (1984) 455.
7 J. R. Rice and G. S. Sih, *J. Appl. Mech.*, *32* (1965), 418.
8 M. Comninou, *J. Appl. Mech.*, *44* (1977) 631.
9 J. W. Hutchinson, M. E. Mear and J. R. Rice, *J. Appl. Mech.*, *54* (1987) 828.
10 J. J. Gilman, *J. Appl. Phys.*, *31* (1960) 2208.

Materials Science and Engineering, A107 (1989) 49-61

On Microstructural Evolution and Micromechanical Modelling of Deformation of a Whisker-reinforced Metal–Matrix Composite*

T. CHRISTMAN, A. NEEDLEMAN, S. NUTT and S. SURESH

Division of Engineering, Brown University, Providence, RI 02912 (U.S.A.)

(Received June 1, 1988)

Abstract

The precipitation characteristics, the mechanisms of accelerated aging, and the variation of uniaxial tensile stress–strain behavior in response to controlled variations in matrix microstructure were investigated for a 2124 Al–SiC whisker composite. The yield strength of the composite was found to be independent of matrix aging condition. However, the overall ductility decreased monotonically with an increase in aging time. A finite element analysis of the constitutive response of the composite is presented. The results of these calculations, as well as the predictions of several models for composite strengthening available in the literature, were compared with the experimental results. The presence of brittle whiskers in aluminum leads to a significant build-up of hydrostatic stresses in the matrix during plastic deformation. Void formation in the matrix of the composite as well as at the whisker–matrix interface appears to play an important role in controlling the overall failure mechanisms. Transmission electron microscopy observations of void formation at whisker ends are described for composite specimens strained in tension at room temperature and at 300 °C. A detailed discussion of matrix deformation and interfacial debonding is presented in an attempt to identify the origins of low ductility in discontinuously reinforced metal–ceramic composites.

1. Introduction

With recent advances in processing technology, the ability to produce, in economically feasible quantities, a wide range of metal–matrix composites is increasing dramatically. Metals, reinforced with brittle particles, often referred to as discontinuously reinforced metal–matrix composites, constitute a large portion of these advanced materials. Particle-reinforced metal–matrix composites are both machinable and workable using conventional processing techniques, and the manufacturing of these materials can easily be scaled up to production quantities. Experimental results of stress–strain relations for these materials have been reported previously [1–5], although the effects of systematic variations in the matrix microstructure on the overall composite properties have not been examined. Recent work has demonstrated that aging-induced precipitation and microstructural evolution in the matrix of whisker-reinforced composite materials can be significantly accelerated compared with those of the unreinforced matrix material subjected to identical heat treatments [6–8]. These results indicate that conventional heat treatments for unreinforced commercial aluminum alloys should not be directly applied to the microstructural design of composite materials although this is often the practice [1–5, 9, 10]. A thorough examination of microstructural evolution in the matrix of the composite and its effects on overall mechanical behavior is critical to a more complete understanding of the constitutive response and to the evaluation of composite strengthening theories. The low ductility exhibited by discontinuously reinforced metal–matrix composites is the primary obstacle preventing their introduction into many structural applications. Yet the influence of controlled matrix microstructural variations on the strain-to-failure of whisker-reinforced metal–matrix composites remains poorly understood. This report will focus on experimental observations and finite element analysis of the effects of matrix microstructural variations on the uniaxial stress–strain response of a discontinuously reinforced metal–matrix composite in an attempt to better understand the failure mechanisms.

*Paper presented at the symposium on Interfacial Phenomena in Composites: Processing, Characterization, and Mechanical Properties, Newport, RI, June 1–3, 1988.

0921-5093/89/$3.50

© Elsevier Sequoia/Printed in The Netherlands

The material selected for this study was a 2124 Al-15 wt.%(13vol.%)SiC whisker reinforced metal-matrix composite obtained from ARCO Chemicals, Greer SC, produced using powder metallurgy techniques. The 2124 Al matrix material had a nominal composition, in weight percent. of 4%Cu-2%Mg-0.4%Mn, with the balance Al. For comparison where appropriate, an unreinforced alloy of 2124 Al, that was identically processed from the same powder batch and subjected to identical solutionizing and aging treatments, was also studied. The whiskers used in this study were the highest quality available and were classified as F-9. The average dimensions of the whiskers before processing were 0.5 μm in diameter and 25 μm in length. However, due to the severe deformation involved in processing of the composite material, significant breakage of the whiskers occurred and the average length of the whiskers in the as-extruded material was about 2.5 μm. A systematic microstructural characterization and aging study of the same extruded bars of the composite and control alloy was performed by Christman and Suresh [6] and will be briefly reviewed in a later section (the reader is referred to the original paper for a more complete discussion). Furthermore, composite damage mechanisms operative during uniaxial tensile tests at high temperatures will be discussed and compared with damage mechanisms at room temperature.

A finite element unit cell model was used to predict the uniaxial stress strain response of the composite material as a function of matrix microstructural variations. The model approximates the stress-strain response of a single, rigid cylindrical inclusion in an elastic power-law hardening viscoplastic matrix material. The matrix and whisker parameters were taken directly from experiments (when possible), thereby minimizing the number of adjustable variables. The experimental observations were compared with the numerical predictions and the implications of the results are discussed in the context of the mechanisms responsible for the high values of yield strength and the low values of ductility displayed by the material.

2. Microstructural evolution

Recently, Christman and Suresh [6] conducted a study of the microstructural evolution and aging kinetics in the 2124 Al-SiC whisker composite and control alloy used in this study, utilizing analytical transmission electron microscopy techniques, matrix microhardness measurements and conductivity measurements. The aim of the work reported in ref. 6 was to examine the effects on the matrix of the composite produced by the introduction of the whiskers in controlled microstructures by a comparison of reinforced and unreinforced materials.

The composite and control alloy were received in the as-extruded condition, solution-treated at 504 °C for 4 h, water quenched, and subsequently aged at 177 °C for various times. The microstructural condition of the matrix material was determined by microhardness measurements (Fig. 1(a)) and by analytical electron microscopy. With the addition of the SiC whiskers, the peak aging time of the matrix of the composite is drastically reduced from 12 h (for the control alloy) to about 3 h. Another interesting feature of this

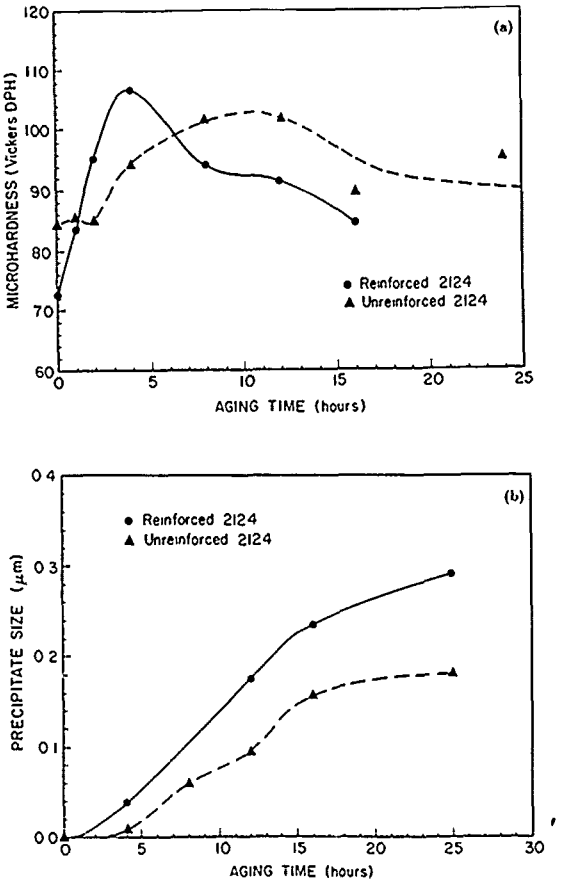

Fig. 1. The variation of (a) microhardness and (b) precipitate size with aging time (after ref. 6).

graph is that there is no appreciable vertical shift in the microhardness values, that is the composite matrix is not significantly harder than the unreinforced material. This result suggests that it would be possible to use the bulk mechanical properties of the control alloy for the matrix properties of the composite in theoretical calculations of the constitutive response of the composite, with proper adjustments for changes in the aging curves. This inference has a strong bearing on the evaluation of composite strengthening theories which will be discussed in a later section.

The transmission electron microscopy (TEM) results showed that the age-hardening precipitates, S′, evolve into corrugated sheets after nucleating on dislocations and growing in the three preferential (001) directions. This type of precipitation sequence is typical of Al–Cu–Mg alloy systems and is well documented in the literature [11–13]. There is little preferential precipitation or precipitate-free zones at or near the whisker–matrix interface. The rate of nucleation of the precipitates, however, was different between the reinforced and unreinforced materials. The reinforced material showed evidence of S′ nucleation after less than 1 h of artificial aging at 177 °C, whereas the unreinforced material required up to 4 h of aging at this temperature before any S′ could be detected, Fig. 1(b).

The accelerated aging of the composite matrix material is aided by a decrease in the incubation time for the nucleation of age-hardening precipitates. The large thermal contraction mismatch between the aluminum matrix and the SiC whiskers gives rise to residual stresses upon cooling from the solutionizing temperature. Dislocations are punched out from whisker ends during cooling to relieve part of the residual stresses at the interface. For 2124 Al–13.2vol.%SiC composite, the dislocation punching distance (calculated from ref. 14) is sufficiently large to cover the majority (approximately 75%) of the matrix with excess dislocations. Transmission electron microscopy studies by Christman and Suresh [6] indicate that the dislocations in the matrix of the composite serve as nucleation sites for the formation of S′ precipitates during the aging of the composite. This facilitates the attainment of peak matrix hardness at much shorter times than in the control alloy.

The theory for accelerated aging listed above is supported by a wide variety of evidence (Christman and Suresh [6]):

(1) TEM studies of the composite material and unreinforced alloy reveal increased dislocation density in the matrix of the composite.

(2) TEM studies also reveal that the strengthening precipitates nucleate preferentially along dislocation lines.

(3) Little preferential precipitation or precipitate free zone at or near the whisker interfaces was observed.

(4) Quantitative analysis of the growth kinetics of the strengthening precipitates for both the reinforced and unreinforced materials shows a shift in nucleation time but not in growth kinetics.

(5) Measurements of changes in electrical conductivity are consistent with the proposed model.

(6) Cold working of the unreinforced material also produces an accelerated aging effect.

(7) Recent *in situ* TEM experiments have demonstrated dislocation punching at whisker ends during cooling of the metal–matrix composites [15].

(8) Calculations of dislocation punching distance agree well with the observed dislocation distribution.

3. Experimental method

The composite material selected for this investigation was the same material used in the previously mentioned characterization study [6] and was a 2124 powder metallurgy aluminum alloy containing 13.2 vol.% SiC whiskers. In order to form a basis for comparison, a control alloy with an identical processing history from the same powder batch containing no reinforcement was also studied. The material was received as-extruded, in bars measuring 12.74 mm × 127 mm × 1500 mm in size. The heat treatments were designed to achieve identical values of microhardness in the unreinforced control alloy and in the matrix of the reinforced material. The heat treatment schedules were chosen to obtain two underaged conditions, the peak aged condition, and two overaged conditions as outlined in Table 1. After heat treatment, the samples were stored in a commercial freezer in order to prevent any aging at room temperature.

Tensile tests were performed on an Instron screw-driven testing machine at room temperature using samples conforming to ASTM standard E8-83 for sub-size specimens. The samples were machined prior to heat treatment because machining has been shown to alter the aging state

TABLE 1 All samples solutionized 504 °C for 4h and water quenched

Aging time (h) at 177 °C		
Condition	*Reinforced*	*Unreinforced*
UA1	1	1
UA2	2	4
PA	4	12
OA1	12	16
OA2	16	24

of the material [16]. The strain rate applied to the samples was 2.7×10^{-4} s^{-1} and strain was monitored with a clip gage type extensometer mounted on the sample. Load and strain output were recorded directly on a HP model 7044A XY recorder for subsequent analysis. Microscopic examination of the fracture surfaces was performed with an AMR model 1000A scanning electron microscope.

4. Finite element formulation and material model

The finite element analysis is based on a convected coordinate Lagrangian formulation of the field equations with the initial unstressed state taken as a reference. All field quantities are considered to be functions of convected coordinates, y^i, which serve as particle labels, and time, t. This formulation has been employed extensively in previous finite element analyses, see, for examples, refs. 17–19.

Attention is confined to quasi-static deformations and, with body forces neglected, the rate form of the principal of virtual work is written as

$$\Delta t\int_V [\dot{\tau}^{ij}\delta E_{ij}+\tau^{ij}\dot{u}_{,i}^{\ k}\delta u_{k,j}]\,dV$$

$$=\Delta t\int_S \dot{T}^i\delta u_i\,dS-\left[\int_V \tau^{ij}\delta E_{ij}\,dV-\int_S T^i\delta u_i\,dS\right] \quad (1)$$

Here, τ^{ij} are the contravariant components of the Kirchhoff stress ($\tau=J\sigma$, with σ being the Cauchy stress) on the deformed convected coordinate net and V and S being the volume and surface, respectively, of the body in the reference configuration; $\dot{(\cdot)}=\partial(\ )/\partial t$ at fixed y^i and the second term on the right-hand side represents an equilibrium correction term that is used in the numerical procedure to reduce drift from the equilibrium path due to the discrete time step. The nominal traction components, T^i, and the Lagrangian strain components, E_{ij}, are given by

$$T^i=(\tau^{ij}+\tau^{kj}u_{,k}^{\ i})\nu_j \quad (2)$$

$$E_{ij}=\tfrac{1}{2}(u_{i,j}+u_{j,i}+u_{,i}^{\ k}u_{k,j}) \quad (3)$$

where ν is the surface normal in the reference configuration, u_j are the components of the displacement vector on base vectors in the reference configuration, and $(\ )_{,i}$ denotes covariant differentiation in the reference frame.

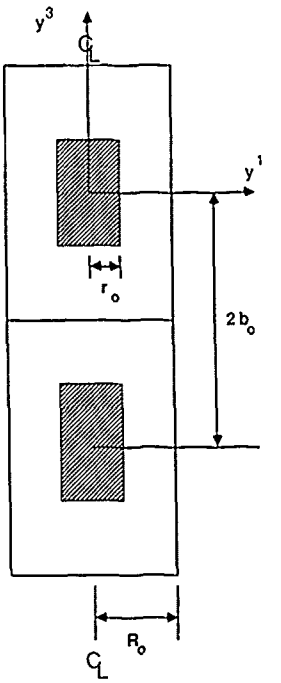

Fig 2 A schematic diagram of the finite element model. The tensile axis, the y^3 axis, is taken to be the centerline. Because of symmetry conditions, it is only necessary to analyze one quadrant of the unit cell.

A cylindrical coordinate system (r,θ,z) is used where the identifications $y^1=r, y^2=\theta$ and $y^3=z$ are made. As shown in Fig. 2, we consider circular cylindrical fibers of radius r_0 embedded in a circular cylindrical cell of radius R_0 and length $2L_0$ and with an initial spacing of $2b_0$ between fiber centers. Attention is confined to axisymmetric deformations so that all field quantities are independent of θ and within each cell symmetry is assumed about the center line. Furthermore, the circular cylindrical cell surrounding each fiber is required to remain a circular cylinder throughout the deformation history. As discussed by Tvergaard [20], this axisymmetric configuration can be considered an

approximation to a three-dimensional array of hexagonal cylinders.

The boundary conditions for the axisymmetric region analyzed numerically are:

$$\dot{u}^3 = 0 \qquad \dot{T}^1 = 0 \qquad \text{on } z = 0 \tag{4}$$

$$\dot{u}^3 = \dot{U}_3 = \dot{\varepsilon}_\infty (b_0 + U_3) \qquad \dot{T}^1 = 0 \quad \text{on } z = b_0 \tag{5}$$

$$\dot{u}^1 = \dot{U}_1 \qquad \dot{T}^3 = 0 \qquad \text{on } r = R_0 \tag{6}$$

Here, $\dot{\varepsilon}_\infty$ is a prescribed constant while $\dot{U}_1$ is determined from the condition that the average lateral traction rate vanishes, *i.e.*

$$\int_0^{b_0} \dot{T}^1 \, dz = 0 \qquad \text{on } r = R_0. \tag{7}$$

In addition to the boundary conditions (4) to (7), there is the requirement that displacement components vanish on the surface of the rigid fiber.

In some calculations, a second set of boundary conditions was employed consisting of (4) and (5), but with (6) and (7) replaced by $\dot{T}^1 = 0$ on $r = R_0$, so that every point along $r = R_0$ is stress free. Under these conditions the outer sidewall of the cell does not remain straight and vertical. Of course, for the entire tension specimen, $\dot{T}^1 = 0$ on the outer boundary of the specimen. However, when, as here, the fibers are much smaller than the specimen, the condition that the circular cylindrical cell remain a circular cylinder comes from enforcing geometric compatibility (within the axisymmetric approximation) for a uniform array of fibers perfectly aligned with the tensile axis. Relaxing the boundary condition (6) and (7) permits, in a highly approximate manner, consequences of deviations from this highly constrained fiber distribution to be explored. In subsequent discussion, predictions based on (6) and (7) are referred to as results "with constraint" and predictions based on $\dot{T}^1 = 0$ on $r = R_0$ are referred to as results "without constraint".

The material is characterized as an isotropically hardening elastic viscoplastic solid and the total rate of deformation, **D**, is written as the sum of an elastic part, $\mathbf{D}^e$, and a plastic part, $\mathbf{D}^p$, with

$$\mathbf{D}^e = \frac{1+\nu}{E} \hat{\boldsymbol{\tau}} - \frac{\nu}{E} (\hat{\boldsymbol{\tau}} : \mathbf{I}) \mathbf{I} \tag{8}$$

$$\mathbf{D}^p = \frac{3\dot{\bar{\varepsilon}}}{2\bar{\sigma}} \boldsymbol{\tau}' \tag{9}$$

where $\hat{\boldsymbol{\tau}}$ is the Jaumann rate of Kirchhoff stress, **I** is the identity tensor, **A**.**B** denotes $A^{ij}B_{ji}$, $\dot{\bar{\varepsilon}}$ is the effective strain rate, E is the Young's modulus, ν is Poisson's ratio and

$$\boldsymbol{\tau}' = \boldsymbol{\tau} - \tfrac{1}{3}(\boldsymbol{\tau} : \mathbf{I})\mathbf{I} \qquad \bar{\sigma}^2 = \tfrac{3}{2}\boldsymbol{\tau}' : \boldsymbol{\tau}' \tag{10}$$

$$\dot{\bar{\varepsilon}} = \dot{\varepsilon}_0 [\bar{\sigma} / g(\bar{\varepsilon})]^{1/m} \qquad g(\bar{\varepsilon}) = \sigma_0 (\bar{\varepsilon}/\varepsilon_0 + 1)^N$$

$$\varepsilon_0 = \sigma_0 / E \tag{11}$$

Here, $\bar{\varepsilon} = \int \dot{\bar{\varepsilon}} dt$ and the function $g(\bar{\varepsilon})$ represents the effective stress *vs.* effective strain response in a tensile test carried out at a strain rate such that $\dot{\bar{\varepsilon}} = \dot{\varepsilon}_0$. Also, σ_0 is a reference strength and N and m are the strain hardening exponent and strain rate hardening exponent, respectively.

Combining eqns. (8) and (9) and inverting gives,

$$\hat{\boldsymbol{\tau}} = \frac{E}{1+\nu} \left[\mathbf{D} + \frac{\nu}{1-2\nu} \mathbf{I}(\mathbf{I} : \mathbf{D}) \right] - \frac{3\dot{\bar{\varepsilon}}}{2\bar{\sigma}} \mathscr{L} : \boldsymbol{\tau}' \tag{12}$$

For use in eqn. (1), standard kinematic relations are used to express eqn. (12) as a relation between the contravariant components (on the current base vectors) of the convected rate of Kirchhoff stress, $\dot{\tau}^{ij}$, and Lagrangian strain rate, $\dot{E}_{ij}$.

The deformation history is calculated in a linear incremental manner and, in order to increase the stable time step, the rate tangent modulus method of Peirce *et al.* [21] is used. This is a forward gradient method based on an estimate of the plastic strain rate in the interval between t and $t + \Delta t$. The incremental boundary value problem is solved using a combined finite element Rayleigh-Ritz method, Tvergaard [19].

5. Experimental results

Representative stress-strain curves for the unreinforced control alloy and the reinforced composite material are shown in Fig. 3. The addition of the whiskers causes an increase in the elastic modulus, 0.2% offset yield strength and ultimate strength, and a decrease in the strain to failure for the composite material. These effects are well documented in the literature [1-5, 9, 10]. What is more surprising, however, are the effects of aging state on the stress-strain behavior of the composite material. Though the aging curve for the unreinforced control alloy (variation of 0.2% offset yield strength as a function of aging time) exhibits the well known "bell-shaped" curve, the composite yield strength is independent of aging time (Fig. 4(a)). The ultimate strength of the

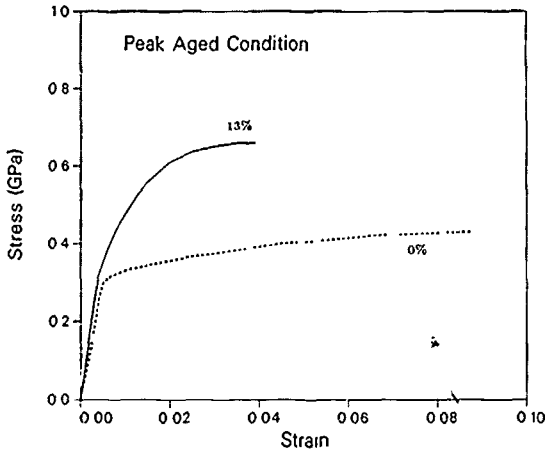

Fig. 3. Representative stress–strain curves for the composite material (labelled 13%) and the unreinforced control alloy (labelled 0%). The increase in the Young's modulus, yield strength, and ultimate strength and decrease in the ductility for the composite material should be noted.

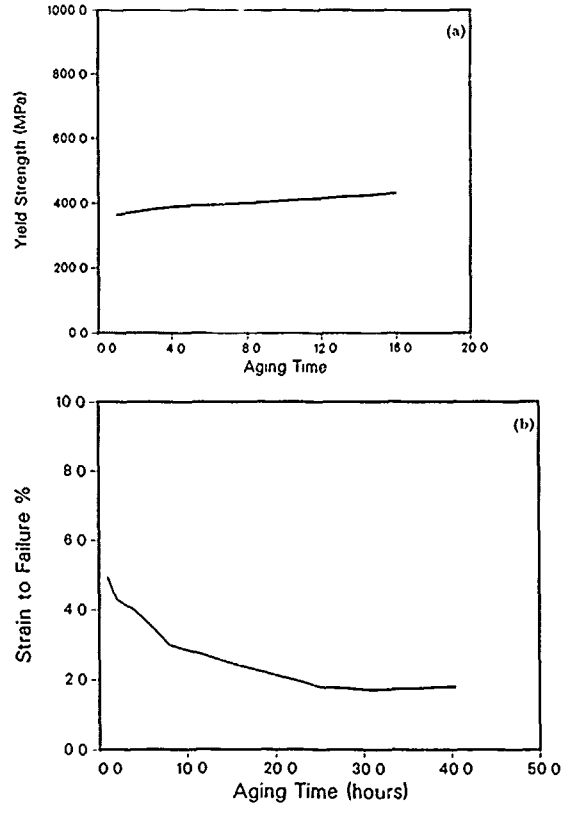

Fig. 4. The variation of (a) the yield strength and (b) the ductility with aging time.

composite (about 650 MPa) is also independent of aging time. However, the strain-to-failure of the composite is a strong function of aging time, decreasing monotonically from about 5% in the as-quenched condition to about 1.5% in the severely overaged microstructure, Fig. 4(b).

Microscopic examination of the fracture surfaces revealed a dimpled fracture surface for both the reinforced and unreinforced materials. The fracture surface of the unreinforced material contained a rather even distribution of large dimples connected by sheets of smaller dimples indicating a pattern resulting from ductile void growth, coalescence and failure, Fig. 5. The fracture surface of the reinforced material contained only small dimples similar to the small dimples on the fracture surface of the unreinforced material, Fig. 6(a). The aging time had no detectable effect on the appearance of the fracture surface. Whisker pullout was sometimes observed; although, the pulled-out whiskers were coated with matrix material, Fig. 6(b). This demonstrates that the failure of the composite was predominantly through the matrix and not along the matrix–reinforcement interface. Similar conclusions were also obtained in the fracture studies on SiC whisker and particulate reinforced 2XXX and 7XXX alloys [22].

6. Observations of void formation at elevated temperatures

One mechanism that appears to contribute to the unusually low ductility of Al–SiC whisker composites involves the formation of voids at fiber ends. Nutt and Duva [23] have observed voids forming at room temperature in a 6061 alloy reinforced with SiC whiskers strained to various amounts. Nutt and Needleman [24] have developed a quantitative description of the void nucleation process at fiber ends and compared the predicted and observed modes of failure initiation. While further studies are needed to establish the link between void formation at whisker ends and overall failure mechanisms at room temperature, our recent work indicates that cavitation at whisker ends plays a greater role in controlling the overall constitutive response of Al–SiC composites at elevated temperatures than at room temperature.

The initiation of voids at whisker ends was studied in the same 2124–SiC whisker-reinforced composite described earlier. When the test temperature is increased, the tensile ductility of the Al–SiC composites increases significantly [25]. We have explored this temperature-dependent phenomenon through TEM observations of spec-

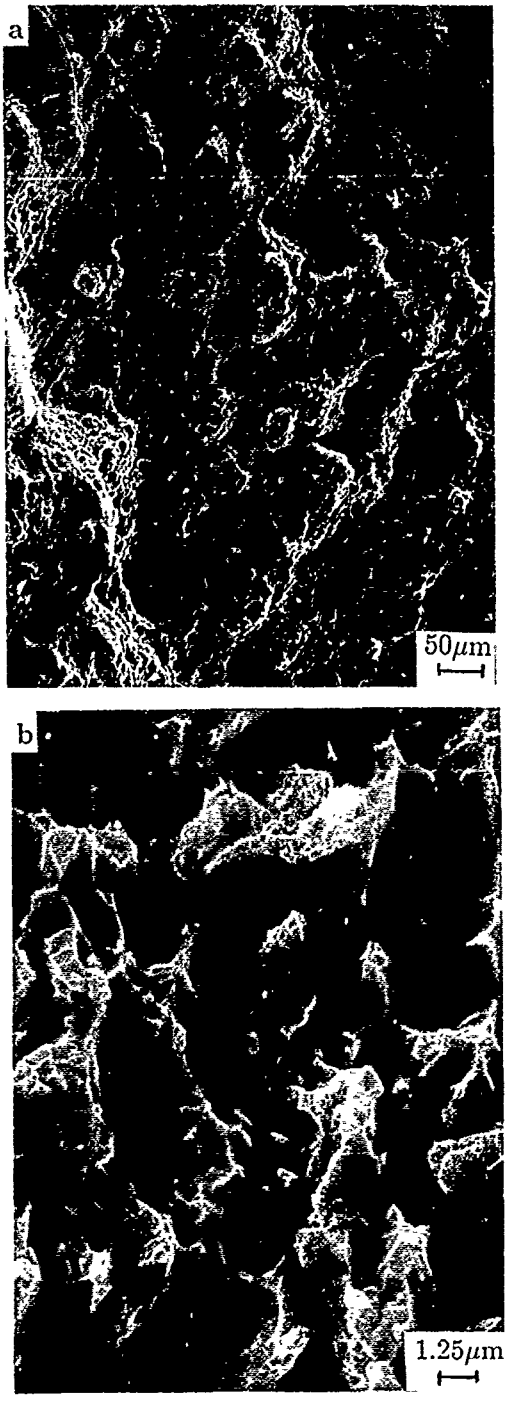

Fig 5 Fracture surface morphology of the unreinforced control alloy (a) showing the distribution of the large dimples and (b) showing the distribution of the small dimples

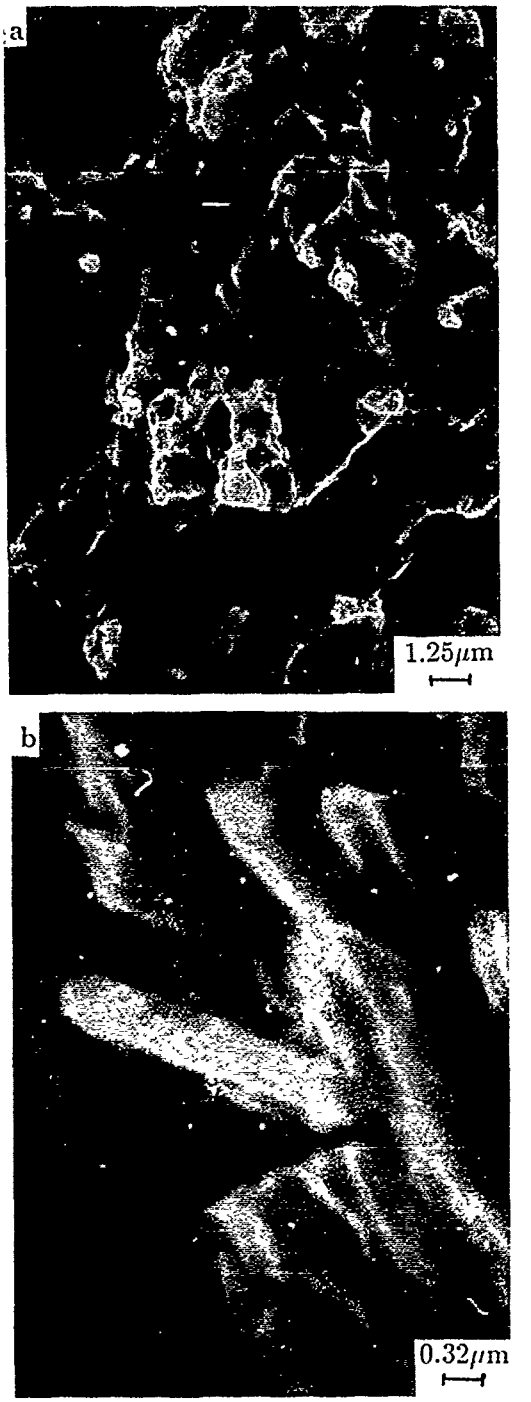

Fig. 6. Fracture surface morphology of the composite material. The similarity of (a) to Fig. 5(b) should be noted. A pulled out whisker coated with matrix material is shown in (b).

imens tested in tension at 300 °C. In these experiments, we have used the specimens in the naturally aged condition, as the specimens tested at 300 °C quickly achieve a severely overaged matrix microstructure. After the tensile tests, TEM specimens were sectioned from tensile specimens that had undergone different amounts of plastic strain. Voids were typically observed at fiber ends in specimens with macroscopic plastic

strains ranging from 3% to 12.5%. The voids generally formed at the corner on the fiber end, as shown in Fig. 7(a), and intense plastic deformation occurred in the vicinity of the fiber end, as evidenced by the high dislocation density in that region. Glide of the dislocations was inhibited by the coarse age-hardening precipitates that grew during the high temperature test, although the high local stresses still produced large plastic strains in this region. With increasing strain, additional voids formed at other corner sites of the same fiber end (Fig. 7(b)), and eventually the voids coalesced to form one large void equal in width to the fiber diameter.

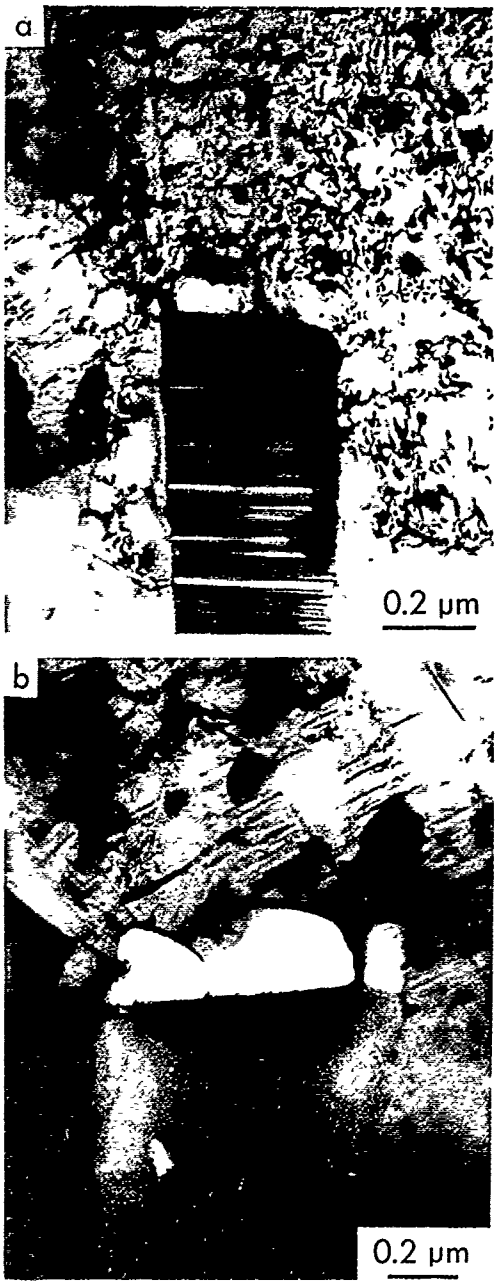

Fig. 7. Void nucleation at fiber ends in 2124 Al–SiC whisker composite deformed at 300 °C to a tensile strain of 0.12. (a) Void at corner of fiber end surrounded by dislocated matrix. (b) Coalescence of voids formed at different sites on the fiber end.

After macroscopic tensile strains of 12.5%, elongated cavities were often observed at fiber ends, as shown in Fig. 8(a). The salient features of the cavitation mechanism are: (1) the cavity width does not exceed the fiber diameter, (2) there is no apparent separation along the fiber side, and (3) the tip of the cavity has retained the same basic shape displayed by much smaller cavities associated with lower strain levels. Furthermore, similar elongated cavities were observed at fiber breaks, as shown in Fig. 8(b). These observations indicate that large amounts of shearing at or near the interface can occur after decohesion at the fiber end, and that the load-bearing capacity of the fibers can be severely reduced.

Patterns of void evolution observed in 2124 Al–SiC composites tested at 300 °C resemble the observations from room-temperature tests in other composite systems in that voids nucleate near the corners of fiber ends and subsequently coalesce to form a single void. However, the distribution of voids differs in that voids nucleate throughout the gage length during the high-temperature tests, while in room-temperature tests the voids are confined to regions very near the fracture surface. Thus, one effect of temperature is to allow the damage to accumulate in the composite microstructure prior to failure, thereby increasing the ductility. These observations suggest that one path to improving the room-temperature ductility of Al–SiC composites would be to identify microstructural parameters that could control the development of cavitation. Toward this end, calculations based on an interface decohesion model are being carried out to determine the effects of microstructural parameters on void formation.

7. Discussion

The results of the tensile tests conducted in this study are useful for the evaluation of composite strengthening theories. The Modified Shear Lag Model [26] predicts the yield strength of the composite material using a model based on simple transfer of shear across the whisker–matrix inter-

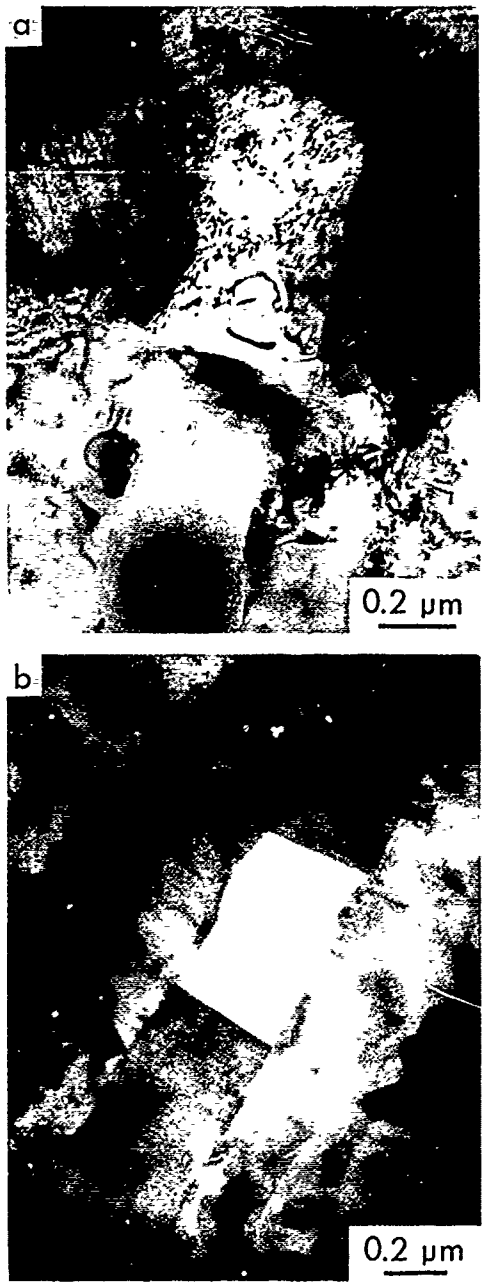

Fig. 8. Void growth in 2124 Al-SiC whisker composite deformed in tension at 300 °C. (a) Elongated cavity at the fiber end surrounded by dislocations. (b) Cylindrical cavity at the fiber break.

face with an additional term used to account for load transfer across the ends of the whiskers. This theory, as well as the widely known rule of mixtures theory, are not in qualitative agreement with the experimental observations as they would also predict that the yield strength of the composite material would increase with an increase in the yield strength of the matrix. The Enhanced Dislocation Density Model [27] attempts to predict the yield strength of discontinuously reinforced metal–matrix composites based on a modified shear lag model taking into account the differences in dislocation densities between the reinforced and unreinforced materials. The qualitative predictions of this theory, however, are in contradiction with the experimental observations of the present study. If the yield strength of the matrix of the composite is significantly different from that of the unreinforced alloy, then one would expect to see this difference reflected as a uniform increase in the microhardness values for the matrix of the composite material. Figure 1(a) indicates that the matrix of the composite material has about the same hardness as the unreinforced alloy. Also, this theory would predict that the yield strength of the composite material will mirror that of the unreinforced alloy as a function of aging time, although this is not observed experimentally. Thus the Enhanced Dislocation Density Model is not in qualitative agreement with the experimental results and therefore is of questionable value for identifying the strengthening mechanisms for the present material.

In ref. 28 a self-consistent formulation for the hardening behavior of discontinuously reinforced metal–matrix composites was developed, in an attempt to predict the yield strength and hardening exponent. The analysis in ref. 28 is based on a path independent deformation theory of plasticity and depends on the use of Ilyushin's theorem [29]. In this formulation the hardening exponents of the reinforced and unreinforced materials are identical. This is contradictory to the present experimental observation that there is a difference of about a factor of three between the hardening exponent of the reinforced and unreinforced materials. In view of the lack of an adequate, analytically tractable model for the yield and hardening behavior of materials reinforced with discontinuous fibers, a finite element method was used in this study.

The finite element method possesses several inherent advantages over many of the more analytical methods. First, geometrical effects, such as corners at fiber ends, can be handled in a straightforward manner. The simplification (required in many theoretical developments) of reducing the inclusion from a cylinder to an ellipsoid is not necessary. Second, the calculation of stress and strain contours within the matrix and at the

matrix–reinforcement interface are possible. Third, complete stress–strain responses, as opposed to certain portions of the stress–strain curves, are predicted. Therefore, a finite element approach is appealing for this application. Here, an axisymmetric finite element unit cell model is employed where the aspect ratio of the whisker is the average aspect ratio observed experimentally and the aspect ratio of the unit cell is taken to be approximately equal to the whisker aspect ratio. A similar finite element model, but using a full three-dimensional cell geometry, is described in ref. 30.

The finite element method predictions for uniaxial loading are qualitatively in agreement with the experimental results. Figure 9(a) shows the predicted stress–strain curves as a function of the volume fraction of reinforcement for whisker-reinforced 2124 Al in an underaged state. The effects of matrix aging condition on the stress–strain response are plotted in Fig. 9(b).

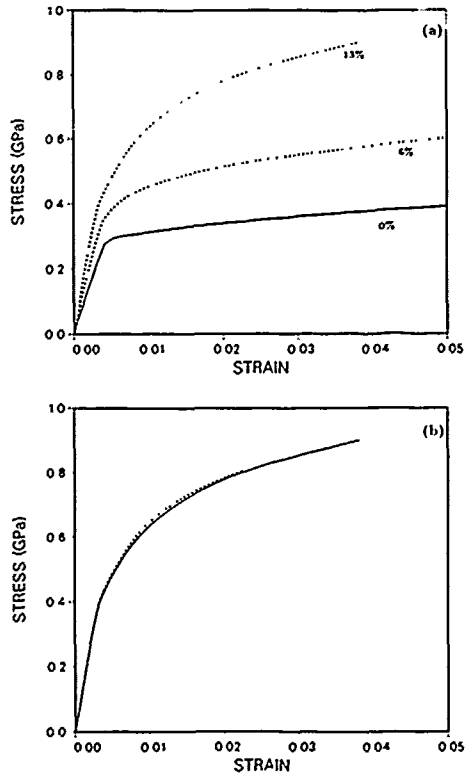

Fig. 9. Qualitative response of the finite element model. (a) Finite element predictions as a function of volume per cent of the reinforcement phase. (b) Finite element predictions as a function of matrix aging condition, the dashed line is for the peak-aged microstructure and the solid line is for an underaged condition.

The finite element model correctly predicts that the yield strength of the composite material is independent of matrix variations due to aging and that the strain-hardening exponent of the composite be quite different from that of the unreinforced material.

The quantitative predictions for stress–strain response, however, are not within acceptable bounds of the experimental results. Figure 10 shows the predicted and experimental stress–strain curves for an underaged condition in the composite material. The calculated curves, with a traction-free lateral side and with the sidewall constraint representing the periodic array imposed, bound the experimental results, although, they are not sufficiently close to be of use.

The analysis of the effects of the sidewall constraint on the response of the unit cell is useful in attempting to understand the underlying strengthening mechanism for these materials. Without the imposed constraint, there is little increase in the yield strength of the composite over that of the unreinforced control alloy. The increase in yield strength of these materials appears to originate not from direct load transfer to the reinforcement phase but from the constraint of geometrical compatibility.

The distribution of hydrostatic stress within the unit cell, with and without the sidewall constraint, elucidates this mechanism further for identical geometries and aging states at similar values of far-field axial strain, Fig. 11. The differ-

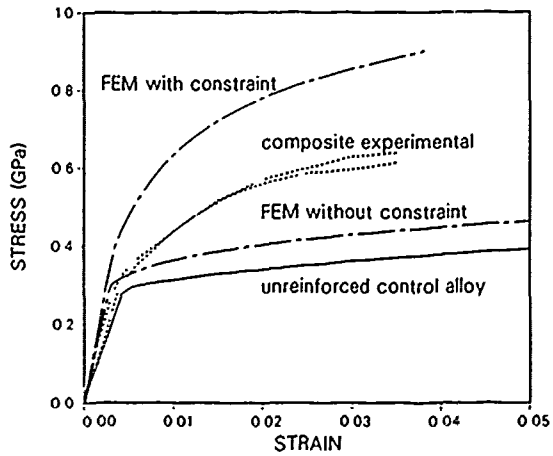

Fig. 10. Comparison of the finite element predictions with and without the sidewall constraint with the experimental results. The finite element predictions bound the experimental results but are too far apart to be of quantitative value.

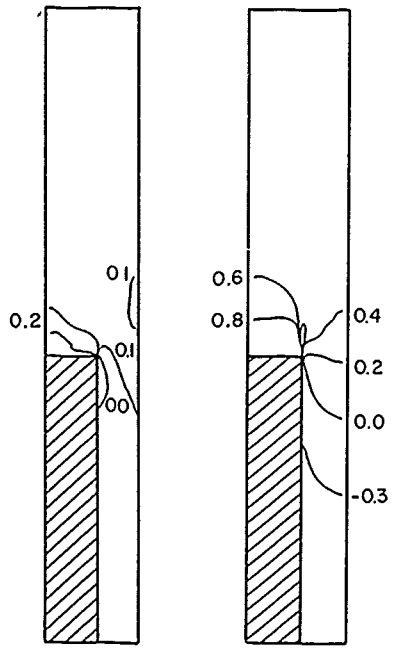

Fig. 11. Distribution of hydrostatic stress (in GPa) within the unit cell, with and without the sidewall constraint. The values of far field axial strain is almost identical in both cases. The shaded portion of the figure represents the whisker.

ence in far-field axial stress is about 300 MPa, which is approximately equal to the difference in the values for hydrostatic stress within the upper region of the cell. As far-field strain accumulates, the sidewall in the upper portion of the cell attempts to contract at a greater rate than in the lower portion of the cell. The sidewall constraint forces the lateral side to remain straight, thereby generating large compressive hydrostatic stresses within the lower portion of the cell and large tensile hydrostatic stresses within the upper portion of the cell. It is these tensile hydrostatic stresses which appear to increase the yield strength of the composite material rather than direct load transfer to the reinforcement phase.

The cell model, "with constraint", *i.e.* based on the boundary conditions (6) and (7), represents an ideal regular array of perfectly aligned fibers and appears to overpredict the levels of hydrostatic stress generated within the material. In certain regions of the cell, the tensile hydrostatic stress component reaches three times the yield strength of the matrix material. At the present time, it is not clear that such high levels of hydrostatic tension are actually achieved and there are a variety of mechanisms that could act to reduce the hydrostatic tension. For example, deviations from the aligned end-to-end fiber geometry assumed in the calculations would be expected to lead to reductions in the hydrostatic tension levels achieved. Indeed, preliminary analysis of this effect by the authors indicate significant reductions are so attained.

In the calculations discussed so far the fiber has been taken to be rigid. A few calculations were carried out accounting for fiber elasticity. In these calculations Young's modulus for the SiC fibers was taken to be 450 GPa and Poisson's ratio, $\nu = 0.17$ [31]. Compared with the rigid fiber analysis, there is a reduction in the Young's modulus of the composite of 8%–10%. Also, the peak hydrostatic tension is reduced by 5%–10% when fiber elasticity is accounted for. These calculations show the quantitative magnitude of effects associated with fiber elasticity and indicate that in the Al–SiC system investigated there is no qualitative difference in behavior arising from the assumption of rigid fibers.

The present finite element model makes no attempt to predict ductility. However, the predictions, in conjunction with the experimental results, provide some insight into possible failure modes at room temperature. The failure of the composite appears to be strongly dependent on the matrix material. Recent work by Christman and Suresh [32] on the response of the composite material and control alloy to fatigue loading demonstrated that under these conditions the behavior of the composite is controlled by the failure of the matrix material. The lack of exposed whiskers on the fracture surface and the strong dependence of the ductility on aging raise questions as to the relative roles of voids at the whisker–matrix interface and those within the matrix of the composite.

The large amounts of local deformation observed on the fracture surface in the form of dimples suggests that a void formation mechanism is present. This is consistent with the high levels of hydrostatic stress predicted by the finite element model. Even though the existence of the high levels of hydrostatic tension predicted by the finite element model is uncertain, the existence of significant tensile hydrostatic stresses within the matrix material appears plausible. The generation of these localized tensile hydrostatic stresses, in the matrix slightly above the whisker, may be a driving force for void formation in the matrix material at relatively low values of far-field axial strain.

It should be stated that other metal–matrix composite materials in other studies have displayed strikingly different fractographic features and failure modes [33, 34]. The dependence of ductility on reinforcement chemistry and morphology, matrix chemistry and processing techniques is evident, although not well documented or characterized. The need for systematic studies of the dependence of ductility in metal–matrix composite systems on these parameters is clear. A basis for such a study should be a thorough investigation of ductility in a single metal–matrix composite system.

8. Concluding remarks

In this study, the uniaxial tensile stress–strain response of a 2124 Al–SiC whisker metal–matrix composite was investigated as a function of controlled matrix microstructural variations. The 0.2% offset yield strength of the composite material was independent of aging time despite a significant change in the yield strength of the unreinforced control alloy. Several models available in the literature for composite strengthening were reviewed and discussed in relation to the experimental results of this study and an earlier microstructural characterization study [6]. A finite element unit cell model was shown to predict the correct qualitative trends, although good quantitative accuracy was lacking. The results of the finite element model were discussed in an attempt to develop a better understanding of the strengthening mechanisms in these materials.

The mechanisms involved in the tensile quasi-static failure of the metal–matrix composite were investigated at room temperature and at 300 °C. Void formation mechanisms appeared to play a dominant role in the failure behavior at both temperatures. Although the precise role of the voids in the fracture process remains unclear at this time, voids nucleating at whisker ends appear to be more predominant at elevated temperatures than at room temperature. Further investigation is required to determine the dominant characteristics of voids formed at the whisker–matrix interface and those formed within the matrix of the composite. In addition, the mechanisms influencing the strong dependence of ductility on aging condition remain to be demonstrated.

Acknowledgments

The work of T. Christman and S. Suresh was supported by National Science Foundation Grant NSF-ENG-8451092. Support for A. Needleman and S. Nutt was provided by the Office of Naval Research through contracts N0001486-K-0261 and N00014-86-K-0125. The authors also gratefully acknowledge the use of Brown University Materials Research Group Central Facilities, funded by the National Science Foundation.

References

1 H. J. Rack and J. W. Mullins, in *High Strength Powder Metallurgy Aluminum Alloys*, The Metallurgy Society of AIME, Warrendale, PA, 1985, p. 155.
2 T. G. Nieh and R. F. Karlak, *J. Mater. Sci. Lett.*, *2* (1983) 119.
3 M. D. Skibo, *SNL Rep. SAND81-8212* 1981 (Sandia National Laboratories), 1981.
4 D. L. McDanels, *Metall. Trans. A*, *16* (1985) 1105.
5 G. Mott and P. K. Liaw, *Rep. 86-7D4-MAMAX-P1*, 1986 (Westinghouse R & D Center).
6 T. Christman and S. Suresh, *Acta Metall.*, *36* (1988) 1691.
7 I. Dutta and D. L. Bourell, to be published.
8 T. G. Nieh and R. F. Karlak, *Scr. Metall.*, *18* (1984) 25.
9 W. A. Logsdon and P. K. Liaw, *Eng. Fracture Mech.*, *24* (1986) 737.
10 A. P. Divecha, S. G. Fishman and S. D. Karmarkar, *J. Met.*, *33* (1981) 12.
11 R. N. Wilson and P. G. Partridge, *Acta Metall.*, *13* (1965) 1321.
12 G. C. Weatherly and R. B. Nicholson, *Philos. Mag.*, *17* (1968) 801.
13 D. J. Thompson, *Metall. Trans. A*, *6* (1975) 671.
14 M. Taya and T. Mori, *Acta Metall.*, *35* (1987) 155.
15 M. Vogelsang, R. J. Arsenault and R. M. Fisher, *Metall. Trans. A*, *17* (1986) 379.
16 T. Christman and S. Suresh, unpublished results, Brown University, Providence, 1987.
17 A. Needleman, *J. Mech. Phys. Solids*, *20* (1972) 111.
18 A. Needleman, in E. H. Lee and R. L. Mallet (eds.), *Plasticity of Metals at Finite Strain: Theory, Computation and Experiment*, Rensselaer Polytechnic Institute, Troy, NY, 1982, p. 387.
19 V. Tvergaard, *J. Mech. Phys. Solids*, *24* (1976) 291.
20 V. Tvergaard, *Int. J. Fracture*, *18* (1982) 237.
21 D. Peirce, C. F. Shih and A. Needleman, *Computers Struc.*, *18* (1984) 875.
22 D. L. Davidson, *SRI Rep. N00014-85-C-0206*, 1987, (Southwest Research Institute).
23 S. R. Nutt and J. M. Duva, *Scr. Metall.*, *20* 1986 1055.
24 S. R. Nutt and A. Needleman, *Scr. Metall.*, *21* 1987 705.
25 V. C. Nardone and J. R. Strife, *Metall. Trans. A*, *18* 1987 109.
26 V. C. Nardone and K. M. Prewo, *Scr. Metall.*, *20* 1986 43.

27 R. J. Arsenault, *Mater. Sci. Eng., 64* (1984) 171.
28 J. M. Duva, *J. Eng. Mater. Tech., 106* (1984) 317.
29 A. A. Ilyushin, *Prikl. Mat. Mekh., 10* (1946) 347.
30 J. M. Papazian and A. Levy, *Symp. on Interfacial Phenomena in Composites, Newport RI, June, 1988.*
31 C.-H. Andersson and R. Warren, *Composites, 15* (1984) 16. , .
32 T. Christman and S. Suresh, *Mater. Sci. Eng., A 102(2)* (1988) 211–216.
33 C. P. You, A. W. Thompson and I. M. Bernstein, *Scr. Metall., 21* (1987) 181.
34 J. J. Lewandowski, C. Liu and W. H. Hunt, Jr., in *Powder Metallurgy Composites*, The Metallurgical Society of AIME, Warrendale PA, in press.

Materials Science and Engineering, A107 (1989) 63–69

The Influence of Hydrostatic Pressure on the Ductility of Al–SiC Composites*

A. K VASUDEVAN and O. RICHMOND
Alcoa Research Centre, Pittsburgh (U.S.A.)

F. ZOK and J. D. EMBURY
McMaster University, Hamilton (Canada)

(Received June 1, 1988)

Abstract

Tensile tests with superimposed hydrostatic pressures were performed on two types of metal matrix composite: 2014 Al with 20% SiC particles and 2124 Al with 14% SiC whiskers. In the materials with SiC particulate, the ductility increases rapidly with pressure and the mode of damage initiation is by particle fracture. Materials containing SiC whiskers exhibit a different fracture mode involving whisker matrix decohesion, and strain localization which results in shear fracture.

1. Introduction

The mechanical response of metal–matrix composites can be considered in terms of various microstructural features, such as the particle–matrix interfaces and the work hardening characteristics of the matrix, and the process of damage accumulation which precedes fracture. Much of the work in the present conference relates to the detailed characterization of interfacial structures and their role in the process of load transfer in metal–matrix composites. The present paper explores the pressure dependence of flow and fracture in both particulate- and whisker-reinforced Al–matrix composites. The results suggest that a combination of studies of the mechanical response under superimposed pressure, detailed metallographic and fractographic studies, and micromechanical analyses can yield information which is complementary to the detailed structural studies of interfaces. The work serves to delineate some of the critical damage processes which limit the ductility of metal–matrix composites.

2. Materials and experimental procedures

Mechanical tests were performed on two types of SiC-reinforced Al–matrix composites and compared with the results of tests performed on the matrix materials without the reinforcing phase.

One composite was a commercial 2014 Al alloy containing 20% SiC particles. This material was heat treated to the T6 condition (Fig. 1(a)). The average particle size was 13 μm and the average aspect ratio was 1.23 measured in the plane containing the tensile axis. Approximately 5% of the SiC particles were greater than 40 μm in size and had aspect ratios of the order of 4.

The second material was a 2124 Al alloy containing 14% SiC whiskers which were 1 μm in diameter and 5 to 10 μm in length (Fig. 1(b)). Two ageing treatments were undertaken in order to examine the influence of precipitates located at the SiC–matrix interfaces on the ductility of the composite. The ageing times were selected to maintain constant matrix strength (as determined from microhardness measurements) as shown in Fig. 2. Transmission electron microscopy (TEM) observations indicated many more intermetallic compounds precipitated at the interfaces in the overaged condition than in the underaged condition.

Tensile tests were conducted in a Harwood pressure unit with superimposed pressures up to 1000 MPa. The tensile samples had a gauge length of 15.2 mm and a gauge diameter of 3.2

*Paper presented at the symposium on Interfacial Phenomena in Composites: Processing, Characterization, and Mechanical Properties, Newport, RI, June 1–3, 1988.

0921-5093/89/$3.50

© Elsevier Sequoia/Printed in The Netherlands

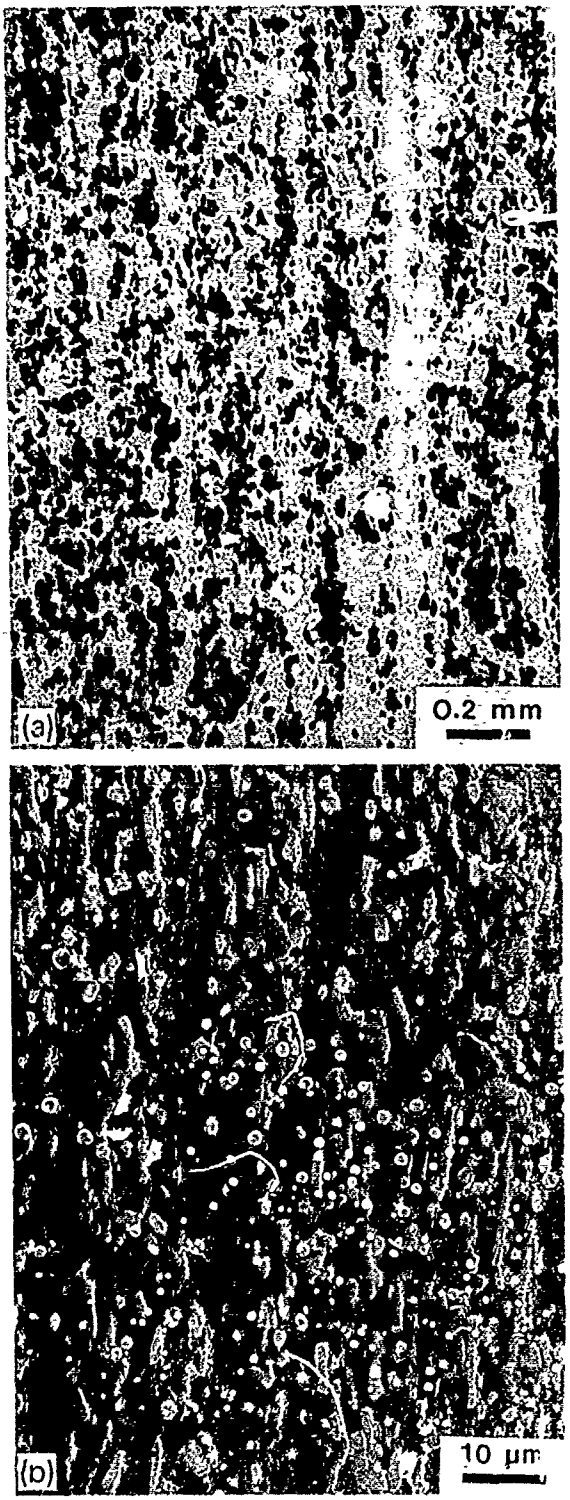

Fig. 1. Undeformed microstructures of (a) particulate-reinforced and (b) whisker-reinforced composites.

mm. Detailed metallography was performed both on fracture surfaces and on longitudinal sections taken through fractured samples. Additional

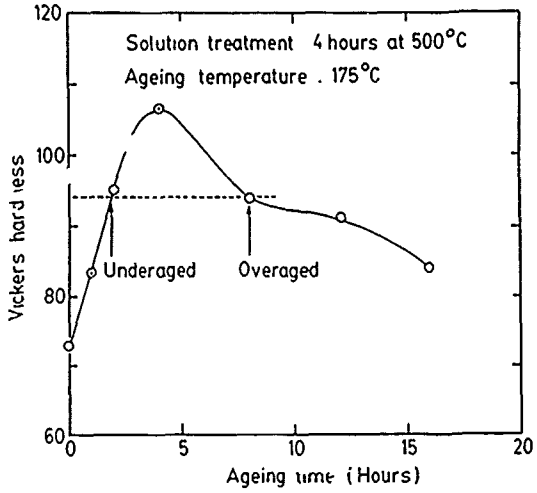

Fig 2. Variation of matrix microhardness with ageing time. Ageing times of 2 h and 8 h were selected for the present study.

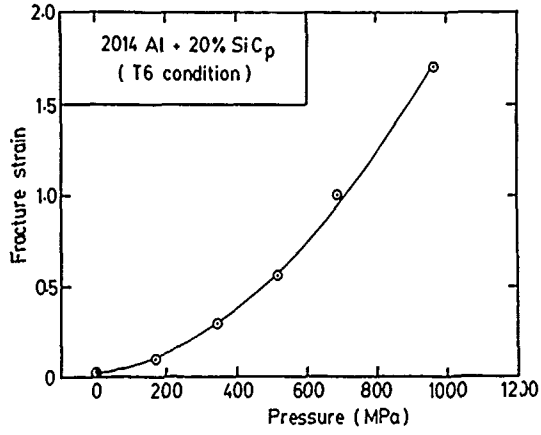

Fig. 3. Influence of hydrostatic pressure on the fracture strain of the particulate-reinforced composite.

metallographic studies and TEM studies of interfaces in these materials are currently in progress and will be reported elsewhere.

3. Results

For clarity, the results are reported in separate sections dealing with particulate- and whisker-reinforced composites.

3.1. Particulate-reinforced composites

The influence of superimposed hydrostatic pressure on the ductility of the particle-reinforced composites is shown in Fig. 3. The ductility is strongly pressure dependent over the entire range. The fracture surfaces at all pressures were inclined at about 45° to the tensile axis.

The origins of fracture in Al–SiC particulate composites have previously been suggested to be either the fracture or decohesion of the SiC particles [2] or failure within the Al alloy matrix [4]. To distinguish between fracture and decohesion of the SiC particles in the present study, matching fracture surfaces were carefully examined. Figure 4 shows an example of matching fracture surfaces, where the corresponding letters on the micrographs show matching halves of fractured SiC particles; particle–matrix decohesion was rarely observed. Longitudinal sections through the fractured samples also revealed a number of fractured particles below the fracture surface. Particle fracture was often associated with the more elongated particles which were aligned with the tensile direction.

In order to gain further insight into the problem of damage accumulation during deformation it is useful to compare the flow curves of both the composite and matrix materials at various superimposed pressures. Figure 5 shows that the yield stress and ultimate tensile strength of the unreinforced matrix material is essentially independent of pressure. This is in contrast to the marked pressure dependence of the flow behaviour of the composite shown in Fig. 6 together with the flow curve obtained in compression. It is evident that the tensile flow stress at a given plastic strain increases with superimposed pressure until it approaches the behaviour in compression. Similar flow behaviour has been observed in iron compacts with various initial porosities [3]. The results can be interpreted in the following way.

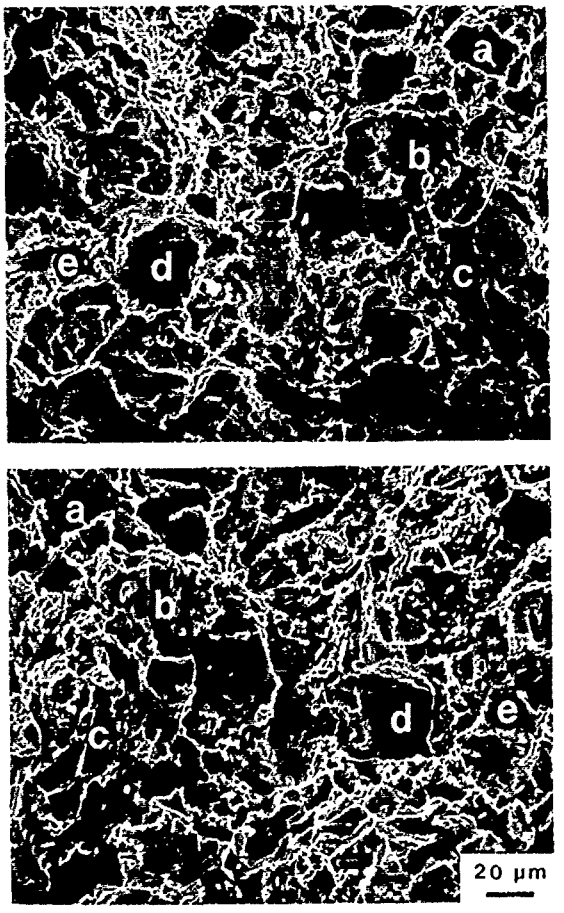

Fig. 4 Matching fracture surfaces of the particulate-reinforced composite.

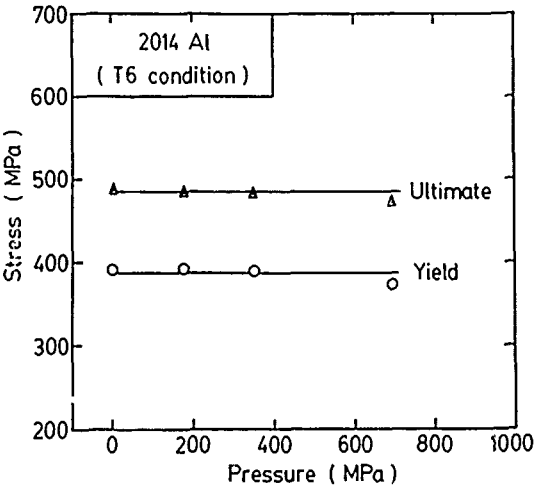

Fig. 5. Influence of hydrostatic pressure on the yield and ultimate tensile strengths of the unreinforced 2014 aluminium alloy.

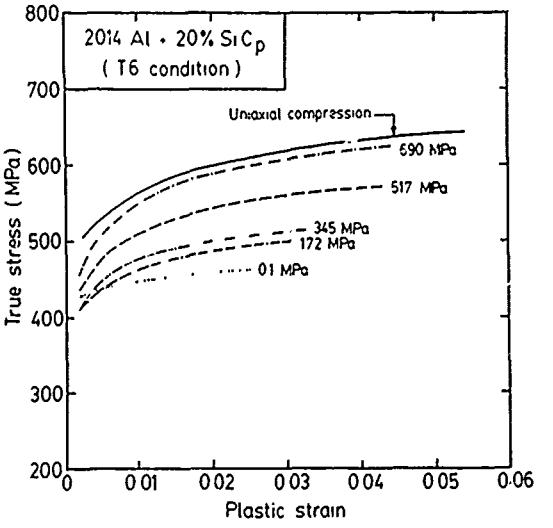

Fig. 6. Variation of the tensile flow behaviour of the particulate-reinforced composite with hydrostatic pressure. Also shown is the compressive flow curve at atmospheric pressure.

During deformation of the composites, the differences in elastic and plastic properties of the matrix and the reinforcing phase result in a rapid increase in the stress supported by the reinforcing phase. This is reflected in the high work hardening rate of the composite at small plastic strains. However, the stresses borne by the reinforcing phase can cause fracture or debonding of the reinforcing phase which significantly lowers the work hardening rate of the composite. The fracture events are pressure dependent and thus the pressure dependence of the flow curves in Fig. 6 indicate in a quantitative manner the pressure dependence of the damage accumulation rate.

This process can be considered in terms of a simple model of damage accumulation by expressing the flow stress of the composite σ as

$$\sigma = \sigma_0(1 - D)$$

where σ_0 is the flow stress achieved in the absence of damage and D is a damage parameter which can vary from 0 at the onset of flow to 1 at fracture, *i.e.* it reflects the loss of load bearing capacity. The net work hardening rate can then be written as

$$\frac{d\sigma}{d\varepsilon} = \frac{\partial \sigma_0}{\partial \varepsilon}(1 - D) - \sigma_0 \frac{\partial D}{\partial \varepsilon}$$

The damage accumulation rate, $\partial D/\partial \varepsilon$, decreases with hydrostatic pressure and thus the flow curves of the composite are pressure dependent. At sufficiently high pressures the damage rate will be suppressed so that the behaviour is similar to that in compression.

3.2. *Whisker-reinforced composites*

The influence of pressure on the ductility of whisker-reinforced composites is shown in Fig. 7. There was no apparent influence of ageing treatment on the ductility of the composites. The fracture surfaces at all pressures were inclined at about 45° to the tensile axis. At atmospheric pressure the fracture surface exhibited an equiaxed dimple structure similar to that usually observed in ductile fracture. As the pressure was increased a greater proportion of the fracture surface consisted of elongated shallow dimples characteristic of shear failure (Fig. 8).

The failure mechanism associated with the dimpled regions was revealed by examining matching fracture surfaces. An example is shown in Fig. 9. This figure illustrates that failure involved the decohesion and pull out of whiskers

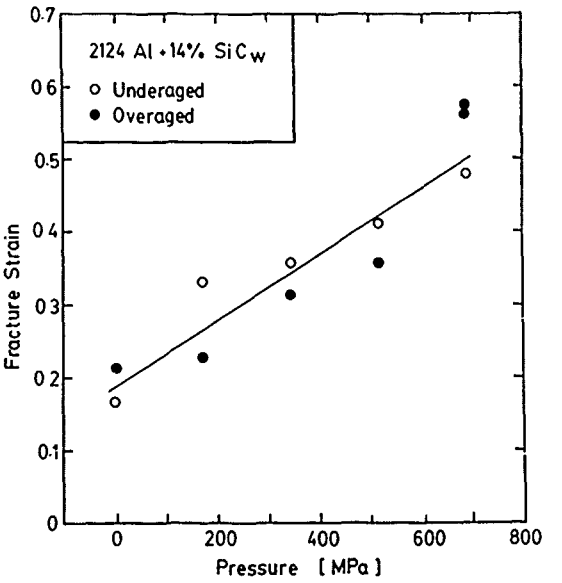

Fig. 7. Influence of hydrostatic pressure on the fracture strain of the whisker-reinforced composites.

from the matrix. Longitudinal sections also revealed evidence of whisker–matrix decohesion (Fig. 10).

The sheared regions of the fracture result from the presence of localized shear bands of the order of 5 μm in width in which the whiskers are rotated away from the tensile axis until a critical point at which shear failure occurs (Fig. 11). Similar behaviour has been observed in directionally solidified Al–Al_3Ni eutectic alloys in which localised shear bands are observed to initiate at the surface [5]. The surface initiation may be associated with the organization of surface rugosities in accordance with some recent continuum models, but further detailed metallographic studies are required to quantify this process.

4. Concluding discussion

Although the mechanical response of composite materials under pressure does not yield direct structural information regarding the local properties of interfaces, it provides a useful framework for delineating competitive processes of fracture and instability for a variety of stress states. In addition, the experimental observations may be compared with the results of micromechanical models which attempt to infer local properties within the reinforcing phase and at the interfaces.

Let us consider first the mechanical response of 2014 Al containing particulate SiC. The

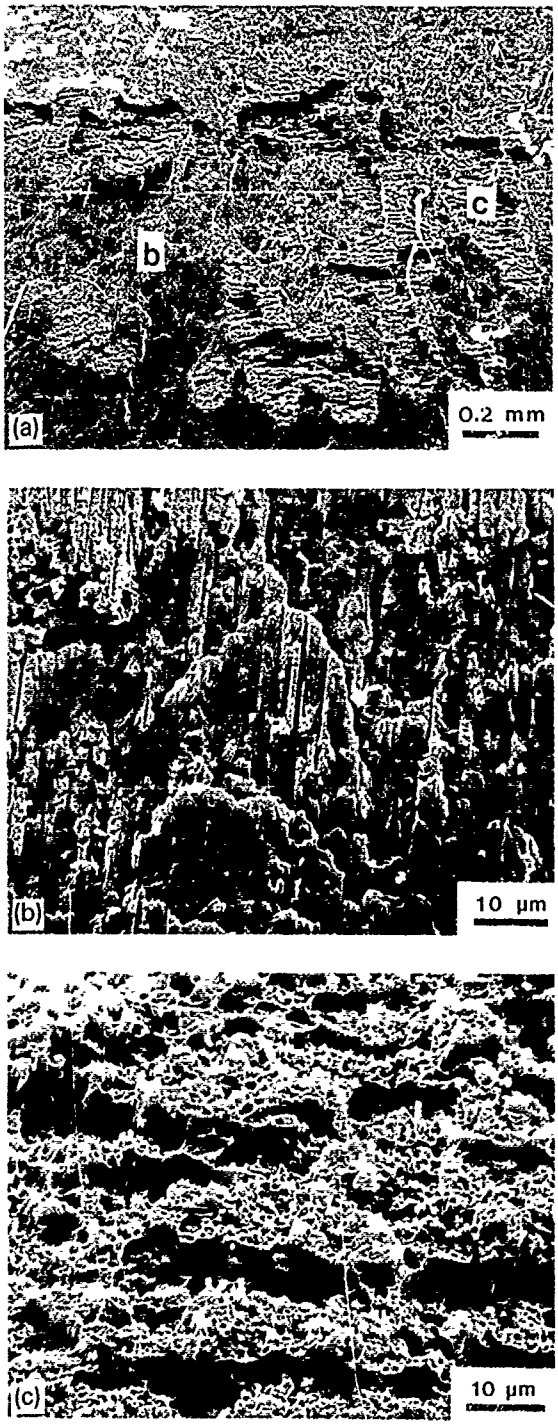

Fig 8 Fracture surface of the whisker-reinforced composite tested at a pressure of 690 MPa. The shear and ductile regions which are shown at higher magnification in (b) and (c) should be noted.

results indicate that fracture is initiated by brittle fracture of the particulate phase. Furthermore, the fracture appears to occur first at the most elongated particles and in clusters of particles. This suggests that refinement of particle size and homogenization of the particle distribution may improve the fracture resistance of the particle-reinforced composites. The beneficial effects of particle homogenization have previously been reported by Hunt *et al.* [1].

The rapid increase in ductility with superimposed pressure suggests that control of the stress state may be of value in producing formable composites. In addition, the pressure dependence of the flow curves gives a direct indication of the magnitude of damage accumulation due to particle fracture and its importance relative to strain hardening.

The stresses responsible for the fracture of the particulate phase are difficult to estimate. The local stresses operative at the particle involve transformation stresses due to differences in thermal expansion coefficients and elastic moduli, the unrelaxed stresses due to inhomogeneous plastic flow around the particulate phase and the influence of the superimposed hydrostatic pressure. However, the response of the material to hydrostatic pressure suggests that this may be a quantitative method of elucidating the local fracture events by varying the magnitude of the transformation stresses and monitoring their interaction with the superimposed pressure.

Turning to the whisker-reinforced composites, the results indicate a more complex fracture process involving whisker–matrix decohesion and strain localization. The data do not, however, provide any conclusive evidence regarding the role of interfacial precipitates in the deformation and fracture behaviours of the composites. Further detailed studies will be required to delineate such effects.

At high superimposed pressures, where the ductility of the material increases but the overall work hardening rate decreases, the dominant mode of failure is by shear. The occurrence of the shear failure can be considered in terms of the following sequence of events. When whisker fracture or debonding occurs, there is locally a loss in both load bearing capacity and work hardening rate resulting in localization. The localization is accentuated because the strains in the shear band are sufficiently large to cause rotation of the whiskers away from the tensile axis. The whisker rotation is itself a form of strain softening which, together with the dilatant process of debonding, leads to shear failure.

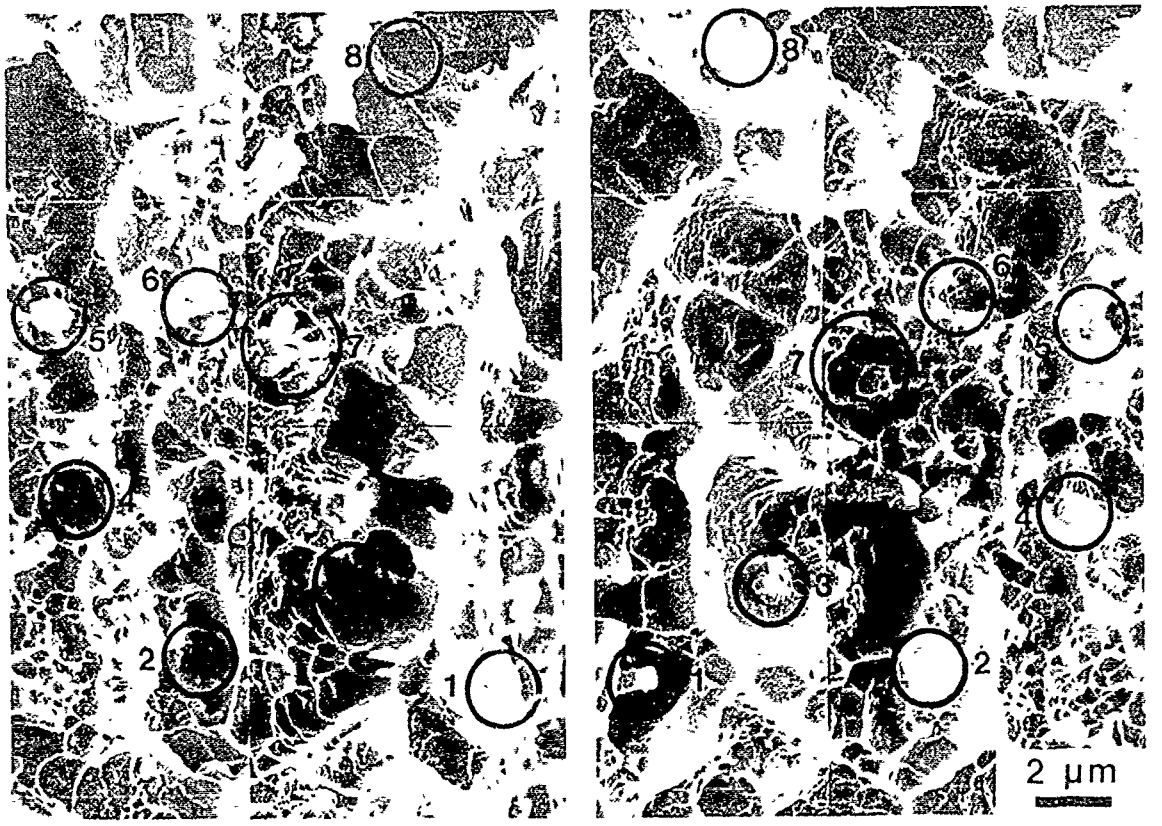

Fig. 9. Matching fracture surfaces of the whisker reinforced composite showing whisker matrix decohesion in the ductile regions

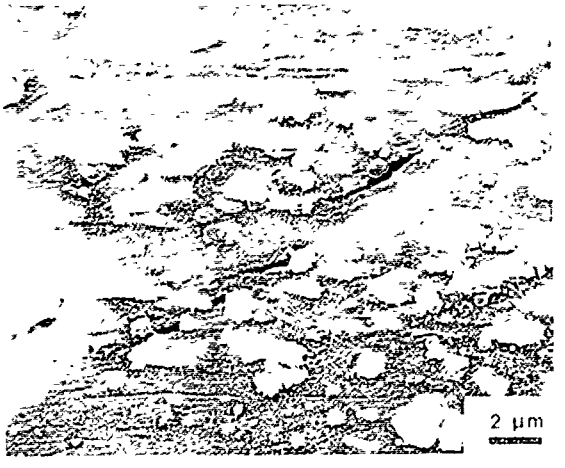

Fig. 10. Whisker matrix decohesion below the fracture surface

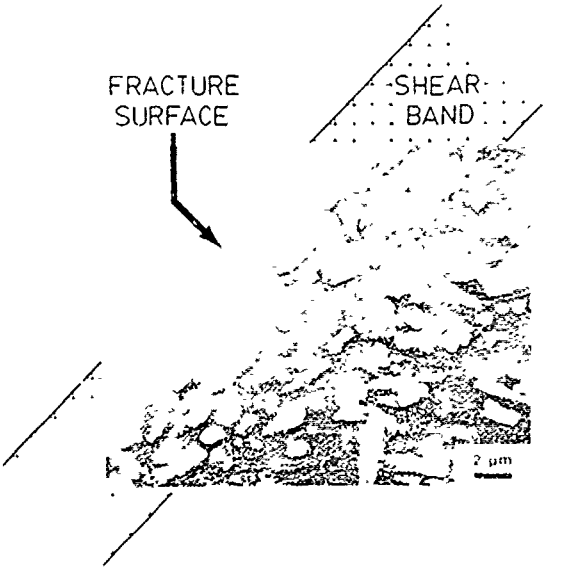

Fig. 11. Strain localization and whisker fractures near the fracture surface

Acknowledgments

The authors are grateful to General Motors and Professor S. Suresh of Brown University for the provision of materials, and to NSERC Canada for research support. In addition they wish to acknowledge Dr. M. Shehata of CANMET for providing the quantitative metallographic data on the particulate reinforced com

posite, Mr. L. Hilty for assisting with the high pressure tests, Mrs. T. Castillo for metallographic assistance, and Mr. L. Luo for the compression data on the particulate-reinforced composite.

References

1 R. W. Hunt, R. Young and O. Richmond, in F. L. Matthews, N. C. R. Buskell, J. M. Hodgkinson and J. Morton (eds.), *6th Int Conf. on Composite Materials*, Vol. 2, Elsevier Applied Science, London, 1987, pp. 209–223.

2 J. J. Lewandowski, C. Liu and W. H. Hunt, in M. Kumar, K. Vedula and A. M Ritter (eds.), *Powder Metallurgy Composites*, The Metallurgical Society of AIME, Warrendale, PA, to be published.

3 W. A. Spitzig, R. E. Smelser and O. Richmond, *Acta Metall., 36* (1988) 1201–1211.

4 C. P. You, A. W. Thompson and I. M. Bernstein, *Scr. Metall., 21* (1987) 181–185.

5 F. Zok, J. D. Embury, M. F. Ashby and O. Richmond, in *9th Riso Int. Symp. on Metallurgy and Material Science, Mechanical and Physical Behaviour of Metallic and Ceramic Composites, Riso National Laboratories, Roskilde, 1988*, to be published.

II PROCESSING

Microstructural Aspects of Aluminium–Silicon Carbide Particulate Composites Produced by a Casting Method*

D. J. LLOYD, H. LAGACE, A. McLEOD and P. L. MORRIS

Alcan International Ltd., Kingston Laboratories, P.O. Box 8400, Kingston, Ontario K7L 4Z4 (Canada)

(Received June 1, 1988)

Abstract

When metal matrix composites are produced by molten metal methods there are some unique factors which have to be considered. In this paper, the microstructure of SiC-reinforced aluminium alloys produced by this method are considered. It is shown that the stability of SiC in the melt is dependent on the matrix alloy involved and that only alloys with high silicon contents have a low reactivity with this reinforcement. With other alloy matrices, SiC reacts to form Al_4C_3, and the nature of this reaction and its kinetics are considered in this paper. Initially, the reaction rates are very rapid but almost saturate after about 1 h. It is also shown that the distribution of the reinforcing particles is dependent on the solidification rate because particles are rejected and pushed ahead of the meniscus. At low solidification rates, and hence for large cell sizes, the reinforcing particles are clustered and form a network which delineates the cell walls. Because the SiC particles are in the interdendritic regions they will be associated with any coarse intermetallic particles present and this can influence the fracture behaviour.

1. Introduction

When composites are produced by a molten metal method, the phenomena encountered are rather different from those occurring when the composites are produced by the more usual powder metallurgy method. The contact time between the reinforcement and the molten metal can be quite long, so the reactivity between the two has to be considered. The molten composite is then solidified which means that solidification effects can be important. The cast ingot is then fabricated to its final shape and may be heat treated. At this stage, the phenomena occurring in the cast and powder composites are expected to be very similar.

In this paper, some of these factors are considered for SiC particulate reinforcement in aluminium alloys. It will be apparent that some of the effects are specific to SiC reinforcement while others are of a more general nature. The composites have been produced by a molten metal mixing technology developed by Dural Aluminum Composite Corporation (DACC).

2. Reactivity

Several studies [1–3] have shown that SiC will react with molten aluminium to form Al_4C_3 according to the reaction

$$4Al + 3SiC \rightarrow Al_4C_3 + 3Si \quad (1)$$

This reaction has several detrimental effects which are as follows: (a) it produces the reaction product Al_4C_3 at the interface between the reinforcement and the matrix, which could result in a degradation of the reinforcement strength and the interfacial strength; (b) the reaction product Al_4C_3 is unstable in some environments, so it increases the corrosion susceptibility of the alloy, (c) the reaction increases the silicon content of the alloy and hence the matrix composition of the alloy may be changed significantly if extensive reaction occurs.

The increase in silicon content can be seen quite easily in the case of extreme reaction, because increasing the silicon content usually results in a decrease in the melting point of the alloy. An example is shown in Fig. 1 where the differential scanning calorimeter (DSC) trace of a 6061 composite in the as-cast condition is com-

*Paper presented at the symposium on Interfacial Phenomena in Composites: Processing, Characterization, and Mechanical Properties, Newport, RI, June 1–3, 1988.

0921-5093/89/$3.50

© Elsevier Sequoia/Printed in The Netherlands

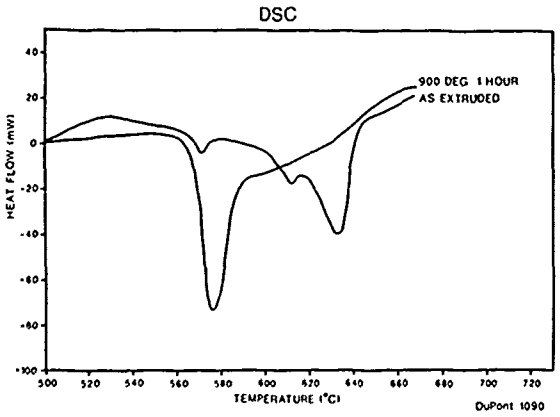

Fig. 1. Influence of remelting on the DSC trace.

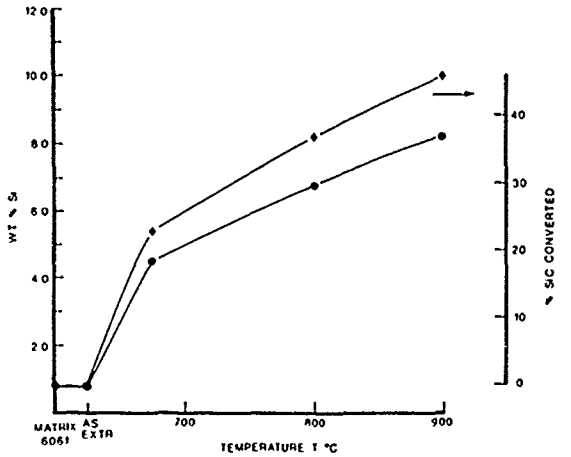

Fig. 2. Extent of SiC converted to Al_4C_3 in 6061–20vol.%SiC after holding for 1 h at different temperatures.

pared with the trace of the same composite after remelting and holding at 900 °C. The DSC trace of the as-extruded composite shows a large endothermic peak owing to general melting at 633 °C and two small incipient melting endothermic peaks at 570 and 611 °C. In the 6000 series alloys, the following invariant reactions may be associated with the peak at 570 °

$Al + Si + FeMg_3Si_6Al_8$ at 567 °C

$Al + Si + FeSiAl_5$ at 575 °C

$Al + Si$ at 577 °C

The peak at 611 °C is very close to the melting temperature for the invariant reaction

$Al + FeSiAl_5$ at 612 °C

After remelting and holding for 1 h at 900 °C, the DSC trace is quite different with a major endothermic melting peak at 577 °C, which is the temperature for Al–Si eutectic melting. This shows that holding for 1 h at 900 °C increased the silicon content to close to the binary eutectic silicon content for this alloy, and this silicon can only have been produced by the conversion of SiC into Al_4C_3 and silicon. As pointed out by Jun and Lloyd [4], changes in the liquidus provide a method of quantitatively measuring the extent of the reaction, provided the effect of silicon on the liquidus of the alloy is known. Figure 2 shows the extent of unprotected SiC converted to Al_4C_3, after holding the 6061–SiC composite at different temperatures.

In practice, the kinetics of the reaction are important and these can be followed by a variety of methods including X-ray diffraction. From eqn.

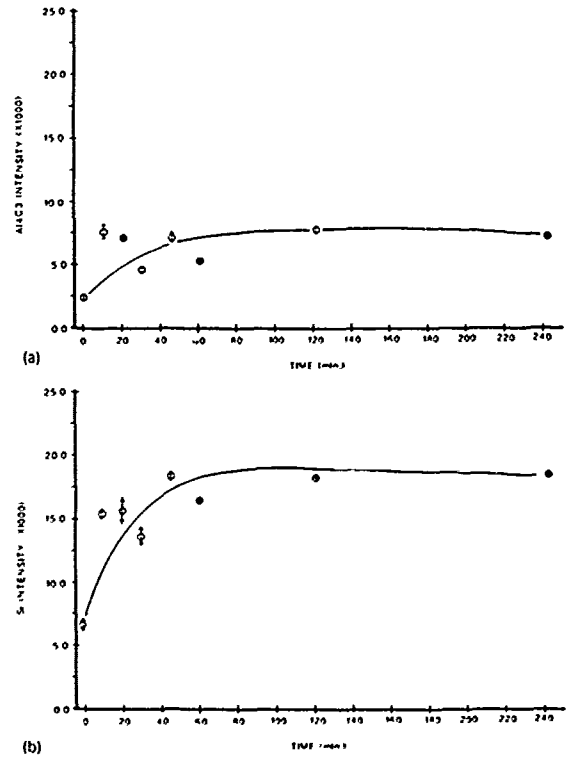

Fig. 3. Rate of reaction to form Al_4C_3 in 6061–SiC: (a) Al_4C_3 peak intensity for AA6061–20vol.%SiC at 800 °C; (b) silicon peak intensity for AA6061–10vol.%SiC at 800 °C.

(1), monitoring the intensity of the Al_4C_3 or silicon diffraction peaks indicates the progress of the reaction. Figure 3 shows the extent of reaction with time in a 6061 matrix. Initially, the reaction occurs very rapidly but it is almost saturated after

60 min and the extent of reaction increases with increasing temperature. The kinetics are not parabolic but are best represented by two linear regions with the region after 60 min having a much lower rate constant. The reaction rate is expected to decrease with time because the local silicon content increases. However, provided the temperature is kept sufficiently low, or the SiC is protected, only a limited amount of Al_4C_3 is formed.

DACC uses a proprietary surface treatment and processing route to inhibit Al_4C_3 formation. Under optimum conditions, clean interfaces are formed (Fig. 4). When reaction occurs, a thin reaction product layer is first formed along the interface (Fig. 5). Energy-dispersive X-ray analysis in scanning transmission electron microscopy of this layer showed aluminium, silicon and magnesium peaks, indicating the presence of Al_4C_3 and Mg_2Si. As more extensive reaction occurs, Al_4C_3 crystals grow out from the interface (Fig. 6) and eventually large crystals of Al_4C_3, which are often faulted, are formed (Fig. 7). In a 6061 matrix the Al_4C_3 is often associated with the intermetallic Mg_2Si (Fig. 7) which is formed by reaction between the magnesium in the matrix and the silicon produced by the reaction.

Therefore, it is seen that process control is critical if degradation of the reinforcement is to

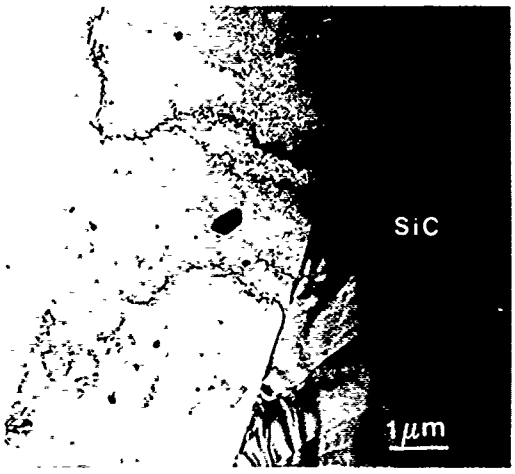

Fig. 4. Clear interface in 6061–SiC.

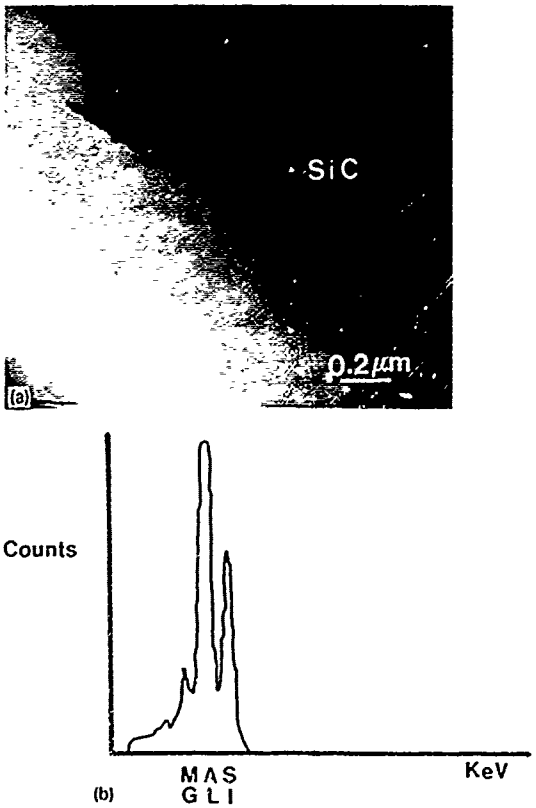

Fig. 5. a Thin reaction layer along interface and b the EDS trace.

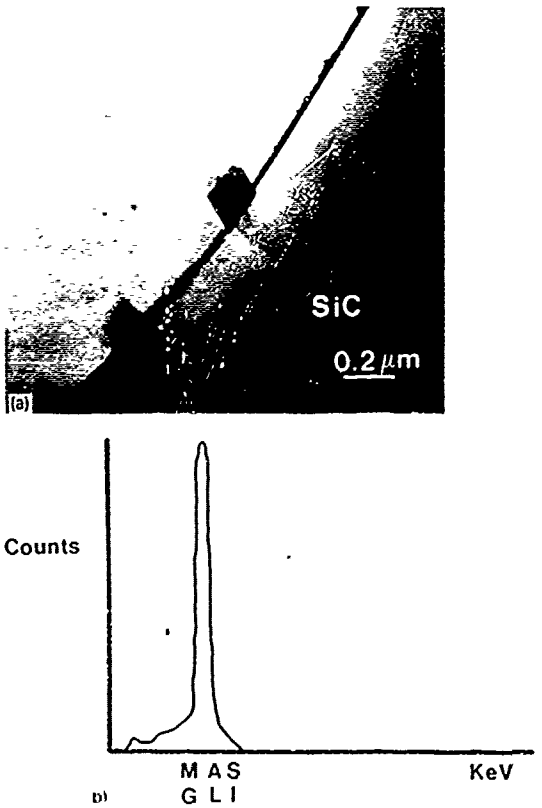

Fig. 6. a Al_4C_3 crystals nucleated at the interface and b the EDS trace.

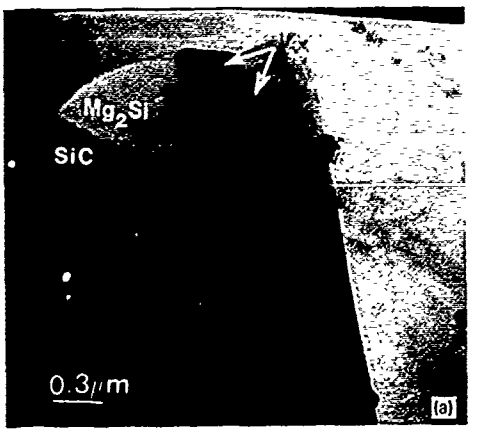

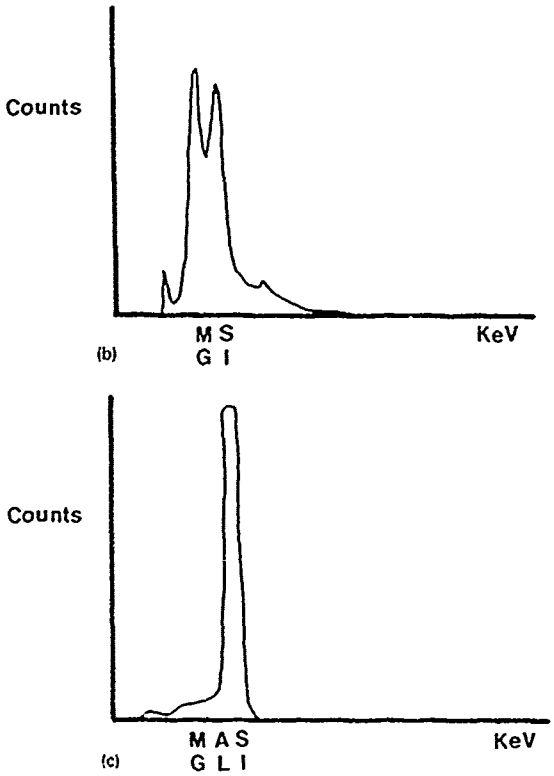

Fig. 7. (a) Large Al_4C_3 crystals associated with Mg_2Si, and (b), (c) the EDS traces.

be avoided. The particular reinforcement used is obviously important but so is the matrix alloy. From eqn. (1), SiC reacts with aluminium to form Al_4C_3 and silicon. This means that there is a silicon content level in the matrix where equilibrium conditions will inhibit Al_4C_3 formation. The silicon content level required can be calculated from the excess molar free energy for the reaction [5] and the activity coefficient. The silicon content levels required at different temperatures are shown in Fig. 8 [6]. These results show that casting alloys with high silicon contents will have a high resistance to Al_4C_3 formation. At temperatures below 750 °C no detectable Al_4C_3 formation occurs during up to 2 h in A356–15vol.%SiC containing 7 wt.% Si, which is slightly below the optimum silicon content level for complete stability. The interface between the reinforcement and the matrix in this composite, cast at 710 °C and solution treated and aged according to standard practice, shows little evidence of a reaction product (Fig. 9).

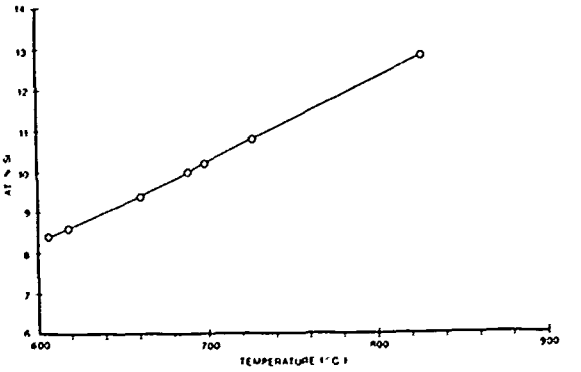

Fig. 8. Minimum silicon content level required to prevent Al_4C_3 formation in aluminium at different temperatures.

From this discusson, it is apparent that there is more flexibility in processing casting alloys, as compared with the wrought alloys with low silicon contents.

3. Solidification

After the reinforcement is incorporated into the melt, the composite is cast into a mould. During solidification, the SiC particles are rejected at the meniscus and pushed ahead of the solidification front to be trapped finally by converging dendrite arms in the intercellular regions. This means that the solidification cell size, and hence the solidification rate, *i.e.* the cooling rate during solidification, influences the distribution of SiC in the final ingot.

Figure 10 shows the microstructure at two cooling rates in 6061–20vol.%SiC and in A356–15vol.%SiC solidified very slowly in a casting. The composite in Fig. 10(a) was solidified at a cooling rate of 20 °C s^{-1} which gives a solidification cell size approximately equal to the SiC particle size. As a result, very little particle push-

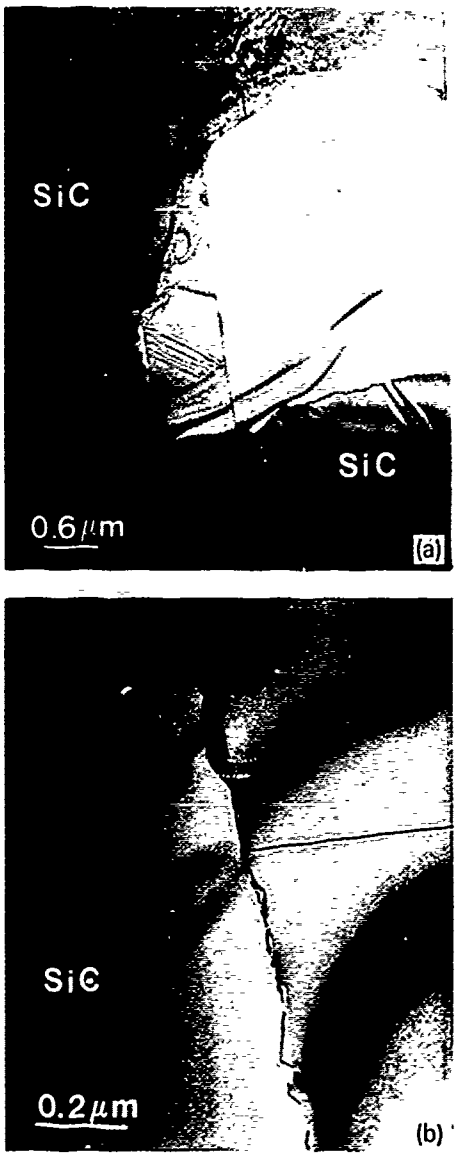

Fig. 9. Interfaces in remelted A356-SiC.

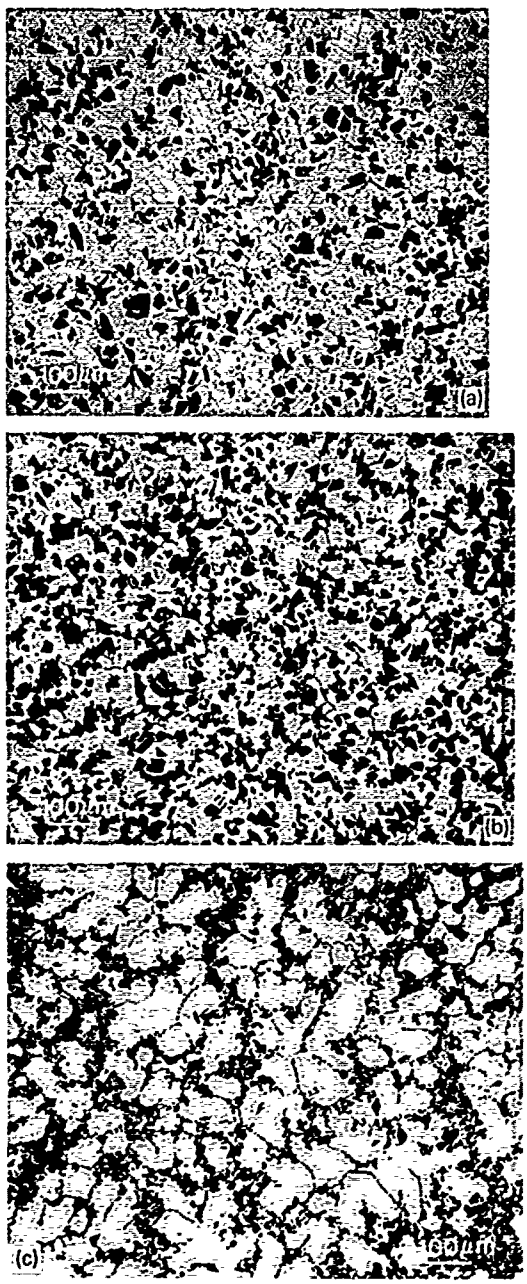

Fig. 10. Microstructure and SiC distribution after solidifying 6061-20vol.%SiC at a cooling rate of a 20 °C s^{-1} and b. 1.0 °C s^{-1}, and (c) slowly solidified A356-15vol.%SiC.

ing occurred during the solidification. If the solidification rate is slower, *e.g.* solidified at a cooling rate of 1.0 °C s^{-1} as in Fig. 10(b), the solidification cell size is several times larger than the particle size, particle pushing is more extensive and the reinforcement distribution is more clustered. At extremely low solidification rates the solidification cell size can be an order of magnitude larger than the SiC particle size, and then particle pushing during solidification results in an SiC particle network delineating the cell boundaries, as in Fig. 10(c). It should also be noted that, because the SiC is in the interdendritic regions, any coarse constituent particles will also be associated with the reinforcement.

Secondary fabrication, such as extrusion, can modify the particle distribution but complete declustering cannot be achieved even at the highest extrusion ratios.

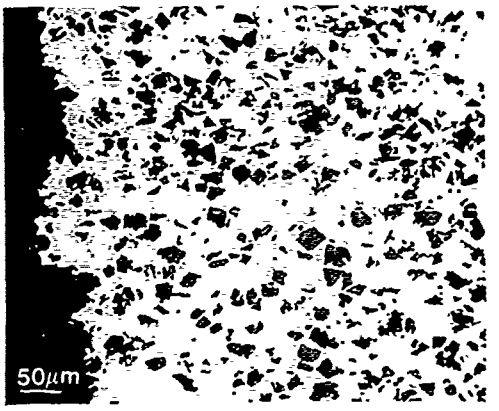

Fig. 11. Fracture path in 6061–20vol.%SiC in T4 temper.

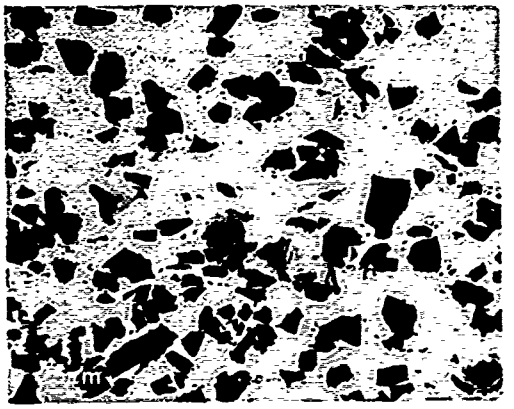

Fig. 12. Crack extending through SiC and associated intermetallic particle.

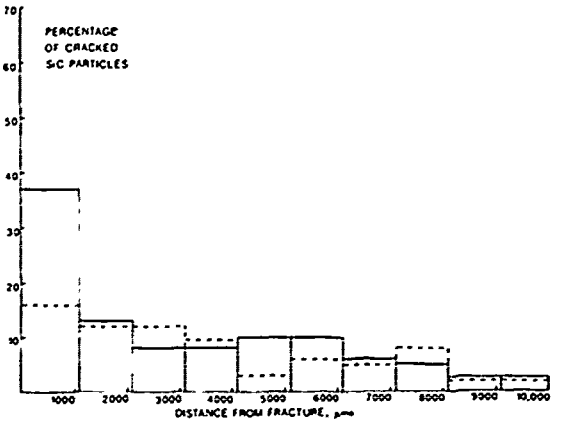

Fig. 13. Extent of SiC particle cracking *vs.* distance from the main crack. The broken line is for 6061–10vol.%SiC and the solid line for 6061–20vol.%SiC.

4. Fracture

For brevity, a detailed consideration of the mechanical properties of cast composite will not be entered into. However, it is appropriate to consider briefly the fracture processes involved, because fracture of particulate composites made by powder metallurgy have been studied [7, 8]. Tensile fracture of extruded 6061–SiC in various heat treatments shows a mixed fracture path (Fig. 11) with the crack propagating through reinforcing particles, through the particle–matrix interface, and through the matrix. This material was extruded at 450 °C with an extrusion ratio of 20:1, which results in there being very few cracked SiC particles after extrusion. However, there is the occasional void associated with clusters of SiC particles. These voids are the remnants of voids present in the as-cast billet which have not been closed during extrusion.

Some SiC particles are associated with coarse intermetal particles and, during straining, these intermetallics crack and the crack then propagates through both the intermetallic and the SiC particles (Fig. 12). The extent of SiC fracture away from the main crack depends both on the extent of aging and on the volume fraction of reinforcement. In the solution-treated condition, where the fracture strain is about 7% at 20 vol.% and over 10% at 10 vol.%, extensive particle fracture and voiding occurs over the whole gauge length. In the peak aged condition, where the tensile elongation is about 2%, the damage is more localized, particularly in the composite with the higher volume fraction. Figure 13 shows the extent of SiC particle fracture with distance from the main crack in 10 and 20 vol.% composites in the T6 temper. Examination of the different fracture surfaces in the scanning electron microscope shows that the extent of ductile dimpling is decreased progressively with increasing SiC content and with the extent of aging (Fig. 14). In the composite materials, fine dimples occur in the regions of matrix between the particles which have undergone ductile tearing (Fig. 15). From these observations it is apparent that the fracture process in these materials is quite complex, involving several different phenomena. Voids associated with clusters of particles will open up and grow during straining. It is not clear whether the failure observed in the particle–matrix interface is due to the opening up of incipient voids or to intrinsic failure of the interface. In addition to

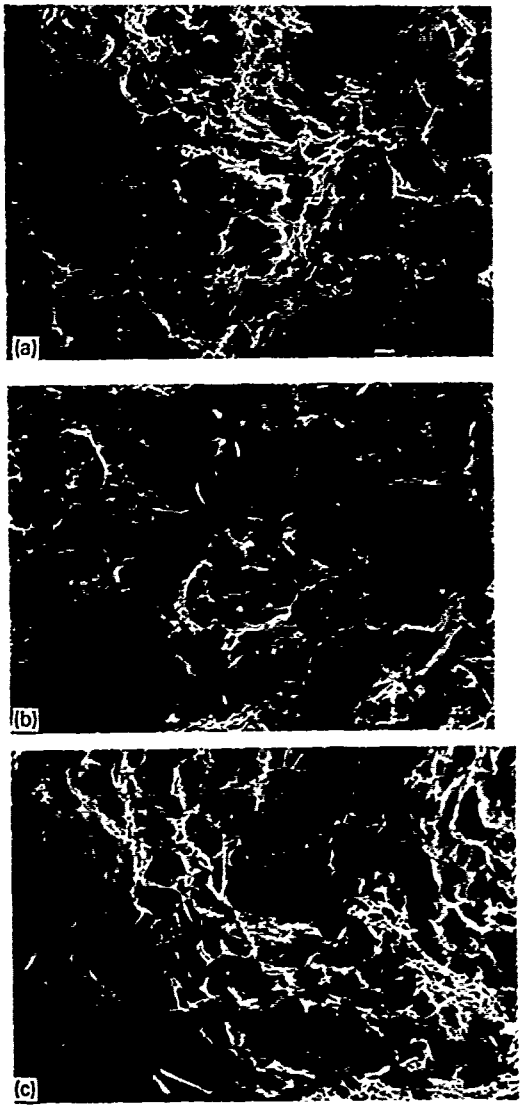

Fig. 14. Fracture surfaces in (a) 6061, (b) 6061 - 10vol.%SiC and (c) 6061 - 20vol.%SiC all in T4 temper.

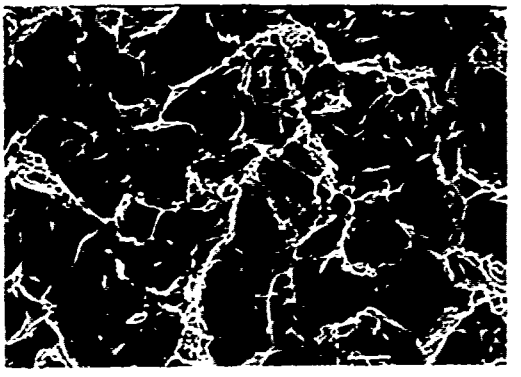

Fig. 15. Fine dimples in the fractured matrix between particles.

voiding, some SiC particles, and any coarse intermetallics associated with them, crack during tensile straining. Cracks produced by voiding or by particle fracture then link by ductile failure of the matrix. To optimize the tensile elongation it will be necessary to limit particle clustering, to eliminate any voids associated with the particle clusters, and to control the alloy composition and heat treatment so that no coarse intermetallics are present in the microstructure.

5. Summarizing remarks

When metal matrix composites are produced by the casting method, several factors have to be considered which differentiate them from composites produced by the powder metallurgy route. With SiC reinforcement, the technology has to limit Al_4C_3 formation, which can be done by process control or by a suitable choice of matrix alloy. The distribution of the reinforcement is a function of the solidification rate: in general the higher the solidification rate, the more uniform the distribution. Because the SiC is situated in the interdendritic regions, the alloy metallurgy has to be controlled carefully to prevent brittle intermetallics being associated with the reinforcement and this, of course, is also a consideration in composites made by the powder metallurgy route.

There are still many aspects of the behaviour of particulate composites, especially those associated with fracture, which are not fully understood. However, the progress made to date indicates that these composites have considerable potential as general engineering materials.

Acknowledgments

The authors thank Alcan International and Dural Aluminum Composite Corporation for permission to publish this paper. They would also like to thank their colleagues in the MMC group for their contributions to many parts of this work.

References

1 R. Warren and C.-H. Anderson, *Composites*, *15* 1984 101

2 T. A. Chernyshova and A. V. Rebrov, *J. Less Common Met.*, *117* 1986 203

3 W. C. Moshier, J. S. Ahearn and D. C. Cooke, *J. Mater. Sci., 22*(1987) 1154.
4 D. J. Lloyd and I. Jin, *Metall. Trans.*, in the press.
5 J. L. Murray and A. J. McAlister, *Bull. Alloy Phase Diag., 5*(1984) 7.
6 E. W. Dewing and D. J. Lloyd, *Int. Symp. on Advanced Materials, Canadian Institute of Mining and Metallurgy, Montreal, August 1988*, in press.
7 J. J. Lewandowski, C. Lui and W. H. Hunt, in P. Kumar, K. Vedula and A. Ritter (eds.), *Powder Metallurgy Composites*, The Metallurgical Society of AIME, Warrenda PA, 1987, p. 117.
8 Y. Flom and R. J. Arsenault, *Proc. 6th Int. Conf. on Composite Materials and 2nd European Conf. on Composite Materials, London, 1987*, Vol. 2, Elsevier, London, 1987, p. 189.

Materials Science and Engineering, A107 (1989) 81–91

Development of Nickel Aluminide Matrix Composites*

J.-M. YANG

Department of Materials Science and Engineering, University of California, Los Angeles, CA 90024 (U.S.A.)

W. H. KAO

Materials Science Laboratory, The Aerospace Corporation, El Segundo, CA 90245 (U.S.A.)

C. T. LIU

Metals and Ceramics Division, Oak Ridge National Laboratory, Oak Ridge, TN 37831 (U.S.A.)

(Received June 1, 1988)

Abstract

Nickel aluminide matrix composites reinforced with continuous fibers, discontinuous fibers and particulates are attractive materials for high temperature structural applications. They possess excellent high temperature strength, good creep and oxidation resistance, as well as lower density than superalloys. A variety of alloys based upon Ni_3Al have been successfully produced and are reported to have improved properties over stoichiometric Ni_3Al. These alloys are all candidate matrix materials for intermetallic matrix composites. This paper provides a comprehensive overview of the recent development of nickel aluminide matrix composites. Various processing techniques such as hot pressing, diffusion bonding, hot extrusion, reactive sintering, and liquid infiltration have been employed to consolidate the composites. The interface compatibility between various reinforcements and nickel aluminide matrices are examined. Finally, the mechanical properties and the directions for future development of various nickel aluminide matrix composites are discussed.

1. Introduction

Ordered intermetallic alloys such as nickel aluminides are attractive materials for high temperature structural applications due to their high strength retention at elevated temperatures, combined with low density and good oxidation resistance [1, 2]. Because of the long-range ordered structure, intermetallic alloys tend to have smaller self-diffusion coefficients than those of disordered alloys. The restricted atomic mobility generally results in excellent corrosion and creep resistance [3]. Also, nickel aluminide is the most important strengthening constituent of commercial nickel-based superalloys and is responsible for their high temperature strength and creep resistance. The yield strengths of various conventional alloys and advanced intermetallic alloys as a function of temperatures are shown in Fig. 1 [1]. The high temperature strength of advanced intermetallic alloys at 850 °C is superior to that of nickel-based superalloys. However, the applications of polycrystalline aluminides as engineering materials has been limited primarily because of

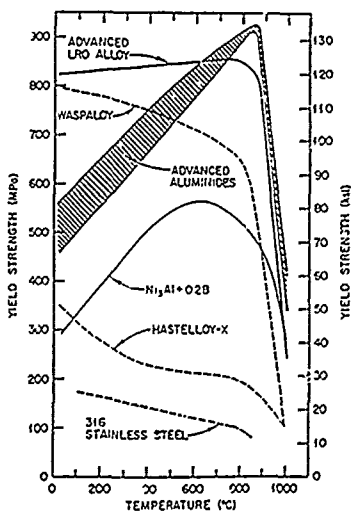

Fig. 1. Yield strength of various alloys and advanced intermetallic alloys as a function of temperature [1]

*Paper presented at the symposium on Interfacial Phenomena in Composites: Processing, Characterization, and Mechanical Properties, Newport, RI, June 1–3, 1988.

0921-5093/89/$3.50

© Elsevier Sequoia/Printed in The Netherlands

the severe problem of poor ductility and brittle intergranular fracture at ambient temperatures. Factors which may lead to the brittle failure of intermetallic alloys include a limited number of easy slip systems, large slip vectors, restricted cross-slip and difficulty of transmitting slip across grain boundaries [4]. Nevertheless, significant improvement in the ductility and toughness has been achieved through various metallurgical techniques such as processing control, grain refinement, microalloying, macroalloying, and rapid solidification [5, 6]. For example, it has been found that the addition of a small amount of boron into Ni_3Al increases the grain boundary adhesion, thereby inhibiting brittle intergranular fracture of polycrystalline Ni_3Al [7]. A tensile elongation greater than 50% with virtually 100% transgranular failure has been achieved in Ni-24at.%Al containing about 0.5 at.% B [8-10]. A comprehensive discussion of the toughening of various intermetallic alloys is summarized in refs. 4-6.

The breakthrough in intermetallic alloy technology has also opened up a significant opportunity for developing a new class of intermetallic matrix composites. The incorporation of particulates, whiskers or continuous fibers into the intermetallic alloy matrix should produce a composite which possesses a lower density, improved tensile strength and creep resistance. Potential applications of these novel intermetallic composites include hypersonic aircraft, space vehicles, and jet engines, etc., where light weight and sufficient specific stiffness and strength at elevated temperature are required. Figure 2 shows the calculated specific strength of various alloys and aluminide matrix composites as a function of temperature [11]. It is clear that the SiC fiber-reinforced aluminide matrix composites have much better specific properties than nickel-based superalloys.

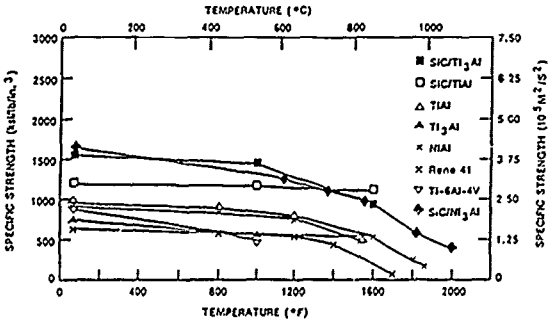

Fig. 2. Calculated specific strength as a function of temperature for various alloys and SiC/aluminide composites [11].

Recently, extensive work on developing processing techniques, optimizing the interface compatibility and characterizing the mechanical properties of composites based upon Ni_3Al matrix alloys are being conducted in many laboratories. The purpose of this paper is to provide a comprehensive overview of the recent development of nickel aluminide matrix composites based upon Ni_3Al. NiAl will be excluded from our discussion because of its poor high temperature strength and low ductility at room temperature.

2. Design of Ni_3Al matrix alloys

Current efforts on alloy design of Ni_3Al have been focused on four areas: (1) improvement of ductility at ambient temperatures, (2) enhancement of high temperature strength by solid solution effects, (3) alleviation of dynamic embrittlement in oxidizing environments, and (4) fabrication improvement [1]. Based upon these efforts, a variety of matrix alloys have been developed including IC-15 (Ni-24.0at.%Al-0.24at.%B), IC-50 (Ni-23at.%Al-0.5at.%Hf-0.2at.%B), IC-218 (Ni-16.5at.%Al-8.0at.%Cr-0.4at.%Zr-0.1at.%B), and IC-221 (Ni-16at.%Al-8.0at.%Cr-1at.%Zr-0.1at.%B) [1]. Another type of alloy is represented by nickel-iron aluminide with composition ranges (at.%) of: Ni-18.5 $\pm$ 1.5%Al-13.5 $\pm$ 2.5%Fe-5.5 $\pm$ 2.5%Cr-0.25 $\pm$ 0.15%Zr(Hf)-0.1 $\pm$ 0.04%B. These alloys have also been developed for potential structural use at elevated temperatures.

In these aluminides, chromium is added for reducing dynamic embrittlement in oxidizing environments at elevated temperatures, and zirconium or hafnium is added for improving high-temperature strength via solid-solution hardening effects. Microalloying with boron enhances grain boundary cohesive strength and increases ductility at ambient temperatures. Addition of iron to nickel-iron aluminides is to improve hot fabricability. Excellent tensile and creep properties as well as oxidation resistance have been achieved in Ni_3Al alloys which serve as attractive matrix materials for composite development.

3. Processing development

Various processing methods have been employed to consolidate the nickel aluminide

matrix composites with continuous and discontinuous ceramic fibers, as well as particulates. The most representative processes are discussed in the following.

3.1. Hot pressing/hot isostatic pressing

Hot pressing or hot isostatic pressing of mixtures of prealloyed matrix powders and reinforcements has been used extensiveiy to fabricate metal matrix composites. This method is particularly suitable for particulate, whisker and short fiber reinforced nickel aluminide matrix composites. Povirk *et al.* [12] used a hot pressing technique to consolidate both IC-15 and IC-218 matrix composites with short alumina fibers. Composites were fabricated by mixing the nickel aluminide powders (normally 100 mm diameter) with up to 20 vol.% alumina fibers (3 mm in length) in a hexane slurry with a high shear mixer. The mixtures were dried and then hot-pressed in graphite dies. The IC-15 matrix composite was consolidated at 1300–1350 °C for 1 h with a pressure of 20 MPa; a temperature of 1250–1300 °C using 20 MPa pressure for 1.5 h was sufficient for IC-218 matrix. The lower processing temperature for IC-218 was mainly due to the addition of chromium which disorders the material at high temperatures and enhances the diffusion kinetics. In both cases, high density with low porosity were achieved in the composites. However, some fiber clusters and a substantial amount of fiber breakage occurred during the processing of the composites.

Bose *et al.* [13] have successfully consolidated an IC-218 matrix composite with 5 vol.% short alumina fibers by hot isostatic pressing at 1100 °C for 1 h and at a pressure of 172 MPa. However, fiber alignment in the composite cannot be achieved by HIPing, if directional properties are desired. In addition, it appears that the 5 vol.% of alumina fibers is too low to provide adequate mechanical properties for structural use. An initial effort to align the short alumina fibers in IC-218 matrix by using injection molding and subsequently HIPing has been attempted, but the results have not been reported [13].

3.2. Diffusion bonding

Diffusion bonding is one of the most popular methods to fabricate metal matrix composites with continuous fibers [14]. The fiber array is generally made by winding the fibers on a drum, and then spraying them with a binder to form a unidirectional tape. The precollimated fiber tape can also be made by plasma spraying. The nickel aluminide matrix alloy can be fabricated into the form of a thin sheet. The preform tape can then be sandwiched between layers of thin nickel aluminide matrix foils and consolidated into fully densed composite by applying heat and pressure in vacuum or in an inert atmosphere. Nieh *et al.* [11] have made reaction couples for compatibility studies by diffusion bonding IC-50 sheets (0.5 mm) and SiC (SCS-6) fibers at 700–1100 °C for 1 to 6 h under vacuum (10^{-3} Pa). To our knowledge, no nickel aluminide matrix composite plates with continuous fibers have been produced to date. The optimum processing conditions such as temperature, pressure, atmosphere and time to produce void-free nickel aluminide matrix composites need to be developed.

3.3. Hot extrusion

A hot extrusion technique has been used to fabricate TiC and Al_2O_3 particulate-reinforced IC-221 composites [15]. In this process, the gas atomized matrix powders were mixed with TiC or Al_2O_3 particulates. The mixtures were then vacuum hot pressed to ingot and subsequently HIPed at 1162 °C/105 MPa/3 h to 97% density, then hot extruded to rod at 1150 °C to form a fully dense composite billet. Direct hot extrusion from loose powder mixtures is also being studied at various laboratories. Temperature and extrusion ratio are the important processing parameters which must be optimized.

3.4. Reactive sintering

Reactive sintering has been developed by Bose *et al.* [16] to consolidate nickel aluminide matrix composites with discontinuous alumina fibers. In this process, the elemental nickel and aluminum powders were mixed in the stoichiometric ratio, along with 3 vol.% of short (3–5 mm) alumina fibers and boron. The mixtures were then cold isostatically compacted into rods and encapsulated in stainless steel under vacuum (5×10^{-3} Pa) and hot isostatically pressed. This is a relatively new process to fabricate composites. The major advantage of this process is that the reaction to form the compound may occur at temperatures far below the melting point of the compound. The lowest-melting eutectic forms in the Ni–Al system at 640 °C. At moderate temperatures, the elemental aluminum powders react and form the desired compound, usually in a

highly exothermic reaction. Once the reaction starts, the heat of reaction causes the lower-melting constituent to form a liquid to produce a rapid densification. For example, reactive sintering of Ni_3Al+B with alumina fibers has been carried out at 800 °C for 30 min at a pressure of 104 MPa. This is in contrast to 1100–1300 °C for hot pressing or HIPing. However, the actual temperature at the reaction front has not been measured, but was estimated to be around 1500 °C. As a result, one must consider the high reaction front temperature and duration which might play dominant roles in determining the interface compatibility. Sintering temperature, heat rate, particle size, composite dimension and reaction environment are the key processing parameters controlling the quality of the composite. Reactive sintering of the Ni_3Al+B with Y_2O_3 coated SiC fibers has been made at 750 °C for 10 min. A post reaction heat treatment at 1300 °C/1 h was also used to homogenize further the matrix microstructure. However, it is clear that the fiber volume content in the composite needs to be increased in order to obtain the desirable strengthening effect from the reinforcements.

3.5. Liquid infiltration/pressure casting

Liquid infiltration/pressure casting has been used to fabricate a Ni_3Al (IC-50) matrix composite with alumina fibers [17]. The precollimated fibers were placed into a mold, and the molten Ni_3Al matrix was infiltrated into the pre-evacuated and preheated mold followed by a solidification process. The casting process was carried out at temperatures between 1400 and 1700 °C under 2.7 MPa of argon gas pressure. The key issue in solidification processing is wetting between the reinforcement and the liquid matrix [18]. Wetting of the fiber surface with a liquid matrix is necessary to promote the formation of a chemical bond at the interface. Extensive work has been conducted to study the wetting behavior of various carbides, oxides and borides with nickel [19]. The wetting angle at a specific temperature between Ni and various potential reinforcements is summarized in Table 1. It is shown that, even at 1500 °C, the angle of contact between Al_2O_3 and liquid nickel is 125°, *i.e.* no wetting occurs. However certain alloying additions such as titanium could change the Ni–Al_2O_3 systems from non-wetting to wetting [20] and can also improve the wetting between Al_2O_3 fibers and Ni_3Al [17]. Similar studies need to be performed to understand the wetting of Ni_3Al alloys with various potential reinforcements.

In addition to the above-mentioned processing techniques, several other methods have also been used to strengthen the nickel aluminide matrix. For example, mechanical alloying followed by HIPing was used to fabricate oxide (Y_2O_3, Al_2O_3, or ThO_2) dispersion strengthened IC-50 alloys [21]. In this case, a dramatic increase in yield strength at room temperature was achieved. This was attributed to the influence of fine dispersoids on the refinement of the matrix grain size during consolidation, rather than the Orowan strengthening mechanism.

4. Interface compatibility

The nature and properties of the interface are of paramount importance in determining the performance of the composite. Although the development of reinforcement/matrix interaction zone of some thickness is desirable for establishing sound interfacial bonding, overgrowth of the interaction layer will be detrimental to the composite properties [14]. Also, the selection of an appropriate diffusion barrier material to prevent deleterious interaction relies on a detailed knowledge of the interaction between the reinforcement and the matrix. Therefore, it is of considerable importance to understand the compatibility between the nickel aluminide matrix and various reinforcements.

4.1. Interface chemical reactions

4.1.1. Al_2O_3/Ni_3Al

The interactions between Al_2O_3 fibers and both IC-15 and IC-218 matrices have been

TABLE 1 The wetting between nickel and various potential reinforcements [19] (temperature °C–contact angle)

	SiC	B_4C	TiC	ZrC	HfC
Ni	1450–65	1460–88	1380–23	1380–24	1380–23
	Al_2O_3	SiO_2	ZrO_2	TiB_2	ZrB_2
Ni	1500–150	1500–125	1500–130	1480–40	1500–42

TABLE 2 Reaction between Al_2O_3 and various nickel-based alloys and nickel aluminides [12, 16, 20, 22–27]

Fiber	*Matrix*	*Reaction products*	*Remark*
Single-crystal Al_2O_3	Ni	$NiAl_2O_4$	Heat treated at 1300 °C for 100 h in helium
Single-crystal Al_2O_3	Ni–20Cr	Ni–Cr–Al Spinel	Heat treated at 1300 °C for 100 h in helium
Single-crystal Al_2O_3	Hastelloy-X	No reaction products	Heat treated at 1300 °C for 100 h in helium
Single-crystal Al_2O_3	NASA Nifeco 5	No reaction products	Heat treated at 1300 °C for 100 h in helium
Single-crystal Al_2O_3	Inconel-718	No reaction products	Heat treated at 1100 °C for 100 h in vacuum
Single-crystal Al_2O_3	Ni–10Cr	No reaction products	Heat treated at 1100 °C for 100 h in vacuum
Al_2O_3 powder	Ni	Ni_2Al_3	Hot pressed at 1350 °C, 2 h
Polycrystalline Al_2O_3	IC-15	No reaction products	Hot pressed at 1300 °C, 0.5 h
Polycrystalline Al_2O_3	IC-218	No reaction products	Hot pressed at 1250 °C, 0.5 h
Polycrystalline Al_2O_3	Ni_3Al+B	No reaction products	Reactive sintering at 800 °C, 0.5 h

studied [12]. The chemical interactions of various types of Al_2O_3 with nickel-based alloys and nickel aluminides are summarized in Table 2 [12, 16, 20, 22–27]. No continuous reaction phases between the alumina fibers and both IC-15 and IC-218 nickel aluminides were observed from TEM micrographs and microdiffraction patterns. Concentration profiles measured across the interface by EDS also revealed no evidence of interface reaction in the composite. The TEM results did indicate, however, that the matrix was in intimate contact with the fiber surface, suggesting that bonding between the Al_2O_3 fiber and the matrix had occurred [12]. Metallographic examination also showed no apparent attack of the alumina fibers by Ni_3Al+B (IC-15) matrix after reactive sintering [16]. However, previous studies had indicated that the single-crystal Al_2O_3 fiber reacted extensively with Ni and Ni–20% Cr to form $NiAl_2O_4$ spinel and Ni–Cr–Al spinel, respectively, after heat treatment at 1300 °C for 100 h in a helium atmosphere [22]. It was believed that the reaction was the result of nickel reacting with Al_2O_3 in the presence of sufficient free oxygen. On the other hand, by alloying the nickel matrix with 10% Cr, it was found to be possible to prevent the spinel formation even after a 100 h vacuum anneal at 1100 °C [26]. Thus, even though the as-processed Al_2O_3/nickel aluminide composite does not show any chemical reaction, a reaction might take place during high temperature service environments. It is apparent that more work is necessary to understand thoroughly the compatibility between various alumina fibers and nickel aluminide matrix under various thermo-mechanical environments.

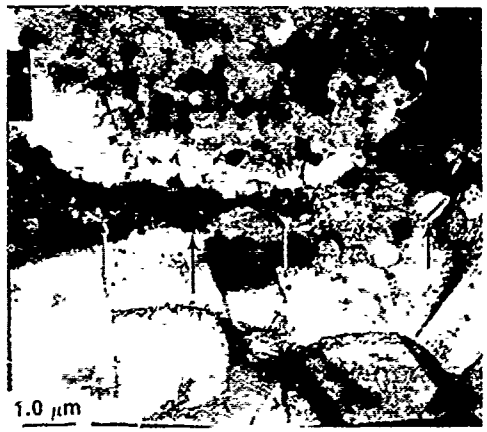

Fig 3 Bright-field TEM micrograph of an annealed IC-218/Al_2O_3 composite showing ZrO_2 particles on an alumina fiber. Arrows point to the zirconia particles.

Zirconia particles, 1–2 μm in diameter, were observed along the fiber/matrix interface in an Al_2O_3/IC-218 composite (Fig. 3) [12]. The formation of zirconia particles resulted from the reaction of zirconium in solution in the matrix with excess oxygen that was present during hot pressing. Similar zirconia particles were also observed at grain boundaries in the hot pressed IC-218 alloys. However, the size of the particles was much smaller (150–300 nm in diameter) in the unreinforced alloys. Zirconia particles in the IC-218 matrix away from the interface were the same size as those in the unreinforced alloys. The unusually large size of zirconia particles was attributed to enhanced nucleation at the fiber surface [12]. Cracks were observed between the ZrO_2 particles and the IC-218 matrix, indicating relatively poor bonding at the interface. The

presence of the ZrO_2 particles will have a detrimental effect on the mechanical properties of the composite. It is possible to eliminate the presence of zirconia particles by reducing the zirconium content or by replacing the zirconium with hafnium in Ni_3Al alloys.

4.1.2. TiC/Ni_3Al

The interaction between TiC and nickel processed by internal carburization has been investigated [28]. It was found that TiC particles were too soluble in the nickel matrix and coarsened too rapidly at temperatures above 800 °C. It was suggested that a highly alloyed matrix might be more effective to decrease the solubility of TiC in the matrix and to lower the diffusion rate of titanium and carbon. In the case of TiC/IC-221, it was also found by SEM/EDS that zirconium and boron diffused to the TiC particle surface after heat treatment at 1100 °C for 100 h [15]. However, the detailed reaction has not yet been studied.

4.1.3. SiC/Ni_3Al

The interface reactions of AVCO's SCS-6 fiber with both IC-50 and IC-221 matrices have been investigated. The reaction between SCS-6 fibers and IC-50 matrix resulted in the formation of multilayer reaction products at the interface [11]. Similar results have been observed for the solid-state reaction between SiC and various nickel-based alloys [29]. Elemental analysis using electron microprobe indicated that the hafnium and boron in IC-50 were not present in the reaction layer, nor did they segregate to reaction layers during the reactions. A significant amount of nickel was detected at the reaction surface of SiC after high temperature heat treatment, while no silicon or carbon was detected at the aluminide reaction surface. This suggested that nickel is the dominant diffusing species responsible for the overall reaction. Severe reaction between SCS-6 fibers and Ni_3Al + B matrix after reactive sintering at 750 °C for 10 min was also observed [16]. Again, this might be due to the effect of high reaction front temperature as stated earlier. The chemical reactions of various SiC with nickel-based alloys and nickel aluminides are summarized in Table 3 [11, 16, 29–37].

It has further been shown that the reaction between SiC fiber and IC-50 is very similar to the reaction between SiC and nickel-based superalloys, except the reaction rate for the former is about five times slower than the latter [11, 29]. Since the nickel-based superalloy contains a large amount of γ' (which is primarily nickel aluminide), the overall chemical reactivities for the superalloy are expected to be similar to those of the nickel aluminide. The rate difference is connected with the fact that nickel aluminide is essentially a stoichiometric compound. In order to react with SiC, chemical debonding of the compound must take place prior to the reaction. In the case of the nickel-based superalloy, nickel is not only present in the γ' precipitates, but also in the solid solution matrix. It is the nickel in the solid solution matrix that leads to the faster reaction in the SiC/superalloy than in the SiC/nickel aluminide system. It has been shown that the carbon-rich layer outside the SiC fiber is not an effective diffusion barrier to prevent the chemical reaction between the SiC fiber and nickel aluminide matrix [11]. Thus, it is apparent that a diffu-

TABLE 3 Reactions between SiC and various nickel-based alloys and nickel aluminides [11, 16, 29–37]

SiC	*Ni-based alloy*	*Reactions*	*Remark*
SiC	Ni	δ-Ni_2Si + graphite	Hot pressed at 1000 °C, 100 h
SiC	Ni–20Cr	δ-Ni_2Si + graphite + η'-Cr_3Ni_5SiC	Hot pressed at 1150 °C, 100 h
SiC	Hastelloy-X	Multilayer reaction products	Hot pressed at 1150 °C, 100 h
SiC	Rene '77	Multilayer reaction products	Hot pressed at 1150 °C, 100 h
SiC fiber	Hastelloy-X	Multilayer reaction products	HIPed at 1150 °C, 100 h
SiC fiber	Waspalloy	Multilayer reaction products	HIPed at 1150 °C, 100 h
SiC fiber	NiCrAl	Multilayer reaction products	HIPed at 1150 °C, 100 h
SCS-6 fiber	Ni_3Al + B	Multilayer reaction products	Reactive sintering at 750 °C 10 min
SiC	IC-50	4-layer reaction products	Diffusion bonded at 900 °C, 1 h
SCS-6 fiber	IC-50	4-layer reaction products	Diffusion bonded at 1100 °C, 1 h
SCS-6 fiber	IC-221	Multilayer reaction products	Hot pressed at 980 °C, 1 h

sion barrier must be developed for the SiC/Ni_3Al composite system.

The reaction between SCS-6 fibers and IC-221 in a composite prepared by hot pressing at 980 °C is shown in Fig. 4. Below 980 °C, multilayer reaction products formed at the interface. The thickness of the reaction zones increases as the composites were subjected to longer time exposure. However, when the composite was subjected to thermal exposure at 980 °C for more than 3 h in vacuum, a rapid increase in reaction zone thickness has been observed as shown in Fig. 5. The elemental distribution across the reaction zone is shown in Fig. 6. The detailed chemical composition and microstructure of the reaction products will be reported elsewhere [37].

4.1.4. B_4C/B-Ni_3Al

Optical micrographs of as-processed B_4C/B fiber-reinforced IC-221 matrix composites prepared by hot pressing at temperatures of 780 °C and 980 °C are shown in Figs. 7 and 8, respectively [37]. It is clear that even at a low processing temperature (780 °C), extensive reactions occurred between the fiber and the matrix. Even with B_4C coating, nickel can still diffuse rapidly into the fiber and react with boron to form Ni_2B or Ni_3B_2. At higher processing temperature (980 °C), the whole fiber reacted with IC-221 as shown in Fig. 8. Previous studies had shown that boron reacted extensively with nickel at temperatures above 700 °C [38]. Thus, the B_4C/B fiber is not a suitable reinforcement for nickel aluminide, unless an effective diffusion barrier coating is used.

4.1.5. TiB_2/Ni_3Al

Titanium diboride is one of the most promising candidates as reinforcement and coating

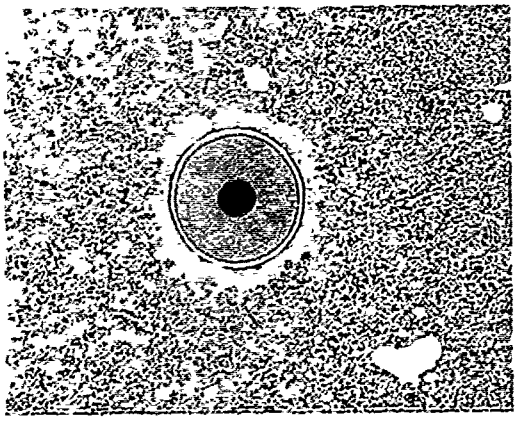

Fig. 4. Chemical interactions of SCS-6 fiber with IC-221 matrix after hot pressing at 980 °C for 2 h.

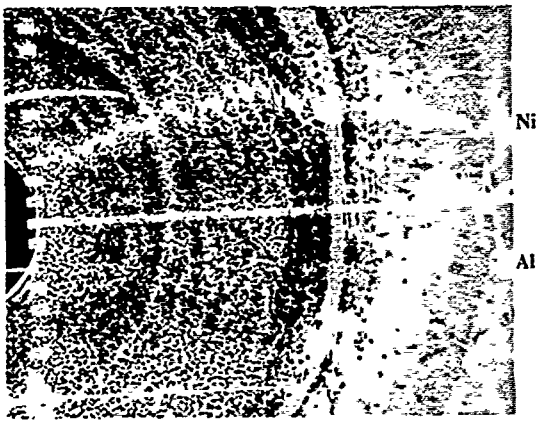

Fig. 6. Elemental distribution from the reaction layers of SCS-6/IC-221 after heat treatment at 980 °C for 6 h.

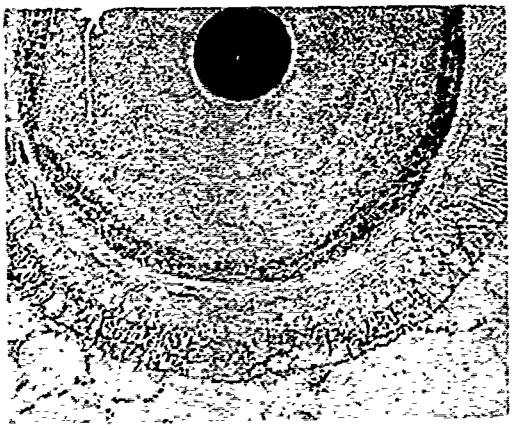

Fig. 5. Chemical interactions of SCS-6 fiber with IC-221 matrix after heat treatment at 980 °C for 6 h.

Fig. 7. Chemical interactions of B_4C/B fiber with IC-221 matrix after hot pressing at 780 °C for 1 h.

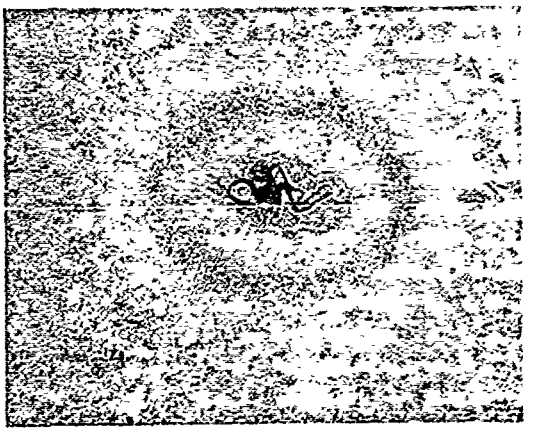

Fig. 8. Chemical interactions of B_4C/B fiber with IC-221 matrix after hot pressing at 980 °C for 1 h.

material for titanium aluminide matrix composites due to its chemical stability [39]. However, a distinct intergranular phase between TiB_2 and Ni_3Al has been observed in a TiB_2-Ni_3Al specimen processed by hot pressing at 1550 °C for 2 h under vacuum (10^{-2} Pa [40]. The intergranular phase has been identified as boride tau phase—$(Ni_xTi_y)_{23}B_6$ by using Analytical Electron Microscopy. Aluminum was not detected in the intergranular tau phase. The formation of this interphase is attributed to the high processing temperature during liquid-phase sintering. However, the boride tau phase may not be present in the TiB_2-reinforced NiAl composites produced by solid-phase processing techniques. The interface reactions of TiB_2/Ni and TiB_2/Ni_3Al samples processed at 1200 °C are being investigated [41, 42]. Meanwhile, it has been reported that no reaction occurred between TiB_2 particulates and NiAl matrix processed by XD synthesis followed by hot pressing [43]. The lack of reaction in TiB_2/NiAl composite is presumably due to the fact that the chemical activity of Ni in NiAl is three orders of magnitude lower than that of Ni_3Al [44].

4.2. Control of interface reactions

A substantial amount of research on controlling the interface reaction has been performed [20]. In order to minimize the excessive reinforcement/matrix interaction and to achieve reasonable service life, it is necessary to suppress the formation of undesirable compounds or to reduce the diffusion rate at the interface. Fiber surface coating has been shown as one of the most effective methods to provide a diffusion barrier to arrest possible forming of unwanted phases at the interface and fiber degradation. The coating layer also provides wetting for a molten matrix alloy if a liquid-phase fabrication method is used.

Based upon the results obtained from the above studies, it has been identified that nickel is the dominant diffusion species during the interaction between SiC and various nickel aluminides [11]. Therefore, an obvious way to restrict the interaction is by selecting a barrier to slow down the diffusion of nickel. Comparing the diffusion coefficients of nickel in various materials, oxides are one of the most effective diffusion barriers for nickel. Nieh *et al.* studied the interface interaction between the SiC fiber and IC-218 matrix foils which were preoxidized to form an Al_2O_3 film [11]. The results show that there is no or little interaction between the preoxidized IC-218 matrix and SCS-6 fibers even at 1100 °C. However, preoxidizing the matrix foil might result in poor bonding during the composite consolidation.

Bose *et al.* have shown that by coating a thin layer of Y_2O_3 on the SCS-6 fiber by CVD can protect the fiber from the matrix during the reactive sintering cycle [16]. The fact that Y_2O_3 prevents the destruction of SiC fiber during processing is consistent with the findings of Mehan *et al.* that Y_2O_3 protects SiC in contact with nickel-based alloys [34]. It has also been found that HfC is an effective diffusion barrier for preventing the deleterious reaction between SiC fiber and the nickel-based superalloys (Hastelloy-X and Waspalloy) [36]. These preliminary results have confirmed that oxides and carbides are good diffusion barriers in inhibiting SiC/nickel aluminide reaction. However, it is necessary to develop a reliable, continuous and cost-effective coating technique, and to understand the influence of the interface layer on the composite strength and the stability and reliability of the barrier under various service environments. A thermodynamic code—FACT (Facility for the Analysis of Chemical Thermodynamics)—has been developed recently by Baal and Palton to study the compatibility among fibers, matrices and coatings [45]. This code calculation can be used as a general guideline for controlling and predicting the interface reactions.

Recently, a new technique to coat a thin layer of Al_2O_3 on the SCS-6 and B_4C/B fiber surfaces from an organometallic precursor solution has been investigated [46]. The fibers were passed

through solution followed by hydrolysis or pyrolysis of the organometallic compound to form Al_2O_3 on the fiber surfaces. Preliminary experimental results show that the solution-coated fibers can reduce the interaction with nickel aluminide matrix. Further work is unde. way to explore the potential of this promising process. Preliminary study on CVD-coated B_4C/B with Al_2O_3 has proven to be successful in preventing interface reaction between the B_4C/B fiber and IC-221 matrix [46].

5. Mechanical properties

The combination of high strength, high stiffness reinforcements and the high temperature strength, low density matrix should result in composites with attractive mechanical properties. However, only very limited mechanical property data for the Ni_3Al matrix composites have been reported. Table 4 summarizes the preliminary results of the yield strength, and the breaking strain of some nickel-aluminide-based composites. It is shown that by adding 20 vol.% of random Al_2O_3 short fibers into IC-15 and consolidating by hot pressing, has resulted in a yield strength (four-point bending) of up to 550 MPa and more than 5% of strain-to-failure [12]. The annealed Al_2O_3/IC-15 composite showed an elongation to failure of 10% under uniaxial tension. The fracture surface showed that the cracks often deflected along the fiber/matrix interface generating matrix microcracks. These results suggest that, at room temperature, a nickel aluminide matrix is sufficiently ductile to resist cracks introduced from fiber breakage. The results for Al_2O_3/IC-218 under bending showed brittle failure with a maximum strain of less than 1% and fracture strength of less than 200 MPa. The low ductility was attributed to the weak bonding between the large ZrO_2 particles and the matrix at the interface, as discussed above.

Moore *et al.* [13, 16] have also found that the incorporation of random alumina fibers in Ni_3Al + B produced no strengthening and actually caused a decrease in tensile strength due to the sharply lowered ductility of the composite. However, the heat-treated IC-218 containing 5% random Al_2O_3 short fibers processed by reactive hot isostatic pressing had 6% elongation at room temperature [16]. SEM fractographic analysis of the composite fracture surface showed that matrix fracture is mainly transgranular, although the ductility of the composite was low. The poor mechanical properties are generally attributed to the randomness of the fiber orientation, fiber clustering, relative poor bonding, and the brittleness of the alumina fibers. Recently, IC-221 matrix composites reinforced with 25 vol.% of Al_2O_3 and TiC particulates produced by hot extrusion have shown a substantial improvement in specific modulus over the matrix alloy [15].

The inferior properties obtained in the Al_2O_3-reinforced composites seem mainly due to the poor fabrication processes. The mechanical properties of composites are strongly affected by their constituents as well as processing conditions. It is apparent that the optimum processing conditions for incorporating any of the potential reinforcements discussed above have not been developed. A nickel aluminide matrix composite with superior performance can only be achieved with controlled microstructure and optimum interface bonding.

6. Directions and future outlook

Ni_3Al matrix composites are promising materials for various high temperature structural applications. However, their potential has not yet

TABLE 4 Mechanical properties of nickel aluminide and composites [12, 13, 16]

Material	*Test temperature* (°C)	*Yield strength* (MPa)	*UTS* (MPa)	*Strain* (%)	*Remark*
IC-218	25	663	1408	23.5	As HIPed 1150 °C
Al_2O_3/Ni_3Al + B	25	474	548	1.0	As HIPed 800 °C
Al_2O_3/IC-218	25	663	893	3.5	Asa HIPed 1150 °C
Al_2O_3/IC-218	25	499	756	6.0	HiPed and heat treated at 1150 °C
Al_2O_3/IC-218	600	814	849	1.0	As HIPed at 1150 °C
Al_2O_3/IC-15	25	500	–	> 5	As hot pressed 1300 °C, bending
Al_2O_3/IC-218	25	–	170-100	< 1	As hot pressed 1250 °C, bending

been fully explored. Considerable research effort is still needed to address the scientific and technological issues concerning the development of this novel high temperature structural composite. Some of the critical issues are summarized as follows.

6.1. Development and optimization of processing methods

The processing techniques for fabricating the nickel aluminide matrix composites are in the early stages of development. In this regard, much can be learned from the aluminum and titanium matrix composites which have been studied extensively. Essentially, all of the processing methods used in the fabrication of the aluminum and titanium matrix composites are adaptable to the nickel aluminide matrix composites. Due to the unique properties of nickel aluminides, the development of novel processing methods together with modifying the existing techniques should be pursued. Optimum processing conditions should be developed by concentrating on a selected processing approach and relate the properties of the composite to interfacial and microstructural features. Hasty judgements based on preliminary data to eliminate or include any material or process should be discouraged, especially in view of the unique behavior and rapid advancement of monolithic nickel aluminide alloys.

6.2. Optimization of reinforcement/matrix interface

It is well established that the interface plays a dominant role in controlling the load transfer efficiency, as well as the failure behavior of the composites. The understanding of the interface reaction products and their growth kinetics are necessary in order to optimize the process parameters during fabrication and service environments. The selection of chemically compatible reinforcements is desirable but is often unachievable during the service conditions. When excessive reactions occur at the interface as in the case of SiC and nickel aluminide alloys, a diffusion barrier is needed. An efficient diffusion barrier material must be able to bond well with the reinforcement and matrix, and possesses adequate strength.

In the case of nickel aluminide, work performed so far seems to indicate that aluminum oxide is probably a material with minimum interface reactions. It is therefore recommended that more effort be concentrated on the understanding of the reactions and kinetics between Al_2O_3 and various nickel aluminide alloys. The development of an Al_2O_3 coating to prevent the reaction degradation of continuous B_4C/B and SiC fibers is also needed. In addition, matrix alloy modifications to promote the wetting between Ni_3Al and various reinforcements for liquid infiltration manufacturing processes are required.

6.3. Development of new matrix alloys

The nickel aluminides recently developed are certainly promising for structural applications at elevated temperatures, yet additional developmental work is needed for further improving their mechanical and metallurgical properties. These include: (a) optimize the microstructure and properties of the alloy through control of the relative amounts of Al, Cr, Zr(Hf); (b) improve cold and hot fabricability, (c) improve the weldability and corrosion resistance through control of minor alloy additions.

It must be noted that the mechanical property improvements achieved in the newer nickel aluminide alloys should not be the only consideration in the selection and design of composite matrices systems. This is due to the fact that the properties of a composite are often dominated by the properties of the reinforcements, particularly for continuous fiber-reinforced composites. In the selection of matrix materials, the chemistry differences between the various nickel aluminide alloys is obviously a more important factor in controlling the interface reactions, therefore, the service life of the composites.

6.4. Characterization of fracture and deformation mechanisms

Mechanical property measurements on a composite system are essential, but the failure/deformation mechanisms and fracture modes need to be investigated simultaneously. It is premature to abandon a system based simply on preliminary mechanical properties data. It is felt that microanalyses such as interfacial and microstructural characterization must be correlated with both static and dynamic properties in order to establish the potential usefulness of the nickel aluminide composite systems. A database containing information on processing/microstructure/properties relationships is needed for design and life predictions. Particular attention should be paid to

the understanding of the strength, deformation mechanism, and failure modes of the composites at elevated temperatures.

Acknowledgment

W. H. Kao would like to acknowledge the support of the Aerospace Sponsor Research Fund, The Aerospace Corporation. C. T. Liu would like to acknowledge the financial support from the Office of Energy Utilization Research, Energy Conversion and Utilization Technology Program, DOE.

References

1 C. T. Liu, in B. L. Bramfitt, R. C. Benn, C. R. Brikman and G. F. Vander Voorf (eds.), *MiCon 86. Optimization of Processing, Properties, and Service Performance through Microstructural Control*, ASTM STP 979, 1988, p. 222.
2 N. S. Stoloff, in C. C. Koch, C. T. Liu and N. S. Stoloff (eds.), *High-Temperature Ordered Intermetallic Alloys*, Materials Research Society, Pittsburgh, PA, 1984, p. 3.
3 D. P. Pope, in N. S. Stoloff, C. C. Koch, C. T. Liu and O. Izumi (eds.), *High-Temperature Ordered Intermetallic Alloy* II, Materials Research Society, Pittsburgh, PA, 1987, p. 3.
4 I. Baker and P. R. Munroe, *J. Met.*, *40* (1988) 28.
5 C. C. Koch, C. T. Liu and N. S. Stoloff (eds.), *High-Temperature Ordered Intermetallic Alloy* I, Materials Research Society, Pittsburgh, PA, 1984.
6 N. S. Stoloff, C. C. Koch, C. T. Liu and O. Izumi (eds.), *High-Temperature Ordered Intermetallic Alloy* II, Materials Research Society, Pittsburgh, PA, 1987.
7 K. Aoki and O. Izumi, *J. Jpn. Inst. Met.*, *43* (1979) 38.
8 C. T. Liu, C. L. White and J. A. Horton, *Acta Metall.*, *23* (1985) 213.
9 S. C. Huang, A. I. Taub and K. M. Chang, *Acta Metall.*, *32* (1984) 1703.
10 A. I. Taub, S. C. Huang and K. M. Chang, *Metall. Trans. A*, *15* (1984) 399.
11 T. G. Nieh, J. J. Stephens, J. Wadsworth and C. T. Liu, in *Proc. Int. Conf. on Composite Interface*, 1988, in the press.
12 G. L. Povirk, J. A. Horton, C. G. McKamey, T. N. Tiegs and S. R. Nutt, *J. Mater. Sci.*, to be published.
13 B. Moore, A. Bose, R. M. German and N. S. Stoloff, in *High Temperature/High Performance Composites*, Materials Research Society, Pittsburgh, 1988, in the press.
14 T. W. Chou, A. Kelly and A. Okura, *Composites*, *16* (1985) 187.
15 G. E. Fuchs and W. H. Kao, *Inter. P/M Conf.*, Orlando, FL, June, 1988.
16 A. Bose, B. Moore, N. S. Stoloff and R. M. German, in *Proc. Conf. on P/M Aerospace Materials, Lucern, Switzerland, November, 1987*, *J. Met.*, *40*, 1988, 14.
17 S. Nourbakhsh, S. L. Liang and H. Margolin, *Advanced Manufacturing Process.*, *3*, 1988, 37.
18 K. C. Russel, J. A. Cornie and S. Y. Oh, in A. K. Dhingra and S. G. Fishman (eds.), *Interfaces in Metal Matrix Composites*, AIME, 1986, p. 61.
19 S. T. Mileiko, in A. Kelly and S. T. Mileiko (eds.), *Fabrication of Composites*, North-Holland, New York, 1985, p. 221.
20 A. G. Metcalfe, in A. G. Metcalfe (ed.), *Interfaces in Metal Matrix Composites*, Academic Press, New York, 1974, p. 65.
21 C. C. Koch, J. S. C. Jang and S. G. Donnelly, *Oak Ridge National Laboratory Contract Report* 19X-43368C, 1987.
22 L. J. Westfall, *NASA* TM X-3333, 1976.
23 R. L. Mehan and M. J. Noone, in K. G. Kreider (ed.), *Metal Matrix Composites*, Academic Press, New York, 1974, p. 159.
24 C. T. Lynch and J. P. Kershaw, *Metal Matrix Composites*, CRC Press, Cleveland, OH, 1972.
25 T. L. Moore, in *Defense Materials Information Center Memorandum 243*, 1969.
26 L. A. Gonzalez (ed.), *Introduction to Metal Matrix Composite Materials*, DOD Metal Matrix Composites Information Analysis Center, Santa Barbara, CA, 1982.
27 I. P. Arsentyeva and M. M. Ristic, in G. S. Upadhyaya (ed.), *Sintered Metal-Ceramic Composites*, Elsevier, New York, 1984, p. 181.
28 R. J. Murphy and N. J. Grant, *MIT Report 703*, 1968.
29 E. L. Hall, Y. M. Kouh, M. R. Jackson and R. L. Mehan, *Metall. Trans. A*, *14* (1983) 781.
30 M. R. Jackson, R. L. Mehan, A. M. Davis and E. L. Hall, *Metall. Trans. A*, *14* (1983) 355.
31 R. L. Mehan and D. W. McKee, *J. Mater. Sci.*, *11* (1976) 1009.
32 M. R. Jackson, R. L. Mehan and M. R. Jackson, *Ceramic Engineering and Science Proc.*, Vol. 7, 1981, p. 787.
33 R. L. Mehan and R. B. Bolon, *J. Mater. Sci.*, *14* (1979) 2471.
34 R. L. Mehan, M. R. Jackson and M. D. McConnell, *J. Mater. Sci.*, *18* (1983) 3195.
35 J. A. Cornie, C. S. Cook and C. A. Anderson, *NASA*-Cr-134956, 1976.
36 J. A. Cornie, *NASA* CR-135301, 1977.
37 J.-M. Yang, W. H. Kao and C. T. Liu, *Interface Characterization of Fiber-Reinforced Nickel Aluminide Matrix Composites*, in preparation.
38 R. F. Schneidmiller and J. E. White, *SAMPE*, paper E-53, 1966.
39 F. E. Wawner, *Universal Technology Corporation Contract Report* F33615-84-C-5127, 1986.
40 P. Angelini, P. F. Becher, J. Bentley, C. B. Finch and P. S. Sklad, in J. H. Crawford, Y. Chen and W. A. Sibley (eds.), *Defect Properties and Processing of High-Technology Nonmetallic Materials*, Materials Research Society, Pittsburgh, PA, 1984, p. 299.
41 J.-M. Yang and W. H. Kao, unpublished results.
42 T. N. Tiegs, Oak Ridge National Laboratory, private communication.
43 R. K. Viswanadham and J. D. Whittenberger, in *High Temperature/High Performance Composites*, Materials Research Society, Pittsburgh, 1988, in the press.
44 R. Hultgren, P. D. Desai, D. T. Hankins, M. Gleiser and K. K. Kelley, *Selected Value of the Thermodynamics Properties of Binary Alloys*, ASM, Metal Parks, OH, 1973, p. 191.
45 W. T. Thompson, *FACT Booklet*, Royal Military College, Canada, 1988.
46 P. C. Brennan, W. H. Kao and J.-M. Yang, unpublished results.

Processing and Properties of Metal Matrix Composites Containing Discontinuous Reinforcement*

M. G. McKIMPSON and T. E. SCOTT

Institute of Materials Processing, Michigan Technological University, Houghton, MI 49931 (U.S.A.)

(Received June 1, 1988)

Abstract

Metal matrix composite materials which utilize discontinuous-type reinforcement undergo unit operations associated with ingot, powder or cast metal manufacturing in addition to their own unique operations. An attempt is made to summarize the scope of operations for both cast- and powder-based processing and identify processing issues which cause matrix–reinforcement interface and property variability in discontinuous metal matrix composites.

1. Introduction

Of all the variable factors contributing to the properties of metal matrix composites (hereafter MMCs), probably the single most important one is the interface between the matrix and the reinforcing phase. Considerable effort has been devoted to interface characterization of MMC materials. However, it is very difficult to make unambiguous correlations between interface structure and MMC properties because the latter are influenced by a myriad of other factors—many of them quite subtle—which need to be carefully controlled.

It is from this perspective that MMC processing, properties and interfaces are described in this paper.

Although several processing methods have been used to produce MMC [1], the focus of this paper is on discontinuous metal matrix composites (hereafter DMMCs) which are reinforced with whiskers, chopped or milled fibers, or particulate of ceramic materials. Processing of commercial DMMC materials generally involves at least two operations—production of the composite material itself and fabrication of this composite into useful product forms. Both operations can affect the properties and interfacial characteristics of the final material. The processes used for producing composite billets will be discussed first. To facilitate discussion, these processes have been subdivided into three categories: molten metal processing, powder processing and deposition processing. Fabrication processes for these composite billets will then be considered.

*Paper presented at the symposium on Interfacial Phenomena in Composites: Processing, Characterization, and Mechanical Properties, Newport, RI, June 1–3, 1988.

2. Billet processing

2.1. Molten metal processing

Of the three categories, this one encompasses the widest range of variations. Three papers [2–4] have reviewed and summarized the body of knowledge regarding molten metal processing of DMMC. Considering the recent date of these reviews, there is little value in paraphrasing them. Instead, we will provide a brief description of molten metal processes that have been commercialized or appear to be moving in that direction. Other molten metal processes which have been explored, but do not appear to offer much promise of being commercialized, will simply be cited with rather terse commentary.

Conventional casting [2–15], compocasting [16–29] and standard squeeze casting [30–37] methods for making DMMC, including some interesting hybrids, have all been thwarted by one major problem: the extreme difficulty of simultaneously obtaining sufficient wetting of the reinforcement by the molten matrix metal without incurring excessive or disastrous reactivity between the components.

Only two cases of apparent success in making DMMC billets by molten metal processes without the use of reinforcement preforms are known to the authors. Of course this status is subject to rapid change.

Magnesium alloys seem to have an inherent ability to adequately wet Al_2O_3 and SiC reinforcement [14]. Commercial production of molten

0921-5093/89/$3.50

© Elsevier Sequoia/Printed in The Netherlands

metal processed magnesium-based DMMC is imminent. Otherwise, successful production of DMMC material by casting is dependent on the use of a proprietary process for coating silicon carbide particulate (hereafter SiC_p) [15]. Mechanical properties of these and other DMMC produced by less promising processes are given in Table 1.

TABLE 1 Mechanical properties of cast/deposited DMMC

Matrix	*Reinforcement* (vol.%)	*Process*	*Yield stress* (MPa)	*Ultimate stress* (MPa)	*Elongation* (%)	*Modulus* (GPa)	*Ref.*
6061-T6	Tokai β-SiC_w (17) Slip cast preform	Squeeze infiltration at 100 MPa + extr. 25:1 at 530 °C, 1 m/min; HT 1H/530 °C + WQ + 8H/175 °C	421	529	4.8	110	50
As above	As above	Squeeze infiltration at 100 MPa as cast	—	460	—	—	50
As above	0	Squeeze infiltration at 100 MPa extr. 25:1 at 530 °C, 1 m/min	274	309	16	70	50
AS7G03 (Al-7Si + 0.25-0.4 Mg)	Chopped Nicalon fibers (15)	Compocast + squeeze cast at 25 MPa	200	—	—	—	29
As above	0	As above	100	—	—	—	29
As above	Chopped Nicalon fibers (15)	As above + HT 8H/540 °C + 4H/160 °C	225	—	—	—	29
As above	0	As above	170	—	—	—	29
A357 casting alloy	SiC particulate (20)	Permanent (steel) mold cast + HIP	386	393	—	100	15
As above	0	As above	214	283	—	72	15
AZ91 Mg alloy	SiC particulate (20)	Die cast	217	—	0.7	—	14
As above	0	As above	161	—	3	—	14
2024-T4	142 μm Al_2O_3 (20 wt.%)	Compocast + squeeze cast at 200 MPa	—	207	0.3	—	21
As above	16 μm Al_2O_3 (20 wt.%)	As above	—	139	0.4	—	21
As above	5 μm Al_2O_3 (20 wt.%)	As above	—	165	0.5	—	21
As above	5 μm Al_2O_3 (5 wt.%)	As above	249	345	3.4	—	21
As above	0	As above	268	388	8.2	—	21
Al-3 Mg	125-180 μm zircon particles (20 wt.%)	Vortex-stirred casting + forged 20% at 475 °C	68	82	3.8	—	5
As above	As above	Vortex-stirred casting	63	73	3.7	—	5
As above	0	Vortex-stirred casting + forged 20% at 475 °C	83	166	38.5	—	5
Al-12Si-1 Cu-1 Ni	Saffil-RF fiber (20) preform	Squeeze infilt. 750 °C/150 MPa + stabilized 4 h/235 °C	283	312	—	95.2	46
As above	0	As above	210	297	—	71.9	46
As above	Tokamax SiC_w (20) preform	As above	298	384	—	111	46
Commercially pure Al	120 μm, spherical sand (18)	Modified spray roll + 50% H.R. + 0.5 H/500 °C + 50% C.R. + 0.5 H/500 °C	—	94	5	—	83
As above	120 μm wedge shaped sand (20)	As above	—	145	3	—	83
As above	80 μm wedge shaped SiC (22)	As above	—	110	8	—	83
As above	0	As above	—	127	22	—	83

Squeeze infiltration, in its most successful form for MMC production, involves placing a preheated preform of reinforcement into a preheated die or mold, filling the die with molten matrix metal, squeezing the molten metal into the preform using a hydraulic press with a preheated ram, holding the pressure during solidification, releasing the pressure and ejecting the resulting composite. This process typically has a cycle time of a few minutes, maximum. Preforms can be made by stacking fiber bundles or woven fibers, or they may be formed from whiskers or chopped fibers by blending them with fugitive organic binders and inorganic binders (*e.g.* SiO_2). The organic binders provide shape-making ability and the inorganic binders provide strength (after firing) for machining and handling. Although other terms, such as liquid metal forging [32] and pressure casting [33], have been used to identify this process, we prefer the designation "squeeze infiltration" for processes which employ reinforcement preforms.

Fukunaga and colleagues [38–40], and others more recently [41–53], have examined the squeeze infiltration process. Several aspects have been analyzed, including thermal parameters [38] elastic deformation and fracture behavior of preforms [43], melt infiltration characteristics [43], heat flow and solidification [43], critical pressures for infiltration [41], interfacial structure [52] and infiltration kinetics [53].

Squeeze infiltration provides good as-cast properties but it may be limited in the sizes and shapes of product that can be produced. Toyota [54] has commercialized this process to make MMC diesel pistons. Representative mechanical properties of squeeze infiltration produced DMMC are included in Table 1.

2.2. *Powder processing*

Powder processing has been used to fabricate materials in a number of composite systems, including Al-SiC [55], Al-Glass [56], Al-Metglass [57], Cu-B_4C [58], Cu-TiO_2 [59], stainless steel-Al_2O_3 [60], and tool steel-VC [61]. The techniques used for producing these materials are similar to those used for powder metallurgy (PM) processing of unreinforced materials, they involve converting the matrix alloy into a powder, blending this powder with the reinforcing phase and consolidating the composite blend into a solid billet. Most matrix alloys can be converted quite readily into powder. Some materials, however, may require specialized and expensive conversion techniques. Many titanium alloys, for example, are produced using PREP (Plasma Rotating Electrode Process) atomization in order to minimize contamination [62].

The matrix and reinforcing powders may be mixed together using a variety of techniques, these include dry blending in a tumbler [59], wet blending in a slurry [63, 64] or co-milling in an attritor [56, 65, 66]. Either coated [59, 64, 67] or uncoated reinforcement may be used. As in powder metallurgy, the ease of mixing will depend on the size (and size difference) of the two phases, the morphology of each powder, the density difference between the two materials and the resilience of each phase [68]. In wet blending applications, surface chemistry effects may also be important [69].

The blend of the matrix and reinforcement powders is then outgassed and consolidated using conventional powder metallurgy techniques. Since composite powders often compact less readily and densify more slowly [70] than their unreinforced counterparts, most DMMC materials are consolidated using pressure-assisted techniques such as vacuum hot pressing [55, 71], hot isostatic pressing [58, 72] and direct powder extrusion [56, 73]. Reactive phase sintering [74] and reactive phase hot isostatic pressing [75] have also been used for some materials. A number of composites have been prepared by conventional pressing and sintering [59, 76], but these materials generally do not exhibit full theoretical density.

2.2.1. *Powder processing of commercial aluminum-SiC composites*

Since powder processing has been used to produce such a variety of composite materials using a variety of synthesis routes, it would be futile to try to discuss the processing methods used in each system. Rather, it appears more appropriate to outline some of the processing techniques used in one particular system—we have chosen commercial SiC-reinforced aluminum composites—in the hope that this may illustrate some of the issues involved in processing other composites.

Silicon carbide reinforced aluminum composites fabricated using powder techniques have been reviewed by several authors, including Nair *et al.* [55] and Divecha *et al.* [77]. In commercial materials, the reinforcement is generally either SiC_p having a size of approximately 3 to 5 μm or SiC whiskers (SiC_w) having a diameter of approx-

imately 0.5 μm. The matrix material is frequently inertly-atomized −325 mesh powder having a composition similar to wrought 6061 or 2124.

According to the patent literature [63, 78], the aluminum and SiC powders are blended using a slurry-based technique which involves suspending both powders in an organic solvent such as toluene or alcohol. This solvent may contain a polymeric binder such as polystyrene, polyisobutanol or acrylic resin. The wet blending is needed to assure complete deagglomeration of the reinforcement, even though it may cause some degradation of the reinforcement and may introduce organic contaminants into the material. A micrograph of a well-mixed blend is shown in Fig. 1. Note that both the SiC whiskers and the spherical aluminum powder particles appear well dispersed.

After drying, the blend is cold compacted into a die and placed in a vacuum hot-press. The press chamber is evacuated to about 25 Pa and heated to about 430 °C [63]. This outgassing treatment volatizes any remaining additives from the blending operation and removes residual moisture from the aluminum powder [79]. It may, however, also change the mechanical characteristics of the surface oxides on the aluminum powder [80] and alter the surface chemistry of the powders. Organics from the blending additives or volatile alloying elements from the aluminum powder, for example, may deposit on the SiC. Such deposition could contribute to the Mg enrichment of the Al–SiC interface which has been reported by Nutt and Carpenter [81]. The degassing cycle should be tailored to the alloy composition because the form of hydrated oxide on the matrix particles varies with composition.

After outgassing, the blend is heated to a temperature just above the solidus of the matrix alloy and pressed. Consolidation, under pressures of 15 to 20 MPa [63], generally results in billets having densities from 98% to 100% of full theoretical density. The microstructure of a typical billet is shown in Fig. 2. It consists of discrete aluminum regions completely embedded in a continuous brittle "cermet" network rich in SiC. The aluminum-rich regions are remnants of the original aluminum powder particles; the cermet network is the remnant of the tangled SiC exoskeleton which encased each aluminum particle in the blend. The structure illustrates why many composites are fabricated using −325 mesh powder. Billets produced from fine powders exhibit a finer distribution of aluminum-rich regions and require less mechanical working to attain a uniform reinforcement distribution.

2.3. Deposition processing

Deposition is a recent DMMC processing development. As such, few detailed characterizations of the structure or properties of deposition-produced material have been reported. A low-pressure plasma deposition (LPPD) process is being developed to make DMMC [82]. Both matrix and reinforcement are injected with an inert carrier gas into a plasma jet which is contained in a low-pressure (4–8 kPa) chamber. While entrained in the high-velocity plasma stream, the individual particles melt or become very soft. When the molten or softened particles strike a substrate, circular splats are formed. The

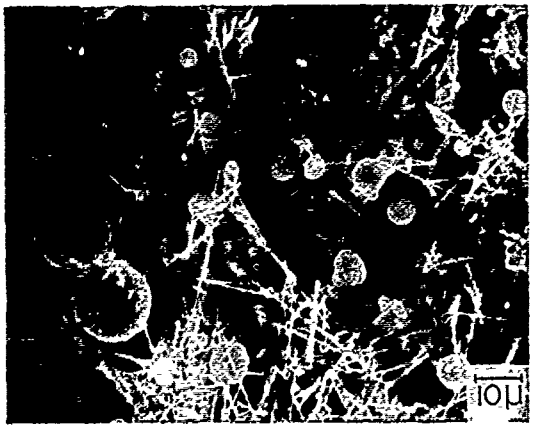

Fig. 1. A well-mixed aluminum–SiC blend containing 20 vol.% SiC_w. Note that both the whiskers and the aluminum powder particles appear well dispersed.

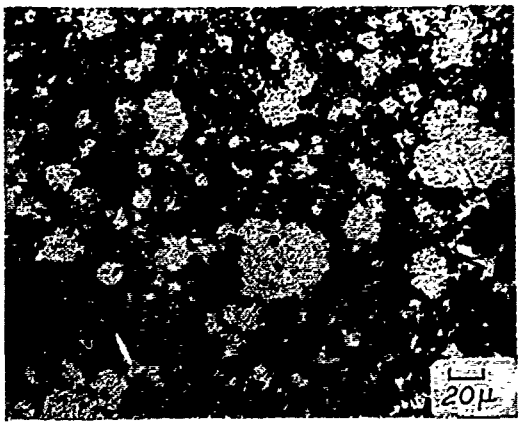

Fig. 2. Microstructure of an as-pressed 2124–20 vol.% SiC_w billet.

process continues until a bulk product has been deposited. The resulting near-theoretically dense composite consists of a uniform distribution of reinforcement which is well bonded to the fine-grained, rapidly-solidified matrix. Heat treatment increases the density to 100% of theoretical.

Singer and Ozbek [83] have experimented with a modification of the spray rolling process [84] (precursor to the Osprey process [85]) which allows them to inject reinforcement particulate into an atomized stream of molten matrix metal. In their method, a homogeneous mixture of matrix and reinforcement is created in flight. This homogeneous stream is directed onto a preheated moving substrate to form a coherent strip consisting of uniformly distributed reinforcement embedded in rapidly solidified matrix. After a hot roll, anneal, cold roll, re-anneal cycle, the strip product was free of porosity. However, interfacial bonding was primarily mechanical as illustrated by the fact that DMMC made with spherical particulate was weaker than the unreinforced matrix while composite made with irregular particulate of the same material at about the same size was stronger as indicated in Table 1. This process is being developed for commercial use [86].

A wire-fed flame spraying process has been used [87] to build up a DMMC deposit of pure aluminum reinforced with SiC whiskers. An air cap, which included a modified nozzle with two whisker injection ports, was attached to a flame spray gun so that whiskers, propelled by N_2 gas, could be sucked into the flame spray by the negative pressure generated by the flow of compressed oxyacetylene fuel gas. Molten aluminum droplets, propelled from the feed wire by the flame and compressed-air stream, combined with SiC whiskers to produce composite preforms in flight. The preforms accumulated to form a relatively thick deposit on the substrate. This deposit was stripped off the substrate and then forged at 600 °C. Five minutes were required to build up a deposit over 5 mm thick containing 13.6 vol.% SiC_w. Forging reduced the porosity to 1.7 vol.% but caused whisker breakage. The forged composite tensile strength was 90% greater than the unreinforced matrix alloy which had been processed identically.

Since deposition processes for making DMMC are only in the exploratory stage, it is difficult to comment substantively on their relative merits. However, under proper and controlled operating conditions, these new processes promise excellent potential for producing DMMC with uniformly dispersed reinforcement.

2.4. Sources of interface and property variability in billet processing

There are many interdependent variables to consider in designing an effective DMMC material. Since the upper bound on DMMC properties is established by the properties of the matrix and reinforcement material, careful selection of these components is necessary. However, the full potential of these composites cannot be realized unless the effectiveness of load transfer from matrix to reinforcement is maximized. This is only possible when the pre-selected size and shape of the reinforcement is retained by the final product and when an adherent interface is developed between the reinforcement and matrix.

In the following sections, the effects of reinforcement, matrix, and processing method on DMMC properties and interfaces are discussed.

2.4.1. Reinforcement

Two choices must be made regarding reinforcement: one is the type of material and the other is the supplier.

When selecting the reinforcement material, its chemical compatibility with the matrix and the following aspects must be considered:

size—diameter and aspect ratio;
shape—chopped fiber, whisker, spherical or irregular particulate, flake, etc.;
surface morphology—smooth or corrugated and rough;
poly- or single-crystal;
structural defects—voids, occluded material, second phases [88, 89];
surface chemistry—*e.g.* SiO_2 or C on SiC_w or other residual films;
impurities—Si, Na and Ca in sapphire whiskers [90];
inherent properties—strength, modulus, and density.

Even when a specific type has been selected (*e.g.* beta SiC_w) reinforcement inconsistency will persist because many of the aspects cited above, plus contamination from processing equipment and feedstock [91], vary among producers.

Most of the reinforcement variability is eliminated once a particular type of reinforcement and its producer are chosen. However, on a cautionary note, if reinforcement is obtained from a

given supplier over a period of time, it would be prudent to verify that the reinforcement characteristics have not changed as a result of process modifications.

Ceramic reinforcement material is often coated, generally with a metal. These coatings are applied for three purposes: (a) to protect reinforcement from damage in handling and from excessive reaction with the matrix metal; (b) to promote wetting; and (c) to improve dispersibility prior to addition to the matrix. Coatings are applied in a variety of ways including CVD, several forms of PVD, electroplating, cementation, plasma spraying [1] and by sol gel processes [92]. Factors such as strength, ductility, adherence, porosity, contamination, reactivity and coating uniformity can vary substantially with coating method. Sometimes the choice of coating material dictates the method of application; in other cases, the coating method should be evaluated in terms of cost and performance requirements.

Choice of coating material involves compromises [93] between cost, wettability, excessive reactivity with the matrix, and effects of dissolved coating material on the properties and heat treatment responses of the matrix itself. To enhance wettability, an alternative to metallic coatings is to coat the reinforcement with an oxide fluxing compound to eliminate the oxide film often associated with molten matrix material [94].

In addition to the coating material and its method of application, coating thickness is also a potential source of interface and property variability. Excessively thick coatings may not permit effective load transfer to the reinforcement or they may debond due to stresses developed during the deposition process [95]. If coatings are too thin, they may be abraded off too easily or they may dissolve too quickly to provide adequate protection in molten matrix metal.

2.4.2. *Matrix material*

Because it is much more than a dispersing glue in DMMC [96], the matrix alloy should be chosen only after giving careful consideration to its chemical compatibility with the reinforcement (or coating), to its ability to wet the reinforcement (or coating), and to its own characteristic properties and processing behavior.

Historically, commercial DMMC producers have elected to use commercial wrought or casting alloy compositions for the matrix material. This selection is understandable but not necessarily the best one. For example, commercial wrought alloys generally contain relatively high solute concentrations. As a result, coarse, brittle constituent (intermetallic) particles form during solidification and, sometimes, during heat treatment or hot working. These constituent particles can be tolerated to a degree in unreinforced matrix material, but the presence of brittle reinforcement greatly reduces this tolerance in DMMC material; ductility and toughness [97, 98] become very sensitive to additional brittle particles. In fact, the recognition that brittle intermetallic particles limit fracture toughness [99] led to the development of "cleaner" aluminum alloys (2124 and 7475) to replace the standard 2024 and 7075 alloys in toughness critical applications. Since the reinforcement is added to the matrix metal to provide added strength and stiffness for most DMMC, it seems unnecesary to sacrifice ductility and toughness by maintaining the solute level used in commercial unreinforced alloys for strengthening.

Commercial wrought alloy compositions also include solute additions to control grain size. In the case of aluminum alloys, manganese and zirconium are used for this purpose. These elements combine with aluminum during elevated temperature treatments to form dispersoid particles which inhibit grain growth. Although these grain-growth-inhibiting dispersoid particles are not as deleterious to toughness as constituent particles, their presence is not required in DMMC because the reinforcement itself generally inhibits grain growth [100].

One very crucial issue to consider in selecting the matrix alloy composition involves the natural dichotomy between wettability of the reinforcement and excessive reactivity with it. Good load transfer from the matrix to the reinforcement depends on the existence of a strongly adherent interface. In turn, a strong interface requires adequate wetting of the reinforcement by the matrix. However, the attainment of wetting and aggressive reactivity are both favored by strong chemical bonding between matrix and reinforcement. Obviously, the desired compromise permits sufficient reactivity for wetting without vigorous reaction which can seriously degrade the reinforcement [95, 101]. Adjusting or controlling chemical composition to accomplish this delicate compromise is difficult—many subtleties are involved. To illustrate the complexity, several

examples concerning alloy additions to aluminum matrix metal relative to Al–SiC DMMC are itemized below:

lithium [93, 102] and magnesium [20, 43, 52, 93] promote wetting and interfacial bonding without producing excessive Al–SiC reactivity;
indium, lead and thallium [103] reduce the surface tension of molten aluminum;
tantalum, vanadium, zirconium, titanium, hafnium and niobium enhance molten aluminum's ability to wet SiC but the extent of reaction is limited to a thin, stable carbide reaction product at the interface [104];
silver, as a coating, does not react with SiC but is readily wetted by aluminum [105];
gold, copper, and palladium react relatively virorously with SiC [105];
aluminum reacts with SiC to form Al_4C_3;
silicon additions mitigate the formation of Al_4C_3 [106–109] without affecting wettability [106]. (Similar alloying effects on the suppression of interface reaction have been noted [110] in Ti–B MMC.)

As a note to interface analysts, Al_4C_3 reacts with moisture in the air or in sample polishing media to form Al_2O_3 [106]. Consequently, care should be exercised when examining Al–SiC interfaces for Al_4C_3.

Additional factors to consider relative to the matrix metal and its interaction with the reinforcement are illustrated by other systems:

low concentrations of impurities in the matrix can interfere with matrix–reinforcement bonding [90];
with oxide reinforcement, oxygen in the matrix assists [20], and may be essential [111], to matrix–reinforcement bonding;
dissolution of the reinforcement may affect the matrix properties significantly [112, 113].

These are just examples of the subtleties involving the matrix metal, including its intentional alloying additions and the insidious impurities of various origins.

2.4.3. Billet processing method

The properties of most composites are determined by a complex interplay between the interfacial and microstructural characteristics of the material. Production of high-strength DMMC with high ductility and toughness such as described by Niskanen and Mohn [114] appears to require a strong, high-integrity matrix–reinforcement interface and a uniform microstructure free of internal discontinuities which might cause premature failure of the material. Attaining one without the other is of limited value. Accordingly, the processing methods developed for these materials seek to balance the two, sometimes contradictory, requirements. The primary causes for failure to achieve these requirements during DMMC billet production processes are discussed here.

A uniform reinforcement distribution is essential to effective utilization of the load-carrying capacity of the reinforcement. Non-uniform distributions of reinforcement in the early stages of processing tend to persist to the final product in the form of streaks or clusters [47] of uninfiltrated reinforcement with their attendant porosity [115], all of which lower ductility, strength and toughness of the material. Several sources or causes of non-uniform reinforcement distributions may be identified as follows.

(a) Inadequate deagglomeration of the reinforcement before mixing with the matrix material; this is especially troublesome with whiskers and other high-aspect-ratio forms of reinforcement.

(b) Inability to disperse the reinforcement in molten matrix metal due to sedimentation (density differences) and surface tension of the melt; this is a major reason that several molten metal processes have not been successful.

(c) Compocast and PM processed DMMC billets have inherent non-uniform reinforcement distributions which arise from the fact that the reinforcement is confined to the boundaries of the solid matrix particles. The nature of this non-uniform distribution, shown in Fig. 2, has also been revealed in compocast [115], squeeze cast [21] and hybrid squeeze cast [29] composites.

Despite the importance of a uniform reinforcement distribution, too much exuberance for achieving this goal can cause reinforcement damage or breakage. Stirring [20, 26], squeezing [35, 41, 43, 47] and blending operations have all caused reinforcement breakage, especially when the reinforcement aspect ratio is high. Aspect ratios of whiskers and chopped fibers have been reduced by factors three or more [35, 47].

It is appropriate at this point to return briefly to the issue of wetting *versus* excessive matrix–reinforcement reactivity as it relates to

process selection. Since interface reactions continue well after the time wetting has occurred, the potential for a process to produce excessive reaction product and its undesirable consequences can usually be correlated with time at higher temperatures, particularly at temperatures above the liquidus of the matrix material. Assuming the processes are conducted properly, the following process hierarchy for avoidance of excessive reaction product is suggested.

(a) Deposition processes, while employing high temperatures, involve rapid solidification and high-temperature matrix–reinforcement durations of milliseconds typically.

(b) Squeeze infiltration processing permits control of superheat by proper adjustment of preform and tooling temperatures [38, 43] while the high pressures are conducive to rapid heat extraction; these factors combine to hold solidification durations to seconds.

(c) During partial-liquid-phase hot-pressing of PM billets, temperatures barely exceed the solidus but time at high temperatures can be substantial depending on pressures and equipment design.

(d) Conventional, compo- and squeeze casting all involve relatively high temperatures, generally well above the liquidus (except for compocasting), and rather extended cooling times.

While this hierarchy clearly reveals the process of choice in terms of interface reactivity, this is by no means the only basis for selecting a DMMC process.

Only recently has the effect of reinforcement on solidification structures become apparent. There is now a convincing body of evidence [29, 40, 43, 116] that reinforcement modifies dendrite structure and that solute-rich zones engulf the reinforcement particles. This solute-enriched zone solidifies eutectically to produce a network of brittle intermetallics and brittle reinforcement encompassing solute-impoverished matrix grains. This probably explains, in part at least, the billet structure in Fig. 2 and the observations of intermetallic phases observed in DMMC products [81, 100]. At least one producer [114] has sought to modify the matrix chemistry of aluminum-based DMMC material in order to minimize the intermetallics.

A final issue worthy of mention is contamination of powder processed billets. As with all PM materials, contamination and variability of both the matrix and reinforcement powders is always a concern, since both can introduce heterogeneities into the final microstructure. In powder processed DMMC this problem is aggravated by the abrasive reinforcement particles which readily create and collect wear debris during cleaning, pretreating (if used) and mixing operations. This debris is difficult to detect and remove, especially from blends of reinforcement and matrix particles. Enumerable premature DMMC fractures were traced to the presence of debris in test samples of finished product during the earlier development of these materials.

3. Deformation and thermal processing

Most DMMC billets intended for engineering applications receive some sort of thermal and/or deformation processing before use. Like many wrought materials, billets processed using liquid-phase or partial-liquid-phase techniques are frequently given a high temperature homogenization treatment. The objective of this treatment is to minimize solute concentration gradients in the composite without inducing excessive coarsening of dispersoids, constituent phases or reaction-product layers. Because of differences in both billet microstructure and coarsening kinetics, appropriate homogenization cycles for composites may be quite different from those used for unreinforced materials. Since cast DMMC materials exhibit a smaller dendrite secondary arm spacing than unreinforced alloys [116], for example, they may require shorter homogenization times. With appropriate schedules, homogenization may be quite beneficial. Skibo [117] found that homogenizing 2024 aluminum matrix composites for 72 h at 510 °C produced improved response to heat treatment and higher strengths. Similarly, Liaw and Gungor [118] showed that a 2124–25 vol.% SiC_p DMMC containing copper-rich eutectic could attain a 50% improvement in ultimate tensile strength through control of homogenization.

3.1. Deformation processing

After homogenization, DMMC materials for structural applications are frequently given some sort of deformation processing. Most SiC-reinforced aluminum DMMC billets are first broken down by extrusion. This extrusion is typically done using a streamlined extrusion die [119] and an extrusion ratio of at least 10 or 20 to 1.

Although few extrusion temperatures are quoted in the open literature, Divecha and Fishman [120] did report extruding material containing 15 vol.% SiC_w at 480 °C. After extrusion, the composite may be forged or hot rolled (either perpendicular or parallel to the original extrusion direction [55]) into final shape. Hot rolling temperatures of 450 °C [120] and 427 °C to 510 °C [121] have been reported.

One of the major purposes of deformation processing is to improve the strength and ductility of the composite. It has been recognized for some time [77, 122] that improving reinforcement distribution uniformity should improve the strength and ductility of DMMC materials. In 1982, Harrigan *et al.* [121] demonstrated that hot rolling billets of SiC_p-reinforced 6061 alloys to rolling reductions of at least 80% both improved the SiC_p distribution and dramatically increased the ductility and strength of the materials. Similarly, Nieh and Karlak [123] found that hot rolling of SiC_w-reinforced 2024 and 6061 alloys at 27.8 °C above the solidus temperature of the matrix produced significant increases in elongation, and they attributed this increase to the increased uniformity of the rolled microstructure.

Hot working clearly does improve the microstructural uniformity of DMMC materials. Figure 3 shows the microstructure of a PM-processed 2124-20 vol.% SiC_w billet (the same billet as that shown in Fig. 2) after extrusion. The top photo represents an L-LT section [124], the right photo shows an L-ST section and the left photo shows an LT-ST section. Extrusion has largely broken up the prior SiC-rich cermet network in the billet, producing a more uniform SiC distribution. As in wrought materials, extrusion may also help heal residual porosity and other defects in the billet microstructure.

Additional mechanical working can improve microstructural uniformity even more. Figure 4 shows the microstructure of the same material after it was subsequently hot rolled down to 1.8 mm sheet. The structure is now fairly uniform. Figures 2 and 4 also illustrate why some composites—especially PM-based composites—often require a substantial amount of mechanical working. Most −325 mesh aluminum powders have a mean particle diameter on the order of 20 μm. As shown in Fig. 4, an aluminum-20 vol.% SiC_w composite with a uniform reinforcement distribution has an interparticle spacing on the order of 2 μm. Assuming uniform deformation, a 100 to 1 extrusion ratio would be required to reduce the 20 μm dimension down to the required 2 μm spacing.

In addition, mechanical working—especially extrusion—tends to align whisker and chopped fiber reinforcements parallel to the working direction. This alignment can strongly affect the mechanical properties of the material. Table 2, for example, shows tensile properties obtained on two 2124T6-20 vol.% SiC_w composites containing different degrees of whisker orientation. The corresponding whisker orientation distributions for the materials are shown in Figs. 5 and 6. Both composites exhibited the same mean SiC_w aspect ratio. They were cut from the same extrusion.

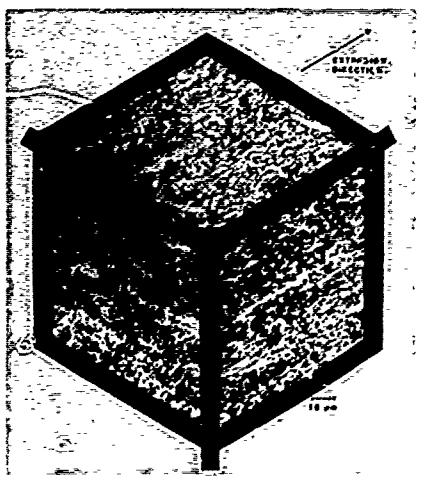

Fig. 3. Microstructure of a 2124-20 vol.% SiC_w extrusion. The material was obtained by extruding the billet shown in Fig. 2 using an extrusion ratio of 11:1.

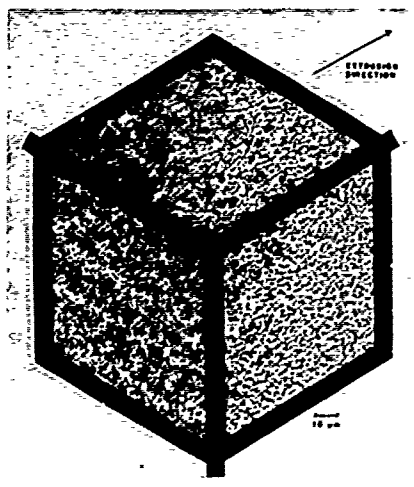

Fig. 4. Microstructure of a 1.8 mm gauge hot rolled 2124-20 vol.% SiC_w sheet. The material was obtained by rolling the extrusion shown in Fig. 3.

TABLE 2 Tensile properties of 2124-20% SiC_w composites

	Composite A		*Composite B*	
	Long.	*Trans.*	*Long.*	*Trans.*
0.2% yield strength (MPa)	517	530	646	495
Tensile strength (MPa)	652	691	817	595
Young's modulus (GPa)	116	121	130	106
Total elongation (%)	5.0	6.8	3.7	4.5

Each result represents the mean of triplicate tensile tests.

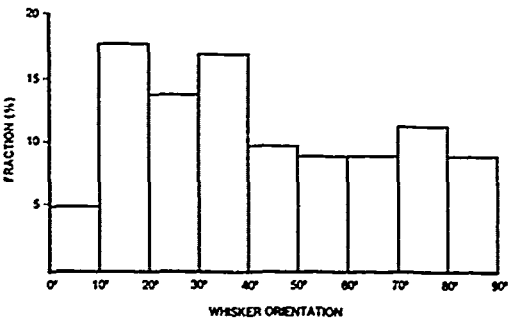

Fig. 5. SiC whisker orientation distribution observed in Composite A.

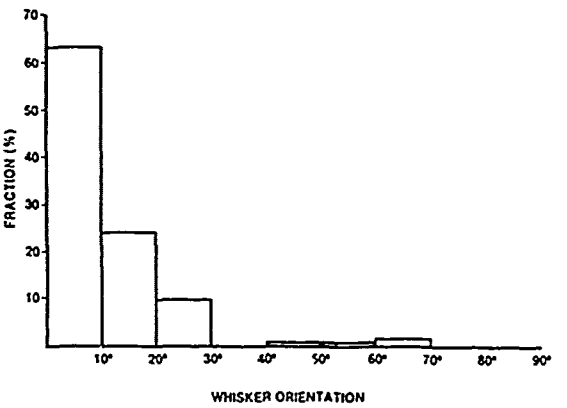

Fig. 6. SiC whisker orientation distribution observed in Composite B.

hot rolled using the same practices and given the same heat treatment. Composite A, however, received a proprietary working treatment before rolling to modify whisker alignment.

Deformation may also crack or fracture some of the reinforcement particles. Webster [125] cited one study in which 0.5 μm diameter SiC_w reinforcement having an initial mean length of 49μm was blended with aluminum powder, pressed into a billet and then extruded using a 16 to 1 extrusion ratio. After billet compaction, the mean length of the whiskers was found to be 33 μm; after extrusion, this mean length was reduced to 9 μm. Since the amount of reinforcement damage in a DMMC material is likely to vary with a number of process variables, including reinforcement content, extrusion schedule and die design, these data should clearly not be considered typical of all DMMC, or even all SiC_w-reinforced, materials. Nevertheless, they at least illustrate the magnitude of the problem.

Discontinuously-reinforced metal matrix composites are also somewhat more difficult to hot work than unreinforced materials. At hot working temperatures, for example, SiC-reinforced aluminum alloys generally exhibit higher flow stresses, and sometimes lower elongations, than their unreinforced counterparts [126]. These higher flow stresses increase both the amount of mechanical energy required for deformation and the local heating of the workpiece. Accordingly, DMMC materials must generally be hot worked at both lower strain rates and lower temperatures (or with tighter temperature control) than unreinforced materials to avoid incipient melting and hot cracking problems. Workpiece lubrication also appears to be more critical for the composites.

The effect of hot working on the metal-reinforcement interface in DMMC materials has not been widely investigated. Most authors agree that this deformation does not disrupt the SiC–matrix bond in SiC-reinforced aluminum alloys [55]. Indeed, the deformation may improve bonding by "smearing" nascent metal across the surface of the reinforcement particles. In other composite systems, however, deformation may cause local tearing near matrix-reinforcement interfaces because of strain incompatibilities. As in unreinforced materials, the working is also likely to alter the grain structure of the matrix alloy. In addition, the elevated temperature exposure required for working may promote dispersoid coarsening and interfacial reactions.

3.2. Heat treatment

After working, DMMC composites, particularly commercial aluminum–SiC composites, may be heat treated to attain optimum properties. The heat treatments used are generally similar to

those used in unreinforced alloys of similar composition. Indeed, some investigators have used the same heat treatments for DMMC composites as for the unreinforced alloys. Aging kinetics in DMMC materials, however, are generally quite different, and usually much faster, than in unreinforced materials [127–132]. The difference is particularly dramatic for heat treatment sequences such as T8 aluminum tempers which incorporate stretching or other forms of plastic deformation. The distribution of matrix phases in DMMC materials also appears to be more heterogeneous than in unreinforced materials [81]. Some aluminum–SiC composites, for example, exhibit precipitation of phases at the SiC–matrix interface [81]. Heat treatment may also introduce vastly different residual stresses into the matrix of the composite than into the matrix of an unreinforced alloy [133].

TABLE 3 Tensile properties of 2124 - 15% SiC_w rolled sheet

	1979 [120][a] *Long.*	*1988* [114]	
		Long.	*Trans.*
0.2% yield strength (MPa)	—	573	386
Tensile strength (MPa)	442	718	559
Young's modulus (GPa)	95.8	114	95
Total elongation (%)	0.006	5.3	8.5
Fracture toughness (MPa-$M^{1/2}$)	—	59	64

[a]Matrix alloy actually 2024 rather than 2124.

4. Concluding comments

In this review, we have attempted to outline some aspects of composite processing which can affect the interfacial and mechanical properties of metal matrix composites containing discontinuous reinforcement. We have also tried to touch on some of the interrelationships between interfaces, microstructures and mechanical properties which exist in these materials. Clearly, the processing of these DMMC materials has not yet evolved to the point where one can study the effects of interfaces on structure-sensitive properties (such as tensile properties) without making detailed reference to the microstructure of the composite.

In the last decade, great strides have been made in processing of DMMC materials such as aluminum–SiC composites. In 1979, Divecha and Fishman [120] reported mechanical properties on some of the first laboratory samples of rolled 2024–15 vol.% SiC_w sheet which they produced using whiskers obtained from Silag Inc. These properties are shown in Table 3. In 1988, Niskanen and Mohr [114] reported mechanical properties they obtained on hot rolled 2124T6–15 vol.% SiC_w sheets fabricated using state-of-the-art processing technology and current-generation whiskers from Silag (now Advanced Composite Materials, a division of Tateho America). These data are also shown in Table 3. The improvement, especially in ductility and toughness, is quite dramatic.

Nevertheless, effects of microstructural variables on the performance characteristics of DMMC materials, and the associated microstructural variability of these materials, are likely to remain as important technical issues for a number of years. At present, for researchers who are seeking to reduce the effects of these microstructural variables on composite behavior, we can only offer the following suggestions.

(1) Whenever possible, use reinforced materials as both control and experimental samples. Because of the different consolidation, mechanical working and heat treatment characteristics of reinforced and unreinforced materials, it is extremely difficult to produce unreinforced materials which are metallurgically equivalent to the matrix of the reinforced materials.

(2) Carefully evaluate and, whenever possible, quantify differences in reinforcement distribution and morphology between experimental and control samples. Reinforcement distribution can often be assessed using quantitative microscopy [134]. Morphology may have to be assessed by extracting the reinforcement from the composite.

(3) Verify that observed differences in material behavior cannot be attributed to unintentional extrinsic factors such as porosity, reinforcement agglomerates, large constituent particles or foreign contaminants. Generally, this means that bulk material should be tested after extrusion or other mechanical working and that all mechanical testing should be accompanied by routine fractography.

(4) When reporting data on experimental composites, try to report the date the material

was produced in addition to the source and composition of this material. If the composite was not obtained from a standard commercial source, also include a low-magnification micrograph (100-400×) of the material. This information will aid in differentiating the composite from other generations of material having a similar composition.

These suggestions are clearly not a panacea for all of the problems associated with studying metal matrix composites containing discontinuous reinforcement. But they may at least help identify what aspects of composite behavior are due to processing limitations rather than to inherent metallurgical characteristics of the material.

Acknowledgments

The authors, by way of this acknowlegment, very sincerely thank Betty Hiltunen and Terry Anderson for their skills and, especially, for their patience and extra time devoted to the preparation of this paper.

References

1. T. W. Chou, A. Kelly and A. Okura, *Composites, 16* (1985) 187.
2. P. K. Rohatgi, R. Asthana and S. Das, *Intn. Metall. Rev., 31* (1986) 115.
3. A. Mortensen, J. A. Cornie and M. C. Flemings, *J. Met., 40* (1988) 12.
4. S. J. Harris, *Met. Sci. Technol., 4* (1988) 231.
5. U. T. S. Pillai, R. K. Pandu and K. D. P. Nigan, in W. C. Harrigan, J. Strife and A. K. Dhingra (eds.), *Proc. 5th Int. Conf. on Composite Materials, ICCM, V*, Metallurgical Society, Warrendale, PA, 1985, p. 895.
6. A. K. Gupta, T. K. Dan and P. K. Rohatgi, *J. Mater. Sci., 21* (1986) 2413.
7. A. K. Jha, T. K. Dan, S. V. Presad and P. K. Rohatgi, *J. Mater. Sci., 21* (1986) 3681.
8. D. Nath, R. Asthana and P. K. Rohatgi, *J. Mater. Sci., 22* (1987) 170.
9. U. T. S. Pillai, R. K. Pandey and P. K. Rohatgi, *Eng. Fract. Mech., 28* (1987) 461.
10. A. K. Gupta, T. K. Dan, P. K. Rohatgi and D. Nath, *J. Mater. Sci. Lett., 6* (1987) 35.
11. S. Das, R. Asthana and P. K. Rohatgi, in E. A. Starke and T. H. Sanders (eds.), *Conf. on Aluminum Alloys, Their Physical and Mechanical Properties*, Vol. I, Engineering Materials Advisory Services, Ltd., West Midlands, UK, 1986, p. 95.
12. P. K. Rohatgi, S. Das and R. Asthana, in E. A. Starke and T. H. Sanders (eds.), *Conf. on Aluminum Alloys, Their Physical and Mechanical Properties*, Vol. I, Engineering Materials Advisory Services, Ltd., West Midlands, UK, 1968, p. 169.
13. R. G. Buchheit, W. Ruch and F. E. Wawner, in E. A. Starke and T. H. Sanders (eds.), *Conf. on Aluminum Alloys, Their Physical and Mechanical Properties*, Vol. I, Engineering Materials Advisory Services, Ltd., West Midlands, UK, 1986, p. 181.
14. T. Crisafulli, *American Metal Market/Metalworking News*, May 27, 1985, and Anon., *Metall. Eng.*, Sept. (1986) p. 60.
15. D. M. Schuster, M. Skibo and F. Yep, *J. Met., 39* (1987) 60 and Anon., *High-Tech Materials Alert* (April 1988).
16. R. Mehrabian, R. C. Riek and M. C. Flemings, *Metall. Trans., 5* (1974) 1899.
17. R. Mehrabian, A. Sato and M. C. Flemings, in *Light Metals*, Vol. II, TMS-AIME, Warrendale, PA, 1975, p. 177.
18. R. Mehrabian and M. C. Flemings, in *New Trends in Materials Processing*, American Society for Metals, Metals Park, OH, 1976, p. 98.
19. A. Sato and R. Mehrabian, *Metall. Trans. B, 7* (1976) 443.
20. C. G. Levi, G. J. Abbaschian and R. Mehrabian, *Metall. Trans. A, 9* (1978) 697 and in J. A. Cornie and F. W. Crossman (eds.), *Failure Modes in Composites IV*, TMS-AIME, Warrendale, PA, 1977, p. 370.
21. F. M. Hosking, F. Folgar Portillo, R. Wunderlin and R. Mehrabian, *J. Mater. Sci., 17* (1982) 477.
22. P. R. Gibson, A. J. Clegg and A. A. Das, *Foundry Trade J., 152* (1982) 253, 262.
23. M. Kiuchi, S. Sugiyama, N. Endo and N. Kuwaski, *J. Jpn. Soc. Technol. Plast., 24* (1983) 974.
24. M. Kiuchi, S. Sugiyama and N. Endo, *J. Jpn. Soc. Technol. Plast., 24* (1983) 1113.
25. P. K. Ghosh, S. Ray and P. K. Rohatgi, *Trans. Jpn. Inst. Met., 25* (1984) 57.
26. F. A. Girot, L. Albingre, J. M. Quenisset and R. Naslain, *J. Met., 39* (1987) 18.
27. F. Girot, J. M. Quenisset, R. Naslain, R. Coutand and T. Macke, in F. L. Matthews, N. C. R. Buskell, J. M. Hodginson and J. Morton (eds.), *Proc. 6th Int. Conf. on Composite Materials, ICCM VI*, Elsevier Applied Sciences, London, 1987, p. 2330.
28. M. A. Bayoumi and M. Suery, in F. L. Matthews, N. C. R. Buskell, J. M. Hodginson and J. Morton (eds.), *Proc. 6th Int. Conf. on Composite Materials, ICCM VI*, Elsevier Applied Sciences, London, 1987, p. 2481.
29. C. Milliere and M. Suery, *Mater. Sci. Technol., 4* (1988) 41.
30. S. Rajagopal, *J. Appl. Metalworking, 1* (1981) 3.
31. G. Williams, and K. M. Fisher, *Met. Technol.*, July (1981) 263.
32. E. L. Kotzen, *Metalcasting and Molding Processes*, AFS, Des Plaines, IL, 1981.
33. J. A. Cornie, A. Mortenson, M. N. Gungor and M. C. Flemings, in W. C. Harrigan, J. Strife and A. K. Dhingra (eds.), *Proc. 5th Int. Conf. on Composite Materials, ICCM V*, Metallurgical Society, Warrendale, PA, 1985, p. 809.
34. M. A. H. Howes, *J. Met., 38* (1986) 28.
35. B. F. Quigley, G. J. Abbaschian, R. Wunderlin and R. Mehrabian, *Metall. Trans. A, 13* (1982) 93.
36. A. A. Das and S. Chatterjee, *Metall. Mater. Technol., 13* (1981) 137.
37. B. Zantout, A. a. Das and J. R. Franklin, in *The Metallurgy of Light Alloys, Spring Residential Conference,*

Institute of Metallurgists, London, 1983, p. 215.
38 H. Fukunaga and M. Kuriyama, *Bull. Jpn. Soc. Mech. Engrs., 25*(1982) 842.
39 H. Fukunaga and K. Goda, *Bull. Jpn. Soc. Mech. Engrs., 27*(1985) 1245.
40 H. Fukunaga and K. Goda, *Bull. Jpn. Soc. Mech. Engrs., 28*(1985) 1.
41 T. W. Clyne and M. G. Bader, in W. C. Harrigan, J. Strife and A. K. Dhingra (eds.), *Proc. 5th Int. Conf. on Composite Materials, ICCM V*, Metallurgical Society, Warrendale, PA, 1985, p. 755.
42 T. W. Clyne, M. G. Bader, G. R. Cappleman and P. A. Hubert, *J. Mater. Sci., 20*(1985) 85.
43 T. W. Clyne and J. F. Mason, *Metall. Trans. A, 18*(1987) 1519.
44 A. Mortensen and J. A. Cornie, *Metall. Trans. A, 18* (1987) 1160.
45 J. Dinwoodie, E. Moore, C. A. J. Langman and W. R. Symes, in W. C. Harrigan, J. Strife and A. K. Dhingra (eds.), *Proc. 5th Int. Conf. on Composite Materials, ICCM V*, Metallurgical Society, Warrendale, PA, 1985, p. 671.
46 L. Ackermann, J. Charbonnier, G. Desplanches and H. Koslowski, in W. C. Harrigan, J. Strife and A. K. Dhingra (eds.), *Proc. 5th Int. Conf. on Composite Materials, ICCM V*, Metallurgical Society, Warrendale, PA, 1985, p. 687.
47 A. Sakamoto, H. Hasegawa and Y. Minoda, in W. C. Harrigan, J. Strife and A. K. Dhingra (eds.), *Proc. 5th Int. Conf. on Composite Materials, ICCM V*, Metallurgical Society, Warrendale, PA, 1985, p. 699.
48 Y. Sawada and M. G. Bader, in W. C. Harrigan, J. Strife and A. K. Dhingra (eds.), *Proc. 5th Int. Conf. on Composite Materials, ICCM V*, Metallurgical Society, Warrendale, PA, 1985, p. 785.
49 J. A. Cornie, A. Mortensen, M. N. Gungor and M. C. Flemings, in W. C. Harrigan, J. Strife and A. K. Dhingra (eds.), *Proc. 5th Int. Conf. on Composite Materials, ICCM V*, Metallurgical Society, Warrendale, PA, 1985, p. 809.
50 K. Ohori, H. Watanabe and Y. Takeuchi, *Mater. Sci. Technol., 3*(1987) 57.
51 T. Imai, Y. Nishida, M. Yamada, H. Matsubara and I. Shirayanagi, *J. Mater. Sci. Lett., 6*(1987) 343.
52 G. R. Cappleman, J. F. Watts and T. W. Clyne, *J. Mater. Sci., 20*(1985) 2159.
53 G. P. Martins, D. L. Olson and G. R. Edwards, *Metall. Trans. B, 19*(1988) 95.
54 T. Donomoto, N. Miura, K. Funatani and N. Miyake, *Ceramic Fiber Reinforced Piston for High Performance in Diesel Engine*, SAE Technical Paper No. 830252, Detroit, MI, 1983.
55 S. V. Nair, J. K. Tien and R. C. Bates, *Int. Metall. Rev., 30*(1985) 275.
56 K. U. Kainer, H. W. Bergmann and B. L. Mordike, *Powder Metall., 27*(1984) 30.
57 A. K. Jha, G. S. Upadhyaya and P. K. Rohatgi, in G. S. Upadhyaya (ed.), *Sintered Metal-Ceramic Composites*, Elsevier, New York, 1984, p. 259.
58 J. E. Smogeresky, H. J. Rack and G. B. Brassell, *Development of a Nonvolatile Boron Carbide-Copper Cermet Neutron Shield for High Performance Shipping Cask*, SAND-80-08002C, 1981.
59 K. G. K. Varrier and P. K. Rohatgi, *Powder Metall., 29* (1986) 65.
60 S. K. Mukherjee and G. S. Upadhyaya, in G. S. Upadhyaya (ed.), *Sintered Metal-Ceramic Composites*, Elsevier, New York, 1984, p. 253.
61 E. Y. Gutmanas, D. B. Goldman, S. Hart and D. Zak, *Powder Metall. Int., 18*(1986) 401.
62 F. H. Froes and D. Eylon, *Powder Metall. Int., 17*(1985) 163.
63 J. F. Dolowy, B. A. Webb and E. C. Supan, *U.S. Patent* 4,259,112, 1981.
64 S. Takahashi in W. C. Harrigan, Jr., J. Strife and A. K. Dhingra (eds.), *Proc. 5th Int. Conf. on Composite Materials, ICCM V*, Metallurgical Society, Warrendale, PA, 1985, p. 747.
65 D. L. Davidson, *Metall. Trans. A, 18*(1987) 2115.
66 N. C. Kothari, *Powder Metall. Int., 18*(1986) 321.
67 Y. Sakai, *Bull. Jpn. Soc. Mech. Engrs., 27*(1984) 1807.
68 J. C. Williams, *Powder Technol., 15*(1976) 245.
69 G. D. Parfitt, in N. Harnby, M. F. Edwards and A. W. Nienow (eds.), *Mixing in the Process Industries*, Butterworth, Boston, MA, 1985, p. 95.
70 M. F. Ashby, S. Bahk, J. Bevk and D. Turnbull, in J. W. Christian, P. Haasen and T. B. Massalski (eds.), *Progress in Materials Science*, Vol. 25, Pergamon, New York, 1982, p. 1.
71 P. R. Roy and C. Ganguly, in G. S. Upadhyaya (ed.), *Sintered Metal-Ceramic Composites*, Elsevier New York, 1984, p. 159.
72 C. J. Skowronek, A. Pattnaik and R. K. Everett, *Dispersion and Blending of SiC Whiskers in RSP Aluminum Powders*, NRL-MR-5750, 1986.
73 R. J. Lederich and S. M. L. Sastry, *Mater. Sci. Eng., 55* (1982) 143.
74 M. S. McLean, *Metal Powder Rep., 42*(1987) 111.
75 A. Bose, B. Moore, R. M. German and N. S. Stoloff, 1988 TMS-AIME Annual Meeting, Phoenix, AZ.
76 A. Sharma, P. R. Soni and T. V. Rajan, *Metal Powder Rep., 43*(1988) 37.
77 A. P. Divecha, S. G. Fishman and S. D. Karmarkar, *J. Met., 33*(Sept. 1981) 12.
78 P. E. Hood and J. O. Pickens, *U.S. Patent* 4,463,058, 1984.
79 T. G. Nieh, R. A. Rainen and D. J. Chellman, in W. C. Harrigan, Jr., J. Strife and A. K. Dhingra (eds.), *Proc. 5th Int. Conf. on Composite Materials, ICCM V*, Metallurgical Society, Warrendale, PA, 1985, p. 825.
80 G. Staricek, *Observation of Oxide Skin in Powder Metallurgy Aluminum Alloys*, AFWAL-TR-83-4157, 1984.
81 S. R. Nutt and R. W. Carpenter, *Mater. Sci. Eng., 75* (1985) 169.
82 M. R. Jackson and R. L. Mehan, in F. L. Matthews, N. C. R. Buskell, J. M. Hodginson and J. Morton (eds.), *Proc. 6th Int. Conf. on Composite Materials, ICCM VI*, Elsevier Applied Science, London, 1987, 2431 and Anon., *Adv. Mat. Proc.*, (Jan., 1988), p. 85.
83 A. R. E. Singer and S. Ozbek, *Powder Metall., 28*(1985) 72.
84 A. R. E. Singer, *J. Inst. Met., 100*, 1972, 185.
85 R. W. Evans, A. G. Leatham and R. G. Brooks, *Powder Metall., 28*(1985) 13.
86 Anon., *Chem. Engr.*, (April, 1988), p. 18.
87 Y. Tsunekawa, M. Okumiya, I. Nishi and K. Okumura, *J. Mater. Sci. Lett., 6*(1987) 191.
88 S. R. Nutt, *J. Am. Ceram. Soc., 71*(1988) 149.

89 S. R. Nutt, *J. Am. Ceram. Soc., 67*(1985) 428.
90 W. Bonfield, in A. G. Metcalfe (ed.), *Interfaces in Metal Matrix Composites*, Academic Press, New York, 1974, p. 363.
91 F. Ordway, P. J. Lare and R. A. Hermann, AFML-TR-71-252, Wright-Patterson Air Force Base, OH, March 1971.
92 H. H. An and T. S. Luhman, 1988 TMS-AIME Annual Meeting, Phoenix, AZ.
93 F. Delannay, L. Froyen and A. Deruyttere, *J. Mater. Sci., 22*(1987) 1.
94 J. P. Rocher, J. M. Quenisset and R. Naslain, *J. Mater. Sci. Lett., 4*(1985) 1841.
95 H. Landis, J. Unnam, S. V. N. Naidu and W. Brewer, *SAMPE Q.* (July, 1981) 19.
96 K. K. Chawla, *J. Met., 37*(1985) 25.
97 G. T. Hahn and A. R. Rosenfield, *Metall. Trans. A, 6* (1975) 653.
98 J. G. Kaufman and J. S. Santner, in J. E. Campbell, W. W. Gerberich and J. H. Underwood (eds.), *Application of Fracture Mechanics for Selection of Metallic Structural Materials*, American Society for Metals, Metals Park, OH, 1982, p. 169.
99 J. T. Staley, in *Properties Related to Fracture Toughness*, STP 605, ASTM, Philadelphia, PA, 1976, p. 71.
100 C. P. You, A. W. Thompson and I. M. Bernstein, *Scr. Metall., 21*(1987) 191.
101 S. Ochiai and K. Osamura, *Metall. Trans. A, 18* (1987) 673.
102 A. K. Dhingra, *Philos. Trans. R. Soc. London, Ser. A, 294*(1980) 151.
103 Y. Kimura, Y. Mishima, S. Umekawa and T. Suzuki, *J. Mater. Sci., 19*(1984) 3107.
104 T. Choh and T. Oki, *Mater. Sci. Technol., 3* (1987) 378.
105 K. Alsafi, C. J. Raub and E. Raub, *Metall. Mat., 36* (1982) 258.
106 V. Laurent, D. Chatain and N. Eustathopoulos, *J. Mater. Sci., 22*(1987) 244.
107 R. Warren and C. H. Anderson, *Composites, 15* (1984) 16.
108 T. Iseki, T. Kameda and T. Maruyama, *J. Mater. Sci., 19* (1984) 1692.
109 K. Kannikeswaran and K. Y. Tin, *J. Met., 39* (1987) 17.
110 P. R. Smith and F. H. Froes, *J. Met., 36* (1984) 19.
111 J. V. Naidich, *Prog. Surf. Membr. Sci., 14* (1981) 353.
112 A. G. Metcalfe, in A. G. Metcalfe (ed.), *Interfaces in Metal Matrix Composites*, Academic Press, New York, 1974, p. 65.
113 E. L. Hall, Y. M. Kouh, M. R. Jackson and R. L. Mehan, *Metall. Trans. A, 14* (1983) 781.
114 P. Niskanen and W. R. Mohn, *Adv. Mater. and Processes, 133* (March 1988) 39.
115 P. K. Ghosh and S. Ray, *J. Mater. Sci., 21* (1986) 1667.
116 A. Mortensen, M. N. Gungor, J. A. Cornie and M. C. Flemings, *J. Met., 38* (1986) 30.
117 M. D. Skibo, *Stiffness and Strength of SiC Al Composites*, SAND81-8212, 1981.
118 P. K. Liaw and M. N. Gungor, 1987 TMS Fall Meeting, Cincinnati, OH.
119 H. J. Rack and P. W. Niskanen, *Light Metal Age, 42* (Feb. 1984) 9.
120 A. P. Divecha and S. G. Fishman, in K. J. Miller and R. F. Smith (eds.), *Proc. 3rd Int. Conf. on Mechanical Behavior of Material*, Pergamon, New York, 1980, p. 351.
121 W. C. Harrigan, Jr., G. Gaebler, E. Davis and E. J. Levin, in J. E. Hack and M. F. Amateau (eds.), *Mechanical Behavior of Metal Matrix Composites*, Metallurgical Society, Warrendale, PA, 1983, p. 169.
122 D. M. Riggs and P. Gellis, *The Effect of Mechanical Working on SiC Whisker-Reinforced Aluminum Alloys*, AMMRC TR 80-11, 1980.
123 T. G. Nieh and R. F. Karlak, *J. Mater. Sci. Lett., 2* (1983) 119.
124 J. R. Pickens, *Metall. Trans. A, 17* (1986) 1095.
125 D. Webster, *Metall. Trans. A, 13* (1982) 1511.
126 J. R. Pickens, T. J. Langan, R. O. England and M. Liebson, *Metall. Trans. A, 18* (1987) 303.
127 W. C. Harrigan, M. T. Ristow, J. F. Doloway and B. A. Webb, 1983 TMS-AIME Annual Meeting, Atlanta, GA.
128 J. M. Papazian, in *Proc. 6th Annual Discontinuous Reinforced Aluminum Composite Working Group Meeting*, MMCIA Report No. 00479, Santa Barbara, CA, April 1984, p. 223.
129 T. G. Nieh and R. F. Karlak, *Scr. Metall., 18* (1984) 25.
130 T. A. Christman and S. Suresh, *Acta Metall., 36* (1988) 1691.
131 I. Dutta and D. L. Bourell, 1987 TMS Fall Meeting, Cincinnati, OH.
132 G. M. Janowski and B. J. Pletka, 1987 TMS Fall Meeting, Cincinnati, OH.
133 R. J. Arsenault and M. Taya, *Acta Metall., 35* (1987) 651.
134 W. A. Spitzig, J. F. Kelly and O. Richmond, *Metallography, 18* (1985) 235.

Materials Science and Engineering, A107 (1989) 107–116

Fabrication of Intermetallic Matrix Composites*

R. M. GERMAN and A. BOSE

Materials Engineering Department, Rensselaer Polytechnic Institute, Troy, NY 12180-3590 (U.S.A.)

(Received June 1, 1988)

Abstract

Research into the fabrication of intermetallic matrix composites is presented using the Ni_3Al–Al_2O_3 system as the baseline. The approach combines reactive sintering, powder injection molding, and hot isostatic compaction to form an aligned fiber composite. The individual components to this process are described with example microstructures and mechanical properties. The initial successes and problems are described. The paper concludes with a description of the major remaining processing challenges in the fabrication of intermetallic matrix composites.

1. Introduction

Intermetallic compounds are emerging as the next generation of high temperature, oxidation-resistant materials. Among the intermetallic compounds, Ni_3Al is the most popular and forms the basis for our efforts. An important attribute of this compound is its anomalous thermal hardening behavior, where the strength increases with temperature up to approximately 800 °C. Thus, alloys based on Ni_3Al offers a strength advantage over other high temperature alloys at temperatures around 600 to 900 °C. Additionally, Ni_3Al exhibits advantages in terms of creep resistance, stress rupture resistance, and fatigue crack growth rates in comparison with superalloys [1].

In spite of all the advantages, the initial commercial interest in Ni_3Al was low because of its intrinsic brittleness. However, alloying with boron improves the ductility of Ni_3Al; the addition of 1000 ppm of boron imparts up to 50% elongation at room temperature in an otherwise brittle compound [2]. Another concern is the environmental stability of Ni_3Al at high temperatures. The ductility decreases sharply at temperatures greater than 600 °C [3]. One solution to this problem is to add chromium to the system [4]. Thus, the advanced nickel aluminides contain various alloying additions to overcome earlier problems and improve properties.

The current effort is directed at high temperature structural materials fabricated from the light weight corrosion-resistant high strength composites, via the use of intermetallic compounds as the matrix phase. This paper reports on a fabrication route applicable to Ni_3Al-based composites. Casting is one possible route, but it has several problems, especially for composites. Alternatively, powder metallurgy based fabrication has some obvious merits. This paper presents the logic and problems associated with a powder metallurgy based fabrication of an Ni_3Al matrix composite with alumina fibers as the reinforcing phase.

2. Fabrication logic

The fabrication logic for the Ni_3Al–Al_2O_3 composite involves three initially parallel efforts. First, matrix fabrication to full density via powder metallurgy processes is needed. Two approaches are available for this: reactive sintering elemental powders and hot isostatic compaction of pre-alloyed powders. The former was selected for this research because of powder availability, especially small particle sizes; there are fiber alignment problems with the coarse pre-alloyed particles. This is evident in Fig. 1 which contrasts the fracture surfaces of molded samples using small and coarse particles. The fiber alignment is superior with the smaller particle size matrix phase.

The second parallel research effort was in fiber incorporation and alignment in the matrix. For this research, powder injection molding with an organic binder was identified as most viable. This

*Paper presented at the symposium on Interfacial Phenomena in Composites: Processing, Characterization, and Mechanical Properties, Newport, RI, June 1–3, 1988.

0921-5093/89/$3.50

© Elsevier Sequoia/Printed in The Netherlands

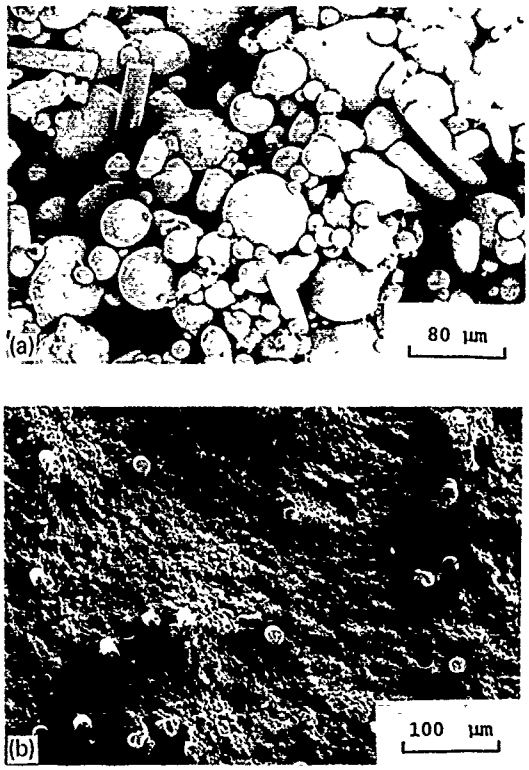

Fig. 1. Scanning electron micrographs contrasting the fracture surfaces for molded fiber-powder composites with differing particle sizes (alumina diameter was 20 μm in both cases): (a) coarse 70 μm powder with 5 vol.% alumina fiber showing poor alignment, and (b) small 5 μm iron powder with 5 vol.% alumina fiber showing good alignment.

process allows incorporation of the fibers and powders into a viscous mass that can be subjected to extrusion or injection molding. With proper tooling design and flow, the fibers can be aligned in the molded structure. Fiber alignment is then dependent on the elongation flow of the mass as it undergoes shear in passing through a cross-sectional area change. To maximize fiber alignment, it is most desirable to have long, thin fibers with a low mass. Furthermore, as the flow velocity and fluid viscosity increase, the fiber orientation improves. The final fiber alignment depends on the flow conditions. Figure 2 shows how expanding flow leads to perpendicular fiber orientation while contracting flow gives longitudinal orientation. As a demonstration of this concept, Fig. 3 is an optical micrograph taken from a molded mixture of iron powder and alumina fibers formed by binder-assisted molding.

Finally, it is evident that full densification is not possible via pressureless sintering when reinforcing ceramic phases are incorporated in the reac-

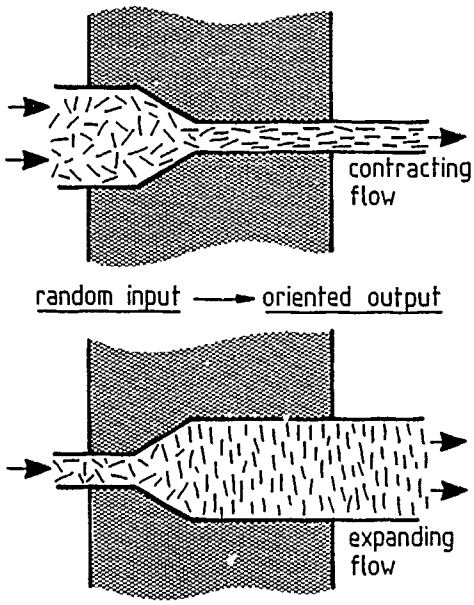

Fig. 2. A sketch of the fiber alignment possibilities using binder-assisted molding and either an expanding flow or contracting flow to induce specific fiber orientations from a random mixture.

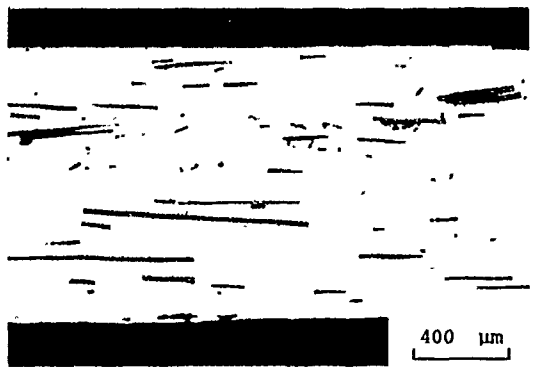

Fig. 3. An optical micrograph taken from a sectioned sample of iron particles and alumina fiber showing the alignment possible with elongation flow in the presence of a binder.

tive sintering mixture. Figure 4 shows the microstructure after reacting a compact containing alumina fibers. The large porosity is characteristic of the densification restraining effect from the fibers. Consequently, a third research area was initiated that combines the attributes of hot isostatic compaction and reactive sintering. By this process, termed reactive hot isostatic pressing (RHIP), full density Ni_3Al-Al_2O_3 composites have been fabricated. Full density composites have also been fabricated by conventional hot isostatic compaction of a pre-alloyed Ni_3Al powder mixed with Al_2O_3 fibers.

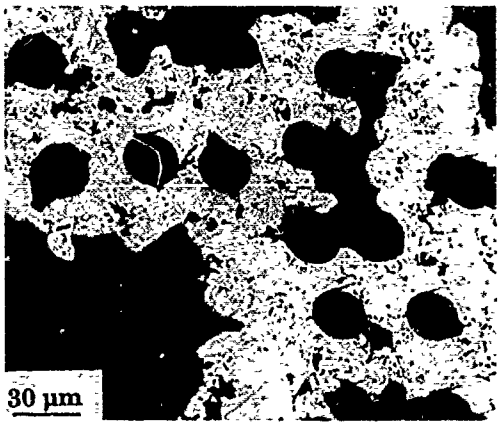

Fig. 4. A metallographic cross-section taken through a reactively sintered compact containing alumina fibers. In this case the fibers prevented significant densification during reactive sintering.

TABLE 1 Powder characteristics

Property	*Nickel*	*Aluminum*
Vendor	INCO	Valimet
Designation	123	H-3, H-10, H-15, H-30 and H-90
Powder type	carbonyl	gas atomized
Purity (%)	99.99	99.7
FSSS size (μm)	2.8	3, 10, 15, 30, 95
Apparent density (g cm^{-3})	2.2	—
Major impurities (ppm)	Ca = 10 Fe = 30	Fe = 1200 volatiles = 200

As detailed in this paper, there are problems remaining with the overall fabrication approach. In spite of these problems, sufficient progress has been made to isolate possible benefits and key research areas. A remaining problem is with the interfacial character of the composite. Improved bonding between the fiber and matrix is needed and an organic binder is needed that does not contaminate the reactive sintering.

3. Experimental materials and procedures

The research relied on reactive sintering of elemental powders to form Ni_3Al. The nickel powder was type 123 from INCO. Various aluminum powders were obtained from Valimet, designated as H-3, H-10, H-15, H-30 and H-95 with nominal particles sizes of 3, 10, 15, 30 and 95 μm. Table 1 gives the characteristics of these powders and Fig. 5 provides scanning electron micrographs. Prior experiments have determined that the 15 μm aluminum particle size was optimal.

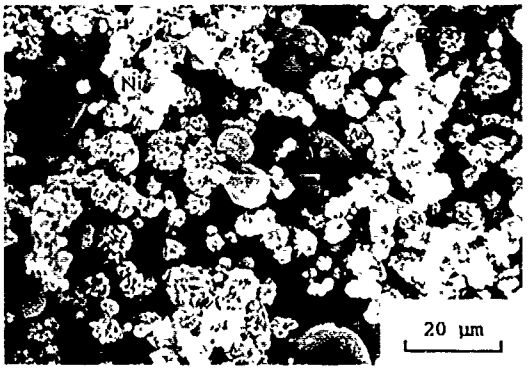

Fig. 5. Scanning electron micrograph showing the nickel and aluminum powders used in the reactive sintering experiments.

The stoichiometric Ni_3Al composition was formed with 86.7% Ni.

Mixing of the loose powders was carried out in a turbula mixer for 30 min. Compaction pressures near 300 MPa were typically applied to the mixed powder, giving green densities equal to 70% of theoretical. Reactive sintering was performed in a horizontal laboratory tube furnace. For vacuum sintering a pressure of less than 10^{-2} Pa was typical. The sintering temperature was 750°C, with a heating rate of 30 K min^{-1} and a hold time of 15 min. Figure 6 is a schematic diagram showing the general fabrication process and key variables.

Chopped Du Pont FP alumina fibers 20 μm in diameter and initially 40 mm long were used to form the composite (after mixing the fibers were roughly 3 to 5 mm long). A scanning electron micrograph of this fiber is shown in Fig. 7. Additionally, -325 mesh boron powder from Cerac was added to some compositions to improve ductility.

A pre-alloyed nickel aluminide powder was also used to provide a baseline material. The powder was produced at Homogeneous Metals by gas atomization, giving an average particle size of 70 μm. As seen in Fig. 8, the particles were spherical in shape. The composition of the powder was 7.67% Cr, 8.18% Al, 0.80% Zr, 0.02% B, balance Ni, which is close to the alloy designated IC-218.

For fiber orientation in molding, a low-density polyethylene wax was selected. The wax was a homopolymer designated A6, from Allied, with a softening temperature of 90°C. The polyethylene wax was melted and combined with the powders and fibers in a double planetary mixer under vacuum at 130°C, with a final mixing time of 30

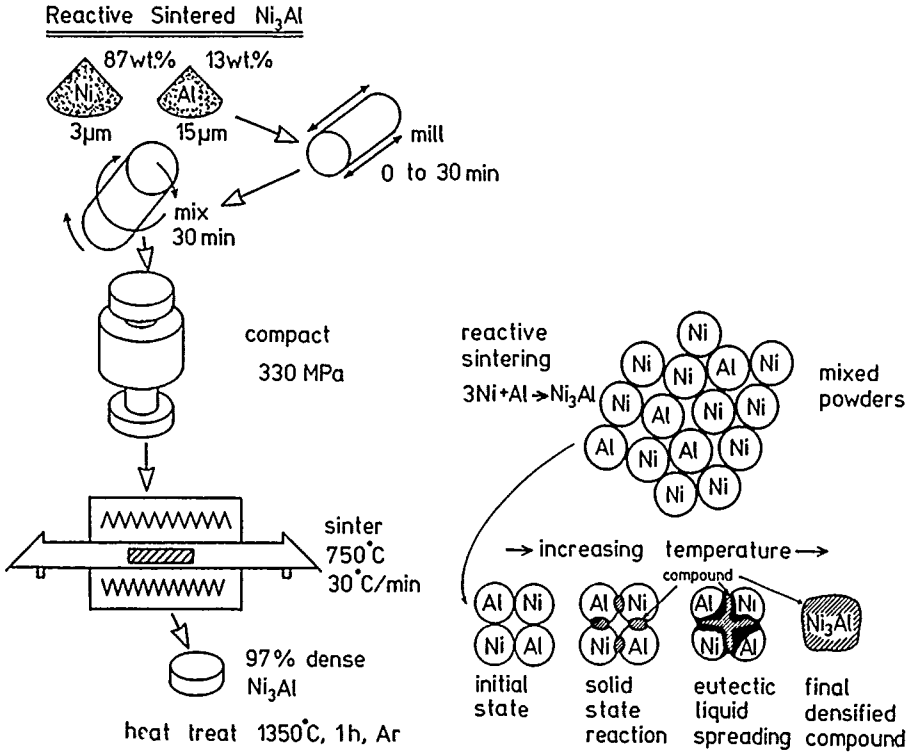

Fig 6 A schematic diagram of the processing sequence developed in this research for the fabrication of dense Ni_3Al through reactive sintering of the component powders.

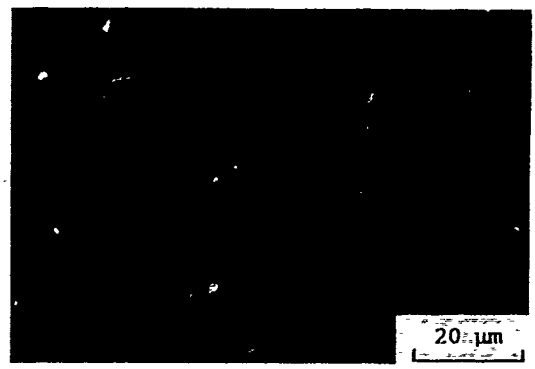

Fig. 7. A scanning electron micrograph of the alumina fiber used in the fabrication of the composites.

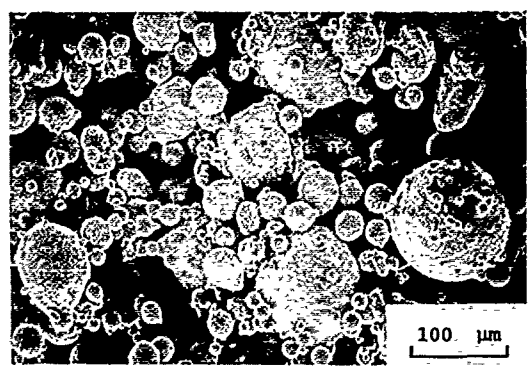

Fig. 8. The pre-alloyed IC-218 atomized Ni_3Al based powder.

min. For injection molding, a sample of 1 kg of the IC-218 with 5 vol.% alumina fiber was mixed with polyethylene wax. The wax was initially melted in the heated basket of a double planetary mixer, and the fibers introduced into the melted wax Subsequently, the particles were added to give a final composition of 66 vol.% solids, composed of 5 vol.% fiber. This mixture was molded in a reciprocating screw type injection molding machine at a pressure of 7.5 MPa and a temperature of 125°C. The mold produced two different types of tensile bars: one is shown in Fig. 9 as molded and after presintering. On cooling, the samples were carefully released from the mold and the tensile bars were cut from the gates. The binder was thermally removed from the compacts by a wicking treatment where fine alumina powder is used to soak out the wax during heating.

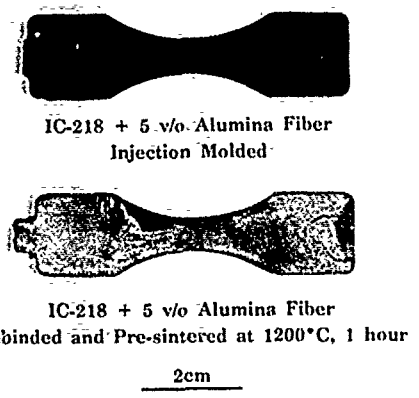

Fig. 9. A photograph of two injection molded tensile bars formed from the IC-218 intermetallic powder with 5 vol.% of alumina fiber, molded with polyethylene wax as the binder. The upper bar is as-molded, while the lower bar is debinded and pre-sintered at 1200 °C for 1 h.

4. Processing routes

4.1. Reactive sintering

Reactive sintering of Ni_3Al involves the formation of a transient liquid phase [5, 6]. The initial compact is composed of mixed nickel and aluminum powders in the 75:25 atomic stoichiometry which are heated to approximately 700 °C where they react to form Ni_3Al. Heat is liberated because of the thermodynamic stability of the compound. Consequently, reactive sintering is nearly spontaneous once the liquid forms. The liquid provides a capillary force on the structure which leads to densification. The liquid is transient since the process is conducted at a temperature below the melting temperature of the compound, typically near the eutectic.

Figure 10 shows the Ni–Al binary phase diagram [7, 8]. The system is characterized by five intermetallic compounds, with particular interest in this study on Ni_3Al. For this system, reactive sintering near 640 °C (the lowest eutectic temperature), is most appropriate. Nickel and aluminum powders are randomly mixed in a stoichiometric ratio. This mixture is sintered under precise conditions of atmosphere, heating rate, time and temperature. At the first eutectic temperature, liquid forms and rapidly spreads throughout the structure. The liquid consumes the elemental powders and forms precipitated Ni_3Al behind the advancing liquid interface. Interdiffusion of nickel and aluminum is quite rapid in the liquid phase and the compound generates heat which further accelerates the reaction. If

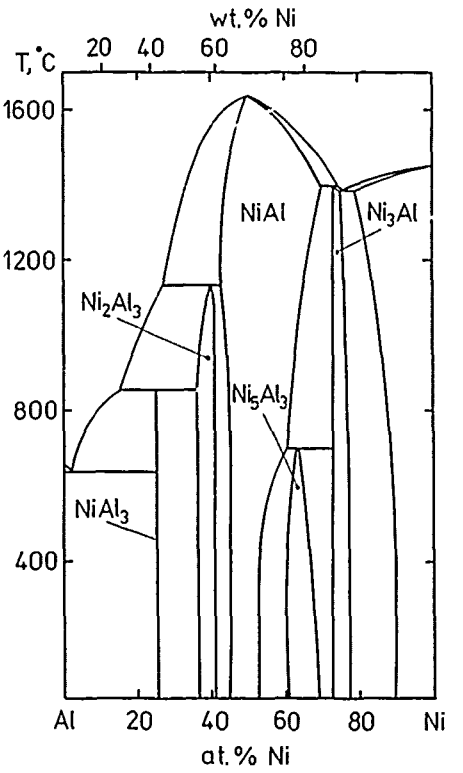

Fig. 10. The nickel–aluminum binary phase diagram [7, 8].

the reaction is controlled, then the compound will be nearly dense and suitable for containerless hot isostatic compaction to full density. Boron is added at concentrations up to 0.1 wt.% to improve the final ductility.

4.2. Injection molding and fiber alignment

Injection molding of a 5 vol.% alumina fiber reinforced nickel aluminide has been performed. Injection molding is important in attaining the desired fiber orientation in the matrix while forming complex shapes. Full density has not yet been achieved with this process, but it is expected that final densification will probably involve hot isostatic pressing using the hot glass envelope technique.

Molding was performed in various heated and chilled die cavities, using packing pressures up to 14 MPa. No significant problems were encountered in either mixing or molding. However, the removal of the polyethylene wax from the molded component proved to be difficult, hence various debinding conditions were studied. Initial debinding was carried out on the mixture without fibers. Considerable slumping and shape distortion was observed when the binder was removed without

any support, even with slow heating rates. By embedding the compact in loose alumina powder (1 μm particle size) the rate of binder removal was improved by wicking of the binder from the compact into the alumina by capillary action. As an example of the rapid debinding cycle, the pellet was embedded in alumina powder and heated in dry hydrogen with the following cycle: 1 K min^{-1} to 150 °C, hold for 60 min, 2 K min^{-1} to 400 °C, hold for 120 min.

Some problems with slumping and shape distortion were encountered when a mixture of the pre-alloyed IC-218 was prepared without fibers. However, for the composite mixture (powder plus fiber) this was significantly reduced. The fibers and supporting alumina wick provided sufficient support to offset the low viscosity condition during debinding. A major difficulty was encountered in that the polyethylene wax binder contaminated the test samples and impeded densification in reactive sintering. This is a major problem that is being addressed in our current research.

4.3. Full densification

In spite of near full densification via reactive sintering, pores often form near the center of large compacts after the reaction, leading to reduced mechanical properties. The formation of large pores relates to the heating conditions; the liquid first forms near the surface and the reaction motion is toward the center. The result is a void due to mass depletion at the center of the compact. It was hypothesized that the residual porosity could be removed by pressurizing the compact during the reaction. This process is termed reactive hot isostatic pressing (RHIP).

Experiments involving simultaneous reaction and hot isostatic compaction were performed near the Ni_3Al stoichiometric composition. Compacts were prepared with and without boron additions, and with either alumina or yttria phases. The powder mixtures were cold isostatically pressed at 208 MPa into rods of approximately 20 mm diameter with a length of 160 mm. The pressed green density was approximately 70% of theoretical. These rods were inserted in thin walled stainless steel tubes. The tubes were evacuated, sealed, and hot isostatically pressed at 800 °C for 30 min at a pressure of 104 MPa. The heating rate was 10 K min^{-1} to the maximum temperature. To compare with the properties of the boron-treated alloy, an undoped elemental nickel–aluminum mixture was fabricated under similar conditions. In a separate set of experiments, RHIP was performed at 1100 °C for 60 min under a pressure of 172 MPa.

To get a fully densified composite, reactive hot isostatic pressing was carried out using randomly mixed particles. One composite was fabricated with 3 vol.% of randomly oriented alumina fiber. In another experiment, 20 vol.% of yttria powder was incorporated in the boron-treated mixture of elemental nickel and aluminum powders. The reactively hot isostatically pressed composite was dense and test bars machined from the HIP can were mechanically tested.

Finally, compacts of the pre-alloyed IC-218 powder were formed by hot isostatic compaction with and without alumina fibers. These compacts provided the baseline against which the other fabrication approaches could be evaluated. For these samples the consolidation took place at 1100 °C and 172 MPa for 1 h.

5. Results

With the successful development of reactive sintering for the fabrication of Ni_3Al, some mechanical property assessments were performed. Transverse rupture strength and tensile specimens were tested, giving strength estimates of 470 MPa (transverse rupture) and 230 MPa (tensile), which agree with the published values for unalloyed Ni_3Al [4, 9]. The samples gave some ductility, with the elongation being in the range of 1%. The bulk hardness was 52 HRA and the microhardness was measured as 264 Knoop (100 g load), which agrees favorably with a value of 240 measured on hot isostatically compacted and extruded pre-alloyed powder compact. Furthermore, preliminary oxidation tests on the material indicate good resistance up to 900 °C.

The compacts formed by reactive sintering were largely free of pores and represent better comparison specimens with cast alloys. The mechanical properties of the RHIP samples are listed in Table 2. Also, the properties of the pre-alloyed powder consolidated by hot isostatic compaction are given in Table 2. Generally, the strengths are comparable to prior reports for cast, unalloyed Ni_3Al [10]. However, the ductility with boron is lower in the RHIP material than in the HIP material. The addition of alumina fibers increased the yield strength and decreased the ductility. The hot tensile properties (600 °C,

TABLE 2 Tensile properties of RHIP compounds at 25 °C

Composition	*RHIP conditions*	*Yield strength* (MPa)	*Ultimate strength* (MPa)	*Elongation* (%)
Ni_3Al	800 °C, 30 min, 104 MPa	—	363	0
Ni_3Al+B	800 °C, 30 min, 104 MPa	265	722	10
Ni_3Al+B/Al_2O_3	800 °C, 30 min, 104 MPa	474	548	1
Ni_3Al+B	1100 °C, 60 min, 172 MPa	494	677	2
Ni_3Al+B	1100 °C, 60 min, 172 MPa + heat treat 1050 °C, 1 h + 800 °C, 24 h, vacuum	591	827	5

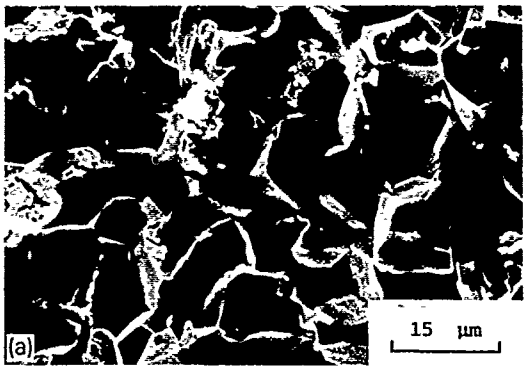

Fig. 11. Fracture surfaces for reactively hot isostatic compacted Ni_3Al specimens fabricated (a) without boron and (b) with boron at 0.06 wt.%. The untreated sample has lower ductility and intergranular fracture.

3×10^{-3} Pa) of the boron-treated Ni_3Al–Al_2O_3 were measured. The yield strength and the ultimate tensile strength were 544 and 617 MPa, respectively, with a ductility of 0.4%, the higher strengths at the elevated test temperature are typical of the Ni_3Al-type alloys.

Figure 11 compares the fracture surfaces for the RHIP specimens fabricated with and without boron additives. The RHIP Ni_3Al failed by an intergranular mode whereas the boron-treated RHIP Ni_3Al displayed a mixed mode of failure. This may be explained by the boron distribution

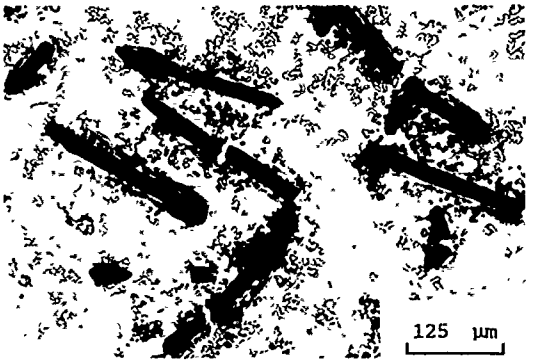

Fig. 12. Optical micrograph showing the microstructure after RHIP processing of the Ni_3Al matrix composite containing randomly oriented alumina fibers (3 vol.%).

in the initial powder mixture, which is reflected in the final RHIP properties. Polycrystalline Ni_3Al is intrinsically brittle, yet the addition of boron results in a ductility increase [4, 10]. Uniform segregation of boron to the grain boundaries results in improved ductility in cast and pre-alloyed powder products. In the RHIP product, the boron is initially inhomogeneously distributed. The short processing time does not allow the boron to enter solution and attain a uniform distribution along the grain boundaries during cooling. Instead, there are local areas rich in boron which contribute to the ductility, whereas other areas fracture intergranularly. This explains the mixed mode of fracture shown by the boron-treated Ni_3Al samples.

The presence of either the yttria particles or the alumina fibers sharply reduced the ductility of both the RHIP and hot isostatically compacted pre-alloyed materials. The samples were fully densified, as illustrated in Fig. 12 for the Ni_3Al containing alumina. Note that the alumina fibers were not aligned. Both ceramic phases increased the RHIP yield strength to some extent, but not the HIP pre-alloyed. The randomly aligned fibers were poorly bonded to the matrix and initiated

failure at low strains. Figure 13 shows a scanning electron micrograph of the fracture surface of the alumina-fiber containing sample.

The optical micrograph of the RHIP boron treated Ni_3Al shown in Fig. 14 displays no retained porosity. However, there are areas of a second phase which is aluminum-rich. This phase can be partially removed by high temperature heat treatment, resulting in improved strength as illustrated in Table 2. The heat treatment has not been optimized. We suspect that these aluminum-rich regions result from the short duration of the liquid during RHIP. The applied pressure removes the residual porosity, but also causes the aluminum-rich liquid to flow into pores, leaving a nonhomogeneous microstructure.

6. Discussion

The reactivity of the nickel and aluminum powders results in relatively high sintered densities (97% of theoretical) with low apparent sintering temperatures (the reaction can be initiated as low as 550°C) and short sintering times. The high final density results from the presence of a liquid during a portion of the sintering cycle. Any processing conditions which influence the reaction between the constituent powders will alter the amount of liquid, length of time the liquid is present, and its distribution in the microstructure. In transient liquid-phase sintering, liquid quantity, distribution and duration dictate the final sintered density and mechanical properties [11–13]. The role of the various process parameters can be explained in terms of their effects on the liquid-phase formation and distribution during sintering.

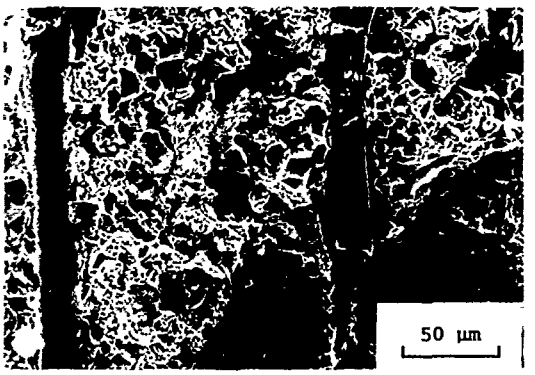

Fig. 13. Scanning electron micrograph of the fracture surface of the Ni_3Al–Al_2O_3 composite fabricated by reactive hot isostatic compaction.

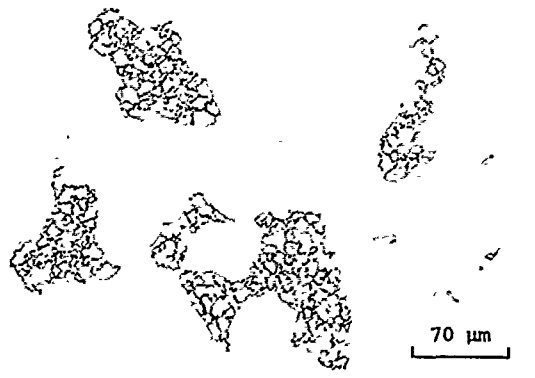

Fig. 14. An optical micrograph of the reactive hot isostatically compacted Ni_3Al treated with boron, but not subjected to heat treatment after reacting.

Control of the processing conditions and particle sizes of the elemental powders allows the intermetallic compound to be synthesized at temperatures less than half of its melting point (1385°C) and in times less than 15 min. This success can be attributed to the following factors: (1) the reaction is exothermic and spontaneous once initiated, due to the heat liberated in forming Ni_3Al; (2) the proper particle size ratio of the elemental nickel and aluminum powders ensures that an interconnected network of liquid can form during the reactive sintering process; (3) rapid heating minimizes solid-state interdiffusion which inhibits the reaction; and (4) sintering in vacuum prevents heat loss and gas entrapment within the pores.

A liquid is formed by heating mixed elemental powders through the lowest eutectic temperature in the Ni–Al phase diagram (at 640°C). This aluminum-rich liquid reacts with the nickel and generates heat which melts (within seconds) the remaining aluminum. Under proper conditions, densification and compound formation occurs simultaneously.

In injection molding, major problems were associated with removal of the binder after molding. The interparticle friction is a key to dimensional control during the debinding process. A major problem was slumping which occurred with the coarse spherical pre-alloyed powder during binder removal. Fiber additions and embedding in alumina greatly increased the resistance to distortion, allowing rapid debinding by wicking with shape retention. Samples formed from the composite were successfully processed using embedding alumina and slow heating rates. With a higher volume fraction of alumina fibers

the system will be stiffer during debinding and distortion will be minimized.

Reactive hot isostatic compaction gives near full density Ni_3Al from inexpensive elemental powders. The product strength is comparable with previous reports for wrought Ni_3Al. Further efforts are needed to optimize the microstructure (fiber alignment and homogeneity). However, a major benefit is that compositional variations can be explored rapidly by this route. Furthermore, processing temperatures are low and times are short. This may be of most benefit in the fabrication of high-performance composites since the small particles (5–8 μm in this case) needed for fiber alignment are available in the elemental powders.

The future activities must focus on some key issues as isolated by this research. First, fiber alignment techniques have been mastered based on use of binder-assisted molding. Unfortunately, the reactivity of the compacts is degraded by residual binder when the reaction begins. A new binder is needed to provide the lubrication and flow characteristics for fiber alignment, while simultaneously not contaminating the interfaces in the mixture. When this problem is cured, then debinding can occur at temperatures below the initiation temperature for reactive hot isostatic pressing. Finally, then, specific attention can be addressed to improving the final microstructure, boron distribution, and interfacial quality between the fiber and matrix. An alternative based on small particles of pre-alloyed Ni_3Al consolidated by hot isostatic compaction is also possible. The fibers could be aligned in processing and full densification attained by the simultaneous pressure and sintering cycle.

7. Conclusions

This paper describes the initial progress in applying low temperature reactive sintering to the fabrication of Ni_3Al–Al_2O_3 composites using mixed elemental powders. Full densification is possible through appropriate selection of particle sizes, composition, heating rate, consolidation pressure, temperature, and hold time, Densification depends on the amount of liquid formed at the first eutectic temperature and the connectivity of this liquid during the reaction. In this sense, reactive sintering is analogous to transient liquid-phase sintering. Since the liquid persists for only a short time, it is important that the several process parameters be carefully controlled to optimize the sintered density. By reacting the material under an applied stress, reactive hot isostatic compaction, full density composites have been fabricated from simple elemental powder blends.

The process outlined in this paper for forming intermetallic matrix composites may have general applicability to other systems. Elemental powders are relatively inexpensive, widely available, easily mixed to adjust composition, can be alloyed using other additives, and are easily compacted. The low processing temperature contributes to the novel nature of the final material. Consider the relatively low processing temperatures that are being applied to the fabrication of high temperature materials. The total processing time is short and the product is dense with good strength and ductility. By performing the reactive sintering process under an imposed external stress via hot isostatic compaction, full density composites have been fabricated. The remaining challenge will be to combine fiber alignment via injection molding with the reactive hot isostatic compaction process. This requires attention to the development of new binders and interfacial strengthening agents.

Acknowledgments

This investigation was sponsored by Defense Advance Research Project Agency and Office of Naval Research through the Center for Design, Analysis and Fabrication of Innovative High Temperature Structural Composites at Rensselaer Polytechnic Institute. We wish to thank Professors Stoloff and Duquette and our co-workers Barbara Lograsso, Norm Gendron, John Warren, Brian Moore, and Karl Hens.

References

1 N. S. Stoloff, in C. C. Koch, C. T. Liu, N. S. Stoloff (eds.), *High Temperature Ordered Intermetallic Alloys*, Materials Research Society, Pittsburgh, PA, 1985, p. 3.
2 K. Aoki and O. Izumi, *J. Jpn. Inst. Met., 43* (1979) 1190.
3 A. I. Taub, S. C. Huang and K. M. Chang, in C. C. Koch, C. T. Liu, N. S. Stoloff (eds.), *High Temperature Ordered Intermetallic Alloys*, Materials Research Society, Pittsburgh, PA, 1985, p. 221.
4 C. T. Liu and V. K. Sikka, *J. Met., 38* (1986) 19.
5 D. M. Sims, A. Bose and R. M. German, *Prog. Powder Metall., 43* (1987) 575.
6 R. M. German, *Liquid Phase Sintering*, Plenum, New

York, 1985, p. 157.
7 M. Hansen and K. Anderko, *Constitution of Binary Alloys*, 2nd ed., McGraw-Hill, New York, 1958.
8 I. M. Robertson and C. M. Wayman, *Metallography, 17* (1984) 43.
9 W. M. Schulson, *Int. J. Powder Metall., 23* (1987) 25.
10 C. T. Liu and C. L. White, in C. C. Koch, C. T. Liu, N. S. Stoloff (eds.), *High Temperature Ordered Intermetallic Alloys*. Materials Research Society, Pittsburgh, PA, 1985, p. 365.
11 W. H. Baek and R. M. German, *Int. J. Powder Metall., 22* (1986) 235.
12 W. H. Baek and R. M. German, *Powder Metall. Int., 17* (1985) 273.
13 R. M. German and J. W. Dunlap, *Metall. Trans. A, 17* (1986) 205.

Materials Science and Engineering, A107 (1989) 117–125

Ceramic–Ceramic Composites with Reaction Bonded Matrices*

JOHN S. HAGGERTY

Materials Processing Center, Massachusetts Institute of Technology, Cambridge, MA 02139 (U.S.A.)

(Received June 1, 1988)

Abstract

Reaction bonded ceramic matrix composites offer the potential of improved, reliable high temperature properties with near net-shape processing. Reaction bonded CMCs consolidate by filling the void space within the green part with reaction product, rather than shrinking as occurs during conventional sintering, so sintering aids are not required to relieve stresses through particle/reinforcement rearrangements. The absence of sintering aids in the grain boundaries gives superior high temperature and corrosion properties. Even though processing temperatures are lower than those used in conventional sintering processes, times are long and the internal atmosphere is active with respect to the reinforcement phase. It is particularly critical to avoid degrading the load-bearing reinforcements or their protective coatings in the porous, low modulus matrices. Recently developed high strength, oxidation resistant, reaction bonded Si_3N_4 that reacts to completion in unusually short, low temperature nitriding cycles, makes these composites feasible for the first time.

1. Introduction

Recently, the perfection of ceramic materials has been improved dramatically as researchers have sought means of improving property values and making parts with adequate levels of reliability. This research has focused on eliminating defects through the use of improved powders and processing techniques [1]. Strengths exceeding 700 MPa with low fracture toughness materials ($K_{Ic} \approx 2.0$–3.0 MPa $m^{1/2}$) are being reported, indicating the achievement of very high levels of microstructural and surface perfection.

Although dramatic, these strength levels cannot be approached as design stresses. Even presuming that parts could be reliably made with maximum flaw dimensions limited to 5–15 μm, it is unlikely that this level of perfection would be retained when parts were subjected to normal impacts and chemically active environments. Thus, strength and reliability remain compromised by service exposures, even though we have now learned enough about processing to make defect-free parts in many cases. Attaining higher fracture toughness values is the key for achieving adequate reliability with ceramic parts used at high stress levels.

Significantly improved toughness values in monolithic ceramics, like Si_3N_4 and ZrO_2 based materials, have been achieved by materials scientists. Although K_{IC} values have been improved for these ceramics when used at low to moderate temperatures, there have been no solutions that apply for high temperature applications. The metastable phases responsible for the high toughness values in the ZrO_2 based materials are lost with exposures to even moderate temperatures (500–600 °C) [2]. High fracture toughness values are achieved in Si_3N_4 by optimizing the alpha/beta ratio in high density materials [3, 4] that employ large quantities of liquid-phase sintering aids, typically these sintering aids limit the service temperature to a maximum of 1200 °C. All of the more refractory monolithic materials, such as SiC, have fracture toughness values ($K_{IC} = 2.3$–3.5 MPa $m^{1/2}$) that make them so sensitive to damage incurred during service that design stresses must be limited to levels far below the strengths of defect-free, as-processed samples.

Composites represent an important opportunity for improving the toughness and reducing the flaw sensitivity of ceramic materials used at temperatures ranging from low to high values. Figure

*Paper presented at the symposium on Interfacial Phenomena in Composites: Processing, Characterization, and Mechanical Properties, Newport, RI, June 1–3, 1988.

0921-5093/89/$3.50

© Elsevier Sequoia/Printed in The Netherlands

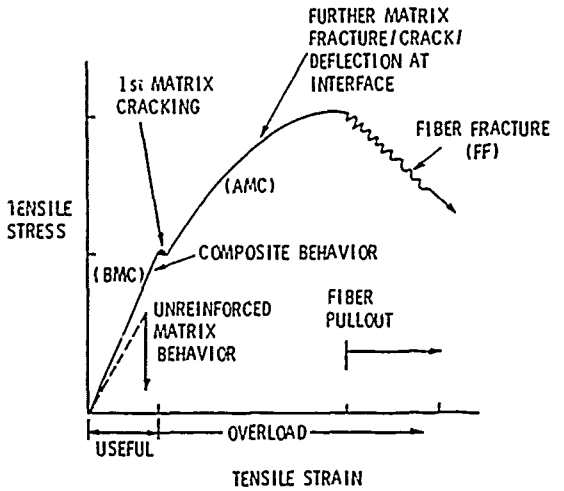

Fig. 1. Ideal stress–strain behavior of ceramic matrix composite reinforced unidirectionally with long, weakly bonded fibers [5] BMC denotes before matrix cracking and AMC after matrix cracking regions of the stress–strain curve.

1 is an idealized stress–strain curve [5] for a unidirectionally reinforced, uniaxially loaded ceramic matrix composite. The toughening represented by the area under this idealized stress–strain curve has in fact been observed in many cases. Significantly increased fracture toughness values have also been observed with random, short fiber reinforced crystalline- and glass-phase ceramic matrices [6, 7]. Toughening in these ceramic matrix composites (CMCs) results primarily from a combination of matrix microcracking and crack deflection with short fiber and whisker reinforcements and a combination of fiber pull-out and crack bridging mechanisms with continuous or long fiber reinforcements [8, 9]. Tough composite ceramics are tolerant of overstrains, they can be made insensitive to matrix flaw size, and they are resistant to impact, machining and thermal shock damage. Properly designed composites should extend useful properties to very high temperatures.

Ceramic composites based on crystalline matrices have not achieved the same level of improvement as those based on glass matrices [6]. Although these crystalline-matrix composite materials should exhibit superior mechanical and thermodynamically controlled properties, processing issues have made it virtually impossible to fabricate high density parts without resorting to combinations of liquid-phase sintering mechanisms, high consolidation pressures and high processing temperatures.

Shrinkage of the matrix around the rigid, dimensionally stable fibers is a persistent, fundamental problem for crystalline matrix composites. Stresses that result can arrest the densification process and/or cause cracks to form in the matrix [10]. Stresses have been relieved by using liquid-phase sintering aids that permit rearrangement of powder particles, a feature that severely limits service temperature levels. With or without liquid-phase sintering aids, most researchers have resorted to hot pressing or HIPing to achieve high densities. These pressure-induced densification processes are costly, cannot easily produce complex shapes, and do not provide precise dimensional control; also, the high pressures frequently damage the fibers.

Reaction bonding, or either reaction sintering or reaction forming as the process is sometimes called, circumvents these issues that have remained primary obstacles to successful application of crystalline matrix composites. Reaction bonding is particularly applicable for cases where net shape formation and high temperature capabilities are important. In the most highly developed reaction bonded material, a green body made from silicon powder is nitrided to form a reaction bonded silicon nitride (RBSN) part. Consolidation in the net shape fabrication process occurs by filling the void space between silicon particles with the Si_3N_4 reaction product. Reaction bonding of silicon carbide (RBSC) is also an established process. Other reaction formed borides, carbides, nitrides, oxides and silicides can be contemplated. Two important advantages of this type of process for crystalline CMCs are the absences of both shrinkage during reaction bonding, and liquid-phase sintering aids.

2. Reaction bonded ceramic matrix composites

2.1. General background

Research with reaction bonded ceramic matrix composites has been limited despite their potential advantages. Low strength and only moderate resistance to internal oxidation have been the principal sources of hesitancy about using this matrix material for CMCs. Fortunately there is important related research with SiC fiber reinforced hot pressed and sintered Si_3N_4 (HPSN and SSN) that defines both the potential as well as difficulties that can be anticipated with the RBSN/SiC composites [7, 11, 12]. The best HPSN matrix samples used short, randomly oriented, small diameter whisker type fibers while the most successful RBSN matrix samples

employed large diameter, unidirectional, continuous fibers made by the CVD technique.

In the United States, research with reaction bonded matrices has beer done primarily at Georgia Tech, Los Alamos National Laboratory, MIT, NASA-Lewis, Norton Co. and Rutgers University. These studies have used RBSN matrices in combination with SiC fibers or whiskers as reinforcements because of the modulus differential and probable thermal expansion coefficient and thermodynamic compatibilities up to ≈1450 °C. Recently, there has been some interest in sintered or HIPed reaction bonded silicon nitride matrices that add a sintering aid for Si_3N_4 to the silicon/reinforcement mixture [13, 14]. After the silicon powder is nitrided, parts are densified with normal Si_3N_4 densification heat treatments. These latter processes may achieve superior dimensional control through reduced shrinkage, but the resulting parts will not enjoy any advantages with respect to their high temperature properties or in terms of other characteristics, like corrosion resistance, that are dominated by grain boundary phases.

Very significantly improved fracture toughness levels (up to 12.5 MPa $m^{1/2}$) were achieved using uncoated VLS SiC whiskers to reinforce HPSN [7] in one of the first investigations of the Si_3N_4/SiC CMC system. Demonstrating K_{IC} values that are approximately twice the levels normally measured for highly optimized HPSN, clearly indicates that this ceramic composite system has merit. More recent studies with the same type of composite materials have also demonstrated difficulties that are inherent to these high modulus, high temperature materials. Using rice hull derived whiskers in HPSN [10] gave maximum K_{IC} values (up to 6.5 MPa $m^{1/2}$) that are less than state-of-the-art levels [3, 4] for HPSN (up to 8.9 MPa $m^{1/2}$). Using a different (unspecified process) SiC whisker in sintered Si_3N_4 (SSN), other authors [12] observed only degraded toughness and strength values. Creep rates for $T \geqslant 1200$ °C observed for similar CMCs were unimproved or degraded by SiC whisker additions, effects that were attributed to liquid-phase in the grain boundaries [15, 16]. It is likely that the differences between the initial and the latter results arise largely from the strengths of the reinforcement fibers that were used; however, other factors such as purity of the constituent materials and amount of sintering aid would certainly play important roles. This first result should be viewed as an indication of the property levels that are accessible with RBSN/SiC composites if they are processed correctly. Further improvements will almost certainly be achieved with optimizations of the fiber–matrix bonding, the fiber architecture, and processing details.

The RBSN/SiC composite system introduces several additional issues that must be resolved successfully in making these materials. Pores throughout the RBSN matrix must remain open and connected with the ambient atmosphere to achieve complete nitridation of interior regions, but must close off quickly to prevent internal oxidation. One important consequence of the relatively high matrix porosity levels is that loads are largely carried by the SiC fibers since the matrix's modulus of elasticity decreases (rates varying between linear and exponential) with increasing porosity. Consequently, it is critical that the fibers and their coatings not be degraded appreciably either by the nitriding process or by service exposures. The absence of matrix shrinkage makes it especially important to achieve defect-free green microstructures since no void-filling rearrangements occur during consolidation. Historically, the low density levels have also resulted in poor matrix strength and uncertain resistance to oxygen penetration to the matrix–fiber interfacial region. While nitriding is undertaken at temperatures as much as 400 °C below hot pressing or sintering temperatures used for Si_3N_4 (typically 1650–1800 °C), the times are long (up to 200 h) and the atmospheres are chemically active [17]. The fibers and their coatings have proven vulnerable to interactions with the silicon particles, at least during the initial stages of the nitriding process. Despite these additional problems, the initial results with RBSN/SiC CMCs are very promising and they provide clear directions for future research.

2.2. *Results with RBSN/SiC composites*

Two of the most thorough investigations of RBSN/SiC CMCs were undertaken simultaneously and independently by NASA-Lewis [18–21] and the Norton Co. [22–24]. These programs initially focused on the use of the large diameter (about 144 μm) CVD SiC fibers produced by the AVCO Co. These fibers were selected because of their high strength, thermodynamic stability and low surface-to-volume ratio. Unidirectional and cross-ply composites were made by hand layup and pressing. Using

unidirectional as-received, SCS-6 type SiC fibers that had coatings about 2–4 μm thick with a variable Si/C ratio on top of an amorphous carbon layer, NASA achieved very impressive improvements relative to the values measured for monolithic RBSN made from the silicon powders used in this study. Ultimate flexural surface stress at failure (3 and 4 point loading) increased up to 9.5 times, the flexural stress at which the matrix first cracked increased up to 2.7 times, and the failures were not brittle, even in tension. Thermal shocking by quenching from 1200 °C into water had no effect on room temperature properties. Work of fracture values for the Norton composites improved 10–20 times relative to monolithic RBSN: otherwise, the results were similar to those reported by NASA. Properties generally improved with increasing volume fraction of the fibers.

Microstructural analysis indicated that debonding during fracture occurred by splitting along the carbon rich coating–matrix interfaces. Hence, the development of reduced nitriding schedules through the use of small, high purity silicon powders was one of the important accomplishments of both research programs; NASA showed that properties degraded with longer time and higher-temperature nitriding schedules and with thinner coatings on the fibers. The mechanisms responsible for the degradation were not completely identified, but increasing bond strengths between the fiber and matrix appear likely.

Cross-plied laminates made at NASA also showed great promise. The strains at first matrix failure were unchanged from the unidirectional composites, indicating that the same level of matrix perfection had been achieved with the more complex architectures. Because the modulus was reduced, the strength at first matrix cracking was lower for the cross-plied composite, as was the ultimate strength. NASA indicated that improved properties in cross-plied composites would come from improved matrix strength and fiber–matrix bonding; we would also suggest the use of smaller diameter fibers.

No transverse or shear data were reported for either RBSN study. It is likely that the transverse and shear strengths of the unidirectional RBSN composites also would be lower than those of the RBSN matrices. Weakly bonded fibers act as flaws to stress components aligned perpendicular to the fiber axes, thereby degrading transverse and shear strengths. For this reason and factors relating to formability, small diameters will likely be favored over large diameters for weakly bonded reinforcement fibers. The use of small diameter SiC fibers will accentuate processing issues that must be resolved before they can be utilized to advantage in RBSN matrix composites.

Norton has also demonstrated the feasibility of using long, uncoated and coated polymer derived SiC reinforcement fibers in an RBSN matrix. The key to this success was using nitriding schedules that had been reduced from 100–140 h to either 8 or 48 h at 1350 °C because each of the five fiber types studied still was at least partially amorphous. The means by which this reduction was accomplished was not revealed; however, both Norton and Rutgers [25] indicated that nitriding kinetics are enhanced by the presence of the SiC fibers. Postulated mechanisms include enlarged channel dimensions into the interior of the matrix and the presence of accelerators such as Fe and SiO.

Using the uncoated Nicalon™ Ceramic Grade and Dow Corning MPDZ grade polymer-derived SiC fibers, Norton observed non-brittle failures when the shorter (8 h) nitriding cycle was used. All other combinations gave completely brittle failures at stress levels that were below strengths of monolithic RBSN. Any toughening should be viewed as highly encouraging since only a very small range of process conditions was accessible that achieved complete nitridation without damaging the polymer derived fibers. Subsequent studies with different coatings on Nicalon™ fibers showed that the thickest carbon coatings gave the best properties. All of the investigated coatings (Al_2O_3, SiC, Si_3N_4 and C) reacted to some extent during nitriding, tending to bond the fibers to the matrix. The carbon coatings reacted with the unreacted silicon, forming SiC. Thicker carbon coatings worked because they were thick enough to survive the nitriding schedule and also formed a weak region at the location where silicon was first detected in the reaction zone between the coating and matrix.

Four groups have studied short, randomly oriented fiber reinforced RBSN, a CMC that should have the potential of matching the results achieved by Los Alamos with the HPSN/SiC$_w$ CMCs. Georgia Tech [26] investigated the use of several types of fibers in RBSN matrices, including polymer derived Nicalon™ and rice hull-derived whisker Silar™ SiC fibers. The nitriding

schedule employed by Georgia Tech was so severe (150 h with temperatures up to 1400 °C) that all of the fibers were degraded or completely converted to Si_3N_4. As a consequence, the mechanical properties were poor even by comparison with monolithic RBSN. Rutgers [25] investigated SiC whisker reinforced RBSN composites made by colloidal pressing. Their best materials achieved nearly complete reaction without damaging the SiC whiskers in parts with reasonably high matrix densities ($\leqslant 59$ %) and correct volume fractions (20–40 %) of whiskers. Though strengths were 2.4–4.0 times higher than would be expected for the achieved matrix densities, they were not improved over conventional, good quality RBSN. Fracture toughness and work of fracture measurements were not made. Los Alamos [27, 28] has studied RBSN/SiC composites that are based on the high purity, high strength SiC whiskers made by the VLS process at that laboratory. Using conventional nitriding schedules, the small diameter whiskers were completely converted to Si_3N_4, precluding any hope of reinforcement. Los Alamos found that the nitriding accelerators such as iron oxide actually enhance the attack of the SiC whiskers even though they reduce the severity of the nitriding schedule. In collaboration with Los Alamos, MIT incorporated the VLS SiC whiskers into very high purity Si powders (final matrix density ≈ 70 %) and subjected the parts to the nitriding schedule in use at MIT at that time (1 h, 1400 °C). These results showed that the combination of high purity and reduced nitriding conditions permitted complete nitridation without any evidence of attacking the uncoated fibers [27]. The SEM micrograph of a fracture surface shown in Fig. 2 shows pull-out lengths equal to many fiber diameters. The use of high purity materials would appear to eliminate any fundamental barrier to making these composites.

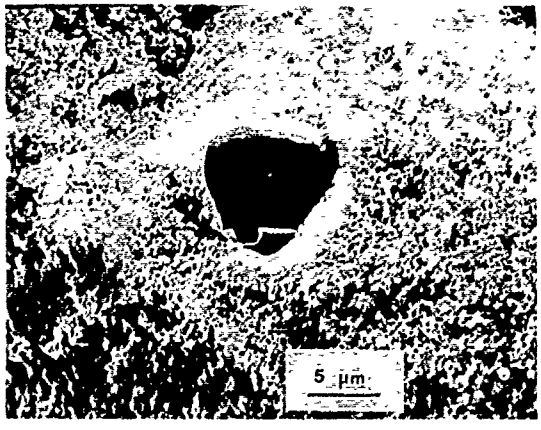

Fig. 2. SEM fracture surface of SiC VLS-whisker reinforced RBSN part made from laser-derived silicon. Extensive pull-out and an absence of fiber degradation are illustrated.

In combination, these results with the RBSN/SiC system demonstrate the feasibility of making this composite and achieving improved properties. They also make clear several issues that must be resolved to make them practical. Most importantly, the nitriding temperature and time must be minimized without using nitriding accelerators to avoid damaging the fibers. Matrix strength must be improved to avoid premature matrix cracking, thereby exposing the reinforcements to damage from the ambient atmosphere. Similarly, related research shows that the inherent oxidation resistance of the RBSN matrix must be improved.

2.3. RBSN improvements

As part of an extensive ceramics processing research program, MIT has synthesized nearly ideal silicon powders from laser heated silane (SiH_4) gas [29–31] and has developed powder handling, dispersion, shaping and drying techniques that permit defect-free, green parts to be made without introducing contaminants [32]. The green silicon bodies have been made into high quality RBSN parts.

Many of the RBSN properties have been measured already [32, 33]. A ball-on-ring biaxial strength test was used to determine the room temperature strengths of the nitrided samples in the as-processed condition and after exposures to 1000 and 1400 °C air (with and without post-oxidation etching); fracture toughnesses were measured using a Vickers indenter and by analysis of fracture surfaces and measured strengths; hardness was measured by the Vickers technique. Oxidation resistance was measured for 1000 and 1400 °C exposures to air for 1 and 50 h. Nitriding kinetics have been modelled experimentally and mechanistically [34]. Results show that RBSN's deficiencies as a CMC matrix have been largely corrected.

If the powders remain free of contaminants through all of the fabrication steps, parts nitride to completion at unusually low temperatures and in short times [32]. Our standard nitriding schedule employs a 1 °C min^{-1} ramp to 1200 °C fol-

lowed by a 0.5 °C min^{-1} ramp from 1200 to 1400 °C and a 1 h hold. The total exposure of 7 h to nitriding temperatures ($T \geqslant 1200$ °C) represents a major reduction from normal schedules. More recent results [34] show that this time period can be reduced dramatically. If as-synthesized purities are maintained until the nitriding step, these silicon parts will react to completion in much less severe combinations of time and temperature, such as 1 h at 1150 °C or 10 min at 1250 °C. The use of a pre-nitriding nucleation step allows complete conversion in 1 h at 1050 °C. Preliminary nitriding studies, of these high purity silicon powders in the presence of high purity SiC powders, indicate that the SiC enhances the reaction rate [35]. Beyond a simple, important corroboration of the Norton and Rutgers observations, these results do not yet provide any basis for mechanistic interpretation. However, it is evident that nitriding times and temperatures can be reduced by using high purity, small diameter powders and correct processing techniques.

Figure 3 shows average fracture stresses for lapped, as-processed MIT RBSN samples having densities of ≈ 65 % (300 MPa) and ≈ 75 % (>31 MPa). The error bars correspond to the standard

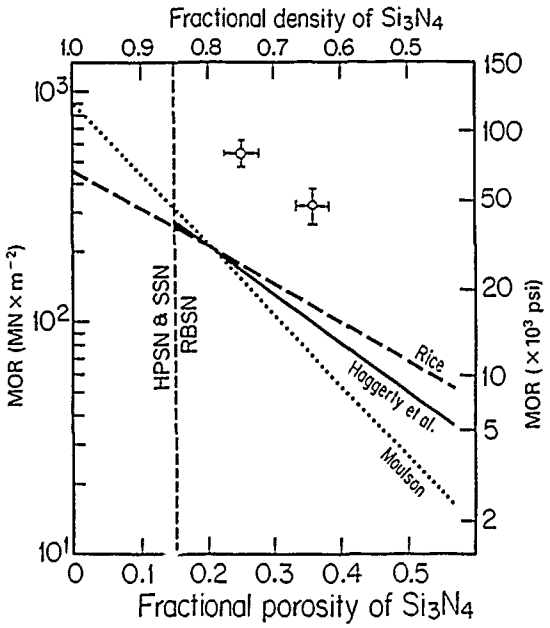

Fig 3. Room temperature strength of silicon nitride vs. density. Experimental data points were derived for MIT RBSN having two density levels; standard deviations are shown. The lines are drawn from literature surveys cited in ref. 36.

deviations in density (± 2–3 %) and strength (± 55 MPa). Fracture sources were usually either 5–15 μm diameter voids, or occasional lenticular cracks less than 50 μm deep. Recently improved processing techniques have yielded ≈ 75 % dense RBSN samples with strengths up to 695 MPa. For comparison, Fig. 3 also includes three different lines representing least-square fits of exponential functions to RBSN, SSN and HPSN strength data from the literature [17, 36, 37]; these data represent both laboratory and commercial samples with all surface finishes. Silane-originating RBSN specimens, that were diamond lapped to 4 μm, exhibit average strengths that are 2.5 to 5.0 times the average reported values at both corresponding density levels. The more recent 75 % dense samples exhibited by far the highest strengths ever reported for RBSN. Exposure to 1000 and 1400 °C air for 1 and 50 h had no measurable effect on the room temperature strengths [33] of etched and unetched samples. These room temperature strength levels are well into the range previously observed only with high density, high purity Si_3N_4 [4, 38]. The absences of both liquid-phase sintering aids in this material and oxidation induced defects should result in the highest strength Si_3N_4 at elevated temperatures.

Vickers hardness values were determined on polished surfaces using 300 and 500 g loads. Observed hardness values ranged from 3.5 to 11.0 GPa, as density increased from 60 to 80 % [32, 39]. The hardness of 77 % dense RBSN (≈ 10 GPa) is higher than that of 85 % dense, highly optimized commercial RBSN (≈ 8.3 GPa) [40]. Calculated from analysis of flaw-size strength results, the K_{IC}s are 2.35 and 2.70 MPa $m^{1/2}$ for the 67 and 77 % dense RBSN respectively [33, 41]; these values are higher than optimized commercial RBSN (≈ 2.0 MPa $m^{1/2}$) [40] and approach those of high density, high purity Si_3N_4 [4]. As is typical, the indentation technique gave slightly lower values (2.1 MPa $m^{1/2}$, [39]) for 77 % dense RBSN.

Figure 4 summarizes the results of the oxidation studies [33] for the 77 % dense RBSN, along with the results reported by others for RBSN [42] and HPSN [43]. The 77 % dense SiH_4-originating RBSN exhibits up to two orders of magnitude lower weight gain than results for two more dense RBSN materials, and up to an order of magnitude better behavior than HPSN. The high purity RBSN samples formed protective films less than 1 μm thick for all combinations of investigated

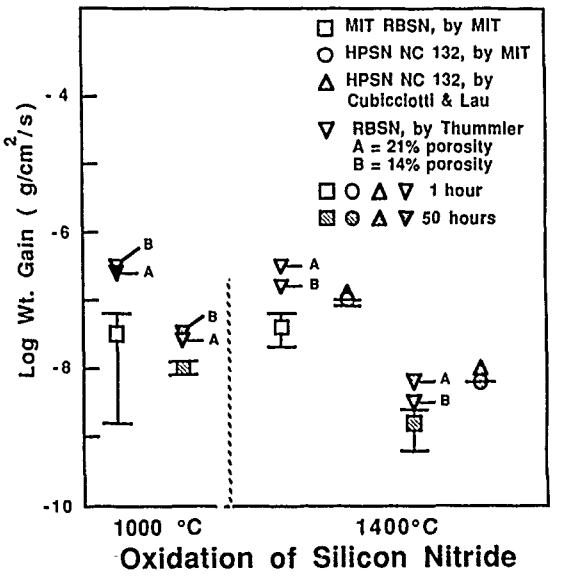

Fig. 4. Oxidation weight gains for RBSN and HPSN samples at 1000 and 1400 °C for 1 and 50 h. MIT measurements and data cited in the literature are shown. Procedures and citations are given in ref. 33.

times and temperatures. Previous results with the SiH_4-originating RBSN show that our low density specimens undergo significant internal oxidation before saturation is attained at 1250 °C [32], as was anticipated from Thummler's results [42]. Although our results have not been analyzed mechanistically, it would appear that the same microstructural features that give high strengths for the SiH_4-originating RBSN also give it improved oxidation resistance relative to more dense RBSN. This superior performance very likely results from a combination of our samples having very small pore diameters, uniform microstructures, and an absence of impure grain boundary phases. The impure grain boundary phase is responsible for the surface defects that cause strength reductions in HPSN after high temperature oxidizing exposures [44] and allows rapid transport of oxygen into the interior of the parts.

At least on an experimental basis, these results indicate that the principal deficiencies exhibited by RBSN as a composite matrix have been resolved. Nitriding kinetics, matrix strength, and oxidation resistance have all been improved to needed levels.

3. Summary and conclusions

If processing issues can be resolved, ceramic matrix composites based on reaction bonding forming processes offer important opportunities for structural ceramics that must exhibit reliable, superior properties at temperatures extending to high levels. Composites, more than monolithic ceramics, are likely to achieve high fracture toughnesses that can survive high and cyclic temperature exposures because they do not depend on metastable effects or on intergranular microcracking through impure grain boundary phases. Although high purity crystalline CMCs should exhibit the best properties based on thermodynamic characteristics and other properties, these materials have not been made successfully by conventional ceramic powder processing routes because of excessive stresses that result from shrinkage and differential thermal expansion coefficients. Reaction bonding may resolve these issues because consolidation occurs without shrinkage as the reaction product fills the void space between particles and there is no need to employ additives that concentrate in grain boundaries. The absence of shrinkage has obvious economic importance by permitting net-shape fabrication of complex parts.

Reaction forming by the reaction bonding route appears to have significant advantages relative to the related chemical vapor infiltration (CVI) type processes. In the CVI processes, very critical levels of supersaturation, temperature and pressure must be maintained that allow deposits to grow deep within a porous part having a complex pore structure. The deposition processes are slow (weeks to months), and the outer surfaces frequently close off, terminating further internal deposition until the part has had its exterior surface removed by machining. Reaction bonding, as practised with Si_3N_4, permits rapid, full penetration reactions without surface closure, if done correctly.

Reaction bonding does introduce new, difficult processing issues that must be resolved to make them feasible. Although the processing temperatures for Si_3N_4 matrix CMCs are reduced, the combination of longer times, free silicon and frequently employed nitriding accelerators, tends to degrade the fibers, whether coated or not. This potential degradation is critical because fibers must be load bearing in the reduced-modulus, porous matrix. This degradation is particularly serious for the small diameter fibers that must be employed to achieve adequate shear and transverse properties. The solution to these problems appears to be one of lessening the nitriding sche-

dule through the route of using small diameter, very high purity materials for the reinforcement and the Si powder. Appropriate high purity coatings could block adverse effects of lesser purity reinforcements while protecting them from attack. Once the silicon has been converted to Si_3N_4, service temperature levels can very likely be raised beyond those that degrade fibers during nitriding.

The procedures developed at MIT for making RBSN have already achieved the superior matrix properties needed for high performance composites, and have reduced nitriding times and temperatures to values that do not cause either degradation of the silicon whiskers or development of excessively strong matrix–fiber bonds. Strength (up to 695 MPa), fracture toughness (up to 2.7 MPa $m^{1/2}$), and hardness (up to 11 GPa) values essentially equal those of fully dense, high purity Si_3N_4. Because pores are extremely small in diameter and are uniformly distributed, oxidation resistance of this RBSN is excellent; the formation of an effective passivating layer is particularly important with respect to protecting the reinforcements in these porous matrix composites. With their low specific gravities (≈ 2.0), composites based on a RBSN matrix should exhibit exceptional specific properties for the entire temperature range of interest.

The RBSN–SiC composite is an important system based on the demonstrated properties of the constituent materials and the characteristics of the fabrication process. It also serves as a model system for other potential reaction bonded matrices.

References

1 H. K. Bowen, *J. Mater. Sci. Eng., 44* (1980) 1–56.
2 A. H. Heuer, Case Western Reserve University, Cleveland, OH, private communication.
3 Y. Tajima, K. Urashima, M. Watanabe and Y. Matsuo, *Proc. Ist Int. Conf. on Ceramic Powder Processing Science*, Am. Ceram. Soc., Nov. 1–4, 1987.
4 R. W. Rice, K. R. McKinney, C. CM. Wu, S. W. Freiman and W. J. M. Donough, *J. Mater. Sci., 20* (1985) 1392–1406.
5 J. J. Mecholsky, *Am. Ceram. Soc. Bull., 65* (2) (1986) 315–322.
6 K. M. Prewo, J. J. Brennan and G. K. Layden, *Am. Ceram. Soc. Bull., 65* (2) (1986) 305–313.
7 P. D. Shalek, J. J. Petrovic, G. F. Hurley and F. D. Gac, *Am. Ceram. Soc. Bull., 65* (2) (1986) 351–356.
8 R. W. Rice, *Ceram. Eng. Sci. Proc., 2* (7–8) (1981) 661–701.
9 A. G. Evans, *Mater. Sci. Eng., 71* (1985) 3–21.
10 A. G. Evans, Defect Properties and Processing of High-Technology Nonmetallic Materials, *Materials Research Soc. Symp. Proc., 60* (1986) 63–78.
11 S. T. Buljan, J. G. Baldoni and M. L. Huckabee, *Am. Ceram. Soc. Bull., 66* (2) (1987) 347–352.
12 R. Lundberg, L. Kahlman, R. Pompe, R. Carlsson and R. Warren, *Am. Ceram. Soc. Bull., 66* (2) (1987) 330–333.
13 J. Heinrich, E. Backer and M. Bohmer, *J. Am. Ceram Soc., 71* (1) (1988) C-28.
14 J. L. Huang, 90th Annual Meeting of the American Ceramic Society, Cincinnati, OH, May 1988, paper 129-C-88.
15 J. R. Porter, F. F. Lange and A. H. Chokshi, in P. F. Becher, M. V. Swain and S. Somiya (eds.), *Materials Research Soc. Symp. Proc., 78* (1987) 289–294.
16 R. D. Nixon, S. Chevacharoenkul, M. L. Huckabee, S. T. Buljan and R. F. Davis, in P. F. Becher, M. V. Swain and S. Somiya (eds.), *Materials Research Soc. Symp. Proc., 78* (1987) 295–302.
17 A. J. Moulson, *J. Mater. Sci., 14* (1979) 1017–1051.
18 R. T. Bhatt, *NASA Techn. Rep. 85-C-14*, July 1985.
19 R. T. Bhatt, *NASA Techn. Rep. 86-C-2*, Jan. 1986.
20 R. T. Bhatt and R. E. Phillips, *J. Compos. Mater.*, to be published.
21 R. T. Bhatt and R. E. Phillips, *J. Am. Ceram. Soc*, to be published.
22 N. D. Corbin, G. A. Rossetti and S. D. Hortlime, *Ceram. Eng. Sci. Proc., 7* (7–8) (1986) 958–968.
23 N. D. Corbin, C. A. Willkens and S. D. Hartline, *NASA Conf. on Metal Matrix, Carbon, and Ceramic Matrix Composites Proc.*, Cocoa Beach, FL, Jan. 1987, to be published.
24 N. D. Corbin, C. A. Willkens and S. D. Hartline, *NASA Conf. on Metal Matrix, Carbon, and Ceramic Matrix Composites Proc.*, Cocoa Beach, FL, Jan. 1987, to be published.
25 F. Takao, W. R. Cannon and S. C. Danforth, in G. L. Messing, K. S. Mazdiyasni, J. W. McCauley and R. A. Haber (eds.), *Advances in Ceramics*, Vol. 21—*Ceramic Powder Science*, Am. Ceram. Soc., Westerville, OH, 1987.
26 T. L. Starr and J. N. Harris, *Development of Advanced Fiber Reinforced Ceramics, Final Report for Oak Ridge National Laboratory*, subcontract 19X-43369C, U.S. Dept. of Energy Contract DE-AC05-840R21400, 1987.
27 F. D. Gac, G. F. Hurley, J. J. Petrovic, W. J. A. Parkinson and P. D. Shalek, LANL-1. *Short Fiber Reinforced Structural Ceramics*, Los Alamos National Laboratory, Los Alamos, NM, 1986.
28 F. D. Gac, *Investigation of VLS Silicon Carbide Whisker Reinforced Reaction Bonded Silicon Nitride*, Ph.D. Thesis, University of Washington.
29 W. R. Cannon, S. C. Danforth, J. H. Flint, J. S. Haggerty and R. A. Marra, *J. Am. Ceram. Soc., 65* (7) (1982) 324–330.
30 W. R. Cannon, S. C. Danforth, J. H. Flint, J. S. Haggerty and R. A. Marra, *J. Am. Ceram. Soc., 65* (7) (1982) 330–335.
31 J. H. Flint and J. S. Haggerty, *Proc. Ist Int. Conf. on Ceramic Powder Processing Science*, Am. Ceram. Soc., Orlando, FL, Nov. 1987, to be published.
32 J. S. Haggerty, J. H. Flint, G. J. Garvey, J-M. Lihrmann and J. E. Ritter, in W. Bunk and H. Hauser (eds.),

Ceramic Materials and Components for Engines, Verlag Deutsche Keramische Gesellschaft, April 1986, pp. 147–154.
33 J. S. Haggerty, A. Lightfoot, J. E. Ritter, S. V. Nair and P. Gennari, *Ceram. Eng. Sci. Proc., 9* (7–8) (1988) 1073–1077.
34 B. W. Sheldon and J. S. Haggerty, *Ceram. Eng. Sci. Proc., 9* (7–8) (1988) 1061–1071.
35 B. W. Sheldon, J. H. Flint and A. Lightfoot, MIT, Cambridge, MA, unpublished results.
36 J. S. Haggerty, G. Garvey, J-M. Lihrmann and J. E. Ritter, *Materials Research Soc. Symp. Proc., 60* (1986) 51–62.
37 R. W. Rice, *J. Mater. Sci., 12* (7) (1977) L627.
38 J. A. Palm and C. D. Greskovich, *Am. Ceram. Soc. Bull., 59* (4) (1980) 447.
39 W. A. Dunlay, *Mechanical Properties of Laser Synthesized Reaction Bonded Silicon Nitride*, M.S. Thesis, Mechanical Engineering Department, University of Massachusetts, Amherst, MA, Sept. 1987.
40 S. C. Danforth and J. S. Haggerty, *J. Am. Ceram. Soc., 64* (4) (1983) C-58.
41 J. S. Haggerty, J. E. Ritter and S. V. Nair, 90th Annual Meeting of the American Ceramic Society, Cincinnati, OH, May 1988, paper 12-SIII-88.
42 F. Porz and F. Thummler, *J. Mater. Sci, 19* (1984) 1283–1295.
43 D. Cubicciotti and K. H. Lau, *J. Am. Ceram. Soc., 61* (11–12) (1978) 512–517.
44 K. Jakus, J. E. Ritter and W. P. Rodgers, *J. Am. Ceram. Soc., 67* (7) (1984) 471–475.

Materials Science and Engineering, A107 (1989) 127–132

Dispersion Processing of Creep Resistant Whisker-Reinforced Ceramic-Matrix Composites*

JOHN R. PORTER

Rockwell International Science Center, Thousand Oaks, CA 91360 (U.S.A.)

(Received June 1, 1988)

Abstract

SiC whisker-reinforced Al_2O_3 composites, with enhanced strength and creep failure strains, have been fabricated by dispersion processing, pressure filtration and hot pressing. This method minimizes flaws that otherwise cause premature failure. High stress creep measurements demonstrate that true steady-state creep does not develop in these composites for whisker loadings above some critical level; creep rates continue to decrease with increasing creep strain. Also, an anelastic strain recovery is observed on load removal at creep temperatures. Existing creep models are inadequate to explain these observations. The development of new models for composite creep requires measurements on composites with systematically varied microstructures, which currently are being prepared.

1. Introduction

Whisker-reinforced ceramic-matrix composites have potential applications as high temperature structural materials in, for example, advanced heat engines. In previous experiments, a 15 vol.% SiC-whisker reinforced Al_2O_3 was shown to creep up to two orders of magnitude more slowly than a control fine-grained polycrystalline Al_2O_3 [1, 2]. The stress exponent for creep, n, in the expression $\dot{\varepsilon} = A\sigma^n$, where $\dot{\varepsilon}$ is the steady-state outer-fiber strain-rate, σ is the outer-fiber stress and A is a constant, was $\simeq 5$ in the composite compared to $\simeq 2$ for the Al_2O_3. However, premature failure limited the total outer-fiber strains observed in these composites to $\simeq 1\%$.

Processing flaws were identified as the creep failure origins in the conventionally processed composites and a dispersion-processing/pressure-filtration/hot-pressing technique was developed to fabricate composites devoid of strength-limiting flaws [2]. The creep experiments reported here for the dispersion-processed composites show that existing models for composite creep are inadequate to explain the observed creep response and new concepts behind a model under development are introduced.

A secondary consequence of the dispersion processing approach is that oxidation rates at creep temperatures are reduced in the absence of processing flaws. The reactions observed on composite oxidation are presented later.

2. Processing

The processing procedure has been described previously [2] and related experiments have recently been described by Sacks *et al* [3]. Composites were fabricated from SiC whiskers (Silar SC9, ARCO Chemical Co., Greer, SC) and high purity Al_2O_3 powder (AKP30, Sumitomo Chemical America, Inc., New York, NY). Similar SiC whiskers, characterized in detail by Nutt, are typically < 0.5 μm in diameter with an aspect ratio up to 100 [4, 5]. Figure 1 shows a scanning electron micrograph of whiskers sedimented from a suspension in water; most whiskers lie, as expected, approximately parallel to the plane of the micrograph. The whiskers are randomly oriented within that plane but there is clearly short-range texture and whiskers tend to align approximately parallel to their nearest neighbors. This arrangement of whiskers is likely to be reproduced in the composite.

No sintering additives, such as MgO, are used in the fabrication of the composites. Normally, MgO additions to monolithic polycrystalline

*Paper presented at the symposium on Interfacial Phenomena in Composites: Processing, Characterization, and Mechanical Properties, Newport, RI, June 1–3, 1988.

0921-5093/89/$3.50

© Elsevier Sequoia/Printed in The Netherlands

Fig. 1. Scanning electron microscope of SiC whiskers after sedimentation from suspension in water.

Al_2O_3 prevent abnormal grain growth; in this case the whiskers appear to perform a similar role.

As-received whiskers and Al_2O_3 powders are known to contain soft and hard agglomerates. These can be removed from dilute, aqueous dispersions by ultrasonic agitation, which breaks up the soft agglomerates, followed by the sedimentation of remaining hard agglomerates and whisker "nests". Al_2O_3 can be dispersed in water at $pH = 2$ and subsequently flocculated when the pH is increased to $pH \geq 5$. In contrast, SiC is dispersed at high pH ($pH = 9-11$) and is flocculated when the pH is lowered to $pH \leq 5$. Adjustments to pH are made by additions of nitric acid (to lower pH) and ammonium hydroxide (to raise pH).

Particles are dispersed in water by mutual electrostatic repulsion. For Al_2O_3 particles in a low pH dispersion, excess H^+ ions adsorb onto the exposed O^{2-} ions, giving each of the particles a net positive charge. For the SiC whiskers, dispersed at high pH, excess OH^- groups adsorb onto exposed Si^{4+} ions giving each whisker a net negative charge. Flocculation occurs when these dispersing charges are removed and van der Waals forces provide a net interparticle attraction. Heteroflocculation, whereby Al_2O_3 particles become electrostatically attracted to the SiC whiskers, may be anticipated if slurries are mixed at a suitable pH. Empirically, high green densities and homogeneous composite microstructures have resulted from mixing slurries at $pH = 2$. To verify that heteroflocculation is occurring at $pH = 2$, a single, large β SiC whisker (provided by J. J. Petrovic, Los Alamos National Laboratory) was immersed in a dilute Al_2O_3 slurry (~ 1 vol.%) at $pH = 2$ for 10 min, gently removed, dried and examined in a scanning electron microscope, where Al_2O_3 particles were observed sticking to the surface.

It is interesting to note that if dispersed SiC whiskers in a dilute slurry (after "nest" removal) are allowed to settle, a sediment with ≃ 20% solid fraction results. The implication for these particular whiskers is that it should be possible to prepare a fully dense composite with up to 20 vol.% whisker loading without significantly damaging the individual whiskers. For greater whisker loadings, whiskers would have to be either more precisely aligned, elastically deformed or broken during hot pressing if full density is to be obtained.

Composite green bodies are produced by mixing dispersed slurries in selected proportions (using both mechanical and ultrasonic agitation), adjusting pH and consolidating into a disc by pressure filtration. After mixing, the pH of the resulting slurry is essentially neutral ($pH \simeq 5-7$). Parameters which can be varied prior to pressure filtration are (1) the ratio of Al_2O_3 to SiC (determined by desired composite whisker loading), (2) the pH of the mixed slurry, and (3) the solids loading of the mixed slurry.

During pressure filtration, the filtration pressure is only adjustable within a limited range: above 20 MPa tends to result in filter cake cracking on removal from the die and less than 5 MPa results in a dilatant filter cake, containing excess moisture, which cannot support its own weight. Hot pressing times, temperatures and pressures are variable. Recently reported work suggests that the hot pressing temperature may influence composite fracture toughness, presumably by modifying the whisker/matrix interface structure [6]. In the present work, all hot pressing has been performed at 1650 °C, 24 MPa and typically 1 hour, sufficient to complete densification.

Composites with a 15 vol.% SiC whisker loading were routinely made with a uniform green color, indicative of a homogeneous distribution of whiskers. Light microscopy of such composites demonstrated that whiskers were textured and tended to be oriented in a plane normal to the filtration/hot pressing axis. Energy dispersive X-ray line profiles (obtained in a scanning electron microscope using a defocused probe) across the thickness of disc cross-sections confirmed that no gross segregation occurred during processing, which may have been expected if differential sedimentation had occurred in the mixed slurry.

More extensive localized texturing occurs in

composites with lower whisker loadings. Figure 2 shows two discs of the composite with a 5 vol.% whisker loading after hot pressing. One disc was pressure filtered at $pH=2$ and the other at $pH=5$. Although microchemical analysis line profiles indicate a homogeneous distribution of SiC within the Al_2O_3 matrix, the marbling of the color suggests domains of whisker texturing, presumably as a result of flow within the slurry.

The results suggest that on mixing the dispersed slurries heteroflocculation does occur and as a result gross segregation of the whiskers within the slurry is not observed. However, on slurry mixing and during pressure filtration, liquid flow appears to promote some localized whisker texturing.

3. Creep

Creep tests have been conducted on composites with both 5 vol.% and 15 vol.% SiC whiskers at 1500 °C in air. 1500 °C, while above the anticipated maximum operating temperature for these materials in structural applications, allows tests to be conducted in reasonable times. The processing method eliminated the flaws which would have induced premature failure, allowing samples to be deformed to large flexural strains. During creep testing, a topochemical reaction scale developed on the samples; the reaction sequence is addressed in the next section.

Creep testing was performed in four-point flexure using sapphire pivots. Load/load-point-deflection data are converted to outer-fiber stress/outer-fiber strain using the analysis on Hollenberg, Terwilliger and Gordon [7]. However, this analysis invoked four assumptions which affect the accuracy of the reduced stress/strain-rate data, namely (1) that strains are small, (2) that the material behaves similarly in tension and compression, (3) that true steady-state conditions prevail, and (4) that the standard creep relationship $\dot{\varepsilon}=A\sigma^n$ holds.

The 5 and 15 vol.% whisker loadings result in significantly different creep responses in the composites. Figure 3 shows typical creep curves for each loading. The 5 vol.% loading case exhibited steady-state creep behavior immediately upon

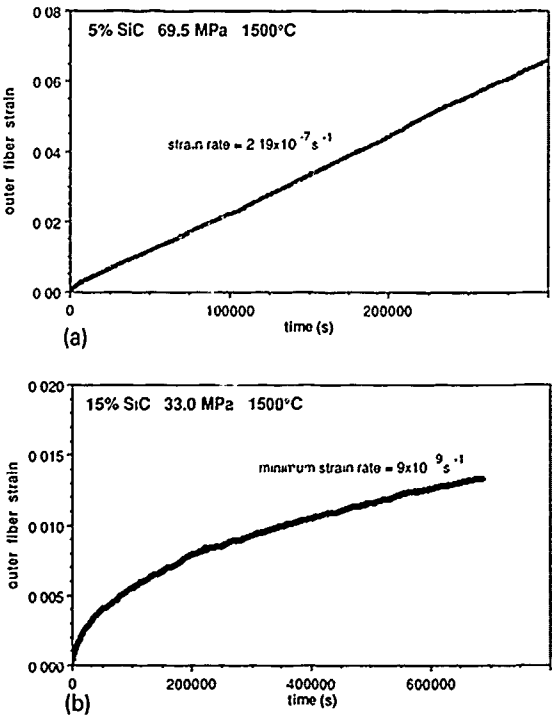

Fig. 3. Creep curves: (a) 5 vol.%, (b) 15 vol.% SiC whisker-Al_2O_3 composite.

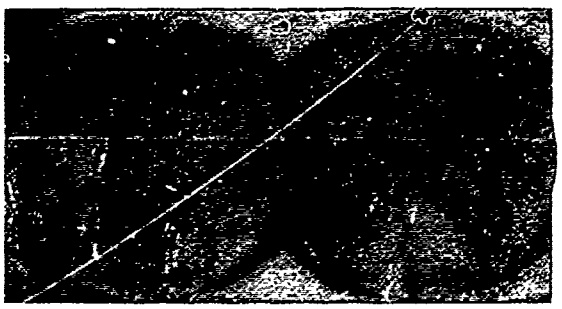

Fig. 2. Hot pressed discs of 5 vol.% SiC whisker-Al_2O_3 composite showing marbling due to localized whisker texturing, pressure filtered at pH 2 and at pH 5.

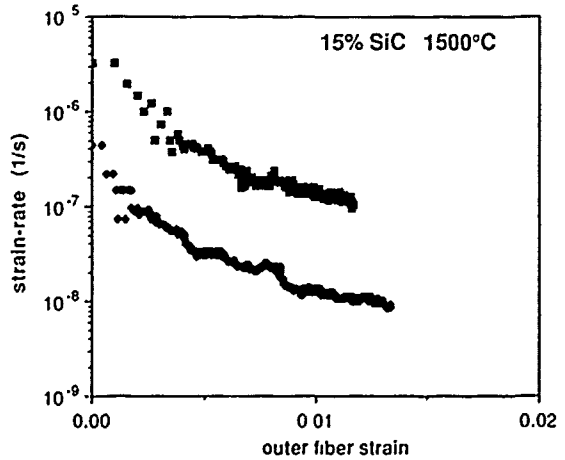

Fig. 4. Creep data for 15 vol.% SiC whisker-Al_2O_3 composite (Fig. 3b) plotted as ln $\dot{\varepsilon}$ vs. ε: ■, 50.5 MPa; ◆, 33.0 MPa.

loading whereas the 15 vol.% composite exhibited a continuously decreasing creep rate during deformation, which is more clearly depicted in Fig. 4, a plot of $\dot{\varepsilon}$ *vs.* ε. Since the Hollenberg analysis does not strictly apply for such non-steady-state behavior, the actual values of stress and strain, calculated for an assumed stress exponent of 2, are inaccurate. However, the calculated values still allow comparative behavior to be investigated. Figure 5 shows a creep curve for a 15 vol.% composite which was deformed at a nominal 50.5 MPa for 50 000 s at which point the load was removed. The sample exhibited an anelastic response whereby approximately 15% of the total accumulated strain was recovered within 10 000 s of load removal. Figure 6 consists of creep curves for 0, 5 and 15 vol.% SiC plotted as ln $\dot{\varepsilon}$ *vs.* ln σ from which values for the creep stress exponent, n, can be obtained. The data for unreinforced Al_2O_3 were corrected for an error which was present when previously reported [1]. For the 15 vol.% samples, minimum strain-rates observed during each test were plotted.

Significant creep rate reductions result from the whisker reinforcement of Al_2O_3. However, the different creep responses of the 5 and 15 vol.% SiC composites suggest that different mechanisms for creep operate in each case. The creep response of fiber-reinforced composites has been modelled by Kelly and Street [8], but their modelling assumed aligned, non-deforming fibers in a deforming matrix such that the fibers carried a fraction of the load, thereby reducing the load on the deforming matrix. The dotted and dashed lines in Fig. 6 correspond to the predicted reductions in creep rate of the Al_2O_3 matrix using the Kelly and Street model for non-deforming fibers with an aspect ratio of 50 for 5 and 15 vol.% loadings. The measured creep-rates were lower than predicted by Kelly and Street and there was clearly a change in slope for the 15 vol.% composite not predicted by the model. Similar modelling, but incorporating a deforming whisker network, is therefore proposed to model the whisker composites.

On 5 vol.% whisker loading, creep rates are reduced by approximately two orders of magnitude, but the creep stress exponent is essentially unchanged from that measured in the fine-grained polycrystalline Al_2O_3. Kelly and Street allowed for load to be transferred to the fiber rein-

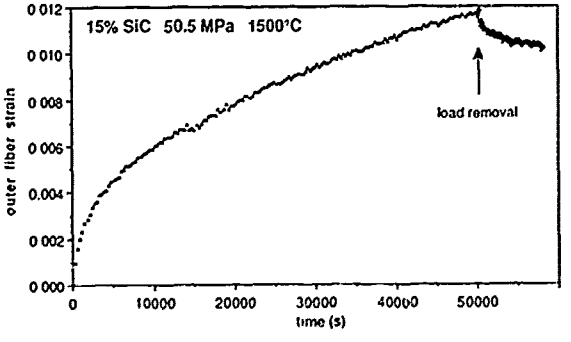

Fig 5 Strain recovery after load removal in 15 vol.% SiC whisker-Al_2O_3 composite.

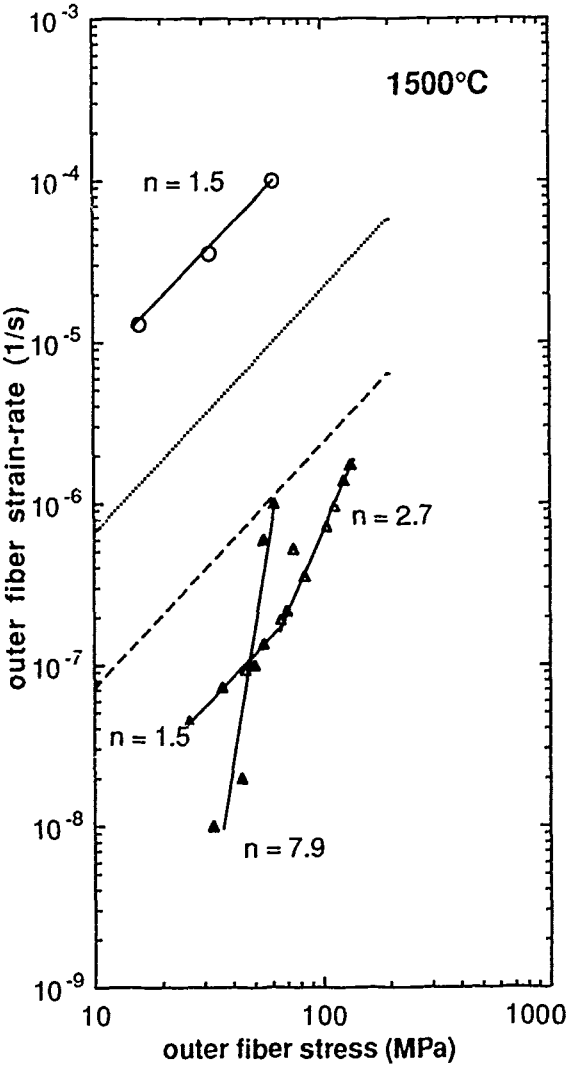

Fig. 6. Composite creep curves for 0 (○), 5 (△) and 15 (▲) vol.% SiC whisker-Al_2O_3 composites. Minimum observed strain rates are plotted for the 15 vol.% SiC material. Kelly and Street predictions for 5 (dotted line) and 15 (dashed line) vol.% short fiber (aspect ratio = 50) reinforcements of the matrix Al_2O_3 are included for comparison [8].

forcement but did not consider a change in the creep mechanism for the matrix itself. One proposed creep mechanism applicable to Al_2O_3 is diffusion-accommodated grain boundary sliding limited by the rate of creation or annihilation of point defects at grain boundaries [9]. Whisker reinforcement at 5 vol.% may simply inhibit this mechanism by either (1) mechanically restricting grain boundary sliding or (2) further limiting the sources and sinks of point defects. The change of slope observed for the composite at 70 MPa may indicate a transition to another creep mechanism.

An alternative explanation, however, utilizes the idea of a whisker network deforming in parallel with the matrix. Now, with a 5 vol.% SiC whisker loading, steady-state creep conditions prevail and there is no strain recovery on load removal. This result would ensue if, during creep, the whiskers, while not deforming, are isolated and free to rotate towards alignment with the applied stress. Kelly and Street identified a model originally developed by Riseman and Ullman for the increase in viscosity of a Newtonian fluid on the incorporation of rigid fibers [8, 10]. While attractive, this model requires extremely dilute loadings to be valid and therefore is not appropriate for this case and new modelling is required.

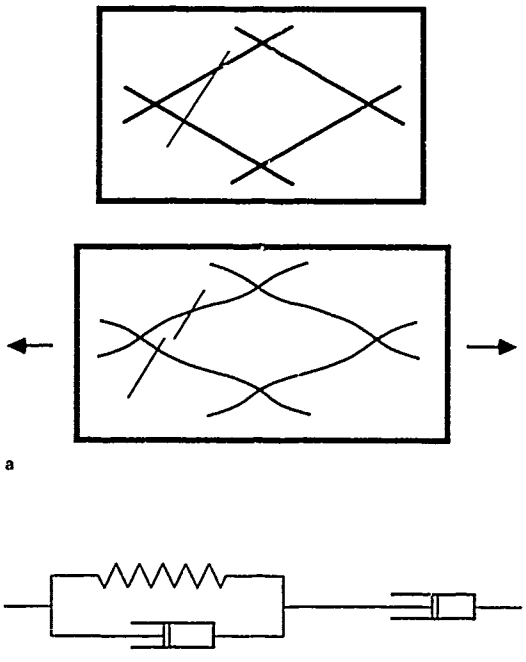

a

b

Fig. 7. (a) Schematic of deformation model for 15 vol.% SiC whisker–Al_2O_3 composite. (b) Spring-dashpot model for observed anelastic response.

The anelastic behavior observed in the 15 vol.% SiC composite requires a different interpretation. For the higher loading whisker composite, a more appropriate model requires a network of interconnected whiskers which are not free to rotate about their points of intersection (nodes), possibly as a result of whisker entanglement. Such a network would have a lower modulus than an individual whisker in tension. To sustain the observed 15% strain recovery on load removal, strain would have to be accumulated in the whisker network by the elastic bending of whiskers. Presumably, the high whisker loading partially inhibits non-recoverable strain accommodation by whisker rotation. This behavior is shown schematically in Fig. 7(a), where the angles between whiskers at nodes remain constant during creep and some non-recoverable deformation results from whisker failure. To a first approximation, such a model is simply an anelastic Voigt element (a spring and dashpot in parallel) in series with another dashpot (representing the non-recoverable deformation), as shown schematically in Fig. 7(b). Mathematically, such a system would exhibit the response:

$$\varepsilon = \frac{\sigma}{E}\left\{1 - \exp\left(\frac{t}{T}\right)\right\} + Bt$$

where E represents the modulus of the whisker network and B and T are constants. This simple representation approximates the measured response but needs to be refined. Since the modulus of the whisker network is clearly not constant with strain, replacing E with $E = f(\varepsilon)$ will be required.

If the hypothesis of a deforming network of whiskers is confirmed, then the implication for composite design is that a uniaxially aligned whisker-reinforced composite would be more creep resistant in a direction parallel to the whiskers than the two-dimensionally aligned composites fabricated to date.

4. Oxidation

Oxidation of the composite is a multistage process involving the reaction between SiC, Al_2O_3 and O_2 ultimately to produce mullite ($Al_6Si_2O_{13}$) and CO_2 [11]. The dispersion-processed composites exhibit oxidation kinetics a factor of six times slower than the dry-powder-processed composites previously investigated [11]. Figure 8

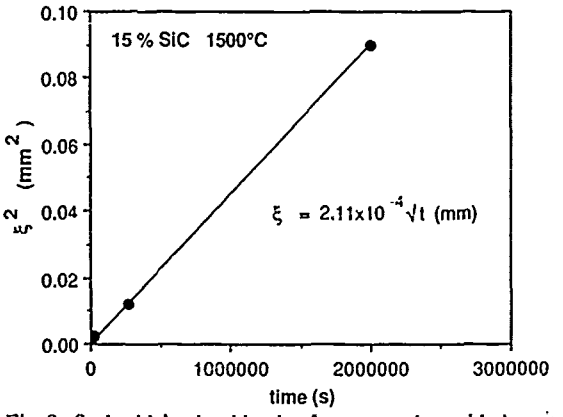

Fig. 8 Scale thickening kinetics for composite oxidation at 1500 °C.

is a plot of the square of mullite scale thickness *vs.* time at 1500 °C for the 15 vol.% SiC composite. Examination of the reaction interface reveals an intermediate black layer between the green unreacted core and the white mullite outer scale. Nutt has reported evidence for graphitic carbon in the vicinity of the reaction interface, using transmission electron microscopy [12]. X-ray diffraction of some exposed black region shows a number of peaks in addition to the expected Al_2O_3 and mullite peaks, although confirmation of specific phases is hindered by peak overlaps. One strong peak at 22° (4.04 Å), is indicative of cristobalite.

Oxidation of the composite would preclude its uncoated application at elevated temperatures; however, even after long exposure times, transmission electron microscopy observations show no evidence of a reaction between the whiskers and the matrix in the core region. This suggests that a coating which could protect the composite from oxygen may eliminate the $SiC/Al_2O_3/O_2$ compatibility problem.

5. Conclusions

SiC whisker-reinforced Al_2O_3 composites are significantly more creep resistant than unreinforced, polycrystalline alumina. A model for the composite consisting of an interconnected whisker network in a deforming matrix has been proposed. If verified in future work, the implication of the model is that significant further improvements in the creep response can be expected if uniaxially aligned composites can be fabricated.

Oxidation of the composites during high temperature exposure to air urges the development of a suitable protective coating. The observation that no reaction occurs in the core regions of samples demonstrates that the system is indeed stable if the composites can be superficially protected.

Acknowledgments

This work was supported by the Rockwell International Independent Research and Development Program. The author acknowledges pleasurable constructive discussions with B. N. Cox and P. E. D. Morgan.

References

1 A. H. Chokshi and J. R. Porter, *J. Am. Ceram. Soc., 68* (1985) C144.
2 J. R. Porter, F. F. Lange and A. H. Chokshi, *Am. Ceram. Soc. Bull., 66*(1987) 343.
3 M D. Sacks, H.-W. Lee and O. E. Rojas, *J. Am. Ceram. Soc., 71*(1988) 370.
4 S. R. Nutt, *J. Am. Ceram. Soc., 69*(1984) 428.
5 S. R. Nutt, *J. Am. Ceram. Soc., 71*(1988) 149.
6 *Comline Industrial Report, No. 871119*(1987) 17.
7 G. W. Hollenberg, G. R. Terwilliger and R. S. Gordon, *J. Am. Ceram. Soc., 54*(1971) 196.
8 A. Kelly and K. N. Street, *Proc. R. Soc. London, Ser. A, 328*(1972) 283.
9 B. Burton, *Mater. Sci. Eng., 10*(1972) 9.
10 J. Riseman and R. Ullman, *J. Chem. Phys., 19*(1951) 578.
11 J. R. Porter and A. H. Chokshi, in J. A. Pask and A. G. Evans (eds.), *Ceramic Microstructures '86: Role of Interfaces*, Plenum, New York, 1988, p. 919.
12 F. Lin, T. Maneb, A. A. Morrone and S. R. Nutt, paper presented at Am. Ceram. Soc. Annual Meeting, 1988.

III BIMATERIALS AND BICRYSTALS

Materials Science and Engineering, A107 (1989) 135–143

Sandwich Test Specimens for Measuring Interface Crack Toughness*

ZHIGANG SUO and JOHN W. HUTCHINSON

Division of Applied Sciences, Harvard University, Cambridge, MA 02138 (U.S.A.)

(Received June 1, 1988)

Abstract

A crack lying along one interface on an elastic sandwich structure is analyzed. When the thickness of the middle layer is small compared with the other length scales of the structure, a universal relation is found between the actual interface stress intensity factors at the crack tip and the apparent mode I and mode II stress intensity factors associated with the corresponding problem for the crack in the homogeneous material. Therefore, if the apparent stress intensity factors are known, for example calculated from the applied loads as if the structure was homogeneous, this information can be immediately converted into the interface stress intensity factors with the universal relation. This observation provides the theoretical basis for developing sandwich specimens for measuring interface crack toughness. The universal relation reveals the extent to which the asymmetry inherent to a bimaterial interface induces asymmetry in the near tip crack field. In particular, the result of the study can be used to infer whether stress intensity factors for a homogeneous body can be used with good approximation in place of the actual interface stress intensity factors. A proposal for simplifying the approach to interfacial fracture is made which plays down the role of the so-called oscillatory interface singularity stresses.

1. Introduction

Cracks in homogeneous, isotropic materials tend to propagate under mode I conditions in which only normal stress acts on the plane of separation ahead of the tip. For this reason, the development of fracture mechanics for such materials has tended to place heavy emphasis on mode I conditions. By contrast, the fracture mode on an interface of dissimilar materials is often mixed. Differences between elastic properties across an interface will generally disrupt the symmetry even when the geometry and loading are otherwise symmetric with respect to the crack. Moreover, an interface between dissimilar materials is frequently the weakest fracture path in a composite body, and an interface crack will tend to stay in the interface even when subject to loading combinations which give rise to shear stress as well as normal stress on the interface ahead of the tip. Some potential applications of interface fracture mechanics, such as fiber debonding from a matrix due to pull-out, involve substantial shear contributions. Thus, in general, the interfacial fracture mode is inherently mixed, and a complete characterization of an interface requires toughness data over the full range of mode combinations. Recent efforts in this direction are found in [1, 2].

A special class of sandwich specimens have been devised recently for experimental determination of interfacial toughness [3, 4], or for other related purposes such as evaluation of the toughness of adhesive joints [5, 6]. The common feature of these specimens is that each of them is homogeneous except for a very thin layer of second material which is sandwiched between the two halves comprising the bulk of the specimen. The thickness of the layer is typically a hundredth or even a thousandth of the length scale of the overall geometry (Fig. 1). A pre-existing crack lies along one of the interfaces. With such specimens, it has generally been the practice to use the stress intensity factor (or factors if mixed mode conditions pertain) determined for the homogeneous specimen with no layer to characterize the interface crack in the presence of the layer. In this paper we determine a universal relation between the stress intensity factors for the homogeneous specimen or body and the actual interfacial stress intensity factors for the crack between the layer

*Paper presented at the symposium on Interfacial Phenomena in Composites: Processing, Characterization, and Mechanical Properties, Newport, RI, June 1–3, 1988.

0921-5093/89/$3.50

© Elsevier Sequoia/Printed in The Netherlands

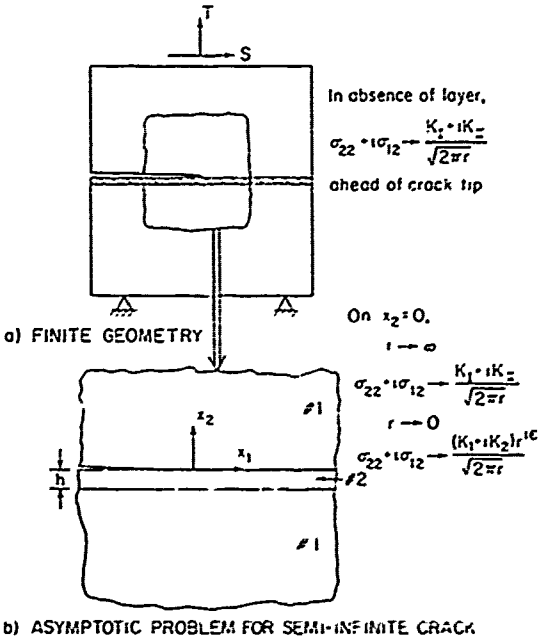

Fig. 1. Schematic of asymptotic problem.

and the material bonded to it. The universal relation is asymptotic in that it requires the thickness of the layer, h, to be very small compared with the crack length and to all other in-plane length scales of the specimen.

The mathematical problem analyzed is introduced in Fig. 1. A thin layer of material 2 is sandwiched in a homogeneous body of material 1. Each material is taken to be isotropic and linearly elastic. Attention is restricted to the plane problem, either plane strain or plane stress. The crack lies along one of the interfaces (the upper interface in Fig. 1) coincident with the x_1-axis with the tip at the origin. As indicated in Fig. 1, the asymptotic problem for the semi-infinite interface crack will be considered, as is appropriate when the layer thickness, h, is very small compared with all other in-plane length scales. The crack tip field of the homogeneous problem (with no layer present) is prescribed as the far field in the asymptotic problem. Thus the far field is characterized by the mode I and mode II stress intensity factors, K_1 and K_{II}, induced by the loads on the reference homogeneous specimen. The interface crack tip field is characterized by a different set of interfacial stress intensity factors, K_1 and K_2, which will be defined precisely in Section 2 below. The universal relation developed in the next section connects these two sets of the stress intensity factors. An analogous problem and similar arguments can be found in [7] for a crack parallel to, but slightly displaced from, an interface.

With the universal relation in hand, we outline in Section 3 the procedure to convert the experimental data (*e.g.* the critical external loads) to interfacial toughness using two particular specimen configurations as illustrative examples. A proposal for simplifying the interpretation and presentation of interfacial toughness will be discussed in Section 4.

2. The universal relation

As observed in [8] the non-dimensional elastic moduli dependence of bimaterial systems, for traction prescribed plane elasticity boundary value problems, may be expressed in terms of two (rather than three) special combinations. The Dundurs' parameters adopted in this work are defined as

$$\alpha=\frac{\Gamma(\kappa_2+1)-(\kappa_1+1)}{\Gamma(\kappa_2+1)+(\kappa_1+1)}$$
$$\beta=\frac{\Gamma(\kappa_2-1)-(\kappa_1-1)}{\Gamma(\kappa_2+1)+(\kappa_1+1)} \qquad (1)$$

Subscripts 1 and 2 refer to the two materials in Fig. 1, $\kappa=3-4\nu$ for plane strain and $(3-\nu)/(1+\nu)$ for plane stress, $\Gamma=\mu_1/\mu_2$, ν is the Poisson ratio, and μ is the shear modulus. The physically interesting values of α and β are restricted to a parallelogram enclosed by $\alpha=\pm 1$ and $\alpha-4\beta=\pm 1$ in the α, β plane. This will be of advantage later on when discussions of any functions depending on material moduli are made. Both α and β vanish when the dissimilarity between the materials does.

Two other bimaterial constants, Σ and ε, may help understand the roles that α and β play, respectively, *i.e.*

$$\Sigma=\frac{c_2}{c_1}=\frac{1+\alpha}{1-\alpha} \qquad \varepsilon=\frac{1}{2\pi}\ln\frac{1-\beta}{1+\beta} \qquad (2)$$

where the compliance parameter c is related to Young's modulus E by

$$c=\frac{\kappa+1}{\mu}=\begin{cases}8/E & \text{for plane stress}\\ 8(1-\nu^2)/E & \text{for plane strain}\end{cases} \qquad (3)$$

From (2), α can be readily interpreted as a measure of the dissimilarity in stiffness of the two

materials. Material 1 is stiffer than 2 as $\alpha > 0$ and material 1 is relatively compliant as $\alpha < 0$. The parameter ε, and thus β, as will be clear soon, is responsible for the oscillatory behavior at the interface crack tip, and it will be proposed in Section 4 that taking $\beta = 0$ may be a sensible simplifying approximation in many cases.

With K_1 and K_2 as the two interface stress intensity factors and with $K = K_1 + iK_2$ as the complex interface intensity factor [$i = (-1)^{1/2}$], the traction in the interface a distance r ahead of the crack tip is given by

$$\sigma_{22} + i\sigma_{12} = \frac{K}{(2\pi r)^{1/2}} r^{i\varepsilon} \tag{4}$$

The associated crack face displacements a distance r behind the crack tip are

$$\delta_2 + i\delta_1 = \frac{c_1 + c_2}{2(2\pi)^{1/2}(1 + 2i\varepsilon)\cosh(\pi\varepsilon)} K r^{1/2} r^{i\varepsilon} \tag{5}$$

The energy release per unit of new interfacial crack area, $\mathcal{G}$, related to the complex stress intensity factor by

$$\mathcal{G} = \frac{c_1 + c_2}{16\cosh^2 \pi\varepsilon} |K|^2 \tag{6}$$

These results for the interface singularity field were contained in a number of papers in 1965 [9–11]. The present normalization of the interfacial stress intensity factors follows [1] and [7]. The interfacial stress intensity factors for various crack configurations have not been well documented, yet some important problems have been analyzed. Two examples are depicted in Fig. 2. For a semi-infinite crack along the interface between two elastic half-spaces loaded by equal but opposite tractions $\sigma_{22} + i\sigma_{12} = -T(x_1)$ on the crack faces,

$$K = \left(\frac{2}{\pi}\right)^{1/2} \cosh \pi\varepsilon \int_{-\infty}^{0} \frac{T(t)}{(-t)^{1/2 + i\varepsilon}} \, dt \tag{7}$$

In the case of a finite crack of length $2a$ on the interface between two half-spaces which are subjected to equal but opposite tractions $\sigma_{22} + i\sigma_{12} = -T(x_1)$ on the crack faces, the stress intensity factor at the right-hand side tip is

$$K = \left(\frac{2}{\pi}\right)^{1/2} \cosh \pi\varepsilon (2a)^{-1/2 - i\varepsilon} \int_{-a}^{+a} \left(\frac{a + t}{a - t}\right)^{1/2 + i\varepsilon} T(t) \, dt \tag{8}$$

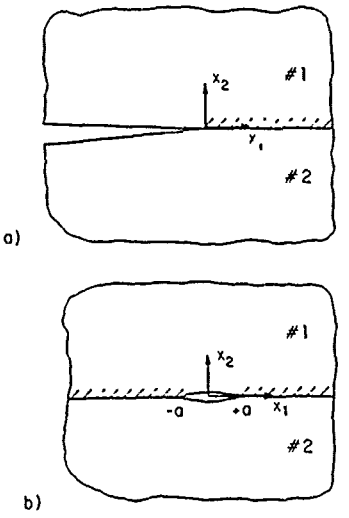

Fig. 2. Two basic interface crack configurations.

When $\beta \neq 0$, and thus by (2) $\varepsilon \neq 0$, K_1 and K_2 do not strictly measure the normal and shear traction singularities, respectively, on the interface since the two traction components do not decouple independent of r due to the term $r^{i\varepsilon} = \exp[i\varepsilon \ln r]$ in (4). Moreover, crack face interpenetration is implied by (5) at sufficiently small r (usually exceedingly small r) when $\varepsilon \neq 0$, as has been discussed in [9]. However, when $\beta = 0$, K_1 and K_2 do measure the normal and shear traction singularities on the interface ahead of the crack tip with the standard definition for the intensity factors. The utility of taking $\beta = 0$ as a pragmatic approximation will be discussed in Section 4. At this point we simply note that interpretation of the interface intensity factors is much clearer when $\beta = 0$, interpenetration is no longer an issue, and it will be argued that little of physical consequence is lost by taking β to be zero in most instances.

The far field for the asymptotic problem in Fig. 1 is characterized by mode I and mode II stress intensity factors, K_I and K_{II}, for the homogeneous specimen. With $K^\infty = K_I + iK_{II}$ as the apparent, or applied, (complex) stress intensity factor, the traction a distance r far ahead of crack tip is

$$\sigma_{22} + i\sigma_{12} = \frac{K^\infty}{(2\pi r)^{1/2}} \tag{9}$$

The energy release rate computed using the far field is

$$\mathcal{G} = \frac{c_1}{8} |K^\infty_1|^2 \tag{10}$$

By elementary energy arguments, or by application of the J-integral, one notes that the energy release rate in (6) and (10) must be equal and thus

$$|K| = p|K^\infty| \tag{11}$$

where

$$p = \left(\frac{1-\alpha}{1-\beta^2}\right)^{1/2} \tag{12}$$

Following an argument similar to that used in ref. 7, dimensional considerations (*cf.* (4) and (9)) and linearity require that

$$Kh^{i\varepsilon} = aK^\infty + b\overline{K^\infty} \tag{13}$$

where $\bar{}$ denotes complex conjugation and a and b are dimensionless complex constants depending only on α and β. Equations (11) and (13) imply

$$|a|^2 + |b|^2 = p^2 \qquad \bar{a}b = a\bar{b} = 0 \tag{14}$$

The solution to (14) which gives $K = K^\infty$ in the limit $\alpha = \beta = 0$ is

$$a = pe^{i\omega} \qquad b = 0 \tag{15}$$

where ω is a real function of only α and β. Now it is possible to rewrite (13) as

$$Kh^{i\varepsilon} = pK^\infty e^{i\omega} \tag{16a}$$

or

$$K_1 + iK_2 = p(K_1 + iK_{II})h^{-i\varepsilon}e^{i\omega} \tag{16b}$$

The universal relation (16) thus has been fully determined apart from $\omega(\alpha, \beta)$. An integral equation formulation of the interface crack problem is given in Appendix A. The function $\omega(\alpha, \beta)$ extracted from the numerical solution to the integral equation is presented in Table 1. As discussed in Appendix A, the error is believed to be within a few tenths of a degree.

The basic relation (16) can be expressed another way. Noting $|Kh^{i\varepsilon}| = |K|$, one can write

$$Kh^{i\varepsilon} = |K|e^{i\psi} \tag{17}$$

as in [1], where ψ is a real phase angle. With $\phi = \tan^{-1}(K_{II}/K_I)$ so that

$$K^\infty = |K^\infty|e^{i\phi} \tag{18}$$

Equation (16) can be written equivalently as

$$|K| = p|K^\infty| \qquad \psi = \phi + \omega(\alpha, \beta) \tag{19}$$

In words, the complex interface stress intensity factor combination $Kh^{i\varepsilon}$ has magnitude scaled by a factor p and phase angle shifted by ω with respect to the far field stress intensity factor.

For material combinations with $\beta = 0$ and thus $\varepsilon = 0$, K_1 and K_2 have conventional interpretations, as already emphasized, and (16) becomes

$$K = (1-\alpha)^{1/2}K^\infty \exp[i\omega(\alpha, 0)] \tag{20}$$

independent of h. Now, $\psi = \tan^{-1}(K_2/K_1)$ measures the relative proportion of "mode II" to "mode I" on the interface. By (19), the shift in the relative proportion in the applied (remote) field to that in the interface field is given by $\omega(\alpha, 0)$. From Table 1, it is noted that this shift is not large, varying from 4.4° for $\alpha = -0.8$ (when the layer material is stiff compared with the bulk material) to $-14.3°$ for $\alpha = 0.8$ (when the layer material is relatively compliant). Thus, for example, a mode I specimen with a sandwich layer will not be "mode I" at the interface crack tip, but the shift will not be large. Much to the expectation of the designers of these kind of specimens, the fracture mode at the crack tip is essentially the same as that induced for the crack in the corresponding homogeneous specimen under the same external loading, but with a scaling factor p.

TABLE 1 $\omega(\alpha, \beta)$ (in degrees)

β \ α	−0.8	−0.6	−0.4	−0.2	0.0	0.2	0.4	0.6	0.8
−0.4	2.2	3.5							
−0.3	3.0	4.0	3.3	1.4					
−0.2	3.6	4.1	3.4	2.0	−0.3	−3.3			
−0.1	4.0	4.1	3.3	2.0	0.1	−2.3	−5.5	−10.8	
0.0	4.4	3.8	2.9	1.6	0.0	−2.1	−4.7	−8.4	−14.3
0.1			2.3	1.1	−0.5	−2.3	−4.5	−7.4	−11.6
0.2					−1.3	−3.0	−4.9	−7.3	−10.5
0.3							−5.8	−7.8	−10.4
0.4									−11.1

3. Applications

The application of the universal relation to a particular sandwich specimen is straightforward. One may start with any specimen which has been successfully used for homogeneous crack fracture test. Proper techniques are required to sandwich a second material layer into the bulk of the specimen and ensure that the crack stays along one of the interfaces, as discussed in [4]. Critical external loads are recorded as the crack starts to propagate. The apparent stress intensity factor, K^{∞}, is then calculated from the critical external loads as if the specimen were homogeneous. The actual interfacial stress intensity factors are readily evaluated using the universal relation (16), or its simplified version (20). Two particular specimens are discussed below for purpose of illustration.

First consider the specimen shown in Fig. 3. A layer of material 2 with thickness h is sandwiched in a large plate of material 1, with overall length scale L. A crack of length $2a$ is introduced at the center of the specimen along the interface. To apply the universal relation, the specimen should be devised such that h is very small compared with the crack half-length a. We will also assume that $L \gg a$ so that the formula for the infinite plane applies, but any formula which accounts for the influence of L on the intensity factors for the homogeneous problem could be used. A uniaxial tensile stress σ is applied at an angle θ to the direction of the layer and crack. The apparent stress intensity factor is simply that of an internal crack in an infinite homogeneous plate due to remote stress [12], *i.e.*

$$K^{\infty} = K_{\mathrm{I}} + \mathrm{i}K_{\mathrm{II}} = \sigma(\pi a)^{1/2}\sin\theta\, \mathrm{e}^{\mathrm{i}\theta} \tag{21}$$

The interface stress intensity factor is then obtained by substituting (21) into (16). That is

$$Kh^{\mathrm{i}\omega} = p\sigma(\pi a)^{1/2}\sin\theta\exp[\mathrm{i}(\theta+\omega)] \tag{22}$$

With $\beta = 0$, the interface stress intensity factors are

$$K_{\mathrm{I}} = \sigma[\pi(1-\alpha)a]^{1/2}\sin\theta\cos(\theta+\omega)$$

$$K_{\mathrm{II}} = \sigma[\pi(1-\alpha)a]^{1/2}\sin\theta\sin(\theta+\omega) \tag{23}$$

Observe that (23) implies the toughness $|K_c|$ can be measured using this specimen over a wide range of phase angles $\psi = \tan^{-1}(K_2/K_1)$ by continuously varying the direction of the load θ.

Next consider the double cantilever beam (DCB) specimen proposed in [4], consisting of a thin film of medium 2 bonded between substrates of medium 1 (Fig. 4). The apparent stress intensity factor associated with the corresponding homogeneous specimen, determined from the previous numerical solution [13] in terms of applied load per unit thickness P, crack length a, and half-height l, is

$$K^{\infty} = K_{\mathrm{I}} = Pl^{-3/2}a[3.467 + 2.315(l/a)] \tag{24}$$

Substituting (24) into (16) gives the interface stress intensity factor of the crack tip as

$$Kh^{\mathrm{i}\omega} = pPl^{-3/2}a[3.467 + 2.315(l/a)]\mathrm{e}^{\mathrm{i}\omega} \tag{25}$$

If the simplifying assumption is made, *i.e.* $\beta = 0$, (25) becomes

$$K = (1-\alpha)^{1/2}Pl^{-3/2}a[3.467 + 2.315(l/a)]\mathrm{e}^{\mathrm{i}\omega} \tag{26}$$

Since ω is typically very small according to Table 1, this is essentially a mode I specimen, as anticipated [4].

4. On the virtues of taking $\beta = 0$

By conducting fracture tests over a full range of external loading (*i.e.* a full range of $\phi = \tan^{-1}(K_{\mathrm{II}}/K_{\mathrm{I}})$, one generates a locus of the critical combinations of the interface intensity factors, K_1 and K_2. A thorough discussion of several approaches to recording and using interfacial fracture data is given in [1]. In particular, if

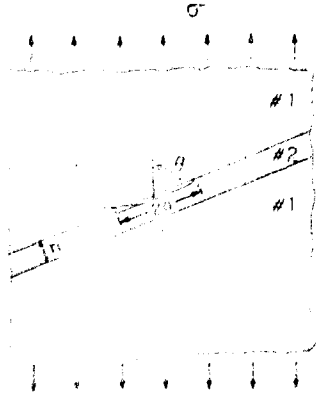

Fig. 3. Sandwich layer and interface crack in finite plane at angle θ to applied tension.

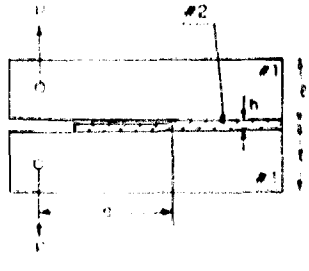

Fig. 4. Double-cantilever beam specimen with sandwich layers.

full accounting for the ε-effects is made, then a critical value of $K = K_1 + iK_2$ must be reported in units of stress σ and length L as

$$K = \Lambda \sigma L^{1/2 - i\varepsilon} \tag{27}$$

where Λ is a dimensionless complex number. A peculiar consequence of (27) is that the phase, *i.e.* the relative proportion of K_1 to K_2, changes when length units are changed. Moreover, from (4) it can be seen that the relative proportion of shear to normal stress acting on the interface directly ahead of the tip is not constant but varies (weakly) according to $r^{i\varepsilon} = \exp(i\varepsilon \ln r)$ when $\varepsilon \neq 0$.

Plane strain values of α, β and ε were listed in [7] for six representative material pairs. In most of these cases, ε is very small, often less than 0.01 in magnitude, even when α is substantial corresponding to ratios of 4 or 5 of the plane strain modulus $E/(1-\nu^2)$ of the two materials. At the present stage of the development of the mechanics of interfacial fracture it is likely that other problems and issues, such as the difficulty in preparing specimens and in measuring interfacial toughness, are much more pertinent than ε-effects. Certainly, there is no compelling experimental evidence to date which suggests an important role for ε, and various proposals for ignoring ε-effects have been considered [1]. A consistent approach proposed in [14] is to systematically take $\beta = 0$, both in the determination of critical toughness data from test specimens and in subsequent application of such data to predict fracture. Of the two non-dimensional parameters, α and β, measuring dissimilarity in material elastic properties, α appears to be the more important. For example, in the present solution (16), β enters in the factor p only as β^2 and for a typical plane strain β value makes a very small numerical contribution to p. Similarly, its lowest-order influence on the relation between K and the energy release rate in (6) is only of order β^2 through $\cosh \pi\varepsilon$. It is also noted that ω in Table 1 is a stronger function of α than of β and for typical β values is hardly influenced. A similarly weak dependence on β of the solution variables for intensity factors for a crack kinking out of an interface was noted in [14]. Curiously, the several solutions for intensity factors for cracks on the interface between two semi-infinite blocks of materials produced in 1965 [9–11], two of which are listed here as (7) and (8), have no dependence on α but do depend weakly on ε and, therefore, on β. This may partly explain why ε-effects may have been overemphasized. In any case, at this stage in the development of the subject it seems sensible to take $\beta = 0$, especially when β is small, in view of the clarification in interpretation and simplification in approach which thereby follows. A safe procedure would be to report data in a manner which would permit conversion to an ε-based scheme at a later date if that turns out to be necessary. Guidelines can be found in ref. 1.

Acknowledgments

This work was supported in part by DARPA University Research Initiative (Subagreement P.O. VB38639-0 with the University of California, Santa Barbara, ONR Prime Contract N00014-86-K-0753), by the National Science Foundation under Grant MSM-84-16392, and by the Division of Applied Sciences, Harvard University. Discussions with B. Budiansky, A. G. Evans and K. S. Kim have been most helpful.

References

1 J. R. Rice, *J. Appl. Mech.*, *55* (1988) 98–103.
2 P. G. Charalambides, J. Lund, A. G. Evans and R. M. McMeeking, *A Test Specimen for Determining the Fracture Resistance of Bimaterial Interfaces*, in the press (1987).
3 K. M. Liechti and W. G. Knauss, *Exp. Mech.*, *22* (1982) 383–391.
4 T. S. Oh, R. M. Cannon and R. O. Ritchie, *J. Am. Ceram. Soc.*, *70* (1987) C-352–C-355.
5 W. A. Zdaniewski, J. C. Conway, Jr. and H. P. Kirchner, *J. Am. Ceram. Soc.*, *70* (1987) 110–118.
6 H. Chai and S. Mall, *Int. J. Fracture*, *36* (1988) R3–R8.
7 J. W. Hutchinson, M. E. Mear and J. R. Rice, *J. Appl. Mech.*, *54* (1987) 828–832.
8 J. Dundurs, in *Mathematical Theory of Dislocations*, American Society of Mechanical Engineering, New York, 1969, pp. 70–115.
9 A. H. England, *J. Appl. Mech.*, *32* (1965) 400–402.
10 F. Erdogan, *J. Appl. Mech.*, *32* (1965) 403–410.
11 J. R. Rice and G. C. Sih, *J. Appl. Mech.*, *32* (1965) 418–423.
12 H. Tada, P. C. Paris and G. R. Irwin, *The Stress Analysis of Cracks Handbook*, Del Research, St. Louis, MO, 1985.
13 S. M. Wiederhorn, A. M. Shorband and R. L. Moses, *J. Appl. Phys.*, *39* (1968) 1569–1572.
14 M.-Y. He and J. W. Hutchinson, *Kinking of Crack out of an Interface*, to be published in *J. Appl. Mech.*
15 M. D. Thouless, A. G. Evans, M. F. Ashby and J. W. Hutchinson, *Acta. Metall.*, *35* (1987) 1333–1341.
16 Z. Suo and J. W. Hutchinson, *Interface Crack Between Two Elastic Layers*, Harvard University Report MECH-118, 1988.

Appendix A. Integral equation formulation and solution

In this Appendix we set up and solve the integral equation for the plane elasticity problem specified in Fig. 1. Similar solution procedure can be found in refs. 7, 15, 16. A layer of material 2 is sandwiched in an infinite medium of material 1. Each material is taken to be isotropic and linearly elastic with the x_1-axis coincident with the upper interface. The thickness of the layer is set to be unity since the h dependence is known. A semi-infinite crack lies along the x_1-axis with the tip at the origin. The external loading is prescribed in the far field as the standard crack tip field of a homogeneous crack characterized by the classical stress intensity factor

$$K^{\infty} = K_{\mathrm{I}} + \mathrm{i}K_{\mathrm{II}} \tag{A1}$$

Let $b_i(\xi)$ be the x_i component of an edge dislocation located on the interface at $x_1 = \xi$. The stresses at point $x_1 = x$ on the interface induced by the dislocation are given by

$$\sigma_{22}(x) + \mathrm{i}\sigma_{12}(x) = \frac{2\bar{B}(\xi)}{x-\xi} + 2\pi\beta\mathrm{i}\delta(x-\xi)\bar{B}(\xi) + B(\xi)F_1(x-\xi) + \bar{B}(\xi)F_2(x-\xi) \tag{A2}$$

where $\delta(x)$ is the Dirac delta function and

$$B(\xi) = \frac{1+\alpha}{c_2(1-\beta^2)}\frac{1}{\pi\mathrm{i}}[b_1(\xi) + \mathrm{i}b_2(\xi)] \tag{A3}$$

and the complex-valued functions $F_i(\zeta)$ are constructed in Appendix B. The functions F_1 and F_2 are well behaved in the whole range $-\infty < \zeta < +\infty$, with asymptotes

$$F_1(\zeta) = O\left(\frac{1}{\zeta}\right), F_2(\zeta) = O\left(\frac{1}{\zeta}\right) \qquad \text{as } \zeta \to \infty \tag{A4}$$

The semi-infinite crack is represented by a distribution of dislocations lying along the negative x_1-axis such that the traction vanishes along the negative x_1-axis. That is, the distribution $B(\xi)$ for $\xi < 0$ must be governed by

$$\int_{-\infty}^{0}\left(\frac{2}{x-\xi} + F_2(x-\xi)\right)\bar{B}(\xi)\,\mathrm{d}\xi + \int_{-\infty}^{0} F_1(x-\xi)B(\xi)\,\mathrm{d}\xi + 2\pi\beta\mathrm{i}\bar{B}(x) = 0 \qquad \text{for } x < 0 \tag{A5}$$

where the first integral is the Cauchy principal value integral.

The crack face displacements are related to the dislocation distribution by

$$\delta_1(x) + \mathrm{i}\delta_2(x) = \int_{x}^{0}[b_1(\xi) + \mathrm{i}b_2(\xi)]\,\mathrm{d}\xi = \pi\mathrm{i}c_2\frac{1-\beta^2}{1+\alpha}\int_{x}^{0} B(\xi)\,\mathrm{d}\xi \qquad \text{for } x < 0 \tag{A6}$$

The relation between the complex stress intensity factor K and the dislocation distribution B can be derived by combining (5) and (A6). That is

$$\bar{K} = (2\pi)^{3/2}(1-\beta^2)^{1/2}\lim_{x\to 0^-}\frac{B(x)}{(-x)^{-1/2-\mathrm{i}\varepsilon}} \tag{A7}$$

The behavior of $B(\xi)$ as $\xi \to -\infty$ can be specified to give the correct far field loading (A1), *i.e.*

$$B(\xi) = (2\pi)^{-3/2}\frac{1-\alpha}{1-\beta^2}\bar{K}^{\infty}(-\xi)^{-1/2} \qquad \text{as } \xi \to -\infty \tag{A8}$$

Notice that with asymptotic behaviors (A4) and (A8), the integrands in (A5) are integrable.

Make the change of variables

$$x = \frac{u-1}{u+1} \qquad -1 < u < 1$$

$$\xi = \frac{t-1}{t+1} \qquad -1 < t < 1 \tag{A9}$$

and let

$$\zeta \equiv x - \xi = \frac{2(u-t)}{(u+1)(t+1)} \tag{A10}$$

Then with $A(t) \equiv B(\xi)$, the integral equation (A15) can be reduced to

$$\int_{-1}^{1}\frac{\bar{A}(t)}{u-t}\,\mathrm{d}t + \pi\beta\mathrm{i}\bar{A}(u) + \int_{-1}^{1}\frac{F_1(\zeta)A(t) + [1+t+F_2(\zeta)]\bar{A}(t)}{(1+t)^2}\,\mathrm{d}t = 0 \qquad \text{for } -1 < u < 1 \tag{A11}$$

where the first integral is the Cauchy principal value integral. With the asymptotic behaviors

(A7) and (A8) in mind, one can take the approximation for $A(t)$ as

$$A(t)=\left(\frac{1-t}{2}\right)^{-1/2-i\varepsilon}\left[a_0\left(\frac{1+t}{2}\right)^{1/2}+(1+t)\sum_{k=1}^{N}a_k T_{k-1}(t)\right] \tag{A12}$$

where

$$a_0=(2\pi)^{-2/3}\frac{1-\alpha}{1-\beta^2}\bar{K}^{\infty} \tag{A13}$$

and $T_j(t)$ is the Chebyshev polynomial of the first kind of degree j, and the a values are complex coefficients which must be determined in the solution process. When substituted into (A11), the representation for A leads to an equation of the form

$$\sum_{k=1}^{N}[a_k I_1(u,k)+\bar{a}_k I_2(u,k)]+a_0 I_3(u)=0 \tag{A14}$$

where the terms I_j for $j=1, 3$ involve integrals such as

$$I_1(u,k)=\int_{-1}^{1}F_1(\zeta)T_{k-1}(t)(1+t)^{-1}\left(\frac{1-t}{2}\right)^{-1/2-i\varepsilon}\mathrm{d}t \tag{A15}$$

These integrals must be evaluated numerically for given values of u and k.

The solution procedure is as follows. Let a set of $2N$ real unknowns be the real and imaginary parts of a_k for $k=1, N$. This set of $2N$ unknowns is used to satisfy the real and imaginary parts of (A11) at N Gauss-Legendre points $\{u_i\}$ on the interval $-1<u<1$. Once the a values have been determined, the complex stress intensity factor can be computed, using (A7) and (A12), from

$$\bar{K}=(2\pi)^{3/2}(1-\beta^2)^{1/2}\left(a_0+2\sum_{k=1}^{N}a_k\right) \tag{A16}$$

The general expression for K in (14) applies to the present case with $K_I=1$ and $K_{II}=0$, or equivalently, with $K^{\infty}=1$, and $h=1$, so that

$$K=pe^{i\omega} \tag{A17}$$

which yields $\sin\omega$ and $\cos\omega$ independently. The relation $\sin^2\omega+\cos^2\omega=1$ provides a consistency check on the accuracy of the solution. The results reported in Table 1 were computed with N between 10 and 20. The consistency check was satisfied to better than 0.3%. It is believed that the error of ω is within a few tenths of a degree.

Appendix B. A dislocation in the sandwich structure

The dislocation solution used as the kernel in the integral equation (A5) is summarized here.

The plane elasticity problem is specified in Fig. 5. An edge dislocation with components b_1 and b_2 at the origin lies on the upper interface of the bonded sandwich structure. The solution to the problem in Fig. 5 is obtained by the similar superposition technique used in [16]. Only the final results are reported below. The stresses at $(\zeta, 0)$ induced by the dislocation at the origin are given by

$$\sigma_{22}(\zeta,0)+i\sigma_{12}(\zeta,0)=\bar{B}\left(\frac{2}{\zeta}+2\pi\beta i\delta(\zeta)+F_2(\zeta)\right)+BF_1(\zeta) \tag{B1}$$

where $\delta(x)$ is the Dirac delta function and

$$B=\frac{1+\alpha}{c_2(1-\beta^2)}\frac{1}{\pi i}(b_1+ib_2) \tag{B2}$$

The complex-valued functions $F_i(\zeta)$ are determined by

$$\begin{aligned}F_1(\zeta)&=[Q_2(\zeta)-R_1(\zeta)]+i[Q_1(\zeta)+R_2(\zeta)]\\F_2(\zeta)&=[Q_2(\zeta)+R_1(\zeta)]+i[R_2(\zeta)-Q_1(\zeta)]\end{aligned} \tag{B3}$$

where the Q and R are defined by Fourier integrals

$$\begin{aligned}Q_1(\zeta)&=\int_0^{\infty}(-A_1)\cos\zeta\lambda\,\mathrm{d}\lambda\\R_1(\zeta)&=\int_0^{\infty}(-A_1+A_2)\sin\zeta\lambda\,\mathrm{d}\lambda\\Q_2(\zeta)&=\int_0^{\infty}(-B_1)\sin\zeta\lambda\,\mathrm{d}\lambda\\R_2(\zeta)&=\int_0^{\infty}(B_1-B_2)\cos\zeta\lambda\,\mathrm{d}\lambda\end{aligned} \tag{B4}$$

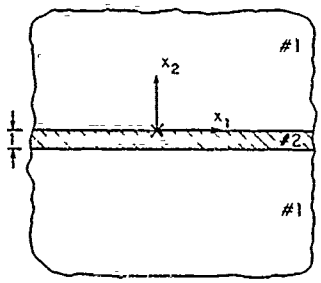

Fig. 5. Geometry for dislocation solution used in constructing the integral equation.

The A and B are solved from the linear algebraic equations

$$[P_1 P_2]\begin{bmatrix} A_1 & B_1 \\ A_2 & B_2 \\ A_3 & B_3 \\ A_4 & B_4 \end{bmatrix} = \begin{bmatrix} 0 & 0 \\ 0 & 0 \\ X_1 & Y_1 \\ X_2 & Y_2 \end{bmatrix} \tag{B5}$$

where $P_1 = CD$ and

$$C = -\begin{bmatrix} e^{\lambda} & -\lambda e^{\lambda} & e^{-\lambda} & -\lambda e^{-\lambda} \\ -e^{\lambda} & (1+\lambda)e^{\lambda} & e^{-\lambda} & (1-\lambda)e^{-\lambda} \\ 0 & \frac{\Sigma}{2}e^{\lambda} & 0 & -\frac{\Sigma}{2}e^{-\lambda} \\ 0 & \frac{\Sigma}{2}e^{\lambda} & 0 & \frac{\Sigma}{2}e^{-\lambda} \end{bmatrix}$$

$$D = \frac{1}{1+\alpha}\begin{bmatrix} 1+\beta & -\beta \\ 0 & 1-\beta \\ \alpha-\beta & \beta \\ -2(\alpha-\beta) & \alpha-\beta \end{bmatrix}$$

$$P_2 = \begin{bmatrix} 1 & -\lambda \\ 1 & 1-\lambda \\ \frac{\alpha-\beta}{1-\alpha} & -\frac{\alpha-\beta}{1-\alpha}\lambda - \frac{1}{2} \\ \frac{\alpha-\beta}{1-\alpha} & \frac{\alpha-\beta}{1-\alpha}(1-\lambda) + \frac{1}{2} \end{bmatrix} e^{-\lambda} \tag{B6}$$

where $\Sigma = (1+\alpha)/(1-\alpha)$, and

$$\begin{aligned} X_1 &= \left[-\frac{\alpha-\beta^2}{1-\alpha} + \frac{(\alpha-\beta)(1-\beta)}{1-\alpha}\lambda\right]e^{-\lambda} \\ X_2 &= \left[\beta + \frac{(\alpha-\beta)(1-\alpha)}{1-\alpha}\lambda\right]e^{-\lambda} \\ Y_1 &= \left[-\beta + \frac{(\alpha-\beta)(1-\alpha)}{1-\alpha}\lambda\right]e^{-\lambda} \\ Y_2 &= \left[\frac{\alpha-\beta^2}{1-\alpha} + \frac{(\alpha-\beta)(1-\alpha)}{1-\alpha}\lambda\right]e^{-\lambda} \end{aligned} \tag{B7}$$

Materials Science and Engineering, A107 (1989) 145-157

Elastic–Plastic Analysis of a Collinear Array of Cracks on a Bimaterial Interface*

C. F. SHIH and R. J. ASARO

Division of Engineering, Brown University, Providence, RI 02912 (U.S.A.)

(Received June 1, 1988)

Abstract

In previous studies, we found that although the near-tip fields of cracks on a bimaterial interface do not have a separable form of the Hutchinson–Rice–Rosengren (HRR) type, they appear to be nearly separable in an annular region well within the plastic zone. Furthermore, the fields bear interesting similarities to mixed mode HRR fields for homogeneous media. Over length scales comparable to the size of the dominant plastic zone, the stress levels in both materials are set by the yield strength of the weaker (lower yield strength) material. Over distances which are small compared with the smallest dimension of the plastic zone (or distances comparable with the crack tip opening displacement), the behavior of the stresses is governed by the strain hardening characteristics of the more compliant (lower hardening) material. Asymptotically, as the crack tip is approached, the material system responds like that of a plastically deforming solid bonded to a rigid substrate; in particular, the stress and the strain fields in the more compliant material behave like those of a material with identical plastic properties bonded to a rigid substrate. Guided by this observation, our attention is directed to the plane strain problem of a deformable material bonded to a rigid substrate. The bimaterial interface is populated by a row of collinear cracks. The body is loaded by remote tension so that the cracks remain effectively open over size scales that are physically relevant. Contained and large-scale yielding solutions for cracks with crack-length-to-ligament ratios that differ by more than two orders of magnitude are obtained by finite element analysis. The solutions reveal that the effects of load (or finite ligament plasticity) and geometry on the near-tip fields are adequately accounted for by the J integral. Furthermore, the near-tip fields appear to possess a structure which is similar to that already presented in previous publications on the small-scale yielding problem. Over the full range of loads considered, the relation between the crack opening displacement (measured at the center of the crack) and the J integral is not sensitive to differences in geometry associated with widely different crack-length-to-ligament ratios.

1. Introduction

Aspects of the structure of small-scale yielding fields at bimaterial crack tips have been investigated independently by Shih and Asaro [1, 2], and by Rice [3]. The form of the structure is sufficiently general that the fields for two plastically deforming materials or an elastic–plastic material bonded onto an elastic (or rigid) substrate can be accommodated. In refs. 1 and 2 numerical solutions have been presented for a boundary layer small-scale yielding formulation and for a full boundary value problem which corroborates certain features of the structure. It was shown that the extent of plasticity and the stress and deformation fields within the dominant plastic zone are determined primarily by the response of the weaker (lower yield strength) solid. The dominant plastic zone develops in the weaker material. Thus, over length scales comparable with the size of the dominant plastic zone, the stress levels are set by the lower of the two yield strengths. In contrast, our numerical solutions suggest that the form of the near-tip fields is governed by the strain hardening characteristics of the more compliant (lower strain hardening) material. If the stress–strain behavior of both materials can be characterized by piecewise linear elastic power law relations, the numerical solutions support an

*Paper presented at the symposium on Interfacial Phenomena in Composites. Processing, Characterization, and Mechanical Properties, Newport, RI, June 1–3, 1988.

0921-5093/89/$3.50

© Elsevier Sequoia/Printed in The Netherlands

observation that, as $r \to 0$, the stress and strain fields in the material with the lower strain hardening capacity asymptotically approach those of a material with identical plastic properties bonded to a rigid substrate. The near-tip stress levels achievable in the material with the higher hardening capacity are limited to those levels attained in the lower hardening material.

In this paper, our objective is to elucidate the effects of crack geometry and of small-scale and finite ligament plasticity on near-tip fields. Guided by the results of our previous studies, our attention in this investigation is directed at the plane strain problem of an elastic–plastic material bonded to a rigid substrate. The boundary value problem considered is that of a row of collinear cracks lying along a bimaterial interface. Crack-length-to-ligament ratios which vary by more than two orders of magnitude are considered. The full range of solutions from contained yielding to fully yielded conditions are obtained by finite element analysis. For the most part, the calculations use a small strain isotropic J_2 deformation theory. This was done to make contact with an analytical investigation of asymptotic crack tip fields which is in progress [4] and to facilitate the connection between the numerically determined near-tip solutions for interface cracks and existing solutions for crack tip fields in homogeneous media. Since deformation theory solutions are sometimes suspect, we have reanalyzed the same boundary value problems for selected load combinations of interest using a small strain and a finite deformation version of J_2 flow (incremental) theory.

For moderately and lightly hardening materials, the solutions from deformation and flow theories show good agreement over length scales which are physically relevant. More importantly, the full field solutions reveal that the effects of load (or finite ligament plasticity) and geometry on near-tip fields are adequately accounted for by the J integral. Throughout this paper, geometry refers to the ratio of the crack length to the ligament length since this is the only geometric parameter of the problem.

2. Review of elasticity and small-scale yielding fields

2.1. Linear elasticity solutions

Figure 1 shows a periodic array of cracks $2a$ long lying on the interface between two semi-

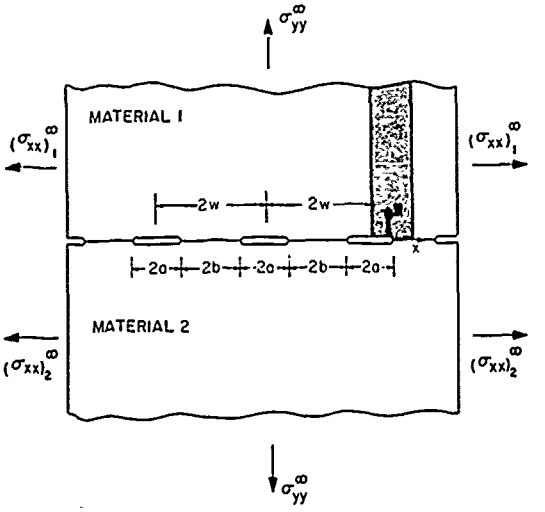

Fig. 1. Infinite row of collinear cracks on a bimaterial interface.

infinite slabs of isotropic elastic solids with differing material moduli. The shear moduli and Poisson's ratios are μ_1, μ_2 and ν_1, ν_2 respectively. The Young's moduli will be denoted by E_1 and E_2. We confine our attention to the right-hand tip of a crack. Let r and θ be the polar coordinates centered at this crack tip. At small distances from the crack tip, the in-plane stresses have the singular form [3, 5–9]

$$\sigma_{ij} = \mathrm{Re}\left\{\frac{Q}{(2\pi r)^{1/2}}\left(\frac{r}{L}\right)^{i\varepsilon}\tilde{\sigma}_{ij}(\theta;\varepsilon)\right\} \tag{1}$$

where $i = -1^{1/2}$, Q is the complex stress intensity factor, and L is a relevant dimension of the crack geometry. For the geometry depicted in Fig. 1, L can be taken to be the total crack length $2a$. The bimaterial constant ε is given by

$$\varepsilon = \frac{1}{2\pi}\ln\left(\frac{1-\beta}{1+\beta}\right) \tag{2}$$

where

$$\beta = \frac{1}{2}\,\frac{\mu_1(1-2\nu_2)-\mu_2(1-2\nu_1)}{\mu_1(1-\nu_2)+\mu_2(1-\nu_1)} \tag{3}$$

The angular variation $\tilde{\sigma}_{ij}(\theta;\varepsilon)$ is complex and depends only on ε (see, for example, Appendix I in ref. 1). It should be noted that $|(r/L)^{i\varepsilon}| = 1$.

It is convenient to express Q in terms of its magnitude $|Q|$ and phase ϕ, namely

$$Q = Q_1 + iQ_2 = |Q|\exp(i\phi) \tag{4}$$

Thus, tractions on the bond line are given by

$$t=(\sigma_{yy}+i\sigma_{xy})_{\theta=0}=\frac{Q}{(2\pi r)^{1/2}}\left(\frac{r}{L}\right)^{i\varepsilon}$$

$$=\frac{|Q|}{(2\pi r)^{1/2}}[\exp i\{\phi+\varepsilon\ln(r/L)\}] \quad (5)$$

and displacement jumps across the crack faces take the form

$$\Delta u=\Delta u_y+i\Delta u_x=(u_y+iu_x)_{\theta=\pi}-(u_y+iu_x)_{\theta=-\pi}$$

$$=\frac{8\Lambda}{(1+4\varepsilon^2)^{1/2}}\frac{|Q|r^{1/2}}{(2\pi)^{1/2}}\exp[i\{-\Theta+\phi+\varepsilon\ln(r/L)\}] \quad (6)$$

where $\Theta=\tan^{-1}(2\varepsilon)$ and for plane strain $\Lambda=\{(1-\nu_1)/\mu_1+(1-\nu_2)/\mu_2\}/4\cosh^2(\pi\varepsilon)$.

The ratio of Q_1 to Q_2, *i.e.* the phase of Q as defined in eqn. (4), does not depend on the relevant length L of the crack geometry. As an example, the relation between Q and the remote traction T ($T=\sigma_{yy}^{\infty}+i\sigma_{xy}^{\infty}$) for an isolated crack of length L lying on a bimaterial interface is $Q=(1+i2\varepsilon)T(\pi L/2)^{1/2}$ [9]. In this case, the connection between the phase ϕ of the stress intensity factor and the phase ψ of the remote load ($T=|T|\exp(i\psi)$) is simply $\phi=\psi+\tan^{-1}(2\varepsilon)$. Thus, changes in crack length at fixed ψ ($|T|$ is free to vary) do not change the phase of Q. Different normalizations of the singular crack tip fields, which result in stress intensity factors that differ by scaling constants involving ε, have appeared in the literature on interface cracks. In ref. 3, a particularly convenient definition of the stress intensity factor K was introduced. The relation between K and Q is

$$Q=KL^{i\varepsilon} \qquad |Q|=|K| \qquad Q\bar{Q}=K\bar{K} \quad (7a)$$

and

$$\phi=\varphi+\varepsilon\ln L \quad (7b)$$

where φ is the phase of K. It should be noted that K uniquely specifies the crack tip fields whereas both Q and a relevant crack dimension L are required for the same purpose. In other words, K fully characterizes the effects of load and geometry on the crack tip field. Consequently, the phase of K depends weakly on the relevant length of the crack geometry. The results contained in eqns. (1), (5) and (6) can be restated in terms of K by using the relationships in eqn. (7).

A relation which will be of use later in the analysis is the energy release rate for the crack advancing along the interface [10, 11]

$$\mathcal{G}=\Lambda Q\bar{Q}=\Lambda K\bar{K} \quad (8)$$

where Λ is a material parameter of the system, defined previously.

The linear elasticity solution for the displacement jumps (eqn. (6)) predicts that overlapping of crack faces always occurs, though the zone of overlap is extremely small compared with L for load states in the range $-45°\leqslant\phi\leqslant45°$, *i.e.* $Q_1>|Q_2|$ (see, for example, refs. 2 and 3). With regard to the present boundary value problem, the cracks are open over length scales of physical relevance for the entire range of loads considered.

2.2. *Structure of the small-scale yielding fields*

In the small-scale yielding formulation, the actual crack problem is replaced by a semi-infinite crack in an infinite medium with the asymptotic boundary condition that, at large values of r, the field approaches that given by eqn. (1). Let σ_{01} and σ_{02} denote the yield strengths of material 1 (top) and material 2 (bottom) respectively (see Fig. 1). It is convenient to denote the lower yield strength by σ_0 ($\sigma_0=\min(\sigma_{01},\sigma_{02})$) and, with no loss of generality, material 1 will be taken to be the weaker (lower yield strength) material in this discussion. The numerical solutions of Shih and Asaro [1, 2] demonstrated that the small-scale yielding fields are members of a family parameterized by an intrinsic phase parameter ξ; the form of these solutions was in fact suggested by dimensional analysis. A similar form for the plastic zone of the interface crack was also suggested by Rice [3] through dimensional analysis and by an examination of the soultions in ref. 1. Zywicz and Parks [12] developed an approximate analysis for the interface crack plastic zone based on the linear elasticity solutions (eqn. (1)) and also arrived at a similar conclusion regarding the dependence of the plastic zone on a parameter ζ similar to ξ.

Under small-scale yielding, ξ varies linearly with the phase of Q(or K) and varies slowly with its magnitude as given by

$$\xi=\phi+\varepsilon\ln\left(\frac{Q\bar{Q}}{L\sigma_0^2}\right)=\varphi+\varepsilon\ln\left(\frac{K\bar{K}}{\sigma_0^2}\right) \quad (9)$$

In the second equality, L has been absorbed in the phase of K. The phase parameter ζ_0 [12] differs inconsequentially from the second expres-

sion in eqn. (9) by a constant involving ε. Dimensional considerations, the linearity of the equilibrium and strain–displacement relations, and the structure of the elastic fields (eqn. (1)) suggest the stress field in the small-scale yielding formulation of the form [2]

$$\sigma_{ij} = \sigma_0 f_{ij}\left[\frac{r\sigma_0^2}{K\bar{K}}, \theta, \text{phase}\left\{\left(\frac{r\sigma_0^2}{K\bar{K}}\right)^{i\Sigma}\right\}; \quad \xi, \text{dimensionless material parameters}\right] \tag{10}$$

The material system parameter Σ, as yet undetermined, involves dimensionless combinations of plasticity parameters A similar result in ref. 3 can be manipulated into the above form.

A rearrangement of the result in eqn. (10) leads immediately to the following expression for the radial distance from the crack tip to the elastic–plastic boundary [1, 2]

$$r_p(\theta) = \frac{K\bar{K}}{\sigma_0^2} R(\theta;\xi) \tag{11}$$

where $R(\theta;\xi)$ is a dimensionless angular function which depends strongly on ξ and weakly on dimensionless groups of elastic and plastic material parameters. The angular function R has a periodicity of π with respect to ξ such that

$$R(\theta;\xi) = R(\theta;\xi + m\pi) \qquad m = 1,2,3,\ldots \tag{12}$$

An equivalent implicit expression for r_p is given in ref. 3. It follows from eqn. (11) that the extent of the dominant (larger) plastic zone is determined by the yield strength of the weaker material and, therefore, over length scales comparable with the size of the dominant plastic zone, the stress levels in both materials are set by the lower yield strength. Various aspects of the fields are discussed in refs. 1, 2 and 13 for different material combinations.

The function $R(\theta;\xi)$ has been determined directly from the plots of small-scale yielding plastic zones which have been obtained for a range of phase angles ξ and several material systems [1, 2]. Alternatively, an estimate of $R(\theta;\xi)$ can be obtained by approximating f_{ij} in eqn. (10) by the linear elasticity fields (eqn. (1)) and assuming that the elastic–plastic boundary is the locus where the effective stress σ_e equals σ_0. The latter procedure has been adopted in ref. 12 to estimate plastic zone sizes and shapes.

2.3. Plausible form of asymptotic fields ($r \to 0$)

It has been noted that, over length scales which are comparable with the size of the dominant plastic zone, the stress levels in both materials are set by σ_0, the yield strength of the weaker material. To understand the behavior of the stresses near bimaterial crack tips (as $r \to 0$), we consider materials with a Ramberg–Osgood-type stress–strain relation. The hardening exponents of the material 1 (top) and material 2 (bottom) are n_1 and n_2. We shall denote the larger of n_1 and n_2 by n, *i.e.* $n = \max(n_1, n_2)$. Shih and Asaro [2] have observed that as $r \to 0$, the stress and strain fields in the material with hardening n asymptotically approach those of a material with the identical plastic properties bonded to a rigid medium. A plausible form of the asymptotic crack tip fields (in the plastically deforming material) for the small-scale yielding problem is

$$\sigma_{ij} = \sigma_0 \left(\frac{K\bar{K}}{\sigma_0^2 r}\right)^{1/(n+1)} h_{ij}(\theta, \hat{r}; \xi) \tag{13}$$

It should be noted that, in eqn. (13), σ_0 and n are the plastic properties of the more compliant material, namely the material with the lower strain hardening capacity. In this equation we have introduced a convenient normalized distance $\hat{r} = r/(K\bar{K}/\sigma_0^2)$ and the implicit dependence of h_{ij} on material parameters is understood. The dimensionless function h_{ij} has a periodic dependence on ξ (with period 2π) and the arguments leading to eqn. (13) require that h_{ij} be bounded as $\hat{r} \to 0$. In other words, relative to $\hat{r}^{-1/(n+1)}$, h_{ij} is a slowly varying function of $\hat{r}$. The form of the linear elastic fields (eqn. (1)) can be rearranged in the form of eqn. (13); then the dependence of h_{ij} on $\hat{r}$ is given by phase$\{(r/L)^{i\varepsilon}\}$.

Under small-scale yielding, $J = \mathcal{J}$ and, noting the relation between $\mathcal{J}$ and $K\bar{K}$ (eqn. (8)), the asymptotic singular fields can be restated as

$$\sigma_{ij} = \sigma_0 \left(\frac{J}{\alpha\sigma_0\varepsilon_0 r}\right)^{1/(n+1)} h_{ij}(\theta, \hat{r}; \xi) \tag{14}$$

where α, σ_0, ε_0 and n are the plastic properties of the more (plastically) compliant material. In eqn. (14), J is Rice's [14] J integral and its role in nonlinear fracture mechanics is the subject of a review article by Hutchinson [15]. As it is our intention to examine near-tip fields under large-scale yielding, it is desirable at this juncture to rescale the dimensionless distance $\hat{r}$ in h_{ij}. A

length which has relevance in both small- and large-scale yielding is J/σ_0. In homogeneous media, the crack tip opening displacement scales linearly with J/σ_0. Hence it is convenient to define the dimensionless radial distance in eqn. (14) as $\hat{r} = r/(J/\sigma_0)$. The asymptotic fields in eqn. (14) nearly scale with J since h_{ij} depends on ξ and, under small-scale yielding, ξ is a slowly varying function of $K\bar{K}/\sigma_0^2$ and therefore of J. To develop this line of argument a little further, we consider a body stressed by tractions whose directions remain fixed while their magnitudes are always linearly proportional to a monotonically increasing single load parameter. Under these conditions, the asymptotic crack tip fields scale precisely with J if h_{ij} does not depend on ξ or if ξ does not depend on $K\bar{K}/\sigma_0^2$. It may also be noted that the stress levels achievable in the stiffer material are limited by the stresses in the more compliant material, as required by the continuity of traction across the interface.

The form of the fields in eqn. (14) has been corroborated by finite element analyses of the small-scale yielding boundary layer formulation for several material combinations [2, 13]. Large-scale yielding solutions to full boundary value problems which we have obtained to date also support the form of the fields in eqn. (14). Of course, the small-scale yielding relation for ξ (eqn. (9)) is no longer applicable to this case. In large-scale yielding, the relation between ξ and the phase and magnitude of the remotely applied traction must be determined for every load combination and for each crack geometry.

At this point, it is instructive to make contact with plastic crack tip fields in homogeneous media. Under mixed mode loading, the Hutchinson–Rice–Rosengren (HRR) singularity [16, 17] for homogeneous media has the form [18]

$$\sigma_{ij} = \sigma_0 \left(\frac{J}{\alpha \sigma_0 \varepsilon_0 r} \right)^{1/(n+1)} \tilde{\sigma}_{ij}(\theta; M^p) \tag{15}$$

where M^p is the mixity of the plastic singular fields based on the relative magnitudes of $\sigma_{\theta\theta}$ and $\sigma_{r\theta}$ along the crack line $\theta = 0$ as $r \to 0$. For the small-scale yielding problem, the relation between M^p and the mixity of the elastic fields M^e (the ratio of K_I to K_{II}) has been given in ref. 18. It may be noted that the mixity of the elastic fields is related to the phase angle of K by $\varphi = (1 - M^e)\pi/2$. The plane strain angular functions $\tilde{\sigma}_{ij}$ for selected values of M^p and n ranging from 2 to 20 are available in a report [19]. In large-scale yielding problems, the relation between M^p and the phase and magnitude of the remotely applied traction must be determined for each load combination and for each crack geometry. Finally, it may be noted that J and M^p completely characterize the effects of load and geometry on the crack tip field. J and ξ have analogous roles for the interface crack.

3. Problem description and numerical procedures

3.1. Material laws

The deformable media are described by a J_2 deformation theory with a Ramberg–Osgood stress–strain relation. In uniaxial tension the material deforms according to

$$\varepsilon/\varepsilon_0 = \sigma/\sigma_0 + \alpha(\sigma/\sigma_0)^n \tag{16}$$

where σ_0 and ε_0 are the yield stress and strain, α is a material constant (taken to be 0.1) and n is the strain hardening exponent. Under multiaxial stress states, the strain is given by

$$\varepsilon_{ij} = \frac{1+\nu}{E} s_{ij} + \frac{1-2\nu}{3E} \sigma_{kk} \delta_{ij} + \frac{3}{2} \alpha \left(\frac{\sigma_e}{\sigma_0} \right)^{n-1} \frac{s_{ij}}{E} \tag{17}$$

Here s_{ij} is the stress deviator, $\sigma_e = (3 s_{ij} s_{ij}/2)^{1/2}$ is the effective stress, and ν and E are the isotropic elastic constants. In eqn. (16) the connection $\sigma_0 = E\varepsilon_0$ was used. Numerical solutions for the range of the strain hardening exponent n corresponding to $n = 1$ (linear elastic) to $n = 10$ have been obtained. However, in the present paper only results for $n = 5$ and selected results for $n = 10$ are presented. Numerical procedures which are well suited for solving deformation plasticity theory problems (or non-linear elasticity problems) are discussed in refs. 1 and 20. The non-linear boundary value problem is solved by the Newton–Raphson method and the initial estimate of the solution is generated by parameter tracking. Near-incompressibility associated with fully developed plastic deformation is handled by selective-reduced integration. The solutions presented in this paper are largely based on the J_2 deformation plasticity theory above.

For selected problems, small strain and finite deformation analyses based on a J_2 flow theory implementation of the stress–strain relation in eqn. (16) have been carried out. The finite ele-

ment solutions are obtained by a semi-implicit method which can handle large plastic deformation as well as finite elastic deformation and which can accommodate the near-incompressibility associated with fully yielded plastic flow [21]. For the range of material strain hardening considered in this paper ($1 \leqslant n \leqslant 10$), we find no difference of any consequence between the three sets of solutions. Only in the vicinity of the interface did we observe some differences between the shear stresses obtained by deformation and flow theories and between the small strain approximation and finite deformation. A full account of the small strain and finite deformation solutions based on J_2 flow theory and particulars of the material description and analysis is given in refs. 13 and 22.

3.2. *Boundary conditions and mesh design*

A schematic diagram of an infinite row of collinear cracks on a bimaterial interface is shown in Fig. 1. Cracks $2a$ long are spaced at constant intervals w. Uniform tension σ_{yy}^{∞} is applied at $|y| \to \infty$. Normal stresses parallel to the bondline $(\sigma_{xx}^{\infty})_1$ and $(\sigma_{xx}^{\infty})_2$ are applied to confer the boundary value problem with reflective symmetry with respect to the vertical planes through the center of the ligament and the crack. Continuity of the extensional strain ε_{xx} across the bonded interface imposes a constraint between the three remote stresses. The loading constraint, when both materials are elastic, is given in ref. 9. In the present investigation, the lower material is taken to be rigid. Thus only the shaded strip indicated in Fig. 1 needs to be considered in the analysis. (It should be noted that the symmetry conditions which we have invoked are more stringent than the conditions associated with periodicity.)

The discretized strip, bounded by the symmetry planes on the left and right vertical edges with the boundary conditions on the top and bottom horizontal edges, is shown in Fig. 2. With the lower material taken to be rigid, the symmetry conditions on the left and right vertical edges can be enforced in the manner indicated. The finite element mesh is constructed with nine-node biquadratic Lagrangian elements. An arrangement of wedge-shaped elements is employed at the crack tip, the innermost ring of elements has linear dimensions of $a \times 10^{-6}$. The upper-half of the near-tip mesh is shown in Fig. 2. Accommodating six orders of magnitude in element size while still preserving the shape of the element is

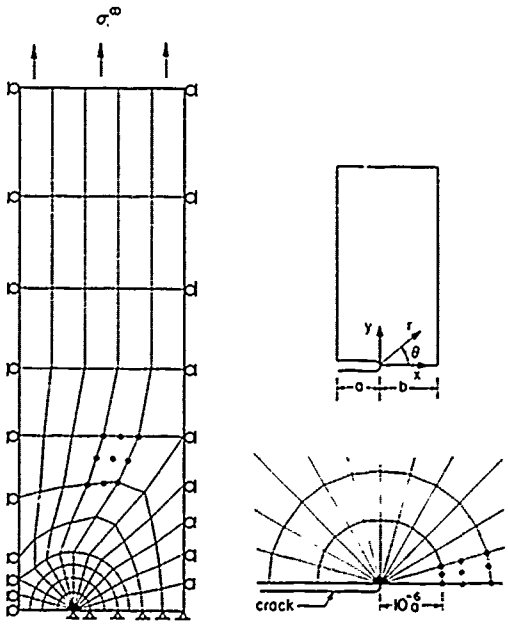

Fig. 2. Finite element model of strip and crack tip region.

accomplished by exponential scaling of element size in the radial direction. Each decade of radial distance is spanned by four annular strips of elements. As laid out in this manner, the domain $a \times 10^{-6} \leqslant r \leqslant a$ is spanned by 24 strips of elements. Within each strip, 12 equally sized elements span the interval $0 \leqslant \theta \leqslant \pi$. A typical mesh has about 400 elements and 1700 nodes. A more complete description of a similar finite element mesh and the element arrangements can be found in an earlier publication [1].

4. Numerical solutions

Finite element solutions have been obtained for a range of strain hardening exponents with $\nu = 0.3$. In the case of $n = 1$, we used the interaction integral method [1] to extract the value of K from the finite element solution. For all the geometries considered, the numerical values agreed with the exact solution of Rice and Sih [9] to better than 1%. To keep the discussion to a reasonable length, we present detailed results for the $n = 5$ material only and include some key results for $n = 10$. Certain features of the solutions for the non-hardening material ($n \to \infty$) are discussed in the concluding section.

Plane strain analyses were carried out for five ratios of crack length to width, $a/w = 2/3$, $1/2$, $1/3$, $1/9$ and $1/100$ respectively (or $a/b = 2$, 1,

1/2, 1/8 and 1/99). Over the range of loads considered, the fields for the $a/w = 1/100$ geometry are almost identical to those for an isolated crack. To study the effect of geometry and ligament plasticity on near-tip fields, solutions for the full range of deformation conditions are obtained. We compare solutions for different geometries with the identical J value to explore the possible role of the J integral as a characterizing parameter. The value of the J integral is extracted from the numerical solutions by the domain integral method which is naturally suited for finite element analysis [23].

4.1. Effective and hydrostatic stress contours

Solutions pertaining to contained yielding conditions for the $n = 5$ material are examined first. Specifically, the stresses for $J/(\sigma_0 \varepsilon_0 a) = 1.0$ are compared. At this J value, the remotely applied stress σ^∞/σ_0 for the five geometries are 0.61, 0.72. 0.78, 0.83 and 0.83 respectively. Effective stress contours $\hat{\sigma}_e = \sigma_e/\sigma_0 = 0.8$, 1.0 and 1.2, for three geometries, ($a/w = 2/3$, 1/2 and 1/100) are plotted in Fig. 3. The cartesian coordinates x and y have their origin at the crack tip and the plane of the crack is $y = 0$. The contour labeled by 1.0 is the elastic–plastic boundary. It can be seen that the plastic zones in the geometries considered are identical in size and shape. Contours of higher values of σ_e/σ_0 are also identically sized and shaped. In Fig. 3(a), the right-hand vertical boundary is also the symmetry plane; the $\sigma_e/\sigma_0 = 0.8$ contour emanating from the crack to the left of the symmetry plane has connected with the corresponding contour which originates from the crack to the right of the symmetry plane. The plastic zone, as estimated by the small-scale yielding result (eqn. (11)) for $J/(\sigma_0 \varepsilon_0 a) = 1.0$ and for ξ appropriate to the $a/w = 1/100$ geometry, is shown in Fig. 3(d); the contours for $\sigma_e/\sigma_0 = 0.8$ and 1.2, which are also estimated by the small-scale yielding solution, have been included. It should be noted that, while the size of the extrapolated plastic zone is only slightly smaller than the actual plastic zone in Fig. 3(c), the protusion along the interface in Fig. 3(d) is more pronounced than that in Fig. 3(c). This is because the small-scale yielding solution predicts shear stresses near the interface which are larger than those for contained yielding.

At $J/(\sigma_0 \varepsilon_0 a) = 6.0$, the ligaments of the three crack geometries $a/w = 2/3$. 1/2 and 1/3 have fully yielded. In the remaining two geometries

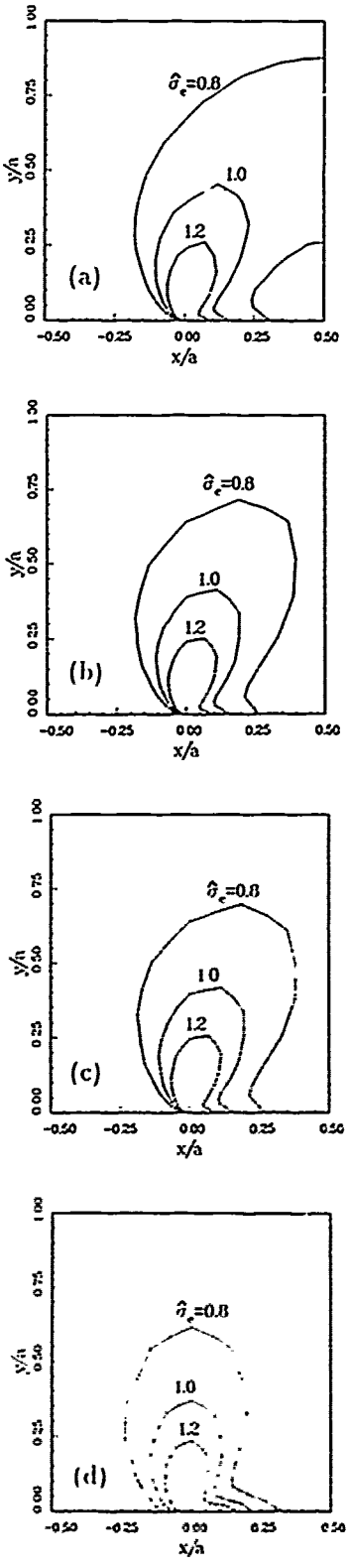

Fig. 3. Effective stress contours for $n = 5$ material for (a) $a/w = 2/3$, (b) $a/w = 1/2$ and (c) $a/w = 1/100$ geometries under contained yielding, and (d) an isolated crack under small-scale yielding: $\hat{\sigma}_e = \sigma_e/\sigma_0$.

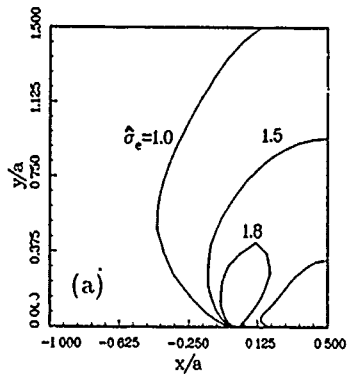

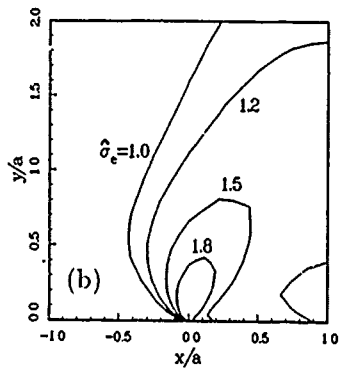

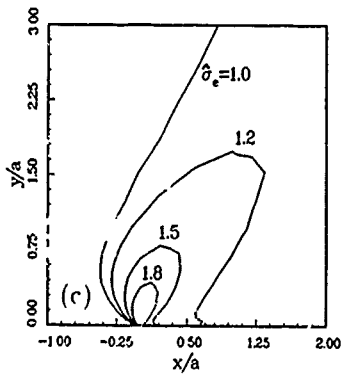

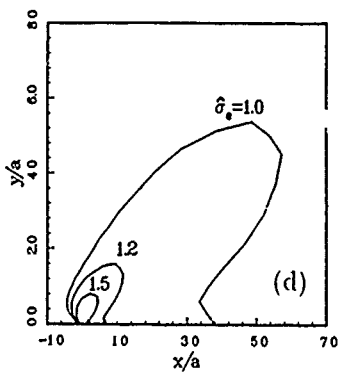

Fig. 4. Effective stress contours for $n=5$ material for (a) $a/w=2/3$, (b) $a/w=1/2$, (c) $a/w=1/3$ and (d) $a/w=1/100$ geometries under large-scale yielding, $\hat{\sigma}_e=\sigma_e/\sigma_0$.

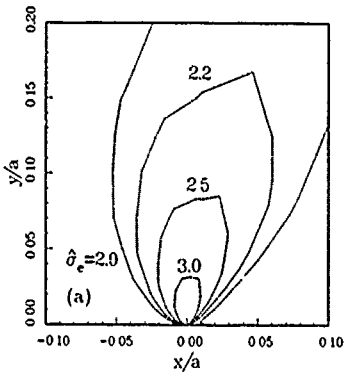

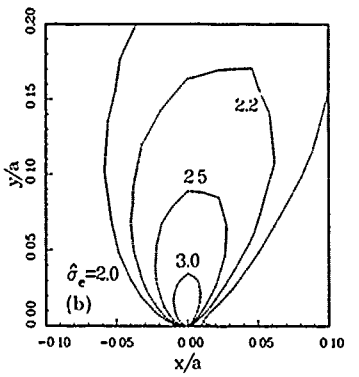

Fig. 5. Effective stress contours for $n=5$ material for (a) $a/w=2/3$ and (b) $a/w=1/100$ geometries under large-scale yielding; $\hat{\sigma}_e=\sigma_e/\sigma_0$.

($a/w=1/9$ and $1/100$) the length of the plastic zone exceeds the crack length but is shorter than the half length of the ligament between two neighboring cracks. At this J level, the applied stresses σ^∞/σ_0 for the five geometries are 1.20, 1.50, 1.68, 1.80 and 1.81 respectively. Effective stress contours for $a/w=2/3$, $1/2$, $1/3$ and $1/100$ are plotted in Fig. 4. Contours for the $a/w=1/9$ geometry are identical to those for $a/w=1/100$. The right vertical boundaries of Figs. 4(a), 4(b) and 4(c) are also planes of symmetry. For these geometries, the plastic zone emanating from the right-hand tip of a crack has linked up with the plastic zone emanating from the left-hand tip of the neighboring crack. While the size and shape of the plastic zones under large-scale yielding are different, a close inspection of the contours for higher stress levels indicates otherwise. The contours of $\sigma_e/\sigma_0=2.0$, 2.2, 2.5 and 3.0 for the $a/w=2/3$ and $1/100$ geometries are plotted in Fig. 5. These contours of high values of σ_e/σ_0 reveal no dependence on a/w ratios.

Hydrostatic stress contours as determined from full field solutions for $J/(\sigma_0\varepsilon_0 a)=1.0$ for the $a/w=2/3$ and $a/w=1/100$ geometries are shown

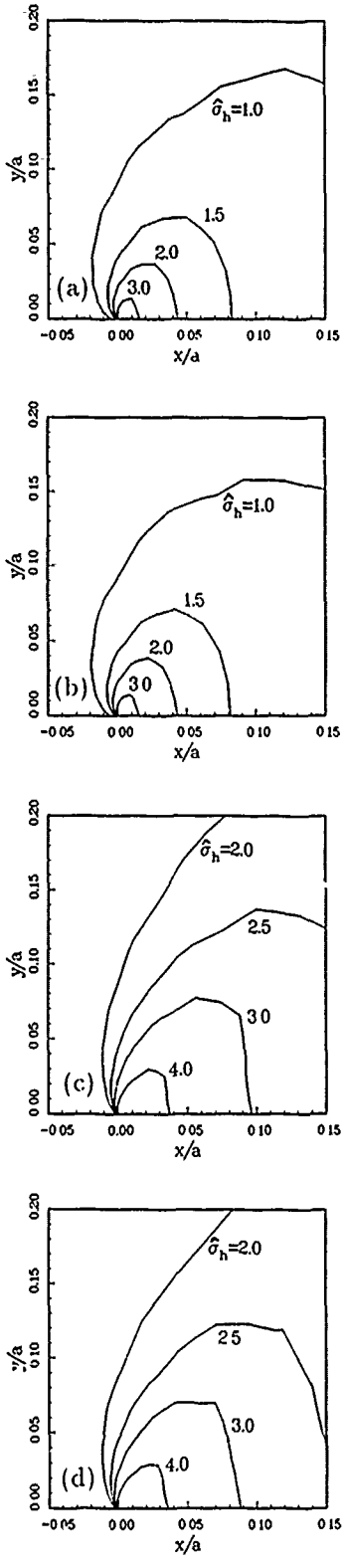

Fig. 6. Hydrostatic stress contours for $n=5$ material for (a) $a/w=2/3$ and (b) $a/w=1/100$ geometries under contained yielding, and for large-scale yielding for (c) $a/w=2/3$ and (d) $a/w=1/100$ ($\hat{\sigma}_h=\sigma_h/\sigma_0$).

in Figs. 6(a) and 6(b) respectively. Contours, based on the large-scale yielding solutions for $J/(\sigma_0\varepsilon_0 a)=6.0$, for the $a/w=2/3$ and $a/w=1/100$ geometries are plotted in Figs. 6(c) and 6(d) respectively. Comparison of the hydrostatic stress contours for these widely different a/w geometries shows no dependence on the a/w ratio.

4.2. *Stresses near the bond line*

The behavior of the hoop stress under small-scale yielding conditions ($J/(\sigma_0\varepsilon_0 a)=0.1$) is examined first. A plot of $\log(\sigma_{\theta\theta}/\sigma_0)$ *vs.* $\log(r/a)$ (along $\theta=1.7°$) is shown in Fig. 7 for $a/w=2/3$ and 1/100; θ is measured from the crack plane. In both geometries, the plastic zone reaches a maximum radial extent of $0.04a$ at $\theta\approx 70°$. The dotted line is the linear elasticity solution according to eqn. (3). The asymptotic $\boldsymbol{K}$ field agrees with the full field solution for the $n=5$ material in the interval $0.01<r/a<0.1$; the interval of agreement, referred to as the zone of $\boldsymbol{K}$ dominance, is indicated in this figure. We may conclude that $\boldsymbol{K}$ (or J) does characterize the effects of load and geometry on the near-tip field for this particular configuration under small-scale yielding conditions.

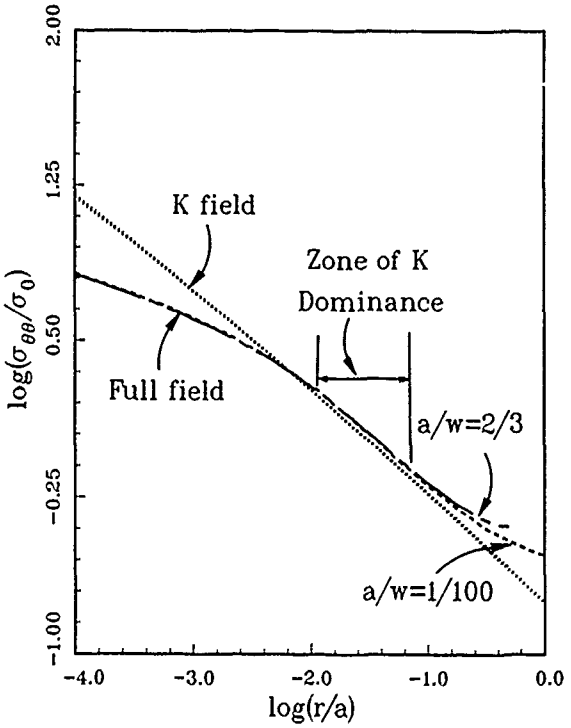

Fig. 7. Hoop stress variations near the interface for $n=5$ material for $a/w=2/3$ and 1/100 geometries, $\hat{J}=J/(\sigma_0\varepsilon_0 a)=0.1$. The K solution is indicated by the dotted line.

To study the structure of the crack tip fields, we introduce normalized stresses defined by

$$\hat{\sigma}_{ij} = \frac{\sigma_{ij}/\sigma_0}{(J/\alpha\sigma_0\varepsilon_0 r)^{1/(n+1)}} \tag{18}$$

If the numerically determined fields possess an HRR structure of the form in eqn. (15) as $r \to 0$, then plots of $\hat{\sigma}_{ij}$ *vs.* r (for fixed θ) will show that the curves approach their respective asymptotes as $r \to 0$. In appropriately normalized plots, e.g. $\hat{\sigma}_{\theta\theta}$ *vs.* r/a (at fixed θ), curves based on solutions for different values of $J/(\sigma_0\varepsilon_0 a)$ and different geometries should converge towards a single curve as $r \to 0$ since the effects of load (or ligament plasticity) and geometry on the near-tip fields are fully characterized by J. On the other hand, if the numerically determined fields are of the form in eqn. (14) as $r \to 0$, then plots of $\hat{\sigma}_{\theta\theta}$ *vs.* r/a will show a weak dependence on r. Additionally, the normalized plots could reveal a weak dependence on geometry and load level since load and geometry effects cannot be fully characterized by J alone.

The soultions for the $n = 5$ material at three J levels and for all five geometries are compared. Specifically, curves of $\hat{\sigma}_{\theta\theta}$ *vs.* $\log(r/a)$ (with θ fixed at 1.7°) for $J/(\sigma_0\varepsilon_0 a) = 0.1$, 1.0 and 6.0 are shown in Fig. 8. As noted previously, these J levels correspond to small-scale contained and large-scale yielding (relative to the crack length) respectively. At $J/(\sigma_0\varepsilon_0 a) = 6.0$, the ligaments of the geometries $a/w = 2/3$, 1/2 and 1/3 have fully yielded. It should also be pointed out that the stresses plotted in all the figures are the actual values computed at the quadrature points — no smoothing was applied to any of the numerically determined fields. It can be seen that the curves based on solutions for different geometries but for the same value of $J/(\sigma_0\varepsilon_0 a)$ merge into what is essentially a single curve. Furthermore, the curves for $J/(\sigma_0\varepsilon_0 a) = 1.0$ and 6.0 are reasonably close together for $r/a < 0.01$. At $J/(\sigma_0\varepsilon_0 a) = 0.1$ the plastic zone extends a distance of about $0.01a$ ahead of the crack tip; hence it is to be expected that those stresses normalized by the singularity of the plastic fields should form a curve which is quite distinct from other curves associated with finite ligament plasticity. At very high J levels, curves of $\hat{\sigma}_{\theta\theta}$ *vs.* $\log(r/a)$ are practically indistinguishable from the curves for $J/(\sigma_0\varepsilon_0 a) = 6.0$. For this reason, the radial variation of the stresses for $J/(\sigma_0\varepsilon_0 a) = 30.0$ (for the five geometries) is indicated by a single broken line. At the latter J value, the ligaments of every geometry, except that of $a/w = 1/100$, have fully yielded.

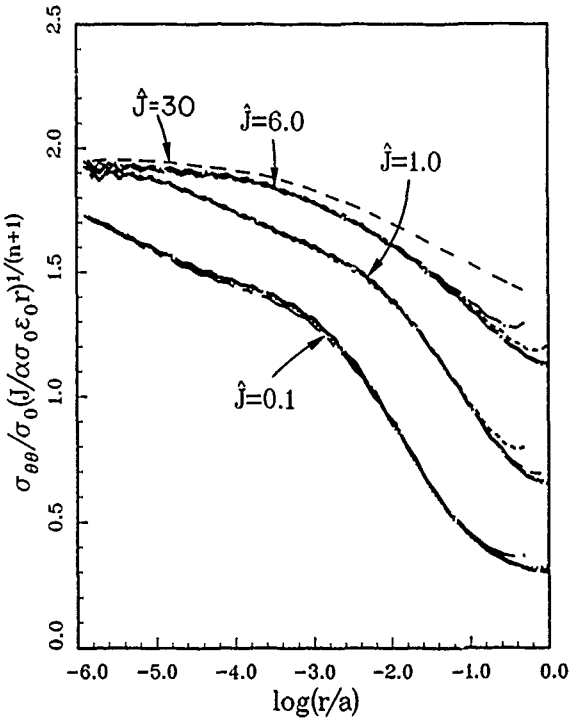

Fig. 8. Hoop stress variations near the interface for $n = 5$ material for $a/w = 2/3$, 1/2, 1/3, 1/9 and 1/100 geometries; $\hat{J} = J/(\sigma_0\varepsilon_0 a) = 0.1$, 1.0, 6.0 and 30.0.

The normalized shear stress $\hat{\sigma}_{r\theta}$ near the interface is plotted against $\log(r/a)$ in Fig. 9 (θ is fixed at 1.7°). Again, the curves show that the effects of geometry are adequately scaled by the J integral. At higher values of J, $\hat{\sigma}_{r\theta}$ varies rather gradually with r/a. It is of interest that the relative magnitude of the shear stress (compared with the hoop stress) decreases as the size of the plastic zone increases and becomes comparable with the crack length (or the relevant crack dimension). This can be seen by comparing the normalized shear and hoop stresses for $J/\sigma_0\varepsilon_0 a = 0.1$, 1.0, 6.0 and 30.0 in Figs. 8 and 9. In contrast, shear and hoop stresses are comparable in magnitude under small-scale yielding conditions.

Solutions for the $n = 10$ material (which is representative of moderate-to-low hardening materials) for the full range of deformation conditions were obtained for the five geometries. These solutions, when plotted in the form as in Figs. 3-9, exhibit precisely the same trends. For this reason, similar plots for the $n = 10$ material will not be shown.

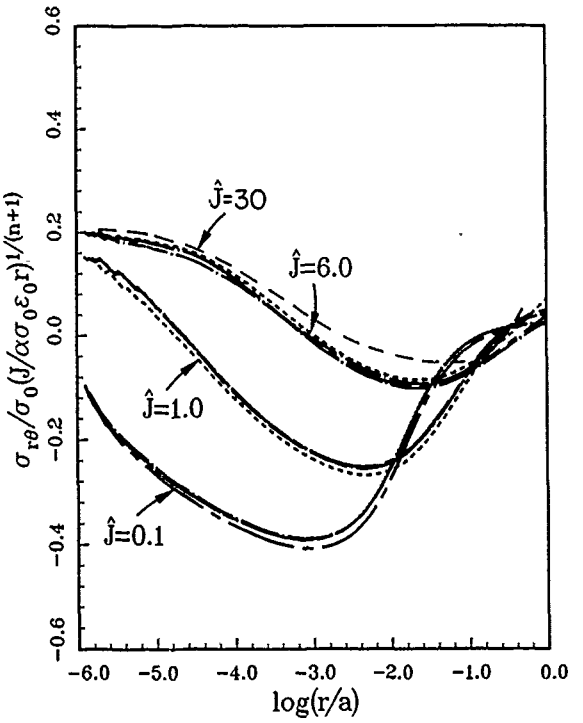

Fig. 9. Shear stress variations near the interface for $n=5$ material for $a/w=2/3$, 1/2, 1/3, 1/9 and 1/100 geometries; $\hat{J}=J/(\sigma_0\varepsilon_0 a)=0.1$, 1.0, 6.0 and 30.0.

4.3. Relations between J, δ and σ^∞

The dependence of J on the remotely applied stress σ^∞ is of interest in fracture analysis. Plots of $J/(\sigma_0\varepsilon_0 a)$ *vs.* the applied stress for the $n=5$ material are given in Fig. 10(a). Up to the maximum load indicated in the figure, we did not find any difference between the J solution for the $a/w=1/100$ geometry and the solution for a geometry with a ligament which is five times larger. Hence, the $a/w=1/100$ geometry is labeled as an isolated crack and the solution is shown by the solid line. The normalized J solution for the $a/w=1/9$ geometry is quite close to the solution for the $a/w=1/100$ geometry and is therefore not included in the figure. It should be noted that the curves rise rapidly for σ^∞/σ_0 greater than about unity, which indicates the beginning of large-scale yielding.

The crack opening displacement δ measured at the center of the crack is plotted in Fig. 10(b). The trends of the curves are similar to those for J in Fig. 10(a). The plots of J *vs.* δ in Fig. 10(c) are obtained by simply replotting the curves of Figs. 10(a) and 10(b). It is quite remarkable that the curves of normalized J *vs.* normalized δ show little dependence on the a/w ratio.

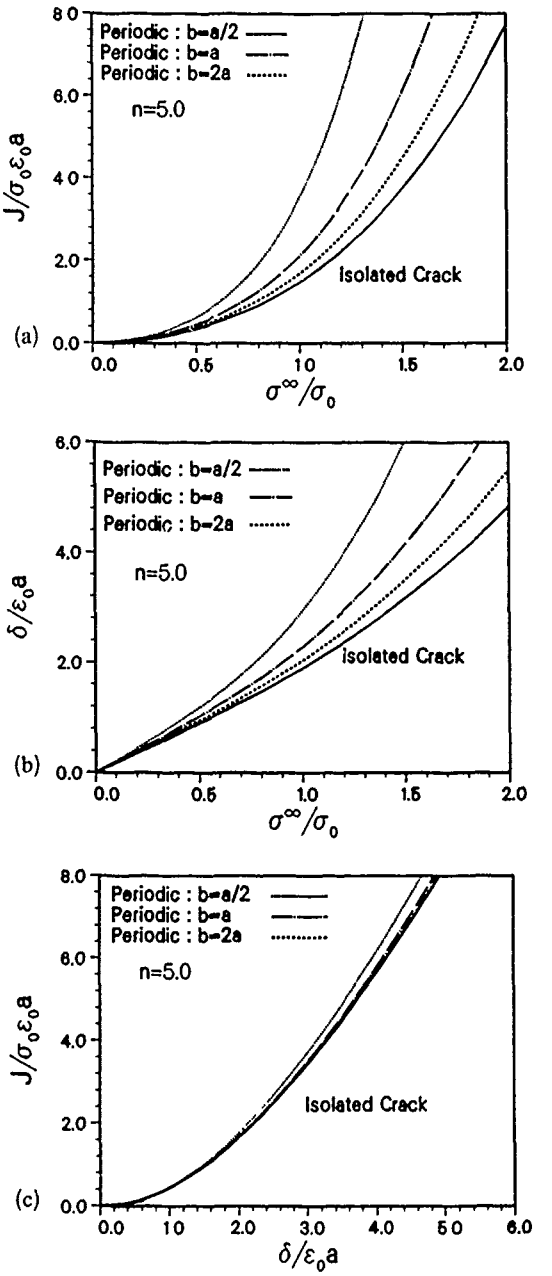

Fig. 10. Effect of the ratio of crack length to ligament length on relationships between J, δ and σ^∞ for $n=5$ material.

The same series of plots for the $n=10$ material is shown in Fig. 11. It should be noted that the curves exhibit trends similar to those in Fig. 10.

5. Discussion

For selected geometries and three material characterizations ($n=5$, 10 and ∞), solutions based on a small strain J_2 flow theory have

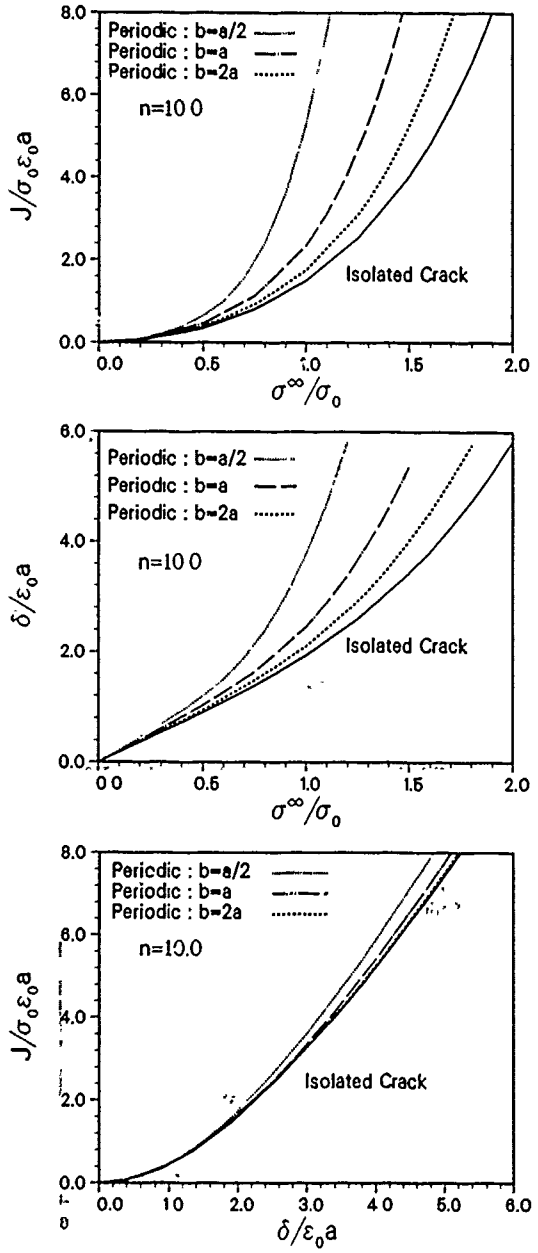

Fig. 11. Effect of the ratio of crack length to ligament length on relationships between J, δ and σ^∞ for $n = 10$ material.

recently been obtained [13]. The plastic zones for the $n = 5$ and $n = 10$ material, and the hydrostatic stress fields are practically identical to those obtained from the corresponding deformation theory solutions. Near the interface, we did find small differences between the solutions. Away from the interface, the fields based on flow and deformation theories are hardly distinguishable from one another. For the elastic-perfect-plastic material ($n \to \infty$), the flow theory solutions show the development of an unloaded elastic wedge-like sector bounded by the interface ($\theta = 0$) and $\theta \approx \pi/6$. The presence of unloaded elastic sectors in elastic-perfect-plastic materials has also been noted by Zywicz [24]. In contrast, solutions for the hardening materials ($n = 5$ and 10) reveal no elastic unloading or indications that elastic unloading may develop. However, the stresses in the vicinity of the interface do show moderate departure from proportional stressing under increasing plastic deformation or remote load. It appears that elastic unloading (under increasing remote load) is a behavior which is peculiar to a non-hardening material perfectly bonded to a stiff substrate. A slight relaxation of the perfect bond assumption and/or a small amount of material strain hardening appear sufficient to prevent its development.

Solutions for the boundary layer small-scale yielding formulation, which take into account fininte geometry changes associated with blunting at the crack tip, have also been obtained. The plastic zones are somewhat similar to those shown in Fig. 3. However, the protrusion of the plastic zone along the interface is only about half of that shown in the plot in Fig. 3(d). The shear stress in the vicinity of the interface is also lower than that predicted by the small strain solution. These aspects, including the crack tip fields for the hardening and non-hardening material, are taken up in ref. 22. A numerical investigation of the process of decohesion along an imperfect interface, which takes into account finite geometry changes, has been carried out by Needleman [25]. He has reported that, under certain conditions, the plastic zone size scales with the value of J.

It is known that, at vanishingly small distances, the elastic interfacial crack solutions ($\varepsilon \neq 0$) predict interpenetration of the crack faces. If the interpenetration zone is much smaller than the crack length, crack face contact can be treated as a small scale non-linear effect and $\boldsymbol{K}$ is still the characterizing parameter for the near-tip state. In any case, the actual situation is somewhat more optimistic than that suggested by the elasticity solution. The results obtained to date indicate that material non-linearity has a mitigating effect on bimaterial crack tip fields in these respects. Under load states that are tension dominated, *i.e.* $\sigma_{yy}^\infty > |\sigma_{xy}^\infty|$, the plastic near-tip fields of interface cracks resemble HRR fields for homogeneous materials because h_{ij} is practically

independent of r over the range of distances which are physically relevant (eqn. (14)). We find no indications of crack face contact over any length scales of physical relevance. Our small strain and finite deformation solutions for the full range of deformation conditions show that the crack tip opens smoothly and that the amount of opening scales nearly linearly with the J integral. Furthermore, the shear stress in the vicinity of the interface is substantially lower than the hoop stress. In contrast, the linear elasticity solutions predict shear and hoop stresses of comparable magnitudes.

In light of the above observations and judging by the results in Fig. 3–9, we conclude that J adequately characterizes the effects of load (or finite ligament plasticity) and geometry on the near-tip field. We should point out that this conclusion pertains to the particular geometric configuration under study. Investigations of different crack geometries are in progress.

Acknowledgments

This investigation is supported by the Office of Naval Research through ONR Grant "Mechanics of Interface Cracks". The computations reported were performed on the Alliant Computer at the Computational Mechanics Facility of Brown University. The acquisition of the Alliant was made possible by grants from the U.S. National Science Foundation (Grant DMR-8714665) and the Office of Naval Research (Grant N00014-88-K-0119), and matching funds from Brown University.

References

1 C. F. Shih and R. J. Asaro, Elastic-plastic analysis of cracks on bimaterial interfaces. part I — small scale yielding, *J. Appl. Mech., 55* (1988) 299-316.
2 C F. Shih and R. J. Asaro, Elastic-plastic analysis of cracks on bimaterial interfaces: part II — structure of small scale yielding fields, submitted to the *J. Appl. Mech.*
3 J. R. Rice, Elastic fracture mechanics concepts for interfacial cracks, *J. Appl. Mech., 55* (1988) 98-103.
4 M. Symington, C. F. Shih and R. J. Asaro, work in progress.
5 M. L. Williams, The stesses around a fault or crack in dissimilar media, *Bull. Seismol. Soc. Am., 49* (1959) 199-204.
6 G. P. Cherepanov, The stress state in a heterogeneous plate with slits, *Izv. Akad. Nauk. SSSR Tekh. Nauk. Mekh. Mashinostr., 1* (1962) 131-137 (in Russian).
7 A. H. England, A crack between dissimilar media, *J. Appl. Mech., 32* (1965) 400-402.
8 F. Erdogan, Stress distribution in bonded dissimilar materials with cracks, *J. Appl. Mech., 32* (1965) 403-410.
9 J. R. Rice and G. C. Sih, Plane problems of cracks in dissimilar media, *J. Appl. Mech., 32* (1965) 418-423.
10 B. M. Malyshev and R. L. Salganik, The strength of adhesive joints using the theory of cracks, *Int. J. Fract. Mech., 1* (1965) 114-128.
11 J. R. Willis, Fracture mechanics of interfacial cracks, *J. Mech. Phys. Solids, 19* (1971) 353-368.
12 E. Zywicz and D. M. Parks, Elastic yield zone around an interfacial crack tip, *J. Appl. Mech.*, in the press.
13 C. F. Shih, R. J. Asaro and N. P. O'Dowd, Elastic-plastic analysis of cracks on bimaterial interfaces: part III — large scale yielding, in preparation.
14 J. R. Rice, A path independent integral and the approximate analysis of strain concentration by notches and cracks, *J. Appl. Mech., 35* (1968) 379-386.
15 J. W. Hutchinson, Fundamentals of the phenomenological theory of nonlinear fracture mechanics, *J. Appl. Mech., 50* (1983) 1042-1051.
16 J. W. Hutchinson, 'Singular behavior at the end of a tensile crack in a hardening material, *J. Mech. Phys. Solids, 16* (1968) 13-31.
17 J. R. Rice and G. F. Rosengren, Plane strain deformation near a crack tip in a power law hardening material, *J. Mech. Phys. Solids, 16* (1968) 1-12.
18 C. F. Shih, Small-scale yielding analysis of mixed mode plane-strain crack problems, *Fracture Analysis, ASTM Spec. Tech. Publ., 560* (1974) 187-210.
19 M. Symington, C. F. Shih and M. Ortiz, Plane strain mixed-mode plastic crack tip fields, *Brown University Report*, 1988.
20 C F. Shih and A. Needleman, Fully plastic crack problems: part I — solutions by a penalty method, *J. Appl. Mech., 51* (1984) 48-56.
21 B. Moran, M. Ortiz and C. F. Shih, Constitutive and computational aspects of finite deformation elastoplasticity, *Brown University Report*, February 1987, to be published.
22 N. P. O'Dowd, C. F. Shih and R. J. Asaro, Elastic-plastic analysis of cracks on bimaterial interfaces. part IV — effects of finite deformation, in preparation.
23 B. Moran and C. F. Shih, Crack tip and associated domain integrals from momentum and energy balance, *Eng. Fract. Mech., 27* (1987) 615-642.
24 E. Zywicz, On elastic-plastic cracks between dissimilar media, *Ph.D. Thesis*, Massachussetts Institute of Technology, 1988.
25 A. Needleman, An analysis of decohesion along an imperfect interface, *Int. J. Fract.*, to be published.

Materials Science and Engineering, A107 (1989) 159–168

On the Mechanics of Adhesion Testing of Flexible Films*

N. ARAVAS

Department of Mechanical Engineering and Applied Mechanics, University of Pennsylvania, Philadelphia, PA 19104 (U.S.A.)

K.-S. KIM

Department of Theoretical and Applied Mechanics, University of Illinois at Urbana-Champaign, Urbana, IL 61801 (U.S.A.)

M. J. LOUKIS

Department of Mechanical Engineering and Applied Mechanics, University of Pennsylvania, Philadelphia, PA 19104 (U.S.A.)

(Received June 1, 1988)

Abstract

The peel test is a simple mechanical test used by microelectronics industries to measure the adhesion of thin films bonded on dielectric substrates. When the film deforms elastically during peeling, the peel force is a direct measure of the adhesive fracture energy. However, when inelastic deformation takes place, the interpretation of the experimental data is not as straightforward. A general formulation of the problem of peeling is given and solutions for metallic and polymeric films are presented. The results of the analysis reveal the effects of several parameters of the peel test, such as the mechanical properties and the thickness of the film, and provide a systematic way for the determination of the adhesive fracture energy from an experimentally measured peel force.

1. Introduction

The peel test is a simple mechanical test which has been extensively used to measure adhesion strength. The test was originally developed by aerospace companies as a method of quality control of bonded aircraft components [1]. More recently, the same test has been used by microelectronics industries to study the adhesion of thin metallic or polymeric films bonded on dielectric substrates. In a peel test, a thin flexible strip that is bonded to a substrate is pulled apart at some angle to the underlying substrate. The peeling force required to separate the strip at a certain rate is recorded and is used for joint design and quality control purposes.

The first theoretical analysis of the peel test was presented in 1953 by Spies [1] who considered the 90° peeling of a thin strip and represented the flexible part of the strip as an elastica and the bonded part as an elastic beam on an elastic (Winkler) foundation. Several elastic analyses of the peel test appeared in the literature since then [2–11]. The effects of plasticity were discussed in refs. 12–14 where several approximate models were used to study the plastic deformation of the strip. An elastoplastic analysis of the peel test has been presented recently by Kim and Aravas [15] who studied in detail the plastic deformation of the strip and calculated the energy dissipated in a peel test. The effects of the speed of peeling on the peel force were considered by Kendall [9] who presented an approximate analysis of the peeling of viscoelastic films.

An analysis of the peeling of elastoplastic and viscoelastic films bonded on rigid substrates is presented in this paper. The deformation of the film is studied in detail using slender beam theory. An energy balance is used to relate the experimentally measured peel force to the adhesive fracture energy. The results of the analysis show that plasticity effects can be very important and that careful interpretation of the experimental data is required when the strip deforms plastically in a peel test. A general formulation of the problem of peeling a linear viscoelastic film from a rigid substrate is presented. The example of a standard three-parameter viscoelastic solid film is considered and an asymptotic solution for the curvature of the film during steady-state peeling is obtained in the form of a perturbation expan-

*Paper presented at the symposium on Interfacial Phenomena in Composites. Processing, Characterization, and Mechanical Properties, Newport, RI, June 1–3, 1988.

0921-5093/89/$3.50

© Elsevier Sequoia/Printed in The Netherlands

sion in a small parameter ε which depends on the speed of peeling and the viscosity of the material. The adhesive fracture energy is also determined in terms of the peel force and the other parameters of the test.

2. Energy balance

A schematic representation of the peel test is shown in Fig. 1. The peel force depends on the adhesion strength as well as on several parameters of the test such as the mechanical properties and the thickness of the film, the angle of peeling, etc. An energy balance is often used to relate the adhesive fracture energy to the experimentally measured peel force [16, 17].

If the film deforms *elastically* during peeling, then part of the work done by the peel force is stored in the elastically deforming system, and the rest is used to provide the energy required to break the interfacial bonding and create the new fracture surface. In steady-state peeling the energy balance can be written as

$$(1-\cos\phi)F\,\mathrm{d}l=\mathrm{d}W^{\mathrm{e}}+\gamma w\,\mathrm{d}l \tag{1}$$

where F is the peel force, ϕ is the peel angle (see Fig. 2), W^{e} is the elastic strain energy of the system, γ is the adhesive fracture energy, w is the width of the film, and $\mathrm{d}l$ is a virtual crack advance. In a steady-state situation, the peel bend remains constant in shape and $\mathrm{d}W^{\mathrm{e}}$ is due to the extension of the film. In most cases $\mathrm{d}W^{\mathrm{e}}$ is small and for an inextensible film is exactly zero. Therefore, eqn. (1) reduces to

$$\gamma=(1-\cos\phi)P \tag{2}$$

where $P=F/w$ is the peel force per unit width of the film. The above equation shows that, for the case of elastic peeling, the peel force is a direct measure of the adhesive fracture energy.

However, the interpretation of the experimental data is not quite as simple as the above analysis would indicate because, in general, there is *inelastic* deformation in the film; in such cases, one has to take into account the energy dissipated as well as the strain energy that remains in the film due to any residual stresses generated in the film after unloading. The energy balance now becomes

$$(1-\cos\phi)F\,\mathrm{d}l=\gamma w\,\mathrm{d}l+\mathrm{d}W^{\mathrm{d}}+\mathrm{d}W^{\mathrm{r}} \tag{3}$$

where W^{d} is the energy dissipation and W^{r} is the residual strain energy. Equation (3) can be also written as

$$\gamma=(1-\cos\phi)P-\psi \tag{4}$$

where

$$\psi=\frac{1}{w}\left(\frac{\mathrm{d}W^{\mathrm{d}}}{\mathrm{d}l}+\frac{\mathrm{d}W^{\mathrm{r}}}{\mathrm{d}l}\right) \tag{5}$$

is the work expenditure per unit width of the film per unit crack advance. The above equation makes it clear that experimental determination of the peel force is not enough for the calculation of the interfacial fracture energy; one needs, in addition, to be able to determine the work expenditure ψ during inelastic peeling.

If inelastic deformation of the film is taking place during a peel test, energy is dissipated in the region near the interfacial crack tip, where singular strains develop, as well as along the inelastically bending part of the film. Elastoplastic finite element analysis of the peel test, however, indicates that the effects of the crack tip singularities are limited to a small region near the crack tip and that bending is the predominant mode of deformation of the film [15]. Therefore, we consider the near tip dissipation to be part of the fracture energy γ and identify ψ with the energy dissipated due to inelastic bending.

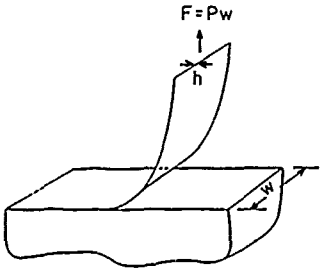

Fig. 1. Schematic representation of the peel test.

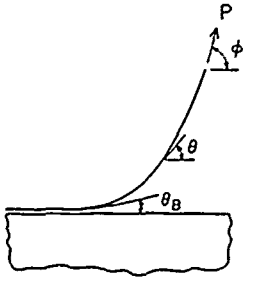

Fig. 2. Schematic diagram of peeling.

In the following, we analyze the deformation of the unattached part of the film during a peel test and present a systematic way for the determination of the fracture energy γ in terms of the peel force and the parameters of the test.

3. Formulation of the problem

In this section we use slender beam theory to analyze the deformation of the film. The governing equations of equilibrium and moment balance are

$$\frac{dT}{ds} - KN = 0 \tag{6}$$

$$\frac{dN}{ds} + KT = 0 \tag{7}$$

and

$$\frac{dM}{ds} + N = 0 \tag{8}$$

where T and N are the axial and shear forces of the beam, $K = d\theta/ds$ is the curvature of the middle surface of the beam, $\tan\theta$ is the slope of the middle surface of the beam, M is the bending moment, and s is the arc length along the deforming film.

Using overall equilibrium we find that

$$T = Pw\cos(\phi - \theta) \quad \text{and} \quad N = Pw\sin(\phi - \theta) \tag{9}$$

The equilibrium equations (6) and (7) are now automatically satisfied and the remaining moment equation (8) becomes

$$\frac{dM}{ds} + Pw\sin(\phi - \theta) = 0 \tag{10}$$

Figure 3 shows a typical section of the deforming film subject to a pure bending moment M. We choose the coordinate axes as indicated and sign conventions so that the indicated moment and the corresponding curvature are positive. The width w is always much larger than the thickness h so that plane-strain conditions prevail. With the usual assumption of beam bending theory that plane sections remain plane and normal to the central axis, the bending strain at any point along the film is given by

$$\varepsilon(s, z) = -zK(s) \tag{11}$$

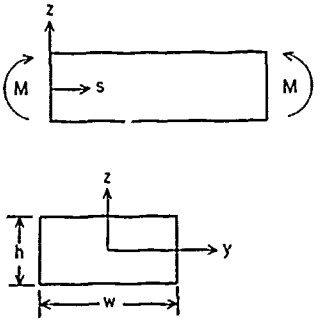

Fig. 3. Beam under pure bending.

The axial and shear forces N and T cause additional strains which are small in metallic films but they can become important when certain polymeric films are peeled [18]. The effects of such additional strains are ignored in the present analysis and they will be addressed in detail in a future publication.

Under these assumptions the work expenditure can be calculated as

$$\psi = \frac{1}{w}\int_{-\infty}^{\infty} M\frac{dK}{ds}\,ds \tag{12}$$

The above equation shows that ψ, and therefore γ, can be easily determined once the moment and curvature distributions are known.

4. Elastoplastic analysis of the peel test

In this section we analyze the deformation of the unattached part of an elastoplastic film during peeling. The material is assumed to obey the von Mises yield condition with associated flow rule. In this paper we consider a perfectly plastic material with yield stress σ_0. The results of the analysis however can be easily extended to include hardening [15].

We study first the deformation of an elastoplastic beam under pure plane-strain bending. When the material is elastically incompressible (Poisson's ratio $\nu = 0.5$) the moment–curvature relations (see Fig. 4) are of the following form:

(a) elastic loading (O–A)

$$m = \frac{2}{3}k \qquad \text{for } 0 \leqslant k \leqslant 1 \tag{13}$$

(b) plastic loading (A–B)

$$m = 1 - \frac{1}{3k^2} \qquad \text{for } 1 \leqslant k \leqslant k_B \tag{14}$$

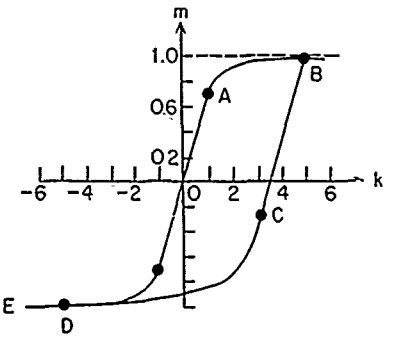

Fig. 4. Moment-curvature relation for a rectangular beam.

(c) elastic unloading (B-C)

$$m = 1 - \frac{1}{3k_B^2} - \frac{2}{3}k_B + \frac{2}{3}k$$

$$\text{for } k_B - 2 \leqslant k \leqslant k_B \tag{15}$$

(d) reverse plastic loading (C-D)

$$m = -1 - \frac{1}{3k_B^2} + \frac{8}{3(k-k_B)^2}$$

$$\text{for } -k_B \leqslant k \leqslant k_B - 2 \tag{16}$$

(e) complete reverse plastic loading (D-E)

$$m = -1 + \frac{1}{3k^2} \qquad \text{for } k \leqslant -k_B \tag{17}$$

In the above equations the dimensionless moment and curvature are defined as

$$m = \frac{M}{M_0} \qquad \text{and} \qquad k = \frac{K}{K_c} \tag{18}$$

where

$$M_0 = \frac{1}{2(3)^{1/2}} w\sigma_0 h^2 \tag{19}$$

is the fully plastic moment of the beam,

$$K_c = \frac{3^{1/2}\sigma_0}{Eh} \tag{20}$$

is the curvature at which yielding first occurs at the outer fibers of the beam, and E is Young's modulus.

A schematic representation of the peel test together with the corresponding moment-curvature diagram is shown in Fig. 5. The curvature at any material point reaches a maximum, k_B, when the material point passes through the interfacial

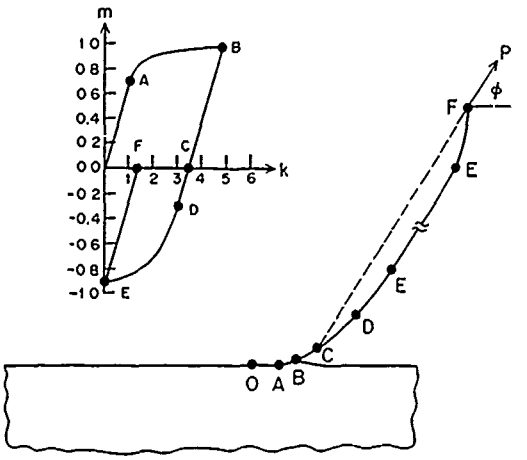

Fig. 5. Configuration of steady-state peeling and the corresponding moment-curvature diagram.

crack tip and it decreases as the point separates from the interface and moves away from it. As the point approaches infinity the curvature must go to zero. Once a material element deforms plastically, it is clear from Fig. 4 that some reverse (negative) moment is necessary for the curvature to become zero again. This means that the film "overshoots" the load axis as shown in Fig. 5, when plastic deformation is taking place during a peel test. Finally, the region marked E-F on Fig. 5 is an "end effect" so that the moment reduces to zero as the point of application of the load is approached.

As mentioned above, we ignore the effects of the axial and shear forces, and determine the work expenditure as

$$\psi = \frac{1}{w}\int_L M(K)\,dK = \frac{3P}{\eta}\int_L m(k)\,dk \tag{21}$$

where L indicates the path O-A-B-C-D-E on the moment-curvature diagram shown in Fig. 5, and

$$\eta = \frac{3Pw}{K_c M_0} = \frac{6EP}{\sigma_0^2 h} \tag{22}$$

is the dimensionless peel force. Using the above equation and the moment-curvature relations (13)-(17) we find that

$$\psi = 0 \qquad \text{for } k_B \leqslant 1 \tag{23}$$

$$\psi = \frac{3P}{\eta}\left(\frac{2}{3k_B} + \frac{1}{3}k_B^2 - 1\right) \qquad \text{for } 1 \leqslant k_B \leqslant 2 \tag{24}$$

and

$$\psi=\frac{3P}{\eta}\left(2k_B-5+\frac{10}{3k_B}\right) \qquad \text{for } k_B\geqslant 2 \qquad (25)$$

The key factor that determines the work expenditure ψ is the maximum curvature k_B. A method for the determination of k_B is given in the following.

Using the dimensionless quantities defined by eqn. (18) we can write the moment equation (10) as

$$\frac{dm}{dl}+\frac{1}{3}\eta\sin(\phi-\theta)=0 \qquad (26)$$

where $l=sK_c$ is the normalized arc length. If we consider the curvature k to be a function of θ, eqn. (26) can be written as

$$k\frac{dm}{dk}\frac{dk}{d\theta}+\frac{1}{3}\eta\sin(\phi-\theta)=0 \qquad (27)$$

where dm/dk is a function of k and can be determined from eqns. (13)–(17). Equation (27) is now a first-order non-linear differential equation which can be used together with the boundary condition $k=0$ at $\theta=\phi$ to determine $k(\theta)$.

If $k_B\leqslant 1$, the film deforms elastically and eqn. (27) becomes

$$2k\frac{dk}{d\theta}+\eta\sin(\phi-\theta)=0 \qquad (28)$$

integration of which yields

$$k=[\eta(1-\cos(\phi-\theta))]^{1/2}=(2\eta)^{1/2}\sin\frac{\phi-\theta}{2} \qquad (29)$$

The maximum curvature is given by

$$k_B=[\eta(1-\cos(\phi-\theta_B))]^{1/2} \qquad (30)$$

where θ_B is the base angle (see Fig. 2) and depends on the properties of the film and the substrate as well as on the strength of the interface. In this case, the film does not overshoot the load axis and both m and k vanish at the point of application of the load.

If $1\leqslant k_B\leqslant 2$, reverse yielding does not take place and points D–E and C–F coincide on the moment–curvature diagram shown in Fig. 5. The m–k relation is given now by eqn. (15), and the solution given by (29) and (30) is still valid. In this case, however, the film overshoots the load axis, there is a residual curvature k_F, and θ_F is in general different from the peel angle ϕ.

Finally, if $k_B\geqslant 2$ reverse yielding is taking place and eqn. (27) becomes

$$2k\frac{dk}{d\theta}+\eta\sin(\phi-\theta)=0$$

along B–D where $k_B-2\leqslant k\leqslant k_B$ (31)

$$\frac{16}{(k-k_B)^2}\frac{dk}{d\theta}-\eta\sin(\phi-\theta)=0$$

along D–E where $0\leqslant k\leqslant k_B-2$ (32)

$$2k\frac{dk}{d\theta}+\eta\sin(\phi-\theta)=0$$

along E–F where $0\leqslant k\leqslant k_F$ (33)

Integration of eqn. (31) yields

$$k=[k_B^2-\eta[\cos(\phi-\theta)-\cos(\phi-\theta_B)]]^{1/2}$$

along B–D (34)

Equation (32) also implies that

$$k=\frac{k_B[k_B\eta(1-\cos(\phi-\theta))]^{1/2}}{2^{3/2}+[k_B\eta(1-\cos(\phi-\theta))]^{1/2}}$$

along D–E (35)

where the boundary condition $k=0$ at $\theta=\phi$ (point E) has been used. Finally, integrating eqn. (33) and using the boundary condition at E we find that

$$k=[\eta(1-\cos(\phi-\theta))]^{1/2} \qquad \text{along E–F} \qquad (36)$$

Matching the solutions (34) and (35) at point D and taking into account that $k_D=k_B-2$ we can easily find that

$$\cos(\phi-\theta_D)=1-\frac{2}{k_B\eta}(k_B-2)^2 \qquad (37)$$

and

$$k_B=1+\frac{1}{12}\eta(1-\cos(\phi-\theta_B))+\left[\left[1+\frac{1}{12}\eta(1-\cos(\phi-\theta_B))\right]^2-\frac{4}{3}\right]^{1/2} \qquad (38)$$

Summarizing, we mention that the work expenditure ψ is given by eqns. (23)–(25), where

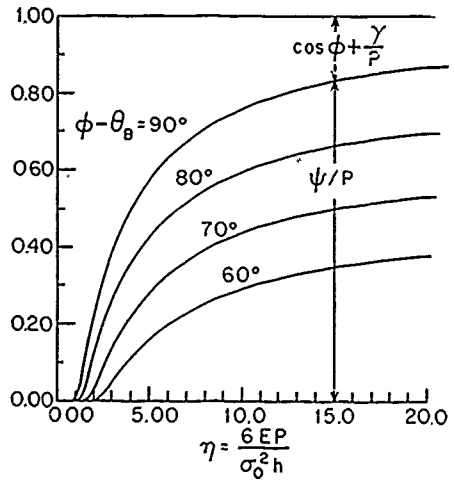

Fig. 6. Normalized work expenditure ψ/P and normalized fracture energy γ/P *vs.* normalized load η for different values of the difference $\phi-\theta_B$.

the maximum curvature k_B is defined in terms of θ_B by eqns. (30) or (38). The base angle θ_B can be either measured experimentally or determined by modelling the attached part of the film as a beam on an elastic (Winkler) foundation [19]. The normalized work expenditure ψ/P and the normalized fracture energy γ/P are plotted in Fig. 6 as functions of the dimensionless peel force η for different values of the difference $\phi-\theta_B$. Figure 6 shows that there is a strong dependence of the work expenditure ψ on θ_B which, for a given adhesion strength, depends on the properties of the film and the substrate as well as on the thickness of the film. Figure 6 also shows that, when the dimensionless load $\eta=6EP/(\sigma_0^2 h)$ is large, the adhesive fracture energy γ is only a small fraction of the peel force P, and that P is mainly a measure of the plastic deformation of the film rather than a measure of the adhesive strength.

5. Analysis of peeling of viscoelastic materials

In this section we analyze the deformation of the unattached part of a viscoelastic film during peeling. The effects of the axial and shear forces are ignored and the film is assumed to be inextensible. We also assume that the substrate is rigid so that the deformation of the attached part of the film is negligible and that viscous deformation occurs at material points on the film only after they separate from the substrate.

We consider a linear viscoelastic material, the stress–strain relation of which under plane-strain tension is given by

$$\mathbf{Q}(\sigma)=\mathbf{R}(\varepsilon) \tag{39}$$

where $\mathbf{Q}$ and $\mathbf{R}$ are linear operators of the form

$$\mathbf{Q}=\sum_{n=0}^{n_q} q_n\frac{\mathrm{d}^n}{\mathrm{d}t^n} \qquad \mathbf{R}=\sum_{n=0}^{n_r} r_n\frac{\mathrm{d}^n}{\mathrm{d}t^n} \tag{40}$$

q_n and r_n are constants and t is time.

The bending moment M on any cross-section of the deforming film is given by

$$M(s)=-w\int_{-h/2}^{h/2} z\sigma(s,z)\,\mathrm{d}z \tag{41}$$

Operating by $\mathbf{Q}$ we find that

$$\mathbf{Q}(M)=-w\int_{-h/2}^{h/2} z\mathbf{Q}(\sigma)\,\mathrm{d}z=-w\int_{-h/2}^{h/2} z\mathbf{R}(\varepsilon)\,\mathrm{d}z \tag{42}$$

Finally, making use of eqn. (11), we find that

$$\mathbf{Q}(M)=I\mathbf{R}(K) \tag{43}$$

where $I=\frac{1}{12}wh^3$ is the moment of inertia of the cross-sectional area of the film. During steady-state peeling $\mathrm{d}s=v\,\mathrm{d}t$, where v is the speed of peeling, and therefore the above equation can be written as

$$\sum_{n=0}^{n_q} q_n v^n\frac{\mathrm{d}^n M}{\mathrm{d}s^n}=I\sum_{n=0}^{n_r} r_n v^n\frac{\mathrm{d}^n K}{\mathrm{d}s^n} \tag{44}$$

Taking into account that $K=\mathrm{d}\theta/\mathrm{d}s$ and using the moment equation (10) we can eliminate M to find

$$-Pw\sum_{n=0}^{n_q} q_n v^n\frac{\mathrm{d}^n[\sin(\phi-\theta)]}{\mathrm{d}s^n}=I\sum_{n=0}^{n_r} r_n v^n\frac{\mathrm{d}^{n+2}\theta}{\mathrm{d}s^{n+2}} \tag{45}$$

which is the governing differential equation for $\theta(s)$. The corresponding boundary conditions are

$$\theta=\theta_B \qquad \text{at } s=0 \tag{46}$$

and

$$\theta=\phi \qquad \text{at } s=\infty \tag{47}$$

The last boundary condition also implies that all derivatives of θ with respect to s are zero at in-

finity. We also have a set of initial conditions at the interfacial crack tip ($s=0$) related to the instantaneous elastic response of the material model.

Once the solution $\theta(s)$ is known, we can calculate the curvature $K=\mathrm{d}\theta/\mathrm{d}s$ and the moment M integrating eqn. (10). Finally, the work expenditure ψ is determined using eqn. (12).

The method is demonstrated in the following section where we consider the peeling of a thin viscoelastic film the constitutive behavior of which is described by the standard three-parameter viscoelastic solid model shown in Fig. 7.

5.1. *Peeling of a three-parameter viscoelastic solid film*

The governing equations in this case are

$$\frac{\mathrm{d}M}{\mathrm{d}s}+Pw\sin(\phi-\theta)=0 \tag{48}$$

and

$$\frac{E_1+E_2}{\mu}M+v\frac{\mathrm{d}M}{\mathrm{d}s}=\frac{IE_1E_2}{\mu}K+IE_1v\frac{\mathrm{d}K}{\mathrm{d}s} \tag{49}$$

where E_1, E_2 and μ are the material parameters shown in Fig. 7. Eliminating the moment M we find

$$\frac{h^3E_1v}{12}\frac{\mathrm{d}^3\theta}{\mathrm{d}s^3}+\frac{h^3E_1E_2}{12\mu}\frac{\mathrm{d}^2\theta}{\mathrm{d}s^2}-vP\cos(\phi-\theta)\frac{\mathrm{d}\theta}{\mathrm{d}s}+\frac{E_1+E_2}{\mu}P\sin(\phi-\theta)=0 \tag{50}$$

which is the governing equation for $\theta(s)$. The corresponding boundary and initial conditions are

$$\theta=\theta_B \qquad \text{at } s=0 \tag{51}$$

$$\theta=\phi \qquad \text{at } s=\infty \tag{52}$$

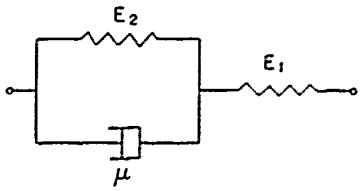

Fig. 7. Three-parameter viscoelastic solid model.

and

$$M=E_1IK \qquad \text{at } s=0 \tag{53}$$

Taking into account that $K=\mathrm{d}\theta/\mathrm{d}s$ and using eqns. (48) and (49) we can write the initial condition (53) in terms of θ as

$$\frac{h^3E_1v}{12}\frac{\mathrm{d}^2\theta}{\mathrm{d}s^2}-\frac{h^3E_1^2}{12\mu}\frac{\mathrm{d}\theta}{\mathrm{d}s}+vP\sin(\phi-\theta_B)=0 \qquad \text{at } s=0 \tag{54}$$

Introducing the dimensionless quantities

$$\varepsilon=\frac{E_1h}{v\mu}\left(\frac{E_1h}{12P}\right)^{1/2} \qquad l=\frac{s}{h}\left(\frac{12P}{E_1h}\right)^{1/2} \qquad \text{and} \qquad E=\frac{E_2}{E_1} \tag{55}$$

we find that the governing equation and the corresponding boundary and initial conditions become

$$\frac{\mathrm{d}^3\theta}{\mathrm{d}l^3}+\varepsilon E\frac{\mathrm{d}^2\theta}{\mathrm{d}l^2}-\cos(\phi-\theta)\frac{\mathrm{d}\theta}{\mathrm{d}l}+\varepsilon(1+E)\sin(\phi-\theta)=0 \tag{56}$$

$$\theta=\theta_B \qquad \text{at } l=0 \tag{57}$$

$$\theta=\phi \qquad \text{at } l=\infty \tag{58}$$

and

$$\frac{\mathrm{d}^2\theta}{\mathrm{d}l^2}-\varepsilon\frac{\mathrm{d}\theta}{\mathrm{d}l}+\sin(\phi-\theta_B)=0 \qquad \text{at } l=0 \tag{59}$$

Considering the dimensionless curvature

$$k=\frac{\mathrm{d}\theta}{\mathrm{d}l}=Kh\left(\frac{E_1h}{12P}\right)^{1/2} \tag{60}$$

to be a function of θ, the governing equation and the corresponding boundary conditions become

$$k\frac{\mathrm{d}}{\mathrm{d}\theta}\left(k\frac{\mathrm{d}k}{\mathrm{d}\theta}\right)+\varepsilon Ek\frac{\mathrm{d}k}{\mathrm{d}\theta}-k\cos(\phi-\theta)+\varepsilon(1+E)\sin(\phi-\theta)=0 \tag{61}$$

$$k=0 \qquad \text{at } \theta=\phi \tag{62}$$

and

$$k\frac{\mathrm{d}k}{\mathrm{d}\theta}-\varepsilon k+\sin(\phi-\theta_B)=0 \qquad \text{at } \theta=\theta_B \tag{63}$$

Integration of the moment equation (48) gives

$$m=\int_{\theta}^{\phi}\frac{\sin(\phi-\theta)}{k}\,\mathrm{d}\theta \tag{64}$$

where the dimensionless moment m is defined as

$$m=\frac{M}{Pwh}\left(\frac{12P}{E_1 h}\right)^{1/2} \tag{65}$$

Finally, using eqn. (12) we find the work expenditure to be

$$\psi=\frac{1}{2}Pk_{\mathrm{B}}^2+P\int_{\theta_{\mathrm{B}}}^{\phi}m\frac{\mathrm{d}k}{\mathrm{d}\theta}\,\mathrm{d}\theta \tag{66}$$

where k_{B} is the curvature of the film at the crack tip, and the first term on the right-hand side is due to the instantaneous elastic response at that point.

In general, the solution of the non-linear eqn. (61) will have to be found numerically. In the following, however, we obtain an approximate closed-form solution for the limiting cases of very fast peeling or very large viscosity μ which make the parameter ε very small. We seek a perturbation expansion in ε for the solution to the problem such that

$$k=k^{(0)}+\varepsilon k^{(1)}+O(\varepsilon^2) \tag{67}$$

Substituting the above expansion into the differential equation (61) and the boundary conditions (62) and (63) and collecting terms having like powers of ε, we obtain the following hierarchy of problems:

For the leading-order problem we have

$$\frac{\mathrm{d}}{\mathrm{d}\theta}\left(k^{(0)}\frac{\mathrm{d}k^{(0)}}{\mathrm{d}\theta}\right)-\cos(\phi-\theta)=0 \tag{68}$$

$$k^{(0)}=0 \qquad \text{at } \theta=\phi \tag{69}$$

and

$$k^{(0)}\frac{\mathrm{d}k^{(0)}}{\mathrm{d}\theta}=-\sin(\phi-\theta_{\mathrm{B}}) \qquad \text{at } \theta=\theta_{\mathrm{B}} \tag{70}$$

At $O(\varepsilon)$ the problem is given by

$$\frac{\mathrm{d}^2}{\mathrm{d}\theta^2}(k^{(0)}k^{(1)})+\frac{1+E}{k^{(0)}}\sin(\phi-\theta)=-E\frac{\mathrm{d}k^{(0)}}{\mathrm{d}\theta} \tag{71}$$

$$k^{(1)}=0 \qquad \text{at } \theta=\phi \tag{72}$$

and

$$\frac{\mathrm{d}}{\mathrm{d}\theta}(k^{(0)}k^{(1)})=k^{(0)} \qquad \text{at } \theta=\theta_{\mathrm{B}} \tag{73}$$

The solutions of the above two problems are easily found to be

$$k^{(0)}=2\sin\frac{\phi-\theta}{2} \tag{74}$$

and

$$k^{(1)}=-2\tan\frac{\phi-\theta}{4} \tag{75}$$

The leading-order solution, $k^{(0)}$, is the elastic solution, and the first-order correction, $k^{(1)}$, introduces the viscoelastic effects. Using eqn. (64) we find that

$$m=m^{(0)}+\varepsilon m^{(1)}+O(\varepsilon^2) \tag{76}$$

where

$$m^{(0)}=\int_{\theta}^{\phi}\frac{1}{k^{(0)}}\sin(\phi-\theta)\,\mathrm{d}\theta=2\sin\frac{\phi-\theta}{2} \tag{77}$$

and

$$m^{(1)}=-\int_{\theta}^{\phi}\frac{k^{(1)}}{k^{(0)2}}\sin(\phi-\theta)\,\mathrm{d}\theta$$

$$=(\phi-\theta)-2\tan\frac{\phi-\theta}{4} \tag{78}$$

Equation (66) now implies that the work expenditure ψ is given by

$$\psi=2P\left[4\left(1-\cos\frac{\phi-\theta_{\mathrm{B}}}{2}\right)-(\phi-\theta_{\mathrm{B}})\sin\frac{\phi-\theta_{\mathrm{B}}}{2}\right]\varepsilon+O(\varepsilon^2) \tag{79}$$

Finally, using the energy balance equation (4) we find that the adhesive energy γ can be written in terms of the peel force P and the other parameters of the test as

$$\frac{\gamma}{P}=1-\cos\phi-2\left[4\left(1-\cos\frac{\phi-\theta_{\mathrm{B}}}{2}\right)-(\phi-\theta_{\mathrm{B}})\times\sin\frac{\phi-\theta_{\mathrm{B}}}{2}\right]\frac{E_1 h}{r\mu}\left(\frac{E_1 h}{12P}\right)^{1/2}+O(\varepsilon^2) \tag{80}$$

As was mentioned in Section 4, the base angle θ_B depends on the thickness of the film as well as on the properties of the film and the substrate.

Solutions for the other extreme cases of very slow peeling or very small viscosity μ, which make ε very large, can be obtained in a similar way. Such solutions will be presented in a future publication together with solutions for intermediate values of ε.

6. Discussion

The analysis presented in Sections 2 to 5 shows that the peel force is a direct measure of the adhesive fracture energy only if both the film and the substrate deform elastically. In such a case

$$\gamma = (1 - \cos\phi)P \tag{81}$$

In the absence of any inelastic deformations the peel force also provides information about the stress field in the region near the interfacial crack tip. The adhesive fracture energy γ is equal to the energy release per unit crack extension along the interface per unit width of the film $\mathcal{G}$, *i.e.*

$$\gamma = \mathcal{G} = \frac{[(1-\nu_1)/G_1 + (1-\nu_2)/G_2]}{4\cosh^2(\pi\varepsilon)}|K|^2 \tag{82}$$

where

$$\varepsilon = \frac{1}{2\pi}\ln\left[\frac{G_1 + G_2(3-4\nu_1)}{G_2 + G_1(3-4\nu_2)}\right] \tag{83}$$

G is the shear modulus, ν is Poisson's ratio, the subscripts 1 and 2 refer to the film and the substrate respectively, and K is the complex interface stress intensity factor as defined in [20] and [21]. These results for the interface singularity field are discussed in detail in refs. 22–24. Combining eqns. (81) and (82) we find that

$$|K| = \left(\frac{4(1-\cos\phi)P\cosh^2(\pi\varepsilon)}{(1-\nu_1)/G_1 + (1-\nu_2)/G_2}\right)^{1/2} \tag{84}$$

The same result can be obtained using the J-integral [25, 26] defined by

$$J = \int_\Gamma \left(WN_1 - \mathbf{T}\cdot\frac{\partial \mathbf{u}}{\partial X_1}\right) ds \tag{85}$$

where Γ is a path in the undeformed configuration from the bottom surface of the crack through material to the upper surface of the crack, W is the strain energy density per unit reference (undeformed) volume, $\mathbf{N}$ is the outward normal to the integration path, $\mathbf{T} = \mathbf{N}\cdot\mathbf{t}^0$, $\mathbf{t}^0$ is the nominal (first Piola–Kirchhoff) stress tensor, $\mathbf{u}$ is the displacement vector, and X is the position of a material point in the undeformed configuration. The J-integral is path independent if the elastic material under consideration is homogeneous, at least in the X_1 direction [27]. Taking the integration path Γ along the boundary of the specimen we find

$$J = P\left(1 - \cos\varphi + \frac{\alpha}{2}\frac{P}{Eh}\right) \tag{86}$$

where E is Young's modulus of the film, $\alpha = 1$ for plane stress and $\alpha = 1 - \nu^2$ for plane-strain conditions far from the crack tip. The last term in the above expression is due to the axial straining of the film. For thin metallic films of thicknesses of the order of 100 μm the ratio P/Eh is of the order of 10^{-4} and can be neglected. Therefore, eqn. (86) can be written as

$$J = (1 - \cos\phi)P \tag{87}$$

For an elastic material $J = \mathcal{G}$ and eqn. (84) follows.

Equation (84) can be also written as

$$|K| = \left(\frac{4\gamma\cosh^2(\pi\varepsilon)}{(1-\nu_1)/G_1 + (1-\nu_2)/G_2}\right)^{1/2} \tag{88}$$

The above equation shows that if the adhesive fracture energy γ is independent of the mode of fracture, then the fracture locus on the complex K plane will be a circle.

The question remains, however, as to whether the adhesive fracture energy γ is independent of the fracture mode and the amount of plasticity in the specimen. One of the advantages of the peel test is that the mode of interfacial fracture and the amount of plasticity in the film can be easily changed by changing the peel angle; a series of peel tests with different peel angles is now underway in an attempt to address this question. Once the peel force is determined, γ can be calculated as described in Sections 4 and 5. It should be noted, however, that part of the so determined γ is associated with energy dissipated in the near crack tip plastic zone. The near tip energy dissipation can be determined using the finite element method and the results of the finite element analysis can be combined with the results presented in this paper in order to determine the

actual adhesive fracture energy, *i.e.* the energy associated with the interfacial debonding. Such work is now underway.

Acknowledgments

It is a pleasure to acknowledge fruitful discussions with Prof. M. W. Nansteel of the University of Pennsylvania on the subject of this paper. The authors acknowledge the support of IBM through Grants PT441614 and 00920. N.A. also acknowledges the support of the NSF under Grant No. MSM-8657860. K.S.K. also acknowledges the support of the ONR under Contract No. N00014-87-K-0493.

References

1 G. J. Spies, *J. Aircraft Eng., 25* (1953) 64.
2 J. J. Bikerman, *J. Appl. Phys., 28* (1957) 1484.
3 D. H. Kaeble, *Trans. Soc. Rheol, 3* (1959) 161.
4 D. H. Kaeble, *Trans. Soc. Rheol. 4* (1960) 45.
5 C. Jouwersma, *J. Polymer Sci., 45* (1960) 253.
6 S. Yurenka, *J. Appl. Polymer Sci., 6* (1962) 136.
7 J. L. Gardon, *J. Appl. Polymer Sci., 7* (1963) 643.
8 E. B. Saubestre, L. J. Durney, J. Haidu and E. Bastenbeck, *Plating, 52* (1965) 982.
9 K. Kendall, *J. Adhesion, 5* (1973) 105.
10 A. N. Gent and G. R. Hamed, *J. Adhesion, 7* (1975) 91.
11 D. W. Nicholson, *Int. J. Fracture, 13* (1977) 279.
12 M. D. Chang, K. L. Devries and M. L. Williams, *J. Adhesion, 4* (1972) 221.
13 W. T. Chen and T. F. Flavin, *IBM J. Res. Dev., 16* (1972) 203.
14 A. N. Gent and G. R. Hamed, *J. Appl. Polymer Sci., 21* (1977) 2817.
15 K.-S. Kim and N. Aravas, *Int. J. Solids Struct., 24* (1988) 417.
16 J. J. Bikerman, *The Science of Adhesive Joints*, 2nd Edn., Academic Press, New York.
17 K. Kendall, *Proc. R. Soc. London, Ser. A, 341* (1975) 409.
18 K.-S. Kim and J. Kim, *J. Eng. Mater. Technol., 110* (1988) 266.
19 K.-S. Kim, University of Illinois at Urbana-Champaign, Department of Theoretical and Applied Mechanics Report No. 472 (1985).
20 J. W. Hutchinson, M. E. Mear and J. R. Rice, *J. Appl. Mech., 54* (1987) 828.
21 J. R. Rice, *J. Appl. Mech., 55* (1988) 98.
22 A. H. England, *J. Appl. Mech., 32* (1965) 400.
23 F. Erdogan, *J. Appl. Mech., 32* (1965) 403.
24 J. R. Rice and G. C. Sih, *J. Appl. Mech., 32* (1965) 418.
25 J. D. Eshelby, in D. Seitz and D. Turnbull (eds.), *Solid State Physics*, Academic Press, New York, 1956, p. 79.
26 J. R. Rice, *J. Appl. Mech., 35* (1968) 379.
27 J. R. Rice, in H. Liebowitz (ed.), *Fracture. An Advanced Treatise*, Vol. 2, Academic Press, New York, 1968, p. 191.

Stress Concentration Along Interfaces of Elastic–Plastic Thin Films*

J. C. LAMBROPOULOS and S.-M. WAN

Department of Mechanical Engineering, University of Rochester, Rochester, NY 14627 (U.S.A.)

(Received June 1, 1988)

Abstract

Finite element techniques are used to calculate the stress concentrations near the free edge and along the interface of thin films which are bonded to stiff substrates. The material of the film is modeled as elastic–plastic with a linear power-law hardening stress–strain curve in simple shear. It is assumed that the film material is characterized by J_2 deformation theory, and that far from the free edges the film is in a state of uniform balanced biaxial stress which may be due to misfit strain, to thermal strain or to intrinsic stress. Emphasis is placed on the stress concentrations in films of small aspect ratio (modeling the early stages of island gro.vth) or of large aspect ratio (modeling epitaxial or layer-by-layer growth) and on the effect of the hardening exponent on the resulting stress concentrations. It is found that stress concentrations are localized near the film–substrate interface, that films of small aspect ratio have smaller stress concentrations than films of large aspect ratio, and that plastic deformation significantly reduces the stress levels near the interface, although close to the free edge the stress levels are still higher than the far field uniform stresses.

1. Introduction

It is well known that thin films grown on substrates are in a state of internal stress which arises as a result of the deposition process (intrinsic stress) or as a result of differential thermal mismatch between film and substrate when the temperature is different from the deposition temperature (thermal stress) [1, 2]. Large values of the internal stress may lead to failure by delamination from the free edge of the film [3], or by buckling and cracking along the interface between film and substrate [4, 5]. The film materials are used in a wide variety of applications, such as optical [6], electronic [7], or magnetic [8].

Stresses near the vicinity of the free edge of an isotropic film were calculated by Aleck [9], and later by Zeyfang [10] and Blech and Levi [11], who established that close to the free edge large peeling and shear stresses develop. Such stresses considerably exceed the far field internal stress of the film [11]. Williams [12] showed that for a film bonded to a rigid substrate stress singularities develop near the point where the interface meets the free edge. Hein and Erdogan [13] calculated the stress singularity for varying stiffness between film and substrate. They showed that when the film is much stiffer the singularity is $-1/2$ for large values of the film material angle. When the substrate is much stiffer, the singularity is generally milder [13]. More recently, Lau, Rahman and Delale calculated the free edge singularity for power-law hardening materials and for a variety of different free-edge material angles [14]. Approximate solutions for the stresses along the interface have been presented by Suhir [15, 16], and by Yang and Freund [17], who have approximated the variation of the stresses through the thickness of the film. Stresses in elastic substrates have been calculated by Hu [18] and by Isomae [19] who were mostly interested in evaluating defect densities induced in silicon substrates due to the thin film internal stresses. Interfacial stress distribution in epitaxial films, which are characterized by considerable elastic anisotropy, have been calculated by Lambropoulos and Wan [20].

As Lau *et al.* have pointed out [14], most studies to date have concentrated on linearly elastic constitutive response for the film or substrate materials. More recently, attempts have been made to include material nonlinearities in the analysis of stresses in film–substrate assemblies. Yang and Freund examined plastic and vis-

*Paper presented at the symposium on Interfacial Phenomena in Composites: Processing, Characterization, and Mechanical Properties, Newport, RI, June 1–3, 1988.

0921-5093/89/$3.50

© Elsevier Sequoia/Printed in The Netherlands

cous material response for the film [17] but, due to the approximation involved, their solution is not valid within 1–2 thickness from the film's free edge. Suhir [16] allowed for nonlinear stiffness of the solder in soldered film–substrate assemblies. Due to the approximations invoked in Suhir's work [15, 16] the traction-free boundary conditions are not satisfied near the film's free edge. As noted above, Lau *et al.* [14] examined singularities in power-law hardening composite wedges. Isomae [21] allowed for linearly viscous response of the film material in an effort to model dislocation generation in silicon substrates with SiO_2 or Si_3O_4/SiO_2 films. In Isomae's work primary emphasis was placed on the stresses induced in the substrate.

Inelastic effects have long been recognized as leading to significant stress relaxation in metallic films. As examples we mention the work of Murakami *et al.* on Pb [22] and the work of Hershkovitz *et al.* on aluminum [23]. Reviews of the deformation mechanisms in thin films have been provided by Koleshko *et al.* [24], by Murakami [25], and by Chaudhari [26]. Kinosita [27] has summarized methods for measuring thin film mechanical properties. Deformation mechanisms include diffusional creep, power-law creep and, at lower temperatures and higher stresses, dislocation glide [25, 26]. As noted above, Isomae [21] used linearly viscous constitutive response for SiO_2 films interacting with silicon substrates.

Concerning plastic deformation of films on substrates by dislocation glide, Hoffman has pointed out that the high stresses along the interface and near the free edge of the film must necessarily lead to plastic flow or fracture, and that the strain gradients are localized near the film edge [3, 28, 29]. Stress–strain curves for gold films measured by Catlin and Walker [30] show a considerable nonlinearity, as do the data of Henning *et al.* on copper and nickel [31].

It is the objective of this report to account for the effect of elastic–plastic relaxation near the free edge and along the film–substrate interface in films which are subjected to a uniform far-field stress (due either to misfit or thermal strain). To simplify the problem, and in view of the studies on stresses in the substrate by Hu [18] and by Isomae [19, 21], we assume that the substrate is rigid, and thus focus our attention exclusively on the film and on the film–substrate interface. We assume that the film is in a state of plane strain, and we account for plastic deformation of the film material via J_2 deformation theory fitted to a linear-power law hardening stress–strain behavior in simple shear. To account for three-dimensional island-like growth (Volmer–Weber growth [32]) and for epitaxial layer growth (Frank and van der Merwe [32]), we consider films whose lateral extent is similar to the thickness of the film or greatly exceeds it. The basic parameters characterizing our model are the ratio of film lateral extent to film thickness, the ratio of misfit to yield strain, and the hardening exponent of the film material.

2. Problem formulation

Figure 1 shows the geometry of a film with thickness h and lateral extent L. The free edge of the film is located along $x=0$, and the film–substrate interface is at $y=0$. For simplicity, and in order to avoid three-dimensional effects, it is assumed that plane-strain conditions prevail along the z direction. For reasons explained in the Introduction, we concentrate our attention on the film and interface. Thus, we assume that the substrate is rigid, and that displacement and traction continuity is satisfied along the interface $y=0$. The sides $x=0$, $x=L$, and $y=h$ are free of tractions. Far from the free edges the film is in a state of balanced biaxial stress, *i.e.* $\sigma_{xx}=\sigma_{zz}$, which, furthermore, is uniform in the y direction.

The film material is taken to be elastic–plastic. Specifically, we assume that in a simple shear test the film material obeys

$$\frac{\varepsilon_{12}}{\varepsilon_0}=\begin{cases}\tau/\tau_0 & \text{if } |\tau|<\tau_0\\ (\tau/\tau_0)^n & \text{if } |\tau|\geq\tau_0\end{cases} \tag{1}$$

where τ_0 is the yield stress in simple shear, ε_0 is the yield strain which is related to τ_0 by $\tau_0=2G\varepsilon_0$, G being the elastic shear modulus, and n is the hardening exponent (Fig. 2). For multiaxial stress states the total strain ε_{ij} is given by

$$\varepsilon_{ij}=\varepsilon_{ij}^{e}+\varepsilon_{ij}^{p}+\varepsilon_{ij}^{T} \tag{2}$$

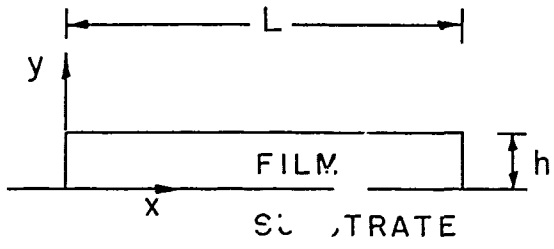

Fig. 1. Film geometry.

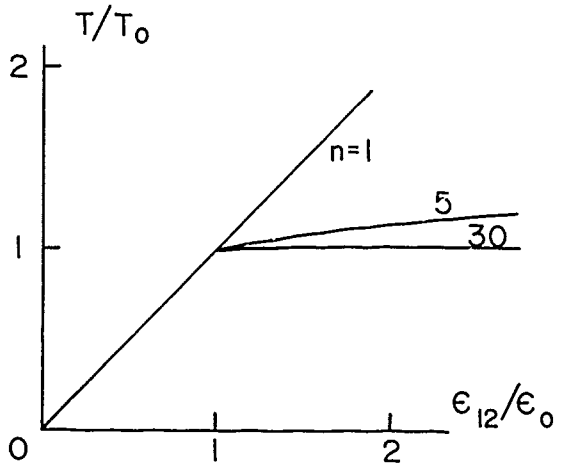

Fig. 2. Linear power-law hardening stress-strain curve in simple shear.

where the elastic strain ε_{ij}^{e} is related to the stress tensor σ_{ij} via the usual linear elastic constitutive response, the plastic strain ε_{ij}^{p} is related to the stress deviator $S_{ij}=\sigma_{ij}-\sigma_{kk}\delta_{ij}/3$ by

$$\varepsilon_{ij}^{p}=fS_{ij} \tag{3}$$

where f is found by invoking J_2 deformation theory, and by fitting eqns. (2), (3) to eqn. (1) with $\varepsilon_{ij}^{T}=0$. Thus, we find that

$$f=\left[\left(\frac{\bar{\varepsilon}}{\varepsilon_0}\right)^{1-1/n}-1\right]\Big/2G \tag{4}$$

where $\bar{\varepsilon}$ is the equivalent shear strain defined as $\bar{\varepsilon}^2=e_{ij}e_{ij}/2$, with e_{ij} the strain deviator. Denoting by τ the equivalent shear stress defined by $\tau^2=S_{ij}S_{ij}/2$, then τ and $\bar{\varepsilon}$ are also related by (1). The last term in eqn. (2) is the misfit strain, which is assumed to consist of only a volumetric component, thus

$$\varepsilon_{ij}^{T}=\varepsilon^{T}\delta_{ij} \tag{5}$$

where δ_{ij} is the Kronecker delta. The assumption that ε_{ij}^{T} is isotropic is exact when ε_{ij}^{T} represents thermal strain due to differential thermal mismatch. For the case of intrinsic stress, the assumption (5) is validated by the physical models of intrinsic stress (such as H_2O vapor, oxygen or impurity absorption in optical thin films [27, 33], or lattice misfit in epitaxial films [34]). For epitaxial films, nevertheless, it may be more appropriate to take $\varepsilon_{xx}^{T}=\varepsilon_{zz}^{T}$, $\varepsilon_{yy}^{T}=0$.

It is convenient to normalize stresses by the yield stress τ_0, strains by the yield strain ε_0, and distances by the film thickness h. Thus, it is clear that the parameters characterizing the present problem are the aspect ratio $L/2h$, the ratio of misfit to yield strain $\varepsilon^{T}/\varepsilon_0$, and the hardening exponent n.

Solving eqns. (2)–(5) for the stresses, we find

$$\sigma_{ij}=\frac{\varepsilon_{ij}}{\eta}+\frac{1}{3}\delta_{ij}\varepsilon_{kk}\left(-\frac{1}{\eta}+\frac{1+\nu}{1-2\nu}\right)-\delta_{ij}\frac{1+\nu}{1-2\nu}\theta \tag{6}$$

where $i, j=1, 2, 3$ and

$$\varepsilon_{zz}=0 \tag{7}$$

from the plane-strain condition. η is defined by

$$\eta=\begin{cases}\bar{\varepsilon}^{(1-1/n)}, & \text{for } \bar{\varepsilon}\geq 1\\ 1, & \text{for } \bar{\varepsilon}<1\end{cases} \tag{8}$$

and ν is the Poisson ratio. The parameter θ is defined by

$$\theta\equiv\varepsilon^{T}/\varepsilon_0 \tag{9}$$

It is immediately clear that the constitutive law of eqns. (6)–(10) is equivalent to that of a nonlinear elastic material. As expected, this is due to the fact that the elastic-plastic response of the film is modeled by using deformation theory of plasticity.

The stresses corresponding to the constitutive law of eqns. (6)–(8) were determined by a displacement-based finite element calculation. Due to the symmetry of the problem, only the domain $0\leq x\leq L/2$ was discretized with the boundary condition that the displacement in the x direction and the shear stress τ_{xy} vanish at $x=L/2$.

The elements used were bilinear isoparametric rectangles with 3×3 Gaussian quadrature. The grid used had approximately 50 nodes in the x direction and 30 nodes in the y direction with higher concentration of elements near the interface and near $x=0$. Convergent solutions were achieved for a given n by using as a first approximation the convergent stress distribution corresponding to the previous value of n. The results for the stress distributions thus determined will be presented and discussed in the next section.

3. Results and discussion

Figures 3 and 4 show the stress distributions σ_{xy} and σ_{yy} versus distance x along the film–substrate interface for several values of the hardening exponent n. To avoid interpolation from the Gaussian quadrature points to $y=0$, we

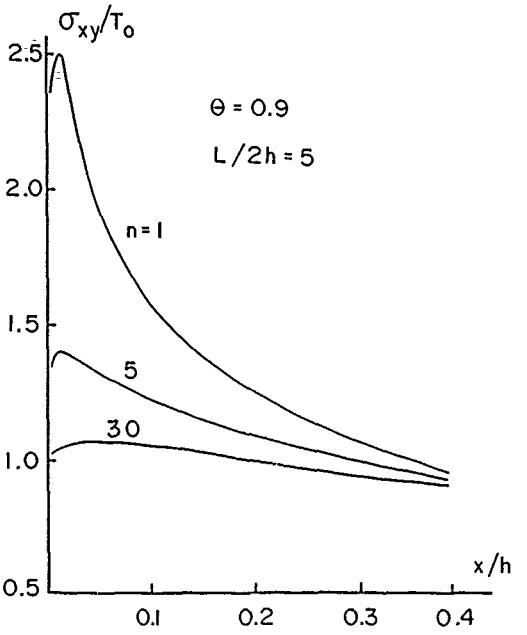

Fig. 3. Shear stress σ_{xy} *vs.* x immediately above the film-substrate interface ($y=0.009h$) for various hardening exponents.

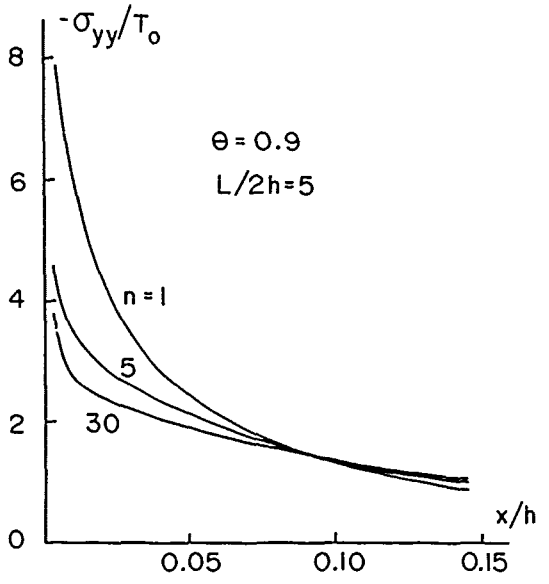

Fig. 4. Peeling stress σ_{yy} *vs.* x immediately above the film-substrate interface ($y=0.009h$) for various hardening exponents.

have plotted the stresses along the centers of the elements closed to the interface, which were located at $y/h=0.009$. These stress distributions can be converted to stress concentrations by picking the maximum value of σ_{xy}/τ_0 (see Fig. 3) or the value of σ_{yy}/τ_0 at the center of the element closest to $x=y=0$ (see Fig. 4), dividing by θ, and

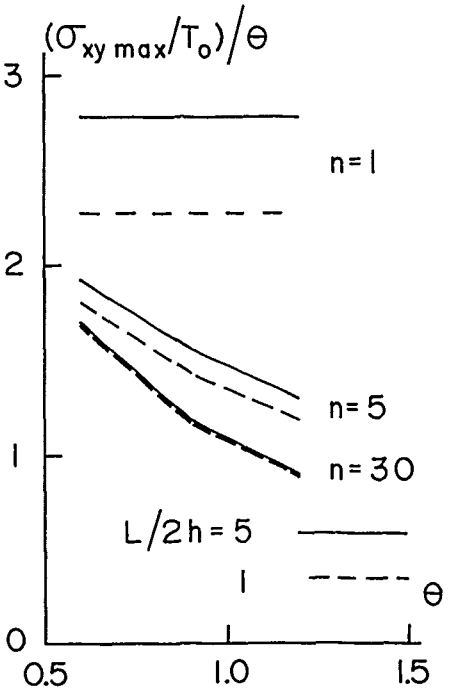

Fig. 5. Non-dimensional shear stress concentration *vs.* non-dimensional load for $n=1, 5, 30$. Solid lines are for thin films ($L/2h=5$). Dashed lines are for thick films ($L/2h=1$).

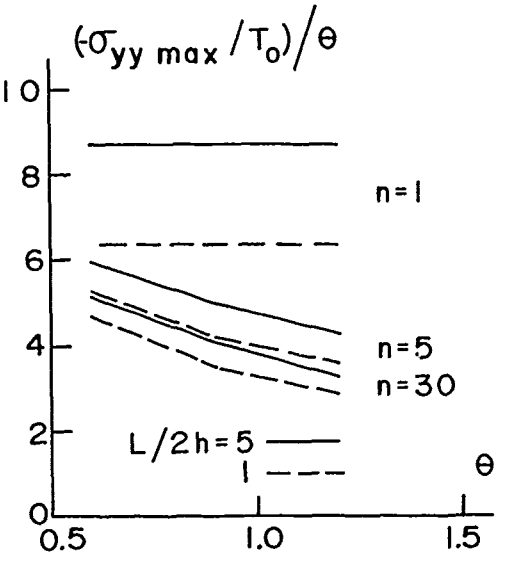

Fig. 6. Non-dimensional peeling stress concentration *vs.* non-dimensional load for $n=1, 5, 30$. Solid lines are for thin films ($L/2h=5$). Dashed lines are for thick films ($L/2h=1$).

by plotting *vs.* θ. The resulting stress concentration factors *vs.* the dimensionless load parameter θ are shown in Figs. 5 and 6 for the shear stress σ_{xy} and for the peeling stress σ_{yy}, respectively, for various values of the hardening exponent n and

for two values of the aspect ratio, 5 and 1, corresponding to thin films ($L \gg h$) and three-dimensional island-like growths ($L \approx h$).

Finally, Figs. 7 and 8 show the development of the dimensions of the plastic zone with the load parameter θ. Specifically, Fig. 7 shows contours of the equivalent shear stress τ for the case of thin films with $n = 30$, for several values of θ; Fig. 8 shows the dependence of the dimensions H, D of the plastic zone on the hardening exponent n for thin films ($L/2h = 5$). In the results shown in Figs. 3–8 the Poisson ratio is taken as 0.3.

It can be easily shown that the far-field material becomes plastic (*i.e.* τ exceeds τ_0) when $\theta = 0.93$. Thus, when $\theta < 0.93$ the plastic deformation is localized near the free edge $x = 0$. As θ approaches 0.93 from below, the extent D of the plastic zone increases rapidly, and extends through the whole of the film as θ exceeds 0.93. Figure 8 shows that the dimension D, H of the plastic zone depend weakly on the hardening exponent n, implying that, for example, linear elastic solutions [9–11, 15, 16] can be used to estimate D and H. On the other hand, as expected, D depends very strongly on the loading parameter θ. Examination of Fig. 7 shows that plastic deformation is localized within a narrow strip which starts at the free edge $x = 0$ and extends parallel to the film–substrate interface. Outside this zone of intense plastic deformation the film material is weakly stressed. If one were to think of plastic deformation in terms of the propagation of interfacial dislocations, Fig. 7 shows that a continuum plasticity approach agrees qualitatively with the fact that interfacial dislocations propagate along the film–substrate interface [32, 34]. Our calculation presently establishes the interface between film and substrate as being extensively deformed into the plastic region. This observation is in agreement with the results of Lau *et al.* [14] in which the angular variation of the stress components resulting from the asymptotic analysis is such that the peeling stress is maximum along the interface.

The stress concentration plots of Figs. 5 and 6 show that bulky films ($L \approx h$, modeling thus island mode of film growth) are in general less stressed than thin films ($L \gg h$, modeling epitaxial mode of film growth [32]). The difference is largest for linear elastic films; it diminishes considerably as hardening diminishes. As the films are progressively stressed into the plastic region, the stress

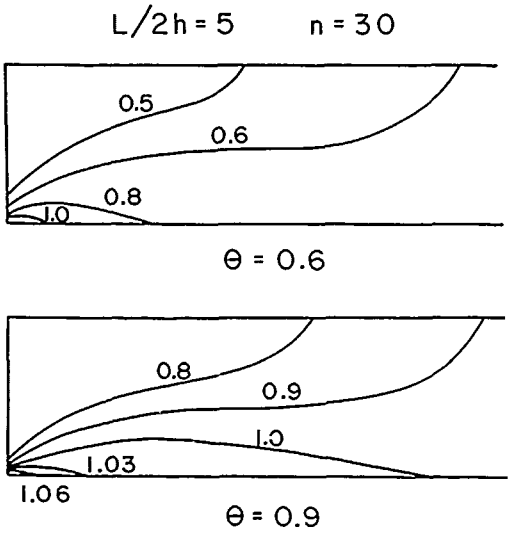

Fig. 7. Contours of equivalent shear stress τ normalized with respect to yield stress τ_0. General yield occurs in the far-field material for $\theta = 0.93$.

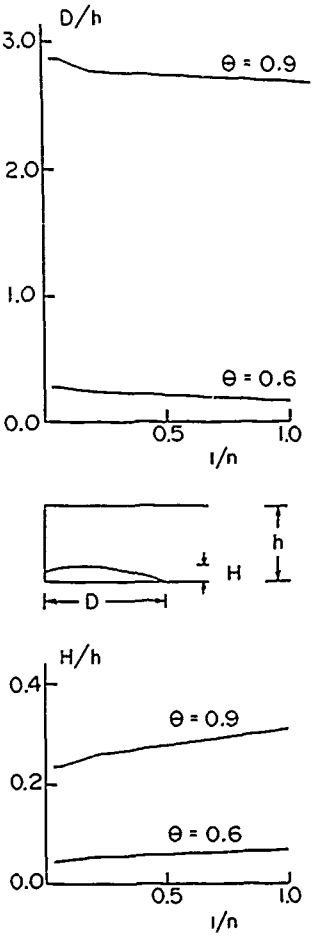

Fig. 8. Variation of extent D and height H of plastic zone vs. strain hardening exponent n. The aspect ratio is $L/2h = 5$.

concentrations diminish as a result of stress relaxation by plastic deformation. Thus, the absolute values of the stresses increase as θ increases, but less rapidly than θ itself.

Figures 3 and 4 show that smaller amount of hardening leads to considerably lower stress values. We note from these figures that within, say, 0.1 h along the interface the stresses exceed considerably the yield stress of the material. Even when $n=30$ the peeling stress is as large as 2–4 τ_0, while the shear stress is no less than τ_0. We note that these stress concentrations are localized within a fraction of the film's thickness from the free edge, and close to the interface (see Fig. 7). As $x/h \to \infty$ both σ_{yy} and σ_{xy} must vanish. When $\theta > 0$ (implying that the far-field material is in compression) the largest value of σ_{yy} is also compressive (Fig. 4), but σ_{yy} changes to tensile with a maximum positive value at a distance of about 0.5–1 thickness along the interface [9–11]. This maximum is diffuse and only a fraction of the far-field stress. It is concluded that when the film is in far-field compression, the anticipated mode of failure is by shearing along the interface. When $\theta > 0$ other modes of failure are also observed (*e.g.* buckling and interfacial delamination [4]). In this context we note that thin polycrystalline metallic films exhibit hardening behavior and yield stress which is quite different from the corresponding quantities for bulk materials. Hoffman [1] has compiled data which show that the hardening (about $1/n$) diminishes as the film thickness increases. Similarly, the yield stress decreases as the thickness increases. Thus, when the thickness is too small, the film may fail in a brittle manner. Such observations are in agreement with experimental observations of Pashley in gold films thinner than 50 nm [35]. For other film materials, such as nickel [1], the plastic and elastic strains at fracture are comparable. The dependence of yield stress on thickness has been modeled by Chaudhari [26, 36] and Ronay [37] who argue that a critical film thickness exists below which plastic flow does not occur and above which the residual elastic strain shows an inverse thickness dependence. When $\theta < 0$ (implying that the far-field film material is in tension), then the large values of the peeling stress along the interface are tensile and considerably exceed the yield stress τ_0 of the film material. We conclude that in this case the anticipated failure mode is by peeling away from the interface. Again, other modes of failure are possible [3].

The use of deformation theory of plasticity to describe the inelastic deformation of the film material is justified by observing that the stresses increase monotonically as the loading parameter θ increases. Furthermore, the calculation presented herein can be used in film growth when h is a monotonically increasing function of time. As discussed above, τ_0 is a decreasing function of h, and $\theta (\equiv \varepsilon^T/\varepsilon_0)$ is a decreasing function of ε_0 or τ_0. We conclude that θ is an increasing function of h, so that deformation theory can be used to model the elastic–plastic deformation of thin films during film growth. Still, deformation theory would be inadequate when significant amounts of unloading are involved. This would be the case when for a film of fixed thickness h the temperature has a sinusoidal dependence on time with a maximum value ΔT such that $\Delta\alpha\Delta T > \varepsilon_0$, $\Delta\alpha$ being the differential thermal mismatch between film and substrate.

All calculations presented herein refer to the case when the angle between the free surface of the film and the interface is $\pi/2$. Once a crack is nucleated (by shearing deformation for $\theta > 0$, and by peeling for $\theta < 0$), the geometry changes radically since now a crack exists along the interface between the film and the substrate. In such a case, the extensive work of Shih and Asaro [38] on cracks between dissimilar elastic–plastic media is to be consulted.

4. Conclusions

Finite element methods were used to determine the stress distributions near the free edge and along the interface in film–substrate assemblies. The film material was assumed to be elastic–plastic characterized by a linear, power-law hardening stress–strain curve in pure shear, and by J_2 deformation theory for multiaxial stress states. The main parameters describing the problem are the hardening exponent n, the ratio of misfit to yield strain, and the aspect ratio of the film. It was found that near the free edge plastic deformation relaxes the elastic stress concentration. Still, near the free edge the shear stresses are no less than the yield stress, and the peeling stresses are at least several times higher than the yield stress. These concentrations are localized within a small fraction (0.1–0.5) of the film thickness from the film's free edge. Far from the free edge the film is in a state of balanced biaxial tension or compression.

The extent of the plastic zone depends weakly on the hardening exponent n, and strongly on the ratio of misfit to yield strain. The zone of plastic deformation is localized within a narrow region along the film–substrate interface, and it propagates parallel to the interface as the misfit strain increases in relation to the yield strain. Plastic deformation reduces the elastic stress concentration both for thin and thick films. When the far-field film material is in compression, the anticipated mode of local failure in the vicinity of the free edge is by shear; when in tension, the local mode of failure is expected to be by peeling. The applicability of deformation theory of plasticity was justified since stresses increase monotonically with the misfit strain. For film growth, deformation theory is again applicable since the yield strain is a decreasing function of film thickness.

Acknowledgments

This work was suported by the Office of Naval Research via grant N00014-87-K-0488, and by the National Science Foundation via a 1988 Presidential Young Investigator Award.

References

1 R. W. Hoffman, in G. Hass and R. E. Thun (eds.), *Physics of Thin Films*, Vol. 3, Academic Press, New York, 1966, p. 211.
2 K. L. Chopra, *Thin Film Phenomena*, McGraw-Hill, New York, 1969.
3 R. W. Hoffman, *Mater. Sci. Eng., 53* (1982) 37.
4 A. G. Evans and J. W. Hutchinson, *Int. J. Solids Struct., 20* (1984) 455.
5 D. B. Marshall and A. G. Evans, *J. Appl. Phys., 56* (1984) 2632.
6 R. R. Austin, R. Michaud, A. H. Guenther, and J. Putman, *Appl. Optics, 12* (1973) 665.
7 R. Rosenberg, T.-S. Kuan, and H. J. Hovel, *Phys. Today, 33* (1980) 40.
8 J. K. Howard, *J. Vac. Sci. Technol. A, 4* (1986) 1.
9 B. J. Aleck, *J. Appl. Mech., 16* (1949) 118.
10 R. Zeyfang, *Solid State Electron., 14* (1971) 1035.
11 I. A. Blech and A. A. Levi, *J. Appl. Mech., 48* (1981) 442.
12 M. L. Williams, *J. Appl. Mech., 19* (1952) 526.
13 V. L. Hein and F. Erdogan, *Int. J. Fract. Mech., 48* (1981) 442.
14 C. W. Lau, A. Rahman and F. Delale, in W. E. Moddeman *et al.* (eds.), *Technology of Glass, Ceramic, or Glass-Ceramic to Metal Sealing*, ASME MD Vol. 4, 1987, p. 89.
15 E. Suhir, *J. Appl. Mech., 53* (1986) 657.
16 E. Suhir, *Calculated Thermally Induced Stresses in Adhesively Bonded and Soldered Assemblies*, AT&T Bell Labs, 1986, to be published.
17 W. Yang and L. B. Freund, *Shear Stress Concentration Near the Edge of a Thin Film*, Brown University, 1986, to be published.
18 S. M. Hu, *J. Appl. Phys., 50* (1979) 4661.
19 S. Isomae, *J. Appl. Phys., 52* (1981) 2782.
20 J. C. Lambropoulos and S.-M. Wan, in R. C. Sundahl *et al.* (eds.), *Electronic Packaging Materials Science, Mater. Res. Soc. Symp. Proc., 108* (1988) 399.
21 S. Isomae, *J. Appl. Phys., 57* (1985) 216.
22 M. Murakami, *Acta Metall., 26* (1978) 175.
23 M. Hershkovitz, I. A. Blech and Y. Komen, *Thin Solid Films, 130* (1985) 87.
24 V. M. Koleshko, V. F. Belitsky and I. V. Kiryushin, *Thin Solid Films, 142* (1986) 199.
25 M. Murakami, in D. E. Schuele and R. W. Hoffman (eds.), *Critical Reviews in Solid State and Materials Sciences*, Vol. 11, CRC, Cleveland, OH, 1984, p. 317.
26 P. Chaudhari, *IBM J. Res. Dev., 13* (1969) 197.
27 K. Kinoshita, *Thin Solid Films, 12* (1972) 17.
28 R. W. Hoffman, *Surf. Interface Anal., 3* (1981) 62.
29 R. W. Hoffman, *Thin Solid Films, 89* (1982) 155.
30 A. Cathin and W. P. Walker, *J. Appl. Phys., 31* (1960) 2135.
31 C. A. Henning, F. W. Boswell and J. M. Corbett, *Acta Metall., 23* (1975) 177.
32 R. W. Vook, *Opt. Eng., 23* (1984) 343.
33 H. K. Pulker and J. Maser, *Thin Solid Films, 59* (1979) 65.
34 I. Markov and S. Stoyanov, *Contemp. Phys., 28* (1987) 267.
35 D. W. Pashley, *Proc. R. Soc. London, Ser. A, 255* (1960) 218.
36 P. Chaudhari, *Philos. Mag. A, 39* (1979) 507.
37 M. Ronay, *Philos. ,Mag. A, 40* (1979) 145.
38 C. F. Shih and R. J. Asaro, *Elastic–Plastic Analysis of Cracks on Bimaterial Interfaces. Part I. Small Scale Yielding*, Brown University, 1987.

Materials Science and Engineering, A107 (1989) 177–184

On Elasticity Solutions for Cracks on Bimaterial and Bicrystal Interfaces*

J. L. BASSANI and J. QU

Department of Mechanical Engineering and Applied Mechanics, University of Pennsylvania, Philadelphia, PA 19104 (U.S.A.)

(Received June 1, 1988)

Abstract

The two-dimensional problem of an interface crack between two anisotropic elastic solids is considered. A necessary and sufficient condition for no oscillations in the singular crack-tip fields is given, and then bicrystals associated with tilt boundaries that satisfy this condition are considered. Explicit solutions for a finite crack along interfaces satisfying this condition are given.

1. Introduction

The two-dimensional interface crack problem in small-strain linear elasticity is the focus of this paper. For brevity, certain mathematical details that are found in two recent papers [1, 2] are omitted, while the emphasis here is on the important results. The reader also is referred to [1, 2] for extensive citations to references on related problems. Particular attention is given in this paper to bimaterials formed by misorienting identical anisotropic solids on either side of the interface. These bimaterials include bicrystals, for example.

Solutions to the classical interface crack problem, in general, display oscillations in the singular crack-tip stress field and interpenetration of the crack faces. Obviously, solutions of this kind can only be valid outside the predicted interpenetration zone. This zone typically is very small compared with the crack length under remote tensile loading, but can be a large fraction of the crack length under shear loading [3]. Several recent papers have focused on these oscillations in the near-tip fields for interface cracks between different isotropic solids, see, for example, refs. 3–5.

In this paper we consider cracks along the interface between anisotropic solids; related investigations include those of Willis [6] and Ting [7]. Since crystals are elastically anisotropic, bicrystal interfaces or grain boundaries between two misoriented but otherwise identical single crystals are a special class of interfaces between dissimilar anisotropic media. A bicrystal is represented through transformations of the reference lattice into two different lattice orientations on either side of the interface. If the transformations are pure rotations about a common axis lying in the interface, the interface is referred to as a tilt boundary. Grain boundary cracks where the crack front is parallel to the tilt axis also are considered.

In this paper a necessary and sufficient condition is given for a non-oscillatory, two-dimensional crack-tip stress field for general bimaterials. Then grain boundary cracks where the crack front is parallel to the tilt axis are considered. In this case, it is seen that the crack-tip stress field has the standard square root singularity without oscillations if the in-plane and anti-plane deformations are decoupled in the interface coordinate system. This result holds for both geometrically symmetric and asymmetric tilt boundaries. Examples are given for f.c.c. bicrystals. Finally, we consider the problem of a finite crack on a bimaterial interface.

2. General solutions in 2D anisotropic elasticity

Consider a two-dimensional deformation in which the three components of displacement depend only on in-plane coordinates, *i.e.* $u_i = u_i(x_1, x_2)$ and $i = 1, 2, 3$ so that $\varepsilon_{33} = 0$. The general anisotropic stress–strain relation is $\sigma_{ij} = C_{ijkl}\varepsilon_{kl}$. We adopt the convention that the Roman indices take on the values 1, 2 and 3 while Greek indices take on the values 1 and 2 only.

*Paper presented at the symposium on Interfacial Phenomena in Composites: Processing, Characterization, and Mechanical Properties, Newport, RI, June 1–3, 1988.

0921-5093/89/$3.50

© Elsevier Sequoia/Printed in The Netherlands

and summation is implied for repeated indices. Then the Navier equations that govern the small-strain elasticity solutions are

$$C_{iak\beta}\frac{\partial^2 u_k}{\partial x_\beta \partial x_a}=0 \tag{1}$$

Define the Fourier transform pair

$$\hat{f}(\xi)=\frac{1}{(2\pi)^{1/2}}\int_{-\infty}^{\infty} f(x)\exp \mathrm{i}\xi x\,\mathrm{d}x \tag{2a}$$

$$f(x)=\frac{1}{(2\pi)^{1/2}}\int_{-\infty}^{\infty} \hat{f}(\xi)\exp -\mathrm{i}\xi x\,\mathrm{d}x \tag{2b}$$

and apply the transform to eqn. (1) over x_1 to obtain

$$\xi^2 C_{i1k1}\hat{u}_k+\mathrm{i}\xi(C_{i2k1}+C_{i1k2})\frac{\partial \hat{u}_k}{\partial x_2} - C_{i2k2}\frac{\partial^2 \hat{u}_k}{\partial x_2^2}=0\,(i=1,3) \tag{3}$$

or, in matrix notation

$$\xi^2\mathbf{Q}\hat{\boldsymbol{u}}+\mathrm{i}\xi(\mathbf{R}+\mathbf{R}^{\mathrm{T}})\frac{\partial \hat{\boldsymbol{u}}}{\partial x_2}-\mathbf{T}\frac{\partial^2 \hat{\boldsymbol{u}}}{\partial x_2^2}=0 \tag{4}$$

where the superscript T stands for the transpose and

$$\mathbf{Q}=(Q_{ik})=(C_{i1k1})=\begin{bmatrix} C_{1111} & C_{1112} & C_{1113}\\ C_{1211} & C_{1212} & C_{1213}\\ C_{1311} & C_{1312} & C_{1313}\end{bmatrix} \tag{5a}$$

$$\mathbf{R}=(R_{ik})=(C_{i1k2})=\begin{bmatrix} C_{1112} & C_{1122} & C_{1123}\\ C_{1212} & C_{1222} & C_{1223}\\ C_{1312} & C_{1322} & C_{1323}\end{bmatrix} \tag{5b}$$

$$\mathbf{T}=(T_{ik})=(C_{i2k2})=\begin{bmatrix} C_{1212} & C_{1222} & C_{1223}\\ C_{2212} & C_{2222} & C_{2223}\\ C_{2312} & C_{2322} & C_{2323}\end{bmatrix} \tag{5c}$$

Given that C_{ijkl} is positive definite with the usual symmetries, Q and T are symmetric and positive definite while R is not; these three matrices have been introduced by Ting [7].

Equation (4) permits solutions of the form

$$\hat{\mathbf{u}}=\boldsymbol{a}\exp(-\mathrm{i}\eta x_2) \tag{6}$$

provided that $\boldsymbol{a}$ and $\eta=p\xi$ satisfy the following eigenvalue equation

$$[\mathbf{Q}+p_n(\mathbf{R}+\mathbf{R}^{\mathrm{T}})+p_n^2\mathbf{T}]\boldsymbol{a}_n=0$$

$$n=1,6 \text{ (no sum on } n) \tag{7}$$

Since Q, R and T are real and are functions only of the material constants C_{ijkl}, p_n and $\boldsymbol{a}_n$ are independent of ξ. Furthermore, $\bar{\boldsymbol{a}}_n$ corresponds to $\bar{p}_n$. Finally, we introduce two matrices P and A by

$$\mathbf{P}=\mathrm{diag}[p_1,p_2,p_3] \tag{8a}$$

$$\mathbf{A}=[\boldsymbol{a}_1,\boldsymbol{a}_2,\boldsymbol{a}_3] \tag{8b}$$

and rewrite eqn. (7) as

$$\mathbf{QA}+\mathbf{RAP}=-(\mathbf{R}^{\mathrm{T}}\mathbf{A}+\mathbf{TAP})\mathbf{P} \tag{9}$$

The general solution to (4) is obtained from superposition of the six particular solutions when the roots are distinct, which from eqns. (6) and (8) can be written as

$$\hat{\boldsymbol{u}}(\xi,x_2)=(2\pi)^{1/2}(\mathbf{AF}\boldsymbol{f}+\bar{\mathbf{A}}\mathbf{G}\boldsymbol{g})H(\xi) +(2\pi)^{1/2}(\bar{\mathbf{A}}\mathbf{F}\boldsymbol{f}+\mathbf{AG}\boldsymbol{g})H(-\xi) \tag{10}$$

where $H(\xi)$ is the Heaviside step function and F and G are the diagonal matrices

$$\mathbf{F}(\xi,x_2)=\mathrm{diag}[\exp(-\mathrm{i}\eta_1 x_2), \exp(-\mathrm{i}\eta_2 x_2),\exp(-\mathrm{i}\eta_3 x_2)] \tag{11}$$

$$\mathbf{G}(\xi,x_2)=\mathrm{diag}[\exp(-\mathrm{i}\bar{\eta}_1 x_2), \exp(-\mathrm{i}\bar{\eta}_2 x_2),\exp(-\mathrm{i}\bar{\eta}_3 x_2)] \tag{12}$$

Recall that ξ and η are related through the eigenvalue $p=\eta/\xi$. In (10), $\boldsymbol{f}$ and $\boldsymbol{g}$ are two vector functions of ξ to be determined from the boundary conditions of a given problem.

3. Infinite bimaterial

Consider a crack along the interface (x_1-x_3 plane) formed by joining two generally anisotropic elastic half spaces. The cartesian coordinate system is centered at the crack tip with the x_3 axis along the crack front and the x_2 axis normal to the interface; see Fig. 1. Let the elastic constants of the two half spaces be $C_{ijkl}^{(1)}$ and $C_{ijkl}^{(2)}$, and then

$$C_{ijkl}=\begin{cases} C_{ijkl}^{(1)} & x_2>0\\ C_{ijkl}^{(2)} & x_2<0\end{cases} \tag{13}$$

Integral representations of the displacements and stresses in the infinite bimaterial, which

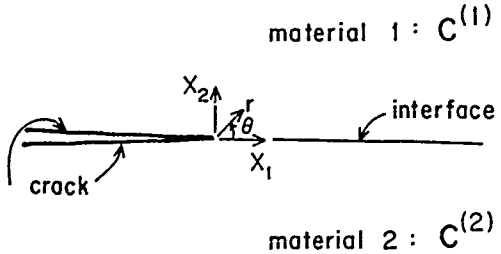

Fig. 1. Interface crack.

follow by inverting (10), are [1, 2]

$$u_1(x_1,x_2)=\tilde{\mathbf{A}}_1\int_0^\infty \mathbf{G}_1(\xi,x_2)g_1(\xi)\exp(-i\xi x_1)d\xi + \mathbf{A}_1\int_0^\infty \mathbf{G}_1(-\xi,x_2)g_1(-\xi)\exp(i\xi x_1)d\xi \tag{14a}$$

$$u_2(x_1,x_2)=\mathbf{A}_2\int_0^\infty \mathbf{F}_2(\xi,x_2)f_2(\xi)\exp(-i\xi x_1)d\xi + \tilde{\mathbf{A}}_2\int_0^\infty \mathbf{F}_2(-\xi,x_2)f_2(-\xi)\exp(i\xi x_1)d\xi \tag{14b}$$

where **A** is obtained from (7)–(9), and

$$\mathbf{G}_1(\xi,x_2)=\mathrm{diag}\{\exp(-i\tilde{\eta}_1^{(1)}x_2), \exp(-i\tilde{\eta}_2^{(1)}x_2),\exp(-i\tilde{\eta}_3^{(1)}x_2)\} \tag{15a}$$

$$\mathbf{F}_2(\xi,x_2)=\mathrm{diag}\{\exp(-i\eta_1^{(2)}x_2), \exp(-i\eta_2^{(2)}x_2),\exp(-i\eta_3^{(2)}x_2)\} \tag{15b}$$

$$\eta_n^{(j)}=\begin{cases} p_n^{(j)}\xi & \xi>0 \\ \tilde{p}_n^{(j)}\xi & \xi<0 \end{cases} \tag{15c}$$

In (14), $g_1(\xi)$ and $f_2(\xi)$ are unknown vectors to be determined by boundary conditions. The stress vector

$$\tau_j(x_1,x_2)=\{\sigma_{12}^{(j)},\sigma_{22}^{(j)},\sigma_{32}^{(j)}\}^{\mathrm{T}} \qquad j=1,2 \tag{16}$$

is given from the following integral expressions [1, 2]

$$\tau_1(x_1,x_2)=-i\tilde{\mathbf{B}}_1\int_0^\infty \xi\mathbf{G}_1(\xi,x_2)g_1(\xi)\exp(-i\xi x_1)d\xi + i\mathbf{B}_1\int_0^\infty \xi\mathbf{G}_1(-\xi,x_2)g_1(-\xi)\exp(i\xi x_1)d\xi \tag{17a}$$

$$\tau_2(x_1,x_2)=-i\mathbf{B}_2\int_0^\infty \xi\mathbf{F}_2(\xi,x_2)f_2(\xi)\exp(-i\xi x_1)d\xi + i\tilde{\mathbf{B}}_2\int_0^\infty \xi\mathbf{F}_2(-\xi,x_2)f_2(-\xi)\exp(i\xi x_1)d\xi \tag{17b}$$

where

$$\mathbf{B}=\mathbf{R}^{\mathrm{T}}\mathbf{A}+\mathbf{T}\mathbf{A}\mathbf{P}=-(\mathbf{Q}\mathbf{A}+\mathbf{R}\mathbf{A}\mathbf{P})\mathbf{P}^{-1} \tag{18a, b}$$

Expressions similar to eqns. (16) and (17) for the other stress components can also be written down. In eqns. (13)–(17), tensor quantities with subscript 1 or 2 correspond to material 1 (upper half space) or material 2 (lower half space), respectively, while components are distinguished by superscripts in parentheses.

Finally, certain properties of the **A** and **B** matrices are noted. First, from eqns. (10) and (14), we see that the displacement vector is the linear superposition of columns of **A**. From eqns. (17), the stresses are expressed in terms of **B**. It has been shown by Stroh [8] that when the six roots of (7) are all distinct that the matrices **A** and **B** are non-singular. However, in some cases even when there are repeated roots, **A** and **B** may still be non-singular as long as the invariant subspace corresponding to that repeated root is complete, *i.e.* the number of linear independent eigenvectors in that subspace is equal to the multiplicity of those roots. Detailed discussions of these degenerated cases may be found from the references cited by Ting [7]. Secondly, $\mathbf{A}\mathbf{B}^{-1}$ is anti-Hermitian, *i.e.* $(\mathbf{A}\mathbf{B}^{-1})^{\mathrm{T}}=-\bar{\mathbf{A}}\bar{\mathbf{B}}^{-1}$ [8]. Thus, the matrix **M** defined as

$$\mathbf{M}^{-1}=i\mathbf{A}\mathbf{B}^{-1} \tag{19}$$

is Hermitian. Moreover, **M** is positive definite. Thirdly, since the vector a_n is uniquely determined by (7) up to an arbitrary multiplicative constant, it can be properly normalized so that the following orthogonality relation holds [7]

$$\mathbf{A}^{\mathrm{T}}\mathbf{B}+\mathbf{B}^{\mathrm{T}}\mathbf{A}=\mathbf{I} \tag{20}$$

4. Singularities at an interface crack tip

Let $x_1=0=x_2$ denote the crack tip, and let r and θ denote the crack-tip polar coordinates where $\theta=0$ along the interface and $\theta=\pm\pi$ along the crack surface as depicted in Fig. 1. The boundary conditions for a traction-free crack with

continuous displacements and tractions across the bimaterial interface are

$$t_1(x_1,0^+)=\mathbf{0} \qquad t_2(x_1,0^-)=\mathbf{0} \qquad x_1<0 \quad (21a)$$

$$u_1(x_1,0)=u_2(x_1,0) \qquad x_1>0 \quad (21b)$$

$$t_1(x_1,0)=t_2(x_1,0) \qquad x_1>0 \quad (21c)$$

To investigate the singular behavior near the crack tip we assume that asymptotically as $r\to 0$

$$u_k(x_1,0^\pm)=\begin{cases}|x_1|^{\delta+1}(\mathbf{A}_k h_k+\bar{\mathbf{A}}_k\bar{h}_k) & x_1>0\\ -|x_1|^{\delta+1}(\exp\pm i\pi\delta\,\mathbf{A}_k h_k & \\ \quad+\exp\mp i\pi\delta\,\bar{\mathbf{A}}_k\bar{h}_k) & x_1<0\end{cases} \quad (22)$$

($k=1,2$; no sum over k)

and

$$t_k(x_1,0^\pm)=$$

$$\begin{cases}(\delta+1)|x_1|^{\delta}(\mathbf{B}_k h_k+\bar{\mathbf{B}}_k\bar{h}_k) & x_1>0\\ -(\delta+1)|x_1|^{\delta}(\exp\pm i\pi\delta\,\mathbf{B}_k h_k & \\ \quad+\exp\mp i\pi\delta\,\bar{\mathbf{B}}_k\bar{h}_k) & x_1<0\end{cases} \quad (23)$$

($k=1,2$; no sum over k)

For non-trivial solutions of the form (22) and (23), the order of the singularity, δ, must satisfy the following characteristic equation [1, 7]

$$\|(1-\exp i2\pi\delta)\mathbf{W}+i(1-\exp i2\pi\delta)\mathbf{D}\|=0 \quad (24)$$

where the real matrices

$$\mathbf{W}=-\mathrm{Re}(\mathbf{A}_1\mathbf{B}_1^{-1}-\bar{\mathbf{A}}_2\bar{\mathbf{B}}_2^{-1}) \quad (25a)$$

$$\mathbf{D}=-\mathrm{Im}(\mathbf{A}_1\mathbf{B}_1^{-1}-\bar{\mathbf{A}}_2\bar{\mathbf{B}}_2^{-1}) \quad (25b)$$

The explicit solution to (24) is [7]

$$\delta=-\tfrac{1}{2}\pm i\gamma \quad (26a)$$

where

$$\gamma=\frac{1}{2\pi}\ln\left(\frac{1+\beta}{1-\beta}\right) \quad (26b)$$

$$\beta=\{-\tfrac{1}{2}\,\mathrm{tr}[(\mathbf{W}\mathbf{D}^{-1})^2]\}^{1/2} \quad (26c)$$

4.1. Nature of singularity

It is readily seen from eqn. (26) that the oscillatory behavior ($\delta\neq 0$ or $\beta\neq 0$) is generally found when material 1 and 2 differ, *i.e.* when W and D are non-zero. Ting [7] has demonstrated the following invariance: once the relative orientation of the anisotropic solids on either side of the interface is specified, the order of the singularity δ is the same for all interfaces between those solids that contain the x_3-axis, where, as before, the crack front is parallel to the x_3-axis.

The following theorem is proven in Section 3 of ref. 1 and is stated here without proof:

Theorem: A necessary and sufficient condition such that δ in (22)-(24) is real is $\mathbf{W}=\mathbf{0}$. Then, $\gamma=0$ in (26) and the crack-tip fields are not oscillatory.

When the two half spaces are distinct but isotropic, β in eqn. (26b,c) simplifies to [1, 3]

$$\beta=\tfrac{1}{2}\frac{\mu_1(1-2\nu_2)-\mu_2(1-2\nu_1)}{\mu_1(1-\nu_2)+\mu_2(1-\nu_1)} \quad (27)$$

where μ_i and ν_i are shear moduli and Poisson's ratio in the respective materials, so that $\gamma=0$ if

$$\frac{1-2\nu_2}{\mu_2}=\frac{1-2\nu_1}{\mu_1} \quad (28)$$

Therefore, when the materials are incompressible, *i.e.* $\nu_1=\nu_2=1/2$, $\beta=0$ so that $\gamma=0$ in (26) and no oscillation is found.

In the next section, we consider an important class of interfaces that make $\mathbf{W}=\mathbf{0}$. These include, for example, certain grain boundaries between bicrystals.

5. Cracks on tilt boundaries

A so-called tilt boundary between two misoriented but otherwise identical single crystals (or misoriented anisotropic solids) has the property that the elastic modulus tensor C on one side of the boundary (interface) can be obtained from that on the other side by a rotation transformation about an axis lying in the boundary. Figure 2 schematically shows such a boundary, where the components of C of material 1 in the (x^1, y^1, z^1) coordinates are the same as the components of C of material 2 in the (x^2, y^2, z^2) coordinates. These (x^A, y^A, z^A) coordinates are most naturally chosen to be the lattice coordinates. However, in the bicrystal coordinates (x_1, x_2, x_3), where $x_2=0$ is the interface plane and the crack front is parallel to the x_3 or tilt axis, C_{ijkl}^1 and C_{ijkl}^2 in (13) differ from reference moduli C_{ijkl}^R only by rotations about the x_3-axis of θ_1 and θ_2, respectively, the misorientation angles. For a given crystal class these reference

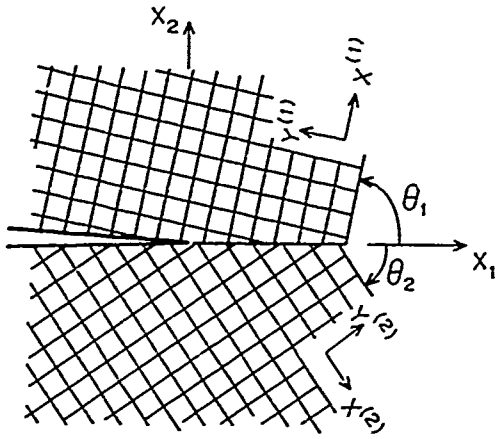

Fig. 2. Grain boundary crack.

moduli may be defined by choosing a particular tilt axis and plane containing that axis from which the tilt angles are measured. Obviously, when $\theta_1 = \theta_2 = 0$, there is no distinct interface.

For equal tilts with respect to the interface plane, that is $\theta_1 = \theta_2$, we refer to the bicrystal as being geometrically symmetric (GS). The GS tilt boundaries are distinct from what we term mechanically symmetric (MS) tilt boundaries, where the latter involve a mirror symmetry in anisotropic elastic properties about the interface plane and traditionally are referred to by crystallographers simply as symmetric tilt boundaries. For (MS) tilt boundaries the 1123, 2223, 3323, 1112, 2212, 3312, 2313, and 1312 components of the reference moduli $C_{ijkl}^{(R)}$ must be zero. Furthermore, in this case when the loading is normal to the interface, *i.e.* Mode I, the solution also has mirror symmetry: $u_i(x_1, x_2) = (1 - 2\delta_{2i})\, u_i(x_1, -x_2)$. The distinction between (GS) and (MS) is elaborated on below.

For cracks on tilt boundaries where the in-plane and anti-plane deformations are decoupled in the interface coordinate system, the singularity is of the standard square-root type with no oscillations, as shown in [1]. By the decoupling between in-plane and anti-plane deformations, we mean $C_{1123} = C_{1113} = C_{2223} = C_{2213} = C_{3323} = C_{3313} = C_{2312} = C_{1312} = 0$, and the stress–strain relation is

$$\begin{bmatrix} \sigma_{11} \\ \sigma_{22} \\ \sigma_{33} \\ \sigma_{23} \\ \sigma_{13} \\ \sigma_{12} \end{bmatrix} = \begin{bmatrix} C_{1111} & C_{1122} & C_{1133} & 0 & 0 & C_{1112} \\ & C_{2222} & C_{2233} & 0 & 0 & C_{2212} \\ & & C_{3333} & 0 & 0 & C_{3312} \\ & & & C_{2323} & C_{2313} & 0 \\ & \text{symmetry} & & & C_{1313} & 0 \\ & & & & & C_{1212} \end{bmatrix} \begin{bmatrix} \varepsilon_{11} \\ \varepsilon_{22} \\ \varepsilon_{33} \\ 2\varepsilon_{23} \\ 2\varepsilon_{13} \\ 2\varepsilon_{12} \end{bmatrix} \tag{29}$$

This decoupling condition must hold for $C_{ijkl}^{(1)}$, $C_{ijkl}^{(2)}$, and $C_{ijkl}^{(R)}$ since if it holds for one it also holds for the other two which only differ by a rotation about the x_3-axis. With decoupling it is seen that the in-plane strains ε_{11}, ε_{22} and ε_{12} do not produce shear stresses σ_{13} and σ_{23}, and similarly the out-plane shear strains ε_{13} and ε_{23} will not produce any in-plane stresses. Furthermore, since for the two-dimensional problems under consideration Q, R, and T in (5) do not depend on C_{3323} and C_{3313}, the decoupling requirements for no oscillations can be relaxed to include non-zero C_{3323} and C_{3313}.

5.1. *Examples*

Bicrystals from simple crystal classes associated with tilt boundaries that satisfy the decoupling condition must necessarily have high symmetry orientations of the tilt axis. For example, in f.c.c. and b.c.c. crystals this includes ⟨100⟩ and ⟨110⟩ tilt axes, and for h.c.p. crystals tilt axes on a basal plane or on a prismatic plane parallel to the *c*-axis also satisfy the decoupling condition.

On the other hand, for a given anisotropy that satisfies the decoupling condition but is otherwise arbitrary, *e.g.* $C_{1121} \neq 0$ in the reference coordinates, one can show that the bicrystal is not necessarily mechanically symmetric (MS). In the mechanically symmetric case where the properties have mirror symmetry about $x_2 = 0$, components of C in the fixed interface coordinates where the index 2 appears an odd number of times, *e.g.* C_{2223}, have opposite sign on either side of the interface, or as noted above eight components of C_{ijkl}^{R} must vanish. As a specific example, consider f.c.c. copper crystals with $C_{1122}/C_{1111} = 0.722$ and $C_{1212}/C_{1111} = 0.447$ in the lattice coordinates. A bicrystal formed by tilting from the $(1\bar{2}0)$ plane by $\theta_1 = \theta_2 = \pi/6$ about the [001] tilt axis certainly satisfies the decoupling condition but is not mechanically symmetric since the reference $(1\bar{2}0)$ plane is not a symmetry plane.

We also note that a MS bicrystal (*i.e.* the interface plane is a plane of mirror symmetry) does not necessarily satisfy the decoupling condition, and therefore can have oscillations in the crack-

tip fields. Consider copper crystals tilted from the (010) plane by $\theta_1 = \theta_2 = \pi/6$ about the [102] tilt axis. This bicrystal satisfies MS (crystallographic symmetry) but not the decoupling conditions since $\mathbf{W} \neq \mathbf{0}$. In this case $\gamma = 0.0126$ in (26). Even though mirror symmetry in the displacement fields leads to zero shear strains along the interface for loading normal to the interface (mode I), the shear stresses are not necessarily zero along the interface.

6. Griffith crack on interfaces for which W = 0

Consider a Griffith crack of length $2a$ along the interface between two semi-infinite anisotropic, linearly elastic solids. The elastic material constants of the inhomogeneous composite solid are given in eqn. (13). The crack tips lie along the interface $x_2 = 0$ at $x_1 = a, -a$. Through linear superposition, the solution corresponding to loading at infinity can be obtained from the solution for loading along the crack faces by self-equilibrated tractions. Even in the case of uniform tractions at infinity, *e.g.* σ_{12}^{∞}, σ_{22}^{∞}, σ_{32}^{∞}, this superposition is simple only if certain combinations of σ_{11}^{∞}, σ_{13}^{∞} and σ_{33}^{∞} are also applied [9]. These latter stress components are discontinuous across the interface. This is a generalization of the isotropic case, where only a discontinuous σ_{11}^{∞} needs to be applied [10].

Let $\boldsymbol{t}(x_1)$ and $-\boldsymbol{t}(x_1)$ denote the traction vectors on the upper and lower surfaces of the crack, respectively. Then, the boundary conditions for the Griffith crack of length $2a$ are

$$\boldsymbol{u}_1(x_1, 0^-) = \boldsymbol{u}_2(x_1, 0^+) \qquad |x_1| > a, \quad (30)$$

$$\boldsymbol{\tau}_1(x_1, 0^-) = \boldsymbol{\tau}_2(x_1, 0^+) \qquad |x_1| < \infty, \quad (31)$$

$$\boldsymbol{\tau}_1(x_1, 0^-) = \boldsymbol{\tau}_2(x_1, 0^+) = -\boldsymbol{t}(x_1) \qquad |x_1| < a, \quad (32)$$

$$|\boldsymbol{\tau}_1(x_1, x_2)| \to 0 \qquad \text{as } |x| \to \infty, \ x_2 > 0, \quad (33a)$$

$$|\boldsymbol{\tau}_2(x_1, x_2)| \to 0 \qquad \text{as } |x| \to \infty, \ x_2 < 0, \quad (33b)$$

where the stress vectors $\boldsymbol{\tau}_j$ are defined in eqn. (16). In eqns. (30)–(33), as before, the tensor quantities with subscript 1 and 2 correspond to material 1 (upper half space) and material 2 (lower half space), respectively, while components are distinguished by superscripts in parentheses.

Applying these boundary conditions to the general integral expressions given in eqns. (14) and (17) leads to dual integral equations for the unknown functions f_j and g_j as given by Bassani and Qu [2]. In the general case, $\mathbf{W} \neq \mathbf{0}$, these equations are coupled. In this section we focus on the finite crack on an interface for which $\mathbf{W} = \mathbf{0}$ in which case the dual integral equations are decoupled.

Define

$$\boldsymbol{h}_a(\xi) = \mathrm{Re}\{\mathbf{B}_2 \boldsymbol{f}_2(\xi)\} \quad (34a)$$

$$\boldsymbol{h}_s(\xi) = \mathrm{Im}\{\mathbf{B}_2 \boldsymbol{f}_2(\xi)\} \quad (34b)$$

so that

$$\boldsymbol{h} = \boldsymbol{h}_a + i\boldsymbol{h}_s = \mathbf{B}_2 \boldsymbol{f}_2(\xi) \quad (34c)$$

In the case where $\mathbf{W} = \mathbf{0}$ the dual integral equations that result from eqns. (14), (17), (30)–(33) with (34) are

$$\int_0^{\infty} [\boldsymbol{h}_s(\xi)\cos(\xi x_1) - \boldsymbol{h}_a(\xi)\sin(\xi x_1)]\,\mathrm{d}\xi = \mathbf{0} \qquad |x_1| > a \quad (35a)$$

$$\int_0^{\infty} \xi[\boldsymbol{h}_s(\xi)\cos(\xi x_1) - \boldsymbol{h}_a(\xi)\sin(\xi x_1)]\,\mathrm{d}\xi = -\tfrac{1}{2}\boldsymbol{t}(x_1) \qquad |x_1| < a \quad (35b)$$

By separating the traction into antisymmetric and symmetric parts about $x_1 = 0$, respectively, it is easily shown that the solutions to eqns. (35a) and (35b) are equivalent to solutions to

$$\int_0^{\infty} \boldsymbol{h}_a(\xi)\sin(\xi x_1)\,\mathrm{d}\xi = \mathbf{0} \qquad x_1 > a \quad (36a)$$

$$\int_0^{\infty} \xi \boldsymbol{h}_a(\xi)\sin(\xi x_1)\,\mathrm{d}\xi = \tfrac{1}{4}[\boldsymbol{t}(x_1) - \boldsymbol{t}(-x_1)] \qquad 0 < x_1 < a \quad (36b)$$

and

$$\int_0^{\infty} \boldsymbol{h}_s(\xi)\cos(\xi x_1)\,\mathrm{d}\xi = \mathbf{0} \qquad x_1 > a \quad (37a)$$

$$\int_0^{\infty} \xi \boldsymbol{h}_s(\xi)\cos(\xi x_1)\,\mathrm{d}\xi = \tfrac{1}{4}[\boldsymbol{t}(x_1) + \boldsymbol{t}(-x_1)] \qquad 0 < x_1 < a \quad (37b)$$

Each pair of equations (36a,b) and (37a,b) are standard dual integral equations for antisymmetric and symmetric loadings, respectively. Their solutions are given by Titchmarsh [11]

$$h_a(\xi)=\frac{1}{2\pi}\int_0^a \eta J_1(\xi\eta)\left\{\int_{-1}^{1} t(s\eta)(1-s^2)^{-1/2}s\,ds\right\}d\eta \tag{38}$$

$$h_s(\xi)=\frac{-1}{2\pi}\int_0^a \eta J_0(\xi\eta)\left\{\int_{-1}^{1} t(s\eta)(1-s^2)^{-1/2}\,ds\right\}d\eta \tag{39}$$

where J_0 and J_1 are Bessel functions of the first kind of order zero and one, respectively.

A particular case of some importance is when the applied traction $t(x)$ is uniform over the crack face. With $t=t_0$ constant, eqns. (38) and (39) reduce to

$$h_a(\xi)=\mathbf{0} \tag{40}$$

$$h_s(\xi)=-(a/2\xi)J_1(a\xi)\,t_0. \tag{41}$$

In this case of uniform tractions [2]

$$\tau_1(x_1,x_2)=\mathrm{Re}\{\tilde{\mathbf{B}}_1\langle \tilde{z}_{1n}/(\tilde{z}_{1n}^2-a^2)^{1/2}-1\rangle\tilde{\mathbf{B}}_1^{-1}\}t_0 \tag{42a}$$

$$\tau_2(x_1,x_2)=\mathrm{Re}\{\mathbf{B}_2\langle z_{2n}/(z_{2n}^2-a^2)^{1/2}-1\rangle\mathbf{B}_2^{-1}\}t_0 \tag{42b}$$

$$u_1(x_1,x_2)=-\mathrm{Re}\{\tilde{\mathbf{A}}_1\langle \tilde{z}_{1n}+\mathrm{i}(a^2-\tilde{z}_{1n}^2)^{1/2}\rangle\tilde{\mathbf{B}}_1^{-1}\}t_0 \tag{43a}$$

$$u_2(x_1,x_2)=-\mathrm{Re}\{\mathbf{A}_2\langle z_{2n}+\mathrm{i}(a^2-z_{2n}^2)^{1/2}\rangle\mathbf{B}_2^{-1}\}t_0 \tag{43b}$$

where

$$z_{jn}=x_1+x_2p_n^{(j)} \tag{44a}$$

with $z_{jn}\to a, -a$ as the crack tips are approached. The bold angle bracket denotes a diagonal matrix, *e.g.*

$$\langle f(z_{jn})\rangle=\mathrm{diag}[f(z_{j1}),f(z_{j2}),f(z_{j3})] \tag{44b}$$

6.1. *Stress intensity factors*

The stress intensity factors are readily obtained from the conventional definitions

$$k=(K_{\mathrm{II}},K_{\mathrm{I}},K_{\mathrm{III}})^{\mathrm{T}}\equiv\lim_{r\to 0}[(2\pi r)^{1/2}\tau_j(r,0)] \tag{45}$$

where the three fracture modes are characterized with respect to the interface coordinate system, *i.e.* mode I corresponds to tensile loading normal to the interface, mode II is shear parallel to the interface, and mode III is anti-plane shear. This definition (eqn. (45)) is valid only when $\gamma=0$ in (26) or $\mathbf{W}=\mathbf{0}$; see also eqn. (23).

With the load vector defined as

$$\mathbf{q}(\eta)=\frac{1}{a\pi}\int_{-a}^{a} t(\eta\xi)(a+\xi)^{1/2}(a-\xi)^{-1/2}\,d\xi \tag{46}$$

it is shown in [2] that when $\mathbf{W}=\mathbf{0}$

$$k=q(1)(\pi a)^{1/2} \tag{47}$$

Hence, for $\mathbf{W}=\mathbf{0}$ not only does the crack-tip stress field have the standard square root singularity, but also from (47): (i) the stress intensity factors are real, (ii) the three fracture modes are decoupled in the sense that $\mathbf{k}$ is parallel to the load vector $\mathbf{q}$, and (iii) for this interfacial Griffith crack the stress intensity factors do not depend on either the material constants or the geometry of the bicrystal. Of course, these features hold for cracks in homogeneous solids, but if $\mathbf{W}\neq\mathbf{0}$ then (i)–(iii) do not hold.

When the crack faces are uniformly loaded, $q(\eta)=t_0=t(\xi)$,

$$k=(K_{\mathrm{II}},K_{\mathrm{I}},K_{\mathrm{III}})^{\mathrm{T}}=t_0(\pi a)^{1/2} \tag{48}$$

Both eqns. (47) and (48) are identical to the results for Griffith cracks in an infinite homogeneous body.

In terms of the stress intensity factors, the crack-tip stress field is expressed in conventional form, as $r\to 0$

$$\tau_1(r,\theta)=\frac{\theta_1(\theta)k}{(2\pi r)^{1/2}}\qquad \text{for } 0<\theta<\pi \tag{49a}$$

$$\tau_2(r,\theta)=\frac{\theta_2(\theta)k}{(2\pi r)^{1/2}}\qquad \text{for } -\pi<\theta<0 \tag{49b}$$

where the normalized matrices

$$\theta_1(\theta)=\mathrm{Re}\{\tilde{\mathbf{B}}_1\langle(\cos\theta+\tilde{p}_n^{(1)}\sin\theta)^{-1/2}\rangle\tilde{\mathbf{B}}_1^{-1}\} \tag{50a}$$

$$\theta_2(\theta)=\mathrm{Re}\{\mathbf{B}_2\langle(\cos\theta+p_n^{(2)}\sin\theta)^{-1/2}\rangle\mathbf{B}_2^{-1}\} \tag{50b}$$

From the definition of τ_j given in eqn. (16), (48) represents the asymptotic behavior of σ_{12}, σ_{22} and σ_{32} at the crack tip. It follows from eqn. (2.18) in ref. 1 that the stress components σ_{11} and σ_{31} can be obtained by multiplying σ_{12} and σ_{32} by p_1 and p_3, respectively (see Qu and Bassani [1] for definitions of p_1 and p_3). Examples of the angular variation of crack-tip stresses, *i.e.* θ_j, are given in ref. 2 for cracks along the grain boundary in f.c.c. copper bicrystals.

6.2. *Crack opening displacements*

With $\mathbf{W}=\mathbf{0}$ and the crack faces uniformly loaded, *i.e.* $q(\eta)=t_0=t(\xi)$, the crack opening

displacement is [2]

$$\mathbf{\Delta}(x_1)=(a^2-x_1^2)^{1/2}\mathbf{D}\boldsymbol{\ell}_0 H(a-|x_1|) \tag{51}$$

Even though the crack opening displacement $\mathbf{\Delta}(x_1)$ has the same x_1 dependence as in a homogeneous medium, it should be emphasized here that, for example, for symmetric mode I loading ($\phi=0$) the crack faces do not open symmetrically, in general. That is, in this case the x_2 component of displacement is not symmetric and the x_1 component of $\mathbf{\Delta}$ does not vanish (since generally the matrix $\mathbf{D}$ is not diagonal). The crack opening modes, unlike the stresses, are coupled. Relative surface sliding may occur even when the crack faces are subjected only to normal loadings.

7. Summarizing remarks

The necessary and sufficient condition for no oscillations in the crack-tip field for a crack along a bimaterial interface is $\mathbf{W}=\mathbf{0}$; see (25) and (26). For the case where the interface is a tilt boundary this condition is satisfied if the in-plane and antiplane deformations of each crystal decouple in the interface coordinate system for both geometrically symmetric and asymmetric boundaries. Furthermore, from the invariance result of Ting [7], it follows that for a given tilt axis and crystal misorientation, $\theta_1+\theta_2$, the order of the singularity δ in (26) is independent of $\theta_1-\theta_2$, *i.e.* independent of the reference plane or boundary plane containing the tilt axis.

The governing dual integral equations for a Griffith crack on the interface between two semi-infinite anisotropic elastic solids can be solved explicitly when $\mathbf{W}=\mathbf{0}$. The crack-tip stresses then have the standard inverse square root singularity, and the corresponding stress intensity factors are separable in the three modes of loading.

Acknowledgments

This work was supported by the NSF/MRL program at the University of Pennsylvania under Grant 8216718. Many discussions with Professor V. Vitek and the support of the University of California, Santa Barbara where this work was completed while one of the authors (J.L.B.) was on sabbatical leave are gratefully acknowledged.

References

1 J. Qu and J. L. Bassani, *J. Mech. Phys. Solids*, (1988) in press.
2 J. L. Bassani and J. Qu, *J. Mech. Phys. Solids*, (1988) in press.
3 J. R. Rice, *J. Appl. Mech., 55* (1988) 98.
4 C. F. Shih and R. J. Asaro, *J. Appl. Mech., 55* (1987) 299.
5 E. Zywicz and D. M. Parks, Elastic Yield Zone around an Interfacial Crack Tip, *Mech. Eng. Rep.*, 1987 (Massachusetts Institute of Technology).
6 J. R. Willis, *J. Mech. Phys. Solids, 19* (1971) 353.
7 T. C. T. Ting, *Int. J. Solids Struct., 22* (1986) 965.
8 A. N. Stroh, *Philos. Mag., 7* (1958) 625.
9 J. Qu and J. L. Bassani, in preparation.
10 J. R. Rice and G. C. Sih, *J. Appl. Mech., 32* (1975) 418.
11 E. C. Titchmarsh, *Introduction to the Theory of Fourier Integrals*, Oxford University Press, Oxford, 1937.

IV CHARACTERIZATION OF INTERFACES

Materials Science and Engineering, A107 (1989) 187–197

Structure and Chemistry of Metal/Ceramic Interfaces*

M. RÜHLE and A. G. EVANS

Materials Department, College of Engineering, University of California, Santa Barbara, CA 93106 (U.S.A.)

(Received June 1, 1988)

Abstract

The present state of knowledge is reviewed concerning the structure and chemistry of metal/ceramic interfaces. Experimental observations are described for several model systems and open problems concerning different aspects of structure and properties of heterophase boundaries are discussed.

1. Introduction

The use of ceramics as structural components, as well as in chemical technology and in electronic devices is steadily increasing because of improved mechanical integrity afforded by enhanced toughness and by process control. Ceramic components must typically be connected to other materials, mainly metals. The requirements that the bonded couple must fulfil are dictated by the functions of the ceramic: physical, chemical, electrical, mechanical. However, in all cases, adequate mechanical integrity is a technical prerequisite, as reflected in the fracture resistance of the interfaces. Metal/ceramic bonded couples are presently being used in electron tubes, multilayer substrates and capacitors, metal matrix composites, automotive power sources, etc. [1–9].

Systematic studies of metal/ceramic interfaces started in the early 1960s. Such studies were directed towards the identification of general rules that govern bonding and interface behavior, both theoretically and experimentally, including the thermodynamics of interfacial reactions, crystallographic relationships and the atomistic structure at the interface. The intention of this article is to review the present state of knowledge concerning the physics, chemistry and structure of interfacial regions between metals and ceramics.

2. The work of adhesion

The driving force for formation of a metal/ceramic interface is the yield in energy when intimate contact is established between the metal and ceramic surfaces [10]. For a high rate of interaction, the surfaces have to be brought into excited states. Therefore, temperature and atmosphere are important variables, as well as the properties and structures of the surfaces.

The simplest description of the physical interaction between a metal and a ceramic is the *work of adhesion*, W_{ad}. Specifically, when clean, defect-free surfaces are brought into contact, energy is released in accordance with the Dupré equation:

$$W_{ad} = \gamma_c + \gamma_m - \gamma_{mc} \quad (1)$$

where γ_c and γ_m are the free energies of the relaxed surfaces of the ceramic and the metal, respectively, γ_{mc} represents the energy of the relaxed interface between the metal and the ceramic. The quantity W_{ad} is thus the reversible work released per unit area of interface formed by two free surfaces. Direct measurement of W_{ad} is not possible [11]. Consequently, in practice, W_{ad} is deduced by measuring the contact angle θ established by a *solid* metal in contact with a ceramic,

$$W_{ad} = \gamma_m(1 + \cos\theta) \quad (2)$$

Adequate measurement of θ and of γ_m constitutes a non-trivial experimental task. Often γ_m is anisotropic and, hence, the crystallography of the surface has to be determined. Furthermore, true equilibrium has to be established by allowing sufficient mass transport and the associated morphological evolution. Measurements on small particles are preferred, although contamination

*Paper presented at the symposium on Interfacial Phenomena in Composites: Processing, Characterization, and Mechanical Properties, Newport, RI, June 1–3, 1988.

0921-5093/89/$3.50

© Elsevier Sequoia/Printed in The Netherlands

during annealing is always a problem [12]. The most acceptable approach involves the deformation and heat treatment of alloys containing particles of ceramic formed by internal oxidation etc. [13, 14]. Plastic straining of the alloy causes particle decohesion. Subsequent annealing then allows mass transport to create an equilibrium void from the initial debond. The angle θ can then be measured on cross-sections through the particles [11]. Different authors [12, 14, 15] measured and calculated values of γ_{mc} and W_{ad}.

Alloying additions strongly influence the thermodynamic quantities [10]. Furthermore, certain alloying additions segregate at the interface, by Gibbsian absorption. As an example, the segregation of chromium at various metal/Al_2O_3 interfaces results in a rearrangement of the interface into a more relaxed structure with a lower interfacial energy, resulting in a lower work of adhesion. Such segregant effects are a major issue in metal/ceramic bonded couples [12, 20, 21].

3. Bonding models

A rudimentary understanding of interfaces can be achieved by adopting phenomenological models. Such models are capable of correlating trends in bonding between different material couples and provide insight into some of the broad issues. However, the detailed understanding of trends in interface structure and properties with alloy composition, segregation, etc., requires more sophisticated atomistic models.

Elucidation of the essential issues, especially the prediction of trends in the work of adhesion (and, eventually, in fracture resistance) with such variables as alloy additions and segregation, requires that bonding be examined at all levels. The eventual objective would be the judicious coupling of information obtained from the most rigorous, but compute bound, quantum mechanical supercell approaches with the results of cluster calculations and of simple continuum, thermodynamic formalisms.

3.1. Continuum models

Interactions across the interface first occur without charge exchange. Such interactions develop between induced dipoles (London), between neutral atoms polarized by a dipole molecule (Debye) and between dipole moments (Keesom). (Another interaction without charge exchange involves anions in the ceramic and image forces in the metal, and occurs when the dielectric constants of the metal and the ceramic are different [23–25].) Together, these interactions constitute the Van der Waals attractions (see for example ref. 22). The London term is generally the most pronounced. For a pair consisting of a metal atom and an oxygen ion, the interaction energy E_p has the form

$$E_p = -\tfrac{3}{2}\frac{\alpha_m \alpha_A}{R^6}\frac{I_m I_A}{I_m + I_A} \tag{3}$$

where R is the distance between the centers of the interacting atoms/ions, α is the polarizability and I the ionization potential, with m referring to the metal and A the anion in the ceramic.

Charge exchange allows ion pairs to form and interact across the interfaces. For example, the interactions between ions of the metal and of oxygen (or other anions) in the ceramic is related to the free energy of metal oxide formation, ΔG° [26, 27]. Furthermore, when the cations of the ceramic are soluble in the metal, dissolution from the interface allows ionic interaction between dissolved cations and the anions in the ceramic.

McDonald and Eberhart [28] examined interactions involving various metals in contact with the (0001) plane of sapphire. For this purpose, they assumed that the (0001) sapphire surface terminates with a layer of close-packed oxygen ions. The metal atoms (to be bonded to Al_2O_3) are then offered two sites; those above the aluminum ions located below the top layer of oxygen ions and those above empty sites. The first site results in attractive dipole forces, as described in eqn. (3), which are about constant for all metal/Al_2O_3 couples. The second metal site forms ionic oxygen–metal bonds having a free energy proportional to ΔG°. By further assuming that all interactions of the dense-packed oxygen plane are occupied with metal atoms, the calculated trends in W_{ad} agree quite well with experimental data for the bonding of Al_2O_3 to simple metals [31]. The very strong bonding of platinum and palladium [19] to alumina is evidently at variance with the simple model. However, aluminum possesses a very high heat of solution in these metals. Consequently, as noted above, bonds could be formed between the oxygen ions and aluminum ions dissolved in the metal. Alternatively, a thin segregated aluminum layer could form between the metal and the Al_2O_3 to enhance the bonding [31].

The McDonald–Eberhart approach provides helpful generalizations. However, a more fundamental, atomistic understanding of the nature of the bonding is needed to adequately understand critically important alloying and segregation effects, as well as trends in the fracture resistance.

3.2. *Atomistic models*

An understanding of the fundamental physics of bonding between a metal and a ceramic requires that quantum mechanical models be developed. The simplest approach involves cluster calculations [30]. Such calculations have established that the primary interactions at metal/oxide interfaces involve the metal (d) and oxygen (p) orbitals, to create both bonding and antibonding orbitals. For copper and silver in contact with Al_2O_3, both states are about equally occupied, resulting in zero net bonding. However, for nickel and iron, fewer antibonding states are occupied and net bonding occurs. The calculations also reveal that a transfer of valence charge occurs, resulting in a contribution to the net ionic bonding which increases in strength as the metal becomes more noble. Consequently, metal-to-alumina bonding strengths are predicted to increase in the order: Ag–Cu–Ni–Fe. This order is generally consistent with the measured trends in sliding resistance as well as with the energies of adhesion. However, it is emphasized that the calculations approximate the interface by an $(AlO_6)^{9-}$ cluster and one metal atom. The selection of the charge to be assigned to this cluster is non-trivial and the choice influences the predicted magnitudes of the energies [32]. To further examine this issue, Anderson *et al.* [33] performed calculations for the Al_2O_3/Pt couple that included more atoms: 31 close-packed platinum atoms and the corresponding numbers of aluminum and oxygen ions. Then, by applying a quantum-chemical superposition technique, including an electron delocalization molecular orbital method, bonding energies were calculated for different atomic configurations of the Pt/Al_2O_3 interface. These calculations confirmed that the bond was strongest when oxidized platinum atoms opposed close-packed oxygen ion planes. However, further quantitative insights did not emerge. Indeed, the preceding models all have the deficiency that they do not fully account for the heterogeneous nature of the interface and cannot, therefore, be expected to accurately predict energies, segregant effects, etc.

Ab initio calculations seem to be essential for a full understanding of the bonding. Louie and coworkers [34, 35] have performed such calculations on metal–semiconductor interfaces. In these calculations, the metal was described by a jellium, so that insight emerged regarding the bonding mechanisms, but not on the atomistic structure. More recently, supercell calculations have been performed that include an interface area and adjacent regions large enough to incorporate the distorted (relaxed) volumes of both crystals. With this approach, the electron distribution around all atoms has been calculated and the atomic potentials evaluated. In a next step, interatomic forces may be calculated and strains determined. Such calculations have been performed rather successfully for the interface between Ge–GaAs [36] and Si–Ge [37]. The crystals adjacent to those interfaces are isomorphous and very nearly commensurate, such that the misfit between lattice planes is very small. However, misfits between metals and ceramics are typically rather large so that extremely large supercells are required. Therefore, only preliminary calculations have been conducted thus far [38]. Nevertheless, the calculations, performed for MgO/Ag, have allowed determination of the atomic potentials surrounding the different atoms, as well as a separation of bonding into different contributions (ionic, covalent and polarization).

With the advent of a new calculational scheme, (Car and Parrinello [39]) involving a combination of molecular dynamics (see *e.g.* Rahman [40]) and density functional theory (Kohn and Sham [41]), it should be possible to conduct computations of *relaxed* interfaces much more efficiently. The scheme should also allow equilibrium computations of metal/ceramic interfaces at finite temperatures. The conduct of such analysis on model interfaces should greatly facilitate the basic understanding of the bonding phenomenon and allow judicious usage of both cluster calculations and continuum thermodynamic formulations.

4. Structure of interfaces

In thermodynamic equilibrium, the atoms and/or ions close to an interface occupy positions that minimize the *total energy* of the system. However, the proximity to equilibrium depends on the conditions used to form the interface. For example, diffusion-bonded interfaces have atomistic arrangements influenced by the orientation of the

two surfaces *prior* to bonding. Additionally, when the bonding is performed at high temperature, chemical gradients often develop and influence the structure (see Section 5) and residual strains form upon cooling. The interface structure thus involves geometric as well as atomistic considerations, conditioned by relaxation mechanisms inherent in each bonding process. Consequently, interface structures are conveniently described by firstly defining generalized geometric parameters for the unrelaxed interfaces. Then, the relaxation mechanism pertinent to each bonding process may be considered. Finally, various geometric and atomistic bonding models, and associated experimental results, may be evaluated.

4.1. Geometrical parameters

An unrelaxed interface can be described by nine geometrical parameters. The required number was evaluated by a thought experiment, similar to that previously used for grain boundaries [42] Six parameters describe the relative orientation and translation of the two crystals. The description of the interface orientation with respect to the crystal requires three additional parameters.

4.2. Process relaxations

The bonding method governs the actual geometrical parameters that describe the interface, by virtue of the imposed geometry and the allowable relaxations. During *diffusion bonding* [6], intimate surface contact at elevated temperatures, subject to a small pressure, generates the bonded interface. This technique, *pre-selects* the (macroscopic) rotation, two components of the translation and the interface orientation. However, some of these geometrical parameters are relaxed by *local* deviations. Specifically, bonding is usually performed at temperatures wherein at least one component may undergo plastic deformation. Consequently, local geometrical relaxation may be accommodated by small-angle grain boundary formation adjacent to the interface. Furthermore, mass transport may allow interface facets to develop that relax the constraint on interface planarity.

Interfaces may also be formed by *internal oxidation* [43, 44]. Such interfaces are not unique, but are related to the precipitate *morphology*, as governed by thermodynamic principles. In particular, since the total energy of the precipitate depends not only on the interfacial energy but also on coherency strains, the interface structure and the shape of the precipitate depend usually on its size [45]. For coherent precipitates, orientation relationships are governed by constraints imposed by interfacial energies, the solubility and lattice parameters, and the most stable morphologies. These relationships should be an integral part of the analysis of the structure of interfaces formed by internal oxidation.

A third way of producing metal/ceramic interfaces is by *evaporation* of the metal onto a clean ceramic surface. The evaporated species is usually highly mobile [46] at high temperature. Consequently, if the metal wets the ceramic, a thin layer forms in an *equilibrium* interfacial configuration. For non-wetting configurations, islands are formed. Then, when the substrate is a single crystal and a one-to-one orientation relationship exists between the two components, the islands may grow together and form a single-crystal film [46]. Alternatively, when different equivalent orientation relationships exist, the islands develop with slightly different orientations. A range of different behaviors is thus expected for interfaces formed by evaporation.

4.3. Geometrical models

Models described by *geometrical* parameters may sometimes be insightful as a basis for the description of *unrelaxed* interfaces. However, it must be appreciated that the direct correlation between such models and interface properties (*e.g.* energy) is not possible [47]. Foremost among such models is a "lock-in" model developed by Gleiter and Fecht [48], deduced from experiments wherein small metallic single crystals were sintered onto a single-crystal ceramic substrate. Interfaces between several alkali halides or rock salt structure oxides and various noble metals were formed in this manner. It was observed that the spheres rotated into orientations which tend to minimize the energy of the sphere/plate boundary. Consequently, the orientation relationships determined by X-ray diffraction may be supposed to reflect a low-energy configuration of those interfaces. Gleiter and Fecht [48] accounted for the observed "stable" configurations by means of a model which describes low-energy interfaces in terms of densely packed atom rows of one crystal nesting in the grooves between similar rows of the other crystal. The requisite periodic matching between (small) multiples of lattice plane spacings was achieved by imposing small

displacements upon certain of the atom rows. The lattice strains from such imposed displacements have thus far been neglected. Nevertheless, in some cases, "lock-in" seemingly describes observations, even when large misfits exist Conformity with the "lock-in" structure has been established for MgO/Au interface formed by evaporation [49] and for gold on KCl (35% misfit) [48]; in both cases, the predicted cube-on-cube orientation was osberved. The "lock-in" concept thus appears to be a useful first-order description in some cases. However, more detailed investigations have revealed important discrepancies. Various observations indicate that small but definite angular off-sets occur between close-packed directions and/or planes. Mulder and Klomp [50] studied orientation relationships in diffusion-bonded sandwiches of polycrystalline copper and platinum foils between identically oriented (parallel) sapphire crystals. As expected, the metal grains developed a preferred orientation, with (111) of the metal parallel to (0001) of the sapphire. However, the grains were rotated within a wide angular range about the close-packed directions. Discrepancies have also been found for the Nb/Al_2O_3 system [51, 52]. Notably, the close-packed planes are not aligned: instead, the (0001) plane of Al_2O_3 and (011) of Nb are tilted by about 3° around an axis parallel to $[11\bar{2}0]\,Al_2O_3$ and $(101)_{Nb}$. This tilt occurs in specimens grown by epitaxy of niobium on (0001) Al_2O_3 [51] and in specimens formed by diffusion bonding [52], even when initially the specimens were adjusted to have parallel close-packed planes. It is also noted that even though MgO/Au has the cube-on-cube orientation predicted by "lock-in", misfit dislocations are observed, indicative of interface strains. Such dislocations are not consistent with the "lock-in" concept.

Relaxation effects are presumably responsible for discrepancies with the "lock-in" model. For example, as noted above, subgrain boundaries in diffusion-bonded Nb/Al_2O_3 provide freedom for some rotation of the niobium lattice. Also, the interface develops facets while retaining the 3° tilt of the two lattices. Clearly, the facets alleviate the misfit strain which would develop if close-packed planes were kept in contact everywhere across the interface.

4.4. *Atomistic models*

The *relaxed* structure of interfaces is obviously of greater significance than the unrelaxed state. Adequate models of this structure do not yet exist, but await comprehensive experimental insight. Experimental studies can be performed either by diffraction [53, 54] or by high-resolution (direct imaging) techniques [55].* With the new generation of electron microscopes, direct imaging of *atomic columns* is possible. Specifically, by aligning along the axis of an interface which possesses only a tilt component, each column of atoms is imaged in one spot, giving a projection of the atomic arrangements in the interface. However, to derive reliable atomic positions, a series of observed images, taken at different focus settings, must be matched quantitatively with computed images, based on an assumed set of atomic coordinates. For matching purposes, image computation and position adjustment is repeated until the best possible fit is reached for the entire through-focus series. This technique is referred to a quantitative high-resolution electron microscopy (HREM) [56]. The interpretation is, of course, most difficult close to the interface where deviations from the perfect lattice are most extreme. Fully quantitative HREM studies have been performed on grain boundaries in germanium [55] and on semiconductor/metal interfaces such as $Si/NiSi_2$ [57].

Quantitative studies of metal/ceramic interfaces have been initiated for the Nb/Al_2O_3 and Au/MgO systems formed using each of the three processes described above. Interpretation of high-resolution images of regions close to a *diffusion-bonded* interface [58] (Fig. 1) requires that image simulations for perfect latttices first be performed. For this purpose, the projected atomic positions and potentials of niobium and Al_2O_3 in the selected orientation have been determined and used to construct the simulated image for a foil having a thickness (12 nm) which corresponds with that for the actual test specimen. It is evident that lens aberration ($C_s = 1.1$ mm, 200 kV) conceals some details of the perfect lattice structure. Nevertheless, it is still apparent (Fig. 1) that the perfect lattice is preserved in the Al_2O_3 up to the interface. Conversely, in the niobium strong deviations occur for distances up to four lattice planes from the interface. However, a periodicity along the interface can be recog-

*Diffraction studies require specimens with interfaces that extend homogeneously over a large area (about 1 mm^2), while direct lattice imaging requires a thin specimen (thickness < 10 nm) plus constraints concerning homogeneity and orientation.

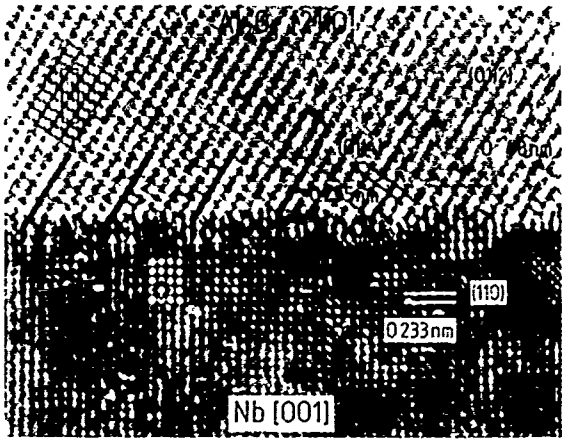

Fig. 1. Lattice image of the regions close to an interface between niobium and Al_2O_3. Orientation relationship between the ceramic and the metal: $0001\ Al_2O_3 \parallel 110\ Nb$ and $[2\bar{1}\bar{1}0]\ Al_2O_3 \parallel [001]\ Nb$. The foil orientation is parallel to $[001]$ Nb. Insets in the high resolution electron microscopy images of niobium and Al_2O_3 represent simulated lattice images. Only four lattice planes within the niobium next to the interface are distorted. Facets can be observed. The periodicity of the interface is indicated.

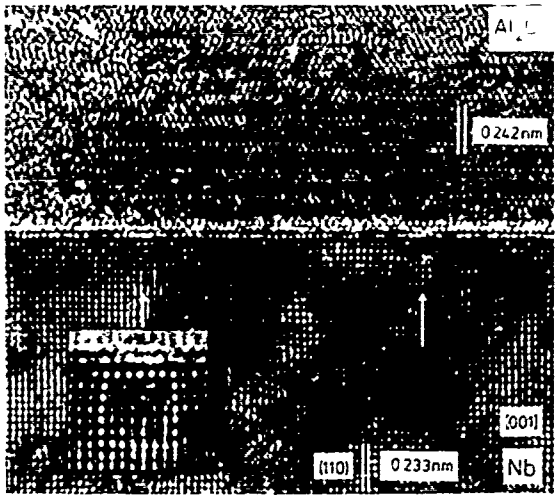

Fig. 2. Lattice image of Nb/Al_2O_3 interface of an internally oxidized Nb/Al alloy. Interface plane parallel to $(0001)\ Al_2O_3 \parallel 110$ Nb and $(01\bar{1}0)\ Al_2O_3 \parallel [001]$ Nb. Misfit dislocations in niobium can be observed (see inset). The extra half plane forming the misfit dislocation does not terminate at the interface [59].

nized within the distorted region. Faceting parallel to the interface also occurs and the interface is slightly inclined with respect to the (0001) plane of Al_2O_3. It is expected that imaging of the same interface with instruments possessing superior resolution would result in a better resolution of the distorted atomistic structure close to the interface. When the results of such studies become available, insightful atomistic models of the interface might be developed.

Interfaces created by *internal oxidation* have well defined geometrical characteristics. Precipitates of α-Al_2O_3 formed in Nb/Al alloys are small and penny-shaped (about 300 nm in diameter) and exhibit a fixed orientation relationship:

$$(0001)_{Al_2O_3} \parallel (110)_{Nb}$$

and

$$[01\bar{1}0]_{Al_2O_3} \parallel [001]_{Nb}$$

High-resolution transmission electron microscopy (TEM) investigation (Fig. 2) has revealed [59], however, that the spacings of the 110 Nb planes ($d = 0.23$ nm) and of the (0001) Al_2O_3 planes ($d_2 = 0.39$ nm) are sufficiently different that misfit dislocations would be predicted with spacing $D \equiv d_1 d_2 / d_2 - d_1 = 8.8$ nm. Weak-beam images confirm such dislocations (Fig. 3) with $D = 9.1 \pm 0.5$ nm. To fully analyze the interface structure, as well as the atomistic structure of the

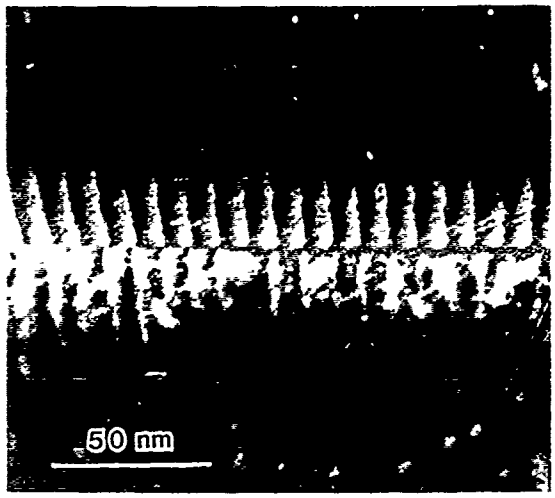

Fig. 3. Weak-beam dark-field image of inclined interfaces of Fig. 2 limiting the α-Al_2O_3 precipitate. Imaging with Nb 010 reflection. Light lines represent the contrast from misfit dislocations.

misfit dislocations, superior resolution (less than 0.2 nm) would be needed.

Finally, it is noted that conventional TEM provides complementary information on defects at or close to the interface, such as dislocation spacings, ledge densities, etc. It is emphasized, however, that a more complete analysis of such defects, including Burgers vector determination, is generally not possible since the materials adjacent to the interface possess usually dif-

ferent lattice parameters and few "common" diffraction vectors exist [60].

5. Chemistry of interfaces

5.1. Theoretical background

In multicomponent two-phase systems, nonplanar interfaces or two-phase product regions can evolve from initially planar interfaces [61], even at constant temperature and pressure. Under the same conditions, the interface stays planar in binary systems. This difference originates with the thermodynamic degrees of freedom, f. For a binary system $f=0$, whereas for ternary or higher-order systems, $f>0$ (Gibbs' phase rule). Consequently, in the latter, interface compositions are in part controlled by the kinetics.

Not all (higher-order) interfaces necessarily develop an unstable morphology during a high-temperature treatment. Analysis of the phenomenon is needed to assess susceptibility. Similar problems exist for solidification and for the oxidation of alloys [62]. Mathematical treatments predict the time evolution of small interface perturbations. The perturbations may occur either due to initial roughnesses or upon small transport fluctuations caused by changes in temperature or by the presence of defects. If perturbations increase in amplitude with time, initially planar interfaces become morphologically unstable. The critical conditions for instability depend primarily on the mobility of the constituents and the thermodynamic properties of the system.

The formalism previously developed for ternary systems [61] can be adapted to metal/ceramic couples, with the three independent components being the two cations and the anion. A schematic ternary phase diagram and the expected concentration profiles are shown in Fig. 4 [63]. In general, the problem is complicated by having several phase fields present, such that intermediate phases form: usually intermetallics with noble metals and spinel (or other oxides) with less noble metals. The actual phases depend on the geometry of the tie lines, as well as on the diffusion paths in the ternary phase field, and cannot be predicted *a priori*.

The diffusion problem has thus far been examined [63] for the simple case wherein no product phases formed, the interfacial stresses were negligible, mass transport occurred by bulk diffusion and local equilibrium was imposed

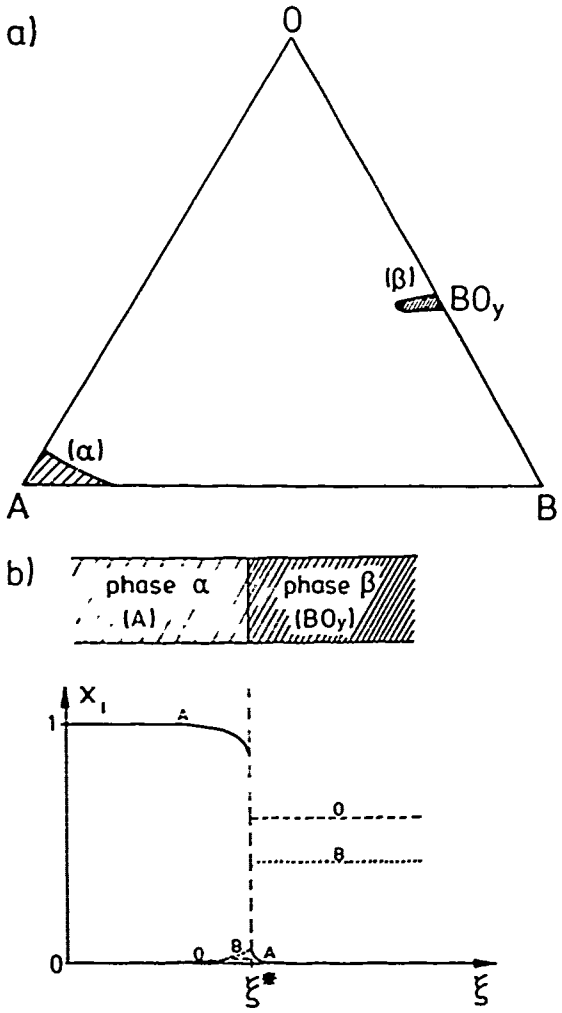

Fig. 4. (a) Schematic ternary phase diagram. Extended phases fields exist near metal A and oxide BO_y. (b) Equilibrium concentration profiles during diffusion bonding between metal phase (A) and oxide BO_y.

everywhere. Even then, a general analytical solution was not possible. However, for several metal/ceramic systems, some further simplifications are appropriate. The oxygen and the metal atoms diffuse on different sublattices allowing the interaction term in the diffusion coefficients to be neglected. (In the niobium–oxygen diffuses on interstitial sites while the aluminum diffuses by vacancies.) Negligible solubility of the metal in the oxide (grad $\mu_{BO}=0$) allows point defect relaxation only in the ceramic. Therefore, for a stoichiometric ceramic, the remaining defect fluxes are small compared with the fluxes in the metal and can be ignored. Subject to the above simplifications, solutions have been obtained for Nb/Al_2O_3 [63, 64].

ferent lattice parameters and few "common" diffraction vectors exist [60].

5. Chemistry of interfaces

5.1. Theoretical background

In multicomponent two-phase systems, nonplanar interfaces or two-phase product regions can evolve from initially planar interfaces [61], even at constant temperature and pressure. Under the same conditions, the interface stays planar in binary systems. This difference originates with the thermodynamic degrees of freedom, f. For a binary system $f=0$, whereas for ternary or higher-order systems, $f>0$ (Gibbs' phase rule). Consequently, in the latter, interface compositions are in part controlled by the kinetics.

Not all (higher-order) interfaces necessarily develop an unstable morphology during a high-temperature treatment. Analysis of the phenomenon is needed to assess susceptibility. Similar problems exist for solidification and for the oxidation of alloys [62]. Mathematical treatments predict the time evolution of small interface perturbations. The perturbations may occur either due to initial roughnesses or upon small transport fluctuations caused by changes in temperature or by the presence of defects. If perturbations increase in amplitude with time, initially planar interfaces become morphologically unstable. The critical conditions for instability depend primarily on the mobility of the constituents and the thermodynamic properties of the system.

The formalism previously developed for ternary systems [61] can be adapted to metal/ceramic couples, with the three independent components being the two cations and the anion. A schematic ternary phase diagram and the expected concentration profiles are shown in Fig. 4 [63]. In general, the problem is complicated by having several phase fields present, such that intermediate phases form, usually intermetallics with noble metals and spinel (or other oxides) with less noble metals. The actual phases depend on the geometry of the tie lines, as well as on the diffusion paths in the ternary phase field, and cannot be predicted *a priori*.

The diffusion problem has thus far been examined [63] for the simple case wherein no product phases formed, the interfacial stresses were negligible, mass transport occurred by bulk diffusion and local equilibrium was imposed

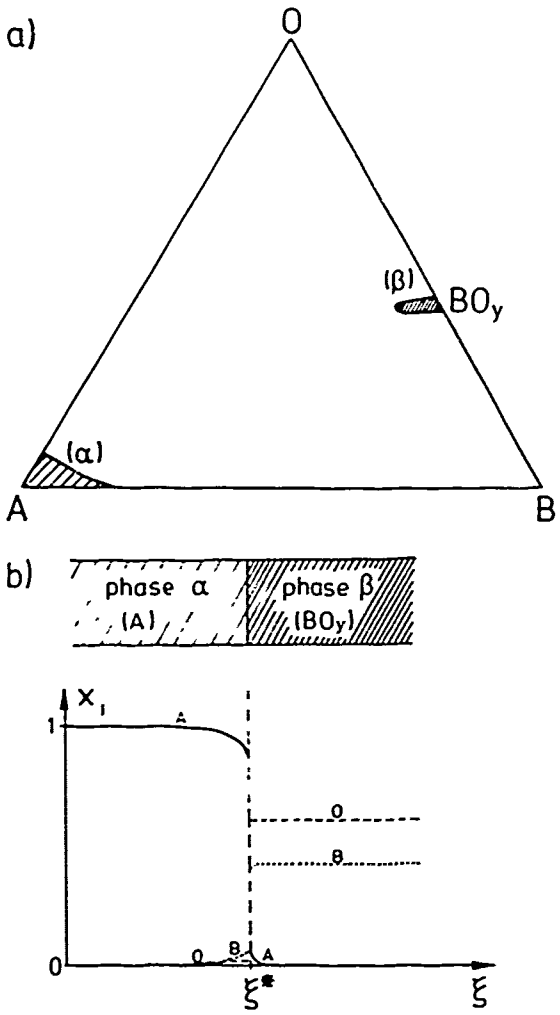

Fig. 4. (a) Schematic ternary phase diagram. Extended phases fields exist near metal A and oxide BO_y. (b) Equilibrium concentration profiles during diffusion bonding between metal phase (A) and oxide BO_y.

everywhere. Even then, a general analytical solution was not possible. However, for several metal/ceramic systems, some further simplifications are appropriate. The oxygen and the metal atoms diffuse on different sublattices allowing the interaction term in the diffusion coefficients to be neglected. (In the niobium–oxygen diffuses on interstitial sites while the aluminum diffuses by vacancies.) Negligible solubility of the metal in the oxide (grad $\mu_{BO}=0$) allows point defect relaxation only in the ceramic. Therefore, for a stoichiometric ceramic, the remaining defect fluxes are small compared with the fluxes in the metal and can be ignored. Subject to the above simplifications, solutions have been obtained for Nb/Al_2O_3 [63, 64].

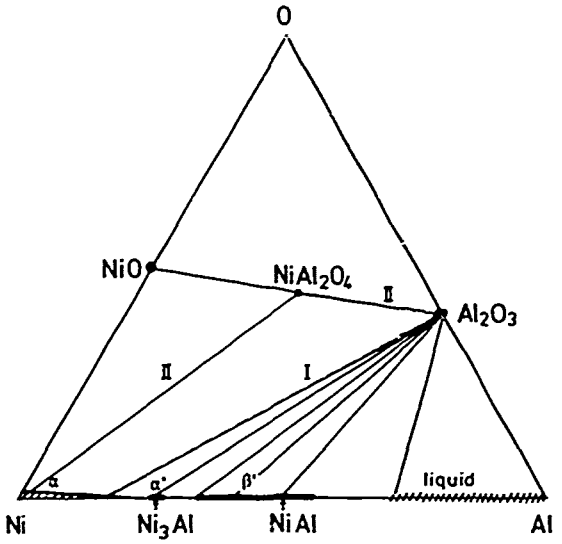

Fig. 6. Ni–Al–O phase diagrams (schematically for $T = 1600$ K). Two reaction paths are possible when nickel is bonded to Al_2O_3: (I) Low oxygen activity, no reaction product forms. (II) high oxygen activity: spinel forms.

ficient oxygen (about 500 ppm solubility), the Ni(O)/Al_2O_3 diffusion couple yields a spinel product layer. Under these conditions, spinel forms, because the new diffusion path in the nickel phase field requires that the tie line connects the metal and spinel field (path II in Fig. 6). The associated thermodynamic and atomistic consideration pertinent to spinel layer formation have been addressed [67, 68]. However, available observations do not unequivocally identify the operative mechanism. It is also noted that the interface between spinel and nickel seems to be unstable, morphological instabilities becoming more apparent with increasing spinel layer thickness.

Bonding of copper to Al_2O_3 seems to require a thin layer of oxygen on the surface of copper prior to bonding and $CuAl_2O_3$ or $CuAl_2O_4$ form [69]. The spinel thickness can be reduced by annealing under extremely low oxygen activities leading first to a "non-wetting" layer of Cu_2O and then to a direct Cu/Al_2O_3 bond. The mechanical stability of spinel-free Cu/Al_2O_3 specimens has not yet been investigated.

Bonding of titanium to Al_2O_3 results in the formation of the intermetallic phases TiAl or Ti_3Al, which probably also include oxygen. The thickness of the reactive layer increases with increasing bonding time and morphologically unstable interfaces develop. A detailed study is again required for the identification of the different stable phases.

Similar studies have been performed for other ceramic partners such as simple cubic oxides (MgO, NiO, ...), sesquioxides (Cr_2O_3, Mn_2O_3, ...), Si_3N_4 and SiC. The situation is much more complicated for the latter materials, since impurities or sintering additives quite frequently diffuse to the interface and form a glassy film. The bonding is then governed by the interfaces between the glass film and both the ceramic and the metal.

6. Sintering of interfacial flaws

Scratches and other defects frequently exist on surfaces which have to be bonded. Long bonding times and high bonding temperatures are required when such flaws are present, because residual defects at the interface restrict the mechanical properties of the metal/ceramic interface. Investigation of the sintering of interface flaws is thus of great importance. The closure of interfacial flaws at *homogeneous* bonds involves several mechanisms [70]: surface diffusion, volume diffusion, diffusion along the interface, power-law creep and plastic yielding. Models for homogeneous interfaces based on these mechanisms qualitatively describe the experimental observations. However, a quantitative comparison has been inhibited by the scarcity of reliable experimental data. For a *heterogeneous* bond and especially for a metal/ceramic interface, additional processes have to be considered [64], namely, the diffusion of metal atoms into the ceramic, dissolution of the ceramic at the interface and diffusion of the species of the ceramic into the metal, chemical reactions between the metal and the ceramic to form a product phase and recondensation of a dissolved ceramic at the interface. The inherent complexity demands a vital role of experiment in ascertaining the most important variables for typical metal/ceramic couples.

For evaluation of the governing transport mechanisms, artificial interfacial defects of different dimensionality and sizes may be introduced into the metallic surfaces [66, 67] prior to bonding: linear flaws by photolithography and other shapes by indentation. After bonding, cross-sections of interfacial fracture surfaces studied by SEM allow determination of the change in flaw size. The depth variations may be measured with a profilometer.

Inspection of results obtained for Nb/Al_2O_3 revealed that the surface of niobium hardly changes, whereas condensation products of Al_2O_3 could be detected on the sapphire. The amount of condensed Al_2O_3 depends on the cooling. From chemistry studies (Section 4), it has already been established that niobium dissolves Al_2O_3 and, upon cooling, Al_2O_3 recondenses at the interface. This mechanism also seems to be involved in the "filling" of the flaws. However, the experimental, as well as the theoretical, studies are not yet sufficient to derive a quantitative description of the process. Studies of this type on other systems are also needed to obtain a comprehensive view of the important issues in diffusion bonding.

7. Conclusions

Although considerable progress has been made in the understanding of structure and chemistry of metal/ceramic interfaces, still many open questions exist. Detailed and careful experimental studies will reveal more insight into the mechanisms of bondings and these experimental studies may challenge further theoretical studies.

Acknowledgment

The authors wish to thank the Defense Advanced Research Projects Agency for financial support through the University Research Initiative Program at UCSB under ONR Contract N00014-86-K-0753.

References

1 E. A. Giess, K. N. Tu and D. R. Uhlmann (eds.), *Electronic Packaging Materials Science. Mater. Res. Soc. Symp. Proc., 40* (1985).
2 K. A. Jackson, R. C. Pohanka, D. R. Uhlmann and D. R. Ulrich (eds.), *Electronic Packaging Materials Science II. Mater. Res. Soc. Symp. Proc., 72* (1986).
3 J. M. Gibson and L. R. Dawson (eds.), *Layered Structures, Epitaxy and Interfaces. Mater. Res. Soc. Symp. Proc., 37* (1985).
4 A. K. Dhingra and S. G. Fishman (eds.), *Interfaces in Metal-Matrix Composites.* The Metallurgical Society of AIME, Warrendale, PA, 1986.
5 M. Rühle, R. W. Balluffi, H. Fischmeister and S. L. Sass (eds.), *Proc. Int. Conf. on the Structure and Properties of Internal Interfaces, J. Phys. Paris, Colloq., C4-46* (1985).
6 Y. Ishida (ed.), *Fundamentals of Diffusion Bonding.* Elsevier, Amsterdam, 1987.
7 J. A. Pask and A. G. Evans (eds.), *Ceramic Microstructure '86: Role of Interfaces.* Plenum, New York, 1987.
8 E. A. Almond, C. A. Brookes and R. Warren (eds.), *Science of Hard Materials, Inst. Phys. Conf. Ser., 75,* Adam Hilger, Bristol, 1986.
9 G. S. Upadhyaya (ed.), *Sintered Metal-Ceramic Composites.* Elsevier, Amsterdam, 1984.
10 K. L. Mittal (ed.), *Adhesion Measurement of Thin Films, Thick Films, and Bulk Coatings, ASTM Spec. Tech. Publ., 640* (1978).
11 B. V. Derjaguim, *Recent Advances in Adhesion,* Gordon and Breach, New York, 1971, p. 513.
12 E. D. Hondros, in R. A. Rapp (ed.), *Techniques of Metals Research Series,* Vol. IV 2, Wiley Interscience, New York, 1970, pp. 293–348.
13 J. W. Hancock, I. L. Dillamore and R. L. Smallman, *6th Plansee Seminar,* Plansee, Reutte, 1968, p. 467.
14 K. E. Easterling, H. F. Fischmeister and E. Navara, *Powder Metall., 16* (1973) 128.
15 M. Nicholas, *J. Mater. Sci., 3* (1968) 571.
16 I. G. Palmer and G. C. Smith, *Proc. 2nd Bolton Landing Conf. on Oxide Dispersion Strengthening,* Gordon and Breach, New York, 1968, p. 351.
17 M. McLean and E. D. Hondros, *J. Mater. Sci., 6* (1971) 19.
18 J. T. Klomp, in J. A. Pask and A. G. Evans (eds.), *Ceramic Microstructure '86. Role of Interfaces.* Plenum, New York, 1987, p. 307.
19 J. T. Klomp, in Y. Ishida (ed.), *Fundamentals of Diffusion Bonding,* Elsevier, Amsterdam, 1987, p. 3.
20 H. F. Fischmeister, E. Navara and K. E. Easterling, *Met. Sci. J., 6* (1972) 211.
21 J. L. Smialek and R. Browning, *NASA Tech. Memo. 87168,* 1987.
22 L. Pauling, *General Chemistry,* 3rd edn., Freeman, San Francisco, 1970, p. 118.
23 E. D. Doyle, J. G. Horne and D. Tabor, *Proc. R. Soc. London Ser. A, 366* (1979) 173.
24 A. M. Stoneham, *Appl. Surf. Sci., 14* (1982–1983) 249.
25 A. M. Stoneham and P. W. Tasker, *Harwell Rep.* T1166 (1985).
26 W. K. Kingery, H. K. Bowen and R. Uhlman, *Introduction to Ceramics,* Wiley, New York, 1976, p. 210.
27 J. T. Klomp, in E. A. Giess, K. N. Tu and D. R. Uhlmann (eds.), *Electronic Packaging Materials Science, Mater. Res. Soc. Symp. Proc., 40* (1985) 381.
28 J. E. McDonald and J. G. Eberhart, *Trans. AIME, 233* (1965) 512.
29 S. V. Pepper, *J. Appl. Phys., 47* (1976) 801.
30 K. H. Johnson and S. V. Pepper, *J. Appl. Phys., 53* (1982) 6634.
31 H. F. Fischmeister, in J. A. Pask and A. G. Evans (eds.), *Ceramic Microstructure '86 Role of Interfaces* Plenum, New York, 1987, p. 1.
32 A. B. Anderson, S. P. Mehandru and J. L. Smialek, *J. Electrochem. Soc., 132* (1985) 1695.
33 A. B. Anderson, C. Ravimohan and S. P. Mehandru, *J. Electrochem. Soc., 134* (1987) 1789.
34 S. G. Louie and M. L. Cohen, *Phys. Rev. B, 13* (1976) 2461.
35 S. G. Louie, J. G. Chelikowsky and M. L. Cohen, *Phys. Rev. B, 15* (1977) 2154.
36 K. Kunc and R. M. Martin, *Phys. Rev. B, 24* (1981) 3445.
37 C. G. Van de Walle and R. M. Martin, *J. Vac. Sci. Technol. B, 3* (1985) 1256.
38 P. Bloechl and O. K. Anderson, to be published.

39 R. Car and M. Parrinello, *Phys. Rev. Lett., 55* (1985) 2471.
40 A. Rahman, in J. W. Halley (ed.), *Correlation Functions and Quasiparticle Interactions in Condensed Matter,* NATO Advanced Study Ser. 35, Plenum, New York, 1977.
41 W. Kohn and L. J. Sham, *Phys. Rev., 140*(1965) A1133.
42 G. Kalonji, *J. Phys. Paris, Colloq. C4, 46*(1985) 249.
43 C. Wagner, *J. Electrochem. Soc., 103*(1956) 571.
44 J. L. Meijering, in H. Herman (ed.), *Advances in Materials Research,* Vol. 5, Wiley Interscience, New York, 1971, p. 1.
45 A. G. Khachaturyan, *Theory of Structural Transformations in Solids,* Wiley, New York, 1983.
46 J. Matthews, *Epitaxial Growth,* Vol. I, Academic Press, New York, 1975.
47 A. P. Sutton and R. W. Balluffi, *Acta Metall., 35*(1987).
48 H. Gleiter and H. S. Fecht, *Acta Metall., 33*(1985) 577.
49 R. H. Hoël, *Surf. Sci., 169*(1986) 317.
50 C. A. M. Mulder and J. T. Klomp, *J. Phys. Paris, Colloq. C4, 46*(1985) 111.
51 D. B. McWhan, *Mater. Res. Soc. Symp. Proc., 37* (1985) 493.
52 M. Florjancic, W. Mader, M. Ruhle and M. Turwitt, *J. Phys. Paris, Colloq. C4, 46*(1985) 129.
53 J. Budai, P. D. Bristowe and S. L. Sass, *Acta Metall., 31* (1983) 699.
54 J. Vitek and M. Rühle, *Acta Metall., 34* (1986) 2095.
55 A. Bourret, *J. Phys. Paris, Colloq. C4, 46*(1985) 27.
56 R. W. Balluffi, M. Rühle and A. P. Sutton, *Mater. Sci. Eng., 89*(1987) 1.
57 J. M. Gibson, R. T. Tung, J. M. Phillips and R. Hull. *J. Phys. Paris, Colloq. C4, 46*(1985) 369.
58 W. Mader and M. Rühle, *Acta Metall.*, in press.
59 W. Mader, *Mater. Res. Soc. Symp. Proc., 82*(1987) 403.
60 R. C. Pond, *J. Microsc., 135*(1984) 213.
61 M. Backhaus-Ricoult and H. Schmalzried, *Ber. Bunsenges. Phys. Chem., 89*(1985) 1323.
62 W. W. Mullins and R. F. Sekerka, *J. Appl Phys , 34*(1963) 323; *35*(1964) 444.
63 M. Backhaus-Ricoult, *Ber. Bunsenges. Phys. Chem., 90* (1987) 684.
64 K. Burger and M. Rühle, *Adv. Ceram.*, in press.
65 K. Burger, W. Mader and M. Rühle, *Ultramicroscopy, 12* (1987) 1.
66 M. Ruhle, K. Burger and W. Mader, *J. Microsc. Spectrosc. Electron., 11*(1986) 163.
67 M. Rühle, M. Backhaus-Ricoult, K. Burger and W. Mader, in J. A. Pask and A. G. Evans (eds.), *Ceramic Microstructure '86: Role of Interfaces,* Plenum, New York, 1987, p. 295.
68 J. A. Wasynczuk and M. Rühle, in J. A. Pask and A. G. Evans (eds.), *Ceramic Microstructure '86. Role of Interfaces,* Plenum, New York, 1987.
69 M. Wittmer, *Mater. Res. Soc. Symp. Proc., 40*(1985) 393.
70 B. Derby and E. R. Wallach, *J. Mater. Sci., 15*(1982) 49; *18*(1984) 427.

Materials Science and Engineering, A107 (1989) 199–205

Characterization of Internal Interfaces in Metals and Alloys by High Resolution Electron Microscopy*

J. M. PENISSON and G. REGHEERE

Departement de Recherche Fondamentale/Service de Physique, CENG, 85X-38041 Grenoble Cédex (France)

(Received June 1, 1988)

Abstract

It is shown how high resolution electron microscopy (HREM) can provide very important structural information on the interface between two different phases. After a brief description of the HREM technique, two different examples are presented. In a stainless steel the orientation relationship between α (b.c.c.) and γ (f.c.c.) is not constant throughout the specimen. Misfit dislocations have been found when the compact planes of both phases are parallel. When they are not parallel a regular array of edge dislocations forming a sub grain boundary is superimposed on the misfit dislocations. In a cobalt-based superalloy, the orientation relationship between the f.c.c. matrix and an ordered precipitate is strict and three sets of edge dislocations have been found associated with a regular array of steps.

1. Introduction

Internal interfaces in materials mainly govern the physical properties of these materials. The understanding and improvement of these properties need a knowledge of the atomic structure of the interfaces. Several different approaches can be made for this study: symmetry properties [1–3], dislocation structure [4], geometrical aspects [5–7] and computer modelling [8]. The interfaces can be divided into homophase and heterophase boundaries. In the first kind the crystallographical structure is the same across the boundary and only the orientation relationship is changing; this is the well-known case of grain boundaries and planar defects like stacking faults and domain boundaries. In heterophase interfaces, the crystallographical and chemical structure as well as the orientation relationship changes across the boundary. The atomic structure of both types of interface can be determined by high resolution electron microscopy (HREM). In the case of grain boundaries (GBs), since the early work [9], numerous examples of GB structure determination have been published in semiconductors [10], in metals [11–14] and in ceramics [15]. In any case the experimental observations have to be compared with calculated models. These computer models can use molecular statics in which the structure is calculated in the absence of thermal vibrations [16, 17] or molecular dynamics [18] which take the effect of temperature into account. To calculate the energy of the system of atoms which constitute the boundary, an interaction potential is used. In most cases this potential is a central pair potential but many-body potentials for transition metals have recently been constructed also [19].

Heterophase interfaces were first studied using conventional electron microscopy [20]. HREM is now widely used. The results concern metallic systems [21] as well as semiconducting materials [22] and ceramics [23], but due to the fact that interaction potentials between different atoms are not known with the same accuracy as those in pure materials the models are not so advanced as for grain boundaries.

In this paper, two different examples will be presented. The first one describes the structure of the interface between α and γ phases in a stainless steel alloy, and it will be shown that the orientation relationship between the two phases is not unique leading to different types of interfaces. In the second example, the interface between the f.c.c. matrix and an ordered phase in a cobalt-based superalloy is investigated. In this alloy the addition of a small quantity of niobium provokes the precipitation of an intragranular

*Paper presented at the symposium on Interfacial Phenomena in Composites: Processing, Characterization, and Mechanical Properties, Newport, RI, June 1–3, 1988.

0921-5093/89/$3.50

© Elsevier Sequoia/Printed in The Netherlands

second phase which is mainly responsible for the mechanical properties of the alloy. In particular the hardness increases strongly when this second phase precipitates.

2. Experimental procedure

2.1. Specimens

The alloys studied have the following compositions (in at.%).

Stainless steel: Fe, 68.7; Cr, 20.6; Ni, 7.7; Mo, 2.4; C, 0.004; Si, 0.54.

The dual phase microstructure is obtained after a series of cold rollings followed by an annealing period.

Superalloy: Co, 37.6; Ni, 36.8; Cr, 22.5; Nb, 3.1.

The alloy is annealed for 24 h at 1200 °C and quenched. After this treatment, the structure is an f.c.c. solid solution. A second annealing is then performed at 800 °C for 24 h. These conditions do not correspond to the maximum hardness, but they have been chosen to obtain well developed precipitates with planar interfaces suitable for high resolution observation.

In both cases, the specimens for HREM have been obtained using an electrolytic cell. For stainless steel specimens, the bath was a mixture of acetic and perchloric acids while it was a saturated CrO_3 solution in acetic acid for the superalloy. Some specimens have been also prepared by ion milling but, in this case, lattice defects were observed and the electrochemical process is preferred.

2.2. High resolution electron microscopy

HREM is now widely used for the determination of interface structure. The HREM technique has been described in detail by Spence [24]. The new generation of microscopes working at medium or high accelerating voltages with very good optical characteristics associated with high tilt angle allows the observation of a wide range of materials. In most of the metallic alloys a resolution of 0.17 nm is needed to obtain high resolution images of the low index crystallographical orientation. Two different microscopes have been used: a JEOL 4000 EX working at 400 kV and the JEOL ARM of the National Center for Electron Microscopy in Berkeley. The 4000 EX has a 0.17 nm resolution at Scherzer defocus and an ultimate resolution better than 0.12 nm [25] so that several different matrix orientations can be observed. On both the stainless steel alloy and the cobalt-based superalloy, the unit cell parameter is 0.36 nm and images have been taken along ⟨011⟩, ⟨111⟩ and ⟨112⟩. The ARM is a versatile microscope in which a very good resolution (better than 0.16 nm ... Scherzer) is associated with a large tilt angle (±40°) of the specimen [26]. In order to prevent the occurrence of radiation damage the accelerating voltage was 800 kV.

An HREM image represents a two-dimensional projection of the atomic potential of the specimen. The specimen must then be perfectly oriented so that no overlap of atomic columns occurs. In the case of an interface, it has to be parallel to the incident beam and in practice for a 10 nm thick specimen the alignment of the interface with respect to the beam must be better than 0.3°. For a complete determination of the structure, the HREM pictures have to be compared with calculated models so that the atomic positions must be unambiguously determined. In this case a precise knowledge of all the optical imaging conditions and specimen characteristics is needed. Defocus is measured on the optical diffraction patterns of the images. Thickness can be estimated by tilting the interface by a known angle. The orientation relationship between the different phases is deduced from both the electron and optical diffraction pattern.

2.3. Image simulations

Images of the different phases present in the alloys have been calculated using a multislice program. The variation with respect to thickness of amplitude and phase of the main diffracted beams have also been calculated; in most of the cases 128 × 128 points are sufficient to obtain a good precision. The numerical values used in all the calculations are:

(i) JEOL 4000 EX: $C_s = 1.05$ mm; Div. = 0.0007 rad; Del = 9 nm [25];
(ii) ARM: $C_s = 2.8$ mm; Div. = 0.0006 rad; Del = 10 nm.

3. Experimental results

3.1. Stainless steel alloy

Figure 1 shows a HREM picture of a typical interface in this alloy. The γ f.c.c. phase has a $[0\bar{1}1]$ orientation and the α b.c.c. phase has a [001] orientation, the interface is seen nearly parallel to the incident electron beam and it is

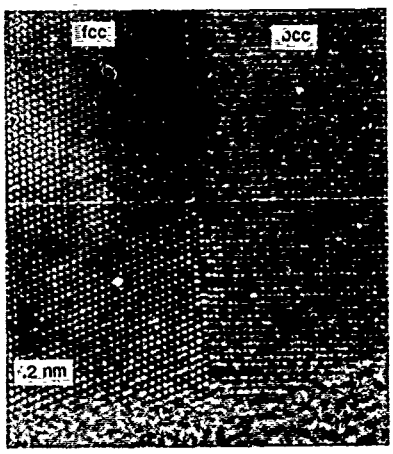

Fig. 1. High resolution image of an interface between f.c.c. and b.c.c. phases in a stainless steel alloy. The interface plane is parallel to the compact planes of both phases. Misfit dislocations (arrowed) are present. Their spacing is 2.2 nm (400 kV).

parallel to the $(\bar{1}11)$ plane of γ. Misfit dislocations are seen end on; their spacing is about 2.6 nm, their Burgers vector is in the boundary plane. The orientation relationship is deduced from the electron diffraction pattern. A careful inspection of this pattern reveals that the orientation is close to the Kurdjumov–Sachs (K–S) and Nishiyama–Wassermann (N–W) orientations. The interface plane is not constant in the specimen; it can be parallel to the compact planes as in Fig. 1 and only misfit dislocations are present. In some cases the compact planes of the two phases are no longer parallel and a regular array of dislocations is present (Fig. 2). Their spacing is 3.5 nm and the deviation angle is between 3° and 4°. Their Burgers vector is equal to $b = \frac{1}{3}[\bar{1}11]$ of the γ f.c.c. phase. The boundary plane can also be in completely different orientation: Fig. 3 shows an example of a boundary nearly parallel to the specimen plane: in this case a moiré pattern reveals the good fit areas.

3.2. *Superalloy*

3.2.1. *Structure of the precipitates*

After annealing at 800 °C for 24 h, plates of a second phase precipitate within the f.c.c. matrix. Energy dispersive X-ray spectroscopy revealed that the composition of the precipitates is $(Ni, Cr, Co)_3Nb$. At the present time this result is only qualitative and in particular the exact concentration of Ni, Cr and Co atoms is not known. In rather similar alloys [27, 28] the precipitates have been identified as orthorhombic β Ni_3Nb. The problem is then to determine whether the

Fig. 2 Interface in a stainless steel alloy. The compact planes of b.c.c. and f.c.c. phases are not parallel and a regular array of edge dislocations is present. Their spacing is 3.5 nm (400 kV).

Fig. 3. Image of an interface perpendicular to the beam. The two phases overlap and form a moiré pattern (400 kV).

presence of Cr and Co atoms introduces a change in the crystallographical structure. Electron diffraction patterns taken in a direction perpendicular to the broad faces of the precipitates show differences with the orthorhombic phase. Some new spots appear and there is a sixfold symmetry axis parallel to the incident beam. These results are consistent with the DO 19 ordered structure and it has been verified that the same diffraction pattern occurs in Ti_3Al which is known to have this ordered structure. As for the β Ni_3Nb structure, the precipitate can be described as the stacking of A and B equivalent planes and the only difference between these two structures is the different ordering of Nb atoms.

3.2.2. Matrix precipitate interface

All the precipitates have been found with their broad faces parallel to 111 matrix planes. The orientation relationship can be written as:

(111)f.c.c.$\parallel(0001)$p

$[1\bar{1}0]$f.c.c.$\parallel[11\bar{2}0]$p

where p stands for the precipitate. The orientation relationship is strict; no deviation, as in the case of stainless steel, has been found and no dislocations with Burgers vector perpendicular to the interface plane have been observed. The orientation relationship corresponds to that found by Kirman [29] between the f.c.c. matrix and β Ni_3Nb in nickel-based alloys. Specimens have been observed along different matrix axes:

(i) *[011] orientation.* In this case, the interface between matrix and precipitate is either parallel to the incident electron beam or in an inclined position. Figure 4 shows such an interface observed parallel to the beam. It is perfectly coherent over large distances and the compact planes of matrix and precipitate are perfectly parallel. The other set of {111} matrix planes parallel to the beam intercept the boundary plane. They correspond to $(10\bar{1}1)$ precipitate planes; there is a 9° angle when they cross the boundary plane. Because of the small misfit between them, dislocations are present. They are associated to a step in the boundary; the step height is one {111} matrix plane although complex steps are also present. Figure 5 is an enlargement of the interface region in a very thin part of the specimen around a dislocation. The position of the interface is determined by looking at the stacking sequence which changes from ABCABC... in the matrix to ABAB in the precipitate. As was pointed out by Sutton [30], the interface position cannot be determined without ambiguity. Some steps not associated with an extra half plane are also found; in the vicinity of these steps the contrast is blurred, suggesting the presence of inclined dislocations. As can be seen from Fig. 4, when the specimen thickness increases, the contrast of the precipitate changes drastically and for example the $(10\bar{1}1)$ planes lose their individuality; this is due to the increasing intensity of superlattice reflections. Because of this contrast change, dislocations become much more difficult to evidence.

(ii) *[111] orientation.* In this orientation the interface can be either inclined or perpendicular to the incident beam. In the latter case, the complete dislocation structure of the interface can be studied. Figure 6 shows three dark field images using three different diffraction vectors. The contrast analysis shows that three sets of pure edge dislocations are present. The dislocation lines are parallel to the $\langle 110 \rangle$ directions. Their spacing is about 10 nm. In some conditions a moiré between the two phases can be seen on the images. Its spacing is about 5 nm and the fringes are 30° away from the dislocation lines.

4. Interpretation of the results

4.1. Stainless steel alloys

The structure of the interface between f.c.c. and b.c.c. phases has been the subject of many publications (for a review see ref. 31) and it has been investigated from the experimental as well as the theoretical point of view in

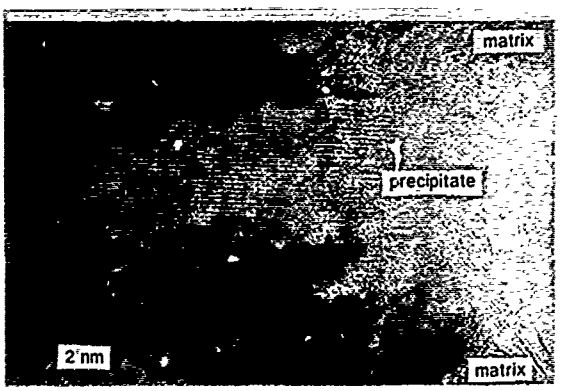

Fig. 4. High resolution image of (Ni, Co, $Cr)_3Nb$ precipitate in a f.c.c matrix. The compact planes of both phases are parallel. Misfit dislocations associated with steps are present. Between them the interface is fully coherent (800 kV).

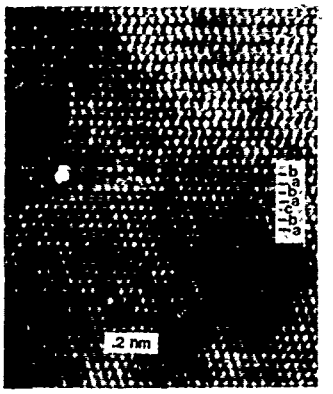

Fig. 5. Enlargement of a region of Fig. 4 around a dislocation. The stacking sequence changes from ABC.... in the f.c.c. matrix to ABAB.... in the precipitate. An extra half plane is present in the matrix and there is a step.

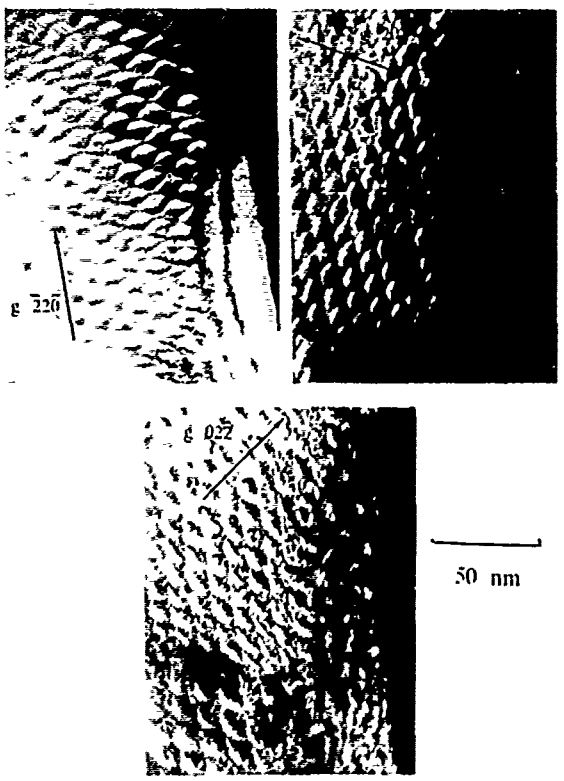

Fig. 6. Dark field images of the same interface using three different diffraction vectors. The contrast analysis leads to the existence of three sets of edge dislocations.

copper–chromium alloy [32]. Our results reveal that the orientation relationship is not constant throughout the sample; it is near N–W and K–S orientations but no exact orientation was observed. The orientation relationships have been investigated in detail by El Hajjaji who determined the values of the coincidence index Σ [33]. In some cases the compact planes of both phases are parallel and the boundary plane lies in this plane. A regular array of misfit dislocations is present, their spacing being approximately 2.2 nm. The Burgers vector is $\frac{1}{2}[101]$ if referred to the f.c.c. phase or $\frac{1}{2}[111]$ if the b.c.c. phase is considered. Both these vectors are inclined with respect to dislocation line and they lie in the boundary plane. The misfit between the two phases is accommodated by the edge component of the dislocations which is:

$\frac{1}{3}\langle 112\rangle$ f.c.c.

The calculated spacing between the dislocations is 2.4 nm which is in good agreement with the experimental value.

In some cases the compact planes are no longer parallel. The deviation angle is accommodated by a regular array of dislocations similar to a pure tilt subgrain boundary. The Burgers vector $b=\frac{1}{3}[\bar{1}1.]$ is perpendicular to the boundary plane and the measured spacing is in agreement with the Frank equation: $d=b/\theta$.

With $b=\frac{1}{3}[\bar{1}11]=0.208$ nm and $\theta=3.5°$, the calculated value is 3.4 nm which is the experimental value.

When the boundary lies nearly perpendicular to the incident beam, the two crystals overlap forming a moiré. The shape and size of this moiré is in good agreement with a geometrical model made of the superposition of the atomic positions corresponding to both phases which are positioned in the observed orientation relationship. No information about atomic relaxations present in the dislocation cores can be obtained from these images. Similar images have been observed on a twist grain boundary in gold [34].

4.2. Superalloy

4.2.1. Crystallography

The precipitation of a second phase inside an f.c.c. matrix leads to the existence of several variants which can be numbered using group theory [1–3]. The application of this theory leads to 12 variants for the f.c.c.–orthorhombic system and only four in the f.c.c.–D019 case. Only four variants were experimentally observed. They correspond to four different {111} interface planes. In a given {111} plane only one variant is present whereas if the precipitate had an orthorhombic structure three different variants would then be present.

4.2.2. Image simulation of the precipitate

In order to test the possibility of distinguishing all the variants present in both possible precipitate structures, images of β Ni_3Nb and the D019 phase have been simulated in the orientations corresponding to the experimental image (in these simulations, a simplified model of the D019 phase containing only nickel and niobium atoms has been used).

[100] and [201] orthorhombic corresponding to $[11\bar{2}0]$ D019

[010] orthorhombic corresponding to [0001] D019.

The calculations show that the three different orthorhombic variants which should be present in each {111} matrix plane are not distinguishable because only small contrast variations are present

which are too small to be experimentally detected. D019 structure can be distinguished from orthorhombic phase (Fig. 7) and fine details of the experimental images can be reproduced in simulated ones. Numerical diffraction patterns have been calculated from both phases and are in agreement with the experimental ones. In {0001} D019 orientation a sixfold symmetry axis is present while it is absent from the diffraction pattern of [010] orthorhombic.

4.2.3. Structure of the interface

All the observations suggest that the interface between the f.c.c. matrix and the precipitate is constituted by a regular array of three sets of edge dislocations parallel to the three ⟨110⟩ matrix directions which lie in the interface plane. This observation excludes the possibility of three sets of 60° dislocations with Burgers vectors $\frac{1}{2}\langle 110\rangle$. The dislocations being pure edge, a possible Burgers vector is $\frac{1}{6}\langle 112\rangle$. This Burgers vector is consistent with the weak beam dark field images. The dislocation spacing can be calculated using the Brooks formula [35]:

$$d = b/\delta$$

where b is the Burgers vectors and δ the misfit

$$\delta = 2\,\frac{d_1 - d_2}{d_1 + d_2}$$

d_1 is the spacing of the {220} matrix planes $d_1 = 0.126$ nm, d_2 is the spacing of the $(22\bar{4}0)$ precipitate planes which are in correspondence with the 220 matrix planes $d_2 = 0.13$ nm. This gives $d = 5.4$ nm. This value is two times smaller than the experimental one and it is of the same order as the experimental spacing of the moiré fringes. The moiré spacing can also be calculated [36]

$$D = \frac{d_1 \cdot d_2}{d_1 - d_2}$$

d_1 and d_2 have the same value as in the misfit expression so that $D = 4.7$ nm which is in good agreement with the experimental value. The only way to obtain an acceptable value for the dislocation spacing is then to increase the modulus of the Burgers vector. If one takes $b = \frac{1}{4}\langle 112\rangle$ then $d = 8.2$ nm which is closer to the experimental value. This Burgers vector is a non-usual one and further experiments are needed to obtain a deeper understanding of the exact structure of the dislocations.

As it was evident from the high resolution pictures, the dislocations which are seen end-on are associated with a monoatomic step. A very simple geometrical model of the interface has been constructed by superposing the {111} matrix plane to the {0001} precipitate plane. Good fit areas are present and they form a triangular array. The number of these good fit zones can be increased by moving the interface plane in the same way as is described for the f.c.c./b.c.c. interface [32]. As the interface plane changes from one {111} matrix plane to a neighbouring one a new good fit area is created. The thickness of the precipitate being approximately constant,

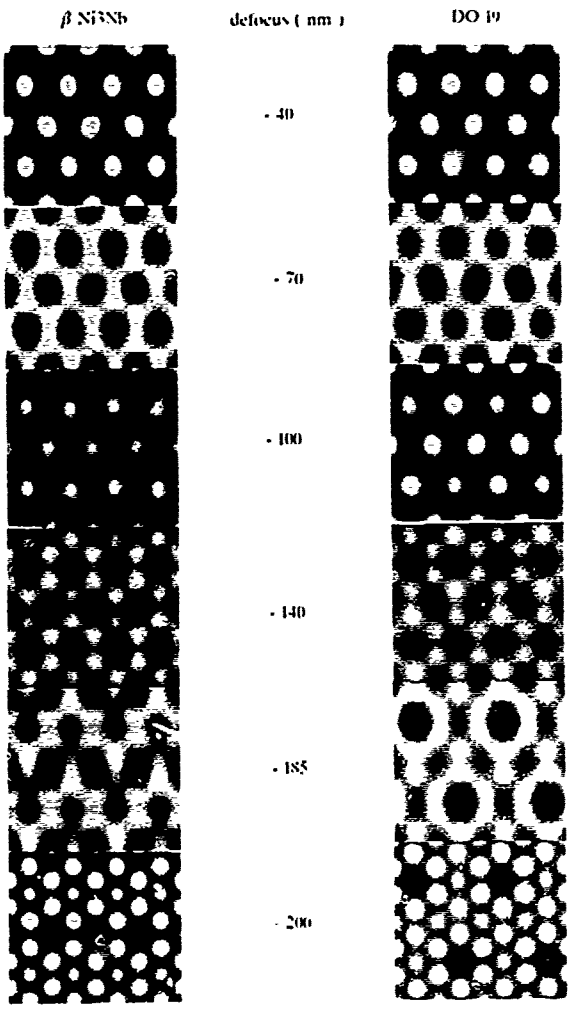

Fig. 7. Simulated images of the two possible structures of the precipitate. On the right is β Ni_3Nb and on the left the D019 structure (in this case a simplified structure is used containing only nickel and niobium atoms). The conditions used in these calculations are: accelerating voltage: 400 kV; $C_s = 1.05$ mm; beam divergence, 0.7 mrad, defocus spread, 9 nm; specimen thickness: 5 nm.

the steps are alternatively up and down with respect to the mean interface plane so that it remains parallel to the {111} matrix plane.

5. Conclusion

Two different types of internal interfaces have been studied by HREM. In a dual-phase stainless steel alloy, the orientation relationship is not constant throughout the specimens and there exists a variety of different interfaces. In particular, the compact planes are not always parallel. The interface is then complex and a tilt subgrain boundary is superimposed on the array of misfit dislocations.

In a cobalt-based superalloy, a D019 ordered phase precipitates and the compact planes of both phases are always parallel. Only misfit dislocations are present, the interface is described as a regular net of three sets of edge dislocations which are associated to monoatomic steps forming also a regular array. Between the dislocations the interface is perfectly coherent.

Acknowledgments

The authors are grateful to Dr. A. Bourret and F. Vanoni for many discussions and criticisms and to C. Bouvier for technical assistance. They also thank Pr. Guiraldenq and Dr. El Hajjaji for providing the stainless steel specimens and for helpful advice. One of us (J.M.P.) would like to thank all the staff of the National Center of Electron Microscopy in Berkeley for the possibility of using the ARM and performing some preliminary image simulations.

References

1 R. Portier and D. Gratias, *J. Phys. (Paris), C4*, 1982, 17.
2 J. W. Cahn and G. Kalonji, *Phase Transformations*, Metallurgical Society of AIME, Warrendale, PA, 1981, p. 3.
3 U. Dahmen and K. H. Westmacott, *Proc. MRS Symp., 62* (1986) 217.
4 G. Shifflet, *Mater. Sci. Eng., 81* (1986) 61.
5 W. Bollmann, *Phys. Status Solidi, 21*, (1974) 543.
6 M. G. Hall, J. M. Rigsbee and H. I. Aaronson, *Acta Metall., 34* (1986) 1419.
7 R. Bonnet and F. Durand, *Philos. Mag., 32* (1975) 997.
8 J. M. Rigsbee and H. I. Aaronson, *Acta Metall., 27* (1979) 351.
9 O. L. Krivanek, S. Isoda and K. Kobayashi, *Philos. Mag., 36* (1977) 931.
10 A. Bourret and J. J. Bacmann, *Surf. Sci., 162*, 1985, 495.
11 J. M. Penisson, T. Nowicki and M. Biscondi, *J. Phys. (Paris)*, to be published.
12 H. Ichinose and Y. Ishida, *J. Phys. (Paris), C4* (1985) 39.
13 W. Krakow, J. T. Wetzel and D. A. Smith, *Philos. Mag. A, 53* (1986) 739.
14 M. Mills, *J. Phys. (Paris)*, to be published.
15 K. L. Merckle and D. J. Smith, *Ultramicroscopy*, 22 (1987) 57.
16 G. Hasson, Y. Boos, I. Herbeuval, M. Biscondi and C. Coux, *Surf. Sci., 31* (1972) 115.
17 V. Vitek, *Dislocations*, Editions CNRS, 1984, p. 435.
18 V. Pontikis, *J. Phys. (Paris), C6* (1982) 65.
19 M. W. Finnis and J. E. Sinclair, *Philos. Mag. A, 50* (1984) 45.
20 G. C. Weatherly and R. B. Nicholson, *Philos. Mag., 17* (1968) 801.
21 J. M. Howe, U. Dahmen and R. Gronsky, *Philos. Mag. A, 56* (1987) 32.
22 J. L. Hutchison, *8th European Congr. on Electron Microscopy, Budapest, 1984*, Vol. 1, p. 505.
23 D. R. Clarke, *Ultramicroscopy, 4* (1979) 33.
24 J. Spence, *Experimental HREM*, Clarendon Press, Oxford, 1981.
25 A. Bourret and J. M. Penisson, *JEOL News, 25E* (1987) 1.
26 G. Thomas, *8th European Congr. on Electron Microscopy*, Budapest, 1984, Vol. 1, p. 683.
27 P. Royer, *Thèse*, Université de Nancy, 1970.
28 J. P. Zhang, H. R. Ye and K. H. Kuo, *Phys. Status Solidi A, 93* (1986) 35.
29 I. Kirman, *J. Iron Steel Inst., 207* (1969) 1612.
30 A. P. Sutton and J. W. Christian, *J. Phys. (Paris), C4* (1982) 197.
31 R. C. Ecob, *J. Microscopy, 137* (1985) 313.
32 M. G. Hall, H. I. Aaronson and K. Kinsman, *Surf. Sci., 31* (1972) 257.
33 M. El Hajjaji, *Thesis*, Université de Lyon 1, France, 1986.
34 W. Mader, G. Necker, S. E. Babcock and R. W. Balluffi, *Scri. Metall., 21* (1987) 555.
35 H. Brooks, *Metal Interface*, American Society for Metals, Cleveland, OH, 1952.
36 P. Hirsch, A. Howie, R. B. Nicholson, D. W. Pashley and M. J. Whelan, *Electron Microscopy of Thin Foils*, Ro. Krieger, Co., 1976.

Materials Science and Engineering, A107 (1989) 207–216

High Resolution Interface Analysis*

R. W. CARPENTER

Center for Solid State Science, Arizona State University, Tempe, AR 85287-1704 (U.S.A.)

(Received June 1, 1988)

Abstract

The structure and composition of interfaces in composites and other structural solids has important effects on their properties and is therefore of great interest. HREM and microspectroscopy are two of the most useful methods for examination of interfaces. HREM methods are the most advanced, and microspectroscopy methods are improving rapidly. The current image resolution limit is ~ 1.6 Å which is sufficient for most interface analysis purposes. The corresponding spatial resolution limit for microspectroscopy is determined by the current in small probes and temporal stability of the probe/specimen. Calculations of probe current vs. size are given and it is shown that current spatial resolution for EELS, for edges containing several thousand counts, is about 5 nm.

The effect of chemical bonding on electron energy loss absorption edges of silicon in its important ceramic compounds is presented and briefly discussed.

Examples of high resolution analysis in several composites and a multiphase ceramic are presented.

1. Introduction

Analysis of interface structure involves chemical distributions on or near the interface plane, relative misorientation across the interface plane, a definition of the interface plane in terms of some convenient coordinate system, and the geometric distribution of atoms at the interface. Typical lengths associated with these observations are fractions of a micron to one or two Ångstroms. Various electron microscopy methods are required to attain the necessary spatial or image resolution for these observations. Relative misorientations across boundaries can be determined by microdiffraction and conventional tilting experiments. Chemical distributions can be determined directly by microspectroscopy using small incident probes, and the geometric distribution of atoms at interfaces can be determined by high resolution imaging. Interfaces can be considered small regions of disorder in solids, and in that context resolution limits associated with these various electron microscopy methods are very important.

For this paper the main topic of interest is local composition change in small regions near interfaces and their structure, and it is useful to consider the factors affecting microspectroscopy resolution. Following this, several current research applications are discussed.

2. Resolution limits

The most familiar resolution limit is the so-called interpretable resolution limit δ associated with high resolution imaging. It corresponds to a spacing (*i.e.* length) in the specimen defined by the first zero of the microscope contrast transfer function, which is dependent on objective lens defocus $D = \Delta f (C_s \lambda)^{-1/2}$ where D is the generalized defocus, Δf is the objective lens defocus, C_s is the objective lens spherical aberration constant and λ is the incident electron wavelength [1]. The Scherzer resolution limit, given by $D = 1$ and $\delta = 0.7 C_s^{1/4} \lambda^{3/4}$ corresponds to spacings in the object imaged without phase reversals of the scattered amplitudes caused by the imaging lens. These images can be interpreted directly, and the best currently available electron microscopes, which generally have maximum operating voltages in the 300–1000 kV range, have interpretable resolution limits in the 1.4–1.8 Å range. This resolution is sufficient for determination of the structure of grain boundaries and interfaces in terms of the distribution of columns of atoms

*Paper presented at the symposium on Interfacial Phenomena in Composites: Processing, Characterization, and Mechanical Properties, Newport, RI, June 1–3, 1988.

0921-5093/89/$3.50

© Elsevier Sequoia/Printed in The Netherlands

when the boundaries are viewed in edge-on projection in crystals even with small unit cells. These experimental methods have been used, for example, to show that all ⟨001⟩ tilt grain boundaries are faceted in NiO [2]; the observations of many large-angle boundaries in this material supported the suggestion that low grain boundary energies are associated with large values of average interplanar spacing at the boundaries and not with low Σ values.

The corresponding resolution limit for local chemical analysis by microspectroscopy methods is the spatial limit, the lower limit of which is given by the incident probe size on a thin specimen. In this context, the microscope pre-specimen lenses are used to form a small focused probe image of the electron source on the specimen, and alignment, defocus, and aberrations of the probe forming lenses have important effects on attainable spatial resolution. Spectra are count rate limited and therefore some time is required for their collection. The count rate limitation brings questions of current in the focused probe into the discussion of probe size, and counting time requirements imply that the time average of the focused probe position relative to the microstructural feature of interest in the specimen during spectrum acquisition will influence spatial resolution.

It is useful to consider probe size and current in terms of aberrations of the probe forming lenses and source brightness, to estimate the current in small probes as a function of probe diameter. Then using measured inelastic scattering cross-sections, collection times for small probe microanalysis can be determined, and attainable spatial resolution can be estimated. For a correctly aligned illumination system the total probe size is given to a good approximation by an incoherent (quadrature) sum of coherent broadening mechanisms [3]

$$d_t^2 = d_g^2 + d_f^2 + d_s^2 \qquad (1)$$

where

$$d_g = \frac{2}{\pi\alpha}\left(\frac{i_b}{\beta}\right)^{1/2} \qquad d_f = (0.61)\frac{\lambda}{\alpha}$$

$$d_s = (0.3)C_s\alpha^3$$

Broadening by diffraction from the probe defining aperture is given by d_f, and by spherical aberration of the pre-specimen probe forming lens by d_s (C_s is the spherical aberration coefficient of the lens). This spherical aberration coefficient can be determined experimentally from wide-angle convergent beam shadow images [4]. The current in a gaussian probe from a source of brightness β is given by d_g. It is assumed in this case that the energy spread in the incident beam from the source is small, so that chromatic aberration broadening can be neglected. The effect of aperture diffraction and spherical aberration, which have different dependences on α, is most easily seen by considering a probe from a point source without considerations of current in the probe, as shown in Fig. 1. Here, contributions to probe size for several values of C_s ranging from 1.5 to 5 mm are given, along with the contribution from aperture diffraction. As C_s decreases, minimum probe diameter decreases and occurs at correspondingly larger values of α. For some particular value of C_s the minimum probe size is $\delta = 0.66 C_s^{1/4}\lambda^{3/4}$, corresponding to the optimum value of $\alpha = 1.05 C_s^{-1/4}\lambda^{1/4}$. Not coincidentally, this value of δ corresponds to the image interpretable resolution or point resolution limit discussed above. In the present context δ corresponds to the image of a point source. Probes corresponding to divergence angles larger than the optimum value are said to be aberration limited because their diameter is determined primarily by C_s. Conversely probes corresponding to divergence angles smaller than the optimum value are called diffraction limited. To obtain more accurate descriptions of diffraction limited probes, wave optical calculations that take explicit account of probe defocus are required. Probes suitable for

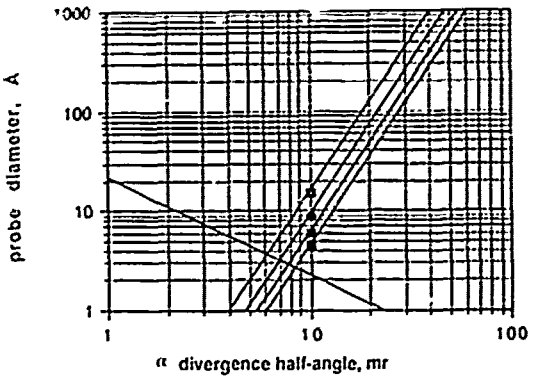

Fig. 1. Dependence of focused probe size at the specimen on aperture diffraction and lens spherical aberration for a point source in the incoherent approximation (100 kV). Several values of C_s are shown: □, 5 mm; ●, 3 mm; *, 2 mm; ■, 1.5 mm.

microspectroscopy usually require values of α larger than optimum to ensure sufficient current for an acceptable count rate. These probes will be aberration limited, and eqn. (1) gives a reasonably accurate description of probe size and current for optimum probe focus at the specimen plane.

When probe current considerations become important the source brightness parameter, β, in d_g, eqn. (1), is important and must be specified. This parameter varies over a wide range for available electron sources, from about 10^5 A cm^{-2} sr^{-1} for tungsten thermionic sources to about 10^8 A cm^{-2} sr^{-1} for FEG sources, with LaB_6 thermionic sources intermediate between the limits [5]. The measured brightness of the FEG analytical microscope used for the experiments discussed in this paper ranges between 5×10^7 and 2×10^8 A cm^{-2} sr^{-1}, depending on the FEG operating parameters. Figure 2 shows total probe diameter as a function of probe current calculated from eqn. (1) for brightnesses characteristic of particular sources. These curves show that FEG sources are required to produce probes smaller than about 25 Å that contain 0.1 to 1 nA. The curves of Fig. 2 were calculated for the optimum value of divergence half angle α, found by minimizing probe diameter with respect to α. This value now depends on brightness as well as C_s and λ, and is given by

$$\alpha_{opt} = 1.18\left\{\frac{4i_b}{\pi^2\beta}+(0.61\lambda)^2\right\}^{1/8} C_s^{-1/4} \qquad (2)$$

where i_b is the probe current and the other parameters were defined earlier. Figure 3 shows the dependence of probe current on optimum divergence. The optimum values of divergence for high brightness FEG sources are approximately half those required for thermionic sources.

Table 1 shows calculated focused probe diameters for the limiting brightness values measured for a particular FEG tip in the analytical microscope used for the measurements reported below, for the limiting beam currents generally considered useful for microspectroscopy. These limiting brightnesses will vary somewhat from one field emitter tip to another, depending on tip radius and other experimental variables [6]. The range for a given tip depends on extractor voltage, operating temperature and flashing procedure.

These small focused probes can easily be imaged in a TEM/STEM analytical microscope to obtain an experimental measurement of probe size. The experiment is straightforward when operating in TEM mode. In STEM operation, to obtain smaller probes, the microscope is operated in diffraction mode and one must adjust the object plane of the transfer lenses to be coincident with the specimen plane without changing

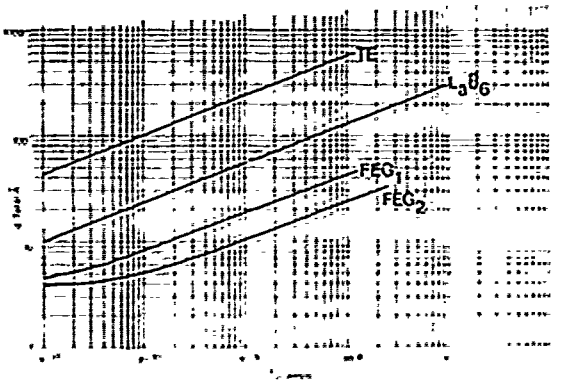

Fig. 2. Probe size as a function of probe current for sources of different brightness β in the incoherent approximation. Aperture and spherical aberration broadening are included. 100 kV. C_s = 1.5 mm. β (A cm^{-2} sr^{-1}): TE = 10^5; LaB_6 = 5×10^6; FEG_1 = 10^8; FEG_2 = 5×10^8.

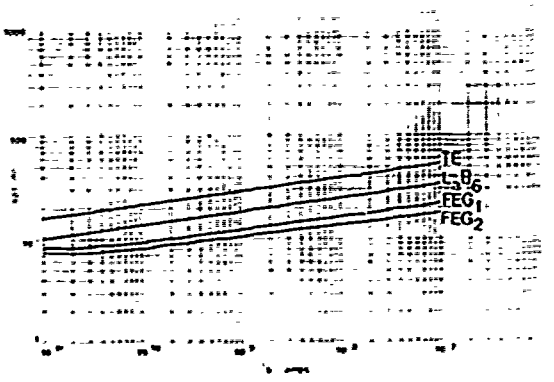

Fig. 3. Optimum divergence half-angle α_{opt} vs. probe current in the incoherent approximation. Aperture and spherical aberration broadening are included. Microscope parameters as in Fig. 2.

TABLE 1 Calculated focused probe diameters at the specimen for measured upper and lower FEG brightness limits, for probe currents of 1 and 0.1 nA. C_s = 1.5 mm, 100 kV, optimum α

i_b (nA)	β A cm^{-2} sr^{-1}	d_g (Å)
1.0	2×10^8	14
0.1	2×10^8	7
1.0	5×10^7	22
0.1	5×10^7	10

the operating mode of the pre-specimen probe forming lenses. Photographically recorded probes for optimum α are shown in Fig. 4. It is worth pointing out that these small probes are nearly HREM images of the electron source, and small misalignments of the illumination system produce distortions that will reduce the basic attainable spatial resolution by at least a factor of 5. These misalignments are obvious in probe images such as Fig. 4, but are difficult to detect by other means. Current distributions in these small probes can be measured directly by scanning them over apertured electronic detectors such as EELS spectrometers or Faraday cups [7]. To obtain a realistic estimate of the attainable spatial resolution in a microspectroscopy experiment, the count rate expected for a given specimen and known incident probe current must be calculated, which leads to a spectrum acquisition time for the desired number of counts in the peak. The acquisition time must be compared with independent measurements of probe/specimen temporal position instability. Positional instability is usually an increasing function of acquisition time, and can easily become limiting, especially for low probe currents.

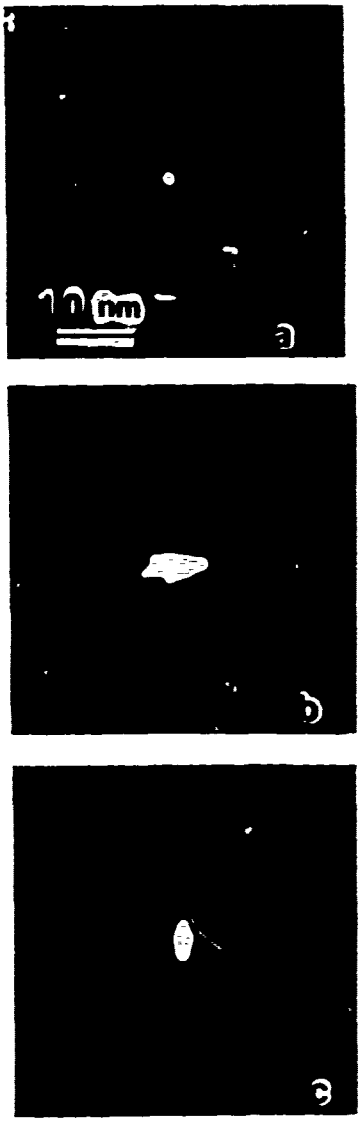

Fig. 4. Photographically recorded STEM probe images. 100 kV, divergence half angle ~ mn, for a field emission source. a. Well aligned probe; probe diameter, ~1.2 nm. b. Distortion caused by displacement of defining aperture by half its diameter. c. Distortion resulting from minor stigmator error.

The net count rate in an ELS absorption edge is given by

$$R = i_p \sigma t N \Delta E \qquad (3)$$

where i_p = focused probe current (electrons s^{-1}); σ = differential cross-section for the core edge of interest at the specified collection angle (nm^2 $atom^{-1}$ eV^{-1}); t = specimen thickness (nm); N = target atom density (nm^{-3}), typically 50 for materials like SiO_2, SiC; ΔE = channel width or probe energy spread (eV), typically 1 eV.

The count rate expression for energy dispersive X-ray spectroscopy (EDS) is similar [8] and a similar method can be used to estimate spatial resolution. Measured values of σ (10 mr collection half angle) at edges of interest such as silicon L or oxygen, carbon or nitrogen K edges in the corresponding compounds with silicon ranged from $10^{-?}$ to $5 \times 10^{-?}$ nm^2 $atom^{-1}$ eV^{-1} [9]. The specimen thickness, t, must be restricted to about 10 nm to avoid undesirable multiple scattering effects. This small thickness does not pose unusually severe experimental difficulties; it is the same as the requirement for interpretable HREM images. All parameters in eqn. (3) are now fixed except the probe current; the upper and lower probe current limits in Table 1 can be used to obtain the limiting count rates. The maximum count rate (for $\sigma = 10^{-?}$ and $i_p = 1$ nA) is about 3×10^{4} counts s^{-1} and the minimum value of R (for $\sigma = 5 \times 10^{-?}$ and $i_p = 0.1$ nA) is about 1600 counts s^{-1}.

The number of counts desirable in an edge depends on the experimental purpose. 5000 is, conservatively, often enough for qualitative analysis and 10 000 or more counts is usually useful for fine structure analysis. On this basis

acceptable counting times, at the energy losses corresponding to the edges of interest here ($\Delta E = 100$ eV for silicon L, and $\Delta E = 283$ and 530 eV for carbon K and oxygen K, respectively) will be between 20 ms and 3 s. For serial EELS collection systems, which require ramping the spectrum channel by channel over an apertured slit/PMT detector, the total spectrum acquisition time is equal to the number of channels scanned times the dwell (*i.e.* counting) time per channel. Typical values for these are 100 ms and 1000, with energy width 1 eV per channel, leading to a total acquisition time of 100 s. Dwell times of 20 ms and 3 s correspond to total acquisition times of 20 s and 50 min, respectively.

Probe position stability, which depends on electrical stability of the microscope, charging along the beam path, etc., has been measured by television recording high magnification ($\simeq 30 \times 10^6$ times) probe images and measuring movement frame by frame. Specimen drift was measured by the usual multiple photographic exposure method; these measurements were made for a liquid nitrogen cooled cryostage at -170 °C. Cold stage use is required to consistently prevent carbon contamination for all extended microprobe experiments. The total probe/specimen positional instability from these two sources can be reduced to about 0.1 nm s^{-1} with careful experimental procedures. For an acquisition time of 20 s (20 ms dwell) the attainable spatial resolution is approximately equal to the largest probe size given in Table 1. For 100 s acquisition times (100 ms dwell) the spatial resolution is limited by probe/specimen positional instability even when high current field emission probes are used. For analysis of multicomponent ceramic microstructures we have found the most useful experimental procedure for high spatial resolution microanalysis to be use of relatively short dwell times (20 to 50 ms) and collection of multiple spectra. The probe is repositioned on the feature of interest between acquisitions, and the individual spectra are summed to obtain the final resultant spectrum. A spatial resolution of 5 nm can be attained for spectra spanning the 0–1000 eV loss range with this procedure if a field emission source and low temperature stage are used.

New parallel detection systems just becoming available give promise of improvements in spatial resolution to near the incident probe size for thin specimens. Actual improvement depends on reduction of total acquisition time, which depends in turn on the net detective quantum efficiency of the parallel detection system relative to the scintillator/PMT serial detection systems currently in use [10–12]. Field emission sources are required to attain high spatial resolution with either serial or parallel detectors.

3. Applications

Silicon and its compounds with oxygen, carbon and nitrogen, such as Si_3N_4, SiO_2 and Si_2N_2O are materials of major interest in ceramics and composites. Analysis of these materials when they are present as small particles or layers in interfaces requires knowledge of their EELS absorption edge shapes in the bulk compounds, since it is expected that local changes in composition or structure will affect electronic structure and bonding [13]. In a recent investigation we have shown that these edge shapes change in a systematic way across the series of materials Si, SiC, Si_3N_4, SiO_2, and also in Si_2N_2O [9, 14]. Examples of experimental silicon L edges, and corresponding theoretical calculations are shown in Fig. 5. Note that the magnitude of the threshold onset peak increases continuously from Si to SiO_2 and that its onset energy increases from Si to SiO_2. The relative minimum between the onset peak and the delayed maximum, at about 125 eV loss, broadens across the series and a small relative maximum appears in this minimum in the Si_3N_4 cross-section curve and is quite prominent in the SiO_2 curve. The delayed maximum itself becomes sharper across the series from Si to SiO_2. Corresponding changes were observed in the K edge anion cross-section curves for SiC, Si_3N_4 and SiO_2. Theoretical analysis of the inelastic scattering in these compounds was carried out using a semiempirical LCAO theory to calculate final state valence shell wavefunctions for the compounds, using Bloch's theorem to account for effects of translational symmetry of the crystals. Plane waves were used for ionization final states far beyond threshold onset, where bonding effects are weak. These wavefunctions were used with a single-electron transition model and the Born approximation to calculate the core shell absorption cross-sections [9, 15]. The results are shown as dotted lines in Fig. 5. There are three primary contributions to the cross-sections. Near onset the compound valence shell final state wavefunctions, which are very sensitive to bond-

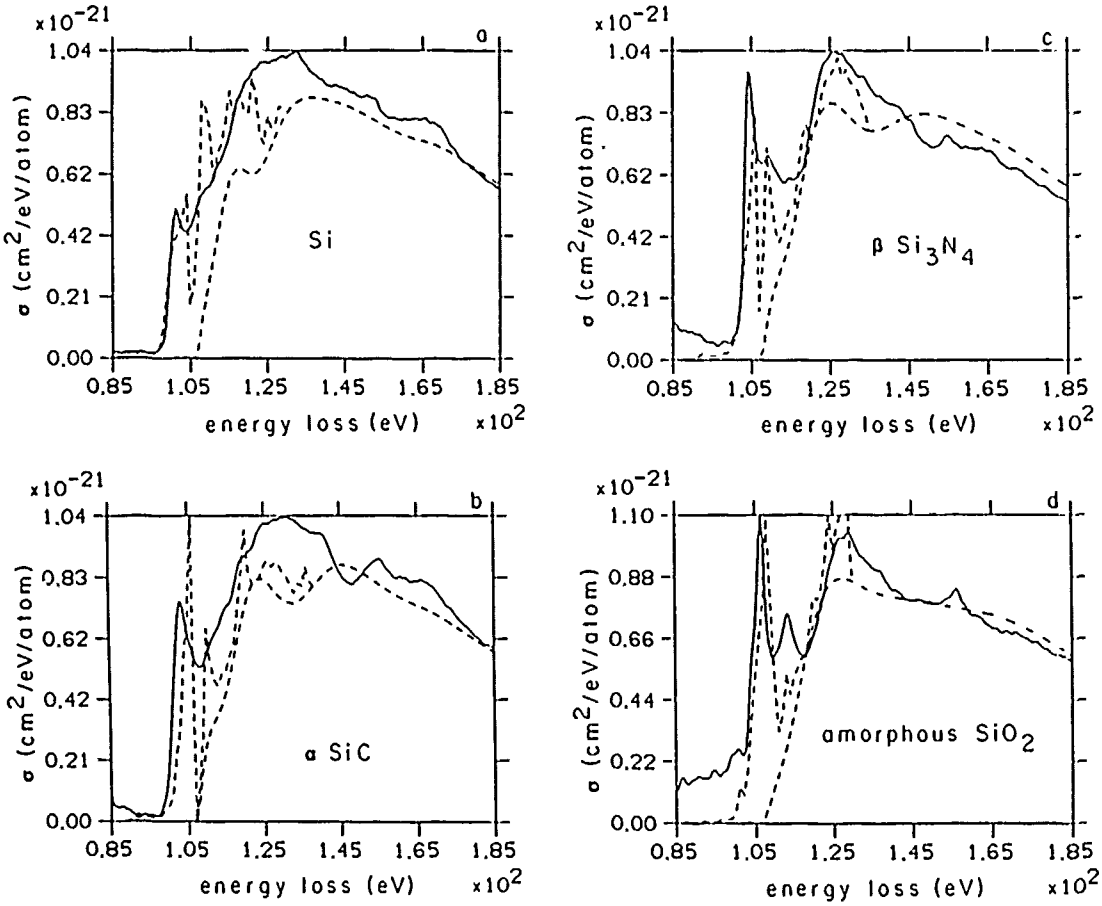

Fig. 5. Silicon L energy loss cross-sections for silicon and some of its important compounds. The solid curve is experimental. The dashed curve beginning at edge onset is the sum of calculated valence shell and ionization cross-sections. The calculated ionization cross-section modulated by near neighbor back-scattering is plotted separately as the dashed curve beginning at 105 eV loss.

ing, control the shape of the curves. Electron transfer from silicon to the ligand atoms occurs in the compounds, to an increasing extent in the progression from Si to SiO_2 and the final state wavefunctions are increasingly dominated by silicon atomic orbitals, so the magnitude of the threshold onset peak in the silicon L edges increases. In this energy loss region the Si 2p→3s and Si 2p→3d partial cross-sections dominate the silicon L edges, with the 2p→3s cross-sections larger. At larger losses, beyond about 125 eV, the atomic ionization cross-section (plane wave final states) dominates the edges, but it is modulated by elastic backscattering of the ionized plane waves by the neighboring atoms surrounding the excited atom, thus the cross-section in this region is not the simple smooth curve expected for a free-atom ionization cross-section. The magnitude of this effect depends on the elastic scattering cross-section of the neighboring atoms, it is stronger for the K shell edges of the ligand atoms because their nearest neighbors are silicon, whereas the nearest neighbors of the silicon atoms are oxygen, nitrogen or carbon. These results furnish a firm fundamental background for microstructural analysis of more complex materials.

Several recent applications to the analysis of complex microstructures illustrate the utility of the technique. The applications were made at about the 5 nm spatial resolution level, and were complemented by EDS, HREM imaging and microdiffraction analysis of the microstructures. Nutt and Carpenter [16] reported an analysis of an aluminum alloy (2124)-silicon carbide metal matrix/ceramic composite in which particular attention was given to the matrix/ceramic interfaces. The material was a discontinuous whis-

ker-reinforced composite made by powder metallurgy methods. The metal ceramic interface contained a discontinuous distribution of small ($\leqslant$10 nm) crystalline precipitates that were shown by EELS to contain oxygen, by EDS to contain magnesium, and by microdiffraction to have structure corresponding to MgO. In regions of the interface not containing these precipitates stepwise EDS analysis across the interface showed a sharp magnesium segregation peak at the interface. The FWHM of the magnesium peak was about 30 nm. Magnesium is a minor constituent of the aluminum alloy matrix, and it was presumed that the MgO particles, which probably did not deviate from the stoichiometric composition, formed as a result of reaction of magnesium with oxide films on the whisker surfaces during heat treatment. HREM produced evidence for a transition zone between the aluminum alloy and the SiC or between the MgO and SiC that may be amorphous. The zone width is small, about 1.5 nm, and below the attainable resolution limit of EELS with serial detection. The composition of this zone should be determinable using a parallel EELS detection system, and is of great interest.

More recently we have examined the non-equilibrium microstructure of a silicon oxynitride ceramic made by hot pressing an equimolar mixture of Si_3N_4 and SiO_2 containing 3 mol.% Al_2O_3 in nitrogen atmopshere at 2000 K [16]. The pressing temperature was above the Si_3N_4–SiO_2 eutectic and Si_2N_2O formed by liquid-phase reaction. The resulting microstructure contained three major phases, shown in Fig. 6. These phases were found to be Si_2N_2O, SiO_2 (amorphous), and Si_3N_4, by quantitative EELS analysis. The silicon L edge from Si_2N_2O is shown in Fig. 7. The shape is very similar to the corresponding edge for SiO_2, despite the fact that in this orthorhombic material three of the silicon nearest neighbors are nitrogen and only one is oxygen. An LCAO calculation similar to those described above was used to calculate the edge shapes, and the results agreed well with experiment. Small crystalline precipitates or second phase particles were observed in the oxynitride plates (Fig. 8) and in the SiO_2 amorphous phase. These contained silicon and variable amounts of nitrogen and oxygen. The small particles in the Si_2N_2O plates obviously have a well-defined habit (long straight edges along (010) Si_2N_2O) and usually have a composition close to Si_3N_4 with a very small oxygen

Fig 6. Low magnification dark field micrograph of Si_2N_2O ceramic taken with section of SiO_2 amorphous ring. Long plates are Si_2N_2O in SiO_2 matrix.

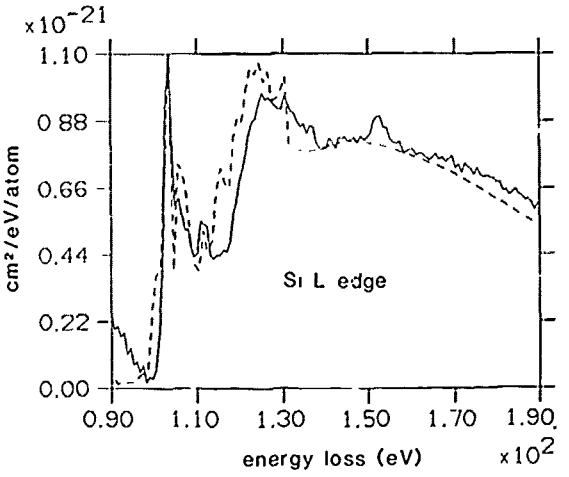

Fig. 7. Electron energy loss cross-section for silicon L in Si_2N_2O. Solid line is experimental. Dashed line is theoretical calculation.

content, however their diffraction patterns do not correspond to α- or β-Si_3N_4. Thus it is difficult to attribute them to residual Si_3N_4 partially reacted to Si_2N_2O. The particles in the matrix are primarily silicon and oxygen and their microdiffraction

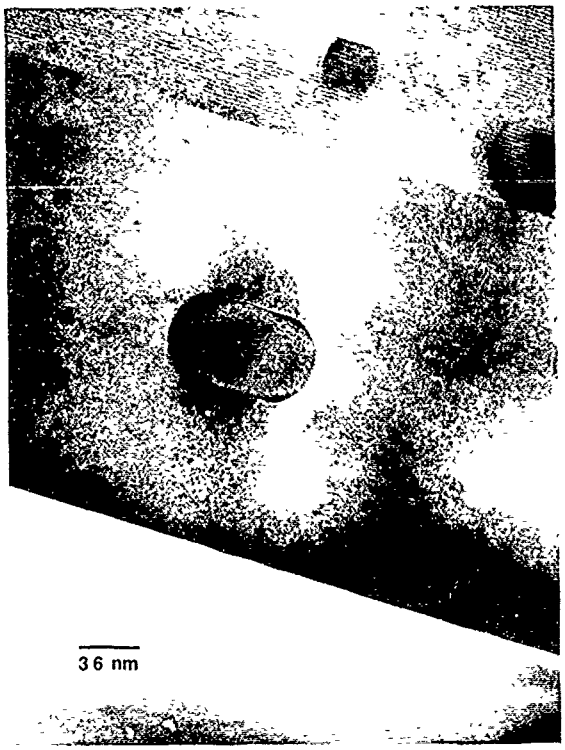

Fig. 8. HREM micrograph of Si_2N_2O plate containing semi-coherent second phase microcrystal. Long edges of microcrystal and axis of oxynitride plates along [010]. See text for discussion.

Fig. 9. Low magnification micrograph of SiC whisker-reinforced Si_3N_4 composite. An SiC whisker oriented nearly normal to its growth axis is visible in the central area. The whisker is faulted normal to its growth axis. Arrowed regions are amorphous, and contain yttrium, aluminum, silicon, oxygen, and a small amount of nitrogen. SiC and Si_3N_4 are in indirect contact in the boxed area.

patterns correspond to crystobalite. Small changes in slope of the energy loss spectra near 73 eV loss, corresponding to the aluminum L edge, indicated the presence of aluminum in all the major phases. EDS showed that aluminum was preferentially partitioned into the SiO_2 phase, and secondarily into the Si_2N_2O, with minimum concentration in the Si_3N_4.

Whisker-reinforced ceramic matrix composites have improved fracture behavior relative to polycrystalline structural ceramics, and their fracture behavior is believed to be dependent on the microstructure of the whisker/matrix interface [17]. These materials have most often been synthesized from mixtures of the ceramic matrix powders and whiskers with sintering aids by hot pressing, and amorphous regions at interfaces and triple junctions similar to those observed in unreinforced polycrystalline ceramics have been reported [18, 19]. Whether these amorphous regions are continuous along the whisker/matrix interfaces is of interest. We have examined relatively flat regions of whisker/matrix interfaces well removed from intersecting grain boundaries using HREM and EELS and do not find imaging or composition evidence for amorphous phases there [20]. One of the composites investigated was Al_2O_3 base, reinforced with 20 vol.% β-SiC whiskers from Tateho Chemical Industries, hot pressed at 1830 °C/60 MPa in vacuum. The other was Si_3N_4 base with 6 wt.% ($Y_2O_3 + Al_2O_3$) added for densification, reinforced with 20 vol.% SiC whiskers from Tokai Carbon, Ltd., hot pressed at 1725 °C/30 MPa in argon. A low magnification image of the Si_3N_4/SiC composite is shown in Fig. 9. An SiC whisker oriented approximately normal to its growth axis is visible in the central region. The whisker/matrix interface is composed of regions with Si_3N_4 in apparent direct contact with SiC (boxed) and irregularly shaped regions that are amorphous (arrowed). A high resolution image of the boxed region is shown in Fig. 10. It can be seen that the carbide and nitride are in direct contact, and no indication for the presence of a second phase was found. EELS examination with an incident probe

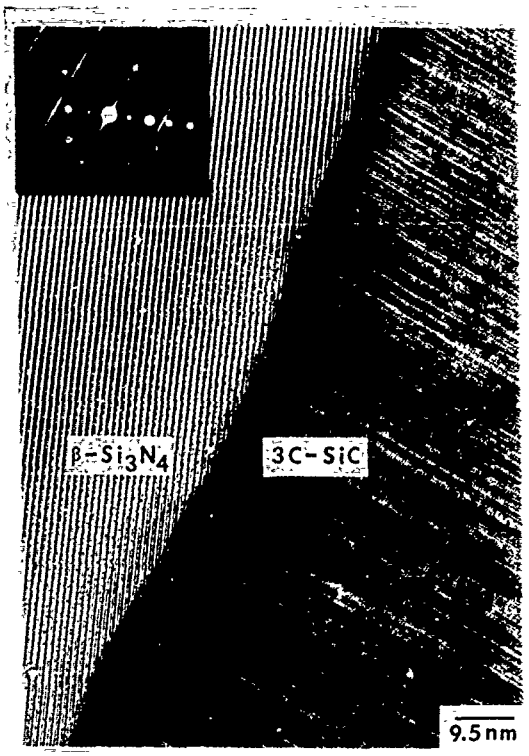

Fig. 10. HREM micrograph (400 kV) of the boxed area of Fig. 9. Note the absence of a thin amorphous zone between the crystals, and the absence of a crystalline reaction zone.

about 5 nm in diameter did not indicate the presence of foreign elements. In particular, oxygen was not detected. The roughness of the interface is small scale, and probably related to the fault plane distribution in the whisker itself, normal to its growth axis. Our observations of the whiskers themselves, before incorporation into composites, indicated that the surface is faceted on a fine scale, corresponding to intersections of the fault planes with the free surface. Similar observations were made for the Al_2O_3/SiC composite, viewing the matrix/whisker interface along the whisker growth axis. It is possible in both cases that the small interface roughness interfered with observations of a very thin amorphous layer by HREM, but other imaging methods also failed to show an amorphous layer in these regions. It is somewhat surprising that no impurity segregation was detected in these regions, given the well-known surface contamination of whiskers. Either the contaminants were removed during processing, or the 5 nm probe effectively reduced the concentration in the irradiated volume below detectability. Future improvements in EELS spatial resolution will be applied to this problem, to obtain spectra more directly related to the boundary plane itself.

A comment concerning electron radiation effects in these materials is useful. Several investigators have noted that mass loss and changes in electronic structure can occur during EELS focused probe experiments in ionic or covalent materials, *e.g.* [21] for copper oxide, where increasing electron doses caused a transformation in shape of the copper L edge to that characteristic of elemental copper with filled 3d shell and a small threshold onset peak. We have observed a similar transformation of the silicon L edge in bulk Si_3N_4 with increasing dose; the edge changed in appearance from characteristic of Si_3N_4 to characteristic of Si (*cf.* Fig. 5 above), indicating nitrogen loss, or at least Si–N debonding. It is expected that these effects may occur more easily in disordered interfaces, and these effects must be considered before segregation is ruled out.

Acknowledgments

Most of the research discussed in this paper was supported by the Division of Materials Sciences, Office of Basic Energy Sciences, U.S. Department of Energy under grant DE-FG02-87ER45305. The electron microscopy was carried out in the NSF/ASU High Resolution Electron Microscopy Facility in the Center for Solid State Science.

References

1 J. C. H. Spence, *Experimental High-Resolution Electron Microscopy*, Clarendon Press, Oxford, 1981.
2 K. L. Merkle, J. F. Reddy, C. L. Wiley and David J. Smith, in J. Pask and A. Evans (eds.), *Ceramic Microstructures '86*, Plenum, New York, 1988.
3 O. C. Wells, *Scanning Electron Microscopy*, McGraw-Hill, New York, 1974, p. 69.
4 R. W. Carpenter, I. Y. T. Chan and J. M. Cowley, in G. Bailey (ed.), *Proc. 40th Annual Meeting Electron Microscopy Society of America*, Claitor's Publ. Co., New Orleans, 1982, p. 696.
5 L. Reimer, *Transmission Electron Microscopy*, Springer, Berlin, 1984.
6 J. F. Hainfeld, *Scanning Electron Microscopy*, Vol. I, IIT Research Institute, Chicago, IL, 1977, p. 591.
7 J. K. Weiss and R. W. Carpenter, in G. Bailey (ed.), *Proc. 46th Annual Meeting Electron Microscopy Society of America*, San Francisco Press, 1988, p. 510.

8 N. J. Zaluzec, in J. J. Hren, J. I. Goldstein and D. C. Joy (eds.), *Introduction to Analytical Electron Microscopy,* Plenum, New York, 1979, p. 121.
9 W. M. Skiff, R. W. Carpenter and S. H. Lin, *J. Appl. Phys., 62*(1987) 2439.
10 R. F. Egerton, *J. Electron. Microsc. Technol., 1*(1984) 37.
11 O. L. Krivanek, *Ultramicroscopy, 22*(1987) 103.
12 M. G. Strauss, I. Naday, I. S. Sherman and N. J. Zaluzec, *Ultramicroscopy, 22* (1987) 117.
13 J. Silcox, in J. J. Hren, J. I. Goldstein and D. C. Joy (eds.), *Introduction to Analytical Electron Microscopy,* Plenum, New York, 1979, p. 295.
14 W. Braue, W. M. Skiff, R. W. Carpenter and H. Ma, in G. Bailey (ed.), *Proc. 45th Annual Meeting Electron Microscopy Society of America,* San Francisco Press, 1987, p. 164.
15 W. M. Skiff, R. W. Carpenter and S. H. Lin, *J. Appl. Phys., 58*(1985) 3463.
16 W. Braue, W. M. Skiff, R. W. Carpenter and H. Ma, in G. Bailey (ed.), *Proc. 45th Annual Meeting Electron Microscopy Society of America,* San Francisco Press, 1987, p. 164.
17 J. Homeny and W. L. Vaughn, *Mater. Res. Bull., 66* (Oct/Nov, 1987).
18 V. K. Sarin and M. Ruhle, *Composites, 18*(1987) 129.
19 S. R. Nutt and D. S. Phillips, in A. K. Ohingra and S. G. Fishman (eds.), *Interfaces in Metal–Matrix Composites,* The Metallurgical Society, Warrendale, PA, 1986, p. 112.
20 W. Braue, R. W. Carpenter and D. J. Smith, in G. Bailey (ed.), *Proc. 46th Annual Meeting Electron Microscopy Society of America*, San Francisco Press, 1988, p. 734.
21 N. J. Long, W. M. Skiff, A. Higgs, R. W. Carpenter and C. E. Lyman, in G. E. Bailey (ed.), *Proc. 43rd Annual Meeting Electron Microscopy Society of America,* San Francisco Press, 1985, p. 408.

Materials Science and Engineering, A107 (1989) 217–223

Interfacial Interactions in Titanium-based Metal Matrix Composites*

D. G. KONITZER

Alcoa Labs, Alcoa Center, Pittsburgh, PA 15069 (U.S.A.)

M. H. LORETTO

Department of Metallurgy and Materials, University of Birmingham, P.O. Box 363, Edgbaston, Birmingham B15 2TT (U.K.)

(Received June 1, 1988)

Abstract

Analytical transmission electron microscopy has been used to assess the nature and the extent of interactions between TiC particulates in Ti6Al4V and in Ti24Al11Nb. It has been found that there appears to be only limited interaction between the TiC and the Ti6Al4V alloy even when the samples are heat treated at 1050 °C for times up to 50 h. The visible interaction is confined to the TiC where it is found that an annulus of non-stoichiometric TiC is formed around the original stoichiometric TiC. In the case of the Ti24Al11Nb alloy there is a clear interaction zone visible where $Ti_3(AlNb)C$ is formed. In addition there is an additional narrow zone within the TiC particles associated with the diffusion of Nb into the TiC in samples heat treated at 1000 °C but Nb is present throughout the particles in specimens heat treated at 1100 °C for 5 h. Non-stoichiometric TiC is also visible in the annuli of the original TiC particles in this composite. The significance of these observations is discussed in terms of the factors which control the extent of the interaction zone.

1. Introduction

Metal matrix composites are seen as a generation of materials which can give significant improvements in properties, but if this hope is to be realized it is essential that the interfacial region between the matrix and the particle or fiber does not fail prematurely. In the case of titanium alloys the extreme reactivity of titanium provides a major difficulty in finding particles or fibers which are not attacked by titanium with the consequent generation of brittle intermetallics. In the case of titanium-based SiC composites [1, 2] it is known, for example, that the interfacial region consists of TiC and Ti_5Si_3—a brittle intermetallic. The present work has been aimed at assessing the stability of TiC particulate in both Ti6Al4V (expressed as wt.%) and in Ti24Al11Nb (expressed as at.%), and this paper summarizes the work which has been completed so far.

2. Experimental

The composites, which contained 10% by volume of TiC, were supplied by Alcoa and were subsequently heat treated for a range of times at temperatures between 900 and 1200 °C. Polished and etched samples were examined optically and using scanning electron microscopy. Analytical transmission electron microscopy was the main technique used to assess the extent of any interfacial interactions, and in this case the samples were prepared by ion beam thinning. The transmission microscopes which were used include a 120 kV Philips 420 and a 400 kV JEOL4000FX, which were interfaced to energy dispersive X-ray (EDX) and electron energy loss (EELS) systems.

3. Results

3.1. Optical and scanning electron microscopy

Typical optical micrographs obtained from the two composites are shown in Fig. 1 and, at the resolution available optically, it appears that the extent of any interaction is larger in the Ti24Al11Nb alloy; in fact there is no interaction visible optically in the Ti6Al4V composite in Figs. 1(a) and 1(b). The interaction is not obvious even in the Ti24Al11Nb but, in both the polished sample (Fig. 1(c)) and in the etched sample (Fig.

*Paper presented at the symposium on Interfacial Phenomena in Composites. Processing, Characterization, and Mechanical Properties, Newport, RI, June 1–3, 1988.

0921-5093/89/$3.50

© Elsevier Sequoia/Printed in The Netherlands

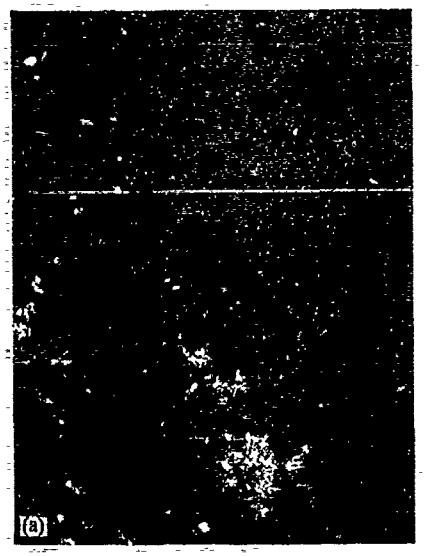

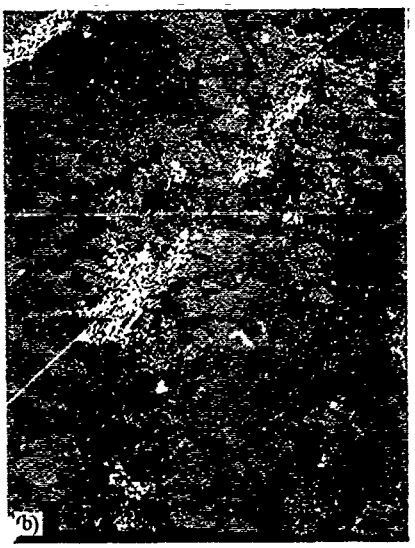

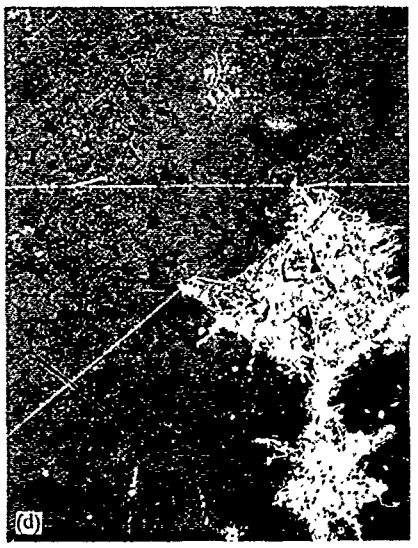

Fig. 1. Optical micrographs of Ti6Al4V–TiC as polished (a) and etched (b) and of Ti24Al11Nb–TiC as polished (c) and etched (d). The samples in (a) and (b) had been heat treated for 2 h at 1050 °C before examination, and the samples in (c) and (d) had been treated at 1000 °C for 2 h. A limited interaction zone around the TiC particles can be seen in the Ti24Al11Nb sample but not in the TiAlV sample.

1(d)) a narrow zone can be seen around each TiC particle.

Similarly scanning electron microscopy shows (Fig. 2) that there is no obvious change around the TiC in the Ti6Al4V samples (Fig. 2(a)), although there is a very narrow region in the image which shows lighter contrast than the rest of the TiC particle. There is again a slight change about 1.0 μm wide, around the TiC particles in the Ti24Al11Nb composite. This difference is just visible in Fig. 2(b).

The extent of any interaction between the TiC and the two matrix alloys is clearly on a scale which is below that at which accurate compositional information can be obtained from bulk samples but detailed information can be obtained using analytical transmission electron microscopy, as discussed below.

3.2. Analytical transmission electron microscopy

3.2.1. Observations on TiAlV–TiC composite

Examination using transmission electron microscopy confirms that there is no obvious interaction zone in the matrix associated with the presence of TiC particles in composites treated over a range of temperatures up to 1050 °C and for times up to 50 h. There is, however, evidence of a reaction zone within the TiC particulates as

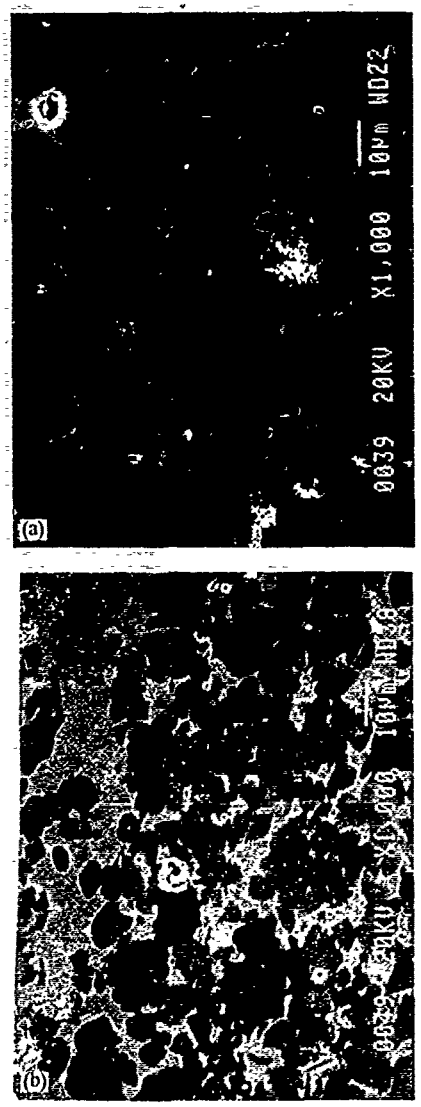

Fig. 2. Scanning electron micrographs using secondary electrons of (a) Ti6Al4V, and (b) Ti24Al11Nb. Any interaction zones are not easily resolved in these micrographs. Samples heat treated at 1050 °C and 1200 °C as in Fig. 1. See text.

can be seen from the micrograph shown in Fig. 3 where a region can be seen around the perimeter of the particle shown in this figure, which is separated from the center of the particle by an array of dislocations. EDX, EELS and diffraction analyses have shown [3] that this annular region is non-stoichiometric TiC, whereas the original TiC added to the composite was stoichiometric and contained virtually no dislocations [3]. The difference between the annulus and the center can be observed directly on the screen when examination is carried out in the diffraction mode, since there are extra diffraction maxima associated

Fig. 3. Transmission electron micrograph of a particle of TiC in Ti6Al4V–TiC showing the presence of a dislocation array within the TiC. This array separates the stoichiometric center of the TiC from the non-stoichiometric annulus. See text.

with the ordering of the carbon vacancies [3], as shown in Fig. 4. It should be noted that this order can be removed by the high energy electrons, within about 20 min examination under normal imaging conditions, and some care is therefore necessary if this technique is used in order to identify ordered regions. The center of this particle and of all other particles examined in similarly heat treated samples were shown to be stoichiometric TiC.

The fact that there is no apparent interaction zone in the Ti6Al4V matrix is surprising. This may be in part due to the fact that the samples which have been examined have been slowly cooled from the heat treatment temperatures so that the structure which has been examined has been influenced by changes which might occur during cooling. In an attempt to investigate this possibility samples have been examined after being quenched from the heat treatment temperature. There was again no apparent difference between samples which had been quenched and those that had been slowly cooled, when using optical and scanning electron microscopy. Thus quantitative analysis of the particle number density in samples which had been either slowly

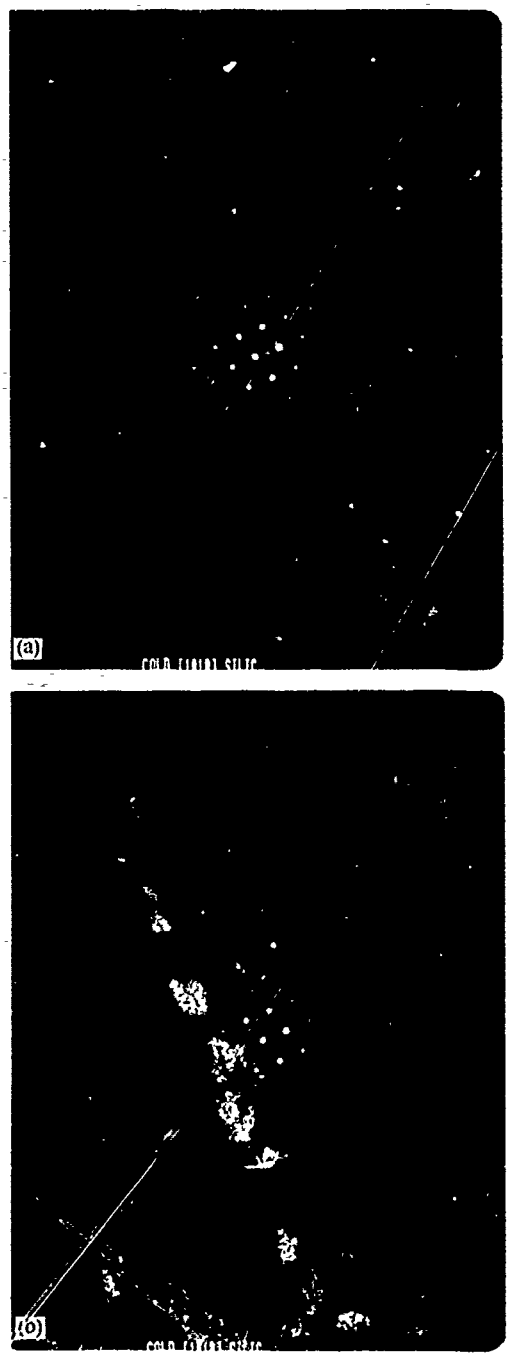

Fig 4 Transmission diffraction patterns obtained (a) from the annulus and (b) from the center of a TiC particle within the Ti6Al4V-TiC composite. Note the extra diffraction maxima from the annulus which are associated with the carbon vacancies.

cooled or quenched revealed no obvious difference. However, examination in transmission showed that the width of the non-stoichiometric TiC was significantly larger in these quenched samples than in the slowly cooled samples, and in some cases no dislocation array could be seen, presumably because the remaining volume consisted totally of the annulus. As mentioned above, the difference between the non-stoichiometric and the stoichiometric core can be quickly qualitatively assessed using the diffraction pattern and approximate widths of the zones could be conveniently obtained using this approach. The typical width in the slowly cooled samples was usually less than 1 μm whereas in the quenched sample the width was about 2 μm.

3.2.2. Observations on TiAlNb–TiC composite

Figure 5 shows a series of micrographs taken from the Ti24Al11Nb-TiC composite which had been heat treated at 1000 °C for 2 h and it is apparent in Fig. 5(a) that the matrix adjacent to the TiC is heavily faulted and that the grain size of this faulted region is smaller than the 10 μm which Fig. 1 shows is typical of the matrix. There also appears to be a slight change in the contrast across the TiC particles, and this can be clearly seen in Fig. 5(b) where the annulus shows different contrast from that in the center of the TiC. In this case, as distinct from the Ti6Al4V case, there is no dislocation wall separating the annulus from the center and no obvious change in the diffraction patterns from the two regions. Observations made on samples which had been heat treated for longer times and higher temperatures revealed some important differences. Thus, in samples heat treated at 1100 °C for 5 h, dislocations were more commonly seen within the TiC particles and diffuse diffraction maxima, which were weaker than those shown in Fig. 4, were occasionally observed.

In order to interpret these observations, diffraction patterns, EDX and EELS spectra were obtained from the heavily faulted region and from the two regions within the TiC particles. The EDX data show that the niobium content of the small-grained, faulted region adjacent to the TiC is significantly lower than that in the matrix. Figure 6 shows spectra obtained from these two regions, which have been normalized to the same titanium count, and it is obvious that there is a change in the NbL:AlK intensity ratio in the interface phase from a value of about 1:1 in the matrix to about 1.2 in the faulted interface phase. Analysis using EELS and using a thin window detector (which allow the presence of light elements to be detected) has also been carried out and a typical EELS spectrum obtained from this

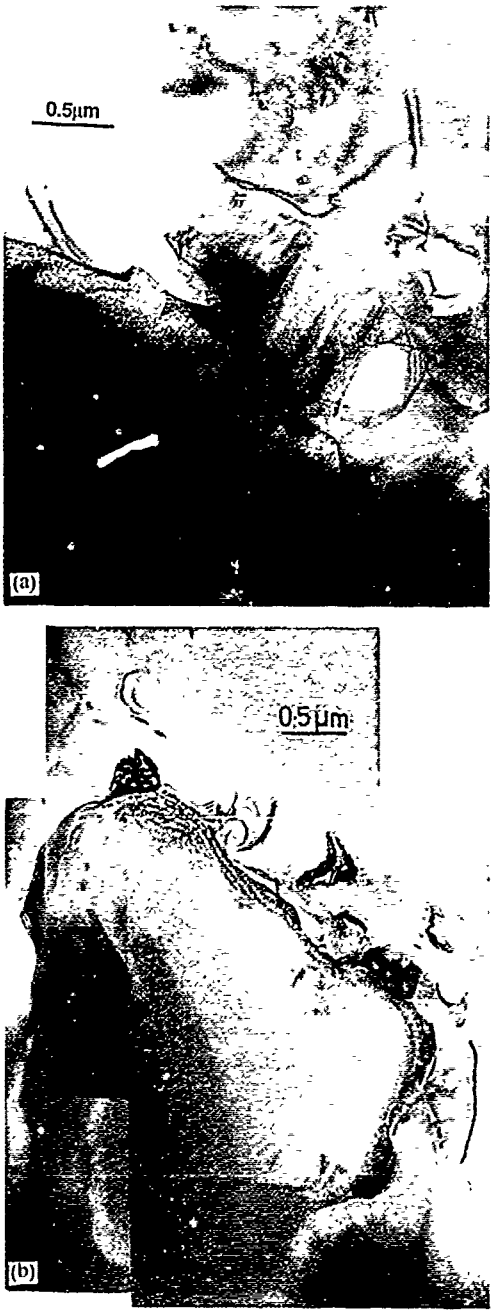

Fig. 5. Transmission electron micrographs of a TiC particle within the Ti24Al11Nb TiC composite showing (a) the presence of the faulted, fine grained phase around the TiC and (b) the annulus around the TiC which shows slightly different contrast from the center.

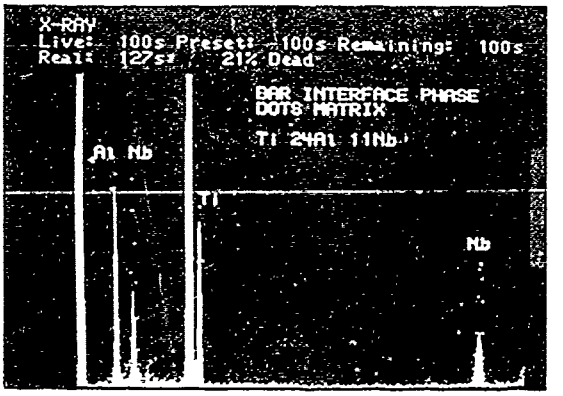

Fig. 6. EDX spectra obtained from the faulted region adjacent to the TiC particle and from the matrix remote from a TiC particle normalized to the same titanium count. It can be seen that the amount of niobium present in the faulted region is significantly less than that in the matrix. See text.

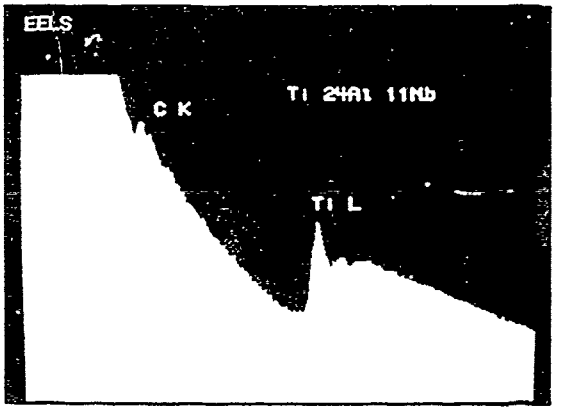

Fig. 7. An EELS spectrum obtained using a thin window detector from the faulted phase adjacent to the TiC particles in Ti24Al11Nb-TiC composite. Note the presence of carbon.

phase is shown in Fig. 7 where it can be seen that there is detectable carbon present. Diffraction analysis of this phase shows [4] that it has a lattice parameter of about 4.15 Å and a space group of $Pm3m$. These facts, taken in conjunction with the analytical data, confirm that the phase formed in the region between the TiC and the matrix is $Ti_3(AlNb)C$, *i.e.* a phase based on the Ti_3AlC phase [5].

The change in contrast, seen in Fig. 5 within the TiC particles, has been investigated using analytical electron microscopy and it has been found that there is a significant amount of niobium within these annular regions in the original TiC particles for samples heat treated at 1000 °C. For samples heat treated at 1100 °C and higher there is detectable Nb throughout the TiC particles and part of two EDX spectra taken from the center and the perimeter of a TiC particle are shown in Fig. 8. These have been normalized to the same titanium count and it is clear that there is more niobium in the annulus than in the center

Fig. 8. Part of two EDX spectra obtained from the annulus and from the center of a TiC particle within the Ti24Al11Nb-TiC composite, normalized to the same titanium count showing niobium is present throughout the particle but at a higher concentration in the annulus.

but that there is a significant niobium content throughout.

It has not been possible to quantify the carbon content across the TiC particles using EDX and EELS and on this basis it is not clear whether there is some depletion of carbon within the annulus. Extra diffraction maxima could however occasionally be observed within the annulus and it is therefore apparent that there is a rim of carbide which is below stoichiometry in these particles as was found in the Ti6Al4V composite.

4. Discussion and conclusions

The results presented above show clearly that the interaction between the TiC particulates and the Ti6Al4V matrix is less extensive than that between the TiC and the Ti24Al11Nb matrix. The interpretation of the observed structures is suggested by the observations made on the quenched Ti6Al4V samples. Thus, the fact that there is a zone denuded of carbon around the center of each TiC particle, and that the size of this zone is smaller in samples which have been slowly cooled, suggests that at the heat treatment temperature there is a state of quasi-equilibrium both between the stoichiometric center of the TiC particle and the annulus (which is non-stoichiometric) and between this non-stoichiometric annulus and the matrix (which would be expected to be saturated with carbon).

The true equilibrium would consist of a uniform non-stoichiometric TiC particle and a saturated solution of carbon in the titanium matrix, but for this condition to be achieved it would be necessary for the carbon from the center to diffuse through the annulus and this would take a very long time to occur. Instead, the composite remains in this metastable state for the annealing times used and, if it is cooled slowly, much of the carbon apparently redeposits on the TiC, so reducing the width of the non-stoichiometric annulus. In the case of the quenched sample, this redeposition cannot occur to the same extent and wider annuli are observed. The solid solubility of carbon in titanium does not decrease significantly until about 600 °C and the fact that there is a relatively wide non-stoichiometric zone, even in slowly cooled samples, presumably reflects the limited temperature range over which there is a significant driving force for reprecipitation of the carbon.

On this basis the apparent lack of interaction between the TiC and the Ti6Al4V matrix simply reflects the fact that the diffusion of carbon from the TiC is reversible in this alloy and the amount of carbon left in solution (which cannot be detected with the techniques used in the present work) is insufficient to cause any significant change in microstructure.

If the situation in the Ti24Al11Nb matrix is now considered in the light of the above discussion, the reason for the change in microstructure is that the carbon, which does diffuse into the matrix, cannot easily redeposit since it forms a stable compound, $Ti_3(AlNb)C$. This compound would be expected to form at the heat treatment temperatures [5] and to remain as a stable phase even during the relatively slow cool. The carbon thus gets trapped in a potential well, and there is therefore evidence remaining in the structure at room temperature that the carbon from the TiC did diffuse into the matrix during the high temperature treatment. In addition there is clearly a driving force for the niobium in the matrix to dissolve in the TiC so forming a solid solution, where the activity of the niobium is reduced below that of the niobium in the matrix. The structure which has been observed after high temperature heat treatment thus consists of (TiNb)C particles surrounded by $Ti_3(NbAl)C$ within the matrix of Ti24Al11Nb.

The above discussion points the way to limit the extent of any interaction zone in titanium-based composites. Thus it is likely that there will be an interaction between most particulates or fibers, when they are heated in contact with tita-

nium, but the influence on the final microstructure will tend to be smaller if the reaction is reversible with temperature. Some interaction is of course necessary, in order to obtain a good bond between the particulate or fiber and the titanium matrix, and it seems that a material such as TiC, which has comparable elastic properties with those of SiC, possesses appropriate stability in some titanium alloys.

Further work is underway to assess the influence of these interfacial reaction products on the mechanical properties of these composites.

Acknowledgments

We would like to acknowledge the assistance of A. J. Burbery and R. B. Tallerico and support from Science and Engineering Research Council for part funding of the 4000FX.

References

1 H. J. Dudek, R. Leucht and G. Ziegler, *Proc. 5th Int. Conf. on Titanium*, Munich, Vol. 4, 1984, p. 1773.
2 A. Brown, *M. Eng. Thesis*, University of Birmingham, 1988.
3 D. G. Konitzer and M. H. Loretto, *Acta Metall.*, accepted for publication.
4 D. G. Konitzer and M. H. Loretto, *Mater. Sci. Technol.*, accepted for publication.
5 S. Sridharan and H. Nowotny, *Z. Metallkd.*, *74* (1983) 468.

V MICROMECHANICS

Materials Science and Engineering, A107 (1989) 227–239

The Mechanical Performance of Fiber-reinforced Ceramic Matrix Composites*

A. G. EVANS

Materials Department, College of Engineering, University of California, Santa Barbara, CA 93106 (U.S.A.)

(Received June 1, 1988)

Abstract

This article evaluates the current understanding of relationships between microstructure and mechanical properties in ceramics reinforced with aligned fibers. Emphasis is placed on definition of the micromechanical properties of the interface that govern the composite toughness. Issues such as the debond and sliding resistance of the interface are discussed based on micromechanics calculations and experiments conducted on both model composites and actual composites.

1. Introduction

Practical ceramic matrix composites reinforced with continuous fibers exhibit important failure and/or damage behaviors in mode I, mode II and mixed mode I–II, as well as in compression. The failure sequence depends on whether the reinforcement is uniaxial or multiaxial and whether woven or laminated architectures are used. However, the underlying failure processes are fully illustrated by the behavior of uniaxially reinforced systems. The basic features are sketched in Fig. 1. The intention of the present article is to provide an assessment of relationships between the properties of the constituents (fiber, matrix, interface) and the overall mechanical performance of the composite. At the outset, it is recognized that the composite properties are dominated by the interface, such that upper bounds must be placed on the interface debond and sliding resistance in order to have a composite with attractive mechanical properties. A major emphasis of the article thus concerns the definition of optimum properties for coatings and interphases between the fibers and the matrix, subject to high temperature stability and integrity. Residual stresses in the composite caused by thermal expansion differences are also very important and are confronted throughout.

The strong dependence of ceramic matrix composite properties on the mechanical properties of the interface generally demands consideration of fiber coatings and/or reaction product layers, at least for high temperature use. Thus, while composites fabricated using low temperature matrix infiltration procedures, such as chemical vapor infiltration (CVI), can create composites that exhibit limited interface bonding and, therefore, have acceptable ambient temperature properties, experience indicates that moderate temperature exposure causes diffusion, coupled with the ingress of oxygen, nitrogen etc., from the environment, resulting in chemical

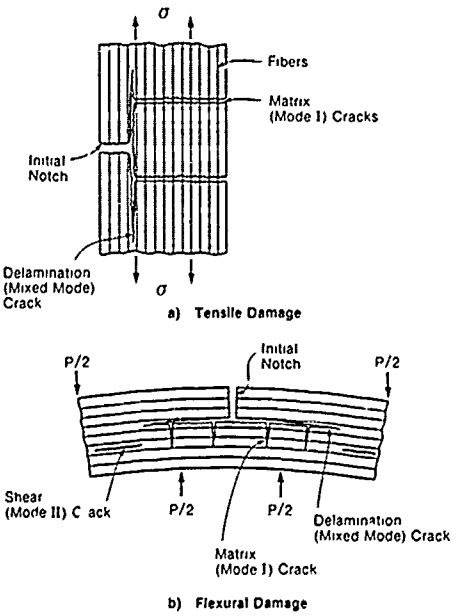

Fig. 1. A schematic illustrating the failure modes observed in high toughness uniaxially reinforced ceramic matrix composites: (a) tension; (b) flexure.

*Paper presented at the symposium on Interfacial Phenomena in Composites. Processing, Characterization, and Mechanical Properties, Newport, RI, June 1–3, 1988.

0921-5093/89/$3.50

© Elsevier Sequoia/Printed in The Netherlands

bonding across the interface. The resultant interphase consisting of oxides, nitrides, carbides (either separately or in combination) invariably have sufficiently high fracture resistance that desirable composite properties are not retained. Consequently, a major objective of this article and of continuing research on ceramic matrix composites is the identification of interphases that are both stable at high temperature and bond poorly to either the fiber or the matrix. Certain refractory metals and intermetallics seem to have these attributes, as elaborated in the following chapters.

The basic philosophy of this article is that the overall mechanical behavior is sufficiently complex and involves a sufficiently large number of independent variables that empiricism is an inefficient approach to microstructure optimization. Instead, optimization only becomes practical when each of the important damage and failure modes has been described by a rigorous model, validated by experiment. The coupling between experiment and theory is thus a prevalent theme. It is also noted that this objective can only be realized if the models are based on homogenized properties that describe representative composite elements, while also taking into account the constituent properties of the fibers, matrix and interface. Models that attempt to discretize microstructural details have little merit in the context of the above objective. In this regard, the present philosophy is analogous to that used successfully to describe process zone phenomena such as transformation and microcrack toughening [10, 16, 22, 11, 4] as well as ductile fracture [15, 20] wherein the behavior of individual particles, dislocations, etc., provides input to the derivation of constitutive properties that describe the continuum behavior.

The behavior of the composite is intimately coupled to some basic features of crack propagation and sliding along interfaces. Indeed, the response of the composite can be simulated by studying interface responses in judiciously selected test specimens. The basic mechanics and the implications of tests used to study interface debonding and sliding are presented first. The characteristics of the damage and fracture processes that occur in each of the important modes depicted in Fig. 1 are then described. Finally, implications for the choice of matrices, fibers and coatings that provide good mechanical properties are discussed.

2. Interface debonding and sliding

2.1. Mechanics of interface cracks

Interface debonding in ceramic matrix composites occurs both at the matrix crack front and in the crack wake (Fig. 2). Both processes are *mixed mode*. Furthermore, debond cracks typically occur between materials (fiber, matrix, coating) having quite different elastic properties. The requisite mechanics thus concern cracks on *bimaterial* interfaces, resulting in a more complex fracture mechanics formulism than the familiar stress intensity factors used in elastically homogeneous systems. The additional features that need to be introduced when considering interface cracks derive from the fact that the mixity of opening and shearing of the surface depends on the modulus mismatch and on the crack length, as well as on the mode of loading. Consequently, the debond resistance of a bimaterial interface must always be characterized by two parameters: the critical strain energy release rate, $\mathcal{G}_{ic}$, and the phase angle of loading ψ_1. The latter quantity is somewhat dependent on the choice of units, for reasons elaborated elsewhere [21]. However, this presents no difficulty, provided that a consistent choice is made. The strain energy release rate, $\mathcal{G}$, and the phase angle can be calculated for any problem of interest and can be expressed in terms of the applied loads, specimen dimensions and debond length.

The basic relationship used to calculate $\mathcal{G}$ and ψ can be defined with reference to Fig. 3. The phase angle is related to the angle of rotation ϕ of the crack surface as the crack opens by [21, 7]

$$\psi = \phi - \frac{\ln r}{2\pi} \ln \frac{(1-b)}{(1+b)} - \tan^{-1}\left(\frac{1}{\pi}\right) \ln \frac{(1-b)}{(1+b)} \qquad (1)$$

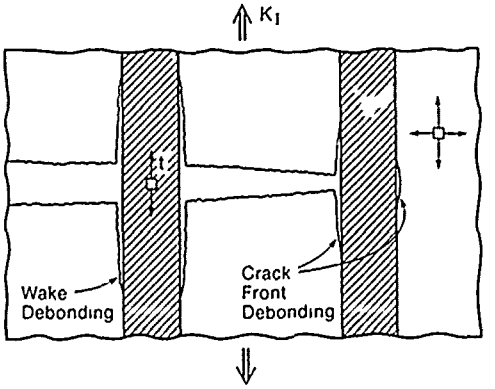

Fig. 2. A schematic illustrating the initial debonding of fibers at the crack front and fiber debonding in the crack wake.

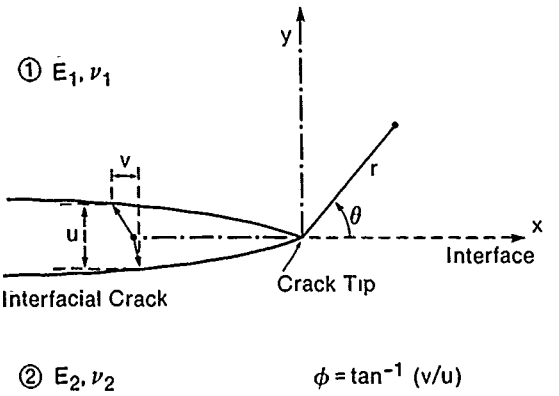

Fig. 3. The displacement of the surface of a crack at a bimaterial interface indicating the shear and opening displacement that accompany it.

with b being one of the Dundurs' parameters [8] (a and b):

$$a=\frac{G_1(1-\nu_2)-G_2(1-\nu_1)}{G_1(1-\nu_2)+G_2(1-\nu_1)}$$

$$b=\frac{1}{2}\frac{G_1(1-2\nu_2)-G_2(1-2\nu_1)}{G_1(1-\nu_2)+G_2(1-\nu_1)} \qquad (2)$$

G is the shear modulus, ν is Poisson's ratio and r is the distance from the crack front. The energy release rate is also related to the crack surface displacements [21, 7].

2.2 Debonding mechanics

Debonding solutions are required for axisymmetric loading, representative of the debonding of fibers (Fig. 2), as well as for planar cracks characteristic of macroscopic delamination (Fig. 1). In both cases, $\mathcal{G}$ and ψ are strongly influenced by the *residual stress*. Furthermore, when the phase angle becomes large, $\psi \to \pi/2$, frictional sliding and crack surface locking effects become important [12]. A comprehensive set of solutions that fully encompass the spectrum of residual stress and of frictional sliding relevant to composites does not yet exist. The known solutions are described below.

Axisymmetric solutions exist for composites with interfaces subject to residual radial *tension*, wherein a net crack opening exists for the full range of applied loads, elastic moduli and fiber volume fractions [6]. All solutions have the general features that $\mathcal{G}$ is small, but non-zero, when the debond length is zero and increases to a steady-state value $\mathcal{G}_{ss}$ when the debond length d exceeds about R. Such behavior indicates the insightful bound that the debond *must* extend without limit when $\mathcal{G}_{ss}$ exceeds $\mathcal{G}_{ic}$ at the appropriate ψ_i which is typically large, indicative of a large ratio of shear to opening.

Rigorous axisymmetric solutions for interfaces subject to residual radial *compression* have not been derived. However, some approximate solutions based on a modified shear lag approach are insightful [24]. This approach has merit when the friction coefficient μ is small ($\mu \lesssim 0.2$). For this case, crack opening does not occur until t reaches a critical value t_c given by

$$t_c/E^f\varepsilon = 1/\nu \qquad (3)$$

where E is Young's modulus.

For $t > t_c$, steady state obtains for long debonds. For $t < t_c$, the debond crack is subject to normal compression and $\mathcal{G}$ diminishes with increase in debond length, d, representative of *stable* debonds. The $\mathcal{G}$ in this instance is strictly mode II and debonding should thus be predicted by equating $\mathcal{G}$ to $\mathcal{G}_{ic}$ at $\psi = \pi/2$. Such predictions have not been attempted. However, it is insightful to note that, for "weak" interfaces ($\mathcal{G}_{ic} \ll \mathcal{G}_{fc}$), the debond length and the slip length, l, are likely to be closely related, with l given by [24]

$$\frac{l}{R} \approx \frac{F\{(1-f)(1-2\nu)+1+f\}}{2\mu(1-f)(1-\nu F)} \qquad (4)$$

where

$$F=(t-p)/E^f\varepsilon$$

For the *plane* delamination problem depicted in Fig. 1, a comprehensive analysis exists [25]. The results indicate that *initial debonding along the interface* is expected, provided that $\mathcal{G}_{ic}$ at $\psi \approx \pi/4$ is less than the critical strain energy release rate for the fiber, $\mathcal{G}_{fc}$, by the ratio that depends somewhat on the elastic properties for fiber and matrix. For the elastically homogeneous case, debonding occurs in preference to fiber failure when

$$\mathcal{G}_{ic}/\mathcal{G}_{fc} \lesssim 1/4 \qquad (5)$$

Further crack front debonding is not addressed by this solution. Useful insights concerning this debonding problem can be gained by interpolating between the above mixed mode solution and that for long, cylindrical debonds in the crack tip

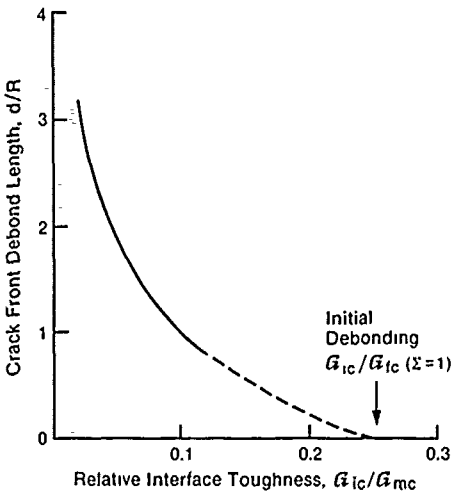

Fig. 4. The energy release rate for crack front debonding.

field [3] (Fig. 4). The latter solution indicates that debond lengths substantially larger than the fiber diameter require very small values of $\mathcal{G}_{ic}$ at the interface compared with that of the matrix crack front, $\mathcal{G}_{mc}$, as given approximately by

$$\mathcal{G}_{ic}/\mathcal{G}_{mc} \approx 0.1R/d \tag{6}$$

Extensive crack front debonding thus appears unlikely in the absence of residual stress, even when $\mathcal{G}_{ic}$ is quite small. This conclusion about crack front debonding is substantially changed when residual stress exists [7].

Initiation of debonding is a necessary but not sufficient condition for good composite properties. It is also required that the debond crack *remain in the interface* and not kink into the fiber to cause premature fiber rupture, either along the crack front or in the crack wake. Analysis of this problem [13] indicates that kinking out of the interface is not expected when eqn. (5) is satisfied.

2.3. The interface fracture resistance

The preceding mechanics provide the essential background needed for the measurement of debond resistances relevant to composite performance. Three basic test methods have been identified [7, 12]: compact tension tests, flexural tests and pull-out tests. The first provides data for $\psi \approx 0$, the last for $\psi \approx \pi/2$ and the flexural test for $\psi \approx \pi/4$. Critical aspects of interface fracture testing concern the initial introduction of a well-defined debond crack and measurement of the residual stress. Another important testing issue concerns friction at the loading points [5]. A procedure that takes frictional effects into account based on measurements of the hysteresis in loading and unloading compliance has been developed and validated. These rigorous demands on the testing needed to generate valid $\mathcal{G}_{ic}(\psi_i)$ data, have limited the extent of available results. Preliminary results indicate that $\mathcal{G}_{ic}$ tends to increase with increase in ψ_i, especially as $\psi_i \to \pi/2$, and furthermore, that the rate of increase depends on the morphology of the fracture interface [12]. Specifically, rough fracture interfaces cause $\mathcal{G}_{ic}$ to increase more rapidly with increase in ψ_i. Analysis of this phenomenon [12] has attributed this trend to the sliding and locking of crack surface asperities that make contact at large phase angles. The material parameter that governs the magnitude of the above effect is [12]

$$\chi = \frac{EH^2}{\mathcal{G}_0 L} \tag{7}$$

where H is the amplitude and L the wavelength of undulations on the fracture interface and $\mathcal{G}_0$ is the intrinsic fracture resistance of the interface. Specifically, large χ results in the greatest effects on $\mathcal{G}_{ic}(\psi_i)$. The quantity χ is a measure of the length of the contact zone, which increases as either H increases or $\mathcal{G}_0$ decreases.

The magnitude of $\mathcal{G}_0$ is clearly influenced by the presence of interphases, the atomistic structure of the interface, etc. However, as yet, residual stress and morphological influences have not been sufficiently decoupled to explore these basic relationships. Nevertheless, preliminary measurements reveal that $\mathcal{G}_0$ is typically quite small for oxides bonded to refractory metals (niobium), to intermetallics (TiAl) and to noble metals (gold, platinum), as well as for oxides bonded with inorganic glasses and for carbides and nitrides having graphite and boron nitride interlayers.

2.4. Debonding during composite fracture

The preceding debonding results, while still incomplete, are consistent with the following sequence of events during matrix crack propagation. Initial debonding occurs along the interface at the crack front, provided that $\mathcal{G}_{fc}/\mathcal{G}_{ic}$ (at $\psi \approx \pi/4$) $\gtrsim 4$. The extent of debonding is typically small when residual compression exists at the interface, but can be extensive when the interface is in residual tension. However, more importantly, further debonding is induced in the crack wake [6]. The extent of debonding is again governed largely by the residual field. Residual

radial tension results in unstable conditions and encourages extensive debonding [6]. Residual compression causes stable debonding [24], with extent determined by the friction coefficient and morphology of the debonded interface. Fracture of the fiber by kinking of the debond crack into the fiber is unlikely [13]. Fiber failure and pull-out toughening thus appear to be governed by the statistics of fiber failure [26].

The above sequence indicates that, while debonding is a prerequisite for high toughness, the properties of the composite are not otherwise limited by the extent of debonding. The basic fracture requirement for the interface is thus

$$\mathcal{G}_{ic}/\mathcal{G}_{fc} \lesssim 1/4$$

at $\psi \approx \pi/4$. Subject to this requirement, the sliding resistance of the debonded interface is the most important interface property, as elaborated in subsequent sections.

There is no direct experimental validation of the preceding hypothesis for ceramic matrix composites. However, various observations of crack interactions with fibers and whiskers are supportive of the general features [2, 29, 27]. In particular, experiments on LAS/SiC composites reveal that as-processed materials with a carbon interlayer debond readily and demonstrate extensive pull-out (Fig. 5), whereas composites heat treated in air to create a continuous SiO_2 layer between the matrix and fiber exhibit matrix crack extension through the fiber without debonding (Fig. 6). Furthermore, composites with a thin interface layer of SiO_2 having a partial circumferential gap exhibit intermediate pull-out characteristics (Fig.

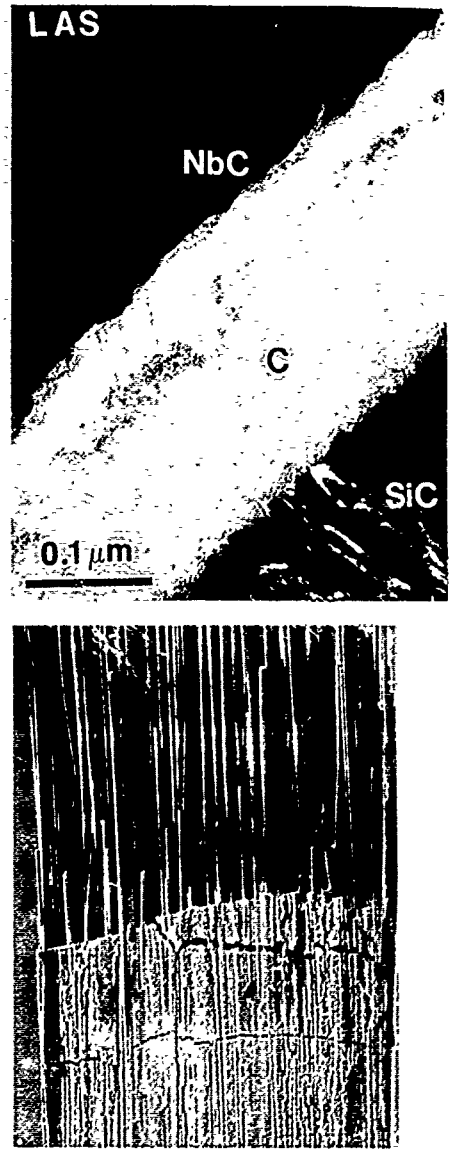

Fig. 5. Interfaces and pull-out in a composite consisting of LAS matrix and SiC (Nicalon) fibers. as-processed indicating carbon interlayer and extensive pull-out.

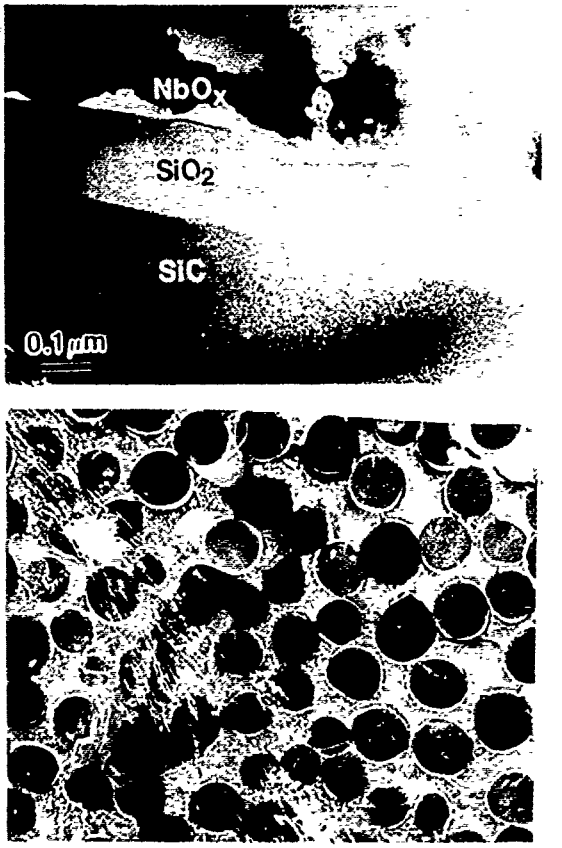

Fig. 6. Heat treated in air for 16 h at 800 °C indicating a complete SiO_2 layer and no pull-out.

7). The associated constituent properties are summarized in Table 1. Based on these properties, the preceding arguments would indicate that crack front debonding should not occur when a complete SiO_2 layer exists at the interface; whereas, appreciable crack front debonding should obtain when the carbon layer is present, in complete accordance with the observations [2, 27]. The composites with only a partial SiO_2 interface layer are also interesting. For these materials, $\mathcal{G}_{ic}$ is related to that fraction of the circumference that bonds the fiber to the matrix. typically 1/3 (Fig.7). Reference to Table 1 and to the initial debonding requirement (eqn. (5)) would thus indicate that debonding, while marginal, is certainly possible.

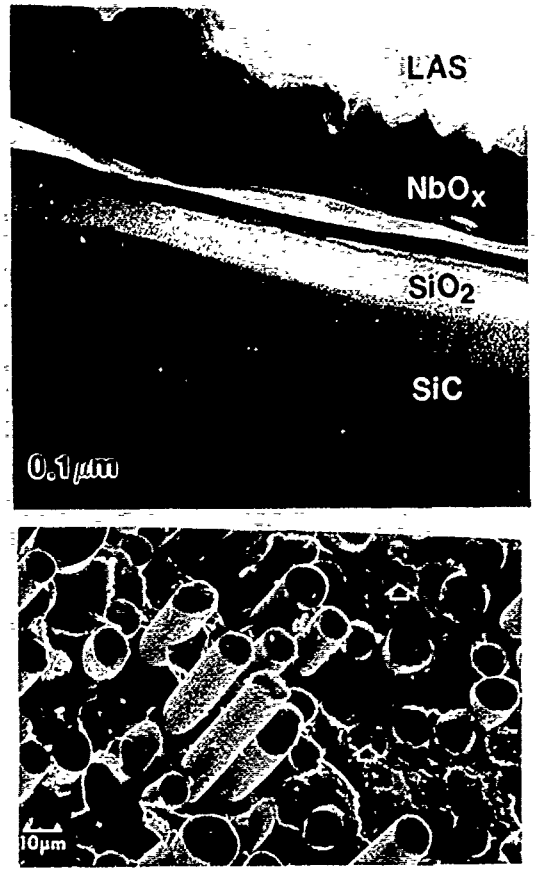

Fig. 7 Heat treated in air for 4 h at 800 °C indicating a partial SiO_2 layer — with gap — and variable pull-out.

TABLE 1 Constituent properties of LAS/Nicalon composites

	E (GPa)	$\mathcal{G}_c$ ($J\,m^{-2}$)	α (K^{-1})
Fiber (Nicalon)	200	4–8[a]	4×10^{-6}
Matrix (LAS)	85	40	1×10^{-6}
Interface			
Amorphous carbon	—	<1[b]	—
Amorphous SiO_2	80	8	1×10^{-6}

[a]Determined from fracture mirror radii.
[b]Determined by indentation: takes into account initial thermal debonding (Fig. 5).

2.5. *Pull-out*

An integral aspect of the analysis of composite fracture involves consideration of fiber failure and of subsequent pull-out. As noted above, fiber failure can usually be described using concepts of weakest link statistics based on the fiber strength parameters S_o and m [26] in accordance with the frequency distribution

$$\int g(S)\,dS = (S/S_o)^m/A_0 \tag{8}$$

where m is the shape parameter and S_0 and A_0 are the scale parameters.

The locations of fiber failure that govern the pull-out distributions can, in principle, be determined from the stresses on the fibers ahead of the matrix crack and in the crack wake. The former analysis has not been attempted, partly because the problem is complex and partly because of a perception that fiber failures close to the crack plane that cause pull-out are most likely to occur in the crack wake, following the debond extension process. However, there is no direct evidence that fiber failure ahead of the matrix crack can be neglected in ceramic matrix composites.

While it is important to be aware of the above uncertainties, it is nevertheless insightful to fully analyze the wake failure phenomenon. Comparisons with experimental fiber pull-out data then allow assessment of the hypothesis. The fiber failure analysis commences with the basic weakest link description of failure. Then, by incorporating an axial fiber stress distribution, the fiber failure locations can be derived [26]. Such analysis has been performed for composites with negligible residual stress and having debonded interfaces subject to a constant sliding stress τ. For this purpose, the fundamental probability density function is [26]

$$\phi(z,t) = \frac{2\pi R m}{S_o^{\,m}}(t - 2z\tau/R)^{m-1}\exp\{-(t/T)^{m+1}\} \tag{9}$$

where

$$T=\left\{\frac{S_o^{\,m}\tau(m+1)}{2\pi R^2}\right\}^{(m+1)}$$

and z is the distance from the crack plane. Then, the cumulative probability that the pull-out length will be $\leq h$ is [27]

$$\Phi(h)=2\int_0^{\infty}\int_0^{h}\phi(z,t)\,\mathrm{d}z\,\mathrm{d}t \qquad (10)$$

Trends in cumulative probability are plotted on Fig. 8, indicating that the pull-out lengths are *inversely dependent on* τ and also tend to increase as m decreases. The effects of residual strain on $\Phi(h)$ are expected to be substantial. Preliminary estimates suggest that the pull-out length usually decreases as the misfit strain ε increases, when the residual stress at the interface is compressive. However, specific trends are sensitive to m, as well as to the friction coefficient μ.

Experimental results concerning trends in the pull-out distribution with interface properties [27] have been obtained for heat-treated LAS/SiC composites, having the features described in the preceding section. The results reveal that as the gap caused by carbon removal is filled with SiO_2, the pull-out distribution gradually changes (Fig. 9). In particular, the median length decreases and that proportion of fibers that actually pull out exhibit length distributions consistent with those predicted by the above weakest link fiber failure analysis (Fig. 9) such that the interface τ increases by about an order of magnitude when a partial SiO_2 layer replaces carbon. This change in τ causes a dramatic change in the mechanical properties of the composite, as elaborated below.

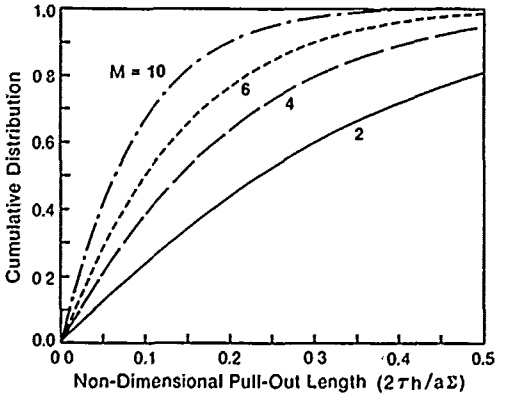

Fig. 8 The cumulative pull-out distribution for several values of the shape parameter, m.

3. Tensile properties: Mode I failure

3.1. Axial stress–strain behavior

The axial tensile properties of ceramic matrix composites are strongly influenced by the relative debond resistance $\mathcal{G}_{ic}/\mathcal{G}_{fc}$, by the friction coefficient along the debonded interface μ and by the residual strain, ε, as intimated in the preceding section. When the interface is in residual tension and when $\mathcal{G}_{ic}/\mathcal{G}_{fc}$ and μ are both small, as exemplified by carbon interlayers between fiber and matrix, experience [27, 18] has indicated that the tensile stress–strain behavior illustrated in Fig. 10(a) is obtained. Three features of this curve are important: matrix cracking at a stress σ_o, fiber bundle failure at σ_u and the pull-out stress. Increases in either $\mathcal{G}_{ic}/\mathcal{G}_{fc}$ or μ cause the stress–strain curve to become linear [27] (Fig. 10(b)). Furthermore, the ultimate strength then coincides with the propagation of a single dominant crack (albeit, sometimes with a desirable "tail" caused by delamination). Composites having this macroscopic characteristic exhibit properties governed by a fracture resistance curve. The individual properties within each of

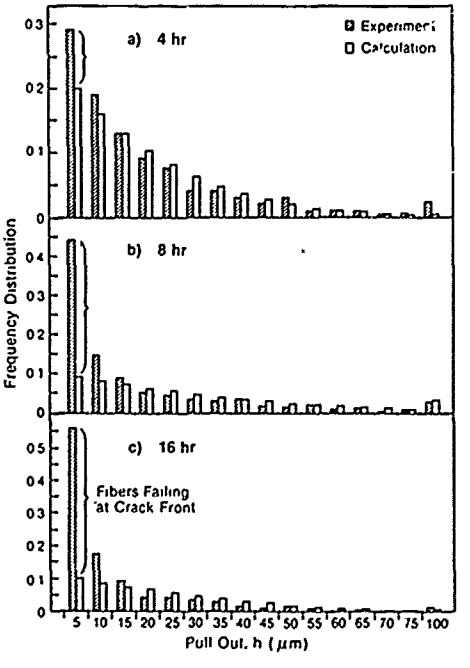

Fig. 9. Histograms indicating trends in pull-out length with heat treatment.

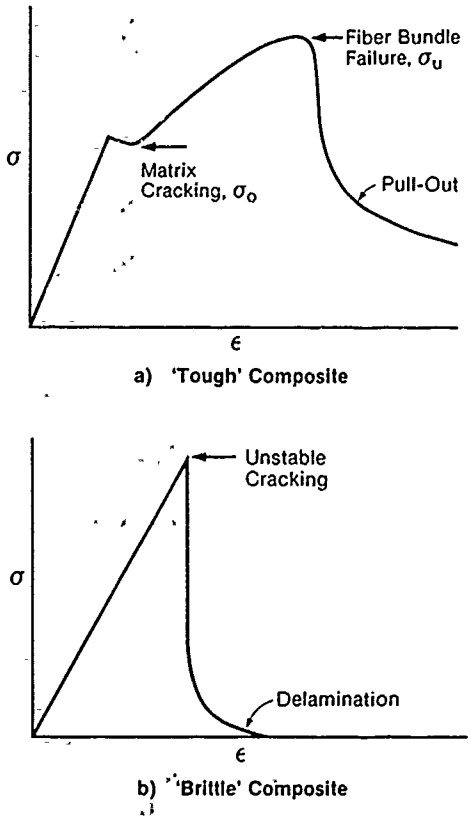

Fig. 10. Tensile stress–strain curves for ceramic matrix composites: (a) small $\mathcal{G}_{tc}$, small μ, (b) small $\mathcal{G}_{tc}$, large μ.

these two regimes are discussed below, as well as criteria that dictate the transition between regimes.

3.1.1. *Matrix cracking*

The stress σ_o at which matrix cracking occurs has been the most extensively studied behavior in ceramic matrix composites [2, 18, 1, 17]. For composites in which q is tensile and the interface properties can be effectively represented by a unique sliding stress, τ, the matrix cracking stress is given by [2]

$$\frac{\sigma_o}{E}=\left\{\frac{6f_v^2E^f\tau\mathcal{G}_{mc}}{(1-f)E(E^m)^2R}\right\}^{1/3}-\frac{p}{E^m} \qquad (11)$$

This result is independent of the matrix crack length because the crack is bridged by fibers. Experiments conducted on a number of ceramic matrix composites have validated eqn. (11). When the interface is subject to residual compression, τ depends on the applied stress and the solution for σ_o is more complex. However, to first order, τ may be simply replaced by μq. At

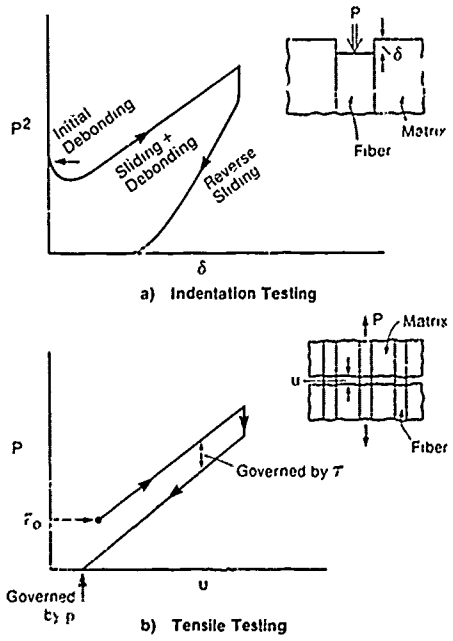

Fig. 11. (a) A load–unload cycle for nanoindentation of a fiber. (b) Crack opening hysteresis for a composite with intact fibers revealing the trends in both sliding resistance and residual stress.

σ_o, multiple matrix cracking is expected [1] and observed [18] with a saturation crack spacing D in the range;

$$\sigma_o R/2f\tau < D < \sigma_o R/f\tau \qquad (12)$$

Experimental observations have again confirmed this feature of matrix cracking.

The most crucial aspects of the above interpretation of steady-state cracking and of behavior prediction concern determination of τ and q for actual composite systems. Both are difficult to measure. Two basic approaches have been used to measure the *sliding resistance* τ. indentation [19] and crack opening hysteresis [18]. Both approaches are readily applicable when $\mathcal{G}_{tc}$ and τ are small. The former method is most insightful when used with a nanoindenter system, whereupon τ can be obtained on single fibers either from a push-through force on thin sections or from the hysteresis in the loading–unloading cycle on thick sections (Fig. 11(a)). However, this method has the obvious disadvantage that the fiber is in axial compression such that the debond interface is also compressed during the test, with attendant changes in τ. Matrix cracking followed by measurement of the crack opening hysteresis (Fig. 11(b)) is more desirable, when feasible, because the fibers are subject to axial tensile load-

ing. However, when appreciable fiber failure accompanies matrix cracking, erroneous results also obtain for this method. Both approaches give about the same value of τ for composites having the following characteristics: tensile residual strain exists at the interface [17], $\mathcal{G}_{ic}/\mathcal{G}_{fc}$ is small and τ is small (less than 10 MPa). Otherwise, both approaches are problematic. Consequently, other approaches applicable to composites having larger τ are being investigated. One of these is discussed in the following section.

3.1.2. The ultimate strength

Following multiple matrix cracking, the fibers are subject to an oscillating stress field The probability of fiber failure within such a stress field subject to weakest link statistics can be readily derived [28]. However, derivation of a load maximum requires that the stress redistribution caused by the fractured fibers be modelled. Such an analysis has not been attempted. Nevertheless, a lower bound for the load can be derived by simply allowing failed fibers to have no load bearing ability. Then, a modified bundle failure analysis allows the ultimate strength to be

$$\sigma_u = f\hat{S}\exp\left[-\frac{\{1-(1-\tau D/R\hat{S})^{m+1}\}}{(m+1)\{1-(1-\tau D/R\hat{S})^{m}\}}\right] \quad (13)$$

where S_o and m are the statistical parameters that represent the fiber strength distribution and

$$\left(\frac{R\hat{S}}{\tau D}\right)^{m+1} = \frac{A_0}{2\pi RL}\left(\frac{RS_o}{\tau D}\right)^{m}\{1-(1-\tau D/R\hat{S})^{m}\}^{-1}$$

with L being the gauge length. In the one composite system for which analysis of the ultimate strength has been performed (LAS/SiC) [27] surprisingly eqn. (13) agrees quite well with measured values.

The ultimate strength anticipated from the above logic is expected to be influenced by the residual stress. Specifically, in systems for which the fiber is subject to residual compression, the axial compression should suppress fiber failure and elevate the ultimate strength to a level in excess of that predicted by eqn. (13).

3.1.3. Resistance curves

When mode I failure is dominated by propagation of a single dominant matrix crack, accompanied by fiber failure and pull-out, the mechanical properties are characterized by a resistance curve. Analysis of this phenomenon utilizes the distribution of fiber failure sites determined in the pull-out analysis (Fig. 8). From such analysis, the mean failure length of all fibers that fail at stress t acting on the fiber between the crack surfaces is first evaluated [26]. Then, by taking into account the reduced stress caused by fiber failure and knowing the associated crack opening, u, the total stress on the fibers between the crack at a fixed crack opening may be determined [26] as plotted on Fig. 12. Several features of the $t(u)$ curve are notable. The initial, rising position is dominated by intact fibers, the peak is dominated by multiple fiber failures, analogous to bundle failure, and the tail is governed by pull-out. The role of the shape parameter, m, on these features is particularly interesting. As m decreases, corresponding to a broader distribution of fiber strengths, more fibers fail further from the matrix crack (Fig. 8) causing the extent of pull-out to substantially increase.

The trends in $t(u)$ directly associate with the two most relevant features of the fracture resistance curves: the asymptotic toughness and the slope (or tearing modulus), respectively. The *asymptotic toughening* can be simply derived from the J integral result,

$$\Delta\mathcal{G}_{ss} = 2f\int_0^{\infty} t(u)\,du \quad (14)$$

The expressions that govern the trends in $\Delta\mathcal{G}_{ss}$ with material properties are unwieldy in form [26]. However, inspection reveals that $\Delta\mathcal{G}_{ss}$ always increases as the scale parameter S_0 in-

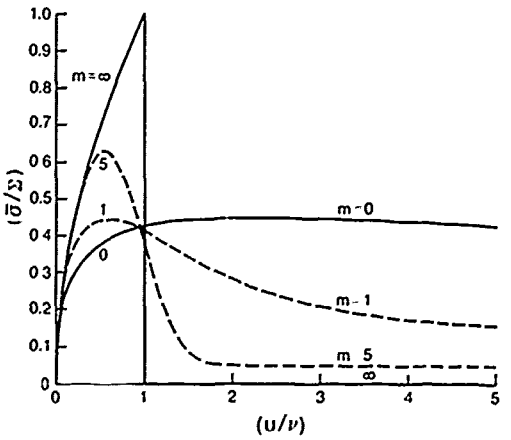

Fig. 12. Trends in non-dimensional crack opening stress, t, with opening u for several values of the shape parameter, m.

creases, thereby establishing that high fiber strengths are invariably desirable. However, the dependence on τ and R is ambivalent. The essential details are highlighted by considering separately the bridging and pull-out contributions to the toughness integral. The *bridging* component

$$\Delta\mathcal{G}_b = 4fTU/(m+1) \tag{15}$$

where $U = T^2R/4E^f\tau(1+\xi)$ is proportional to $[R^{m-5}/\tau^{m-2}]^{1/(m+1)}$. A notable feature is the inversion in the trend so that τ occurs at $m=2$, and R at $m=5$. The corresponding pull-out contribution can be examined by recognizing that the toughening has the form

$$\Delta\mathcal{G}_p \approx \langle h\rangle^2(\tau/R) \tag{16}$$

which, with eqn. (10) for h indicates a toughness proportional to $(R^{m-3}S_o^{2m}/\tau^{m-1})^{1/(m+1)}$. The toughness thus increases with increasing R when $m>5$, and decreases when $m<3$. Conversely, it increases with increasing τ when m is very small (less than or equal to 1), and decreases when $m>2$. These limits arise because of the competing importance of the contribution to toughness from the intact bridging fibers and the failed fibers that experience pull-out. Knowledge of the magnitude of the statistical shape parameter, m, for the fibers *within* the composite is therefore a prerequisite to optimizing the shear properties of the interface for high toughness.

The slope of the resistance curve has not yet been evaluated, because numerical methods are needed to determine the upper limit of eqn. (14), as dictated by the crack opening at the end of the bridging zone.

3.1.4. Property transition

Non-linear macroscopic mechanical behavior in tension is most desirable for structural purposes and thus analysis of the transition between this regime and the linear regime is important. A useful preamble involves comparison of the basic trends in the steady-state matrix cracking stress, σ_o (eqn. (11)), and in the asymptotic fracture resistance, $\Delta\mathcal{G}_{ss}$ (eqn. (14)). The opposing trends with τ suggest the existence of an *optimum* τ that permits good matrix cracking resistance while still allowing high toughness.

More specifically, a property transition is expected when the matrix cracking stress attains the stress needed for fiber bundle failure. One bound on the property transition can be obtained by simply allowing σ_o to exceed the ultimate strength. Then, the parameter B which governs the transition when τ is small is

$$B = \tau E\mathcal{G}_{mc}/S_o^3R \tag{17}$$

Specifically, when B exceeds a critical value, linear behavior initiates. Experiments on heat-treated LAS/SiC composites [27] have examined the conditions with this transition (Fig. 13).

3.1.5. Residual stress

Large mismatches in thermal expansion between fiber and matrix are clearly undesirable. In particular, relatively large matrix expansions, cause premature matrix cracking (eqn. (11)). Such behavior is not necessarily structurally detrimental, but concerns regarding thermal fatigue, the ingress of environmental fluids, etc., have discouraged the development of materials having these characteristics. Conversely, very small matrix expansions thermally debond the fiber from the matrix. When sufficiently extensive, such debonding results in axial separations that negate the influence of the fibers. Consequently, values of $\Delta\alpha \lesssim 3\times10^{-6}\,°C^{-1}$ are required. Indeed, mode I axial properties subject to an interface that easily debonds and slides freely along the debond involve an *optimum* residual stress, with a *maximum* matrix cracking stress, when ε is positive, given by [2]

$$\sigma_o/E = \{(J\mu\mathcal{G}_{mc}/\lambda_2E^{m}R)^{1/2} \tag{18}$$

where $\lambda_2 = 1-(1-E/E^f)/2$.

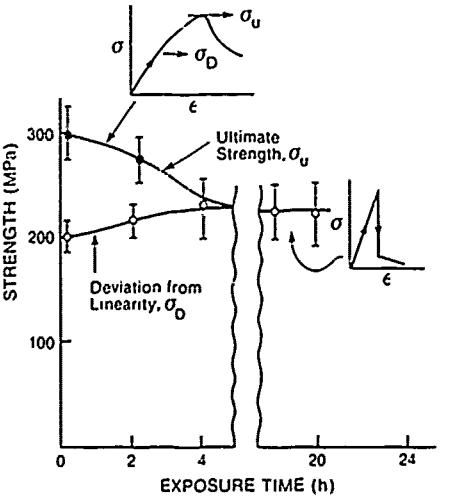

Fig. 13. Effects of heat treatment on the stress–strain behavior of LAS/SiC composites.

When ε is negative, asperities on the debond surface may provide a discrete sliding stress, τ, that depends on such features as the asperity amplitude. For such cases, the optimum residual strain has not been determined. However, it is noted that good properties have been demonstrated for LAS/SiC composites having an expansion mismatch, $\Delta\alpha \approx 3 \times 10^{-6}\,°C^{-1}$.

The fracture resistance is also influenced by the residual stress. However, the sign and magnitude of the change in toughness induced by residual stress depends on the mechanisms of interface sliding and fiber failure. Subject to adequate debonding, the salient result for ceramics reinforced with brittle fibers is that $\Delta\mathcal{G}_{ss}$ is unaffected when ε is negative and the interface is characterized by an unique τ, whereas $\Delta\mathcal{G}_{ss}$ usually decreases with increase in ε when ε is positive because the pull-out lengths decrease, as apparent when τ is equated to μq.

3.2. *Transverse failure*

The transverse strengths of high toughness composites are generally very low. There have been no systematic studies of this property. However, experimental studies on composite laminates [23] indicate that the transverse cracks typically propagate along the interface layer and through the matrix between neighboring fibers. Furthermore, because the interfaces have sufficiently small $\mathcal{G}_{ic}$ to allow debonding, overall failure is preceded by interface failure. This process is assumed to occur at a critical stress, σ_c, which can be determined in a manner analogous to that for the steady-state cracking of thin films [14] to give

$$\sigma^c \approx (2E\mathcal{G}_i/\pi R)^{1/2} - q \qquad (19)$$

In some cases, q is sufficiently large that $\sigma^c < 0$ and the interfaces debond upon cooling (Fig. 5).

4. Mixed mode failure

4.1. *Mode II failure mechanisms*

Flexural tests performed on uniaxial composites reveal that a shear damage mechanism exists (Fig. 1) [18, 23, 9] and that such damage often initiates at quite low shear stresses, *e.g.* 20 MPa in LAS/SiC. The damage consists of echelon matrix microcracks inclined at about $\pi/4$ to the fiber axis. With further loading, the microcracks coalesce, causing matrix material to be ejected and resulting in the formation of a discrete mode II crack. The crack is defined by the planar zone of ejected matrix. The crack also has a microcrack damage zone similar to that present upon crack initiation.

The microcracks that govern mode II failure are presumably caused by stress concentrations in the matrix and form normal to the local principal tensile stress, but then deflect parallel to the mode II plane and coalesce. An adequate model that incorporates the above features has not been developed. Consequently, the underlying phenomena are briefly noted without elaboration. The stress concentrations in the matrix have magnitude governed by the elastic properties, the fiber spacing and the interface strength. The growth and coalescence of the microcracks scales with the matrix toughness $\mathcal{G}_{mc}$. The shear strength seemingly decreases as the mode I toughness increases.

4.2. *Delamination cracking*

Delamination is a common damage mode in the presence of notches (Fig. 14). Delamination cracks nucleate near the notch base and extend stably. The fracture resistance is found to increase with crack extension and, because of the large phase angle, the fracture mechanism is essentially identical to that noted for mode II failure, involving matrix microcracking and spalling. The existence of a resistance curve is attributed to intact fibers within the crack that resist the displacement of the crack surfaces and thus shield the crack tip in a manner analogous to fiber bridging in mode I. However, explicit analysis has yet to be conducted.

5. Microstructure design

Many of the microstructural parameters that control the overall mechanical properties of ceramic matrix composites are now known and validated, as elaborated in the preceding sections. Consequently, various general remarks about microstructure design can be made. However, important aspects of damage and failure are incompletely understood because there have been few organized studies of failure in mode II, mixed mode and transverse mode I. The remarks made in this section thus refer primarily to axial mode I behavior with no special regard to attendant problems in other loading modes.

The basic microstructural parameters that govern mode I failure are the relative fiber-

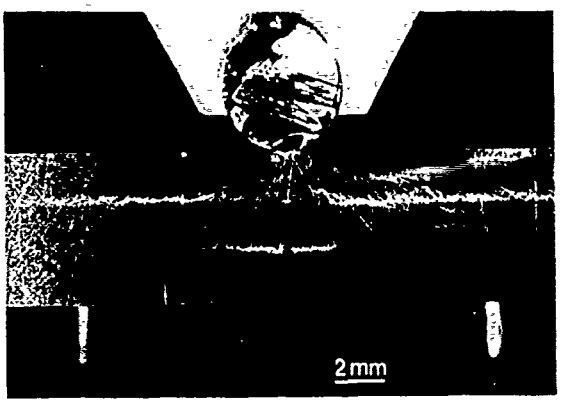

Fig. 14. Delamination cracking in notched flexure tests.

matrix interface debond toughness, $\mathcal{G}_{ic}/\mathcal{G}_{fc}$, the residual strain, ε, the friction coefficient of the debonded interface, μ, the statistical parameters that characterize the fiber strength, S_o and m, the matrix toughness, $\mathcal{G}_{mc}$, and the fiber volume fraction f. The prerequisite for high toughness is that $\mathcal{G}_{ic}/\mathcal{G}_{fc} \lesssim 1/4$. Subject to this requirement, the residual strain must be small ($\Delta\alpha \lesssim 3\times10^{-6}$ °C^{-1}). Furthermore, the friction coefficient along the debonded interface should be small ($\mu \lesssim 0.1$). The ideal fiber properties are those that encourage large pull-out lengths, as manifest in an optimum combination of a high median strength (large S_o) and large variability (small m).

The above conditions can be satisfied, in principle, by creating interphases between the fiber and matrix, either by fiber coating or, *in situ*, by segregation. The most common approach is the use of a dual coating: the inner coating satisfies the above debonding and sliding requirements, while the outer coating provides protection against the matrix during processing. However, the principal challenge is to identify an inner coating that has the requisite mechanical properties while also being thermodynamically stable in air at elevated temperatures. Most existing materials have either carbon or boron nitride as the debond layer. However, both materials are prone to degradation in air at elevated temperatures. More stable alternatives have been proposed (*e.g.* niobium, molybdenum, platinum, NbAl) but have not been evaluated.

References

1 J. Aveston, G. A. Cooper and A. Kelly, *The Properties of Fiber Composites*, JPC Science Technology, 1971, p. 15.
2 E. Bischoff, O. Sbaizero, M. Rühle and A. G. Evans, *J. Am. Ceram. Soc.*, in press.
3 B. Budiansky, J. W. Hutchinson and A. G. Evans, *J. Mech. Phys. Solids, 34* (1986) 167.
4 B. Budiansky, J. W. Hutchinson and J. Lambropolous, *Int. J. Solids Struct., 19* (1983) 337.
5 P. G. Charalambides, H. C. Cao, J. Lund and A. G. Evans, *Mech. Mater.*, in press.
6 P. G. Charalambides and A. G. Evans, *J. Am. Ceram. Soc.*, in press.
7 P. G. Charalambides, R. M. McMeeking and A. G. Evans, *J. Appl. Mech.*, in press.
8 J. Dundurs, *Mathematical Theory of Dislocations*, ASME, New York, 1969, p. 70.
9 A. G. Evans, *Mater. Sci. Eng., 71* (1985) 3.
10 A. G. Evans and R. M. Cannon, *Acta Metall., 34* (1986) 761.
11 A. G. Evans and K. T. Faber, *J. Am. Ceram. Soc., 67* (1984) 255.
12 A. G. Evans and J. W. Hutchinson, *Acta Metall.*, in press.
13 M. Y. He and J. W. Hutchinson, *Harv. Univ. Rep. MECH, 113* (1988; *J. Appl. Mech.*, in press.
14 M. S. Hu and A. G. Evans, *Acta Metall.*, in press.
15 J. W. Hutchinson, *Non-Linear Fracture Mechanics*, Technical University of Denmark, 1979.
16 J. W. Hutchinson, *Acta Metall., 35* (1987) 1605.
17 D. B. Marshall, B. N. Cox and A. G. Evans, *Acta Metall., 33*, (1985) 2013.
18 D. B. Marshall and A. G. Evans, *J. Am. Ceram. Soc., 68* (1985) 225.
19 D. B. Marshall and W. Oliver, *J. Am. Ceram. Soc., 70* (1987) 542.
20 J. R. Rice, in H. Liebowitz (ed.), *Fracture*, Vol. 11 Academic Press, New York, 1968, p. 191.
21 J. R. Rice, *J. Appl. Mech.*, in press.
22 M. Rühle, A. G. Evans, R. M. McMeeking and J. W. Hutchinson, *Acta Metall., 35* (1987) 2701.
23 O. Sbaizero and A. G. Evans, *J. Am. Ceram. Soc., 69* (1986) 481.
24 L. S. Sigl and A. G. Evans, *Mech. Mater.*, in press.
25 Z. Suo and J. W. Hutchinson, *Harv. Univ. Rep. MECH, 118* (1988); *Int. J. Fract.*, in press.
26 M. D. Thouless and A. G. Evans, *Acta Metall., 36* (1988) 517.
27 M. D. Thouless, O. Sbaizero, L. S. Sigl and A. G. Evans, *J. Am. Ceram. Soc.*, in press.
28 D. J. Walls, M.S. Thesis, University of California, Berkeley, 1986.
29 M. Ruhle and A. G. Evans, *Mater. Sci. Eng., A107* (1988) 187.

Appendix A 1. Notation

α	linear thermal expansion coefficient
ε	stress-free strain ($\Delta\alpha\Delta T$): positive refers to residual compression normal to the interface
μ	friction coefficient
ν	Poisson's ratio of composite
ξ	coefficient

Σ	ratio of Young's modulus of fiber to matrix, E^f/E^m.
σ_o	matrix cracking stress
σ_u	ultimate strength
σ^c	stress for transverse interface failure
τ	shear resistance of interface after debonding
$\Phi(h)$	cumulative pull-out distribution
ϕ	crack surface shear angle
$\phi(z,t)$	probability density function for fiber failure
χ	interface fracture parameter $= EH^2/\mathcal{G}_o L$
ψ	phase angle of loading
a	Dundurs' parameter $= \{G_1(1-\nu_2)-G_2(1-\nu_1)\}/\{G_1(1-\nu_2)+G_2(1-\nu_1)\}$
B	Transition parameter
b	Dundurs' parameter $= \{G_1(1-2\nu_2)-G_2(1-2\nu_1)\}/[2\{G_1(1-\nu_2)+G_2(1-\nu_1)\}]$
D	matrix crack spacing
d	debond length
E	Young's modulus of composite
F	non-dimensional stress $=(t-p)/E^f\varepsilon$
f	fiber volume fraction
G	shear modulus
$\mathcal{G}$	strain energy release rate
$\mathcal{G}_{ic}$	critical strain energy release rate for interface
$\mathcal{G}_{ss}$	steady-state strain energy release rate
$\mathcal{G}_{fc}$	critical strain energy release rate for the fiber
$\mathcal{G}_{mc}$	critical strain energy release rate for the matrix
$\mathcal{G}_o$	intrinsic critical strain energy release rate for the interface
$\mathcal{G}_R(\Delta a)$	increase in critical strain energy release rate with increase in crack length Δa
H	amplitude of interface roughness
h	pull-out length
l	slip length
L	gauge length
m	shape parameter for fiber strength distribution
p	residual axial stress in the *matrix*
q	residual compression normal to interface
R	fiber radius
r	distance from crack front
S	fiber strength
S_o	scale parameter for fiber strength distribution
T	pull-out parameter
t	stress acting on fiber between crack surfaces
U	pull-out parameter
u	crack opening displacement
v	crack shear displacement
z	distance from crack plane

Effects of Matrix Microstructure and Particle Distribution on Fracture of an Aluminum Metal Matrix Composite*

J. LEWANDOWSKI and C. LIU

Department of Materials Science and Engineering, Case Western Reserve University, Cleveland, OH 44106 (U.S.A.)

W. H. HUNT, Jr.

ALCOA Laboratories, Alcoa Center, PA 15069 (U.S.A.)

(Received June 1, 1988)

Abstract

This paper presents the results of a study on the effects of matrix microstructure and particle distribution on the fracture of an aluminum alloy metal matrix composite containing 20% by volume SiC particulate. The matrix microstructure was systematically varied by heat treating to either an under- or over-aged condition of equivalent strength, and was characterized using a combination of techniques. Quantitative metallographic techniques were utilized to characterize the material with respect to size, size distribution, and particle clustering, while transmission electron microscopy was utilized to characterize the details of the matrix microstructure in addition to the effects of aging on the character of the particle/matrix interfaces. Fracture experiments were conducted on smooth tensile, notched bend, short-rod toughness, and on specimens designed to permit controlled crack propagation, in an attempt to determine the effects of matrix microstructure and clustered regions on the details of damage accumulation. Large effects of microstructure on the notched properties were obtained with little effect of microstructure on tensile ductility. It is shown that the micromechanisms of fracture are significantly affected by the details of the matrix microstructure, interface character, and degree of clustering in the material. Fracture of the SiC was predominant in the underaged materials, with a preference for failure in the matrix and near the interface in the overaged material. Metallographic and fractographic analyses revealed that clustered regions were preferred sites for damage initiation in both the aging conditions tested, while preliminary results additionally indicate that damage accumulation ahead of a propagating crack also tended to occur in clustered regions.

1. Introduction

Discontinuous metal matrix composites based on aluminum alloy matrices provide a number of advantages over many of the composite systems currently under investigation. In general, the properties of discontinuously reinforced materials are more isotropic than those of continuously reinforced materials. The ability to utilize conventional metalworking processes in the production of the discontinuous materials adds to their appeal. However, despite the great interest in this class of materials, and considerable research into the effects of reinforcement type and volume fraction on macroscopic properties such as stiffness, strength, and ductility, fewer studies have systematically examined the effects of matrix microstructure on the details (*i.e.* micromechanisms) of fracture in these materials. In particular, the effects of the matrix microstructure on the fracture properties have been emphasized in only a few of the studies [1–6]. The present work addresses the issue of the effects of matrix microstructure as well as the degree of particle clustering on the fracture behavior and accumulation of damage in discontinuously reinforced metal matrix composites based on a 7XXX aluminum alloy matrix, and represents a continuation of work reported previously on these systems [2]. Separate reviews of the effects of matrix microstructure and particle distribution on damage processes are summarized below.

Recent researches on the fracture behavior of

*Paper presented at the symposium on Interfacial Phenomena in Composites: Processing, Characterization, and Mechanical Properties, Newport, RI, June 1–3, 1988.

0921-5093/89/$3.50

© Elsevier Sequoia/Printed in The Netherlands

aluminum matrix composites [1–10] have revealed that fracture is often macroscopically brittle (*i.e.* low fracture strain) while SEM fractography has revealed that the fracture surface consists of microvoids of sizes ranging from the submicron to tens of microns [1–3, 6, 10]. The sources of these dimples have been attributed to either fracture or decohesion of the SiC particles, as well as inclusions, precipitates, and grain boundaries. Relatively few studies have focused on the effects of matrix microstructure on the monotonic fracture behavior of these materials. One effective way to examine the effects of microstructural changes on fracture of these materials is to perform testing on specimens heat treated to equivalent strength levels. This eliminates the complications introduced when trying to compare materials of different yielding behavior. Recent work [2, 3] has indicated that although significant changes in the micromechanisms of fracture may accompany changes in the matrix microstructure at an equivalent strength, the uniaxial tensile ductility was relatively unaffected. However, additional work revealed that dramatic changes in the notched bend toughness and short rod fracture toughness were obtained despite the similar uniaxial tensile ductilities. Unfortunately, the low macroscopic ductilities exhibited by reinforced materials often preclude an investigation into the effects of microstructure on the mechanisms of damage accumulation, although some success has been achieved using bluntly notched testpieces [2, 3]. In the present work, the matrix microstructure will be varied independent of the yield strength.

In addition to the importance of the behavior of the matrix microstructure on the macroscopic fracture properties of discontinuously reinforced materials, it has been demonstrated in previous work on both porous materials [11, 12] and in particle hardened materials [13–16] exhibiting some degree of ductility that void nucleation and the final ductility may be sensitive to both the size and distribution of particles. In particular, it has been suggested that local volume fraction (*i.e.* clustering) as opposed to the average volume fraction may be a particularly important parameter in determining the fracture of materials containing dispersions of particles at high volume percentages. Recent advances in techniques for quantifying microstructures with respect to the spatial distribution of particles or porosity may be useful in the analyses of the fracture behavior of discontinuous composites. The intention of the present work was to use recently available quantitative techniques [17] to characterize the effects of matrix microstructure on mechanical properties and to begin to quantify the effects of particle clustering on damage accumulation during deformation in an aluminum alloy reinforced with SiC particles. Attention to the effects of the matrix microstructure independent of the yield strength is emphasized in this work, as the micromechanisms of fracture may be sensitively affected by the details of the matrix microstructure. This work represents recent results of a continuing study of matrix and clustering effects on a number of composites reinforced with different size and volume percent SiC particulate.

2. Experimental details

2.1. Materials and heat treatments

The material used in this study was a powder metallurgy 7XXX aluminum alloy, designated ALCOA MB78, containing 7%Zn, 2%Mg, 2%Cu, 0.14%Zr, balance Al, and was reinforced with 20% by volume of F-600 grade (average size 16 μm) SiC produced by Norton Co. The materials were consolidated by sub-solidus processing to minimize the formation of coarse intermetallic particles during hot pressing. The product form examined was a 1 in × 3 in bar extruded at a 19:1 extrusion ratio. Additional processing details are provided elsewhere [2].

The as-received materials were solution treated at 510 °C/4 h, water quenched, and artificially aged to the under- (*i.e.* UA) or over-aged (*i.e.* OA) conditions by the following treatments: UA, 120 °C/30 min; OA, 120 °C/24 h + 170 °C/30 h. In addition to the composite material, both wrought and P/M control materials (*i.e.* unreinforced) were heat treated to the UA and OA conditions using similar heat treatments.

2.2. Microstructural evaluation

Quantification of the microstructures is a key component in understanding the behavior of these materials. Initial work focused on the characterization of random metallographic sections of the composite. For this work, scanning electron microscope images were analyzed using a Zeiss Videoplan Image Analyzer in order to determine the particle size distribution in the extruded and heat treated product. Subsequently, it was of interest to examine the particle size and

spatial distribution characteristics in selected areas. This was accomplished by using micrographs of the region of interest and analyzing these images with the IBAS 2000 system, which is capable of image enhancement and quantitative data acquisition. For each particle in a field of view, the X and Y coordinates of the particle centroid, particle area, aspect ratio, width, length, and angle with respect to the X-axis were measured. Approximately 10 fields and about 300 particles were measured for each matrix aging condition.

Of specific interest in this work was the relationship between the particle size and spatial distribution characteristics on the accumulation of damage leading to fracture. The role of particle clustering was of particular interest. The data acquired with the IBAS 2000 system allow the generation of the Dirichlet tesselation [17] for the fields. In this construction, a computer algorithm is employed which produces a space filling structure consisting of cells of matrix surrounding each particle. The cell defines that region of the matrix closer to the particular particle than any other. Recent refinements to the algorithm enable the current program to deal specifically with high volume fraction materials containing non-spherical particles. The ability to represent the particles as ellipses rather than circles in two dimensions, and the ability to define the cell boundaries based on the particle surfaces rather than centers has permitted more accurate representations of the microstructures to be constructed.

The tesselated structure allows the metallographic parameter of local area fraction to be defined as the particle area divided by the cell area. In addition, the neighbors are clearly defined as those particles with cell sides in common with the subject particle, and the minimum interparticle spacing as the distance to the closest of the neighbors. These additional parameters available from the Dirichlet tesselation construction are direct measures of the spatial distribution of particles, and are particularly suited for direct comparison to damage accumulation in the microstructure. Figure 1 shows a typical microstructure, its image enhanced version, and the tesselated version of the microstructure where the particles are represented as ellipses. Not all particles in a field can be tesselated due to the need to have all sides of the cell defined by other particles. Particles near the outer portions of the field often do not meet this

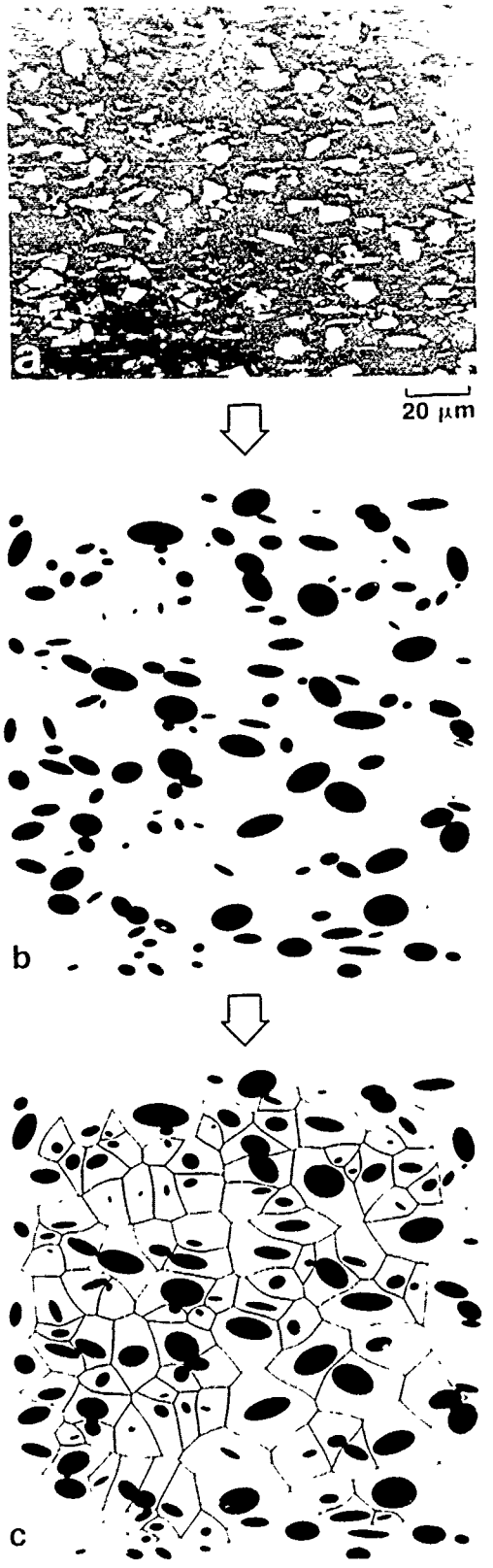

Fig. 1. (a) SEM image of composite microstructure. (b) Computer representation of (a). (c) Tesselated microstructure of (a), (b).

condition. Use of the tesselated structures in conjunction with the mechanical testing work is described below.

It was also of interest to investigate the microstructures of the different matrix aging conditions at higher magnifications to elucidate the fracture micromechanisms. Specimens from both matrix aging conditions in the undeformed state were prepared by thinning with an ion miller equipped with a cold stage and subsequently were examined via transmission electron microscopy (TEM). Special interest was directed towards the interface and near-interface regions. Deformed and fractured specimens were also examined in the TEM by taking foils from directly beneath the fracture surface.

2.3. *Mechanical testing*

Tensile testing was performed on heat treated specimens machined such that the rolling direction was paraliel to the tensile axis on an INSTRON 1125 Universal Testing Machine. Cylindrical tensile specimens with a 5.4 mm diameter and 25.4 mm gauge length were tested at strain rates of 0.00083 s^{-1} and utilized an extensometer to monitor strain. Data including 0.2% offset yield strength, UTS, reduction of area (RA), and work hardening information were obtained.

Fracture initiation studies were conducted on double-notched four-point bend specimens of the geometry shown in Fig. 2. While the details of these specimens have been described elsewhere [2, 3, 18], they have been successfully used to identify microstructural features responsible for fracture initiation in a variety of materials. While one of the notches typically fails, the remaining notch can be subsequently sectioned perpendicular to the notch axis, and polished to reveal the site(s) of fracture initiation.

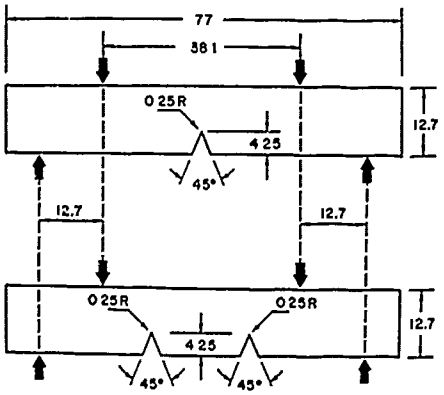

Fig 2 Design of blunt-notch bend bars. Dimensions in mm. Specimen thickness = 12.7 mm.

In addition to the fracture nucleation studies, controlled crack propagation studies were performed on specimens designed to retard the propagation of the crack, so that the sequence of damage accumulation could be determined. Figure 3 schematically illustrates the specimen design, which is a modification of a recent design [19] used to detail the sequence of events in the fracture of materials which fail with low macroscopic ductility. The specimen design consists of a compact tension type specimen which is machined to contain the composite material as well as a backing of a very ductile material. The ductile backing material provides a retarding effect on crack propagation, thereby enabling *in-situ* monitoring of fracture events in materials which fail with low macroscopic ductility. Fracture was monitored using a video camera in conjunction with a high powered optical microscope affixed to an INSTRON Model 1361 Testing Machine. Prior to mechanical testing, the

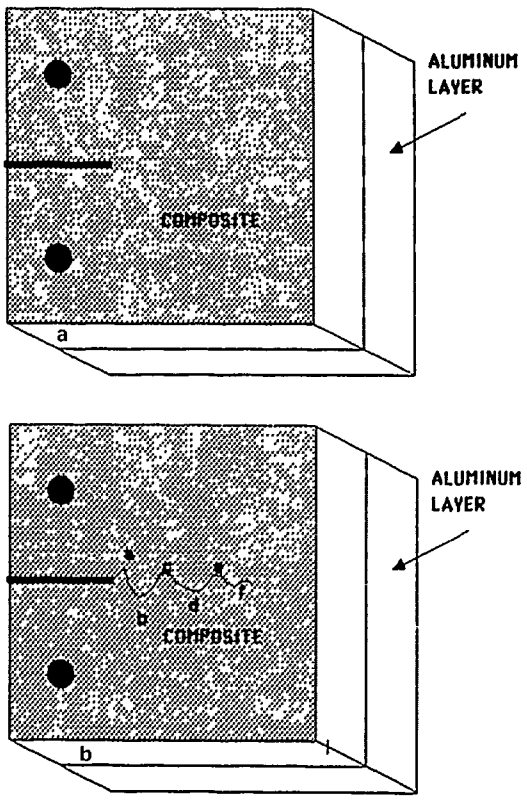

Fig. 3. (a) Specimen design for controlled crack propagation studies. Ductile aluminum backing present on composite specimen. (b) Ductile aluminum layer retards crack growth, permitting *in-situ* fracture monitoring.

microstructure in the notch root region and below were tesselated so that the propensity for damage accumulation in locally clustered regions could be determined at the conclusion of the experiment.

2.4. Quantitative fractography

Fracture surfaces were analyzed using a JEOL 35 SEM equipped with a PGT Microanalysis System. Analyses of the fracture surfaces were performed by matching surface fractography, as well as by quantification of the area fraction and particle size distributions of SiC present on the fracture surface. Particular attention was directed towards examining for evidence of SiC particulate cracking *vs.* decohesion, as well as to the effects of matrix temper on the fracture morphology.

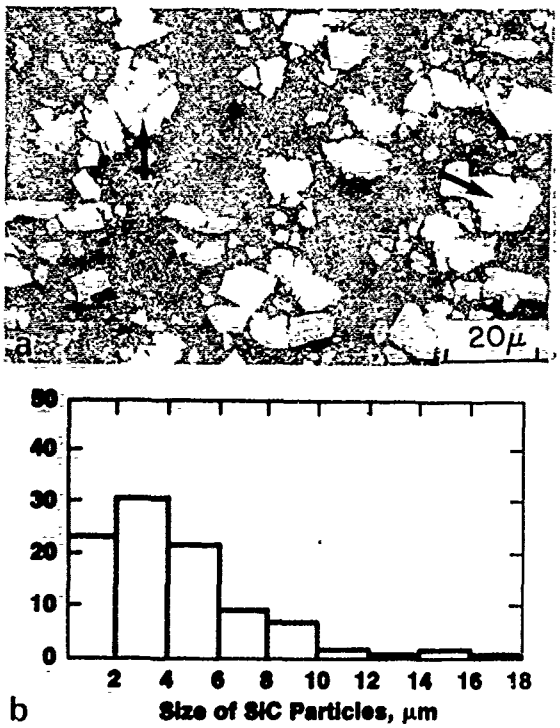

Fig. 4. (a) As-extruded microstructure exhibiting fractured SiC (arrows). (b) Size distribution of SiC particles in as-extruded material.

3. Results

3.1. Undeformed microstructures

Figures 4(a) and 4(b) show the typical microstructures and size distribution of SiC in the metallographic sections of the MB78 composites reinforced with 20% SiC particulate. As shown in previous work [2, 3], fabrication of the material containing F-600 SiC exhibited extensive cracking of the SiC, thereby shifting the average size and size distribution from that of the as-blended powder (*i.e.* 16 μm) to that where the average size of the SiC particulate in the as-extruded product is $\simeq 3$–4 μm. Figure 4(a) illustrates some of the fractured particulate. It was of particular interest in the present work to determine whether these previously fractured SiC particles would be preferential sites for damage accumulation.

Tables 1 and 2 present the quantitative metallographic data for selected regions of the UA and OA matrix conditions, respectively. The data for all of the about 300 particles measured reveal that similar values of area fraction, particle area, and aspect ratio for the two matrix aging conditions were obtained as expected, since these

TABLE 1 Quantitative metallographic data UA condition

Field	*Number of particles*	*Area fraction*		*Minimum spacing*		*Particle area*		*Aspect ratio*	
		Mean	*S.D.*	*Mean* (μm)	*S.D.*	*Mean* (μm^2)	*S.D.*	*Mean*	*S.D.*
1	9	0.22	0.11	1.0	0.8				
2	9	0.12	0.09	2.5	2.4				
3	12	0.36	0.17	0.7	0.5				
4	6	0.11	0.09	1.3	3.0				
5	7	0.23	0.16	1.5	1.5				
6	16	0.26	0.15	0.7	0.7				
7	16	0.23	0.13	1.6	1.2				
Total	75	0.23	0.15	1.3	1.5				
Cells on crack path	23	0.24	0.16	1.5	1.5	28.9	23.8	0.46	0.15
Particles on crack path	17	0.29	0.15	1.2	1.1	35.7	23.8	0.49	0.15
All particles	337	0.25	0.05			24.1	23.8	0.53	0.19

TABLE 2 Quantitative metallographic data OA condition

Field	Number of particles	Area fraction		Minimum spacing		Particle area		Aspect ratio	
		Mean	S.D.	Mean (μm)	S.D.	Mean (μm^2)	S.D.	Mean	S.D.
1	6	0.25	0.11	2.2	3.0				
2	15	0.18	0.15	1.0	1.0				
3	15	0.20	0.15	1.6	1.0				
4	11	0.26	0.17	1.2	0.8				
5	14	0.18	0.09	0.9	0.7				
6	13	0.19	0.08	1.0	0.6				
7	9	0.18	0.14	1.9	1.3				
8	6	0.15	0.10	1.3	1.8				
9	11	0.25	0.14	0.5	0.4				
Total	100	0.20	0.13	1.3	1.2				
Cells on crack path	23	0.26	0.18	1.6	1.8	40.7	42.1	0.51	0.18
Particles on crack path	21	0.30	0.15	1.5	1.6	45.5	41.4	0.51	0.19
All particles	236	0.21	0.04			26.1	27	0.55	0.17

features should not be influenced by aging treatment.

Included in Tables 1 and 2 are the data for the about 100 particles which were tesselated. Comparison of the values of area fraction, particle area, and aspect ratio are similar to those observed for all of the measured particles. The higher standard deviation of the area fraction measurements for the tesselated particles results from the fact that the individual local area fraction for each particle is being measured, as compared to the field averaged value reported for all particles. This higher standard deviation reflects the wide range in local area fractions which is encountered in real microstructures.

TEM of the as-extruded composite exhibited fractured SiC and a high dislocation density at the particle/matrix interface as well as in the matrix, while the interfaces were well bonded (*i.e.* no particle/matrix voids) to the matrix. TEM micrographs of the UA and OA microstructures are shown in Figs. 5(a) and 5(b). Precipitates were not evident either in the matrix or at the SiC particle/matrix interface region in the UA material, while the OA material exhibited precipitation in the matrix as well as at the particle/matrix interfaces. The particles contained Zn, as determined by EDAX analyses on the TEM, and probably represent the $MgZn_2$ precipitate.

3.2. Mechanical properties

Table 3 summarizes the mechanical properties obtained for the composite materials. Slightly lower strengths were obtained for the composites

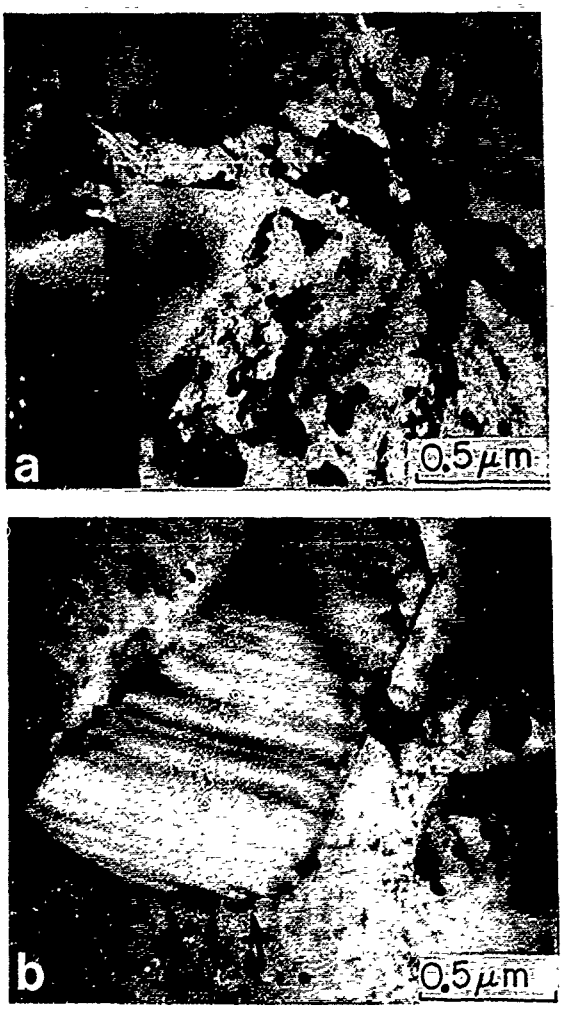

Fig 5 (a) TEM micrograph of UA material. (b) TEM micrograph of OA material. $MgZn_2$ precipitates present at SiC/matrix interface (arrows).

in comparison to the control material as noted in other recent work on these materials [5], while an increased modulus and decreased ductility were also observed for the composite in comparison to the control material [2]. The effect of matrix microstructure (*i.e.* UA *vs.* OA) on the macroscopic tensile ductility was negligible, while the remaining uniaxial tensile properties were similarly negligibly affected by the drastic changes in microstructure provided by the UA and OA heat treatments. This is not necessarily a general observation, as shown in previous work [1–6, 10] where peak aged specimens exhibited significant reductions in ductility in comparison to either under- or over-aged materials. However, matching surface fractography performed on the tensile fracture surfaces did reveal significant effects of the matrix temper on the fracture morphology in the present work. SiC particle cracking was observed in the UA material as Fig. 6 illustrates, with an area coverage of fractured SiC of 18% on the fracture surface. In contrast, the OA material shown in Fig. 7 exhibited only 11% of the surface covered by fractured SiC, and a predominance of fracture near SiC/matrix interfaces. Unfortunately, from these observations alone, it is not possible to determine whether the particles present on the fracture surface were already fractured during processing, or whether they fractured during tensile straining. It is similarly difficult to determine whether fracture is occurring along clustered regions. These points will be returned to in the presentation of the *in-situ* fracture studies which were designed to address these

TABLE 3 Uniaxial tensile properties

Condition	σ_y (MPa)	UTS (MPa)	*n*	RA	*Area fraction fractured SiC on fracture surface*
UA	390	500	0.16	7.9%	18%
OA	405	480	0.16	7.3%	11%

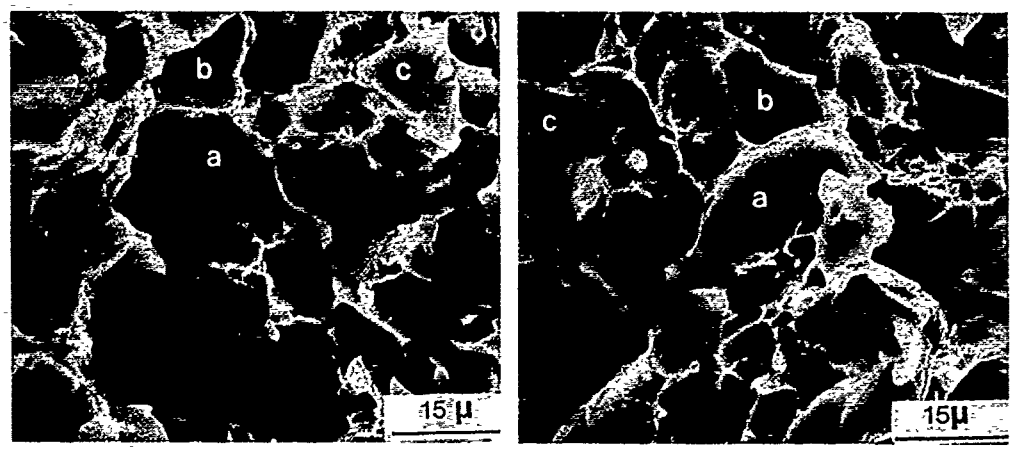

Fig. 6. Matching surface fractograph for UA material. Areas a, b, c contain fractured SiC.

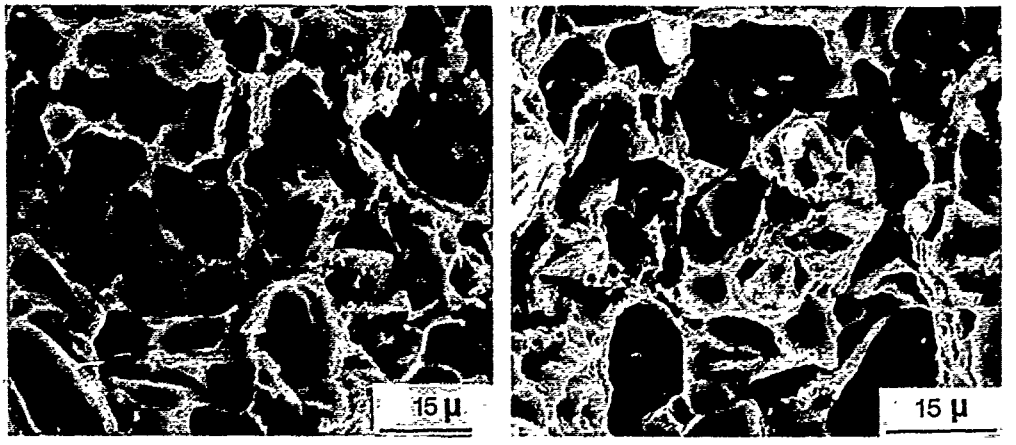

Fig. 7. Matching surface fractograph for OA material. Arrowed regions denote fracture near SiC/matrix interfaces.

Fig. 8. (a) TEM foil taken from below fracture surface in UA tensile specimen. Fractured SiC observed. Arrows indicate subsequent failure in matrix. (b) TEM foil taken from below fracture surface in OA specimen. Void nucleation observed at and near interfaces.

issues. TEM foils taken from below the tensile fracture surfaces in both UA and OA materials similarly reflected the changes in fracture mode observed on the fracture surface, with particulate fracture in the UA condition (*cf.* Fig. 8(a)) and a preference for fracture near the SiC/matrix interface in the OA condition (*cf.* Fig. 8(b)). Evidence of void nucleation below the fracture surface using SEM techniques was not obtained in most of the specimens. Although TEM investigations were successful in locating initiation of fracture, these were similarly difficult to detect.

Despite the similarity in the tensile results (*i.e.* yield strength, RA, *n*) for the UA and OA specimens, the nominal bending stresses at fracture in the UA material were significantly greater than those of the OA material. Values for σ_{nom}/σ_y of the UA material ranged from 1.4–1.7 as compared to 0.9 for the OA material. The details of fracture initiation were studied by sectioning the second notch in the double-notched specimens [2, 18], while fracture toughness data were obtained on short-rod specimens [2]. Short-rod toughness data are shown in Fig. 9 for a range of aging conditions and indicated that the UA material (labelled A) possessed a short-rod toughness significantly in excess of that in the OA material (labelled B). Fracture toughness data obtained in accordance with E-399 revealed similar trends [2, 28]. The controlled fracture experiments conclusively showed that particle fracture was preferred in the UA material, with a change to failure near the interface and in the matrix in the OA material. Figures 10(a–c) present a sequence of photographs depicting damage initiation in the controlled crack propagation specimens for the UA material. Figure 10(a) shows a specimen prior to loading, where the arrowed particles are not yet cracked, while Fig. 10(b) illustrates fracture of a few of the particles (arrowed) during reloading, but prior to matrix fracture. Figure 10(c) shows failure in the matrix and the growth of a macroscopic crack in the UA material where particle cracking is clearly observed. Fracture initiation was observed to occur in SiC particles which were *not* previously cracked during the processing. Similar observations have been made during the controlled propagation of the crack. Figures 11(a) and 11(b) present the crack tip region in the UA material before and after reloading, respectively. The uncracked particles in Fig. 11(a) (*i.e.* prior to reloading) have clearly cracked during reloading in Fig. 11(b), with subsequent failure in the matrix. In contrast to the UA material,

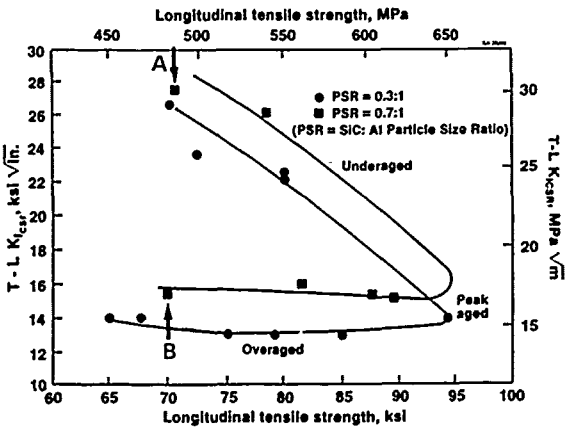

Fig. 9. Short-rod toughness results. UA material shown at "A", OA material shown at "B".

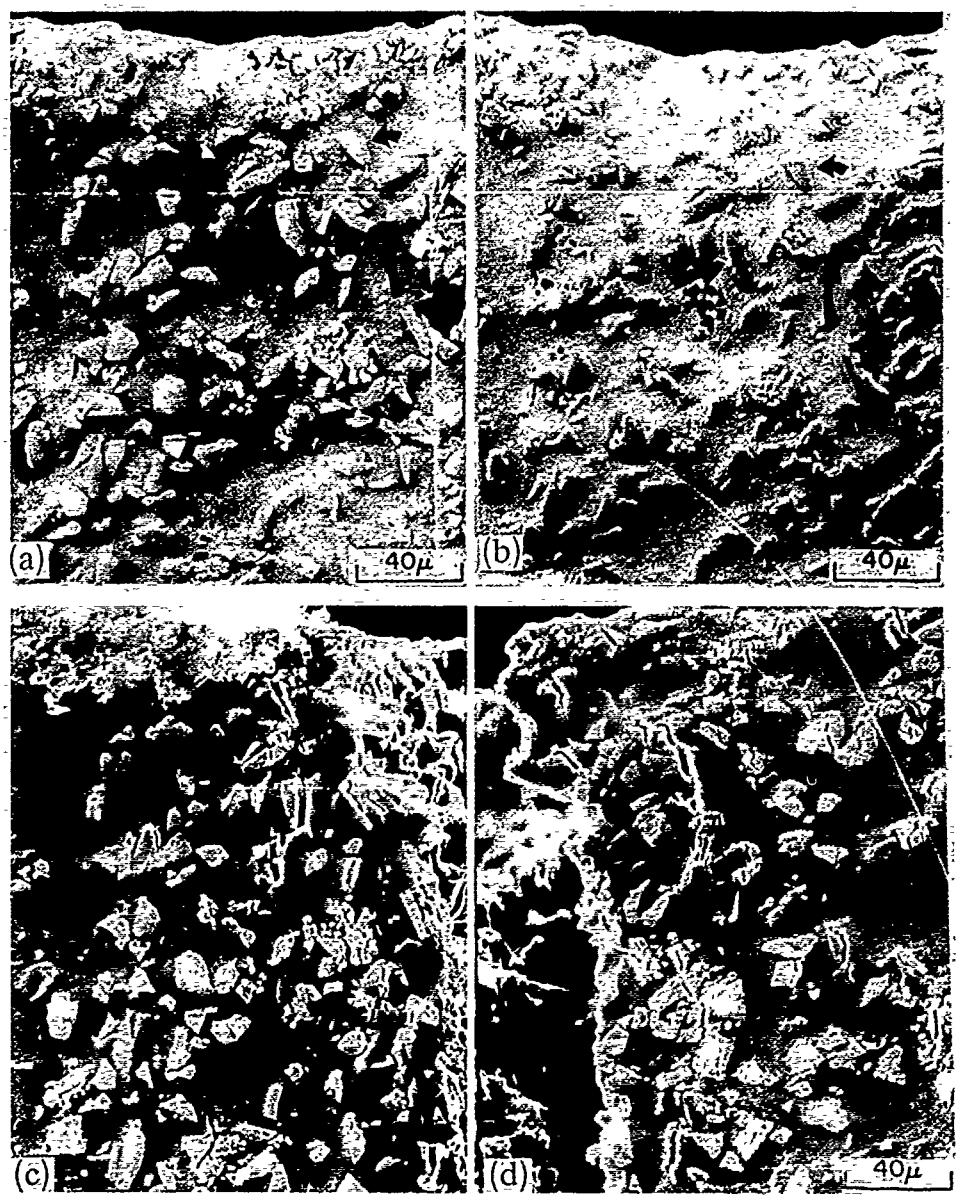

Fig 10. (a) Notch region in UA controlled propagation specimen prior to fracture nucleation at arrowed SiC. (b) Notch region after reloading. Fracture of SiC (curved arrows) observed prior to matrix failure. (c) Notch region after reloading (b). Matrix failure and additional SiC fracture observed. Arrows denote particles in (a), (b).

damage initiation in the OA material was by both matrix failure as well as by separation at and near SiC/matrix interfaces, shown in Fig. 12. The tip of a propagating crack in the OA material is shown in Fig. 13, illustrating fracture at and near the particle/matrix interfaces.

3.3. Microstructural evaluation of deformed/fractured specimens

Of particular interest in this work was the effect of clustered regions on damage accumulation and fracture. To evaluate this, regions such as those shown in Figs. 11 and 13 were tesselated prior to cracking, followed by overlaying the crack on the tesselated microstructures, and identifying the cells intersected by the crack. Figures 14(a)–14(c) present the UA microstructure, an image-enhanced version of the microstructure with the crack path indicated, and its tesselated version which incorporates the same region of the propagating crack. Figures 15(a)–15(c) present the same information for the OA material. The

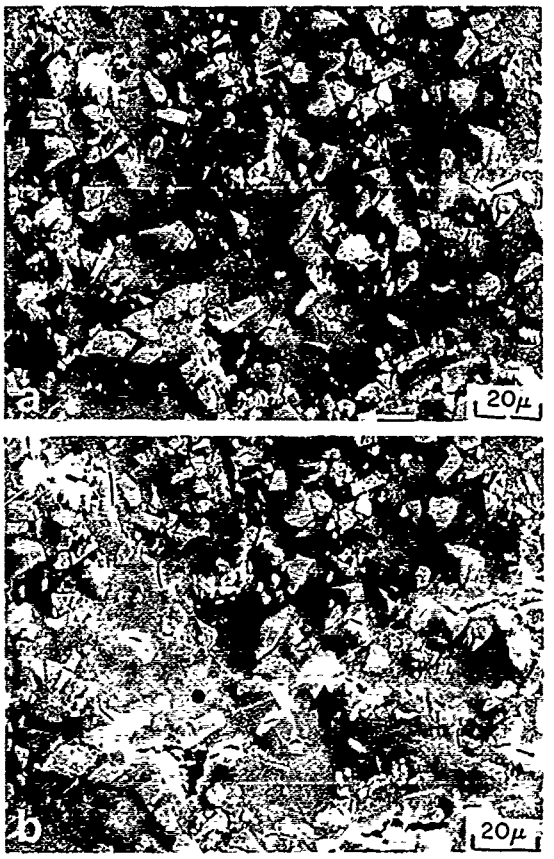

Fig. 11. (a) Crack tip region prior to reloading. Arrows denote unfractured SiC ahead of crack tip, "A". (b) Crack tip region after reloading. SiC fracture ahead of crack tip observed (arrows).

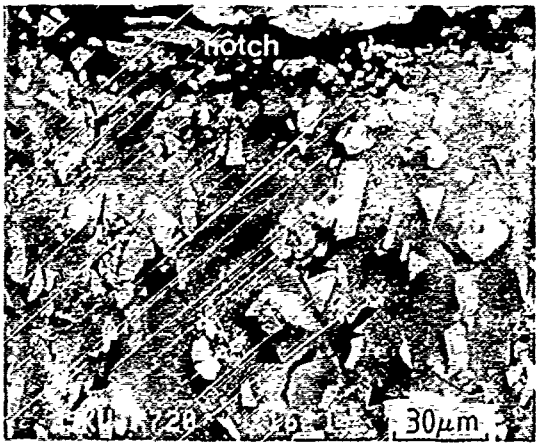

Fig. 12. Notch root region in OA material. Fracture in matrix and near SiC/matrix observed in clustered regions.

metallographic parameters of the intersected cells were then tabulated for comparison to the average values. Approximately 20–25 cells of the about 100 tesselated cells obtained for each matrix condition were intersected by the crack

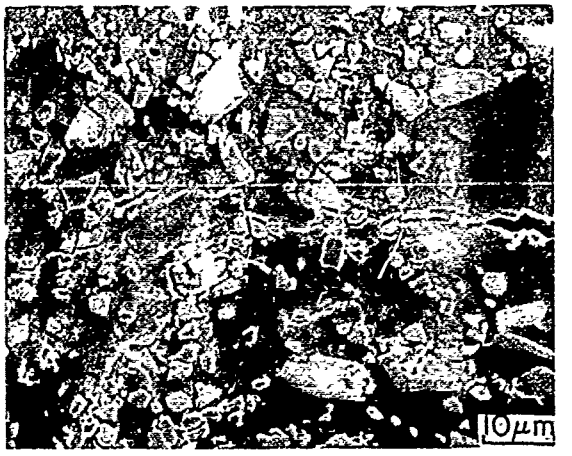

Fig. 13. Crack tip region in OA controlled propagation specimen. Failure near SiC/matrix interface (arrows).

path. Comparison of the particle areas for random fields and those intersecting the crack indicate a tendency for larger particles to be involved in the cracking process, consistent with the results of quantitative fractography performed on fracture surfaces [2, 3]. Although the initiation of damage ahead of the propagating crack was observed to occur in clustered regions, the comparison of the local area fraction values of the intersected cells with the average local area fraction (*i.e.* Tables 1, 2) reveals that the total crack path follows a nearly random path for both the UA and OA materials, despite the change in fracture morphology. It should be noted, however, that by considering the intersected cells, some regions are included in which the particles are not truly intersecting the crack. A further refinement of this analysis is to consider just the cells which contain particles which intersect the crack, which reduces the number of cells considered to about 20 in both cases. When computed in this manner, the analysis reveals that, on average, the crack interacts with local area fractions of particles in excess of the bulk reinforcement level (*i.e.* Tables 1, 2). Although the high standard of deviation of the data does not support this conclusion from a statistical viewpoint, additional work will focus on accumulating a greater number of fields to further elucidate this aspect.

4. Discussion

The present work was intended to investigate the effects of microstructural changes at equivalent strength on the fracture of MMCs containing 20% reinforcement, in addition to beginning to

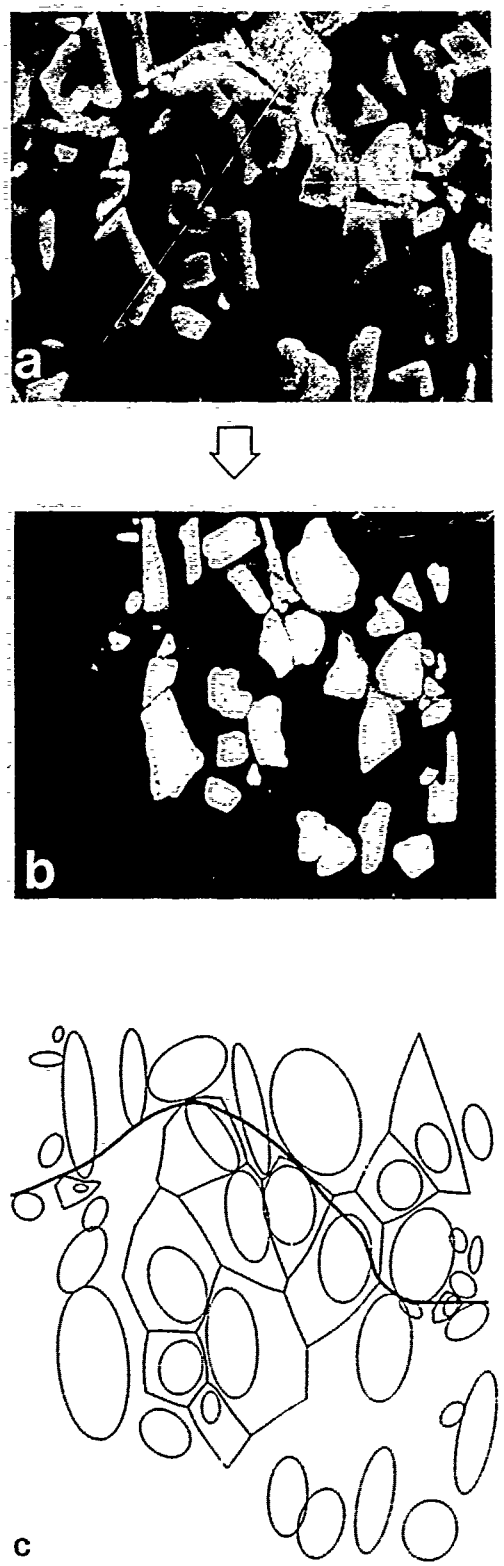

Fig. 14. (a) SEM view of crack path in UA material. (b) Image enhanced version of (a). Crack path shown. (c) Tesselated version of (b). Crack path shown. Particle cracking observed.

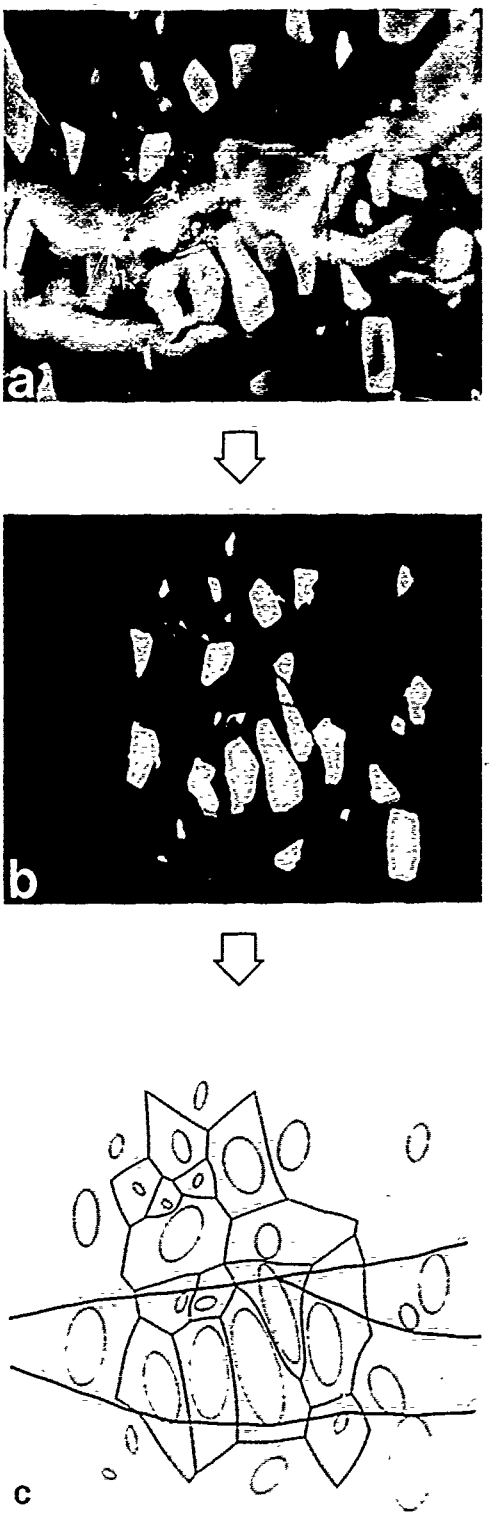

Fig. 15. (a) SEM view of crack path in OA material. (b) Image enhanced version of (a). Crack path shown. (c) Tesselated version of (b). Crack path shown. Failure near SiC/matrix indicated.

evaluate the effects of particle clustering on fracture. The effects of microstructural changes (*i.e.* matrix temper) were shown to exhibit a dramatic effect on the micromechanisms of fracture and various measures of toughness, although their effects on tensile ductility were negligible. The effects of microstructure on the observed properties will be discussed presently, followed by the initial results obtained on clustering effects.

The present work has revealed a dramatic effect of matrix microstructure (*i.e.* temper) on the fracture micromechanisms at an equivalent strength level. In all specimens tested (*i.e.* tensile, bend, toughness), a transition in fracture mode from particle cracking in UA specimens to matrix and "near interface" failure in the OA specimens was obtained. Despite the dramatic changes in failure micromechanisms revealed by both SEM and TEM, uniaxial tensile ductility was not significantly affected (*cf.* Table 3), although the UA microstructure exhibited much better properties in the notched bend and short-rod toughness specimens. The general lack of correlation between smooth tensile and fracture toughness measurements on materials failing by MVC has been covered in a recent review of ductile fracture [20]. Such observations may be rationalized by examining the stages of fracture events leading to catastrophic fracture in the various specimen geometries examined. In smooth tensile specimens, fracture was observed to occur in a macroscopically brittle mode (*i.e.* low ductility) although the fracture surface details revealed micro-void coalescence (*i.e.* MVC). As it has been reviewed that ductile fracture consists of void nucleation, growth, and coalescence stages, the relative importance of each stage should determine the macroscopic ductility of the specimen. In ductile materials reinforced with a high volume fraction of hard second phase particles (*e.g.* SiC), however, it has been suggested that fracture nucleation events may dominate the ductility since the subsequent stages of void growth and coalescence may be extremely rapid once initiation has occurred [13, 21]. Although both microstructures exhibited nearly identical tensile ductilities (*i.e.* RA = 8%), fracture initiation in the two microstructures appears to occur via very different mechanisms, as revealed by the SEM and TEM investigations. The former (*i.e.* UA) failed by particle cracking while the latter (*i.e.* OA) failed by a mixture of matrix and near interface failure. The difficulty in locating fracture sites below the fracture surface similarly supports the contention that fracture nucleation events play a dominant role in the ductility of these materials, and precludes the chance of determining particle clustering effects directly in the fracture of the smooth tensile specimens.

Previous work [2, 3, 6, 22, 28] on a variety of MMCs has indicated that crack initiation in smooth tensile specimens preferentially initiates at large particles, inclusions, and regions of clustered SiC. The present work indicates that UA materials initiate predominantly via a particle cracking mechanism, while the OA materials initiate via matrix and near interface failure. Comparison of the observed ductility to micromechanical models for ductility in particle-hardened materials [23, 24] was performed for the OA material with the Brown/Embury model [23]. Particle/matrix decohesion is assumed in that model with subsequent fracture by rupture of ligaments between voids which occur when the void length becomes equal to the spacing between the void nucleating particles. This model assumes that void coalescence contributes only minimally to the total ductility, and that the ductility is in large part determined by void growth, although the nucleation strain has also been incorporated into the model. At high volume percent reinforcement, (*e.g.* $> 15\%$), the model predicts that the growth of voids provides an insignificant contribution to ductility, while the nucleation strain becomes dominant. The inability to detect void initiation below the fracture surface for both UA and OA materials strongly suggests that nucleation events are dominant in the fracture behavior of the high volume fraction reinforced materials studied presently. Assuming that the nucleation strain corresponds to the fracture strain enables a qualitative comparison of the OA material exhibiting preference for "interface" failure to the original Brown/Embury model [23] where:

$$\varepsilon_T = \ln(1 + \varepsilon_g + \varepsilon_n) = \ln\{(\pi/6f)^{1/2} - (2/3)^{1/2} + \varepsilon_n\}$$

Substituting for $f = 0.2$ and $\varepsilon_n = 0.08$ gives $\varepsilon_T = 0.08$. In contrast, the Evensen–Verk [24] model was utilized for the UA material, which assumes particle cracking as the operative damage initiation mechanism in a ductile surrounding matrix where the growth strain controls ductility:

$$e_G = 0.104\{(2\pi/3f)^{1/2} - (8/3)^{1/2}\}$$

Assuming a nucleation strain of $= 0.1$ provides $\varepsilon_f = 0.20$, an overestimate of ductility. This likely results from the differences in the details of the

micromechanisms of fracture in the present work and those assumed by the model. This will be returned to in the discussion of the controlled crack propagation experiments.

Despite the similarity in the uniaxial tensile ductilities, large effects on both the fracture micromechan[illegible] and macroscopic properties were obtained under more severe stress states. Both the nominal bending stresses at fracture in the notched bend specimens and the short-rod toughnesses were significantly higher in the UA material as compared to the OA material. The blunt notched bend tests failed with a linear load-displacement trace, also suggesting that the details of initiation control the notched properties of MMCs reinforced with high volume fractions of SiC. Although clustered regions were observed to be preferential sites for fracture nucleation in the unbroken notch of the double-notched specimens, the mode of initiation was again different in the UA (*cf.* Fig. 10) and the OA (*cf.* Fig. 12) materials. UA materials exhibited SiC fracture and matrix failure, while OA materials exhibited matrix and near interface failure and less fracture of the SiC. As the notched bend specimens are sensitive to fracture initiation events, it appears that the matrix failure strain of the OA material is considerably lower than that of the UA material when testing is conducted under a strain state more severe than that of uniaxial tension. The uniaxial fracture strains were nearly equivalent at 8%, although it is clear that fracture in the notched bend specimens occurred at lower loads (and lower notch root strains) in the OA material. The controlled fracture propagation studies similarly revealed that the fracture micromechanisms differed in the two materials. Both fracture initiation and propagation occurred at lower loads and crack opening displacements for the OA material. Thus, the fracture strain (*i.e.* local) under stress states more severe than uniaxial tension is considerably different from that obtained under uniaxial conditions. This has been previously observed in a variety of monolithic materials [25, 26], where it has been experimentally observed that the failure strains under plane strain conditions may be considerably lower than those obtained in uniaxial specimens. The present study also indicates that the magnitude of this decrease may depend sensitively on the characteristics of the matrix, since the UA material exhibited significantly higher notch root fracture loads (and strains).

Although the present results show a clear effect of matrix microstructure on the fracture details, previous work [6] on other aluminum based composites (*e.g.* 2XXX series) suggested that the details of the fracture micromechanisms were unaffected by heat treatment. A tendency for particle cracking was exhibited in that work, regardless of matrix temper. Other work on 6XXX and 7XXX alloys indicated a shift in fracture micromechanisms with aging [22], similar to that observed in the present work. These observations indicate that the details of the matrix microstructure and interface region play a dominant role in the fracture micromechanisms, and that relatively subtle differences in aging conditions and matrix compositions may produce the distinctively different properties which have been observed in nominally similar materials. It is interesting to note that the relatively constant low level of fracture toughness observed in the over-aged conditions in the composite materials has also been observed in over-aged Al–Li based alloys, in which grain boundary precipitates reduced the grain boundary cohesive strength [27].

The controlled crack propagation experiments additionally provide some insight with regard to fracture in either the UA or OA composites. As pointed out by Embury [13], nucleation events may dominate the ductility in the case of materials containing high volume fractions of reinforcement. This appears to be particularly true in the present case where little evidence of voiding was observed below the fracture plane in the failed tensile specimens. The Brown/Embury model assumes that coalescence occurs when the vertical void height equals the spacing between particles, which was not observed with the OA materials. The Evensen/Verk [24] model for particle cracking-initiated failure assumes a non-hardening matrix where particle cracks are blunted by displacement of the particle faces, with local plasticity at the tips. This model similarly suggests that void growth and linkup require a large strain. However, the sequential straining experiments indicate that this micromechanism of failure does not appear to describe failure in the UA materials, where particle cracking is followed by little blunting in the matrix prior to subsequent fracture. The failure between adjacent fractured particles appears to occur by intense localized flow in the matrix. The observed micromechanisms suggest that the adaptation of

models used for ductile fracture in other materials (*e.g.* steels containing spheroidized carbides in a ductile α-Fe matrix, brittle Si particles in a ductile Al alloy matrix) may not be applicable in the case of some discontinuous MMCs because of the differences in the micromechanisms of fracture. In the present work, the controlled propagation experiments indicate that fracture in the UA materials occurs via particle cracking in the process zone ahead of the crack, while matrix and near interface failure are obtained in the OA material.

The remaining discussion focuses on a comparison between the tensile fracture surfaces and those observed in the controlled propagation studies. Analysis of the quantitative fractography performed on the OA materials revealed that only 11% of the fracture surface was covered by fractured SiC particles, suggesting that fracture was avoiding the particles in the OA material while selecting nearly the average area fraction in the UA material where 18% of the fracture surface was covered with fractured SiC particles. However, fracture surface observations do not necessarily provide an accurate representation of the fracture path with regard to particle clustering since only half of the fracture surface is being viewed. For example, the tesselated microstructures (*i.e.* Tables 1, 2) indicate that the crack path in the controlled propagation studies was, on average, choosing a random path. To the authors' knowledge, the present work is one of the first attempts to directly compare the progression of cracking with respect to particle clustering. Although only a limited number of cells have been analyzed at present, the quantitative information provided in Tables 1 and 2 indicates that the average local volume fraction of particles intersected by the propagating crack is roughly the average volume fraction (*i.e.* 20%) for both microstructures. However, observations of the regions ahead of the propagating crack revealed damage accumulation in clustered regions as well as differences in the mechanisms of failure in the UA and OA materials. Tables 1 and 2 indicate that damage accumulation and fracture propagation show a greater propensity for preferential fracture in clustered regions when following the more restricted criterion of choosing only those cells in which the particle is actually interacting with the crack. Although this conclusion cannot be statistically supported at this time due to the limited number of cells examined, additional work is being conducted to provide a statistical basis.

Although the quantitative results indicated that a random path was exhibited by the total crack path, damage accumulation was observed to occur in highly clustered regions along parts of the fracture path for both microstructures. The selection of damage accumulation in locally clustered regions, combined with the quantitative analyses which showed that the gross fracture path was essentially random may be related to the orientation of the controlled fracture propagation samples. It was observed that alternating "bands" of high volume fraction reinforcement and low volume fraction regions are present in the direction of crack propagation. This requires that the crack pass through some low volume fraction regions in order to progress. This effectively reduces the values obtained in the calculations of local volume fraction of particles along the total crack path, despite damage accumulation in areas of highly clustered regions. Further experiments are planned where the orientation is changed with respect to the "banding" observed in the composite.

In the present tests, the growth of the crack could be controlled due to the presence of a compliant layer on the specimen. In specimens not containing this compliant layer, however, catastrophic crack propagation typically occurs without significant macroscopic crack opening displacement. Previous arguments [21] have been made that the initiation event may be the critical factor in the fracture of these materials. The present work further illustrates that the examination of fracture surfaces alone may be insufficient to determine whether fracture is initiating or propagating along a path of clustered particles. Thus, as an extension of this work, subsequent work will focus on the relationship between clustered regions and damage accumulation, where similar specimens may again be useful in detailing the accumulation of damage. Composites containing different particle sizes at the same reinforcement level are being tested to evaluate the effects of changes in clustering on the fracture properties. Previous work [2] has indicated that property changes have been obtained by varying the particle size independent of the volume percentage, while property correlations with the amount of clustering were consistent with the trends exhibited.

5. Conclusions

(1) Controlled variations in matrix micro-

structure have been achieved while producing equivalent uniaxial tensile properties.

(2) Despite nearly identical uniaxial tensile properties, substantial differences in fracture micromechanisms and mechanical properties were obtained under test conditions representing more severe stress states (*e.g.* notched bend, short-rod toughness). These property changes were accompanied by a change in fracture mode from predominantly particle cracking in the UA material to failure in the matrix and near the interfaces in the OA material. Quantitative fractography revealed a preference for fracture of the large SiC particles in the size distribution.

(3) The details of damage accumulation and fracture have been determined on specimens designed to permit controlled propagation of a crack. This technique demonstrated that in the UA condition, large uncracked particles are fractured ahead of the crack tip in preference to sampling particles fractured during processing.

(4) Quantitative assessment of the role of particle clustering on damage accumulation, as studied by *in-situ* crack experiments, reveals that damage accumulation occurs preferentially in clustered regions ahead of a blunt notch or propagating crack tip. Subsequent linkage of the main crack to the regions of accumulated damage appears to occur in a nearly random manner. Continuing work is focusing on studying material containing different particle sizes at the same reinforcement level, as these should exhibit different tendencies for clustering.

Acknowledgments

This work was funded by a one-year ALCOA Fellowship for one of the authors (C.L.) while an AIME Research Initiation Grant supported another (J.J.L.). Additional experimental support at CWRU was provided by DARPA-ONR-N000 13-86-K-0773.

References

1 D. L. McDanels, *Metall. Trans. A, 16*(1985) 1105.
2 J. J. Lewandowski, C. Liu and W. H. Hunt, Jr., in M. Kumar, K. Vedula and A. M. Ritter (eds.), *Powder Metallurgy Composites*, TMS-AIME, Warrendale, PA, 1987, pp. 117–139.
3 C. Liu, S. Pape and J. J. Lewandowski, in H. Ishida (ed.), *Interfaces in Polymer, Ceramic, and Metal Matrix Composites*, Elsevier Science, New York, 1988, p. 513.
4 T. Christman, A. Needleman, S. Nutt and S. Suresh, *Mater. Sci. Eng., A107* (1989) 49.
5 J. K. Shang and R. O. Ritchie, *Mater. Sci. Eng.* (1988) in the press.
6 C. P. You, A. W. Thompson and I. M. Bernstein, *Scripta Metall., 21* (1987) 181.
7 A. K. Dhingra, S. G. Fishman and S. D. Karmarkar, *J. Met., 33*(1981) 12.
8 S. V. Nair, J. K. Tien and R. C. Bates, *Int. Metall. Rev., 30* (1985) 275.
9 W. A. Logsdon and P. K. Liaw, *Eng. Fract. Mech., 24* (1986) 737.
10 D. L. Davidson, *Metall. Trans. A, 18*, 1987, 2003.
11 W. A. Spitzig, R. E. Smelser and O. Richmond, *Acta Metall., 36*(1988) 1201.
12 E. M. Dubensky and D. A. Koss, *Metall. Trans. A, 18* (1987) 1887.
13 J. D. Embury, *Metall. Trans. A, 16*, 1985, 2191.
14 G. LeRoy, J. D. Embury, G. Edward and M. F. Ashby, *Acta Metall., 29*(1981) 1509.
15 J. R. Fisher and J. Gurland, *Metall. Sci.* (1981) 193.
16 A. S. Argon, J. Im and R. Safoglu, *Metall. Trans. A, 6* (1975) 825.
17 P. J. Wray, O. Richmond and H. L. Morrison, *Metallography, 16*(1983) 39.
18 J. J. Lewandowski and A. W. Thompson, *Metall. Trans. A, 17*(1986) 1769.
19 J. J. Lewandowski, *Scr. Metall.*, submitted.
20 W. M. Garrison, Jr. and N. R. Moody, *J. Phys. Chem. Solids, 48*(1987) 1035.
21 W. H. Hunt, Jr., O. Richmond and R. D. Young, in F. L. Matthews *et al.* (eds.), *Proc. 6th Int. Conf. on Composite Materials*, Vol. 2, Elsevier, London, 1987, p. 2209.
22 A. Voelkel, unpublished results, 1988.
23 L. M. Brown and J. D. Embury, in *Proc. 3rd Int. Conf. Strength of Metals and Alloys*, Iron and Steel Inst., London, 1975, p. 161.
24 J. D. Evensen and A. S. Verk, *Scripta Metall., 15* (1981) 1131.
25 D. P. Clausing, *U.S. Steel Res. Lab. Report 35.066*, 1972.
26 J. J. Lewandowski and A. W. Thompson, *Metall. Trans. A, 17*(1986) 461.
27 A. K. Vasudevan and R. D. Doherty, *Acta Metall., 35* (1987) 1193.
28 M. Manoharan, C. Liu and J. J. Lewandowski, in K. Salama (ed.), *Proc. ICF7*, Pergamon, Oxford, in press.

Materials Science and Engineering, A107 (1989) 257–259

Theoretical and Experimental Analysis of the Toughening Behavior of Whisker Reinforcement in Ceramic Matrix Composites*

P. F. BECHER, C. H. HSUEH, P. ANGELINI, and T. N. TIEGS

Metals and Ceramics Division, Oak Ridge National Laboratory, Oak Ridge, TN 37831 (U.S.A.)

(Received June 1, 1988)

Abstract

A brief summary of recent analytical solutions which accurately describe the experimentally observed toughening behavior in a variety of whisker reinforced ceramics is presented. These results are found to provide important insights into the whisker, matrix, and interface properties required to obtain further increases in toughness by whisker reinforcement of ceramics.

1. Introduction

SiC whisker reinforcement of ceramics can result in substantial improvements in fracture toughness and resistance to wear, slow crack growth, and thermal shock of ceramics with the incorporation of strong, small diameter ceramic whiskers [1–5]. For example, the critical toughness of very fine grained alumina can be increased from $\leqslant 3$ MPa $m^{1/2}$ to 9 MPa $m^{1/2}$ with the addition of 20 vol.% SiC whiskers. Comparable increases in toughness have been observed in a variety of other whisker-reinforced ceramics [3–4]. In addition, the increased fracture toughness is retained with increasing temperature, *e.g.* up to about 1100 °C in the SiC whisker-reinforced alumina composites [6]. When compared with the continuous fiber-reinforced ceramics at the same reinforcing phase contents, the whisker-reinforced composites exhibit similar toughness values, but have the advantage of composite fabrication by more conventional powder processing techniques.

The mechanisms responsible for such whisker toughening include crack deflection and both whisker bridging and whisker pullout within a zone immediately behind the crack tip [1, 5]. Such processes are noted in fracture surface observations and scanning and transmission electron microscopy studies of cracks in these composites, Fig. 1. Crack tip bridging processes are of considerable interest in fracture processes. A classic example of the formation of a bridging zone is that noted in continuous fiber-reinforced ceramics where toughness is enhanced by the extensive pullout of the fibers in this zone.

2. Theoretical analysis

As noted in Fig. 1, the establishment of a whisker bridging zone in the crack tip wake results in increased toughness, dK^{wr} which is defined as

$$dK^{wr} = 2\sigma^{c}(2D_B/\pi)^{1/2} \quad (1)$$

where σ^c is a closure stress imposed on the crack by the bridging whiskers over a zone of length D_B [1]. In the case of aligned whiskers, the closure stress is the sum of the stress (less than or equal to the whisker tensile fracture strength (σ_f^w)) exerted by each whisker in the bridging zone and is given by

$$\sigma^c = V_f \sigma_f^w \quad (2)$$

where V_f is the volume fraction of whiskers.

When there is a strong toughening contribution from whisker reinforcement, the crack opening displacement (u) at the whisker at the end of the bridging zone can be reduced to the form

$$u = 8(1-\nu^2)\sigma_f^w V_f D_B/\pi E^c \quad (3)$$

where ν is the Poisson's ratio and E^c the Young's modulus of the composite for the whiskers uniaxially aligned parallel to the tensile stress axis [1]. The crack opening displacement at the end of the bridging zone will equal the maximum tensile displacement ($d/$) in the debonded whisker at that point. Thus the crack opening displacement (u)

*Paper presented at the symposium on Interfacial Phenomena in Composites: Processing, Characterization, and Mechanical Properties, Newport, RI, June 1–3, 1988.

0921-5093/89/$3.50

© Elsevier Sequoia/Printed in The Netherlands

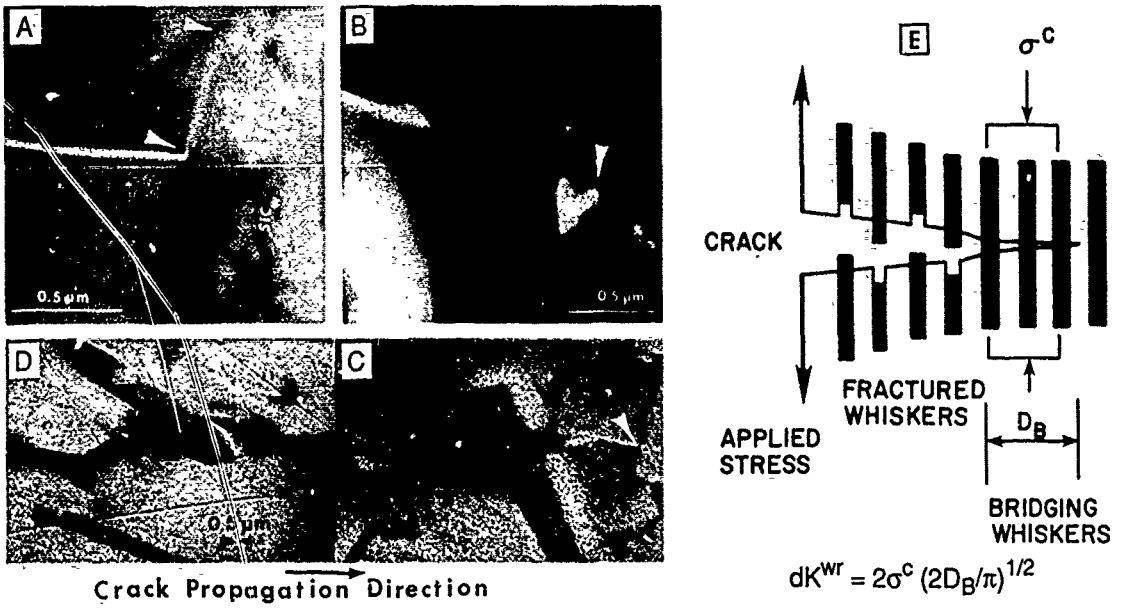

Fig 1. Toughening by whisker reinforcement is associated with the formation of a zone of bridging whiskers behind the crack tip. As the crack tip reaches the whisker, debonding and/or fracture occurs along the whisker–matrix interface (A) which allows the crack tip to advance leaving the whiskers intact and bridging the crack (B, C). At some distance behind the crack tip, whiskers fracture and/or are pulled out of the matrix (D) establishing the whisker bridging zone (E).

can be related to dl and the whisker–matrix interface debond length (l_{DB}) as

$$dl = u = \sigma_f^w l_{DB}/E^w \quad (4)$$

where E^w is the Young's modulus of the whisker. Using the analytical solutions for interface separation versus whisker fracture of Budiansky *et al.* [7], the debonded length of the whisker–matrix interface is

$$l_{DB}/r = \gamma^m/6\gamma^i = \beta \quad (5)$$

where r is the whisker radius and γ^m and γ^i are the fracture energies of the matrix and interface respectively. By substitution of eqns. (4) and (5) into eqn. (3), we obtain the definition of D_B:

$$D_B = (\gamma^m E^c/\gamma^i E^w)[\pi r/48(1-\nu^2)V_f] \quad (6)$$

for bridging whiskers in the region immediately behind the crack tip. The toughening contribution from whisker bridging dK^{wr} is then defined by substitution of eqns. (2) and (6) into eqn. (1):

$$dK^{wr} = \sigma_f^w\{[V_f r/6(1-\nu^2)](E^c/E^w)(\gamma^m/\gamma^i)\}^{1/2} \quad (7)$$

for the case where whisker bridging imposes a uniform closure stress over the bridging zone.

These and companion analytical solutions are found to accurately describe the experimentally observed toughening behavior in a variety of whisker-reinforced ceramics (*eg.* alumina, mullite, and glasses) as shown in Fig. 2. In addition, they provide important insights into the whisker,

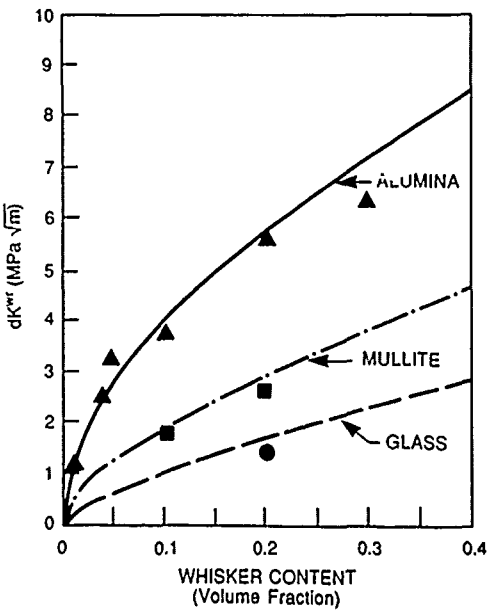

Fig. 2. The fracture toughness of ceramics increases with the addition of strong SiC whiskers. The toughness increase due to whisker bridging predicted by the analytical models (curves) describes that observed experimentally in alumina- (▲), mullite- (■), and glass- (●) based composites.

matrix, and interface properties required to obtain further increases in toughness by whisker reinforcement of ceramics. However, the solutions derived explicitly consider the case of whisker bridging involving strong interfaces where whisker pullout is minimized. Further studies are underway to examine the role of interface properties and the toughening contributions derived from extensive whisker pullout in brittle matrix systems.

Acknowledgments

The research was supported by the U.S. Department of Energy, Office of Basic Energy Sciences, Division of Materials Sciences, and the Office of Transportation Systems, Ceramics Technology for Advanced Heat Engines Project of the Advanced Materials Development Program under Contract DE-AC05-84OR21400 with Martin Marietta Energy Systems, Inc.

References

1 P. F. Becher, C. H. Hsueh, P. Angelini and T. N. Tiegs, *J. Am. Ceram. Soc.* (1988) in press.
2 P. F. Becher and G. C. Wei, *J. Am. Ceram. Soc., 67* (12) (1984) C-267–C-269.
3 P. F. Becher and T. N. Tiegs, in *Engineered Materials Handbook*, Vol. 1: *Composites*, ASM International, Metals Park, Ohio, 1987, pp. 941–944.
4 P. F. Becher, T. N. Tiegs and P. Angelini, in K. S. Mazdiyasni (ed.), *Fiber Reinforced Ceramics*, Noyes Publications, Park Ridge, NJ, in press.
5 P. Angelini, W. Mader and P. F. Becher, in P. F. Becher, M. V. Swain and S. Somiya (eds.), *MRS Proceedings: Advanced Structural Ceramics*, Vol. 78, Materials Research Society, Pittsburgh, PA, 1987, pp. 241–257.
6 P. F. Becher and T. N. Tiegs, *Adv. Ceram. Mater., 3* (2) (1988) 148–153.
7 B. Budiansky, J. W. Hutchinson and A. G. Evans, *J. Mech. Phys. Solids, 34* (2) (1986) 167–189.

Materials Science and Engineering, A107 (1989) 261–268

Dynamic Compressive Fracture in Fiber-reinforced Ceramic Matrix Composites*

JAMES LANKFORD

Department of Materials Sciences, Southwest Research Institute, San Antonio, TX (U.S.A.)

(Received June 1, 1988)

Abstract

High-strain-rate compressive failure mechanisms in fiber-reinforced ceramic matrix composite materials have been characterized. These are contrasted with composite damage development at low strain rates, and with the dynamic failure of monolithic ceramics. It is shown that it is possible to derive major strain-rate strengthening benefits if a major fraction of the fiber reinforcement is aligned with the load axis. This effect considerably exceeds the inertial microfracture strengthening observed in monolithic ceramics, and non-aligned composites. Its basis is shown to be the trans-specimen propagation time period for heterogeneously-nucleated, high-strain kink bands.

1. Introduction

It is by now well known that brittle materials subjected to high rates of loading often exhibit strengths much greater than those characteristic of slow or quasistatic rates [1–5]. The degree of strengthening observed is generally too high, and too strain-rate sensitive, to be explained on the basis of the suppression of thermally activated crack tip processes, although the latter does impart a mild rate-dependent strength benefit [1]. For example, the author has shown that for strain rates $\gtrsim 10^3\ s^{-1}$, obtainable within the split Hopkinson pressure bar (HPB), certain classes of monolithic ceramics (Fig. 1) behave according to [1]:

$$\sigma_c \propto \dot{\varepsilon}^{1/3} \tag{1}$$

where σ_c is the compressive failure (fracture) strength, $\dot{\varepsilon}$ is the imposed strain rate, and n is a constant, usually of the order of 1/3. Others have obtained similar results for rocks, in both compression and tension [2–7]. Where this behavior has not been observed (Fig. 1), fracture mode/microstructural considerations (RB Si_3N_4), or strain-rate limitations inherent in the HPB (Al_2O_3), are thought to be responsible.

In fact, it has been shown by Grady and Lipkin [8] that analyses based on a variety of physical criteria (work of fracture, least action law, inertia of flaws to crack initiation, crack inertia under step loading) all lead inevitably to a tensile fracture relationship like eqn. (1), *i.e.*

$$\sigma_T \propto \dot{\varepsilon}^{1/3} \tag{2}$$

where σ_T is the applied tensile stress at failure. Since brittle compressive failure is known to correspond to the coalescence of a multitude of microscopic cracks nucleated within local tensile regions, it is therefore not surprising that equivalent failure dynamics should obtain for both tension and compression. Generalizing the situation, Grady and Kipp observe [8] that such results

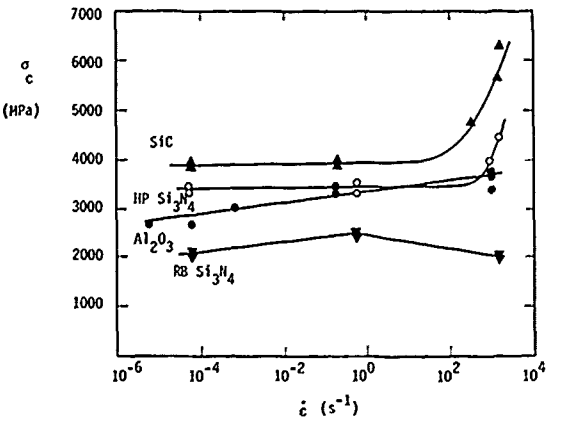

Fig. 1. Compressive strength *vs.* strain rate for several monolithic ceramics at 23 °C. The decrease in strength for reaction bonded (RB) Si_3N_4 at $\dot{\varepsilon} \approx 10^1\ s^{-1}$ is caused by a transition in fracture mode from transgranular to intergranular.

*Paper presented at the symposium on Interfacial Phenomena in Composites. Processing, Characterization, and Mechanical Properties, Newport, RI, June 1–3, 1988.

0921-5093/89/$3.50

© Elsevier Sequoia/Printed in The Netherlands

suggest that a cube-root strain-rate dependence represents the upper limit that can be obtained in the dynamic brittle failure process. This is probably true for monolithic materials, but recent experimental results [9] seem to indicate that the microstructures of ceramic matrix composites can be manipulated to yield a much higher degree of strain-rate sensitivity.

The objective of the present paper is to briefly outline these results, and then establish the principal factors which appear to control the damage development/failure process. A simple basis for treating the problem analytically is presented.

2. Experimental approach

The materials studied have been described in detail elsewhere [9, 10], and so are discussed here only briefly. Thus, the composites (Compglas®, United Technologies Research Center) consisted essentially of a pyroceramic matrix reinforced with about 46% of 15 μm diameter SiC fibers laid up in two variants. In the first (0° variant), the fibers were oriented unidirectionally, and compression specimen axes were aligned with the fibers. For the second variant, fibers were laid up in 200 μm thick planar bundles, with the fibers in alternating layers at 90° to one another. Specimen axes in this case were either parallel to one set of fibers (0/90), or lay at 45° to both sets (45/45). The matrix, which also was tested, was a polycrystalline lithium–alumino–silicate with grains ranging in size from 0.5 to 2.0 μm. Further microstructural details for both matrix and composite are discussed elsewhere [9–12].

Cylindrical compression specimens (10 mm long × 5 mm diameter) were machined from the as-received composite panels and from the monolithic ceramic matrix bodies. Specimens were tested in air at temperatures ranging from 23 °C to 1100 °C, over a strain rate range of 10^{-4} s^{-1} to $> 10^{3}$ s^{-1}. The latter dynamic rates were obtained by means of a split HPB apparatus. Nickel-based superalloy rings were honed so as to just fit the ends of each composite specimen, to prevent failure by brooming.

Damage introduced during dynamic loading (low-strain-rate damage has been discussed elsewhere [10]) was characterized by optical and scanning electron microscopy of impacted but unfailed specimens. This state was achieved by enclosing the latter within slightly shorter high-strength steel sleeves (Fig. 2). Prior to failure, the composites "flow" as damage accumulates [9, 10]; this process can be arrested at any desired strain level by carefully adjusting sleeve lengths to absorb the load at the appropriate point on the stress–strain curve. The intact, but deformed, specimens thereby obtained can then be sectioned and polished for study.

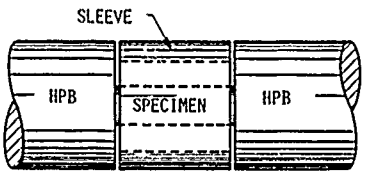

Fig. 2 Schematic of sleeved HPB configuration to permit specimen damage without failure.

3. Results

As shown in Fig. 3, the strength of the composite material is relatively strain-rate independent for $\dot{\varepsilon} \lesssim 10^{2}$ s^{-1}, above which the strength of 0° and 0/90 variants obey

$$\sigma_c \propto \dot{\varepsilon}^{\,0.77} \tag{3}$$

while for the 45/45 material

$$\sigma_c \propto \dot{\varepsilon}^{\,0.3} \tag{4}$$

It should be observed that the relative strength ordering at low strain-rates is preserved within the high-rate regime, and that the strength decrement between 0° and 0/90 variants is essentially constant, *i.e.* $\Delta\sigma_c \simeq 350$ MPa.

For the matrix material alone (Fig. 4), σ_c *vs.* $\dot{\varepsilon}$ is basically constant for temperatures $\leqslant 800$ °C until $\dot{\varepsilon} \approx 10^{3}$ s^{-1}, above which eqn. (4) again holds. Although the strength is quite strain-rate sensitive at 1100 °C, it is interesting to note that at high strain-rates the thermally activated failure process (grain boundary sliding and cavitation, Fig. 5) is defeated. Within this strain-rate regime, pyroceram failure is catastrophic at all temperatures, and brought about by the rapid coalescence of a multitude of microcracks.

It was shown in an earlier paper [10] that at low strain-rates, the composite material fails in compression by matrix microfracture, which accommodates a general fiber buckling process followed by gross failure via localized fiber kinking. This is not what happens at high loading rates. Sections of damaged, but unfailed, sleeved

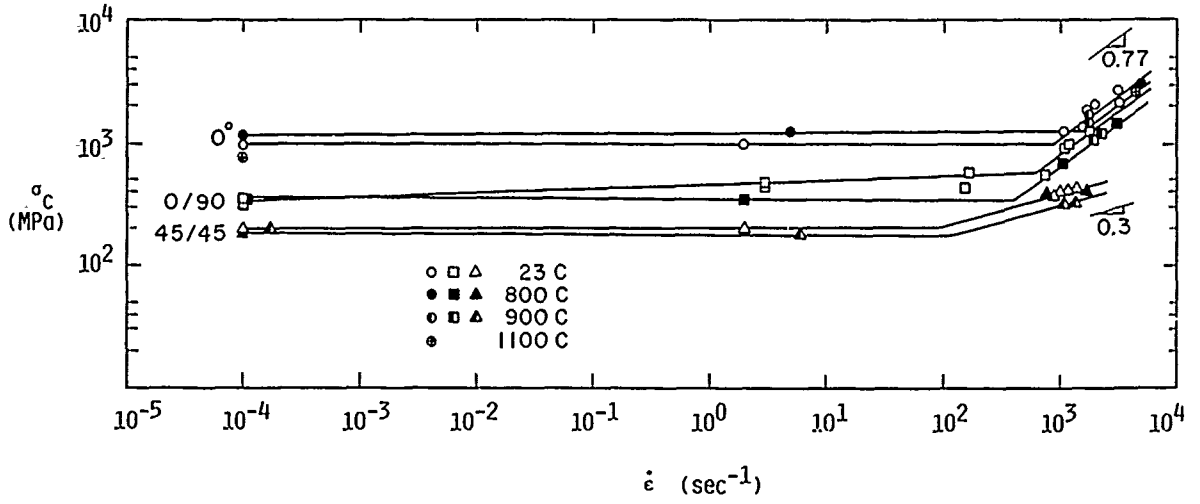

Fig. 3. Compressive strength *vs.* strain rate for SiC fiber-reinforced pyroceram.

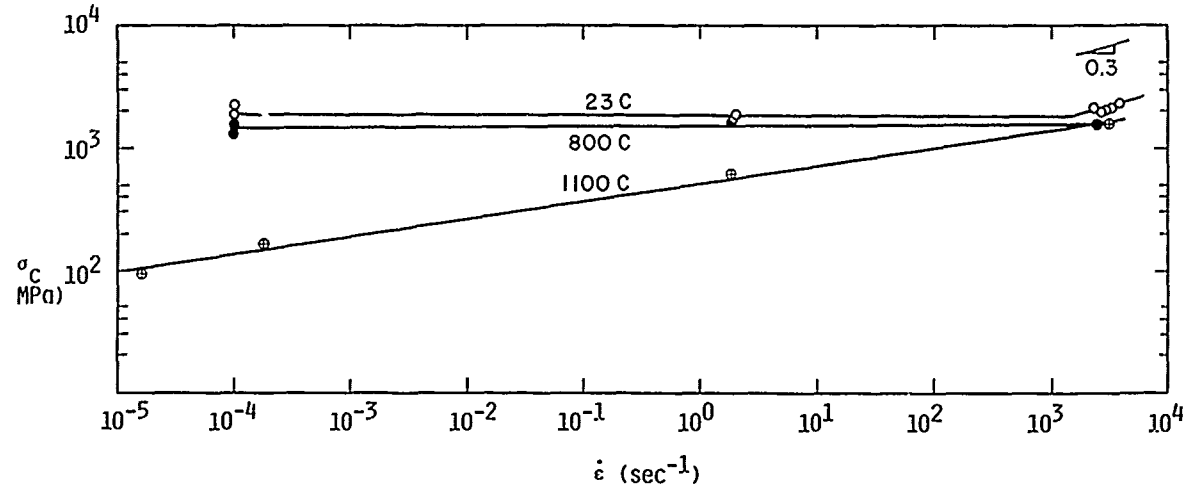

Fig. 4. Compressive strength *vs.* strain rate for pyroceram.

0° and 0/90 HPB specimens reveal no buckling, but instead (Fig. 6) a number of isolated, but macroscopic, shear bands. At least one end (usually both ends) of each such band is associated with a vertical microfracture zone (arrow, Fig. 6); the latter appears to accommodate the intense shear within a given band. Formation of the shear zones occurs at all temperatures studied. Behavior of the 45/45 composite differed in that it simply disintegrated catastrophically, similar to the matrix material itself.

Comparing d and l_0 in Fig. 7, it is evident that kink band shear strains (d/l_0) can easily exceed unity. These are accomplished by the propagation of kinks in SiC fibers (Fig. 8), accompanied by local microfracture and/or matrix flow (arrows, Fig. 9); the latter would require near adiabatic heating. Work is in progress to permit discrimination between these two possibilities.

4. Discussion

The fact that the strengths of the monolithic matrix and the 45/45 composite increase as $\dot{\varepsilon}^{0.3}$ at high loading rates, and that both fail via rapid microcrack coalescence, suggests that inertia-controlled, homogeneous microfracture is responsible for failure. This also suggests that the presence of fibers at other than 0° provides a weakening effect which probably derives from their role as "microanvils", fracturing the matrix at a significantly lower stress than that which

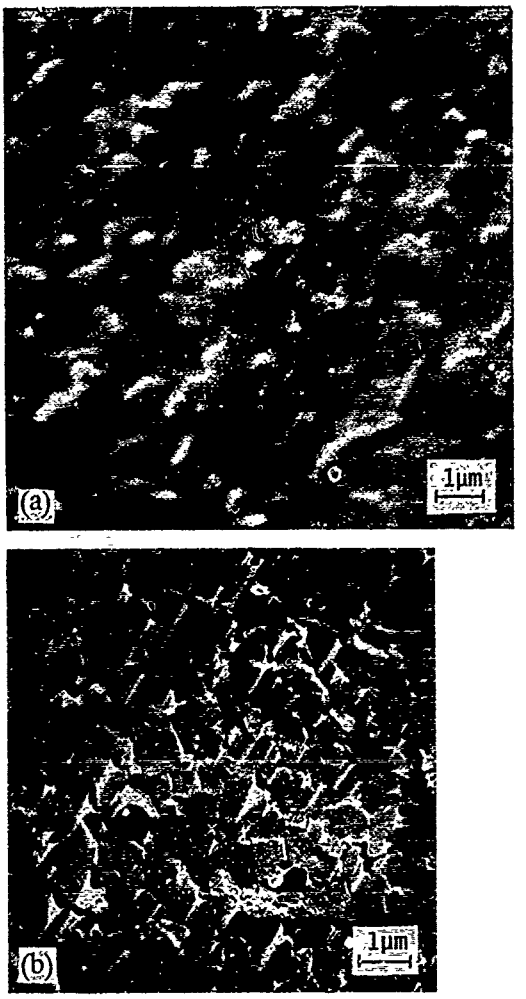

Fig. 5. Deformation mechanisms in pyroceram: $T = 1100$ °C, $\dot{\varepsilon} = 10^{-5}$ s^{-1}. (a) SEM showing grain boundary sliding; (b) TEM surface replica showing cavitation (black dots) caused by grain boundary sliding.

obtains in the pure matrix. It can be shown that this is likely by considering analytically the idealized case of the 0/90 material, in which the 90° fibers form perfect hardness indenters.

Study of sections through such specimens show (Fig. 10) that cracks form between individual fibers as sketched in Fig. 11(a), *i.e.* they follow an arced, non-centerline path. This is reminiscent of the behavior of cone cracks beneath a blunt punch, suggesting that the situation might be idealized as shown in Fig. 11(b). In the vicinity of a round, flat indenter, the maximum tensile stress (which nucleates cone cracks) is approximately

$$\sigma_T^{max} \simeq \frac{P}{\pi a^2}\left(\frac{1-\nu}{2}\right) \tag{5}$$

Fig. 6. Kink band crossing several 0/90 plies: stress axis vertical, $T = 800$ °C, $\dot{\varepsilon} = 2 \times 10^3$ s^{-1}. Arrow indicates zone of microfracture within 90° ply at end of band.

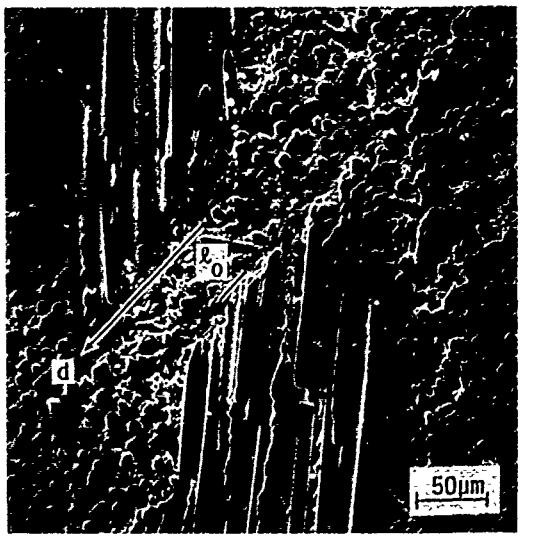

Fig. 7. Kink band in 0/90 composite, showing shear displacement d vs. shear gauge length l_0. $\dot{\varepsilon} = 10^3$ s^{-1}, stress axis vertical.

where P is the applied load, a is the area of contact, and ν is Poisson's ratio. If $a = R/2$ (where R is the fiber radius), and $\nu = 0.25$, then

$$\sigma_T^{max} \simeq 4\sigma(0.375) \tag{6}$$

where σ is the applied compressive stress. Earlier work [1, 13] has shown that microcracking can be

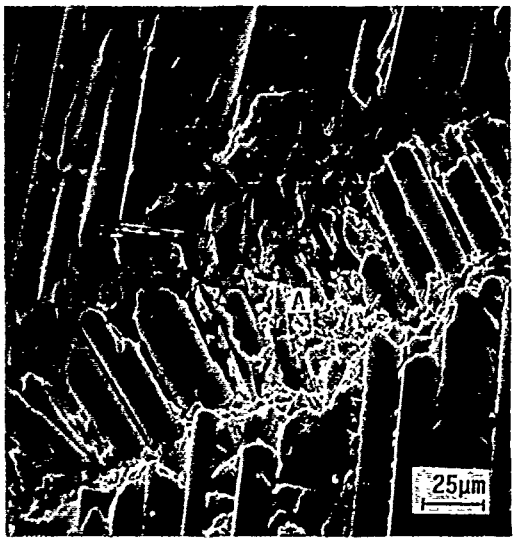

Fig. 8. Kink band in 0/90 composite, showing microfragmentation of matrix to accommodate SiC fiber fracture and rotation: $T = 23$ °C, $\dot{\varepsilon} = 2 \times 10^3\ s^{-1}$, stress axis vertical.

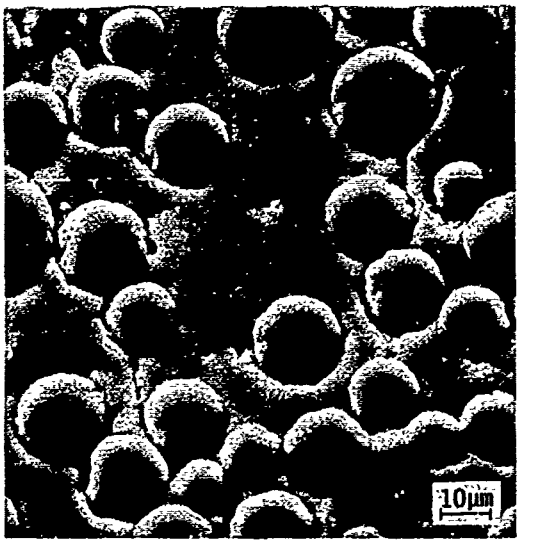

Fig. 10. Section through 90° ply in 0/90 composite, showing non-center-to-center interfiber microfracture. $T = 23$ °C, $\dot{\varepsilon} = 0.6 \times 10^3\ s^{-1}$ stress axis vertical.

Fig. 9. Magnified view of region A in Fig. 8, showing (arrows) possible adiabatic viscous flow in matrix material and SiC fiber; note blunt crack tips in latter, apparent local necking in former.

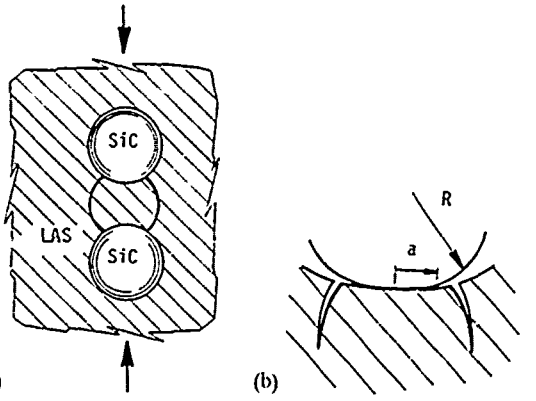

Fig 11 Schematic diagram of matrix microfracture associated with off-axis fibers. (a) non-center-to-center fracture between adjacent fibers, (b) representation of fiber-matrix interaction as punch-cone crack problem.

monitored by acoustic emission, which for 0/90 composites begins when $\sigma = 270$ MPa [13]. From eqn. (6), this means $\sigma_1^{mtx} \simeq 400$ MPa when interfiber matrix microcracking begins, which correlates with the experimentally measured matrix tensile strength, 430 MPa.

The presence of such effective crack initiators in 0/90 material evidently accounts for the persistent difference in strength between 0° and 0/90 composites over the entire strain-rate regime. Further, since the difference exists at high loading rates, tensile microfracture inertia must be included within the observed strain-rate sensitivity for both 0° and 0/90 layups. However, the high-strain-rate specimens actually fail by shear fault nucleation and propagation, the latter can be shown to contribute an additional, significant rate-dependent term.

Specifically, in the most general case, the strain rate at failure is given by

$$\dot{\varepsilon} = \frac{\dot{\sigma}_1}{E} = \frac{\sigma_1}{Et_1} \tag{7}$$

where $\dot{\sigma}_f$ is the compressive stress rate, σ_f is the compressive failure stress, t_f is the time required for failure, and E is the elastic modulus. If failure corresponds only to the propagation of a narrow shear fault, or kink band ($\sigma_f = \sigma_k$), by a characteristic macroscopic dimension l (Fig. 12), then

$$t_f \simeq l/c_s \tag{8}$$

where c_s is the shear velocity. Eliminating t_f yields

$$\sigma_k \simeq \left(\frac{El}{c_s}\right)\dot{\varepsilon} \tag{9}$$

hence

$$\sigma_k \propto \dot{\varepsilon}^{1.0} \tag{10}$$

It should be appreciated that this process cannot take place without local accommodation of the initial 0° kink responsible for shear band formation. Evans and Adler [14], for example, have analyzed the micromechanics of kinking in three-dimensional composites capable of at least some plastic flow. Consideration of their result, which includes a variety of microstructural and material parameters, indicates that the compressive strength depends mainly on the matrix yield strength. In the present instance, the matrix clearly does not yield, but can fragment via local tensile microfracture, and thereby produce a shear instability capable of accommodating a kink by the sliding/rotation of the fragments.

Such accommodation appears to be responsible for the off-fault-plane microfracture attending the ends of the present kink bands (Fig. 6). Since the kink cannot form until the matrix "yields", it is likely that local tensile microfracture precedes dynamic kink formation. This is in accordance with the earlier suggestions that a differing microfracture threshold is responsible for the observed constant (strain-rate independent) difference between 0° and 0/90 compressive strengths.

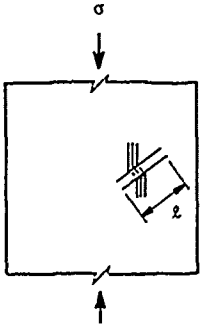

Fig. 12. Schematic diagram of kink band propagation over a macroscopic dimension l.

Accommodation by local microfracture would imply, of course, a cube-root strain-rate contribution to the composite dynamic compressive strength, in addition to the first power factor (eqn. (9)) derived for kink propagation. Unfortunately, it is not as straightforward to produce an equivalent expression for the inertial microcrack term, since modeling to date has dealt only with tensile external loading. For example, for impulsive tensile loading of a penny-shaped crack, Kipp *et al.* [15] have shown that

$$\sigma_f = \left(\frac{9\pi E K_{Ic}^2}{16 N^2 c_s}\right)^{1/3} \dot{\varepsilon}^{1/3} \tag{11}$$

where K_{Ic} is the fracture toughness and N is a crack geometry term. However, while the same strain-rate dependence should obtain for compressive loading, the correct form of coefficient for compression is unknown. That is, the magnitude of the failure stress must reflect the resolution of an applied compressive field into local tensile enclaves due to factors such as geometric flaws (pores, microcracks), intrinsic flaws (twins, dislocations), and elastic compliance mismatch across grain boundaries. Since no such analogue to eqn. (11) is available, the accommodation (via inertial microcracking) contribution to the dynamic kink process cannot be estimated directly.

Accordingly, the composite compressive strength under impulsive loading can be written as

$$\sigma_c = \sigma_0 + \left(\frac{El}{c_s}\right)\dot{\varepsilon} + A\left(\frac{9\pi E K_{Ic}^2}{16 N^2 c_s}\right)^{1/3} \dot{\varepsilon}^{1/3} \tag{12}$$

where σ_0 represents the approximately constant, thermally activated, quasistatic compressive strength, and A is a constant greater than unity representing the resolution (compressive to tensile) and amplification of the applied stress during kink accommodation. For present purposes, let us consider the case of the 0° composite, for which $\sigma_0 \simeq 950$ MPa, $E = 131$ GPa, $c_s = 7.24 \times 10^3$ m s^{-1}, and l is assumed to be approximately 8.5 mm. Figure 13 compares experimental results (average for $T = 23$ °C to 1100 °C) with the first two terms in eqn. (12).

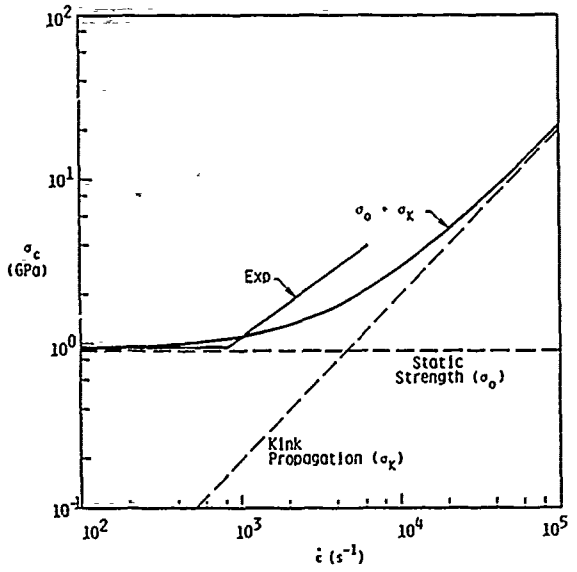

Fig. 13. Experimental *vs.* theoretical (static plus kink propagation) dynamic strength for 0° composite. Addition of inertial kink accommodation term would raise the theoretical curve.

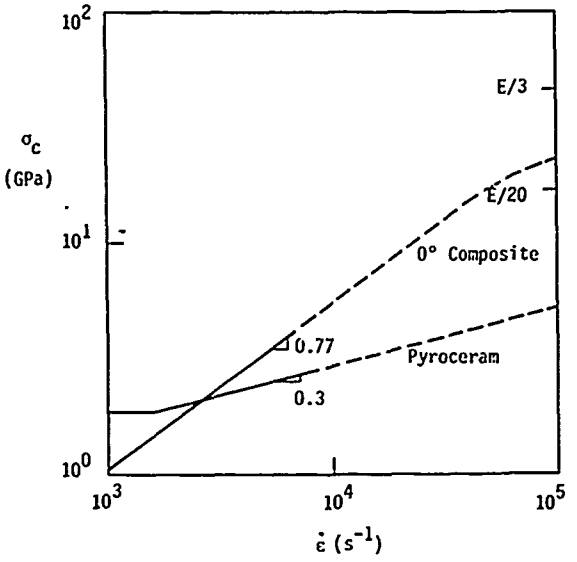

Fig. 14. Extrapolation of composite and pyroceramic dynamic strengths to $\dot{\varepsilon} = 10^5\ s^{-1}$, compared with theoretical ultimate strength.

Agreement seems reasonable, especially considering that, if A were known, inclusion of the inertial kink accommodation term would shift the theoretical curve upward, closer to the experimental results.

It is interesting to compare the behavior of the composite material with its monolithic ceramic matrix, as shown in Fig. 14. Although the former is weaker than the latter for strain-rates less than about $10^3\ s^{-1}$, the situation is reversed once the powerful strain-rate strengthening of the composite begins to dominate the inertial (cube-root) rate hardening of the monolithic material. Extrapolation of this effect, which is a direct result of the time-dependent complexity of the composite failure process, predicts that the reinforced material will achieve its maximum theoretical strength ($E/20$ to $E/3$) at the relatively modest strain rate of about $10^5\ s^{-1}$, while the pyroceram will not reach the same value until $\dot{\varepsilon} \simeq 10^8\ s^{-1}$. This result clearly has interesting implications for practical situations (armor, shock loading). In addition, it is relevant to wonder whether similar complexity in failure, with its associated strain-rate strengthening might be engendered via high-aspect-ratio whisker, versus continuous fiber, reinforcement. That is, it seems likely that composites containing a fairly high density of such fibers, preferentially oriented and extensively overlapping, would also experience kink nucleation and propagation during dynamic loading/failure.

Finally, it should be noted that the macroscopic dynamic strain rates used to correlate the present results do not represent the true state of affairs obtaining within the local kink bands. While macroscopic strains at failure were on the order of 0.01, it will be recalled that strains within discrete shear bands were on the order of 1.0. Accordingly, actual strain rates within these regions must have been well in excess of $10^5\ s^{-1}$; it therefore would not be surprising for the flow process within such a fast deformation field to be adiabatic. This would be in accordance with some of the viscous-like features noted within the kink bands (*i.e.* Fig. 9), and would suggest that matrix flow was beginning to compete with microfracture.

Factors involved in the strain-rate dependence of fiber-reinforced, ceramic matrix composites are summarized schematically in Fig. 15. While the thermally activated and plastic flow plateaus are relatively flat, the transition regime $10^2\ s^{-1} \leqslant \dot{\varepsilon} \leqslant 10^6\ s^{-1}$ is extremely strain-rate sensitive. Both the strain-rate hardening within, and the threshold (minimum $\dot{\varepsilon}$) for, this regime are amenable to optimization by means of composite microstructural modification.

5. Conclusions

It has been shown that compressive strain-rate hardening well in excess of the cube-root theoretical maximum for brittle materials can be

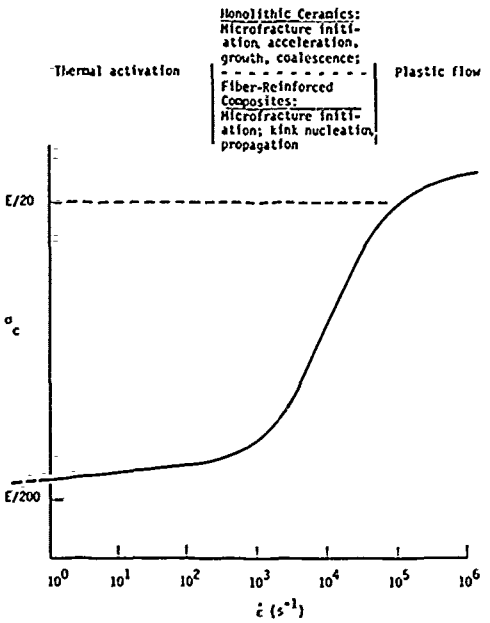

Fig. 15. Schematic representation of damage-strain-rate regimes in ceramics and fiber-reinforced ceramic matrix composites.

achieved, if the failure mechanism can be made sufficiently complex. In particular, fiber reinforcement in the direction of the compression axis necessitates a combined failure mode involving inertia-controlled microcrack accommodation of heterogeneous kink band nucleation, followed by rate-dependent kink propagation. The latter involves very high local strain-rates, so high, in fact, that local heating may be involved in the shear process. The results suggest that a high density of preferentially-oriented, high-aspect-ratio whiskers might provide similar strain-rate strengthening benefits.

Acknowledgments

The support of the Office of Naval Research through Contract No. N00014-84-C-0213 is gratefully acknowledged. In addition, the author appeciates the careful experimental work of Mr. A. Nicholls, and the kind provision of Compglas material by Dr. C. Prewo of United Technologies Research Center.

References

1 J. Lankford, *Fracture Mechanics of Ceramics*, Vol. 5, 1983, pp. 625–637.
2 D. Grady and R. E. Hollenbach, *Geophys. Res. Lett., 6* (1979) 76–76.
3 D. E. Grady and M. E. Kipp, *Int. J. Rock Mech. Min. Sci., 16* (1979) 293.
4 S. J. Green and R. D. Perkins, in K. E. Gray (ed.), *Proc. 10th Symp. on Rock Mechanics*, Am. Inst. of Mining, Metallurgical, and Petroleum Engrs., Austin, TX, 1968.
5 J. Lankford, *J. Am. Ceram. Soc., 65* [18] (1982) C-122.
6 D. L. Birkimer, in K. E. Gray (ed.), *Proc. 12th Symp. on Rock Mechanics*, Am. Inst. of Mining, Metallurgical, and Petroleum Engrs., Austin, TX, 1971.
7 M. J. Forrestal, D. E. Grady and K. W. Schuler, *Int. J. Rock Mech. Min. Sci., 15* (1978) 263–265.
8 D. E. Grady and J. Lipkin, *Geophys. Res. Lett., 7* (1980) 255.
9 J. Lankford, *Composites, 18* [2] (1987) 145–152.
10 J. Lankford, in W. C. Harrigan, J. Strife and A. K. Dhingra (eds.), *Proc. 5th Int. Conf. on Composite Materials (ICCMV)*, TMS-AIME, Warrendale, PA, 1985.
11 K. M. Prewo, *ONR Techn. Rep.*, Contract No. N00014-81-C-0571, 1983.
12 J. J. Brennan, *ONR Techn. Rep.*, Contract No. N00014-82-C-0096, 1984.
13 J. Lankford, *Ceram. Eng. Sci. Proc., 9* (1988) in press.
14 A. G. Evans and W. F. Adler, *Acta Metall., 26* (1978) 725.
15 M. E. Kipp, D. E. Grady and E. P. Chen, *Int. J. Fract., 16* [4] (1980) 471–478.

Behavior of Interface in Alumina/Glass Composite*

ABHAY MAHESHWARI, K. K. CHAWLA

Department of Materials and Metallurgical Engineering, New Mexico Institute of Mining and Technology, Socorro, New Mexico 87801 (U.S.A.)

T. A. MICHALSKE

Sandia National Laboratories, Albuquerque, NM 87185 (U.S.A.)

(Received June 1, 1988)

Abstract

Alumina/glass and alumina/SnO_2/glass laminate composites were prepared and microstructurally characterized by means of scanning electron microscope and electron microprobe. Diffusion profiles obtained by an electron microprobe indicated very little diffusion of tin in the glass region and almost undetectable diffusion of tin in the alumina region. The crack propagation behavior through the interface was studied in the two cases. It was observed that the cracks from the indentations were arrested in the SnO_2 layer and at times got deflected along the alumina/SnO_2 interface. In uncoated samples of alumina/glass the cracks propagated right across the interface unhindered, indicating strong bonding at the interface. Also, the lengths of the cracks produced in the Al_2O_3/glass composites were greater than those produced in Al_2O_3/SnO_2/glass composites. The SnO_2 coating showed the desired crack arresting features.

1. Introduction

Carbon fiber and SiC fiber reinforced glasses and glass ceramics show extensive fiber pullout before fracture [1–3]. The primary reason for this is the rather low value of interfacial bond strength between the fiber and the matrix. The cracks which travel perpendicular to the interface get deflected at the interfacial region and become parallel to the interface. Chemical bonding and mechanical keying are the two main bonding types which are responsible for fiber/matrix interface strength [4]. From the fracture surfaces of such composites it seems that the wettability is rather low and the bond strength is controlled mainly by mechanical keying. The energy expended in fiber matrix debonding leading to fiber pullout causes an increase in toughness or work of fracture of such composite materials [1, 4]. However, the high temperature oxidation of carbon fibers and SiC fibers limit the application of such composites. Alumina fiber reinforced glass was shown to be unaffected by exposure to temperatures up to 1000 °C [5]. However, the alumina/glass system is extremely brittle because of the strong interfacial bonding between the fiber and the matrix. An earlier study [6] has indicated that the diffusion coefficient of alumina in glass is high enough to cause fiber dissolution and strong diffusion bonding. This results in cracks propagating right through the material unhindered, causing a brittle failure. Such a composite does not show any evidence of fiber pullout (Fig. 1) [7].

One way to enhance fiber pullout is to provide a stable interfacial coating between the fiber and the matrix which can act as a diffusion barrier layer at the high temperatures of application. Apart from the properties described above, the coating should also help deflect or arrest the cracks and thereby increase the fracture toughness of the material [8]. One such coating for the system alumina/glass is SnO_2, which is the subject of investigation in this work. The phase equilibrium diagram of alumina/SnO_2, Fig. 2, shows no solid solubility between alumina and SnO_2 [9]. As a result of this thermodynamic stability, no diffusion bonding is expected at the interface Al_2O_3/SnO_2. It has also been indicated by Manfredo and McNally [10] that SnO_2 has very low solubility in silicate melts. The solubility studies of SnO_2 in a soda lime glass, Fig. 3, show less than 0.05 mole fraction solubility of this oxide even at

*Paper presented at the symposium on Interfacial Phenomena in Composites: Processing, Characterization, and Mechanical Properties, Newport, RI, June 1–3, 1988.

0921-5093/89/$3.50

© Elsevier Sequoia/Printed in The Netherlands

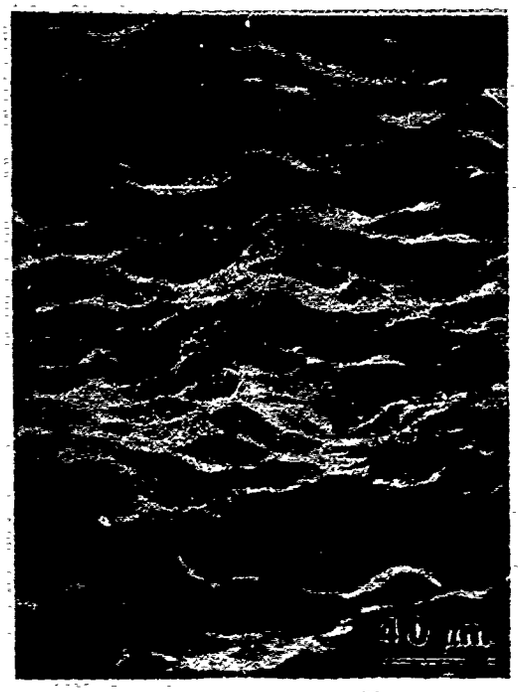

Fig. 1. Fracture surface of an alumina fiber reinforced glass matrix showing no fiber pullout [7].

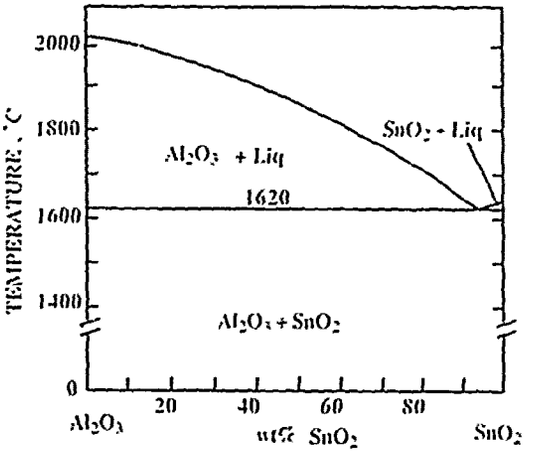

Fig. 2. Equilibrium phase diagram of system Al_2O_3/SnO_2. Note the zero solid solubility between the two components [9].

temperatures as high as 1300°C [10]. Hence, the interface SnO_2/glass is expected to be stable at high temperatures. Apart from the advantages described above, the inherent high thermal stability of this oxide and its relative ease of coating procedure makes it an ideal diffusion barrier layer for the system alumina/glass.

The intent of this work is to study the chemical stability, microstructure and mechanical properties of simple alumina/SnO_2/glass interfaces.

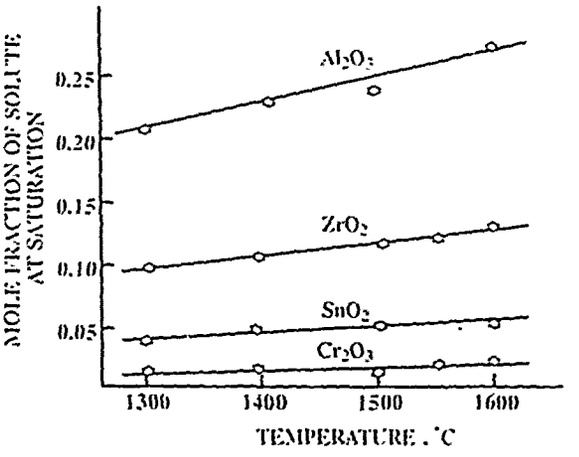

Fig. 3. Comparative solubility of different oxides in a soda-lime glass [10].

TABLE 1 Relevant physical properties of alumina [11]

Phase	$\alpha - Al_2O_3$
Thermal expansion coefficient (K^{-1})	7.4×10^{-6}
Young's modulus (GPa)	390

2. Materials and experimental procedure

Among the materials used for the experimental purpose alumina was obtained from the Coors Porcelain Co. The relevant properties of this alumina is shown in Table 1 [11]. The glass used for the experiment was a borosilicate glass from the Owens Illinois Co. commercially known as N51A. The approximate chemical composition and relevant physical properties are shown in Table 2. The laboratory grade reagent $SnCl_4$ for SnO_2 coating was obtained from Fisher Scientific.

Alumina substrates approximately 1 cm^2 in area and 0.7 mm in thickness were used for making composite laminates of the coated and uncoated variety. These substrates were polished to 600 grit SiC paper and then thoroughly cleaned prior to coating or bonding to the glass.

The tin dioxide coating was deposited in an alumina reactor at temperatures about 750°C. The reagents used were $SnCl_4$, oxygen gas and water vapor. The experimental set up for substrate coating is shown in Fig. 4. The flow rate of oxygen was regulated to 0.5 l min^{-1} which in turn controlled the flow of $SnCl_4$ vapor to the reaction chamber. The X-ray diffraction pattern obtained from the coated interface (see Fig. 5) showed the coating to be primarily SnO_2.

TABLE 2 Nominal chemical composition and physical properties of N51A glass (provided by the manufacturer, Owens, Illinois Inc.)

Composition of N51A glass		*Physical properties*	
Oxide	*wt.%*		
SiO_2	72	Softening point	785°C
B_2O_3	12	Contraction coefficient ($°C^{-1}$)	7×10^{-6}
Al_2O_3	7	(Annealing point to 25°C)	
CaO	1	Young's modulus (GPa)	71.7
Na_2O	6		
K_2O	2		
BaO	<0.1		

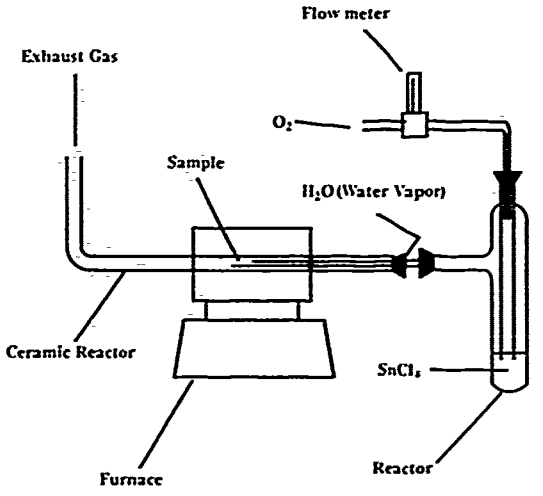

Fig. 4. Experimental set-up for coating of tin dioxide on alumina substrate.

The coated alumina substrates were bonded to N51A glass at temperatures of 850, 900, 950 and 1000°C for 1 h each. The bonded specimens were allowed to cool slowly in the furnace to avoid any cracking. Uncoated samples were also given a similar treatment and the laminates thus produced, Fig. 6, were mounted and polished across the interface for microstructural and other characterization studies.

The diffusion of species across the interface was studied by means of an electron microprobe analyzer. A finely focused beam was used and X-ray data were collected at 2 μm intervals across the tin dioxide interface. The Sn diffusion profiles obtained across the interface for the samples bonded at 850, 900, 950 and 1000°C were analyzed to obtain the diffusion coefficient of tin as a function of temperature. The standards

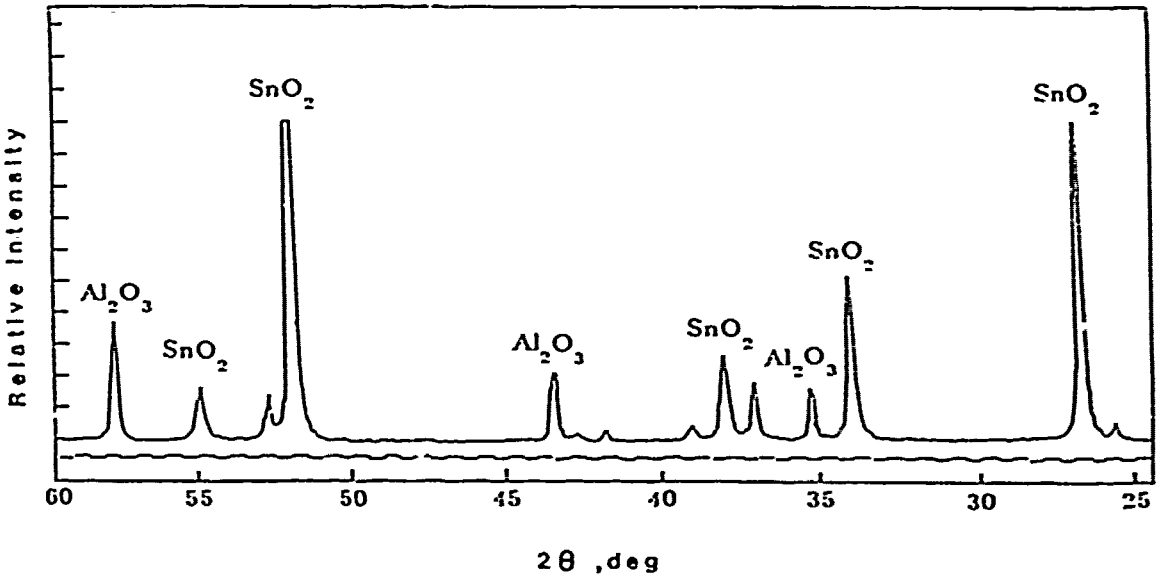

Fig. 5. X-ray diffraction pattern from the coated alumina substrate showing the deposit to be primarily SnO_2.

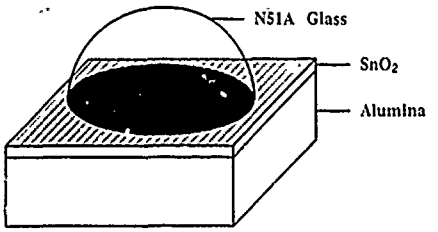

Fig. 6. Schematic of a coated composite sample showing the various components.

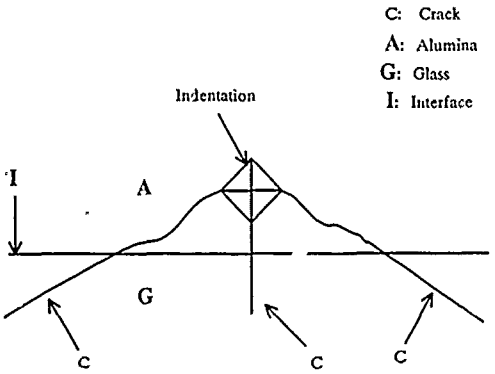

Fig. 7. Schematic of the indentation cracks produced from the tips of the indentations near the alumina side of the interface.

used to calibrate these measurements were the pure samples of alumina, glass and tin dioxide.

The microhardness of the three components of the composite was measured by a diamond pyramid Vicker's microindenter. The load on the indenter was just enough to accommodate the indentations within the thin interphase layer.

To study the behavior of the response of the interface to propagating cracks, a Vickers diamond indenter was used to make indentations in the alumina as well as the glass region of the uncoated and the coated samples. During the indentation procedure the diamond indenter diagonals were kept at approximately 90° to the interface. The schematic of the cracks produced from the tips of these indentations is shown in Fig. 7. A scanning electron microscope was used in the backscattered electron mode to highlight these cracks in the coated as well as in the uncoated samples.

3. Results and discussion

The coatings produced at 750°C substrate temperature for 30 min and 1 h are shown in Figs. 8(a) and 8(b). Note that all of the substrate

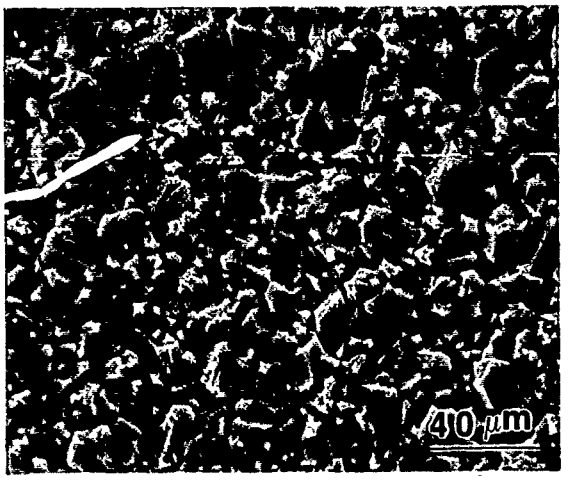

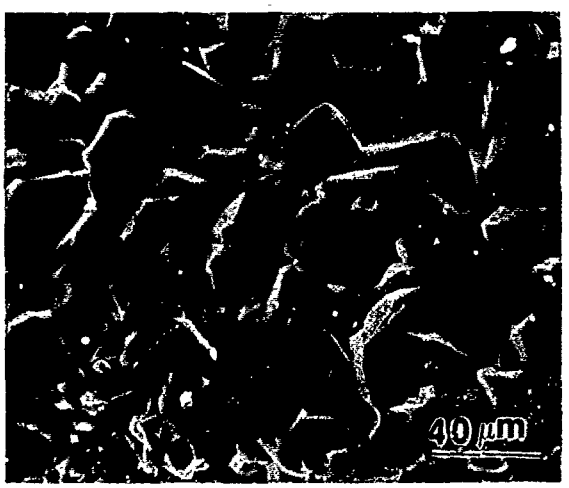

Fig. 8. (a) Alumina substrate coated with SnO_2 at 750°C for 30 min (SEM). Note that the SnO_2 crystals have covered all the exposed surface of the substrate. (b) Alumina substrate coated with SnO_2 at 750°C for 1 h (SEM). Note the varied size distribution of the SnO_2 crystals.

area was covered in 30 min (Fig. 8a). After 1 h, Fig. 8(b), a varied distribution of the crystals was obtained, giving a non-uniform thickness of the coating on the substrate.

Electron microprobe profiles for the composite samples coated with SnO_2 at the interface region at 800°C for 1 h and bonded at temperatures of 850, 900, 950 and 1000°C were obtained to compute the diffusion coefficient of tin into the alumina and the glass region. As predicted by the phase equilibria of SnO_2 and alumina, almost no tin diffusion into Al_2O_3 was noticed from the profiles. Figure 9 shows one such diffusion profile obtained for a sample bonded at 1000°C to N51A glass. Note the flat region on the top of the profile showing the maximum level of concentration of tin in pure tin diox-

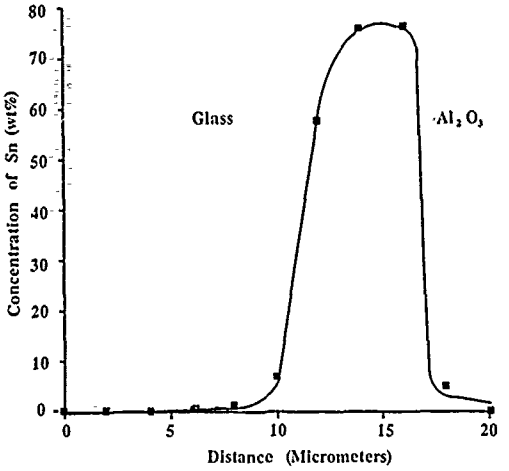

Fig. 9. Tin diffusion profile for coated sample bonded at 1000°C.

TABLE 3 Diffusivity of tin in glass at different temperatures of bonding

Temperature of bonding (°C)	*Time* (h)	*Diffusivity of tin in glass* ($cm^2\ s^{-1}$)
900	1	2×10^{-12}
950	1	5×10^{-12}
1000	1	8×10^{-12}

ide. The very steep slope of the concentration versus distance curve in the alumina side indicates almost no diffusion in the alumina region. The slope in the glass side over the small diffusion distance indicates very little diffusion of tin in the glass region. Diffusion profiles were also obtained for samples bonded at 850, 900 and 950°C. The Matano interface was calculated from these profiles and then a simple Grube's analysis with an error function analytical solution [12] was used to obtain the average chemical diffusivity of tin in the glass. The assumption here is that there is no impingement of the diffusion profiles from the glass and the alumina sides of the SnO_2 interphase layer.

As expected, the microprobe data confirm the absence of tin diffusion into Al_2O_3 and rather small diffusion of tin into glass. The average chemical diffusivity values calculated from the diffusion profiles are given in Table 3. The Arrhenius plot of these diffusivity values, Fig. 10, gives a value of 167 kJ $mole^{-1}$ for the activation energy for diffusion of tin into glass. Taylor *et al.* [13] found an activation energy value of 880 kJ $mole^{-1}$ for diffusion of tin into an aluminosilicate glass. In

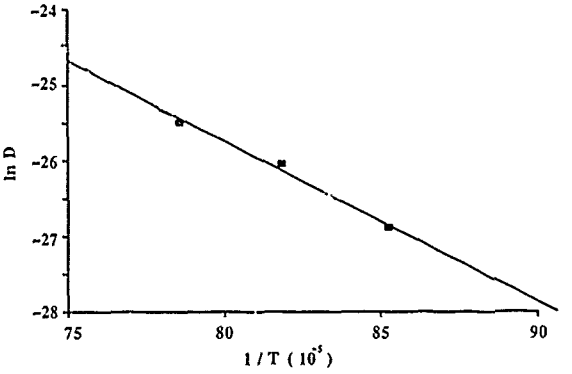

Fig. 10. Arrhenius plot for the diffusion coefficients of tin in glass at 900, 950 and 1000°C.

TABLE 4 Vickers microhardness of SnO_2, Al_2O_3 and N51A glass

Material	*Indenter load* (gf)	*VHN*
Al_2O_3	500	1729
SnO_2	200	1134
Glass	200	631

another study, Eremenko *et al.* [14] reported an activation energy value of 120 kJ $mole^{-1}$ for tin diffusion into a soda lime glass.

The microhardness values shown in Table 4 indicate that the SnO_2 interphase layer is relatively more plastic than alumina. The glass is the softest material among the three.

Indentation cracking is a commonly used method for measuring the toughness of a brittle material. In brittle materials the crack tip plastic zone is very small compared to the crack length; therefore, elastic calculations can be used for studying the crack propagation and strength parameters of these materials [15]. However, it should be admitted that the stress-strain conditions prevailing in an indentation test are difficult to determine unequivocally because of any residual stresses and/or proximity of the interface. The indentation technique can be used as an effective qualitative tool. The indentation induced cracks from the tips of the indentations near the interface in the alumina region propagated asymmetrically toward the interface. The modulus mismatch between the two materials at the interface causes the stress intensity at the crack tip near the interface to be higher, forcing the cracks to change their direction of propagation and veer toward the interface [15]. The

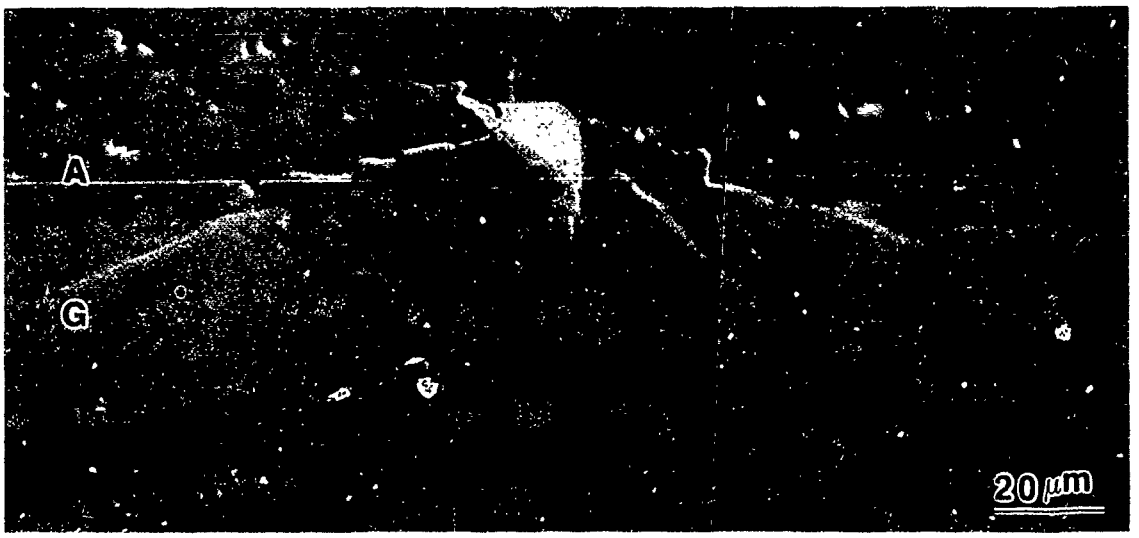

Fig 11 Indentation induced cracks at the interface region of an uncoated alumina/glass sample bonded at 950 °C. Note the cracks emanating from the tips of the indentation travelling unhindered in the glass.

cracks emanating from the indentation tips in the alumina region of an uncoated sample, Fig. 11, have traveled toward the interface and then crossed the alumina/glass interface unhindered into the glass region. The reason for such an efficient crack extension is the very strong bonding between the alumina and the glass that results from alumina diffusing very easily in the glass matrix [7] at the temperatures of composite fabrication. In Fig. 11 we also see that cracks propagating from the alumina to the glass region showed no change in direction upon crossing the interface. For the samples coated with SnO_2 (*i.e.* now we have two interfaces: Al_2O_3/SnO_2 and SnO_2/glass), the cracks from the indentations in the alumina side traveled toward the Al_2O_3/SnO_2 interface and then either deflected along the Al_2O_3/SnO_2 interface or were arrested in the interphase SnO_2. Figure 12 is a scanning electron micrograph of a sample coated at a substrate temperature of 800 °C, bonded to N51A glass at 950 °C and then indented near the interface in the alumina region. The coating thickness is approximately 10 μm. The cracks emanating from the tips of the indentation traveled toward the interface and were deflected at the Al_2O_3/SnO_2 interface. Crack branching along the interface region can be seen in the high magnification micrographs (A and B in Fig. 12). Figure 13 is a scanning electron micrograph of a sample coated at a substrate temperature of 750 °C for 1 h. The cracks emanating from the tips of the indentation have entered the interphase region and have died out after extending for some distance. The reason for such a behavior of the propagating crack may be due to the higher plasticity of the SnO_2 interphase.

It is also of interest to compare the crack lengths at the interface region in the coated sample with those obtained in an uncoated sample. The unhindered cracks in the uncoated samples are extremely long compared to those obtained in the coated samples, showing that the SnO_2 interphase increases the crack propagation resistance of this alumina/glass system.

Although we were not able to find data for the detailed mechanical and physical nature of SnO_2, the suitability of the material for the system alumina/glass is well demonstrated in this study. Thermodynamically, the coating material is extremely stable with alumina and we do not expect any diffusion bonding at the alumina/tin dioxide interface. The only other mode of bonding between the two materials can be a mechanical bonding. Hence, this interface can be treated as a contact interface. Mechanical response of such contact interface to transverse loading has been studied extensively and their stress analysis has been well developed [15]. The failure of such contact depends upon the material properties and the contact geometry. The fracture initiation stress threshold at the contact can be increased by making the coefficient of friction at the contact smaller by the use of a finely polished interface

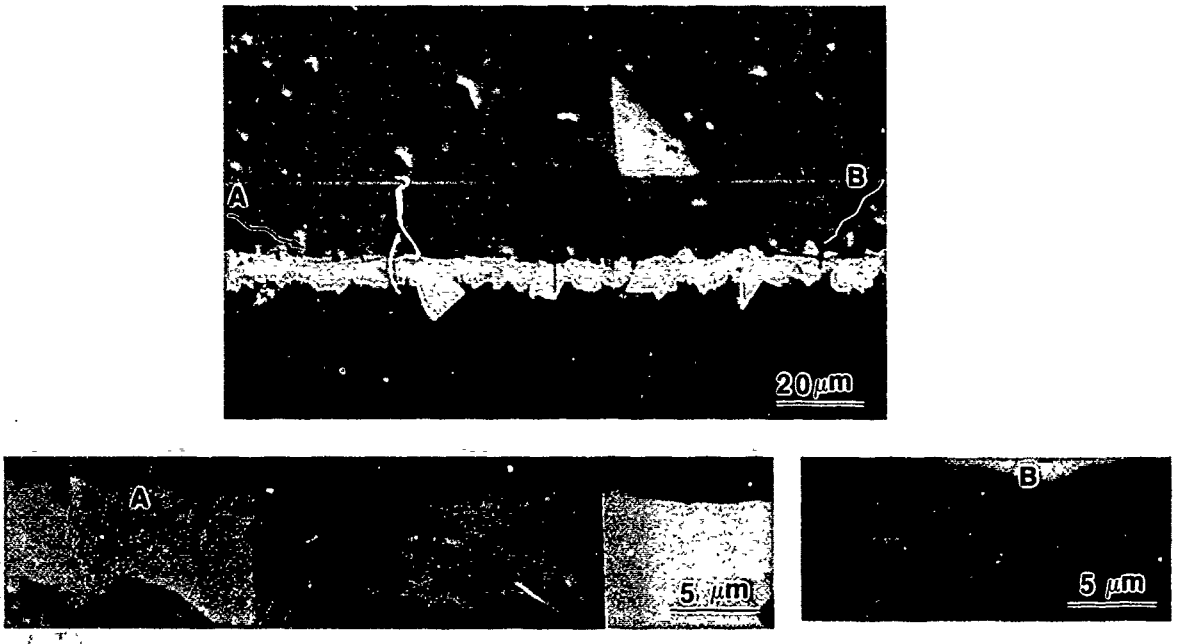

Fig. 12. Coated composite sample indented at the alumina region near the interface (SEM). Note that the cracks have changed their direction and have caused failure of the Al_2O_3/SnO_2 interface. The crack branching phenomenon can be seen in the higher magnification micrographs.

Fig 13. Coated composite sample indented in the alumina region near the interface (SEM). Note that the cracks have extended into the SnO_2 interphase for a small distance before dying out. A, I and G indicate alumina, interphase, and glass, respectively.

[15, 16]. In the future it will be interesting to explore the coefficient of friction between SnO_2 and alumina.

4. Conclusions

From the results and discussions presented in this study we can conclude that the incorporation of SnO_2 diffusion barrier layer is an effective way of creating a weak interfacial bond between the components of alumina/glass composite. SnO_2 is very suitable for the system alumina and glass because of its inherent refractory properties, ease of handling and coating procedure, lack of diffusion bonding between the alumina and the SnO_2 interphase layer, and very small solubility of

SnO_2 in silicate glass. The bond between the alumina and the interphase tin dioxide is weak. The interface layer is quite efficient as a crack arrestor and deflector thereby indicating the potential of obtaining enhanced fracture toughness in alumina/glass composite.

Acknowledgments

Financial support for this work was provided by a grant from the Sandia National Laboratories. We acknowledge useful discussions with Dr. A. D. Romig, Jr., of Sandia National Laboratories, Dr. A. K. Vasudevan of Alcoa Laboratories and J. L. Keddie during the course of this work. Special thanks are due to G. Gray of Alcoa Laboratories for the electron microprobe work.

References

1 J. J. Brennan and K. M. Prewo, *J. Mater. Sci., 17* (1982) 2371.
2 D. C. Phillips, *J. Mater. Sci., 9* (1974) 1847.
3 R. Levitt, *J. Mater. Sci., 8* (1973) 793.
4 K K. Chawla, *Composite Materials. Science and Engineering*, Springer, New York, 1987, pp. 83, 144.
5 J. Bacon, K. Prewo and R. Veltri, *Proc. 1978 Int. Conf. on Composite Materials*, Toronto, AIME, 1978, p. 753.
6 J. L. Keddie and T. A. Michalske, Sandia Report, SAND 87-1884.UC-25, Jan. 1988.
7 T. A. Michalske and J. Hellman, *J. Am. Ceram. Soc., 71* (1988) 725.
8 K. M. Prewo, J. J. Brennan and G. K. Layden, *Ceram. Bull. 65* (1986) 363.
9 V. J. Barczak and R. H. Insley, *J. Am. Ceram Soc., 45* (1962) 144.
10 L. J. Manfredo and R. N. McNally, *J. Am. Ceram. Soc., 67* (1984) C-155.
11 R. N Kleiner, in C. T. Lynch (ed.), *Handbook of Materials Science*, CRC Press, Cleveland, OH, 1975, p. 355.
12 P.G. Shewmon, *Diffusion in Solids*, J. Williams Book Co., Jenks, OK, 1983.
13 R. H. Taylor, J. Robertson, S. B. Morris, J. Williamson and A. Atkinson, *J. Mater. Sci., 15* (1980) 670.
14 V. N. Eremenko, V. M. Sergenkova, V. E. Listounichy and A. V. Murzin, *Dopov. Akad. Nauk. Ukrain RSR, A6* (1975) 560, as cited in Ref. [14].
15 S. Chiang and A. G. Evans, *J. Am. Ceram. Soc., 64* (1983) 4.
16 A. G. Evans, M. C. Lu, S. Schmander and M. Ruhle, *Acta Metall., 34* (1986) 1643.

Author Index

Angelini, P., 257
Aravas, N., 159
Argon, A. S., 41
Asaro, R. J., 145

Bassani, J. L., 177
Becher, P. F., 257
Bose, A., 107

Carpenter, R. W., 207
Chawla, K. K., 269
Christman, T., 49
Cornie, J. A., 41

Embury, J. D., 63
Evans, A. G., 187

German, R. M., 107
Gupta, V., 41

Haggerty, J. S., 117
Hsueh, C. H., 257
Hunt, Jr., W. H., 241
Hutchinson, J. W., 135

Kao, W. H., 81
Kim, K.-S., 159
Konitzer, D. G., 217

Lagace, H., 73
Lambropoulos, J. C., 169
Landis, H. S., 41
Lankford, J., 261
Lewandowski, J. J., 241
Liu, C., 241
Liu, C. T., 81
Lloyd, D. J., 73
Loretto, M. H., 217
Loukis, M. J., 159

Maheshwari, A., 269
McKimpson, M. G., 93
McLeod, A., 73
Michalske, T. A., 269
Morris, P. L., 73

Needleman, A., 49
Nguygen, T., 15
Nutt, S., 49

Penisson, J. M., 199
Phillpot, S., 3
Porter, J. R., 127

Qu, J., 177

Regheere, G., 199
Rice, J. R., 23
Richmond, O., 63
Rühle, M., 187

Scott, T. E., 93
Shih, C. F., 145
Suo, Z., 135
Suresh, S., 49

Tiegs, T. N., 257

Vasudevan, A. K., 63

Wan, S.-M., 169
Wang, J.-S., 23
Wolf, D., 3

Yang, J.-M., 81
Yip, S., 15

Zok, F., 63

© Elsevier Sequoia/Printed in The Netherlands

Subject Index

Adhesion
mechanics of adhesion testing of flexible films, 159
Alloys
characterization of internal interfaces in metals and alloys by high resolution electron microscopy, 199
Aluminium
behavior of interface in alumina/glass composite, 269
development of nickel aluminide matrix composites, 81
effects of matrix microstructure and particle distribution on fracture of an aluminum metal matrix composite, 241
influence of hydrostatic pressure on the ductility of Al–SiC composites, 63
microstructural aspects of aluminium–silicon carbon particulate composites produced by a casting method, 73

Bicrystal
elasticity solutions for cracks on bimaterial and bicrystal interfaces, 177
molecular dynamics study of a bicrystal at elevated temperatures, 15
Bimaterial
elasticity solutions for cracks on bimaterial and bicrystal interfaces, 177
elastic–plastic analysis of a collinear array of cracks on a bimaterial interface, 145

Carbon
influence of hydrostatic pressure on the ductility of Al–SiC composites, 63
microstructural aspects of aluminium–silicon carbon particulate composites produced by a casting method, 73
Computer simulation
role of the densest lattice planes in the stability of crystalline interfaces: a computer simulation study, 3
Creep
dispersion processing of creep resistant whisker-reinforced ceramic-matrix composites, 127
Crystals
role of the densest lattice planes in the stability of crystalline interfaces: a computer simulation study, 3

Deformation
on microstructural evolution and micromechanical modelling of deformation of a whisker-reinforced metal–matrix composite, 49
Dispersion
dispersion processing of creep resistant whisker-reinforced ceramic-matrix composites, 127
Ductility
influence of hydrostatic pressure on the ductility of Al–SiC composites, 63

Embrittlement
embrittlement of interfaces by solute segregation, 23

Fabrication
fabrication of intermetallic matrix composites, 107
Fracture
dynamic compressive fracture in fiber-reinforced ceramic matrix composites, 261
effects of matrix microstructure and particle distribution on fracture of an aluminum metal matrix composite, 241

Glass
behavior of interface in alumina/glass composite, 269

High resolution electron microscopy
characterization of internal interfaces in metals and alloys by high resolution electron microscopy, 199
high resolution interface analysis, 207

Lattice planes
role of the densest lattice planes in the stability of crystalline interfaces: a computer simulation study, 3

Mechanics
mechanical performance of fiber-reinforced ceramic matrix composites, 227
Micromechanical modelling
microstructural evolution and micromechanical modelling of deformation of a whisker-reinforced metal–matrix composite, 49
Molecular dynamics
molecular dynamics study of a bicrystal at elevated temperatures, 15

Nickel
development of nickel aluminide matrix composites, 81

Oxygen
behavior of interface in alumina/glass composite, 269

Particle distribution
effects of matrix microstructure and particle distribution on fracture of an aluminum metal matrix composite, 241

Reaction bonding
ceramic–ceramic composites with reaction bonded matrices, 117
Reinforcement
dispersion processing of creep resistant whisker-reinforced ceramic-matrix composites, 127
dynamic compressive fracture in fiber-reinforced ceramic matrix composites, 261
mechanical performance of fiber-reinforced ceramic matrix composites, 227
microstructural evolution and micromechanical modelling of deformation of a whisker-reinforced metal–matrix composite, 49

© Elsevier Sequoia/Printed in The Netherlands

processing and properties of metal matrix composites containing discontinuous reinforcement, 93
theoretical and experimental analysis of the toughening behavior of whisker reinforcement in ceramic matrix composites, 257

Silicon
influence of hydrostatic pressure on the ductility of Al-SiC composites, 63
microstructural aspects of aluminium–silicon carbon particulate composites produced by a casting method, 73
Solute segregation
embrittlement of interfaces by solute segregation, 23
Stress
stress concentration along interfaces of elastic–plastic thin films, 169
Structure
structure and chemistry of metal/ceramic interfaces, 187

Thin films
stress concentration along interfaces of elastic–plastic thin films, 169
Titanium
interfacial interactions in titanium-based metal matrix composites, 217
Toughening
theoretical and experimental analysis of the toughening behavior of whisker reinforcement in ceramic matrix composites, 257
Toughness
intrinsic toughness of interfaces, 41
sandwich test specimens for measuring interface crack toughness, 135